frontiers | Research Topics

Current insights in drylands

Edited by
Niall Patrick Hanan and Lindsay Beaumont Hutley

Published in
Frontiers in Environmental Science

ISSN 1664-8714
ISBN 978-2-8325-4696-3
DOI 10.3389/978-2-8325-4696-3

About Frontiers

Frontiers is more than just an open access publisher of scholarly articles: it is a pioneering approach to the world of academia, radically improving the way scholarly research is managed. The grand vision of Frontiers is a world where all people have an equal opportunity to seek, share and generate knowledge. Frontiers provides immediate and permanent online open access to all its publications, but this alone is not enough to realize our grand goals.

Frontiers journal series

The Frontiers journal series is a multi-tier and interdisciplinary set of open-access, online journals, promising a paradigm shift from the current review, selection and dissemination processes in academic publishing. All Frontiers journals are driven by researchers for researchers; therefore, they constitute a service to the scholarly community. At the same time, the *Frontiers journal series* operates on a revolutionary invention, the tiered publishing system, initially addressing specific communities of scholars, and gradually climbing up to broader public understanding, thus serving the interests of the lay society, too.

Dedication to quality

Each Frontiers article is a landmark of the highest quality, thanks to genuinely collaborative interactions between authors and review editors, who include some of the world's best academicians. Research must be certified by peers before entering a stream of knowledge that may eventually reach the public - and shape society; therefore, Frontiers only applies the most rigorous and unbiased reviews. Frontiers revolutionizes research publishing by freely delivering the most outstanding research, evaluated with no bias from both the academic and social point of view. By applying the most advanced information technologies, Frontiers is catapulting scholarly publishing into a new generation.

What are Frontiers Research Topics?

Frontiers Research Topics are very popular trademarks of the *Frontiers journals series*: they are collections of at least ten articles, all centered on a particular subject. With their unique mix of varied contributions from Original Research to Review Articles, Frontiers Research Topics unify the most influential researchers, the latest key findings and historical advances in a hot research area.

Find out more on how to host your own Frontiers Research Topic or contribute to one as an author by contacting the Frontiers editorial office: frontiersin.org/about/contact

Current insights in drylands

Topic editors

Niall Patrick Hanan — New Mexico State University, United States

Lindsay Beaumont Hutley — Charles Darwin University, Australia

Citation

Hanan, N. P., Hutley, L. B., eds. (2024). *Current insights in drylands*. Lausanne: Frontiers Media SA. doi: 10.3389/978-2-8325-4696-3

Table of contents

Earth system models for drylands

Dryland cultural services

frontiers | Frontiers in Environmental Science

TYPE Editorial
PUBLISHED 06 March 2024
DOI 10.3389/fenvs.2024.1391211

Editorial: Current insights in drylands

N. P. Hanan[1,2]* and L. B. Hutley[3]

[1]Plant and Environmental Science Department, New Mexico State University, Las Cruces, NM, United States, [2]Jornada Basin Long-Term Ecological Research (JRN-LTER), Las Cruces, NM, United States, [3]Research Institute for the Environment and Livelihoods, Faculty of Science and Technology, Charles Darwin University, Darwin, NT, Australia

KEYWORDS

drylands, soil processes, remote sensing, ecosystem modeling, desert, savanna

OPEN ACCESS

EDITED AND REVIEWED BY
Martin Siegert,
University of Exeter, United Kingdom

*CORRESPONDENCE
N. P. Hanan,
nhanan@nmsu.edu

RECEIVED 25 February 2024
ACCEPTED 29 February 2024
PUBLISHED 06 March 2024

CITATION
Hanan NP and Hutley LB (2024), Editorial: Current insights in drylands.
Front. Environ. Sci. 12:1391211.
doi: 10.3389/fenvs.2024.1391211

Editorial on the Research Topic
Current insights in drylands

Introduction

Drylands occur on all continents and, despite their inherently low productivity, they provide critical services to approximately 2 billion people worldwide via livestock grazing, dryland cropping, fuelwood, timber and other ecosystem functions (Maestre et al., 2021). Drylands feature a diversity of plant forms and functional types, in response to temporal variability of resource availability, primarily driven by infrequent rainfall. This diversity supported coevolution of distinctive wild herbivore communities, many of which have been lost to the combination of agricultural conversion and livestock grazing. In other regions, dryland biodiversity is threatened by woody encroachment occurring in drylands of the Americas, Australia, Africa and Europe, driven by aridification, overgrazing, changes in fire regime and CO_2 fertilization (Archer et al., 2001; Walker et al., 2021); factors which in many cases favor woody life forms over herbaceous vegetation. Such changes in vegetation structure have profound and cascading impacts on dryland biota, soil carbon, water and nutrient cycles, productivity and, ultimately, human livelihoods.

Being water limited, climate change related changes in precipitation amount and timing will have significant consequences for drylands. However, model predictions for rainfall patterns in many drylands are uncertain on the magnitude and even the direction of long-term trends, while future warming trends and thus increasing aridity appears inevitable (Hanan et al., 2021; Masson-Delmotte et al., 2021). Furthermore, certain ecological patterns and processes are amplified in drylands, including the importance of spatial heterogeneity and temporal pulse responses in vegetation, biocrust and bare soil cover. These characteristics create spatial and temporal variability in the physical, biogeochemical and biotic drivers and responses of drylands to changing climate, anthropogenic and natural disturbances, that are both poorly understood and hard to predict. What is clear, however, is that drylands are experiencing concurrent change from population growth, land use pressure and climate change, requiring a continued focus on the current and future dynamics and ecosystem services in these unique landscapes.

The *Current Insights in Drylands* Research Topic was intended to contribute new insight and fill knowledge gaps in dryland ecosystem function. It consists of 11 papers that

address emerging themes across five continents. These include the multi-functional role of dryland soils and importance of connectivity and lateral transport of water and nutrients in drylands in mediating water and nutrient pulses, challenges for remote sensing of vegetation structure and productivity in dryland regions, and the related challenges in representing drylands in global Earth system models.

Soil water, nutrients and connectivity in drylands

Wilcox et al. provide an important conceptual analysis of the impacts of woody encroachment on the ecohydrological connectivity of drylands. The concept of connectivity for both wind and water has long been a theme in dryland ecology (Schlesinger et al., 1990; Okin et al., 2018), altering the extent to which materials (water, sediments, nutrient and propagules) are redistributed in the landscape and creating spatial heterogeneity. Wilcox et al. review six case studies from drylands of the Southern Great Plains and Southwest regions of the United States to provide a conceptual model for how woody plant encroachment modifies connectivity in predictable ways and changes partitioning of rainfall between evapotranspiration, runoff, streamflow and groundwater recharge.

Connectivity processes related to nutrient redistribution were also the theme explored by Zhang et al. who examined how "fertile islands" are associated with woody plants in drylands of northwestern China. They compared nutrient distributions in soils under canopies and in bare soil interspaces, finding clear evidence of "islands of fertility" (Schlesinger et al., 1996), and highlighting the influence of woody plants for ecosystem function in drylands.

Chen et al. provide a baseline study of soil carbon and nutrient stocks of Kyrgyzstan, a major dryland region of Eurasia. Such data are critical for constraining terrestrial ecosystem models simulating carbon fluxes in this region. The study also addressed soil multifunctionality, including an index of microbial community structure linked to soil functions (i.e., enzyme patterns, C and N cycling), providing data to better predict the effects of environmental changes on ecosystem multifunctionality, sustainable use and management of dryland soils to ultimately reduce land productivity decline with impacts on climate change.

Shaukat et al. use a novel approach for land suitability assessments based on electromagnetic induction (EMI) to assess soil conditions for high-value nectar producing shrubs (*Leptospermum nitens*) used for honey production in semi-arid Western Australia. EMI measurements were highly correlated with true electrical conductivities of soils at different depth, providing new opportunities to map 3-dimensional soil properties. Importantly, for this application, *Leptospermum* growth and survival were strongly correlated with soil properties, providing an effective method for site assessments prior to planting.

Our ability to predict trends in dryland precipitation amounts remains relatively poor, but changes in rainfall regimes (timing and size of events) are consistently predicted (Masson-Delmotte et al., 2021). Roby et al. provide an experimental analysis of rainfall redistribution between few large events versus many small events on soil CO_2 efflux in a semi-arid grassland, with fewer, larger rainfall events causing reduced seasonal soil CO_2 efflux. Dryland biota have evolved and adapted to pulse driven resource availability; however, the frequency of extreme events is now increasing, and such mechanistic studies are critical to assess impacts of climate change on soil carbon and nutrient cycling and retention.

Remote sensing of dryland processes

Our ability to measure vegetation structure at regional and continental scales, and detect changes associated with global change drivers, is critical for management and modeling of drylands state and transitions. Drylands feature high levels of both vertical and horizontal spatial heterogeneity, with highly variable density, height and cover of trees and shrubs, overlying herbaceous communities with varying bare soil exposure and highly seasonal dynamics. In particular, contrasting woody and herbaceous plant functional types require appropriately calibrated remote sensing and mapping tools to separate these key components of dryland plant communities. This Research Topic features two papers addressing remote sensing of low density and low stature woody vegetation in drylands, and a third paper focused on the separation of herbaceous biomass as a critical measurement of forage availability in grazed drylands.

Recent research has demonstrated an exciting new Frontier in mapping individual tree canopies over very large areas using commercial very high resolution (<1 m) satellite imagery (Brandt et al., 2020; Hanan and Anchang, 2020; Tucker et al., 2023). In this Research Topic, Marzolf et al. and Kirchhoff et al. use recently released HEXAGON KH-9 and CORONA high resolution (2–3 m) surveillance imagery taken during the 1960-1970s to map and detect change in individual trees and tree cover in dry Argan woodlands of Morocco. They benchmarked the historical imagery with recent WorldView images, and found that HEXAGON images could be used to map individual trees, although smaller trees and shrubs are generally underestimated. They concluded that the HEXAGON images could provide a powerful tool to assess historic tree population change in drylands, especially given that a further 670,000 HEXAGON images worldwide will soon be available, providing unprecedented opportunities for 50-year time-series analysis.

Capturing dynamics of the herbaceous layer in drylands is as important as mapping trees, as grasses support grazing animals and provide food and livelihood security for pastoral and agropastoral societies reliant on livestock. Lo et al. developed 6 metrics derived from satellite data to monitor dry season forage in the Sahel. Dry season biomass assessment is significant as the dry season can be the bottleneck for livestock growth and survival in the Sahel and other grazing lands. Thus, dryland-specific remote sensing is critical to support the monitoring of forage resources for livestock and wildlife in the Sahel and many dryland regions dependent on extensive livestock grazing.

Earth system models for drylands

Drylands cover ~40% of the land surface, and while net primary production and carbon uptake tend to be small, the significant areal

extent of drylands, coupled with strong interannual variability in rainfall and fire, means they play an outsized role in the interannual variability of global atmospheric CO_2 (Poulter et al., 2014; Ahlstrohm et al., 2015). He et al. provide estimates of the uncertainties of gross primary productivity in Chinese semi-arid grasslands based on terrestrial ecosystem models and remote sensing. This study demonstrated the need for uncertainty analysis when GPP is applied to spatio-temporal analysis, and suggested that when comparing and assessing carbon balance, multiple source data sets should be used to avoid misleading conclusions due to uncertainty.

Similarly, Fawcett et al. compared spatial and temporal patterns of MODIS derived GPP and biomass with the TRENDY ensemble of land surface models (LSMs). The models were able to reproduce spatial patterns of dryland productivity, and inter-annual variability, but long-term trends were not well resolved. Spatial patterns of above ground biomass were also not well simulated. They concluded that LSMs may not be well calibrated for dryland environments, likely due to model failures to adequately account for impacts of low plant available moisture, impacts of fire and carbon loss from photodegradation, all processes that drive dryland carbon dynamics. As such, long term predictions of CO_2 fertilization, woody plant encroachment and resultant changes in soil and vegetation carbon sinks remain highly uncertain. Clearly LSMs need continued improvement as at present such model ensembles appear to be poorly constrained for dryland ecosystems.

Dryland ecosystem and cultural services

The papers in this Research Topic highlight some of the recent successes and remaining challenges in understanding dryland processes plus monitoring and modeling change in dryland function and critical physical and biological ecosystem services. The issue discusses both the power and limitations of Earth system models when applied to drylands, as well as remote sensing approaches ideally suited to drylands. Methods suitable for assessing both tree and grass components were recommended: remote sensing-based models to monitor dry season forage, through to the use of historic, high resolution surveillance imagery for high precision detection of tree cover change at multi-decadal scales. Such tools will be enormously powerful given the ever increasing resolution of satellite imagery to track loss and/or gain in woody and herbaceous cover. Woody encroachment was also highlighted as a key process, with wide ranging consequences for ecosystem services such as available moisture, forage productivity and ultimately, livelihoods.

Papers were grouped around three biophysical themes (soil water, nutrients and connectivity, remote sensing of dryland processes, Earth system models for drylands), but global drylands must also be recognized as centers of human development and civilizations over millennia. The paper by Albalawneh et al. highlighted this perspective, using social science survey methodologies and GIS to assess and map cultural ecosystem services (CES) provided by drylands in Jordan. They show the extent to which local communities value drylands as resources well beyond conventional ecosystem services (relating to food, fiber and income production), arguing that CES should be incorporated into development and conservation planning. Albalawneh et al. highlight that drylands are multifunctional landscapes, valued by humans not only for food and fibre production, but also because of their significant social, cultural and spiritual importance.

Author contributions

NH: Conceptualization, Writing–original draft, Writing–review and editing. LH: Conceptualization, Writing–original draft, Writing–review and editing.

Funding

The author(s) declare that financial support was received for the research, authorship, and/or publication of this article. This work was supported by funding from the National Science Foundation to New Mexico State University for the Jornada Basin Long-Term Ecological Research Program (DEB 2025166).

Conflict of interest

The authors declare that the research was conducted in the absence of any commercial or financial relationships that could be construed as a potential conflict of interest.

The author(s) declared that they were an editorial board member of Frontiers, at the time of submission. This had no impact on the peer review process and the final decision.

Publisher's note

References

Ahlström, A., Raupach, M. R., Schurgers, G., Smith, B., Arneth, A., Jung, M., et al. (2015). The dominant role of semi-arid ecosystems in the trend and variability of the land CO_2 sink. *Science* 348, 895–899. doi:10.1126/science.aaa1668

Archer, S., Boutton, T. W., and Hibbard, K. A. (2001). "Trees in grasslands: biogeochemical consequences of woody plant expansion," in *Global biogeochemical cycles in the climate system*. Editors M. Schulze, S. Heimann, E. Harrison, J. Holland, I. Lloyd, C. Prentice, et al. (San Diego, California, USA: Academic Press), 115–130.

Brandt, M., Tucker, C. J., Kariryaa, A., Rasmussen, K., Abel, C., Small, J., et al. (2020). An unexpectedly large count of trees in the West African Sahara and Sahel. *Nature* 587, 78–82. doi:10.1038/s41586-020-2824-5

Hanan, N. P., and Anchang, J. Y. (2020). Satellites could soon map every tree on Earth. *Nature* 587, 42–43.

Hanan, N. P., Milne, E., Aynekulu, E., Yu, Q., and Anchang, J. Y. (2021). A role for drylands in a carbon neutral world? *Front. Environ. Sci. Drylands* 9, 786087. doi:10.3389/fenvs.2021.786087

Maestre, F. T., Benito, B. M., Berdugo, M., Concostrina-Zubiri, L., Delgado-Baquerizo, M., Eldridge, D. J., et al. (2021). Biogeography of global drylands. *New Phytol.* 231, 540–558. doi:10.1111/nph.17395

Masson-Delmotte, V., Zhai, P., Pirani, A., Connors, S. L., Péan, C., Berger, S., et al. (2021). Climate change 2021: the physical science basis. *Contribution Work. group I sixth Assess. Rep. Intergov. panel Clim. change* 2.

Okin, G. S., Sala, O. E., Vivoni, E. R., Zhang, J., and Bhattachan, A. (2018). The interactive role of wind and water in functioning of drylands: what does the future hold? *Bioscience* 68, 670–677.

Poulter, B., Frank, D., Ciais, P., Myneni, R. B., Andela, N., Bi, J., et al. (2014). Contribution of semi-arid ecosystems to interannual variability of the global carbon cycle. *Nature* 509, 600–603. doi:10.1038/nature13376

Schlesinger, W. H., Raikes, J. A., Hartley, A. E., and Cross, A. F. (1996). On the spatial pattern of soil nutrients in desert ecosystems. *Ecology* 77, 364–374.

Schlesinger, W. H., Reynolds, J. F., Cunningham, G. L., Huenneke, L. F., Jarrell, W. M., Virginia, R. A., et al. (1990). Biological feedbacks in global desertification. *Science* 247, 1043–1048.

Tucker, C., Brandt, M., Hiernaux, P., Kariryaa, A., Rasmussen, K., Small, J., et al. (2023). Sub-continental-scale carbon stocks of individual trees in African drylands. *Nature* 615, 80–86. doi:10.1038/s41586-022-05653-6

Walker, A. P., De Kauwe, M. G., Bastos, A., Belmecheri, S., Georgiou, K., Keeling, R. F., et al. (2021). Integrating the evidence for a terrestrial carbon sink caused by increasing atmospheric CO_2. *New Phytol.* 229, 2413–2445. doi:10.1111/nph.16866

frontiers | Frontiers in Environmental Science

TYPE Conceptual Analysis
PUBLISHED 28 September 2022
DOI 10.3389/fenvs.2022.934535

OPEN ACCESS

EDITED BY
Lindsay Beaumont Hutley,
Charles Darwin University, Australia

REVIEWED BY
Mohd Yawar Ali Khan,
King Abdulaziz University, Saudi Arabia
Mandy Slate,
University of Colorado Boulder,
United States

*CORRESPONDENCE
Bradford P. Wilcox,
bwilcox@tamu.edu

SPECIALTY SECTION
This article was submitted to Drylands, a section of the journal Frontiers in Environmental Science

RECEIVED 02 May 2022
ACCEPTED 31 August 2022
PUBLISHED 28 September 2022

CITATION
Wilcox BP, Basant S, Olariu H and Leite PAM (2022), Ecohydrological connectivity: A unifying framework for understanding how woody plant encroachment alters the water cycle in drylands.
Front. Environ. Sci. 10:934535.
doi: 10.3389/fenvs.2022.934535

Ecohydrological connectivity: A unifying framework for understanding how woody plant encroachment alters the water cycle in drylands

Bradford P. Wilcox*, Shishir Basant, Horia Olariu and Pedro A. M. Leite

Department of Ecology and Conservation Biology, Texas A&M University, College Station, TX, United States

Grasslands and savannas in drylands have been and continue to be converted to woodlands through a phenomenon often described as woody plant encroachment. This conversion has profound implications for the ecosystem services that these landscapes provide, including water. In this paper, using examples from six case studies across drylands in the Great Plains and Chihuahuan Desert regions of the United States, we explore the ecohydrological changes that occurred following woody plant encroachment (WPE). In all cases, the increase in woody plant cover brought about modifications in connectivity, which led to profound ecohydrological changes at both the patch and landscape scales. At the wet end of the dryland spectrum (subhumid climates), increases in evapotranspiration following WPE led to reduced streamflows and groundwater recharge. In drier regions, woody plant encroachment did not alter evapotranspiration appreciably but did significantly alter hydrological connectivity because of changes to soil infiltrability. In semiarid climates where rainfall is sufficient to maintain cover in intercanopy areas concurrent with woody plant encroachment (*thicketization*), overall soil infiltrability was increased—translating to either decreased streamflows or increased streamflows, depending on soils and geology. In the driest landscapes, woody plant encroachment led to *xerification*, whereby intercanopy areas became bare and highly interconnected, resulting in higher surface runoff and, ultimately, higher groundwater recharge because of transmission losses in stream channels. On the basis of our review of the studies' findings, we argue that the concept of eco*hydrological connectivity* provides a unifying framework for understanding these different outcomes.

KEYWORDS

ecohydrology, rangelands, runoff, groundwater recharge, dryland

Introduction

Grasslands and savannas represent important types of vegetation cover within drylands globally—particularly those under semiarid and subhumid climate regimes. Prior to the advent of mechanized agriculture, grasslands and savannas accounted for close to 40% of the Earth's surface. Today, these landscapes cover only a little over 20% (Mishra and Young, 2020) and are considered an imperiled biome, threatened by agricultural conversion, overgrazing, altered fire regimes, and invasive plants (Wilcox et al., 2022). A prominent example of these proximate threats is *woody plant encroachment* (WPE)—the process by which grasslands and savannas are converted to woodlands or more densely wooded savannas.

The proliferation of trees and shrubs on rangelands is one of the most striking land-cover transformations of the last 100–200 years, and represents one of the gravest threats to grassland biomes (Sala and Maestre, 2014; Veldman et al., 2015). Much of this transformation has been driven by unsustainable livestock production and overgrazing. In the United States, especially during the late 1800s, overgrazing played a key role in disrupting longstanding fire regimes, which set the stage for the expansion of woody plants (Wilcox et al., 2018). Similar transitions took place in Australia and southern Africa with the arrival of Anglo-European settlers and their livestock (Archer et al., 2017). Although grazing management has improved in all these regions, many drylands remain chronically overgrazed, leading to vegetation regime shifts (Hoover et al., 2020). In addition to overgrazing, other factors contributing to WPE include the dissemination of woody-plant seeds by livestock, eradication of native browsers, increased atmospheric CO_2 concentrations, and a warming climate (Archer et al., 2017).

The world's grasslands and savannas are critically important for livestock production and the pastoral societies that depend on them (Yahdjian et al., 2015; Mishra and Young, 2020). Almost without exception, forage production will decline as woody plants increase (Archer et al., 2017)—as will, in many cases, species richness and biodiversity, especially those species endemic to more open ecosystems (Ratajczak et al., 2012; Archer and Predick, 2014). It is important to note that WPE is not necessarily synonymous with landscape degradation and/or desertification (Eldridge et al., 2011; Bestelmeyer et al., 2018). This is primarily true in the case of subhumid or relatively wet semiarid climates in which both canopy and intercanopy vegetation cover remains high year round (Basant et al., 2020). In some instances, WPE may even slow or reverse degradation or desertification that has already begun (Maestre et al., 2009). Woody plant encroachment that does not increase the extent of bare ground—either because the intercanopy patches remain vegetated with herbaceous plants and/or woody vegetation forms dense thickets—has been described as *thicketization* (Schreiner-McGraw et al., 2020). In contrast, WPE that does increase the extent of bare ground, eventuating in the degradation and heightened soil erosion described as *xerification,* is seen in more arid climates (Li et al., 2007). Heavy grazing by livestock can extend the amount of terrain affected by xerification (Webb et al., 2014).

In addition to causing declines in forage production and biodiversity, WPE can alter biogeochemical, energy, and water cycles in important but not always well-understood ways. In regions having annual rainfall exceeding 400 mm, above-ground carbon storage will generally increase with WPE. However, changes in below-ground carbon are less certain and are often unpredictable (Archer et al., 2017). With respect to climate, Wang et al. (2021) report that WPE can lead to subtle but important changes in temperatures in the Southern Great Plains. They found that daytime temperatures were lower and nighttime temperatures were higher following WPE.

With respect to the water cycle, WPE has the potential to affect primarily two contrasting processes: evapotranspiration and soil infiltrability. As the number and density of woody plants increase, interception and transpiration rates will rise, translating to higher evapotranspiration. At the same time, as woody cover increases, soil infiltrability will be altered through root action and the addition of organic matter (Leite et al., 2020). Historically, most scientific investigations of the mechanisms by which woody plants may alter groundwater recharge or streamflow in drylands have focused on evapotranspiration as the key mechanism (Bosch and Hewlett, 1982). This is true even of frameworks developed quite recently, largely overlooking the importance of changes to soil infiltrability (Huxman et al., 2005; Wilcox et al., 2006). Such frameworks emphasize how WPE may lead to higher evaporative losses in drylands when rainfall is greater than potential evapotranspiration for a period of time. Examples include Mediterranean climate regimes, where rainfall is "out of phase" with potential evapotranspiration; and areas where groundwater levels are shallow enough to be accessed by woody plants.

In the past several years, a number of studies have drawn attention to the fact that changes in soil infiltrability are important as well (Ilstedt et al., 2016; Basant et al., 2020; Leite et al., 2020). In general, infiltrability is higher under the canopy of woody plants than in the intercanopy, as woody roots form a network of macropores that enable preferential water flow, often promoting deep water percolation (Devitt and Smith, 2002; Tobella et al., 2014). In addition, through their canopies and through the accumulation of litter, woody plants provide mechanical protection against soil crusting from solar radiation and raindrop impact. By adding organic matter and promoting microbial activity, leaf litter acts as a soil amendment, enhancing soil structure and aggregate stability (Bochet et al., 1999). It also provides ideal conditions for soil fauna that—like woody roots—improve macroporosity and infiltrability (Marquart et al., 2020). Some woody plants have a strong legacy effect on soils. High infiltrability under canopies can

last long after the plants have died or been removed (Cipriotti and Aguiar, 2017; Williams et al., 2019) and can even increase over time as roots decay (Wu et al., 2021).

As described in this paper, the two phenomena—evapotranspiration and soil infiltration—can have diametrically opposing influences on groundwater recharge and streamflows in drylands. For example, in regions where WPE leads to higher evapotranspiration, groundwater recharge and/or streamflows will decline as woody plant cover increases (Zou et al., 2016). However, for many drylands potential evapotranspiration (PET) greatly exceeds rainfall and there is relatively little "surplus water." Thus, any changes in total evapotranspiration caused by WPE will be quite small. Instead, in these landscapes WPE will often lead to higher soil infiltrability, which—depending on soil and geologic conditions—can either reduce streamflows and groundwater recharge (Wilcox et al., 2008a), increase streamflows and groundwater recharge (Wilcox and Huang, 2010), or have minimal effect (Berg et al., 2016).

Although at first glance these outcomes appear so variable as to defy a unifying explanation, recent research suggests that such an explanation of the influences of WPE on the water cycle (and how those influences vary with scale) is provided by the concept of *ecohydrological connectivity*. As support for this assertion we offer the findings of six case studies carried out in the Southern Great Plains and Southwest regions of the United States and representing a climatic gradient that stretches from subhumid to arid. Each of these studies showed that WPE has altered groundwater recharge and/or streamflows in significant ways.

Connectivity as a unifying concept

Connectivity is broadly defined as the extent to which a system facilitates the transfer of matter and energy within itself (Keesstra et al., 2020). In the field of Earth and environmental sciences, this concept has been increasingly applied as an organizing principle for understanding environmental change and interactions across spatial scales (Peters et al., 2008; Okin et al., 2015; Iwaniec et al., 2021). At the same time, even within the hydrological sciences multiple definitions of the term exist (Bracken et al., 2013; Wohl, 2017). With respect to drylands, Okin et al. (2015) define connectivity as the extent to which materials can move, spread, or be redistributed from one place to another within the landscape—a definition similar to those proposed by others (Tetzlaff et al., 2007; Wohl, 2017). An essential characteristic of connectivity is that it functions spatially in multiple directions, including longitudinal (river channel), lateral (hillslope), and vertical (surface–subsurface) (Keesstra et al., 2018).

The connectivity concept is increasingly being employed by hydrologists and geomorphologists to better understand and describe water and sediment fluxes (Bracken et al., 2013; Bracken et al., 2015; Keesstra et al., 2018). It has been usefully applied by hydrologists in many environments, including wetlands (Cohen et al., 2016; Lane et al., 2018; Leibowitz et al., 2018), river systems (Castello et al., 2013; Jaeger et al., 2014; Goodrich et al., 2018), and arctic regions (Bring et al., 2016; Walvoord and Kurylyk, 2016)—at continental and even global scales (Peters et al., 2008; Good et al., 2015)—but it has been especially useful in clarifying ecosystem function and interaction in drylands (Turnbull and Wainwright, 2019; Saco et al., 2020; Calvo-Cases et al., 2021; Johnson et al., 2021). Okin et al. (2015) argue that connectivity serves as an "organizing principle to understand dryland structure and function at scales from individual plants to entire landscapes." It has proved to be particularly valuable for understanding cross-scale interactions (Peters et al., 2006). For example, as discussed below, changes in infiltrability at the patch scale can have important implications for water fluxes at the landscape and even regional scales.

Depending on the context and the application, various modifiers have been applied to the basic term: *hydrological* connectivity (Bracken et al., 2013), *ecohydrological* connectivity (D'Odorico et al., 2010; Basant et al., 2020), *eco-geomorphological* connectivity (Calvo-Cases et al., 2021), *stream* connectivity (Goodrich et al., 2018), *sediment* connectivity (Bracken et al., 2015), etc. We believe that the term *ecohydrological connectivity* is appropriate when exploring how vegetation influences the water cycle, because of the intimate coupling between biota and the extent of connectedness of the landscape. As noted by Keesstra et al. (2018), biota can promote or impede connectivity. Plants, for example, reduce raindrop impact, modify soils through root activity and the addition of litter, and promote soil infiltrability. In drylands, the patchy nature of vegetation determines connectivity, which in turn controls source–sink dynamics—a critical factor for ecosystem functionality (Reid et al., 1999; Wilcox et al., 2003; Ludwig et al., 2005).

Case studies along a climate gradient

Using examples from six case studies carried out in the United States (Figure 1), we explore the ecohydrological changes that occur concomitant with WPE. Although these changes vary with location, depending on the particular conditions of climate, soils, geology, and topography, we demonstrate that the concept of *ecohydrological connectivity* provides a unifying framework for understanding and even predicting landscape-level ecohydrological responses to WPE.

These case studies, drawn from the Southern Great Plains and Southwest regions of the United States, span the climate spectrum of drylands from subhumid to arid (Figures 2, 3). These landscapes have been dramatically altered by WPE, beginning in the late 1800s—largely in response to a combination of overgrazing, droughts, and altered fire regimes (Bestelmeyer et al., 2018; Wilcox et al., 2018; Wilcox et al., 2022). Each of

FIGURE 1
The six ecoregions represented by the case studies on which our evaluation is based: **(A)**. Case Study 1--Cross Timbers of Oklahoma; **(B)**. Case Study 2--Post Oak Savanna in Texas; **(C)**. Case Study 3—South Texas Shrublands; **(D)**. Case Study 4—Edwards Plateau of Texas; **(E)**. Case Study 5—Rolling Plains of Texas; and **(F)**. Case Study 6—Chihuahuan Desert of New Mexico.

the six sites has been the focus of intensive studies addressing the ecohydrological ramifications of WPE. The case studies are discussed below roughly in the order of annual rainfall (from high to low).

Case Study 1: Cross Timbers—Proliferation of Eastern Red Cedar.

Overview. The states of the Central Great Plains, including Nebraska, Kansas, and Oklahoma, form the epicenter of WPE in the United States (Barger et al., 2011), largely because of the proliferation of eastern red cedar (*Juniperus virginiana*). According to recent assessments, areas dominated by this species are expanding by about 8% a year—which amounts to about 40 km^2/year (Wang et al., 2017; Wang et al., 2018a). This expansion is especially pronounced in the Cross Timbers region of Oklahoma, a mosaic of upland deciduous forest, savanna, and tallgrass prairie that has been transformed by WPE. The climate is subhumid, with an average annual rainfall of around 900 mm and an aridity index (AI) of 0.5–0.6. Although the region is water limited for part of the year, it is on the wetter end of the "drylands" spectrum (Hoover et al., 2020) (Figure 2) and rainfall may exceed potential evapotranspiration during parts of the year (Figure 3).

Over the last several decades, an active research program within the Cross Timbers region has provided much of what we know concerning the ecohydrological implications of the proliferation of eastern red cedar in the Central Great Plains (Zou et al., 2018). In the past decade in particular, this research has provided detailed insights into the effects of encroachment of grasslands and savannas by eastern red cedar (Zou et al., 2014; Zou et al., 2015; Zou et al., 2016; Acharya et al., 2017a; Acharya et al., 2017b; Qiao et al., 2017). Once these areas have undergone encroachment, they essentially become closed-canopy woodlands dominated by eastern red cedar.

This body of work has brought to light such effects as drier soils, less groundwater recharge, and lower streamflow. For example, results from small catchments demonstrated that whereas runoff from grasslands was on average around 10% of precipitation, runoff from the juniper-encroached areas was

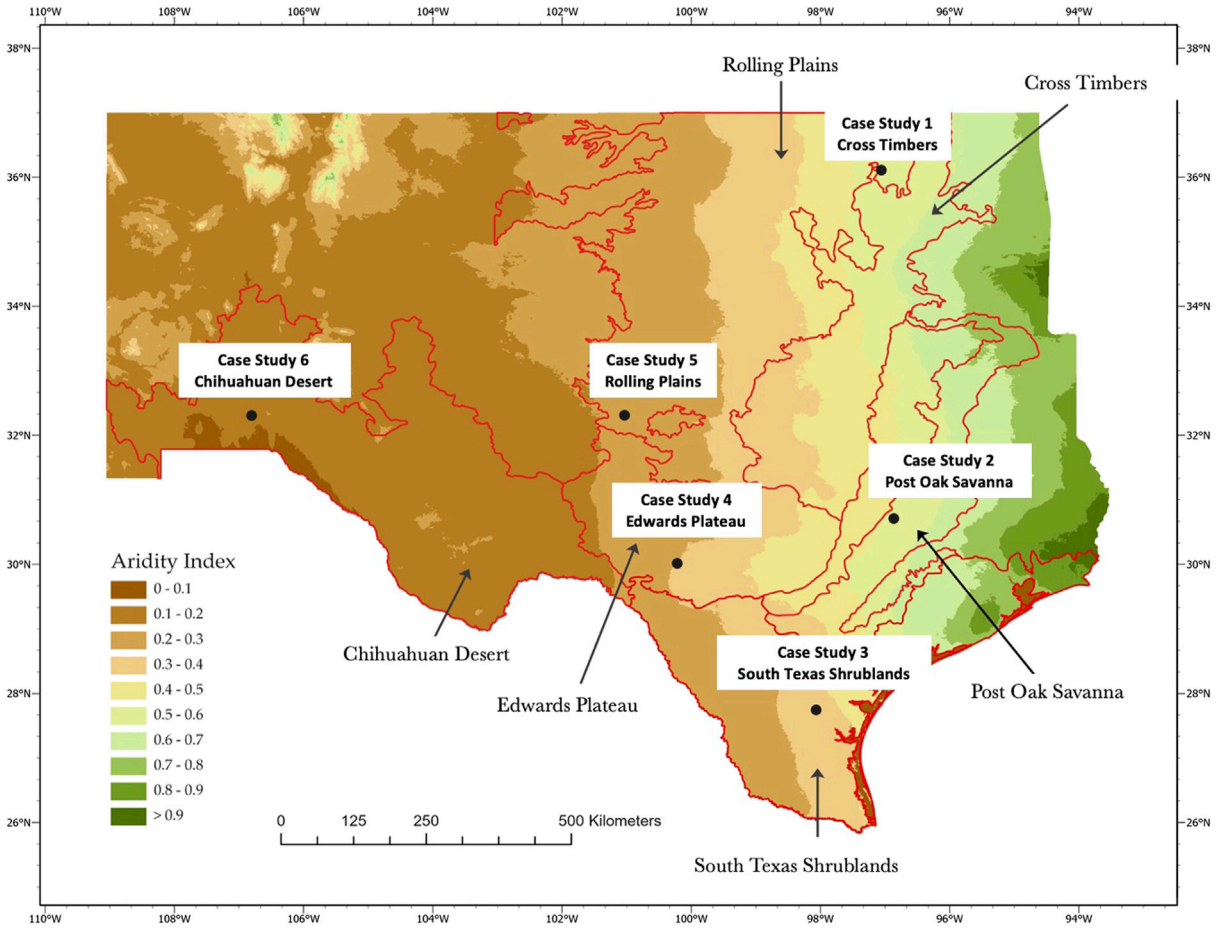

FIGURE 2
Locations of the six study sites within the ecoregions represented by the six case studies.

only 2%. In addition, runoff dynamics were altered: whereas runoff from grasslands was typically generated as saturation overland flow, that from the juniper-encroached sites was generated as infiltration-excess overland flow (Qiao et al., 2017). These ecohydrological changes are being driven largely by higher transpiration and interception losses in the juniper woodlands (Caterina et al., 2014; Wang et al., 2018b; Torquato et al., 2020). Modeling exercises and historical streamflow records suggest that these smaller-scale changes will result in reduced streamflows at larger scales (Zou et al., 2016; Starks and Moriasi, 2017). Interestingly, soil infiltrability is much higher following encroachment but it does not seem to confer any hydrological benefits. Soils are consistently drier in the wooded areas (Zou et al., 2014).

Underlying mechanisms, landscape-scale responses, and changes in connectivity. Woody plant encroachment in and adjacent to the Cross Timbers region of Oklahoma has resulted in higher losses of water via evapotranspiration—owing to increases in both interception and transpiration by trees. These changes have reduced lateral as well as vertical ecohydrological connectivity, with a consequent diminishing of both groundwater recharge and streamflow generation. Modeling work and field observations suggest that these changes translate to larger-scale reductions in streamflows.

Case Study 2: Post Oak Savanna—Thicketization.

Overview. The second case study comes from the Post Oak Savanna (POS) ecoregion, which extends from northeastern to southwestern Texas (Figure 2). Like other oak savannas in the United States, it has been radically transformed by cultivation and subsequent abandonment, altered fire regimes, urbanization, and fragmentation (Hoagland et al., 1999). These factors are, of course, interrelated; but the net result is a highly fractured patchwork of pasturelands, open savannas, and dense woodlands (Figure 1). Many of the remaining woodlands are now *thicketized*, with a dense understory of eastern red cedar and yaupon (*Ilex vomitoria*). True savannas composed of native grasses and a scattering of trees are rare in the POS. Where

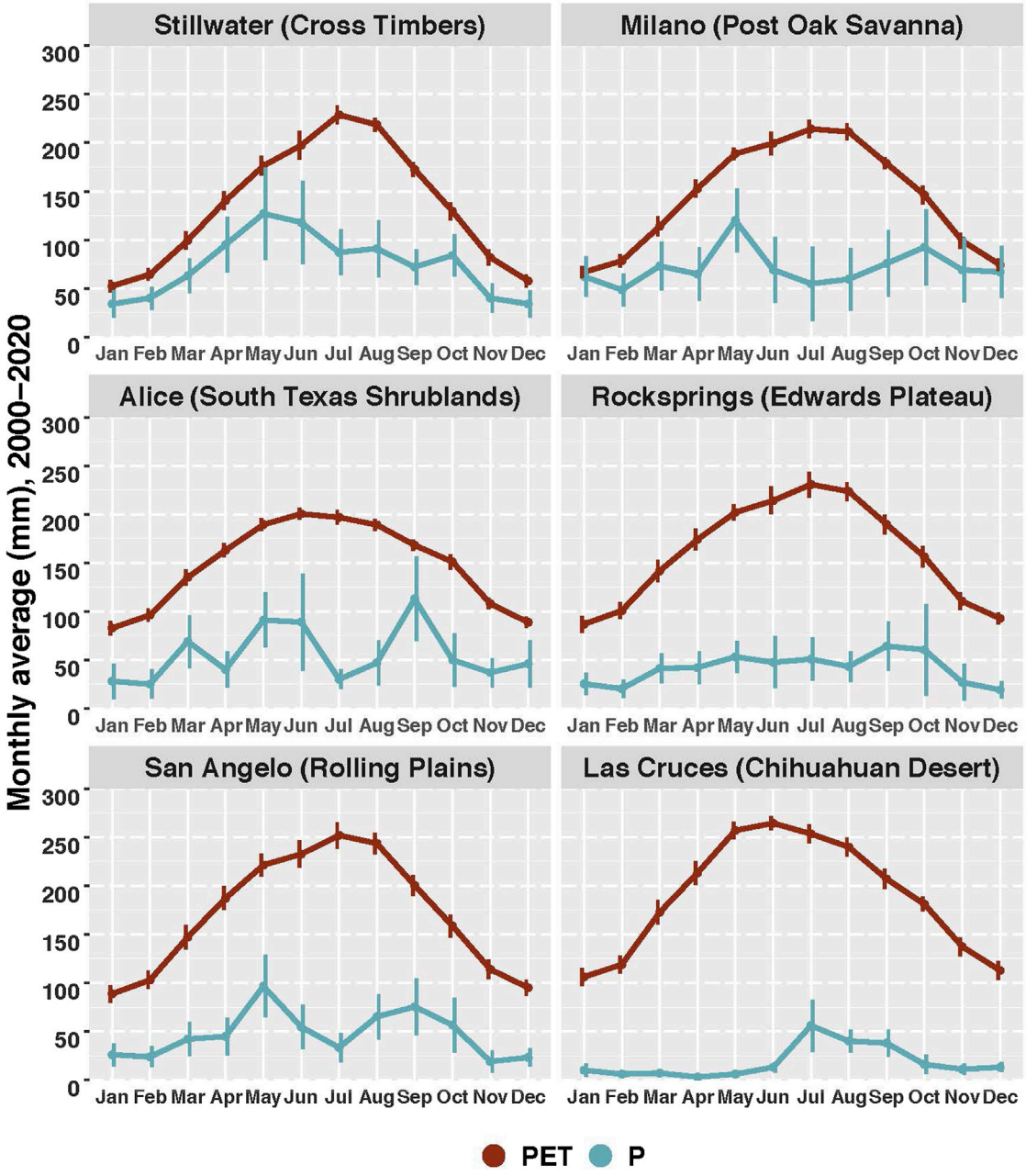

FIGURE 3
Mean values of potential evapotranspiraton (PET) and precipitation (P) for the period 2000–2020 in representative locations for each of the six case studies. PET was calculated using the MOD16 data set (Mu et al., 2011). Vertical bars represent 95% confidence interval.

they exist, the common grass species are big blue stem (*Andropogon gerardi*), indiangrass (*Sorghastrum nutans*), and switchgrass (*Panicum virgatum*). Pastures in the region consist mostly of introduced grasses such as bahaiagrass (*Paspalum notatum*) and bermudagrass (*Cynodon* spp.).

The other significant feature of the POS is that it overlies the recharge zone of the Carrizo–Wilcox aquifer, the third most important aquifer in Texas. Although relatively few field studies have evaluated the influence of vegetation on recharge rates in the Carrizo–Wilcox, modeling work by Keese et al. (2005) suggests that the influence is profound. In a comprehensive evaluation of groundwater recharge across the state of Texas, they found that in addition to soil and climate, vegetation had a marked influence on groundwater recharge rates. Their modeling experiments

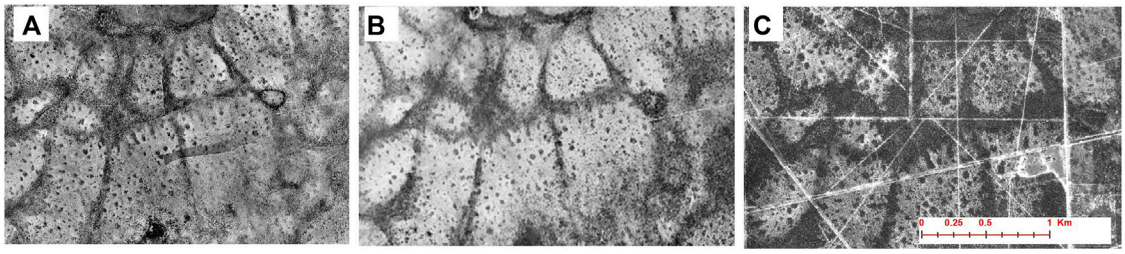

FIGURE 4
Aerial imagery showing changes over time in the study site for Case Study 3 (South Texas Shrublands) **(A)** 1930; **(B)** 1955; and **(C)** 1995. Note that woody vegetation is increasing with time and expanding from the drainage ways to the upland portions of the landscape.

showed that where the dominant vegetation consists of deep-rooted trees, recharge is significantly lower than where shallow-rooted grasses dominate.

The modeling predictions of Keese et al. (2005) have recently been verified by a field study close to Milano, Texas (Basant et al., 2020), where average annual rainfall is around 930 mm/yr and the AI is between 0.5 and 0.6 (Figure 2). This site, like the Cross Timbers region (Case Study 1), sits at the wet end of the dryland spectrum (Figures 2, 3). In this study, the chloride mass balance approach was used to compare long-term recharge rates in thicketized woodlands with those in open pastures. The results were striking: rates of deep drainage (which is equivalent to recharge) in the thicketized woodlands were only around 1 mm/yr—compared with 127 mm/yr in the open pastures. While these results need to be verified at more locations within the POS, they strongly suggest that thicketization dramatically reduces groundwater recharge.

Underlying mechanisms, landscape-scale responses, and changes in connectivity. The dramatic declines in groundwater recharge observed in thicketized woodlands are driven by the higher evapotranspiration rates that accompany WPE and bring about a reduction in vertical connectivity. It is likely that this loss of connectivity would also result in lowered baseflows in the streams that are partially fed by the Carrizo–Wilcox aquifer.

Case Study 3: South Texas Shrublands—Increased Soil Infiltrability.

Overview. Our next example comes from a subtropical savanna in the South Texas Shrublands (Figure 2), where average annual rainfall is around 660 mm/yr (Figure 3) and the AI is between 0.3 and 0.4 (Figure 2). Predominant woody plants include Texas persimmon (*Diospyros texana*) and mesquite (*Prosopis glandulosa*). Common grass species in the intercanopy areas include purple aristida (*Aristida purpurea*), Texas grama (*Bouteloua rigidiseta*), and love grass (*Eragrostis intermedia*). The region is distinct in that it consists of an upland savanna surrounded by a low-lying "drainage-woodlands" area—the result of heavy encroachment by woody plants—that exhibits a banded vegetation pattern (see Figure 4). Woody plants have subsequently expanded into the upland areas as well.

Aerial photographs and travel accounts (Humphrey, 1958) from the early 20th century indicate that the two landforms were even more distinct in the past (Figure 4), when WPE was taking place mostly in the drainage-woodlands. Additional evidence confirming this early pattern of WPE was provided by Boutton et al. (1998), who found a greater accumulation of soil organic carbon as well as a higher mean age of woody plants in the drainage-woodlands than in the uplands. Additionally, on the basis of the mean residence time of ^{14}C and $\delta^{13}C$ in the soil organic carbon of the two landforms, Boutton et al. 1999) suggested that the process of WPE started around 150 years ago—roughly the time of the introduction of heavy grazing.

Basant et al. (2020), working at a location that had been ungrazed by domestic livestock for more than 40 years, tested the prevailing hypothesis that water from the uplands was subsidizing the drainage-woodlands. Over a 3-year period, they monitored runoff from large runoff plots on the uplands as well as soil water in both the uplands and the drainage-woodlands, and found that there was no overland flow from the uplands to the drainage areas.

In addition, when they measured soil infiltrability and compared it with that of an adjacent grazed area, they found much higher levels in the ungrazed study site—with the highest infiltrabilities occurring under the shrub clusters. Some 40 years ago, Weltz and Blackburn (1995) had monitored runoff over a 20-month period at the same site, from large (5 m × 7 m) plots. Their findings showed that at that time (soon after the removal of livestock), runoff was being generated from the upland areas; and that for rainfall events larger than 100 mm, runoff could be as high as 8% of rainfall. It is quite likely that 150 years ago, when the site was subjected to severe overgrazing, runoff from the uplands was much higher than it is today. On the basis of these findings, Basant et al. (2020) hypothesized that historical overgrazing amplified the runoff–runon process, resulting in significant subsidies of water from the uplands to the drainage areas. Then, the combination of relaxation of grazing pressure, increase in woody plants, and subsequent landscape recovery brought about the rise in soil infiltrability that made redistribution of water via surface runoff relatively rare.

It is likely that in addition to modifying soil infiltrability, woody plants have the effect of reducing groundwater recharge,

but only slightly and primarily in wet years. Weltz and Blackburn (1995) found that for a relatively wet year (890 mm), deep drainage in areas that had been cleared of woody plants was 22 mm—whereas in areas not cleared of woody plants, no deep drainage at all was measured. Similarly, Moore et al. (2012) found that long-term recharge was only slightly affected by changes in woody plant cover: in areas cleared of woody plants, annual recharge was around 2 mm/yr, compared with zero where woody plants were not cleared.

Underlying mechanisms, landscape-scale responses, and changes in connectivity. In this landscape, the combination of WPE and the recovery of herbaceous plants that followed the decline in grazing led to increases in soil infiltrability, which in turn dramatically reduced lateral connectivity—with the result that the amount of runoff able to reach the low-lying drainage areas declined steeply. Although WPE also led to slight increases in evapotranspiration and deep drainage, the effect of these increases on total groundwater recharge is small.

Case Study 4: Edwards Plateau—Increasing Groundwater Recharge in Semiarid Karst Landscapes.

Overview. In the Edwards Plateau region of central Texas, average annual rainfall ranges from around 450–800 mm and the AI ranges from 0.2 to 0.4 (Figure 2). In spite of its semiarid climate, the Edwards Plateau is home to numerous perennially flowing springs, streams, and rivers. It is also the source area for the prolific and regionally important Edwards Aquifer, a major source of water for a number of urban areas as well as local agriculture. The explanation for this ecohydrological paradox is the underlying karst geology, which facilitates rapid and abundant groundwater recharge (Wilcox et al., 2007; Wilcox et al., 2008b).

The Edwards Plateau has undergone radical vegetation change as a result of historic overgrazing and subsequent WPE (Figure 1). Beginning in the late 1800s, pristine grasslands were rapidly converted to degraded and overgrazed rangelands; then, with the gradual reduction in grazing pressure (and the general lack of fire), the landscape has transitioned to woodlands dominated by live oak (*Quercus fusiformis*), Ashe juniper (*Juniperus ashei*), and redberry juniper (*Juniperus pinchotii*). A variety of short and mid-height grasses are common in the intercanopy areas.

Recognizing that such large-scale and dramatic changes in vegetation likely have an influence on streamflows (Wilcox, 2007), Wilcox and Huang (2010) explored the extent to which streamflows have changed in the Edwards Plateau. They analyzed long-term trends in streamflow, using data from four of the region's major rivers. Using hydrograph separation techniques, they were able to determine the volumes of baseflows and stormflows—the logic being that while both baseflow and stormflow may be affected by changes in vegetation, the mechanisms by which they are affected are different. Baseflows will be affected by vegetation change that influences groundwater recharge, whereas stormflow will be affected by surface changes that influence overland flow.

Their findings were not only surprising but at first glance counterintuitive. Notwithstanding the prevailing view—in both lay and scientific circles—that woody plants were depleting spring flows, Wilcox and Huang (2010) found that baseflows had effectively doubled in the wake of WPE and overall recovery from overgrazing. It is in light of the known fact that vegetation (and woody plants in particular) enhance soil infiltrability that these results do make sense. For example, several studies have demonstrated that infiltrability under juniper trees is many times higher than in adjacent interspaces (Wilcox et al., 2008b; Leite et al., 2020).

Underlying mechanisms, landscape-scale responses, and changes in connectivity. In the Edwards Plateau region, the expansion of woody plant cover in combination with improved range condition has brought about an increase in soil infiltrability. In this case, even though the higher infiltrability has decreased lateral connectivity, at the same time—because of the high permeability of the karst substrate—it has substantially increased vertical connectivity. As a result, both groundwater recharge and baseflows in the streams and rivers have risen significantly.

Case Study 5: Rolling Plains of Texas—Diminishing Streamflows.

Overview. The North Concho River flows near the boundary between the Edwards Plateau and the Rolling Plains ecoregions in Texas—most of the river basin lying within the Rolling Plains (Figure 1). The average rainfall in this region is around 480 mm/yr and the AI is between 0.2 and 0.3 (Figure 2). The North Concho provides an interesting example of how changes in vegetation cover can translate to large-scale changes in streamflows. Since around 1960, mean annual streamflows have been 70% lower than they were in the first half of the 20th century—a change concurrent with a dramatic expansion of woody plants, in particular mesquite (*Prosopis glandulosa*) (Figure 1). Using the prevailing logic at the time, water planners attributed the decline in streamflows to increasing water use by mesquite; and with the goal of restoring streamflows, they implemented a large-scale brush removal program in the North Concho watershed. Between 2000 and 2005, more than one-third of the 3100-km^2 watershed was cleared of mesquite. However, as reported in Wilcox et al. (2010), this large-scale effort did not result in any perceptible increase in streamflow.

In order to better understand what was driving streamflow in the North Concho, Wilcox et al. (2008a) conducted a detailed analysis of streamflow and precipitation records, going back to around 1915. What they found was that in this region streamflows make up a very small portion of the water budget and that most streamflow is generated from large rainfall events. In other words, most of the streamflow occurs as stormflows and is driven by infiltration-excess overland flow. But they also found that stormflows were much smaller and less frequent after 1960, despite the fact that average precipitation totals had not changed. These findings make sense in light of the extensive vegetation changes that took place over the preceding 100 years. As in the

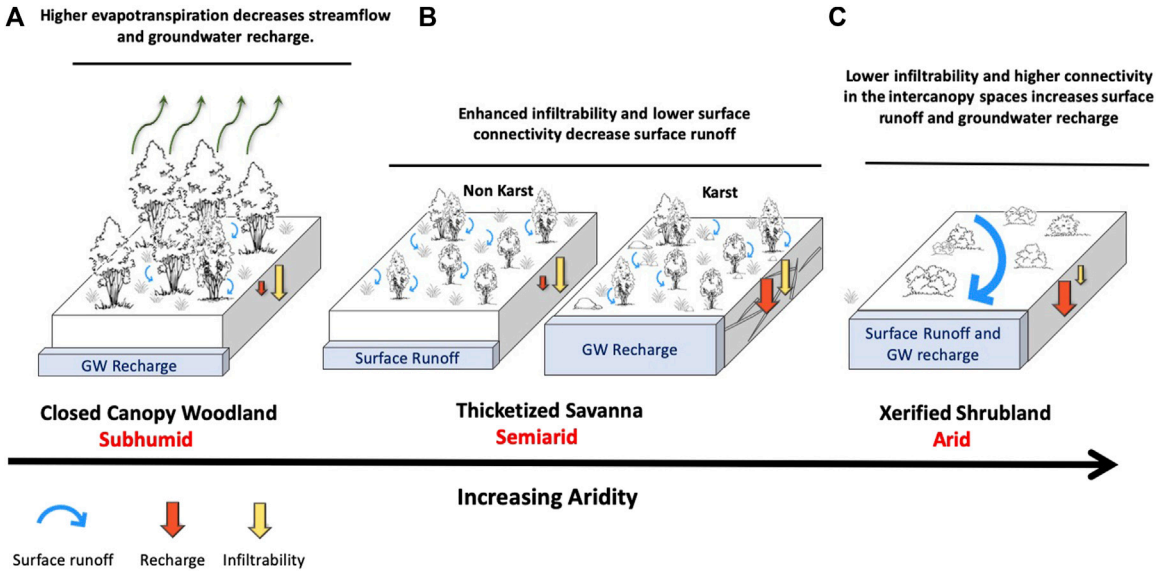

FIGURE 5
Conceptualized framework for understanding how woody plant encroachment modifies ecohydrological processes. **(A)**. *Closed Canopy Woodlands:* In subhumid climates (aridity index 0.5–0.7) woody encroachment will result in higher evapotranspiration leading to lower streamflows and groundwater recharge. **(B)**. *Thicketized Savannas:* in semiarid climates where rainfall is sufficient to maintain vegetated intercanopy areas (aridity index 0.2–0.5) woody encroachment enhances infiltrability (lower connectivity) resulting in less surface runoff. Where substrate is highly permeable such as karst landscapes, groundwater recharge may be increased. **(C)**. *Xerified shrublands:* in arid climates (aridity index <0.2) woody encroachment increases landscape connectivity because of interconnected bare intercanopy patches. As a result surface runoff is increased as is groundwater recharge as a result of higher transmission losses in stream channels.

Edwards Plateau ecoregion (see Case Study 4), overgrazing dramatically altered vegetation cover in the Rolling Plains. Beginning around 1880 and lasting until around 1960, these rangelands were extremely heavily grazed. Then, when the numbers of grazing animals declined precipitously (Wilcox et al., 2012), vegetation cover—both herbaceous and woody—increased dramatically. Certainly, one result of the increase in tree cover has been higher soil infiltrability. For example, Wood et al. (1978) found that in previously heavily grazed rangelands in the Rolling Plains, infiltration rates were twice as high under mesquite canopies than in the intercanopy areas.

Several studies have found that mesquite expansion does increase evapotranspiration by a few millimeters a year (Carlson et al., 1990; Saleh et al., 2009). But as argued by Wilcox et al. (2010), in systems of this nature—in which most streamflow is generated as infiltration-excess overland flow, with only a small percentage coming from deep drainage—changes in evapotranspiration have little bearing on either groundwater recharge or streamflows.

Underlying mechanisms, landscape-scale responses, and changes in connectivity. Like the situation described in Case Study 3, in the North Concho the improved range condition brought about by greatly lowered grazing pressure and the concomitant expansion of woody plants has led to higher soil infiltrability and less overland flow—hence a dramatic reduction in lateral connectivity that has resulted in much lower streamflows.

Case Study 6: Chihuahuan Desert—Increases in Surface Runoff and in Groundwater Recharge.

Overview. In the Chihuahuan Desert, where average annual precipitation is around 230 mm and the AI is <0.1 (Figure 2), large swaths of desert grassland have been converted to shrublands consisting primarily of creosote bush (*Larrea tridentate*). The initial transition from desert grassland to shrubland was most likely driven by overgrazing, but with increasing temperatures and changes in precipitation patterns—including the onset of periodic multi-year droughts—the process is continuing (Bestelmeyer et al., 2018). In addition, once the process has been initiated, self-reinforcing feedback loops may occur that accelerate the shift from grassland to shrubland (D'Odorico et al., 2012; Turnbull et al., 2012). As woody plants become dominant, water, soil, and nutrient resources are concentrated in the shrub clusters—at the expense of intercanopy areas, which gradually turn into bare ground (Schlesinger et al., 1990). With the consequent declines in surface roughness and soil infiltrability, the intercanopy areas become highly interconnected, which gives rise to much greater surface runoff than from desert grasslands. A recent modeling analysis suggests that in such shrublands, the increased surface

runoff significantly augments groundwater recharge (Schreiner-McGraw et al., 2020), owing to the high transmission losses that occur in desert washes during runoff events (Schreiner-McGraw and Vivoni, 2018; Schreiner-McGraw et al., 2019). In this way, the conversion of desert grasslands to shrublands actually increases groundwater recharge.

Underlying mechanisms, landscape-scale responses, and changes in connectivity. At the drier end of the dryland spectrum (<300 mm rainfall/year), WPE leads to increasing bare ground, or *xerification* (Schreiner-McGraw et al., 2020). As noted above, the net result is dramatically higher lateral connectivity via a network of intercanopy patches, which greatly facilitates surface runoff and ultimately leads to higher groundwater recharge via transmission loss in stream channels.

A framework for understanding the ecohydrology of woody plant encroachment

As demonstrated by the case studies presented here, woody plant encroachment in dryland ecosystems does have profound ecohydrological consequences—at multiple scales—driven primarily by changes in evapotranspiration and/or soil infiltrability. The findings of these studies provide evidence for the existence of two thresholds in ecohydrological response to WPE: one occurring at an AI value of around 0.5, and the other at an AI value of about 0.1, which correspond roughly to the dividing lines between the three climate zones of subhumid, semiarid, and arid. We found that ecohydrological responses to WPE differed among the three zones and were related to changes in ecohydrological connectivity. These findings are conceptualized in Figure 5.

For subhumid climates, WPE results in the formation of closed-canopy woodlands and thereby significant increases in evapotranspiration, leading to reduced ecohydrological connectivity (both vertical and lateral). The result, as exemplified by the findings in the Cross Timbers region (Case Study 1) and in the Post Oak Savanna (Case Study 2), is lower groundwater recharge and streamflows. In both of these ecosystems, average annual precipitation is around 900 mm and the aridity index is between 0.5 and 0.6 (Figure 2); rainfall upon occasion may exceed PET, especially during the cooler periods of the year (Figure 3).

Three of the case studies (case studies 3, 4, and 5) are drawn from semiarid climates where annual rainfall ranges from around 400–700 mm and AI from 0.2 to 0.4. Because rainfall is much lower than PET during the entire year (Figure 3), WPE brings about only minor changes in evapotranspiration. At the same time, the higher vegetation cover resulting from WPE, in concert with recovery from historic overgrazing, has led to higher soil infiltrability. These conditions—an absence of overgrazing, sufficient rainfall to maintain vegetation cover in the intercanopy areas, and higher soil infiltrability—dramatically reduce lateral connectivity, which means lower surface runoff. In areas where subsurface vertical connectivity is poor, the consequence is lower streamflows, as seen from the South Texas Shrublands (Case Study 3) and the Rolling Plains (Case Study 5). In contrast, where subsurface connectivity is high, such as in the karst landscapes of the Edwards Plateau (Case Study 4), higher soil infiltrability means enhanced groundwater recharge and baseflows to streams and rivers. It is important to emphasize that in each of the ecoregions represented by these case studies, a gradual rebound from overgrazing took place concomitantly with WPE and there were strong interactions between the two. Together, they have contributed to increased vegetation cover on the landscape and higher soil infiltrability.

At the driest end of the climate gradient, where rainfall is less than 300 mm/yr and AI is around 0.1, WPE results in *xerification*. Intercanopy areas become bare and highly interconnected, leading to higher surface runoff. In areas where runoff is routed into highly transmissible stream channels (as in Case Study 6), groundwater recharge will be increased.

The concept of connectivity, then, provides a unifying framework for interpreting and making sense of findings that initially appear to be incongruent and inconsistent with respect to the ecohydrological effects of WPE. In drylands, changes in woody plant cover—by bringing about changes in evapotranspiration and/or soil infiltrability—fundamentally alter the *ecohydrological connectivity* of these landscapes. The directional change in connectivity can be lateral (overland flow, shallow subsurface flow) or vertical (deep drainage, groundwater recharge). The landscape-scale response to these changes will depend on the nature of the soil and rock substrate as well as the depth to groundwater.

Author contributions

BW Conceptualization and writing SB. Conceptualization, writing and figure preparation HO Conceptualization and writing and figure preparation PL. Conceptualization and writing.

Funding

This work was supported by USDA-NIFA awards 2019-68012-29819 and 2022-67019-36267.

Conflict of interest

The authors declare that the research was conducted in the absence of any commercial or financial relationships that could be construed as a potential conflict of interest.

Publisher's note

References

Acharya, B. S., Halihan, T., Zou, C. B., and Will, R. E. (2017a). Vegetation controls on the spatio-temporal heterogeneity of deep moisture in the unsaturated zone: A hydrogeophysical evaluation. *Sci. Rep.* 7, 1499. doi:10.1038/s41598-017-01662-y

Acharya, B. S., Hao, Y. H., Ochsner, T. E., and Zou, C. B. (2017b). Woody plant encroachment alters soil hydrological properties and reduces downward flux of water in tallgrass prairie. *Plant Soil* 414, 379–391. doi:10.1007/s11104-016-3138-0

Archer, S. R., Anderson, E. M., Predick, K. I., Schwinning, S., Steidl, R. J., and Woods, S. R. (2017). "Woody plant encroachment: Causes and consequences," in *Rangeland systems: Processes, management, challenges*. Editor D. D. Briske (Cham, Switzerland: Springer), 25–84.

Archer, S. R., and Predick, K. I. (2014). An ecosystem services perspective on brush management: Research priorities for competing land-use objectives. *J. Ecol.* 102, 1394–1407. doi:10.1111/1365-2745.12314

Barger, N. N., Archer, S. R., Campbell, J. L., Huang, C. Y., Morton, J. A., and Knapp, A. K. (2011). Woody plant proliferation in North American drylands: A synthesis of impacts on ecosystem carbon balance. *J. Geophys. Res.* 116, G00K07. doi:10.1029/2010jg001506

Basant, S., Wilcox, B. P., Leite, P. M., and Morgan, C. L. (2020). When savannas recover from overgrazing, ecohydrological connectivity collapses. *Environ. Res. Lett.* 15, 054001. doi:10.1088/1748-9326/ab71a1

Berg, M. D., Marcantonio, F., Allison, M. A., Mcalister, J., Wilcox, B. P., and Fox, W. E. (2016). Contrasting watershed-scale trends in runoff and sediment yield complicate rangeland water resources planning. *Hydrol. Earth Syst. Sci.* 20, 2295–2307. doi:10.5194/hess-20-2295-2016

Bestelmeyer, B. T., Peters, D. P. C., Archer, S. R., Browning, D. M., Okin, G. S., Schooley, R. L., et al. (2018). The grassland-shrubland regime shift in the southwestern United States: Misconceptions and their implications for management. *Bioscience* 68, 678–690. doi:10.1093/biosci/biy065

Bochet, E., Rubio, J. L., and Poesen, J. (1999). Modified topsoil islands within patchy Mediterranean vegetation in SE Spain. *Catena* 38, 23–44. doi:10.1016/s0341-8162(99)00056-9

Bosch, J. M., and Hewlett, J. D. (1982). A review of catchment experiments to determine the effect of vegetation changes on water yield and evapotranspiration. *J. Hydrology* 55, 3–23. doi:10.1016/0022-1694(82)90117-2

Bracken, L. J., Turnbull, L., Wainwright, J., and Bogaart, P. (2015). Sediment connectivity: A framework for understanding sediment transfer at multiple scales. *Earth Surf. Process. Landf.* 40, 177–188. doi:10.1002/esp.3635

Bracken, L. J., Wainwright, J., Ali, G. A., Tetzlaff, D., Smith, M. W., Reaney, S. M., et al. (2013). Concepts of hydrological connectivity: Research approaches, pathways and future agendas. *Earth-Science Rev.* 119, 17–34. doi:10.1016/j.earscirev.2013.02.001

Bring, A., Fedorova, I., Dibike, Y., Hinzman, L., Mard, J., Mernild, S. H., et al. (2016). Arctic terrestrial hydrology: A synthesis of processes, regional effects, and research challenges. *J. Geophys. Res. Biogeosci.* 121, 621–649. doi:10.1002/2015jg003131

Calvo-Cases, A., Arnau-Rosalen, E., Boix-Fayos, C., Estrany, J., Roxo, M. J., and Symeonakis, E. (2021). Eco-geomorphological connectivity and coupling interactions at hillslope scale in drylands: Concepts and critical examples. *J. Arid Environ.* 186, 104418. doi:10.1016/j.jaridenv.2020.104418

Carlson, D. H., Thurow, T. L., Knight, R. W., and Heitschmidt, R. K. (1990). Effect of honey mesquite on the water balance of Texas Rolling Plains rangeland. *J. Range Manag.* 43, 491–496. doi:10.2307/4002351

Castello, L., Mcgrath, D. G., Hess, L. L., Coe, M. T., Lefebvre, P. A., Petry, P., et al. (2013). The vulnerability of Amazon freshwater ecosystems. *Conserv. Lett.* 6, 217–229. doi:10.1111/conl.12008

Caterina, G. L., Will, R. E., Turton, D. J., Wilson, D. S., and Zou, C. B. (2014). Water use of Juniperus virginiana trees encroached into mesic prairies in Oklahoma, USA. *Ecohydrology* 7, 1124–1134.

Cipriotti, P. A., and Aguiar, M. R. (2017). Biotic and abiotic changes along a cyclic succession driven by shrubs in semiarid steppes from Patagonia. *Plant Soil* 414, 295–308. doi:10.1007/s11104-016-3131-7

Cohen, M. J., Creed, I. F., Alexander, L., Basu, N. B., Calhoun, A. J. K., Craft, C., et al. (2016). Do geographically isolated wetlands influence landscape functions? *Proc. Natl. Acad. Sci. U. S. A.* 113, 1978–1986. doi:10.1073/pnas.1512650113

D'odorico, P., Laio, F., Porporato, A., Ridolfi, L., Rinaldo, A., and Iturbe, I. R. (2010). Ecohydrology of terrestrial ecosystems. *BioScience* 60, 898–907. doi:10.1525/bio.2010.60.11.6

D'odorico, P., Okin, G. S., and Bestelmeyer, B. T. (2012). A synthetic review of feedbacks and drivers of shrub encroachment in arid grasslands. *Ecohydrology* 5, 520–530. doi:10.1002/eco.259

Devitt, D. A., and Smith, S. D. (2002). Root channel macropores enhance downward movement of water in a Mojave Desert ecosystem. *J. Arid Environ.* 50, 99–108. doi:10.1006/jare.2001.0853

Eldridge, D. J., Bowker, M. A., Maestre, F. T., Roger, E., Reynolds, J. F., and Whitford, W. G. (2011). Impacts of shrub encroachment on ecosystem structure and functioning: Towards a global synthesis. *Ecol. Lett.* 14, 709–722. doi:10.1111/j.1461-0248.2011.01630.x

Good, S. P., Noone, D., and Bowen, G. (2015). Hydrologic connectivity constrains partitioning of global terrestrial water fluxes. *Science* 349, 175–177. doi:10.1126/science.aaa5931

Goodrich, D. C., Kepner, W. G., Levick, L. R., and Wigington, P. J. (2018). Southwestern intermittent and ephemeral stream connectivity. *J. Am. Water Resour. Assoc.* 54, 400–422. doi:10.1111/1752-1688.12636

Hoagland, B. W., Butler, I. H., Johnson, F. L., and Gleen, S. (1999). "The cross Timbers," in *Savannas, barrens, and rock outcrop plant communities of North America*. Editors R. C. Anderson, J. S. Fralish, and J. M. Baskin (New York: Cambridge Press), 231–248.

Hoover, D. L., Bestelmeyer, B., Grimm, N. B., Huxman, T. E., Reed, S. C., Sala, O., et al. (2020). Traversing the wasteland: A framework for assessing ecological threats to drylands. *Bioscience* 70, 35–47. doi:10.1093/biosci/biz126

Huxman, T. E., Wilcox, B. P., Breshears, D. D., Scott, R. L., Snyder, K. A., Small, E. E., et al. (2005). Ecohydrological implications of woody plant encroachment. *Ecology* 86, 308–319. doi:10.1890/03-0583

Ilstedt, U., Tobella, A. B., Bazie, H. R., Bayala, J., Verbeeten, E., Nyberg, G., et al. (2016). Intermediate tree cover can maximize groundwater recharge in the seasonally dry tropics. *Sci. Rep.* 6, 21930. doi:10.1038/srep21930

Iwaniec, D. M., Gooseff, M., Suding, K. N., Johnson, D. S., Reed, D. C., Peters, D. P. C., et al. (2021). Connectivity: Insights from the US long term ecological research network. *Ecosphere* 12, 30. doi:10.1002/ecs2.3432

Jaeger, K. L., Olden, J. D., and Pelland, N. A. (2014). Climate change poised to threaten hydrologic connectivity and endemic fishes in dryland streams. *Proc. Natl. Acad. Sci. U. S. A.* 111, 13894–13899. doi:10.1073/pnas.1320890111

Johnson, J. C., Williams, C. J., Guertin, D. P., Archer, S. R., Heilman, P., Pierson, F. B., et al. (2021). Restoration of a shrub-encroached semi-arid grassland: Implications for structural, hydrologic, and sediment connectivity. *Ecohydrology* 14, 20. doi:10.1002/eco.2281

Keese, K. E., Scanlon, B. R., and Reedy, R. C. (2005). Assessing controls on diffuse groundwater recharge using unsaturated flow modeling. *Water Resour. Res.* 41. doi:10.1029/2004wr003841

Keesstra, S. D., Bagarello, V., Ferro, V., Finger, D., and Parsons, A. J. (2020). Connectivity in hydrology and sediment dynamics. *Land Degrad. Dev.* 31, 2525–2528. doi:10.1002/ldr.3401

Keesstra, S., Nunes, J. P., Saco, P., Parsons, T., Poeppl, R., Masselink, R., et al. (2018). The way forward: Can connectivity be useful to design better measuring and modelling schemes for water and sediment dynamics? *Sci. Total Environ.* 644, 1557–1572. doi:10.1016/j.scitotenv.2018.06.342

Lane, C. R., Leibowitz, S. G., Autrey, B. C., Leduc, S. D., and Alexander, L. C. (2018). Hydrological, physical, and chemical functions and connectivity of non-floodplain wetlands to downstream waters: A review. *J. Am. Water Resour. Assoc.* 54, 346–371. doi:10.1111/1752-1688.12633

Leibowitz, S. G., Wigington, P. J., Schofield, K. A., Alexander, L. C., Vanderhoof, M. K., and Golden, H. E. (2018). Connectivity of streams and wetlands to

downstream waters: An integrated systems framework. *J. Am. Water Resour. Assoc.* 54, 298–322. doi:10.1111/1752-1688.12631

Leite, P. a. M., Wilcox, B. P., and Mcinnes, K. J. (2020). Woody plant encroachment enhances soil infiltrability of a semiarid karst savanna. *Environ. Res. Commun.* 2, 115005. doi:10.1088/2515-7620/abc92f

Li, J., Okin, G. S., Alvarez, L., and Epstein, H. (2007). Quantitative effects of vegetation cover on wind erosion and soil nutrient loss in a desert grassland of southern New Mexico, USA. *Biogeochemistry* 85, 317–332. doi:10.1007/s10533-007-9142-y

Ludwig, J. A., Wilcox, B. P., Breshears, D. D., Tongway, D. J., and Imeson, A. C. (2005). Vegetation patches and runoff-erosion as interacting ecohydrological processes in semiarid landscapes. *Ecology* 86, 288–297. doi:10.1890/03-0569

Maestre, F. T., Bowker, M. A., Puche, M. D., Hinojosa, M. B., Martinez, I., Garcia-Palacios, P., et al. (2009). Shrub encroachment can reverse desertification in semi-arid Mediterranean grasslands. *Ecol. Lett.* 12, 930–941. doi:10.1111/j.1461-0248.2009.01352.x

Marquart, A., Eldridge, D. J., Geissler, K., Lobas, C., and Blaum, N. (2020). Interconnected effects of shrubs, invertebrate-derived macropores and soil texture on water infiltration in a semi-arid savanna rangeland. *Land Degrad. Dev.* 31, 2307–2318. doi:10.1002/ldr.3598

Mishra, N. B., and Young, K. R. (2020). "Savannas and grasslands," in *The handbook of natural resources: Terrestrial ecosystems and biodiversity*. Editor Y. Wang. 2nd ed (Taylor & Francis Group).

Moore, G. W., Barre, D. A., and Owens, M. K. (2012). Does shrub removal increase groundwater recharge in southwestern Texas semiarid rangelands? *Rangel. Ecol. Manag.* 65, 1–10. doi:10.2111/rem-d-11-00055.1

Mu, Q. Z., Zhao, M. S., and Running, S. W. (2011). Improvements to a MODIS global terrestrial evapotranspiration algorithm. *Remote Sens. Environ.* 115, 1781–1800. doi:10.1016/j.rse.2011.02.019

Okin, G. S., Moreno-De Las Heras, M., Saco, P. M., Throop, H. L., Vivoni, E. R., Parsons, A. J., et al. (2015). Connectivity in dryland landscapes: Shifting concepts of spatial interactions. *Front. Ecol. Environ.* 13, 20–27. doi:10.1890/140163

Peters, D. P. C., Bestelmeyer, B. T., Herrick, J. E., Fredrickson, E. L., Monger, H. C., and Havstad, K. M. (2006). Disentangling complex landscapes: New insights into arid and semiarid system dynamics. *BioScience* 56, 491–501. doi:10.1641/0006-3568(2006)56[491:dclnii]2.0.co;2

Peters, D. P. C., Groffman, P. M., Nadelhoffer, K. J., Grimm, N. B., Coffins, S. L., Michener, W. K., et al. (2008). Living in an increasingly connected world: A framework for continental-scale environmental science. *Front. Ecol. Environ.* 6, 229–237. doi:10.1890/070098

Qiao, L., Zou, C. B., Stebler, E., and Will, R. E. (2017). Woody plant encroachment reduces annual runoff and shifts runoff mechanisms in the tallgrass prairie, USA. *Water Resour. Res.* 53, 4838–4849. doi:10.1002/2016wr019951

Ratajczak, Z., Nippert, J. B., and Collins, S. L. (2012). Woody encroachment decreases diversity across North American grasslands and savannas. *Ecology* 93, 697–703. doi:10.1890/11-1199.1

Reid, K. D., Wilcox, B. P., Breshears, D. D., and Macdonald, L. (1999). Runoff and erosion in a pinon-juniper woodland: Influence of vegetation patches. *Soil Sci. Soc. Am. J.* 63, 1869–1879. doi:10.2136/sssaj1999.6361869x

Saco, P. M., Rodriguez, J. F., Moreno-De Las Heras, M., Keesstra, S., Azadi, S., Sandi, S., et al. (2020). Using hydrological connectivity to detect transitions and degradation thresholds: Applications to dryland systems. *Catena* 186, 104354. doi:10.1016/j.catena.2019.104354

Sala, O. E., and Maestre, F. T. (2014). Grass-woodland transitions: Determinants and consequences for ecosystem functioning and provisioning of services. *J. Ecol.* 102, 1357–1362. doi:10.1111/1365-2745.12326

Saleh, A., Wu, H., Brown, C. S., Teagarden, F. M., Mcwilliams, S. M., Hauck, L. M., et al. (2009). Effect of brush control on evapotranspiration in the North Concho River watershed using the eddy covariance technique. *J. Soil Water Conservation* 64, 336–349. doi:10.2489/jswc.64.5.336

Schlesinger, W. H., Reynolds, J. F., Cunningham, G. L., Huenneke, L. F., Jarrell, W. M., Virginia, R. A., et al. (1990). Biological feedbacks in global desertification. *Science* 247, 1043–1048. doi:10.1126/science.247.4946.1043

Schreiner-Mcgraw, A. P., Ajami, H., and Vivoni, E. R. (2019). Extreme weather events and transmission losses in arid streams. *Environ. Res. Lett.* 14. doi:10.1088/1748-9326/ab2949

Schreiner-Mcgraw, A. P., Vivoni, E. R., Ajami, H., Sala, O. E., Throop, H. L., and Peters, D. C. (2020). Woody plant encroachment has a larger impact than climate change on dryland water budgets. *Sci. Rep.* 10, 8112. doi:10.1038/s41598-020-65094-x

Schreiner-Mcgraw, A. P., and Vivoni, E. R. (2018). On the sensitivity of hillslope runoff and channel transmission losses in arid piedmont slopes. *Water Resour. Res.* 54, 4498–4518. doi:10.1029/2018wr022842

Starks, P. J., and Moriasi, D. N. (2017). Impact of Eastern redcedar encroachment on stream discharge in the North Canadian River basin. *J. Soil Water Conservation* 72, 12–25. doi:10.2489/jswc.72.1.12

Tetzlaff, D., Soulsby, C., Bacon, P. J., Youngson, A. F., Gibbins, C., and Malcolm, I. A. (2007). Connectivity between landscapes and riverscapes - a unifying theme in integrating hydrology and ecology in catchment science? *Hydrol. Process.* 21, 1385–1389. doi:10.1002/hyp.6701

Tobella, A. B., Reese, H., Almaw, A., Bayala, J., Malmer, A., Laudon, H., et al. (2014). The effect of trees on preferential flow and soil infiltrability in an agroforestry parkland in semiarid Burkina Faso. *Water Resour. Res.* 50, 3342–3354. doi:10.1002/2013wr015197

Torquato, P. R., Will, R. E., Zhang, B., and Zou, C. B. (2020). *Stand-level transpiration increases after eastern redcedar (juniperus virginianaL.) encroachment into the midstory of oak forests*. *Forests* 11.

Turnbull, L., and Wainwright, J. (2019). From structure to function: Understanding shrub encroachment in drylands using hydrological and sediment connectivity. *Ecol. Indic.* 98, 608–618. doi:10.1016/j.ecolind.2018.11.039

Turnbull, L., Wilcox, B. P., Belnap, J., Ravi, S., D'odorico, P., Childers, D., et al. (2012). Understanding the role of ecohydrological feedbacks in ecosystem state change in drylands. *Ecohydrology* 5, 174–183. doi:10.1002/eco.265

Veldman, J. W., Buisson, E., Durigan, G., Fernandes, G. W., Le Stradic, S., Mahy, G., et al. (2015). Toward an old-growth concept for grasslands, savannas, and woodlands. *Front. Ecol. Environ.* 13, 154–162. doi:10.1890/140270

Walvoord, M. A., and Kurylyk, B. L. (2016). Hydrologic impacts of thawing permafrost-A review. *Vadose Zone J.* 15, 010010. doi:10.2136/vzj2016.01.0010

Wang, J. E., Xiao, X. M., Qin, Y. W., Dong, J. W., Geissler, G., Zhang, G. L., et al. (2017). Mapping the dynamics of eastern redcedar encroachment into grasslands during 1984-2010 through PALSAR and time series Landsat images. *Remote Sens. Environ.* 190, 233–246. doi:10.1016/j.rse.2016.12.025

Wang, J., Xiao, X. M., Basara, J., Wu, X. C., Bajgain, R., Qin, Y. W., et al. (2021). Impacts of juniper woody plant encroachment into grasslands on local climate. *Agric. For. Meteorology* 307, 108508. doi:10.1016/j.agrformet.2021.108508

Wang, J., Xiao, X. M., Zhang, Y., Qin, Y. W., Doughty, R. B., Wu, X. C., et al. (2018b). Enhanced gross primary production and evapotranspiration in juniper-encroached grasslands. *Glob. Chang. Biol.* 24, 5655–5667. doi:10.1111/gcb.14441

Wang, J., Xiao, X., Qin, Y., Droughty, R. B., Dong, J., and Zou, Z. (2018a). Characterizing the encroachment of juniper forests into sub-humid and semi-arid prairies from 1984 to 2010 using PALSA and Landsat data. *Remote Sens. Environ.* 205, 166–179. doi:10.1016/j.rse.2017.11.019

Webb, N. P., Herrick, J. E., and Duniway, M. C. (2014). Ecological site-based assessments of wind and water erosion: Informing accelerated soil erosion management in rangelands. *Ecol. Appl.* 24, 1405–1420. doi:10.1890/13-1175.1

Weltz, M. A., and Blackburn, W. H. (1995). Water budget for south Texas rangelands. *J. Range Manag.* 48, 45–52. doi:10.2307/4002503

Wilcox, B. P., Birt, A., Archer, S. R., Fuhlendorf, S. D., Kreuter, U. P., Sorice, M. G., et al. (2018). Viewing woody-plant encroachment through a social–ecological lens. *BioScience* 68, 691–705. doi:10.1093/biosci/biy051

Wilcox, B. P., Breshears, D. D., and Allen, C. D. (2003). Ecohydrology of a resource-conserving semiarid woodland: Effects of scale and disturbance. *Ecol. Monogr.* 73, 223–239. doi:10.1890/0012-9615(2003)073[0223:eoarsw]2.0.co;2

Wilcox, B. P. (2007). Does rangeland degradation have implications for global streamflow? *Hydrol. Process.* 21, 2961–2964. doi:10.1002/hyp.6856

Wilcox, B. P., Fuhlendorf, S. D., Walker, J. W., Twidwell, D., Wu, X. B., Goodman, L. E., et al. (2022). Saving imperiled grassland biomes by recoupling fire and grazing: A case study from the Great Plains. *Front. Ecol. Environ.* 20, 179–186. doi:10.1002/fee.2448

Wilcox, B. P., Huang, Y., and Walker, J. W. (2008a). Long-term trends in streamflow from semiarid rangelands: Uncovering drivers of change. *Glob. Change Biol.* 14, 1676–1689. doi:10.1111/j.1365-2486.2008.01578.x

Wilcox, B. P., and Huang, Y. (2010). Woody plant encroachment paradox: Rivers rebound as degraded grasslands convert to woodlands. *Geophys. Res. Lett.* 37, L07402. doi:10.1029/2009gl041929

Wilcox, B. P., Owens, M. K., Dugas, W. A., Ueckert, D. N., and Hart, C. R. (2006). Shrubs, streamflow, and the paradox of scale. *Hydrol. Process.* 20, 3245–3259. doi:10.1002/hyp.6330

Wilcox, B. P., Sorice, M. G., Angerer, J., and Wright, C. L. (2012). Historical changes in stocking densities on Texas rangelands. *Rangel. Ecol. Manag.* 65, 313–317. doi:10.2111/rem-d-11-00119.1

Wilcox, B. P., Taucer, P. I., Munster, C. L., Owens, M. K., Mohanty, B. P., Sorenson, J. R., et al. (2008b). Subsurface stormflow is important in semiarid karst shrublands. *Geophys. Res. Lett.* 35, L10403. doi:10.1029/2008gl033696

Wilcox, B. P., Walker, J. W., and Heilman, J. L. (2010). Commentary on "Effect of brush control on evapotranspiration in the North Concho River watershed using the eddy covariance technique" by Saleh et al. (2009). *J. Soil Water Conservation* 65, 83A–84A. doi:10.2489/jswc.65.4.83a

Wilcox, B. P., Wilding, L. P., and Woodruff, C. M. (2007). Soil and topographic controls on runoff generation from stepped landforms in the Edwards Plateau of Central Texas. *Geophys. Res. Lett.* 34, L24S24. doi:10.1029/2007gl030860

Williams, C. J., Pierson, F. B., Kormos, P. R., Al-Hamdan, O. Z., Nouwakpo, S. K., and Weitz, M. A. (2019). Vegetation, hydrologic, and erosion responses of sagebrush steppe 9 Yr following mechanical tree removal. *Rangel. Ecol. Manag.* 72, 47–68. doi:10.1016/j.rama.2018.07.004

Wohl, E. (2017). Connectivity in rivers. *Prog. Phys. Geogr. Earth Environ.* 41, 345–362. doi:10.1177/0309133317714972

Wood, M. K., Blackburn, W. H., Eckert, J., and Peterson, F. F. (1978). Interrelations of the physical properties of coppice dune and vesicular dune interspace soils with grass seedling emergence. *J. Range Manag.* 31, 189–192. doi:10.2307/3897177

Wu, G. L., Cui, Z., and Huang, Z. (2021). *Contribution of root decay process on soil infiltration capacity and soil water replenishment of planted forestland in semi-arid regions*, 404.*Geoderma*

Yahdjian, L., Sala, O. E., and Havstad, K. M. (2015). Rangeland ecosystem services: Shifting focus from supply to reconciling supply and demand. *Front. Ecol. Environ.* 13, 44–51. doi:10.1890/140156

Zou, C. B., Caterina, G. L., Will, R. E., Stebler, E., and Turton, D. (2015). Canopy interception for a tallgrass prairie under juniper encroachment. *Plos One* 10, e0141422. doi:10.1371/journal.pone.0141422

Zou, C. B., Qiao, L., and Wilcox, B. P. (2016). Woodland expansion in central Oklahoma will significantly reduce streamflows – A modelling analysis. *Ecohydrology* 9, 807–816. doi:10.1002/eco.1684

Zou, C. B., Turton, D. J., Will, R. E., Engle, D. M., and Fuhlendorf, S. D. (2014). Alteration of hydrological processes and streamflow with juniper (Juniperus virginiana) encroachment in a mesic grassland catchment. *Hydrol. Process.* 28, 6173–6182. doi:10.1002/hyp.10102

Zou, C. B., Twidwell, D., Bielski, C. H., Fogarty, D. T., Mittelstet, A. R., Starks, P. J., et al. (2018). Impact of eastern redcedar proliferation on water resources in the Great Plains USACurrent state of knowledge. *Water* 10, 1768. doi:10.3390/w10121768

frontiers | Frontiers in Environmental Science

TYPE Original Research
PUBLISHED 03 November 2022
DOI 10.3389/fenvs.2022.1034077

OPEN ACCESS

EDITED BY
Z. Y. Yuan,
Institute of Soil and Water Conservation (CAS), China

REVIEWED BY
Junqiang Yao,
China Meteorological Administration, China
Jingzhe Wang,
Shenzhen Polytechnic, China

*CORRESPONDENCE
Hengfang Wang,
wanghf@xju.edu.cn
Guanghui Lv,
ler@xju.edu.cn

SPECIALTY SECTION
This article was submitted to Drylands, a section of the journal Frontiers in Environmental Science

RECEIVED 01 September 2022
ACCEPTED 14 October 2022
PUBLISHED 03 November 2022

CITATION
Zhang Y, Wang H, Cai Y, Yang Q and Lv G (2022), Fertile Island Effect by Three Typical Woody Plants on Wetlands of Ebinur Lake, northwestern China. *Front. Environ. Sci.* 10:1034077. doi: 10.3389/fenvs.2022.1034077

Fertile Island Effect by Three Typical Woody Plants on Wetlands of Ebinur Lake, northwestern China

Yabei Zhang[1], Hengfang Wang[1]*, Yan Cai[2], Qi Yang[1] and Guanghui Lv[1]*

[1]Key Laboratory of Oasis Ecology, College of the Ecology and Environment, Ministry of Education, Xinjiang University, Urumqi, China, [2]Student Work Department, Tarim University, Aral, China

Desertification poses a permanent threat to the security of arid ecosystems. Perennial arid vegetation plays a crucial role in maintaining the structure and function of arid ecosystems and slowing the process of desertification by forming "fertile islands" under the tree canopy. However, the process of formation and development of these fertile islands remains uncertain. Here, we explored how three typical woody plants (i.e., *Populus euphratica*, *Haloxylon ammodendron*, and *Nitraria tangutorum*) in the Ebinur Lake Basin of northwestern China differed in their soil nitrogen and phosphorus. 1) Significant differences of organic carbon and total and available nitrogen/phosphorus were observed in the soil among the three typical woody plant-dominated ecosystems. *Populus euphratica* had significant differences of N and P contents between the canopy and bare soils, except for ammonium nitrogen. 2) Our RDA analysis revealed that the major factors that influenced the soil nutrient differences among the three vegetations were plant crown width, soil water content, salinity, and pH. 3) The organic carbon content of bare soil was significantly correlated with N and P in all the three vegetations. This study contributes to our understanding of the factors that influence the fertile island effect in arid ecosystems, which may contribute to soil conservation in arid areas.

KEYWORDS

woody plants, fertile island effect, influencing factors, arid area, Ebinur lake basin

Introduction

Soil and plants are important components of terrestrial ecosystems. The physicochemical properties of soil affect the growth and development of plants (Zhang et al., 2019). Plants improve the physicochemical properties of soil through the rhizosphere (Chen et al., 2022) and litter decomposition (Jiang et al., 2020), both of which affect each other through various feedbacks. The rhizosphere/litter decomposition-influence mechanism is more obvious in arid regions (Mora & Lazaro. 2013; Yang et al., 2015). Around perennial plants, due to the combined action of biological and abiotic

processes, soil nutrients gradually flow into the canopy, wheretheir contents are significantly higher than those outside thecanopy, which is evidence of a nutrient-accumulation phenomenon in the spatial distribution that is called the 'fertile island' effect (Chen et al., 2004). Formation of the fertile island effect can promote the growth of plant roots (Zhao et al., 2002) and increase the contents of nutrients and water around plants, thereby improving their survival rates, which is important for renewal and diffusion of plants (Fuhlendorf et al., 2001). The fertile island effect is also the main mechanism by which plants use nutrients and adapt to arid and barren environments.

Scholars in China and abroad have conducted many studies on the effects of plant fertilizer island. The formation of global dry land fertile islands depends, to a large extent, on the local climate, topography, soil characteristics, structure, and properties of plant communities and soil microbial communities (Ochoa-Hues et al., 2017). Researchers used biological and abiotic data on a wide range of drought gradients in eastern Australia to show that the 'fertile island' effect increases with increasing drought levels(Ding and Eldridge, 2020). In a study on soil properties at three different altitudes in the Qilian Mountains, researchers showed that with the increase in altitude, the soil nutrition and microbial-biomass parameters mostly decreased, and the 'fertile island' effect increased(Zhao and An, 2021). In woody plants and shrub communities, such as *Haloxylon ammodendron*, *Tamarix ramosissima,* and *Populus euphratica*, the nutrient enrichment in the topsoil under the canopies was obvious, and the 'fertile island' effect in the upper soil layer was greater than that in the lower soil layer (Reynolds et al., 1999; Chen et al., 2018; Guo et al., 2020; Bomans et al., 2021). Researchers investigated the soil moisture, nutrient content, and fine root density, and they found that the interaction between plants and soil was important for the formation and development of fertile islands and that its influence was not only related to the soil surface but also extended to the depth of the root contact (Cao et al., 2021). Researchers studied the soil nutrient content and microbial community under the canopy of a plant community in the southeast of the Tengger Desert in northwestern China, and they found that the bacterial community was significantly related to the spatial heterogeneity of some of the physical and chemical properties of the soil. The establishment of fertile islands in a desert ecosystem formed soil bacterial communities, which affected the soil characteristics, and the soil was then fed back to the plants, which affected plant growth and development (Li et al., 2021).

However, the focus of these studies is the difference in 'fertile island' effect in different soil depths or different scales or differences in the fat island effect between plants. Few researchers have focused on the effects of plants themselves or soil conditions on the 'fertile island' effect. Therefore, in this study, we analyzed the soil nutrient contents of typical woody plants in arid areas around the Aqikesu River in the Ebinur Lake Basin. The soil nutrient contents under the canopy and bare soil were compared and analyzed, and the following problems were proposed: 1) does the soil under a typical woody plant canopy in the arid area have a 'fertile island' effect? 2) Are there significant differences in different plant nutrient 'fertile island' effect? 3) What factors affect the 'fertile island' effect?

Methods

Overview of the study area

The Ebinur Lake Wetland National Nature Reserve (79°53′-85°02′ E and 43°38′-45°52′ N) is located in the Xinjiang Uygur Autonomous Region. The basin has the continental climate of the northern temperate zone. The climate varies substantially over the four seasons. Rainfall in summer is scarce, and winter is cold and dry. The annual average temperature is 6.6–7.8°C. The annual maximum temperature can reach 44°C, and the minimum temperature can reach 33°C below zero. The annual rainfall is less than 100 mm, and the annual gale weather is 165 days (winds greater than 17 m/s). The typical soil types in the study area are mainly gray desert soil, aeolian sandy soil, gray–brown desert soil, meadow soil, and marsh soil, and the soil in the hidden area is mainly saline soil (Wang et al., 2019; Wang. 2020). The main plants in the study area are *Populus euphratica*, *Haloxylon ammodendron*, *Suaeda glauca,* and *Kalidium foliatum* (Yang et al., 2009).

Sample setting and sample collection

This study is drawn on the results of soil moisture and salinity surveys in previous studies, and we set a transect vertically along the banks of the Achixu River. The transect is about 500 m from the river channel. In the sample belt, the study arranged 30 × 30 m quadrats at 30 m intervals, with a total of 60 quadrats. In addition, the study arranged sample plots about 1 km away from the sample belt, and the study divided the 480 × 600 m sample plots into 320 quadrats of 30 × 30 m. From these 320 quadrats, the study selected the quadrats according to the chessboard interval, for a total of 80 quadrats of 30 × 30 m. The study included a total of 140 quadrats in the transect and plot. Plant quadrat surveys and soil sampling were carried out for each selected quadrat. In the determined standard quadrat, the study selected the soil sampling points by the "diagonal" sampling method, and the study took three portions of soil (three replicates) of 0–10 cm for each quadrat. The study used aluminum boxes to collect the soil samples (the study weighed the quality of the aluminum boxes in advance). After the study completed the aluminum-box collection of the soil, the study

TABLE 1 Study outline of the experimental method.

Main methods of experimental indicators
Organic carbon potassium dichromate dilution heating method
Total nitrogen Kjeldahl determination
Nitrate nitrogen phenol–sulfonic acid method
Ammonium nitrogen indophenol blue colorimetric method
Total phosphorus molybdenum antimony resistance colorimetric method
Available phosphorus sodium bicarbonate molybdenum antimony colorimetric method
Alkali-hydrolyzable nitrogen alkali n-proliferation method

numbered the numbers, immediately weighed the fresh soil, and then brought it back to the laboratory. The study sampled each quadrat by species for crown soil sampling (sampling as close as possible to the root) and randomly selected three plants for each plant (less than three plants, similar plants with the same growth in adjacent quadrats). The study selected three to five sampling points under the canopy and gently shoveled the uppermost layer of litter with a small shovel when sampling. Then, soil samples were collected at 0–10 cm depth at the identified sample sites, and three plants were selected for each species. Finally, the researchers mixed the soil collected under the crowns of the three plants. After collecting the soil under the crown, the researcher collected the bare soil of the corresponding quadrat and put the number into a self-sealing bag. After taking the soil samples back to the laboratory, they were naturally air-dried and pretreated, and the corresponding indexes were measured in the later stage.

Determination items and methods

To measure the 'fertile island' effect, the study measured seven indicators of the soil function related to C, N, and P cycles: organic carbon, total nitrogen, nitrate nitrogen, ammonium nitrogen, alkali-hydrolyzable nitrogen, total phosphorus, and available phosphorus. The study outlines the experimental method as Table 1.

Data processing in the study

The patch distribution pattern of the arid desert ecosystem is strongly affected by vegetation coverage, so the study defined the nutrient-accumulation effect as the relative difference between the plant canopy and the bare area without plant growth (Allington and Valone. 2014). Armas used the relative interaction index (RII) to estimate the accumulation-effect value of each soil index (Armas et al., 2004). The formula of the relative interaction index (RII) is as follows:

$$RII = \frac{X_p - X_n}{X_p + X_n}. \quad (1)$$

In the aforementioned formula, X is the target variable and Xp and Xn are the soil index values of the canopy soil and the bare soil, respectively.

TABLE 2 Difference analysis of soil nutrients under three woody plant canopies.

Nutrient species	Land-use type	*Populus euphratica*	*Haloxylon ammodendron*	*Nitraria tangutorum*
SOC	Cover	13.06 ± 7.70Aa	6.79 ± 8.05Ab	8.77 ± 6.58Aab
	CK	4.66 ± 4.02B	4.66 ± 4.02A	4.66 ± 4.02B
TN	Cover	0.90 ± 0.43Ab	0.58 ± 0.46Aab	0.71 ± 0.44Aa
	CK	0.36 ± 0.20B	0.36 ± 0.20B	0.36 ± 0.20B
TP	Cover	0.61 ± 0.10Ab	0.66 ± 0.32Aab	0.83 ± 0.36Aa
	CK	0.92 ± 0.27B	0.92 ± 0.27B	0.92 ± 0.27A
AP	Cover	41.95 ± 12.97Aa	49.12 ± 24.07Aa	53.22 ± 20.69Ab
	CK	30.60 ± 5.51B	30.60 ± 5.51B	30.60 ± 5.51B
NO_3^--N	Cover	31.07 ± 39.03Aa	27.86 ± 26.12Aa	35.05 ± 32.73Aa
	CK	5.65 ± 7.74B	5.65 ± 7.74B	5.65 ± 7.74B
NH_4^+-N	Cover	9.92 ± 4.30Aa	21.31 ± 56.60Aa	22.60 ± 64.42Aa
	CK	9.76 ± 2.93A	9.76 ± 2.93A	9.76 ± 2.93A
AN	Cover	66.43 ± 38.77Aa	107.77 ± 397.80Aa	93.52 ± 176.2Aa
	CK	35.20 ± 20.39B	35.20 ± 20.39A	35.20 ± 20.39A

Note: $n = 30$. SOC, organic carbon; TN, total nitrogen; NO_3^--N, nitrate nitrogen; NH_4^+-N, ammonium nitrogen; TP, total phosphorus; AP, available phosphorus; AN, alkali-hydrolyzable nitrogen; Cover, sub-crown soil; CK, bare soil; AB: the difference in nutrient contents between sub-crown soil and bare soil; ab: the difference in nutrient contents between sub-crown soil of different plants.

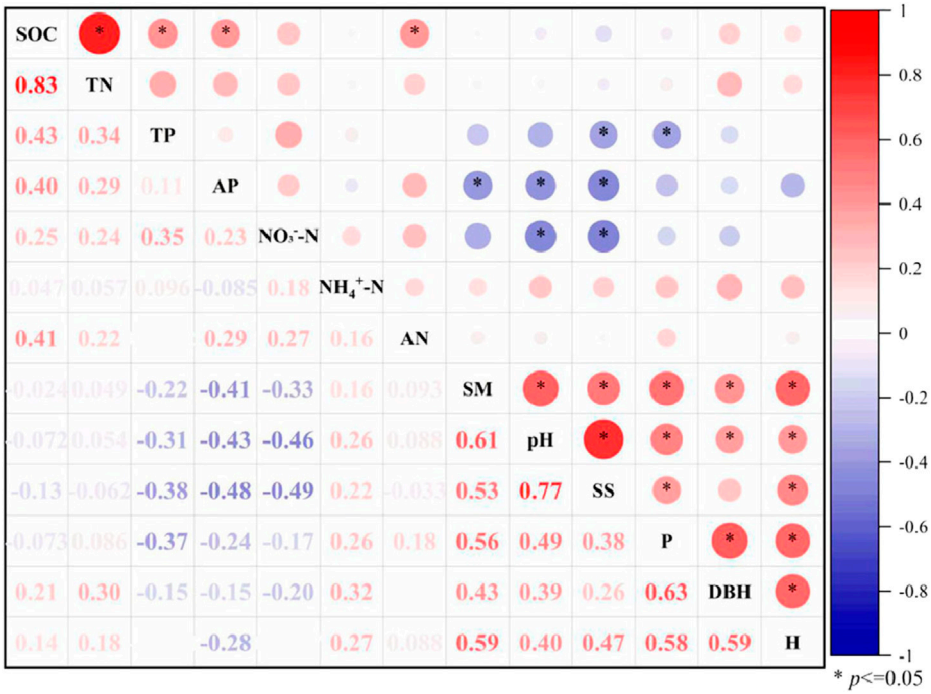

FIGURE 1
Correlation analysis of factors that influence the 'fertile island' effect of different nutrient contents in *Populus euphratica*.

The study used the average method to calculate the nutrient accumulation effect value of each plant (Bowker et al., 2013). The average method of calculating the formula is as follows:

$$M_{RII} = \frac{1}{F}\sum_{i=1}^{F} g(r_i(f_i)). \quad (2)$$

In the aforementioned formula, M_{RII} represents the nutrient accumulation effect, f_i represents the accumulation effect value of different nutrients, r_i is a mathematical function that converts f_i into a positive value, g represents the standardization of all measured values, and F represents the number of measured nutrients.

The study used a paired *t*-test to analyze the differences in soil nutrient properties between the canopy soil and bare soil of *Populus euphratica*, *Haloxylon ammodendron,* and *Nitraria tangutorum* and the analysis of variance to analyze these differences. If the results were obvious, then the study used the least squares difference (LSD) method to conduct the difference test for pairwise comparison of the soil nutrient contents in different habitats. The study used SPSS25 (Statistical Product and Service Solutions) (IBM, New York, NY, United States) to complete the entire statistical analysis and used Origin2022 and Canoco5 (Copyright Petr Šmilauer 2012-2021) to complete the drawing.

Results and analysis

'Fertile island' effect of typical woody plants

The study selected typical desert woody plants from all the plants in the survey area: *Populus euphratica*, *Haloxylon ammodendron,* and *Nitraria tangutorum* and analyzed their 'fertile island' effect. In Table 2, we can see that the nutrient contents of the soil under the *Populus euphratica* canopy were significantly different from those of the bare soil, except for ammonium nitrogen. The nutrient contents of TN, TP, AP, and NO_3^--N in the soil under the *Haloxylon ammodendron* canopy were significantly different from those in the bare soil, while the other nutrient contents had no significant differences. The nutrient contents of the soil organic carbon, TN, AP, and NO_3^--N under the *Nitraria tangutorum* canopy were significantly different from those in the bare soil, and there was no significant difference in the nutrient contents. The contents of the soil organic carbon, TN, and TP under *Populus euphratica* were significantly different from those under *Haloxylon ammodendron*, and the contents of the soil SOC, TN, and TP under *Haloxylon ammodendron* were significantly different from those under *Nitraria tangutorum*. The soil AP content under the *Haloxylon ammodendron* canopy was significantly different from that under *Nitraria tangutorum*. *Populus euphratica* had 'fertile island' effect on nutrients other than NH_4^+-N.

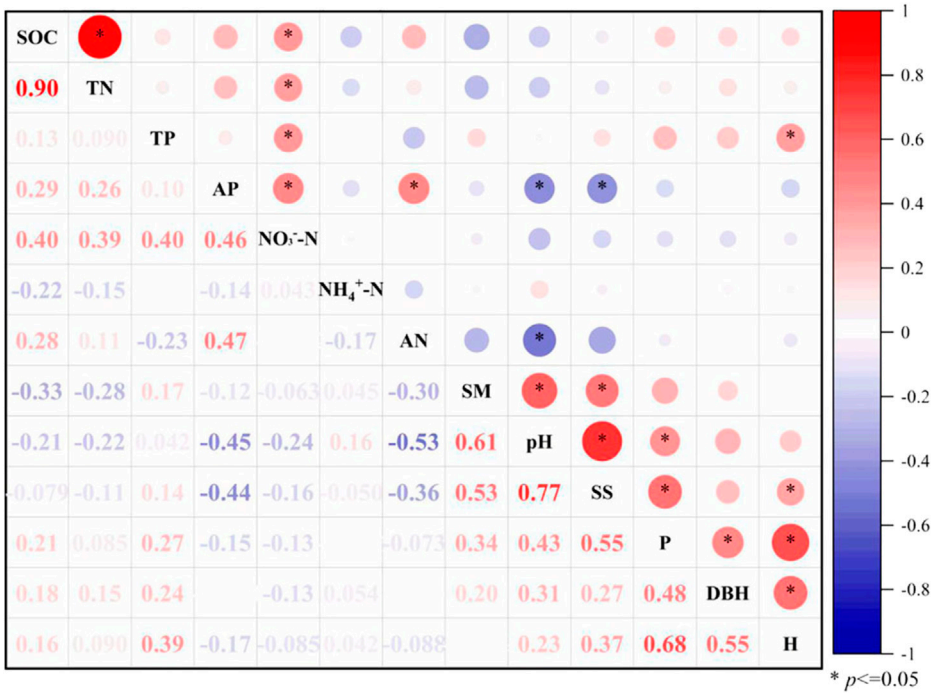

FIGURE 2
Correlation analysis of influencing factors of the 'fertile island' effect of different nutrient contents in *Haloxylon ammodendron*.

Factor analysis of fertile island effect in typical woody plants

As shown in Figure 1, the 'TP-fertile island' effect of *Populus euphratica* was significantly negatively correlated with the soil salt content of the *Populus euphratica* canopy (r = -0.37 and -0.38). The 'AP-fertile island' effect was significantly negatively correlated with the soil water content, pH value, and salt content (r = -0.41, -0.43, and -0.48), and the 'NO_3^--N-fertile island' effect was significantly negatively correlated with the soil pH value and salt content (r = -0.46 and -0.49). There was no significant correlation between the 'fertile island' effect and the plant crown width. The 'fertile island' effect of SOC and TN was significantly positively correlated (r = 0.83), indicating a highly consistent accumulation process and SOC and TN in *Populus euphratica*. The 'fertile island' effect of SOC was significantly positively correlated with the 'fertile island' effect of TP, AP, and alkali-hydrolyzable nitrogen (r = 0.43, 0.40, and 0.41), which indicates that the accumulation of SOC affected the accumulation processes of phosphorus and nitrogen to a certain extent. In addition to DBH and soil salt content, the plant crown width, height, DBH, soil water content, pH, and salt content of *Populus euphratica* were significantly positively correlated.

The 'TP-fertile island effect' of *Haloxylon ammodendron* was significantly positively correlated with the plant height of *Haloxylon ammodendron* (r = 0.39), the 'AP-fertile island' effect was significantly negatively correlated with the soil pH and salinity (r = -0.45 and -0.44), and the 'alkali-hydrolyzable-nitrogen fertile island' effect was significantly negatively correlated with the soil pH (r = -0.53). There were no significant correlations between the 'fertile island' effect and the plant crown width or other influencing factors. The 'fertile island' effect of the SOC and TN was significantly positively correlated (r = 0.90). The SOC, TN, TP, and AP-fertile island effect of the 'NO_3^--N-fertile island' effect are significantly positively correlated (r = 0.40, 0.39, 0.40, and 0.46). The *Haloxylon ammodendron* crown width was significantly positively correlated with soil pH and salinity. The height of *Haloxylon ammodendron* is significantly correlated with soil salinity. There was a significant positive correlation between the soil water content, salt content, and pH (Figure 2).

The 'TP-fertile island' effect of *Nitraria tangutorum* was significantly positively correlated with the crown width and basal diameter of *Nitraria tangutorum* (r = 0.43 and 0.47), the 'AP-fertile island' effect was significantly negatively correlated with the crown width of *Nitraria tangutorum* (r = -0.39), and the 'NO_3^--N-fertile island' effect was significantly negatively correlated with the soil water content and pH (r = -0.44 and

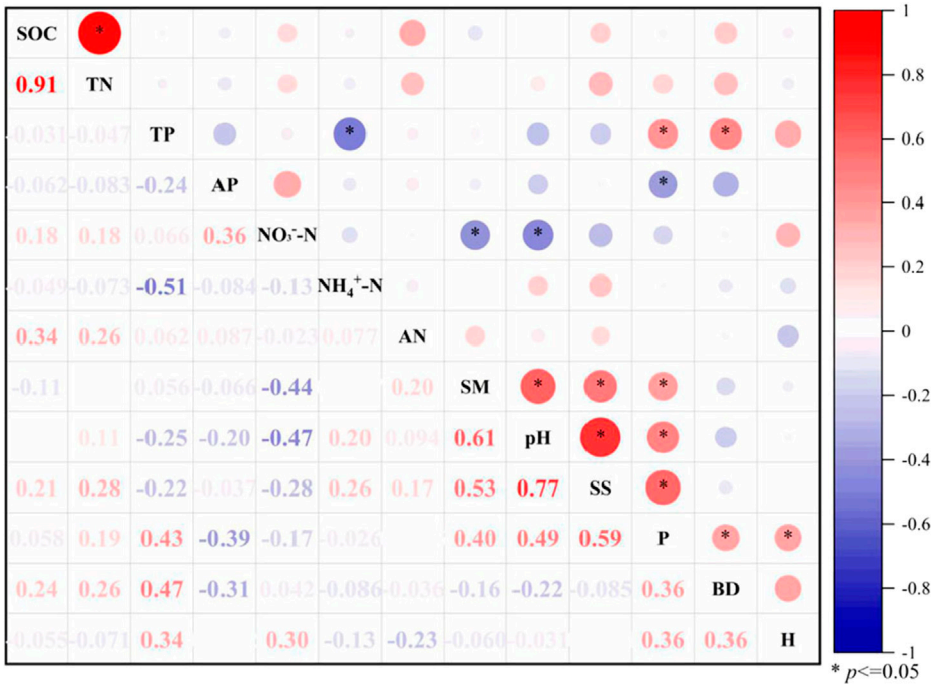

FIGURE 3
Correlation analysis of influencing factors of the 'fertile island' effect of different nutrient contents in *Nitraria tangutorum*.

-0.47). No significant correlation was observed between the nutrient-fertile island effect and the crown width. The 'fertile island' effect of SOC and TN was significantly positively correlated (r = 0.91). The 'NH_4^+-N-fertile island' effect was significantly negatively correlated with the 'TP-fertile island' effect (r = -0.51). The crown width was positively correlated with the soil water content, pH, and salinity. There was a significant positive correlation between the soil water content, salt content, and pH (Figure 3).

Relationship between overall plant nutrient fertile island effect and soil physicochemical properties of bare soil

The analysis of RDA results is shown in Figure 4. The first axis explained 53.84% of the relationship between soil physical and chemical factors and the overall nutrient fertile island effect of plants, and the second axis explained 84.78%. The highest correlation in the first ordination axis was mainly soil NO_3^--N and soil water content, and the highest correlation in the second axis was soil salt content and AN.

This shows that for different species, the first axis mainly reflects the changes in the overall nutrient 'fertile island' effect of plants in soil nitrate nitrogen, water content, and other factors, while the second axis mainly reflects the changes in salt content, alkali-hydrolyzable nitrogen, and other factors. Combining the first two axes, nitrate nitrogen, water content, salt content, and alkali-hydrolyzable nitrogen in bare soil are all soil physical and chemical factors that affect the overall nutrient fertile island effect of plants. In addition, as shown in Supplementary Table S1, the SOC content of bare soil is significantly correlated with the overall nutrient fertile island effect of the three species (p = 0.014). This shows that this environmental factor is the main factor affecting the overall nutrient fertile island effect of species.

Discussion

Differences in the fertile island effect of typical woody plants and their possible influencing mechanisms

In this study, in addition to the TP, we found significant differences in the contents of the SOC, TN, AP, and NO_3^--N in the soil under the canopies and in the bare soil of typical woody plants in arid areas, which was evidence of the 'fertile island' effect in the canopy, which is consistent with the related research (Liu et al., 2016; Cha et al., 2017). *Populus*

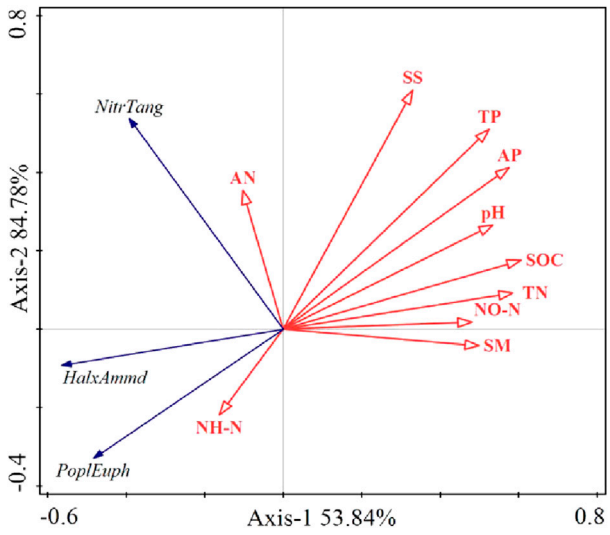

FIGURE 4
Redundancy analysis based on the correlation between soil physico-chemical properties and the overall plant fertile island effect.

euphratica had a 'fertile island' effect for each nutrient, and the contents of the soil SOC and TN under the canopy were higher than those of *Haloxylon ammodendron* and *Nitraria tangutorum*, which is consistent with the research results of Guo et al. (Guo et al., 2020). However, for the other nutrients, we found the highest soil nutrient contents under the crown. On one hand, different plants have different utilizations of soil nutrients in the growth process (Chen et al., 2013; Wang et al., 2020). On the other hand, the biomass and decomposition rates of different plant litters were different (Yang et al., 2012), so the effects of different plants on the soil nutrients were different.

In this study, the plant biological factors and soil physical factors affected the 'fertile island' effect of the TP and AP in the three plants. The reason might be that phosphorus was a limiting factor for plant growth in the study area (Zhang et al., 2019). The main factors that affected the 'fertile island' effect of *Populus euphratica* and *Nitraria tangutorum* were crown width, soil water content, salinity, and pH. The factors that affected the 'fertile island' effect of *Haloxylon ammodendron* were plant height, soil water content, salinity, and pH. The reason for the effect of the canopy width on the 'fertile island' effect might be that the growth of plants under larger canopies and woody canopies increases the threshold wind speed. Therefore, the wind deposits atmospheric dust and windblown sediments from the gaps around plants, which further strengthens the 'fertile island' effect (Yan et al., 2019). Soil water content affects the 'fertile island' effect due to the amount of water content in the soil affecting the content of hydrolase in the soil, which thereby affects the soil nutrient-cycling process, which results in differences in the soil nutrient contents (Zhang et al., 2022). Soil salinization is a common phenomenon in arid areas. Salinity affects the 'fertile island' effect due to salinity and alkaline stress affecting the contents and types of microorganisms and enzymes in the soil, which results in differences in the soil nutrient contents (Cao et al., 2015; Luo et al., 2017).

The main factors that affect the 'fertile island' effect of plants and their possible influencing modes

According to the results, biological factors, such as plant crown width and height, were significantly correlated with soil water content, pH, and salinity. Therefore, we can infer that the formation of the fertile island effect is because of the continuous increase in the biomass during plant growth affecting the animal action around plants, which results in the concentrated distribution of animal action near plants, which is convenient for feeding and avoiding light. These action processes increase the litter, soil microorganisms, and surface residues in the soil under the canopies of plants and affect the physical and chemical properties (Zhong et al., 2017; Li et al., 2018). Researchers have found highly consistent processes and effects of the accumulation of SOC and TN in *Populus euphratica*, *Haloxylon ammodendron,* and *Nitraria tangutorum*. The accumulation of SOC in *Populus euphratica* and *Haloxylon ammodendron* affected the accumulation of phosphorus and nitrogen to a certain extent, which was consistent with the research of Cao et al. (Cao et al., 2016).

Analysis of influencing factors of plant overall nutrient fertile island effect

This study showed that the bare soil SOC was the main factor that affected the overall fertile island effect. Previous studies have shown that the main reason for the accumulation of nutrients under the canopy of plants was the transport of surface soil materials from close distances (C, N, P, and K) (Qu et al., 2015).

However, due to the insufficient collection of influencing factors in this study, we could only predict a part of the fertile island effect. The effects of abiotic factors on the fertile island effect in plants are yet to be studied, especially the effects of biological factors on the fertile island effect. Abiotic processes were insufficient to promote the continuous development of the fertile island, so plant biological processes have more important effects on the fertile island effect (Li et al., 2017). Plant biological processes mainly include animal and microbial processes. The rhizosphere region contains highly diversified microbial communities, and the number of genes is far greater than that of plant genes, which is one of the most complex ecological regions (Mendes et al., 2013). Researchers have found many microorganisms in the rhizosphere, such as bacteria, fungi, oomycetes, nematodes, protozoa, algae, viruses, and archaea (Bonkowski et al., 2009; Buée et al., 2009). In the rhizosphere region, on one hand, plant root exudates attract all kinds of microorganisms to construct rhizosphere microbial groups, and on the other hand, microorganisms regulate the interaction between plants and the environment through various activities, promote plant growth, accelerate the process of plant restoration, and thus improve the ecological environment (Ying, 2019). Therefore, studying microbial and animal processes, and quantifying them into indicators, is important for a more accurate prediction of the plant fertile island effect.

Conclusion

The results showed that soil nutrients under the canopy of *Populus euphratica*, *Haloxylon ammodendron,* and *Nitraria tangutorum* were significantly higher than those under the bare soil, which proved a fertile island effect exists in the canopy of plants.

Among them, *Populus euphratica* had a higher fertile island effect than *Haloxylon ammodendron* and *Nitraria tangutorum* in terms of nutrient content and enrichment rate. Soil water content, salt content, soil pH, and plant crown width were the main factors affecting the nutrient fertile island effect. The influencing factor of the overall nutrient fertile island effect of the three plants is the SOC content in the bare soil. Therefore, in the process of ecological environment protection in arid areas, maintaining the habitat of trees and shrubs can effectively improve soil fertility, slow down desertification in arid areas, and maintain the stability of the ecosystem.

Data availability statement

The original contributions presented in the study are included in the article/Supplementary Material. Further inquiries can be directed to the corresponding authors.

Author contributions

YZ was responsible for article writing and data analysis. QY, YC, and HW were responsible for field investigation and indoor experiment. GL and HW revised the article later.

Conflict of interest

The authors declare that the research was conducted in the absence of any commercial or financial relationships that could be construed as a potential conflict of interest.

Publisher's note

Supplementary material

The Supplementary Material for this article can be found online at: https://www.frontiersin.org/articles/10.3389/fenvs.2022.1034077/full#supplementary-material

References

Allington, G., and Valone, T. (2014). Islands of fertility: A byproduct of grazing? *Ecosystems* 17 (1), 127–141. doi:10.1007/s10021-013-9711-y

Armas, C., Ordiales, R., and Pugnaire, F. I. (2004). Measuring plant interactions: A new comparative index. *Ecology* 85 (10), 2682–2686. doi:10.1890/03-0650

Bomans, A., Cook, A., and Hartley, S., (2021). Bioacoustic monitoring of lower North Island bird communities before and after aerial application of 1080 *N. Z. J. Ecol.* 45. 3435. doi:10.20417/NZJECOL.45.2

Bonkowski, V, Villenave, C., and Griffiths, B. (2009). Rhizosphere fauna: The functional and structural diversity of intimate interactions of soil fauna

with plant roots. *Plant Soil* 321 (1-2), 213–233. doi:10.1007/s11104-009-0013-2

Bowker, M. A., Maestre, F. T., and Mau, R. L. (2013). Diversity and patch-size distributions of biological soil crusts regulate dryland ecosystem multifunctionality. *Ecosystems* 16 (6), 923–933. doi:10.1007/s10021-013-9644-5

Buée, M., Boer, W. D., Overbeek, L. V., et al. (2009). The rhizosphere zoo: An overview of plant-associated communities of microorganisms, including phages, bacteria, archaea, and fungi, and some of their structuring factors. *Plant & Soil* 321 (1-2), 189–212. doi:10.1007/s11104-009-9991-3

Cao, Q., Cao, H. S., Wei, X. L., Karmous, C., and Amara, H. S. (2015). Effects of salt stress on soil microbial biomass carbon and nitrogen and enzyme activity. *J. Soil Water Conservation* 9 (04), 300–304. doi:10.13870/j.cnki.stbcxb.2015.04.054

Cao, Y. F., Ding, J. X., Yu, Y. J., and Shi, J. (2016). Preliminary study on desert shrub Haloxylon ammodendron 'Feidao' in different texture soils. *Soil Sci.* 53 (1), 261–270. doi:10.11766/trxb201508130326

Cao, Yf, Gang, H. B., Yan, L. C., and Li, Y. (2021). Soil texture modulates the intensity of fertile islands through affecting the distribution of shrub fine roots. *J. Arid Environ.* 189, 104503. doi:10.1016/J.JARIDENV.2021.104503

Cha, X. H., Lin, N., Wang, J., and Chen, I. (2017). Nutrient characteristics analysis of 'Feidao' in the oasis-desert transitional zone of southern Xinjiang. *J. Southwest Agric.* 30 (7), 4. doi:10.16213/j.cnki.scjas.2017.7.027

Chen, G. S., Zeng, D. H., Chen, F. S., Fan, Z., and Geng, H. (2004). [A research review on "fertile islands" of soils under shrub canopy in arid and semi-arid regions]. *Appl. Ecol.* 14 (12), 2295–2300.

Chen, S. Y., Yu, H., Feng, Q. S., Xiao, K., and Wang, H. (2013). Study on spatial heterogeneity of soil N/P ratio in Gannan Plateau. *Grassl. J.* 21 (1), 30–36. doi:10.11733/j.issn.1007-0435.2013.01.005

Chen, Y., Yao, Z., Sun, Y., Wang, E., Tian, C., Sun, Y., et al. (2022). Current studies of the effects of drought stress on root exudates and rhizosphere microbiomes of crop plant species. *Int. J. Mol. Sci.* 23 (4), 2374. doi:10.3390/IJMS23042374

Chen, Y. J., Liu, J. Z., Jing, S. H., and Fang, Y. (2018). Research on the phenomenon of 'feidao/gu' under the crown of Tamarix chinensis in the yellow river delta Wetland. *J. Liaocheng Univ. Nat. Sci. Ed.* 031 (1), 56–64. doi:10.19728/j.issn.1672-6634.2018.01.009

Ding, J., and Eldridge, D. J. (2020). The fertile island effect varies with aridity and plant patch type across an extensive continental gradient. *Plant Soil* 254, 173–183. doi:10.1007/s11104-020-04731-w

Fuhlendorf, S. D., and Engle, D. M. (2001). Restoring heterogeneity on rangelands: Ecosystem management based on evolutionary grazing patterns. *Bioscience* 2, 625. doi:10.1641/0006-3568(2001)051[0625:rhorem]2.0.co;2

Guo, X. L., Wang, M. L., Zhao, L. P., and Wang, M. (2020). Effect of Haloxylon ammodendron and Populus euphratica on 'Feidao' in arid areas. *J. Southwest Agric.* 33 (5), 7. doi:10.16213/j.cnki.scjas.2020.5.020

Jiang, Q., He, S. Q., and Gong, Y. B. (2020). Litter nutrient characteristics and potential return ability of different vegetation types. *Resour. Environ. arid areas* 4, 6. doi:10.13448/j.cnki.jalre.2020.108

Li, J., Gilhooly, W. P., Okin, G. S., and Blackwell, J. (2017). Abiotic processes are insufficient for fertile island development: A 10-year artificial shrub experiment in a desert grassland. *Geophys. Res. Lett.* 44 (5), 2245–2253. doi:10.1002/2016GL072068

Li, S., Chen, W., Li, Z., Bu, L., Jin, Z., Wei, G., et al. (2021). Fertile islands lead to more conspicuous spatial heterogeneity of bacteria than soil physicochemical properties in a desert ecosystem. *Catena* 206, 105526. doi:10.1016/J.CATENA.2021.105526

Li, X. F., Zhong, Z. W., Dirk, S., Smit, C., Wang, D., Nummi, P., et al. (2018). Reciprocal facilitation between large herbivores and ants in a semi-arid grassland. *Proc. R. Soc. B* 285 (1888), 20181665. doi:10.1098/rspb.2018.1665

Liu, X. D., Chen, L., Yang, X. G., and Dency, O. (2016). The 'fertilizer island' effect of two kinds of Caragana korshinskii and artemisia lordosis shrub soil nutrients in a desert steppe. *J. Northwest For. Univ.* 31 (4), 8. doi:10.3969/j.issn.1001-7461.2016.04.05

Luo, Q., Wang, Y. G., Deng, C. Y., and Li, S. (2017). Distribution of inorganic carbon in the soil profile of the arid area and its relationship with salinity and alkalinity. *J. Soil Water Conservation* 31 (05), 240–246. doi:10.13870/j.cnki.stbcxb.2017.05.37

Mendes, R., Garbeva, P., and Raaijmakers, J. M. (2013). The rhizosphere microbiome: Significance of plant beneficial, plant pathogenic, and human pathogenic microorganisms. *FEMS Microbiol. Rev.* 37, 634–663. doi:10.1111/1574-6976.12028

Mora, J. L., and Lazaro, R. (2013). Evidence of a threshold in soil erodibility generating differences in vegetation development and resilience between two semiarid grasslands. *J. Arid Environ.* 89 (FEB), 57–66. doi:10.1016/j.jaridenv.2012.10.005

Ochoa-Hues, R., Eldridg, D. J., Delgado-B, M., Soliveres, S., Bowker, M. A., Gross, N., et al. (2017). Soil fungal abundance and plant functional traits drive fertile island formation in global drylands. *J. Ecol.* 106, 242–253. doi:10.1111/1365-2745.12871

Qu, W., Yang, X., Zhang, C., and Chang, P. (2015). Selecting specific PCR primers with MFEprimer. *Methods Mol. Biol.* 24 (04), 201–213. doi:10.1007/978-1-4939-2365-6_15

Reynolds, J. F., Virginia, R. A., Kemp, P. R., de Soyza, A. G., and Tremmel, D. C. (1999). Impact of drought on desert shrubs: Effects of seasonality and degree of resource island development. *Ecol. Monogr.* 69 (1), 69–106. doi:10.1890/0012-9615(1999)069[0069:iodods]2.0.co;2

Wang, H. F. (2020). *Study on plant diversity and ecosystem function in Ebinur Lake Basin*. China: Xinjiang University. doi:10.27429/d.cnki.gxjdu.2020.001436

Wang, J., Ding, J., Li, G., Liang, J., Yu, D., Aishan, T., et al. (2019). Dynamic detection of water surface area of Ebinur Lake using multi-source satellite data (Landsat and Sentinel-1A) and its responses to changing environment. *Catena* 177, 189–201. doi:10.1016/j.catena.2019.02.020

Wang, J., Shi, T., Yu, D., Teng, D., Ge, X., Zhang, Z., et al. (2020). Ensemble machine-learning-based framework for estimating total nitrogen concentration in water using drone-borne hyperspectral imagery of emergent plants: A case study in an arid oasis, NW China. *Environ. Pollut.* 266, 115412. doi:10.1016/j.envpol.2020.115412

Yan, Y., Xu, D., Wang, D., Cai, Y., and Jing, B. (2019). Shrub patches capture tumble plants: Potential evidence for a self-reinforcing pattern in a semiarid shrub encroached grassland. *Plant Soil* 442 (1-2), 311–321. doi:10.1007/s11104-019-04189-5

Yang, X., and Williams, M. (2015). Landforms and processes in arid and semi-arid environments. *Catena* 134, 1–3.

Yang, X. D., Lv, G. H., Tian, Y. H., and Chi, N. (2009). Ecological grouping of plants in Ebinur Lake Wetland nature Reserve, Xinjiang. *J. Ecol.* 12, 2489–2494. doi:10.13292/j.1000-4890.2009.0407

Yang, Y., Ha, S., Sun, B. P., and Xiao, X. (2012). Soil nutrient effects of different vegetation restoration types in the southern margin of Mu Us Sandy Land. *Agric. Sci. Technol.* 28 (8), 1708–1712. doi:10.3969/j.issn.1000-6850.2012.10.007

Ying, M. (2019). Editorial: Biotechnological potential of plant-microbe interactions in environmental decontamination. *Front. Plant Sci.* 10, 1519. doi:10.3389/fpls.2019.01519

Zhang, L., Lv, G. H., and Jiang, L. M. (2019). Analysis of soil driving forces affecting desert plant biomass distribution in Ebinur Lake Basin. *J. Plant Resour. Environ.* 2019(3), 12–18. doi:10.3969/j.issn.1674-7895.2019.03.02

Zhang, X. L., Zhou, J. H., Lai, L. M., and Xia, M. (2019). Leaf traits and ecological stoichiometric characteristics of dominant species in oasis-transition zone-Gobidesert community in the lower reaches of Heihe River. *Appl. Environ. Biol.* 25 (6), 7.

Zhang, Y. L., Lu, Y. X., Yin, B. F., and Chen, R. (2022). Effects of simulated rainfall changes on soil nutrients and enzyme activities in Gurbantunggut Desert. *Ecology* 42 (05), 1739–1749. doi:10.5846/stxb202102170450

Zhao, H. L., Su, Y. Z., and Zhang, T. H. (2002). [Influencing mechanism of several shrubs and subshrubs on soil fertility in Keerqin sandy land]. *Appl. Ecol.* 13 (7), 802–806.

Zhao, R., and An, L. (2021). Plant size of the alpine cushion thylacospermum caespitosum affects soil amelioration at different elevations. *Plant Ecol.* 23, 323–335. doi:10.1007/S11258-020-01108-Y

Zhong, Z., Li, X., Pearson, D., Wang, D., Sanders, D., Zhu, Y., et al. (2017). Ecosystem engineering strengthens bottom-up and weakens top-down effects via trait-mediated indirect interactions. *Proc. R. Soc. B* 284 (1863), 20170894. doi:10.1098/rspb.2017.0894

frontiers | Frontiers in Environmental Science

TYPE Correction
PUBLISHED 15 March 2024
DOI 10.3389/fenvs.2024.1390297

OPEN ACCESS

EDITED AND REVIEWED BY
Niall Patrick Hanan,
New Mexico State University, United States

*CORRESPONDENCE
Hengfang Wang,
wanghf@xju.edu.cn
Guanghui Lv,
ler@xju.edu.cn

RECEIVED 23 February 2024
ACCEPTED 27 February 2024
PUBLISHED 15 March 2024

CITATION
Zhang Y, Wang H, Cai Y, Yang Q and Lv G (2024), Corrigendum: Fertile island effect by three typical woody plants on wetlands of Ebinur Lake, northwestern China.
Front. Environ. Sci. 12:1390297.
doi: 10.3389/fenvs.2024.1390297

Corrigendum: Fertile island effect by three typical woody plants on wetlands of Ebinur Lake, northwestern China

Yabei Zhang[1], Hengfang Wang[1]*, Yan Cai[2], Qi Yang[1] and Guanghui Lv[1]*

[1]Key Laboratory of Oasis Ecology, College of the Ecology and Environment, Ministry of Education, Xinjiang University, Urumqi, China, [2]Student Work Department, Tarim University, Aral, China

KEYWORDS

woody plants, fertile island effect, influencing factors, arid area, Ebinur lake basin

A Corrigendum on
Fertile island effect by three typical woody plants on wetlands of Ebinur Lake, northwestern China

by Zhang Y, Wang H, Cai Y, Yang Q and Lv G (2022). Front. Environ. Sci. 10:1034077. doi: 10.3389/fenvs.2022.1034077

In the published article, there was a spelling mistake in the **title**, **body text**, and **keywords**. The term "fertilizer island effect" has been replaced with "fertile island effect" throughout.

The authors apologize for these errors and state that this does not change the scientific conclusions of the article in any way. The original article has been updated.

Publisher's note

All claims expressed in this article are solely those of the authors and do not necessarily represent those of their affiliated organizations, or those of the publisher, the editors and the reviewers. Any product that may be evaluated in this article, or claim that may be made by its manufacturer, is not guaranteed or endorsed by the publisher.

frontiers | Frontiers in Environmental Science

TYPE Original Research
PUBLISHED 23 September 2022
DOI 10.3389/fenvs.2022.1001984

OPEN ACCESS

EDITED BY
Z. Y. Yuan,
Institute of Soil and Water Conservation (CAS), China

REVIEWED BY
Kai Yue,
Fujian Normal University, China
Yaofeng Wang,
Xinjiang Agricultural University, China
Lei Feng,
Xinjiang Agricultural University, China

*CORRESPONDENCE
Yongdong Wang,
wangyd@ms.xjb.ac.cn

†These authors have contributed equally to this work and share first authorship

SPECIALTY SECTION
This article was submitted to Drylands, a section of the journal Frontiers in Environmental Science

RECEIVED 24 July 2022
ACCEPTED 29 August 2022
PUBLISHED 23 September 2022

CITATION
Chen Y, Zhang S, Li H and Wang Y (2022), Drivers of nutrient content and spatial variability of soil multifunctionality in the topsoil of Kyrgyzstan.
Front. Environ. Sci. 10:1001984.
doi: 10.3389/fenvs.2022.1001984

Drivers of nutrient content and spatial variability of soil multifunctionality in the topsoil of Kyrgyzstan

Yusen Chen[1,2,3†], Shihang Zhang[1,2,4†], Huiliang Li[1,2,3] and Yongdong Wang[1,2,3*]

[1]Xinjiang Institute of Ecology and Geography, Chinese Academy of Sciences, Xinjiang Uygur Autonomous Region, Urumqi, China, [2]University of Chinese Academy of Sciences, Beijing, China, [3]National Engineering Technology Research Center for Desert-Oasis Ecological Construction, Xinjiang Uygur Autonomous Region, Urumqi, China, [4]State Key Laboratory of Desert and Oasis Ecology, Xinjiang Institute of Ecology and Geography Chinese Academy of Sciences, Xinjiang Uygur Autonomous Region, Urumqi, China

Soil nutrient status is a crucial measure of soil fertility, which not only coordinates and provides the nutrients necessary for plant growth, but also stimulates the decomposition of soil humus and biogeochemical cycles. Therefore, understanding the distribution characteristics of soil nutrients in the Kyrgyzstan, while exploring the drivers of their variability, is important for understanding ecological processes and the distribution of soil resources. Simultaneously, the study of the spatial distribution of soil multifunctionality and its drivers across Kyrgyzstan can better elucidate the functions of the entire ecosystem, assist in optimizing the allocation of resources and serve as a reference material for the scientific and rational management of the country's soil ecosystems. In this paper, We have used field sampling data from Kyrgyzstan, to examined the geographic variability and distribution of soil nutrients and soil multifunctionality within different soil depths, as well as the drivers in the country, using a combination of factor analysis and structural equation modeling (SEM). Findings indicated: (1)The topsoil of Kyrgyzstan (0–30 cm) stores 4.24 ± 0.59 Pg of SOC, 0.33 ± 0.06 Pg of total nitrogen (TN), 0.31 ± 0.03 Pg of total phosphorus (TP), and 5.12 ± 1.84 Pg of total potassium (TK). The nutrient reserves of various land-cover categories vary greatly across the nation, with grasslands accounting for the largest reserves (40%) but urban areas allocating the smallest proportion (0.3%). (2): the analysis revealed that using the linear or nonlinear fitting equations, the majority of soil nutrients exhibited a strong correlation with each other and also environmental parameters; (3): in Kyrgyzstan, soil multifunctionality varied substantially from −0.63 to 2.30 across regions. (4): according to the SEM results, NPP, wind speed (VS), MAP, longitude (Lon), SWC, and pH directly affected soil multifunctionality. In addition, several indirect effects of ST, MAT, Sard, and latitude (Lat) on soil multifunctionality were observed. Lon, map, SWC, and pH also had various direct and indirect impacts on soil multifunctionality. The findings of this study shed light on the functions of the entire soil ecosystem in the Kyrgyz Republic that help better predict the effects of environmental changes on ecosystem multifunctionality in drylands and provide a scientific basis for rational utilization

of soil resources, efficient management of dryland soils, and prevention of land productivity decline in the country.

KEYWORDS

soil Nutrients, SMF, Drivers, spatial distribution, structural equation modeling

1 Introduction

Soils participate in and regulate the nutrient cycles within ecosystems, with soil nutrients being one of the most important soil characteristics (Sterner and Elser, 2017). Soil nutrient status is a significant indicator of soil fertility since it not only regulates the delivery of the nutrients required for plant development but also promotes the breakdown of soil humus and biogeochemical cycles (Verhoeven et al.,. 2009). soil organic carbon (SOC), nitrogen (N), and phosphorus (P) make up the majority of the soil nutrients and are essential to plant development and different physiological processes (Meersmans et al., 2008). Plaza et al. (2018) reported that global reserves of soil C, N, and P in the soil surface layer (0–30 cm) were more than 50% of those in the whole soil layer (0–100 cm) (Plaza et al., 2018). For instance, soil organic carbon (SOC) is not only an essential component of soil fertility, but also a vital contributor to agricultural productivity and quality, as well as having important supporting/regulatory functions for ecosystem services. Soil nitrogen and phosphorus affect soil characteristics, plant development (Quilchano et al., 2008), and soil microbial activity (Hati et al., 2008). Compared to other soil nutrients, soil nitrogen and phosphorus are regarded as the fundamental nutrients that most frequently limit soil productivity (Giesler et al., 2002). Soil C, N, and P are the three most abundant elements in living organisms, and their ratios have been identified as important indicators of ecosystem structure and function at macroscopic scales, while also being hypothesized to reflect the composition of living organisms within the ecosystem (Rodríguez et al., 2009). Potassium (K) stimulates photosynthesis, and also enhances plant economic water usage, among other roles, and elemental K has garnered substantial scholarly attention in recent soil nutrient research (Guo et al., 2000). plaza et al. (2018) assessed global soil C, N, and P stocks in the global soil (0–30 cm) and discovered that the elemental stocks in the soil surface layer (0–30 cm) comprised more than fifty percent of the overall soil layer (0–100 cm) (Plaza et al., 2018). In order to achieve integrated management of soil functions and maximize the ecological service value of soil, it is crucial to examine the spatial distribution pattern of nutrients in the soil surface layer, estimate the content of nutrients in the surface layer, and investigate the chemometric relationships between elements. Therefore, the emphasis of this research is on the state of nutrients in the surface soil in Kyrgyzstan.

Soil nutrients are susceptible to intricate scale-dependent relationships and geographical variability, as well as complex linkages between environmental variables that affect the multi-scale variability of soil nutrients (Li et al., 2003). Studies have shown that soil nutrients respond to environmental factors such as soil pH, ambient temperature, and average annual precipitation (Miller et al., 2004; Tian et al., 2018). Liu et al. (2013) demonstrated that land use, precipitation, and temperature had significant effects on both STN and STP; Brovelli et al. (2012) analyzed the dynamics of soil carbon and nitrogen in riparian soils and discovered that soil carbon and nitrogen content varied on a temporal scale in response to changes in climatic conditions and the uptake of inputs from surface vegetation; Wang et al. (2016) demonstrated that precipitation and vegetation changes had significant effects on STN and STP. Existing approaches to assess the multifunctionality of ecosystems include the average approach (Maestre et al., 2021), functional replacement across species (Guo et al., 2017), the single thresholding method (Zavaleta et al., 2010), the multi-threshold method (Byrnes et al., 2014), and factor analysis that have both benefits and drawbacks. In this study, we first calculated the soil versatility index using the average approach and component analysis, then we combined soil pH, soil water content (SWC), soil temperature (ST), mean annual temperature (MAT), mean annual rainfall (MAP), net primary plant productivity (NPP), and sunshine radiation (Sard) with soil nutrients. Finally we performed correlation analysis and adopted the structural equation modeling (SEM) approach. The goal of this study was to investigate the determinants of geographical variation in nutrient concentrations in the topsoil of Kyrgyzstan to expand the related soil research in Kyrgyzstan and eventually benefit local agricultural production.

Ecosystem multifunctionality (EMF) is the capacity of an ecosystem to simultaneously maintain numerous ecosystem functions and services, i.e. the ecosystem's overall function (Zavaleta et al., 2010). Increasingly, researchers are utilizing Soil Multifunctionality (SMF) to describe the multifunctionality of the entire ecosystem (Ding and Eldridge, 2021) Soils play an important role in the terrestrial ecosystem as a whole (Bui and Henderson, 2013); hence, more study on soil multifunctionality will lead to a better understanding of the integrated service capacity of soils. SMF is geographically influenced by various climatic elements (such as precipitation and its seasonality, soil dryness, and soil moisture) and soil characteristics (such as pH and sand content), and increases with plant or soil microbial diversity (Ding and Eldridge, 2021). Quantifying the national SMF of Kyrgyzstan and its drivers can consequently give a reference for the scientific and rational management of the entire national soil environment.

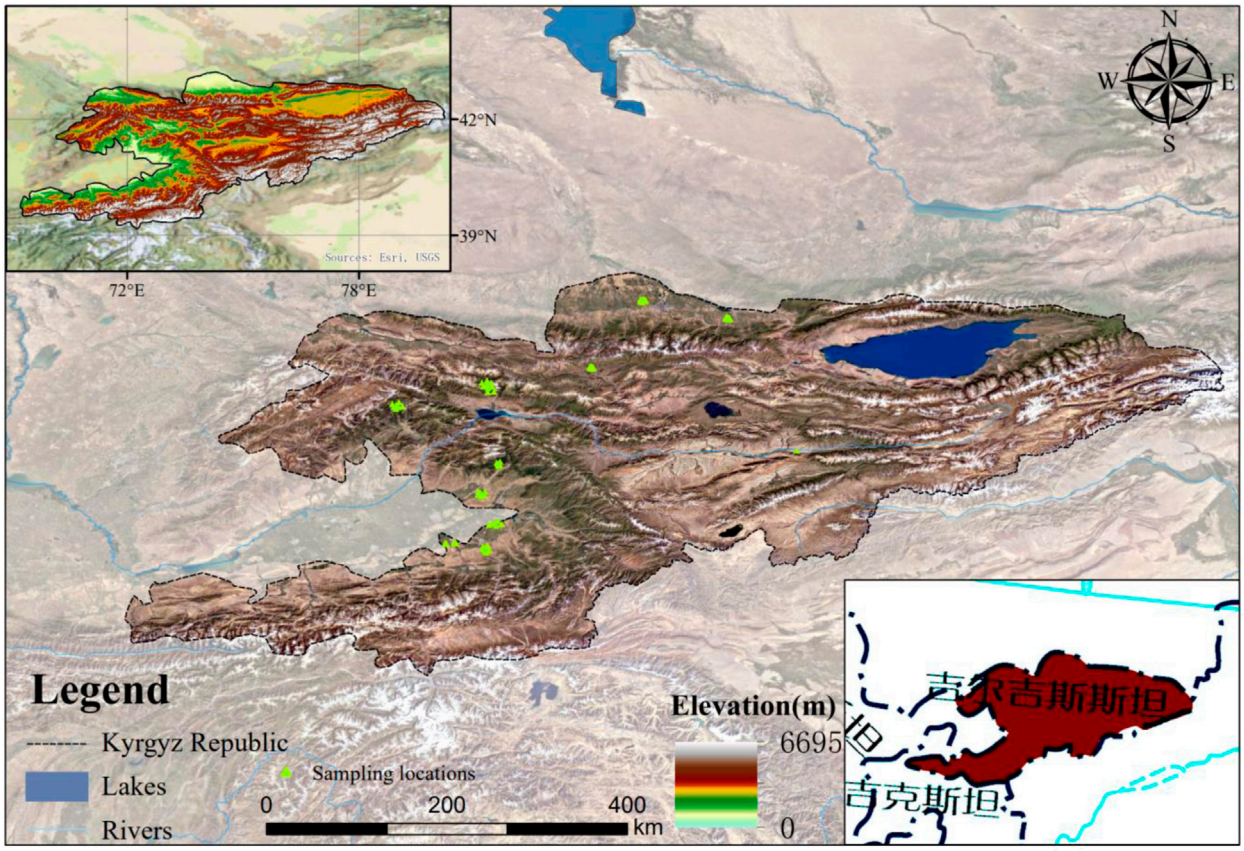

FIGURE 1
Overview of the study area. The map is based on the standard map No. GS (2021)5453 downloaded from the map technology review center of Ministry of natural resources, the standard map is not modified.

This study addresses the following scientific concerns using field measurements of soil nutrients in Kyrgyzstan from 2011 to 2015, as well as data on their physical and chemical qualities and meteorological environment. 1) What are the nutrient stocks, spatial distribution patterns, and influencing factors of Kyrgyzstan's surface soils (0–30 cm)? 2) What are the spatial variability characteristics and driving elements of the SMF? On the basis of the aforementioned scientific concerns, we hypothesize that 1) the distribution of soil nutrients and SMF in Kyrgyzstan is very spatially diverse and 2) temperature and precipitation are likely to be the primary causes of regional variability in nutrients and SMF.

The analysis of the spatial relationships between climate, soil, and plant and soil multifunctionality provides a foundation for local ecosystem management to improve local land-cover efficiency and a reference for the efficient and rational management of soil resources and ecosystems across the nation.

2 Materials and methods

2.1 Overview of the study area

The Kyrgyz Republic is situated in the center of the Eurasian continent (39.18°–43.24°N, 69.23°–80.20°E) and has an area of 199,900 square kilometers, bordering China, Uzbekistan, Kazakhstan, and Tajikistan (Figure 1). The region is mountainous, with the highest peak, called Tomur, rising to approximately 7,000 m, and Issyk-Kul valley framed by mountains, with the lowlands comprising only 15% of the total land area. The average annual precipitation varies between 200 and 800 mm, and the climate is characteristic of the continental temperate zone. The country has abundant water resources, pastures, and arable land, with grasslands constituting 38.5% of the national territory. Agricultural land comprises 19.8% of the total land area.

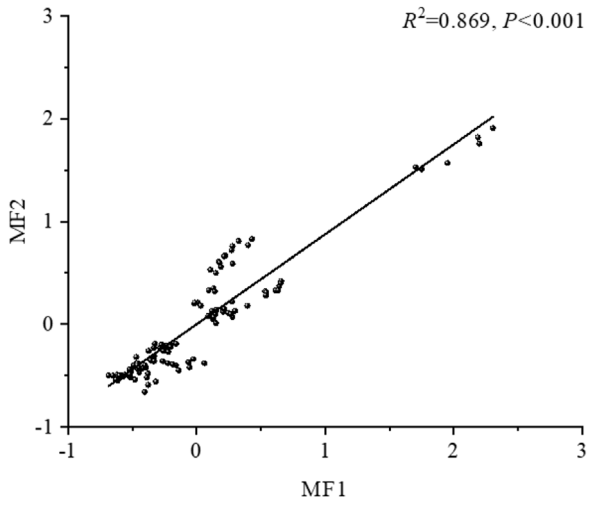

FIGURE 2
Indices of soil multifunctionality derived from the two quantification techniques; MF1: Multifunctionality index calculated using the average approach; MF2: Multifunctionality index calculated using the factor analysis approach.

2.2 Data sources

2.2.1 Surface soil nutrient data

Field surveys and laboratory tests were used to gather data on the nutrient contents of the soil surface. During the field study conducted in Kyrgyzstan between 2011 and July 2015, 136 sampling locations were selected, and land-cover types were collected. The soil pH, organic matter fast-acting potassium (AK) were analyzed for 159 soil samples, and eight ions were evaluated for 41 samples. Data were compiled using 114 soil samples.

2.2.2 Environmental data

The Terra Climatic is a global dataset (http://doi.org/10.1038/sdata.2017.191) of monthly climate water balance and land surface temperature from the University of Idaho. It consists of meteorological data such as precipitation, maximum and minimum temperatures, and variations in pressure of water vapor, wind speed, and solar radiation. The aforementioned meteorological data were obtained from the cloud computing platform (GEE) for reprojection and cropping procedures.

Land cover data were obtained from ESA's global land cover database with coverage at 300-m spatial resolution from 1992 to 2020 (https://cds.climate.copernicus.eu/cdsapp#!/dataset/satellite-land-cover), which classifies the global land surface into 22 categories based on the UN FAO Land Cover Classification System (LCCS).

2.2.3 Sampling and determination of quantitative soil functional indicators

Based on the study conducted by Maestre et al. (2012), thirteen soil functional indicators related to four ecosystem processes (C, N, P, and K) were chosen to assess the multifunctionality of soil in the research area (Maestre et al., 2012). These markers were found to have a close relationship with the cycling and content of carbon, nitrogen, and phosphorus in the ecosystem (Dai et al., 2020; Maestre et al., 2021). These soil indicators essentially reflect different processes of ecosystems, including carbon, nitrogen, and phosphorus sequestration, soil and water conservation, and animal hosting (Chytrý et al., 2010). The average approach and the factor analysis developed by Hooper and Vitousek (1998) were used to calculate the soil multifunctionality index in this study (Hooper and Vitousek, 1998). The results of these two techniques (Figure 2) indicated that the two multifunctionality indices (MF1 and MF2) were quite comparable ($R^2 = 0.866$, $p < 0.001$), and both had significant positive relationships with eight single soil functions (Table 1).

2.3 Calculation of nutrient density and content of the surface soil

The mean value method was first proposed by Hopper and Vitousek (Hooper and Vitousek, 1998), which converts the measured values of ecosystem functions in a sample, then standardises these functional indicators, and finally the multifunctionality index is the calculation of the mean value of each co-functional value to represent it. quantitative characterisation of multiple ecosystem processes, calculated as follows:

$$\mathrm{MF_a} = \frac{1}{F}\sum_{i=1}^{F} g\left(r_i\left(f_i\right)\right) \quad (1)$$

where MFa denotes ecosystem multifunctionality, f_i denotes the measured value of function i, r_i is the mathematical function that converts f_i into a positive value, g denotes the normalisation of all measured values and F denotes the number of functions measured.

Based on the calculation of the mean method, some scholars later began to experiment with factor analysis to obtain similar multifunctionality indices. The thinking behind this calculation is that the parameters of these functional indicators are first downscaled for factor analysis, and then each factor score is obtained, and then each factor score is used to express multifunctionality, and this method can, to a certain extent, measure the trade-offs between the various functions:

$$\mathrm{MF_a} = \sum a_i z_i \quad (2)$$

TABLE 1 Correlation between individual soil functions and soil multifunctionality indices.

	C	N	P	K	C:N	C:P	C:K	N:P	N:K	P:K	AN	AP	AK	MF1	MF2
MF1	0.964**	0.947**	0.387**	0.233*	-0.116**	0.479**	0.831**	0.635**	0.831**	0.402**	0.725**	0.770**	0.652**	1	0.933**
MF2	0.835**	0.870**	0.644**	0.501**	-0.292**	0.244**	0.610**	0.427**	0.673**	0.417**	0.599**	0.907**	0.781**	0.933**	1

where,

$$Z_i = \sum W_{ij} x_{ij} \tag{3}$$

In the above equation, MFa denotes the ecosystem multifunctionality index, z_i is the factor score, ai is the variance contribution of each factor, z_{ij} is the standardised value of variable i at the factor j, and w_{ij} denotes the factor score coefficient of variable i at the factor j.

The nutrient element contents of the soil layers were first determined. Using the depth of each layer as a weighting factor, the average values of physicochemical parameters of the soil profile were determined. Tian et al. (2006) calculated the nutrient density (Density) for a single layer in the soil profile as follows (Tian et al., 2006

$$\boldsymbol{Density} = \frac{\sum_{i=1}^{n} \boldsymbol{B_i D_i C_i}}{\sum_{i=1}^{n} \boldsymbol{D_i}} \tag{4}$$

Where B_i (Bulk density) represents the soil water capacity expressed in g/cm^3 in various places; Di (Depth) denotes the soil depth in cm, and C_i (Content) signifies the nutrient content of the horizontal layer of soil (%). Using spatial interpolation and the usual kriging technique, a geographical distribution map of soil nutrients for Tajikistan was drawn. The raster layer was then formed using the surface with a resolution of 300 m × 300 m, a density value of $Density_i$ (kg/m^2), and an area value of $Area_i$ for each grid square (m^2). Nutrient content was calculated using the following formula (Liu et al., 2011):

$$\boldsymbol{Nutrient\ Storage} = \sum_{i=1}^{n} \boldsymbol{Density_i Area_i} \tag{5}$$

2.4 Statistical analysis

In this study, the relationships between soil pH, soil water content (SWC), soil temperature (ST), mean annual temperature (MAT), mean annual rainfall (MAP), net primary productivity (NPP), mean annual wind speed (VS), the difference in saturated atmospheric pressure (VPD), solar radiation (Sard), and soil nutrients were determined using correlation analysis, and a structural equation modeling (SEM) method was used to identify the drivers for spatial variability in surface soil nutrients in Kyrgyzstan.

Initially, a descriptive statistical analysis of the soil nutrient contents and other related environmental indicators was performed for all regions of the country; the kriging interpolation was used in ArcGIS 10.2 to investigate the spatial distribution of nutrient contents; the correlation analysis of soil nutrients and environmental factors was performed using the "corrplot" package under R version 4.1.1. Different functional models, including linear, quadratic, power, etc. that best fit the SOC, TK, TP, and TK were selected using the "Lavaan" package in R version 4.1.1. The best-fit model selection was based on the model's AIC value; the Origin (version 2021) was used to create simple scatter plots, bar charts, 3D pie charts, etc.

3 Results

3.1 Descriptive statistics of soil nutrient contents and environmental factors

Table 2 shows the changes in soil nutrient contents and environmental factors at representative sample locations in Kyrgyzstan. The mean values for SOC, TN, TP, TK, AN, AP, and AK were 14.80 g/kg, 1.25 g/kg, 0.96 g/kg, 17.88 g/kg, 51.71 mg/kg, 12.84 mg/kg, and 216.18 mg/kg, respectively. The total coefficients of variation (CVs) for all nutrients varied from 0.44 to 0.84, demonstrating a rather substantial geographical variation in soil nutrient concentrations across various locations. The values of mean annual precipitation (MAP) and mean annual temperature (MAT) at each sampling point of the region were 414.81 mm and 6.32°C, respectively, and the coefficient of variation (CV) of MAP was 0.260, while that of MAT was 0.78, indicating that the region has small variations in MAP but large variations in MAT across space. The mean values of VS and Sard were 0.11 and 0.03, respectively, and their CVs were low, indicating the minor variations in VS and Sard throughout the area. The mean values of VS and Sard were 0.11 and 0.03, respectively, with both having modest CV values, showing that regional variations in VS and Sard were negligible. The soils in this region have a mean pH value of 7.82 and a minimum pH value of 6.89, indicating that they are mostly neutral and moderately alkaline.

TABLE 2 Descriptive statistics of soil nutrient contents and environmental factors.

Parameter	MAT	MAP	VS	Sard	pH	SOC	TN	TP	TK	AN	AP	AK
MAX	12.97	726.40	2.37	192.56	7.82	49.12	5.02	2.77	44.13	162.60	44.50	532.00
MIN	−1.23	246.00	1.43	175.46	6.89	5.97	0.26	0.26	9.89	10.80	3.10	78.00
Mean	6.32	414.81	1.71	186.13	7.37	14.80	1.25	0.96	17.87	51.71	12.84	216.16
CV	0.78	0.26	0.11	0.02	0.03	0.58	0.71	0.58	0.44	0.59	0.84	0.47
SD	4.95	107.85	0.18	4.06	0.19	8.65	0.88	0.56	7.82	30.63	10.77	101.88
SE	0.04	0.95	0.002	0.04	0.002	0.08	0.01	0.01	0.07	0.27	0.09	0.89

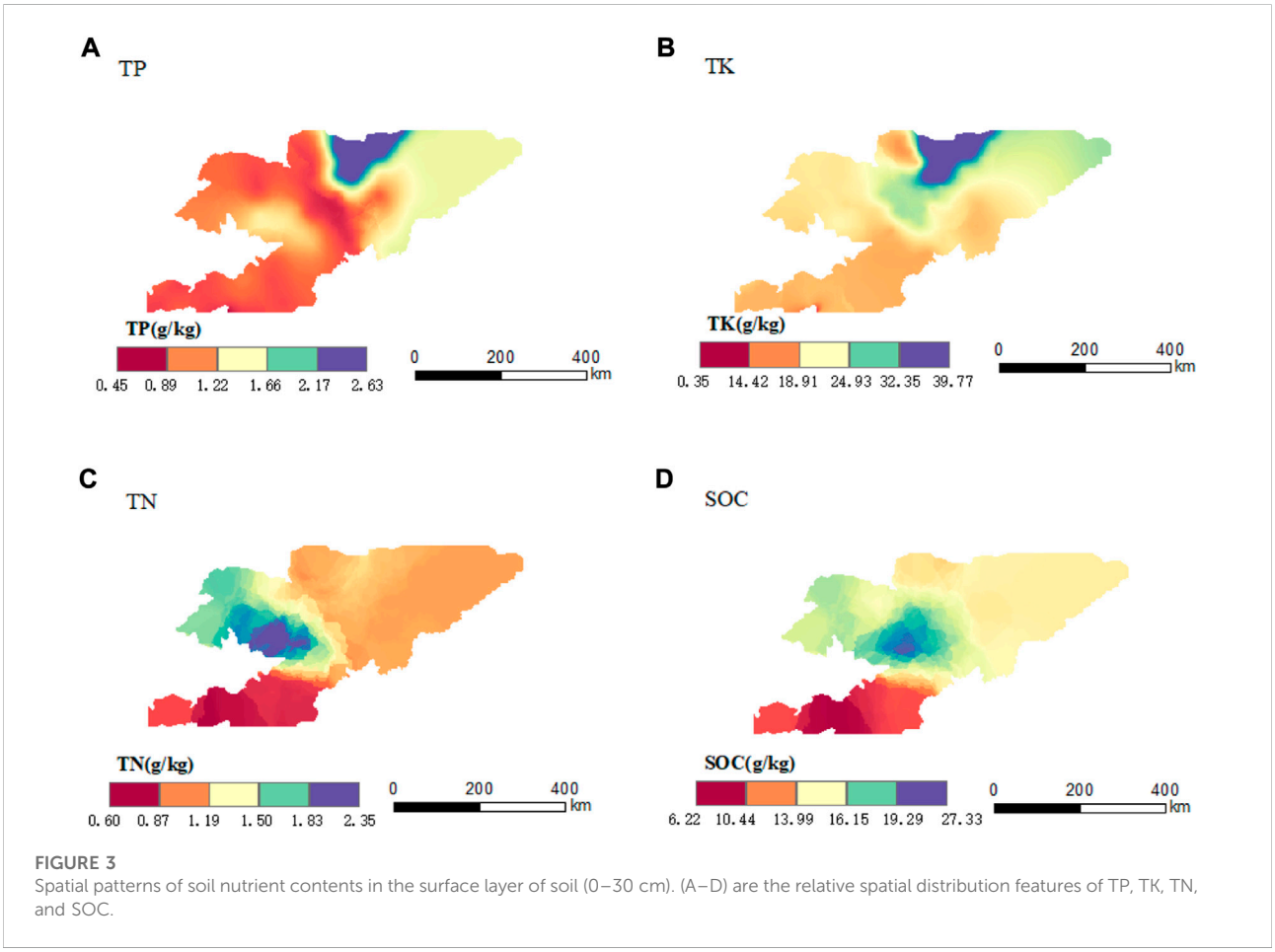

FIGURE 3
Spatial patterns of soil nutrient contents in the surface layer of soil (0–30 cm). (A–D) are the relative spatial distribution features of TP, TK, TN, and SOC.

3.2 Patterns of the spatial distribution of soil nutrient stocks and concentrations in surface soil (0–30 cm)

The average SOC density of surface soil in Kyrgyzstan was 18.25 ± 1.29 kg/m^2, with a content capacity of 4.24 ± 0.59 Pg; the average TN density of surface soil was 1.51 ± 0.24 kg/m^2, with a content capacity of 0.33 ± 0.06 Pg; however, the average TP density was 1.29 ± 0.11 kg/m^2, with a content capacity of 0.31 ± 0.03 Pg, and the average TK density was 23.98 (Figure 3).

Based on the optimal spatial interpolation of SOC, TN, TP, and TK for the entire soil surface in Kyrgyzstan using the ordinary kriging method, the spatial distribution of SOC, TN, TP, and TK contents in soil was mapped, with the SOC content within the range of 13.99–16.15 g/kg and an average of 14.80 g/kg. The average concentrations of TP and TK in the study area were 0.96 g/kg and 17.87 g/kg, ranging from 0.89 to

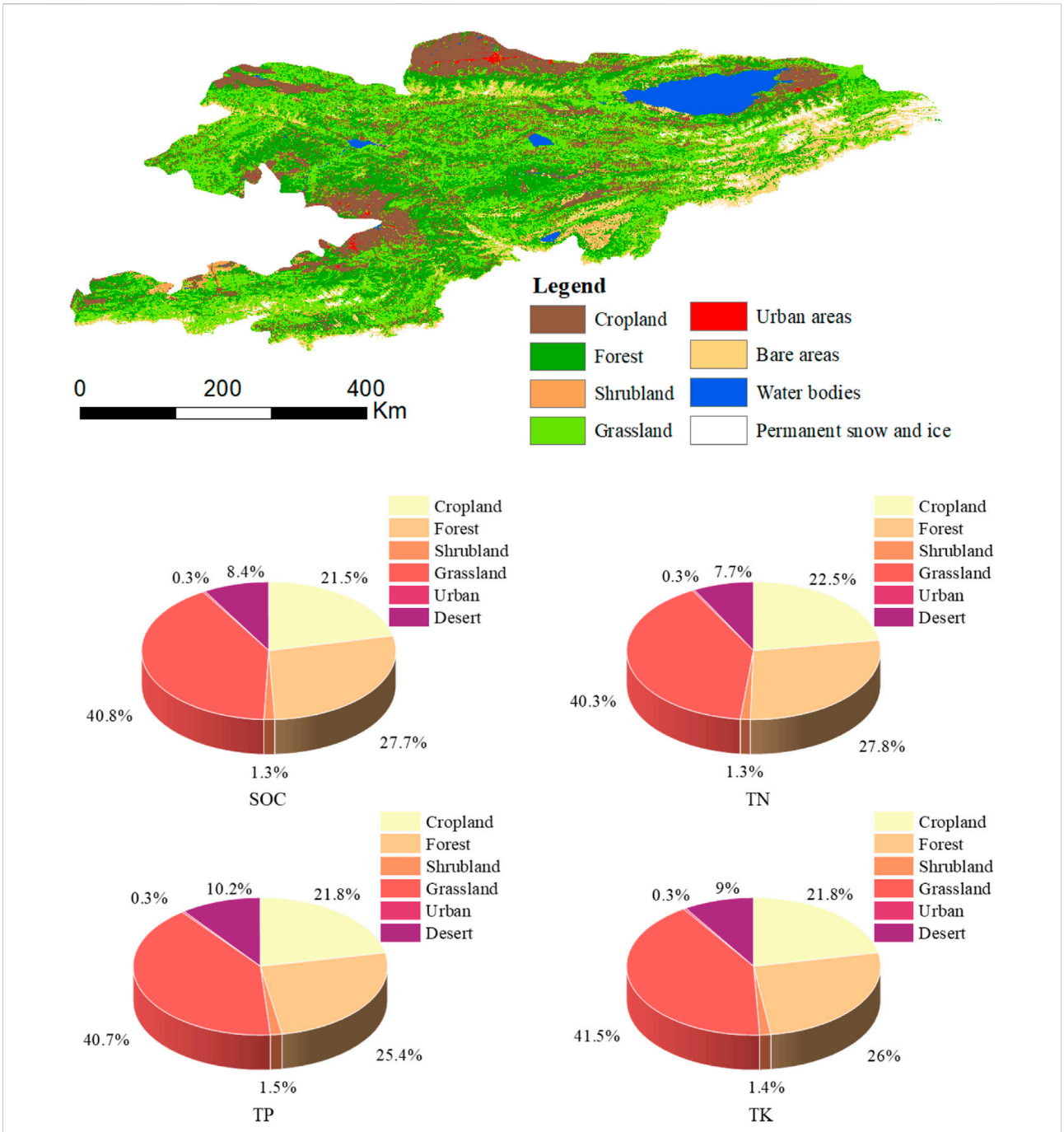

FIGURE 4
Maps of various land-cover types and proportions of nutrient stocks in each land-cover type in Kyrgyzstan.

1.66 mg/kg and 18.91–24.93 mg/kg, respectively, in the whole region. The center of the nation had the highest SOC and TN contents, whose geographic distribution had a high degree of similarity; the Northeast region had the highest contents of TP and TK, whose spatial distribution had a high degree of similarity.

3.3 Proportions of soil nutrient stocks in various land-cover types

To better elucidate the spatial distribution features of soil nutrient contents under various land-cover types, the entire Kyrgyzstan country was categorized into six land-cover types,

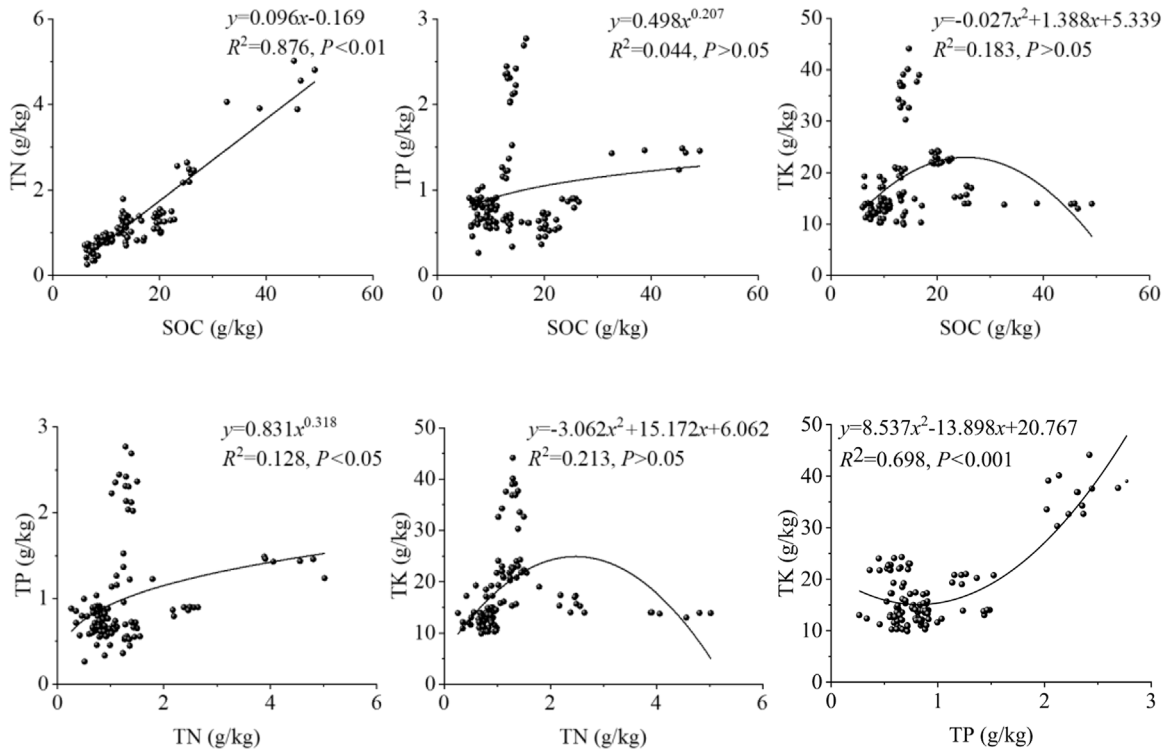

FIGURE 5
Correlations between soil C, N, P, and K contents.

TABLE 3 Correlation coefficients between soil nutrients.

Parameter	SOC	TN	TP	TK	AN	AP
TN	0.936**					
TP	0.177	0.276**				
TK	0.109	0.072	0.758**			
AN	0.750**	0.768**	0.105	0.006		
AP	0.634**	0.658**	0.702**	0.594**	0.320**	
AK	0.503**	0.580**	0.584**	0.373**	0.173	0.782**

Note:**$p < 0.01$.

including grassland, forest, urban, agricultural land, bush, and desert, based on ESA's "Land cover categorization" (see Figure 4, in which permafrost and water areas were not determined). ArcGIS 10.2 was used to calculate the area of each land-cover type, which was paired with data on the nutrient contents of each land-cover type to estimate the nutrient values in these six land-cover categories (Figure 5). As the nutrient densities of soils in various land-cover types considerably varied, so the area of each land-cover type; thus, the soil nutrient stocks in various land-cover types also varied considerably. Among the reserves of various land-cover types, grassland allocated the largest proportion (40%), while urban had the lowest proportion, approximately 0.3%, and the combined nutrients of agriculture, forest, and scrub accounted for approximately 50% of the overall reserves (Figure 4).

3.4 Interactions between soil nutrient contents and environmental variables

Except between SOC and TP, TK, TN, and TK, AN and TP, and TK and AK, there were significant relationships between the contents of most nutrients (Table 3).

The relationship between soil nutrient contents and environmental variables is shown in Figure 6. Overall, most environmental parameters were substantially associated with the contents of soil nutrients. SWC and NPP were substantially related to all seven nutrients. The linear and nonlinear fitting equations revealed (Figure 5) that soil SOC had a highly significant linear relationship with TN, while soil TN had a substantial relationship with TP, and soil TP had a highly significant quadratic relationship with TK.

There was a strong link between soil SOC and all environmental parameters except for VS Only MAP, SWC, VPD, and NPP were substantially related to soil TN levels.

10.3389/fenvs.2022.1001984

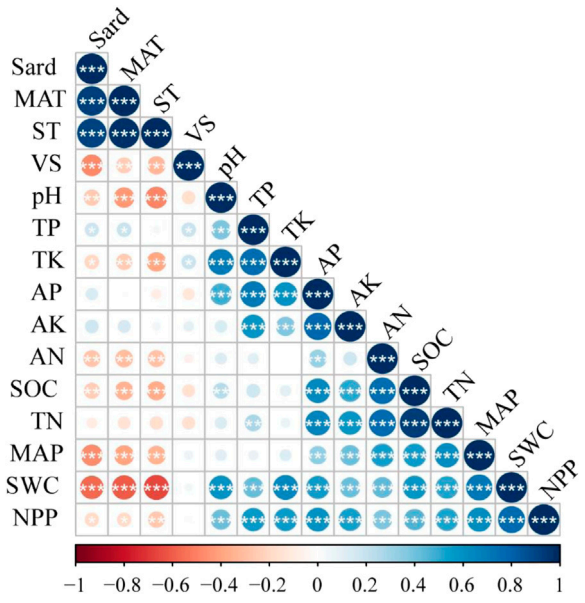

FIGURE 6
Heat map depicting the relationship between soil nutrients and environmental variables.

With the exception of MAP and ST, all environmental parameters were highly significantly linked to soil TP. There were no significant relationships between soil TK, MAP, and VPD. AN demonstrated very substantial associations with the majority of environmental factors, except for pH. There was a high degree of similarity between AP and AK and environmental parameters, exhibiting the correlations between soil nutrients and all environmental factors except for pH (Table 4).

Note: Srad represents solar radiation; MAT stands for mean annual temperature; MAP signifies mean annual precipitation; ST denotes soil temperature; VS stands for mean wind speed at 10 m height; pH represents soil pH; TP: total phosphorus in the soil; TK: total potassium in the soil; AP: fast-acting phosphorus in the soil; AK: fast-acting potassium in the soil; AN: fast-acting nitrogen in the soil; SOC: soil organic carbon; TN: total nitrogen; SWC: soil water content; NPP: net primary productivity.

3.5 The spatial variability of soil multifunctionality by influencing soil properties

Throughout Kyrgyzstan, the soil multifunctionality of soils was spatially heterogeneous (Figure 7), with soil multifunctionality indices ranging from -0.63 to 2.30. The soil multifunctionality values ranged from -0.63 to -0.20, comprising approximately 22.46% of the country's total land area; soil multifunctionality values ranged from -0.20 to 0.16, accounting for approximately 50.40% of the country's total land area; soil multifunctionality values in were within the range of 0.16–0.43, allocating approximately 20.50% of the country's total land area. soil multifunctionality values ranged from 0.43 to 0.77, which comprised approximately 4.18% of the country's land area encompassing the smallest land area, accounting for approximately 2.47% of the nation's land area, with soil multifunctionality values within the range of ~0.77–2.30. From west to east, the soil multifunctionality index in the region generally increases and then decreases, with the highest and lowest soil multifunctionality indices in the central region and the southwest and northwest directions, respectively.

3.6 Relationships between environmental variables and soil multifunctionality

SEM analysis results revealed that the model explained 31% of soil multifunctionality (Figure 8). NPP, SWC, MAP, and pH presented direct beneficial effects on soil multifunctionality, with loadings of 0.29***, 0.33**, 0.32**, and 0.17*, respectively, whereas VS and Lon exerted direct negative effects, with loadings of -0.2* and -0.36*, respectively.

In addition, indirect effects of ST, MAT, Sard, and Lat on soil multifunctionality were detected. Lon, MAP, SWC, and pH had various direct and indirect impacts on soil multifunctionality. As shown in Figure 8, in addition to their direct beneficial effects on soil multifunctionality, the soil indicators SWC and pH also had a favorable effect on soil multifunctionality through modulation of NPP, with loadings of up to 0.19** and 0.41**, respectively.

TABLE 4 Average AIC values of the different fitting results.

Models/parameters based on AIC values	SOC-TN	SOC-TP	SOC-TK	TN-TP	TN-TK	TP-TK
Linear functions	102.5	261.3	200.3	230.3	210.3	214.2
Quadratic functions	190.3	213.6	160.5	210.6	170.3	150.3
Exponential functions	200.8	230.8	190.6	176.5	223.6	203.6
Power functions	210.2	202.6	213.1	220.4	210.3	241.3

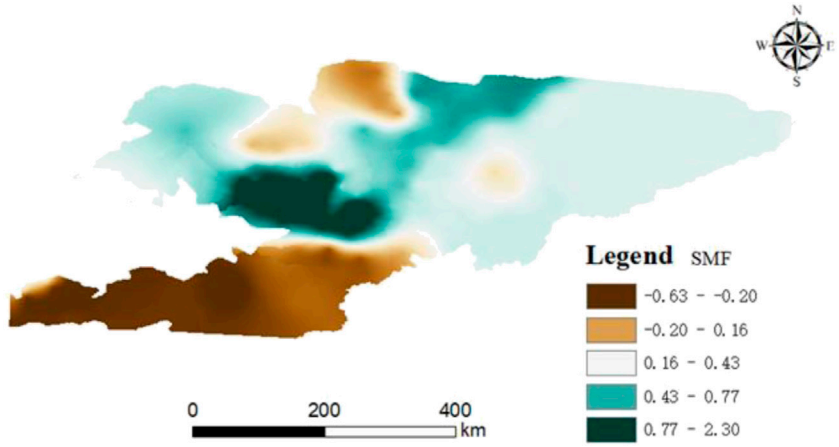

FIGURE 7
Maps of the spatial variability of soil multifunctionality.

The standardized total effects (based on the sum of direct and indirect effects derived from SEM) indicated that MAT, VS, ST, and Lon had a negative relationship with soil multifunctionality, whereas there were positive relationships between all other variables and soil multifunctionality (Figure 9).

4 Discussion

The SOC concentration reflects in part the formation process and fertility level of the soil (Xiong and Li, 1990), and the SOC content of the research area's soil is comparatively high at 14.80 g/kg. N is the most limiting element for plant development (Liu et al., 2017) and also the essential nutrient for all organisms (Galloway et al., 2004), and soil available nitrogen (AN) directly influences the uptake and absorption of other nutrients by nitrogen-fixing plants (Dai et al., 2020). The study area is rich in nitrogen, with 1.25 g/kg of TN and 95.9 mg/kg of AN. P is an essential nutrient element for plant growth, mostly derived from the mineralization of decomposed organic matter and weathering of soil mineral particles; P deficiency may be prevalent in some temperate locations due to its low biological efficiency (Fisher and Dan, 2000). Soil TP content in the study area was high (0.96 g/kg); AP is an important indicator of the soil phosphorus supply capacity and risk of P loss (Zhang and Wu, 2021), with the content of 12.84 mg/kg, marking the study area as the P-rich area; K is an essential element for plant growth and development and can promote photosynthesis of plants, which leads to greater production of compounds, particularly starch; AK content was 0.1–0.2%.

The primary source of soil nutrients is the weathering of minerals in natural settings, but the intensity of human activities and the extent of their impact under various land-cover types are also significant factors influencing soil nutrients. Different land-cover types modify the soil microhabitat, resulting in creating distinct nutrient concentration trends (Zhao et al., 2018). Soil nutrient levels vary dynamically with land-cover and land management approaches, especially abrupt land-use/land cover changes (Gross and Harrison, 2019). In this study, both the soil nutrient concentrations and the land cover area under various land-cover options varied greatly. Grasslands constitute the largest area, approximately 82,400 km^2, while urban areas constitute the smallest area, approximately 0.07 million km^2, making grasslands around 120 times larger than urban areas. The great differences in nutrient content maximized the already-existing differences in nutrient contents. This is compatible with hypothesis (1), as nutrient distribution is highly spatially heterogeneous.

Soil pH is one of the main factors influencing soil chemical, physical, and biological processes and properties (Brady et al., 2008), and it also is one of the most important determinants of soil nutrient transformations and nutrient use efficiency (Lin et al., 2020), which can directly or indirectly influence soil nutrient levels. The soil pH in the study area ranged from 6.890 to 7.820, which is neutral and exhibited a highly positive correlation with soil nutrients, especially SOC, TP, TK, and AN (Figure 6). Plants cannot withstand both low and high pH due to weak aluminum toxicity, availability of certain nutrients under low pH conditions, and poor solubility of certain critical elements under high pH conditions (Tyler, 2003). Therefore, a positive linear relationship between soil pH and nutrients is more common in studies with acidic and neutral soils. The significant positive correlation between vegetation NPP and all soil nutrients in this study may be explained by the fact that the slightly increased soil pH (weakly acidic to weakly alkaline) can create a soil environment that is more suitable for plant growth and, thus, favor the content of soil nutrients in

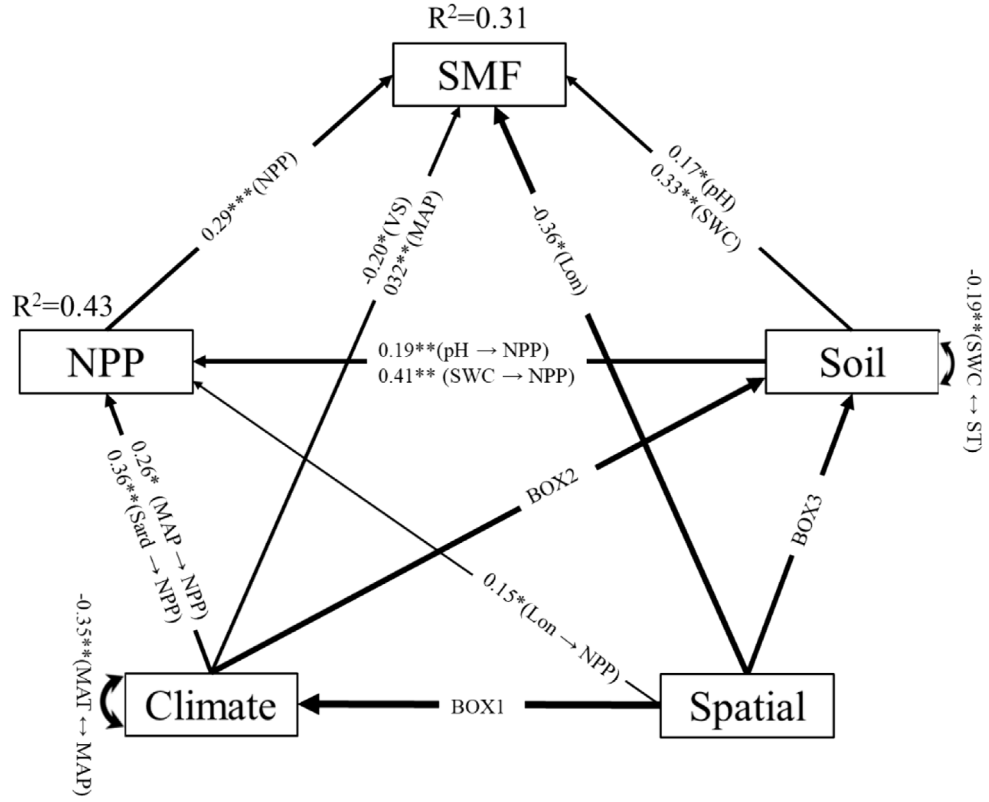

BOX1	BOX2	BOX3	Model fit
0.46**(Lat → VS)	0.61**(MAT → ST)	-0.16*(Lon → ST)	x^2=1.251, p=0.563
0.22* (Lon → VS)	0.25* (MAP→ pH)	0.26** (Lon → SWC)	Chi-square/df=2.58
-0.58** (Lat → Sard)	0.59** (MAP→ SWC)	0.45* (Lat → SWC)	RMSEA=0.018
0.60**(Lat → MAP)	0.15** (Sard → ST)	0.38**(Lon → pH)	p=0.641

FIGURE 8
Results of the SEM analysis showing the direct and indirect effects of environmental variables on soil multifunctionality. Note: *: $p < 0.05$; **: $p < 0.01$; ***: $p < 0.001$.

Kyrgyzstan, showing an overall highly significant positive correlation between soil pH and soil nutrients. This is similar to the results obtained by Zhang et al. (Zhang et al., 2021), who reported that a slight increase in soil pH increased the content of organic carbon and nitrogen in semi-arid steppe soils.

C, N, and P cycles are significantly altered by global changes such as rising temperatures and varying precipitation patterns (Yue et al., 2016). On a regional scale, it has been demonstrated that soil nutrient (C and N e.g.) contents were favorably correlated with precipitation but negatively correlated with temperature (Post et al., 1982; Miller et al., 2004). Precipitation increased SOC and TN stocks by affecting soil moisture and enhancing subsurface biomass (Fang et al., 2018). James et al. (2015) and Rumpel, 2011, and Koel-Knaben (2011) reported that increased precipitation enhanced the transport of dissolved C and N to deeper soil layers (Rumpel, 2011; James et al., 2015). The association between MAP and MAT soil nutrients differed significantly, with the former exhibiting a highly significant positive correlation with soil nutrients but the latter showing a predominantly negative correlation. Kyrgyzstan is considered a dry zone based on the worldwide categorization (Maestre et al., 2021), where soil water content is commonly regarded as a limiting factor for many terrestrial ecosystem processes and a key driver of plant growth and soil microbial activity (Moyano et al., 2013). MAP and SWC exhibited a highly strong positive

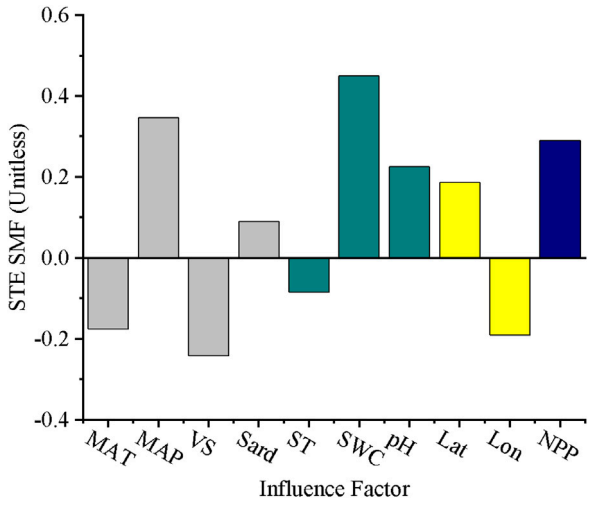

FIGURE 9
The normalized total effects (direct and indirect effects) derived from structural equation modeling (SEM).

correlation, indicating that MAP can influence soil microorganisms and plants through SWC. Increases in precipitation resulted in increased plant productivity and nitrogen inputs in the soil. This effect may be more pronounced in arid and semi-arid regions where plant growth is primarily limited by water supply (Longfei et al.,. 2015); an increase in MAP leads to an increase in soil nitrogen content due to the input of exotic nitrogen, indicating a positive correlation between these two, which is consistent with the findings of this study. The aforementioned data are compatible with hypothesis (2), which states that temperature and precipitation are the primary determinants of the spatial distribution of nutrients.

C and N availability in soil is controlled by not only plant organic matter inputs, apoplankton and roots but also microbial activity (Gavrichkova et al., 2019). Soil bacteria control the formation of soil organic matter (SOM) and the release of extracellular enzymes by C and N turnover (Sterner and Elser, 2017). The elevated temperature immediately accelerated microbial processes and turnover rates, affecting the availability of water and nutrients and, thereby extending the plant growing season (Fang et al., 2017). Hobbie et al. (2002) discovered that climate warming enhanced the decomposition of large amounts of organic carbon present in high-latitude soils (positive feedback in climate warming), which resulted in a release of significant quantities of carbon into the atmosphere as carbon dioxide (Hobbie et al., 2002), thereby decreasing the organic carbon level in the soil. Soil extracellular enzymes catalyze the rate-limiting step of soil organic carbon decomposition, and the rates of their catalysis, production, and degradation are temperature-dependent (Jing et al., 2014). Therefore, an increase in temperature may stimulate soil extracellular enzyme activities, thereby accelerating soil organic carbon decomposition and reducing soil SOC stocks. MAT demonstrated a highly significant negative correlation with SOC. MAT also exhibited a negative correlation with TN but for a highly significant negative correlation with AN. This could be due to the increase in ST with an increase in MAT over a wide range of temperatures, indicating a highly significant positive correlation between these two, leading to promoting the growth of ammonia-oxidizing archaea (AOA) communities and increasing ammonia oxidation rates, the rate-limiting step in nitrification and also an important indicator of soil N cycling (Fierer et al., 2009). MAT had a negative correlation with TN and a strong negative correlation with AN because a portion of the digestive reaction was released into the air in the form of gas (likely with a low flux). Temperature increases contribute to a transition from mostly anabolic to predominantly catabolic pathways in the microbially-driven nitrogen cycle. Increased soil temperature increased the rates of nitrification and denitrification, resulting in an increase in N2O emissions by 227% and a fall in soil TN concentration (Dai et al., 2020). MAP exhibited positive correlations with TP and TK but highly significant positive correlations with AP and AK, whereas MAT had strong negative impacts on TP and TK, but no correlations were detected between AP and AK. This may be a result of draining nutrients in the dry zone region by higher MAP (Liu et al., 2017). MAP was positively correlated with TP and TK; therefore, the increase in MAP may increase the soil SWC, which in turn creates a more suitable environment for the survival of soil microbes and thereby increases their activities and consequently degrades TP and TK, leading to increasing AP and AK. TP and TK increased with leaching on one side, whereas some components were degraded and absorbed by soil microorganisms; therefore, the hypothesis about the lack of significant association between TP and TK and MAP must be confirmed in future trials. Within a limited temperature range, the increase in MAT accelerated the absorption of elemental phosphorus and potassium by bacteria by increasing their activities. In addition, a minor increase in soil temperature accelerated the decomposition of organic compounds like TP and TK by soil enzymes, leading to a reduction in TP and TK contents. VS only demonstrated a significant correlation with TP and TK, presumably because the long-term increase in VS caused the weathering of rocks, making P and K more sensitive to weathering and release. Sard and MAT had a significant positive correlation, and both correlated the same with soil nutrients; therefore, Sard may have influenced soil nutrients through modifying MAT levels and, consequently, MAT levels.

Consistent with hypothesis, the regional distribution of SMF in this investigation is similarly highly varied (1). In this study,

vegetation NPP was the most important factor, exerting a significant direct positive effect on soil multifunctionality. It has been demonstrated that plant species diversity was positively correlated with soil multifunctionality in extremely arid regions, while the correlation was stronger in less arid environments. There was a strong correlation between vegetation NPP and plant species richness (Abatzoglou et al., 2018); therefore, the significant positive influence of NPP on soil multifunctionality observed in our study is consistent with the findings of previous research studies. It has been demonstrated that the pH of the soil environment is the most important factor in determining soil functions (Ding and Eldridge., 2021). Zhang et al. (2021) discovered that a minor increase in soil pH was beneficial to organic carbon and nitrogen content in semi-arid grassland soils, thereby having a substantial favorable impact on changes in soil multifunctionality (Zhang et al., 2021). Both ST and MAT had adverse indirect impacts on soil multifunctionality. Within a particular temperature range, it is possible that a rise in soil temperature would enhance the decomposition and mineralization of organic materials, thus improving soil multifunctionality. Possibly due to the close relationship between seasonal precipitation and soil moisture, soil multifunctionality is limited more by the increase in precipitation than in temperature (Eldridge et al., 2019). Higher SWC concentrations may drive the growth of a plant root and soil microbial activity, further influencing plant metabolism and nutrient loss. In addition, increasing soil moisture can affect CO2 emissions by promoting plant growth and the ensuing allocation of subsurface carbon and carbon substrates (Liu et al., 2017). The majority of studies have demonstrated that soil microbial diversity had a significant effect on soil multifunctionality, and different soil environmental conditions also influenced the relationship between soil microbes and soil multifunctionality, e.g., the relationship between soil microbial diversity and soil multifunctionality was stronger when soil moisture levels were low (Durán et al., 2018). This study has limitations due to a lack of data on soil microorganisms and the relationship between soil microbes and soil multifunctionality. Changes in spatial patterns had both direct and indirect effects on soil multifunctionality, and spatial variability of soil properties is generally controlled by the interaction between biological, chemical, and physical processes occurring simultaneously and at multiple scales (Zuo et al., 2010). Changes in spatial patterns have concurrently contributed to alterations in the weather, soil, and vegetation NPP. Variations in temperature, soil properties, and plants have been proven to exert distinct effects on the regional variability of soil multifunctionality, implying that no individual environmental factor may optimize all soil functions (Ding and Eldridge, n. d.). Spatial variation in soil multifunctionality is not caused by a single environmental variable but rather by a combination of environmental conditions.

5 Conclusion

In this study, field sampling data from Kyrgyzstan were analyzed to characterize the spatial variability of the distribution of soil nutrients and soil multifunctionality at different soil depths in the country using the average approach, factor analysis, and structural equation modeling (SEM) to determine the driving mechanisms. The findings of the study were as follows:

(1) The surface soils (0–30 cm) of entire Kyrgyzstan contain 4.24 ± 0.59 Pg of soil organic carbon (SOC), 0.33 ± 0.06 Pg of total nitrogen (TN), 0.31 ± 0.03 Pg of total phosphorus (TP), and 5.12 ± 1.88 Pg of total potassium (TK). Soil nutrient reserves of various land-cover types vary substantially, with grassland contributing up to 40% to the total soil nutrient reserves and urban areas accounting for approximately 0.3%. Approximately 50% of the total soil nutrient reserves are derived from arable land, woodland, and shrubland.
(2) Fitting linear or nonlinear equations revealed a highly significant linear relationship between soil organic carbon (SOC) and total nitrogen (TN), a significant power function relationship between soil total nitrogen (TN) and total phosphorus (TP), and a highly significant quadratic relationship between soil total phosphorus (TP) and total potassium (TK). Overall, a highly strong positive correlation was observed between NPP and all soil nutrients. Mean annual precipitation (MAP) and soil water content (SWC) demonstrated highly significant positive correlations with soil nutrients, whereas mean annual temperature (MAT) and soil temperature (ST) showed highly significant negative correlations with soil nutrients, and there were differing correlations between other environmental variables and various nutrients.
(3) Soil multifunctionality is spatially heterogeneous throughout Kyrgyzstan, with soil multifunctionality indices ranging from -0.63 to 2.30. From west to east, soil multifunctionality indices showed a generally increasing trend, followed by a decreasing trend in the region, with the highest indices in the central region mostly comprising agricultural and pastoral lands but lower indices in the South-western and Eastern Alpine regions.
(4) SEM analysis showed significant positive direct effects of NPP, SWC, MAP, and pH on soil multifunctionality, while VS and Lon had negative effects on soil multifunctionality. In addition, we found multiple indirect effects of ST, MAT, Sard, and Lat on soil multifunctionality. However, Lon, MAP, SWC, and pH had direct and multiple indirect effects on soil multifunctionality.

This paper investigates soil ecosystem processes and the distribution of soil resources in Kyrgyzstan. The results of this study provide further clarification of the spatial heterogeneity

and driving factors of the entire soil ecosystem functioning in Kyrgyzstan, which helps better predict the impact of environmental changes on the ecosystem multifunctionality in drylands and provides a scientific basis for the rational use of soil resources and efficient management of dryland soils to prevent further land degradation in the country.

Data availability statement

The datasets presented in this study can be found in online repositories. The names of the repository/repositories and accession number(s) can be found in the article/Supplementary Material.

Author contributions

YC and SZ made equally and mainly contribution to this work. YC and SZ are Co-first authors of this article, Other authors have contributed to this article to a certain degree, HL: formal analysis. All authors commented on previous versions of the manuscript. All authors read and approved the final manuscript.

Funding

"This work was supported by [Strategic priority research project of Chinese Academy of Sciences] (Grant numbers [XDA20030102]) [The Key Technical Talent Project of Chinese Academy of Sciences (Research on desertification technology along the "Belt and Road")] Author Yusen Chen has received research support from Xinjiang Institute of Ecology and Geography Chinese Academy of Sciences."

Acknowledgments

I would like to thank the Institute of ecology and geography of the Chinese Academy of Sciences for its help and support in my work.

Conflict of interest

The authors declare that the research was conducted in the absence of any commercial or financial relationships that could be construed as a potential conflict of interest.

Publisher's note

References

Abatzoglou, J. T., Dobrowski, S. Z., Parks, S. A., and Hegewisch, K. C. (2018). TerraClimate, a high-resolution global dataset of monthly climate and climatic water balance from 1958–2015. *Sci. data* 5, 170191–170212. doi:10.1038/sdata.2017.191

Brady, N. C., Weil, R. R., and Weil, R. R. (2008). *The nature and properties of soils*. Upper Saddle River, NJ: Prentice-Hall.

Bui, E. N., and Henderson, B. L. (2013). C:N:P stoichiometry in Australian soils with respect to vegetation and environmental factors. *Plant Soil* 373, 553–568. doi:10.1007/s11104-013-1823-9

Byrnes, J. E. K., Gamfeldt, L., Isbell, F., Lefcheck, J. S., Griffin, J. N., Hector, A., et al. (2014). Investigating the relationship between biodiversity and ecosystem multifunctionality: Challenges and solutions. *Methods Ecol. Evol.* 5, 111–124. doi:10.1111/2041-210x.12143

Chytrý, M., Danihelka, J., Ermakov, N., Hájek, M., Valachovič, M., Koci, M., et al. (2010). Plant species richness in continental southern siberia: Effects of pH and climate in the context of the species pool hypothesis. *Glob. Ecol. Biogeogr.* 16, 668–678. doi:10.1111/j.1466-8238.2007.00320.x

Dai, Z., Yu, M., Chen, H., Zhao, H., Huang, Y., Su, W., et al. (2020). Elevated temperature shifts soil N cycling from microbial immobilization to enhanced mineralization, nitrification and denitrification across global terrestrial ecosystems. *Glob. Chang. Biol.* 26, 5267–5276. doi:10.1111/gcb.15211

Ding, J., and Eldridge, D. J. (2021). Climate and plants regulate the spatial variation in soil multifunctionality across a climatic gradient. *CATENA* 201, 105233. doi:10.1016/j.catena.2021.105233

Durán, J., Delgado-Baquerizo, M., Dougill, A. J., Guuroh, R. T., Linstdter, A., Thomas, A. D., et al. (2018). Temperature and aridity regulate spatial variability of soil multifunctionality in drylands across the globe. *Ecology* 99, 1184–1193. doi:10.1002/ecy.2199

Eldridge, D. J., Delgado-Baquerizo, M., Quero, J. L., Ochoa, V., Maestre, F. T., Garcia-Palacios, P., et al. (2019). Surface indicators are correlated with soil multifunctionality in global drylands. *J. Appl. Ecol.* 57, 424–435. doi:10.1111/1365-2664.13540

Fang, C., Ye, J., Gong, Y., Pei, J., Yuan, Z., Xie, C., et al. (2017). Seasonal responses of soil respiration to warming and nitrogen addition in a semi-arid alfalfa-pasture of the Loess Plateau, China. *Sci. Total Environ.* 590, 729–738. doi:10.1016/j.scitotenv.2017.03.034

Fang, J., Yu, G., Liu, L., Hu, S., and Chapin, F. S. (2018). Climate change, human impacts, and carbon sequestration in China. *Proc. Natl. Acad. Sci. U. S. A.* 115, 4015–4020. doi:10.1073/pnas.1700304115

Fierer, N., Strickland, M. S., Liptzin, D., Bradford, M. A., and Cleveland, C. C. (2009). Global patterns in belowground communities. *Ecol. Lett.* 12, 1238–1249. doi:10.1111/j.1461-0248.2009.01360.x

Fisher, R. F., and Dan, B. (2000). *Ecology and management of forest soils*.

Galloway, J. N., Dentener, F. J., Capone, D. G., Boyer, E. W., Vosmarty, C. J., Seitzinger, S. P., et al. (2004). Nitrogen cycles: Past, present, and future. *Biogeochemistry* 70, 153–226. doi:10.1007/s10533-004-0370-0

Gavrichkova, O., Scartazza, A., Guidolotti, G., Kuzyakov, Y., Calfapietra, C., Mattioni, M., et al. (2019). When the Mediterranean becomes harsh: Heat pulses strongly affect C allocation in plant-soil-atmosphere continuum in *Eucalyptus camaldulensis*. *Environ. Exp. Bot.* 162, 181–191. doi:10.1016/j.envexpbot.2019.02.019

Giesler, R., Petersson, T., and Högberg, P. (2002). Phosphorus limitation in boreal forests: Effects of aluminum and iron accumulation in the humus layer. *Ecosystems* 5, 300–314. doi:10.1007/s10021-001-0073-5

Gross, C. D., and Harrison, R. B. (2019). The case for digging deeper: Soil organic carbon storage, dynamics, and controls in our changing world. *Soil Syst.* 3, 28. doi:10.3390/soilsystems3020028

Guo, L., Cheng, J., Luedeling, E., Koerner, S. E., He, J.-S., Xu, J., et al. (2017). Critical climate periods for grassland productivity on China's Loess Plateau. *Agric. For. Meteorol.* 233, 101–109. doi:10.1016/j.agrformet.2016.11.006

Guo, X., Fu, B., and Chen, L. (2000). The spatio-temporal variability of soil nutrients in zunhua Plain of Hebei Province. *ACTA Geogr. Sin. Ed.* 55, 555–566.

Hati, K. M., Swarup, A., Mishra, B., Manna, M. C., Wanjari, R. H., Mandal, K. G., et al. (2008). Impact of long-term application of fertilizer, manure and lime under intensive cropping on physical properties and organic carbon content of an Alfisol. *Geoderma* 148, 173–179. doi:10.1016/j.geoderma.2008.09.015

Hobbie, S. E., Nadelhoffer, K. J., and Högberg, P. (2002). A synthesis: The role of nutrients as constraints on carbon balances in boreal and arctic regions. *Plant Soil* 242, 163–170. doi:10.1023/a:1019670731128

Hooper, D. U., and Vitousek, P. M. (1998). Effects of plant composition and diversity on nutrient cycling. *Ecol. Monogr.* 68, 121–149. doi:10.1890/0012-9615(1998)068[0121:eopcad]2.0.co;2

James, J., Knight, E., Gamba, V., and Harrison, R. (2015). Deep soil: Quantification, modeling, and significance of subsurface nitrogen. *For. Ecol. Manage.* 336, 194–202. doi:10.1016/j.foreco.2014.10.010

Jing, X., Wang, Y., Chung, H., Mi, Z., Wang, S., Zeng, H., et al. (2014). No temperature acclimation of soil extracellular enzymes to experimental warming in an alpine grassland ecosystem on the Tibetan Plateau. *Biogeochemistry* 117, 39–54. doi:10.1007/s10533-013-9844-2

Li, Z. A., Zou, B., Cao, Y. S., Ren, H., and Liu, J. (2003). Analysis on soil nutrient characteristics of typical hilly degraded wasteland in South China. *Acta Ecol. Sin.* 23, 1648–1656.

Lin, X. B., Sun, Y. M., Jiang, X. F., Huang, S. S., He, S. L., Yu, P. L., et al. (2020). [Soil fertility characteristics and their influencing factors in tea plantations of Jiangxi Pro-vince, China]. *Chin. J. Appl. Ecol.* 31, 1163–1174. doi:10.13287/j.1001-9332.202004.022

Liu, Y., Wang, C., He, N., Wen, X., Gao, Y., Li, S., et al. (2017). A global synthesis of the rate and temperature sensitivity of soil nitrogen mineralization: Latitudinal patterns and mechanisms. *Glob. Chang. Biol.* 23, 455–464. doi:10.1111/gcb.13372

Liu, Z., Shao, M., and Wang, Y. (2011). Effect of environmental factors on regional soil organic carbon stocks across the Loess Plateau region, China. *Agric. Ecosyst. Environ.* 142, 184–194. doi:10.1016/j.agee.2011.05.002

Longfei, C., Zhibin, H., Jun, D., Junjun, Y., and Xi, Z. (2015). Patterns and controls of soil organic carbon and nitrogen in alpine forests of northwestern China. *For. Sci.* 66, 1033–1040. doi:10.5849/forsci.14-231

Maestre, F. T., Benito, B. M., Berdugo, M., Concostrina-Zubiri, L., Delgado-Baquerizo, M., Eldridge, D. J., et al. (2021). Biogeography of global drylands. *New Phytol.* 231, 540–558. doi:10.1111/nph.17395

Maestre, F. T., Quero, J. L., Gotelli, N. J., Escudero, A., Ochoa, V., Delgado-Baquerizo, M., et al. (2012). Plant species richness and ecosystem multifunctionality in global drylands. *Science* 335, 214–218. doi:10.1126/science.1215442

Meersmans, J., De Ridder, F., Canters, F., De Baets, S., and Van Molle, M. (2008). A multiple regression approach to assess the spatial distribution of Soil Organic Carbon (SOC) at the regional scale (Flanders, Belgium). *Geoderma* 143, 1–13. doi:10.1016/j.geoderma.2007.08.025

Miller, A. J., Amundson, R., Burke, I. C., and Yonker, C. (2004). The effect of climate and cultivation on soil organic C and N. *Biogeochemistry* 67, 57–72. doi:10.1023/B:BIOG.0000015302.16640.A5

Moyano, F. E., Manzoni, S., and Chenu, C. (2013). Responses of soil heterotrophic respiration to moisture availability: An exploration of processes and models. *Soil Biol. Biochem.* 59, 72–85. doi:10.1016/j.soilbio.2013.01.002

Plaza, C., Zaccone, C., Sawicka, K., Méndez, A. M., Tarquis, A., Gascó, G., et al. (2018). Soil resources and element stocks in drylands to face global issues. *Sci. Rep.* 8, 13788–8. doi:10.1038/s41598-018-32229-0

Post, W. M., Emanuel, W. R., Zinke, P. J., and Stangenberger, A. G. (1982). Soil carbon pools and world life zones. *Nature* 298, 156–159. doi:10.1038/298156a0

Quilchano, C., Marañón, T., Pérez-Ramos, I. M., Noejovich, L., Valladares, F., and Zavala, M. A. (2008). Patterns and ecological consequences of abiotic heterogeneity in managed cork oak forests of Southern Spain. *Ecol. Res.* 23, 127–139. doi:10.1007/s11284-007-0343-6

Rodríguez, A., Durán, J., Fernández-Palacios, J. M., and Gallardo, A. (2009). Spatial pattern and scale of soil N and P fractions under the influence of a leguminous shrub in a Pinus canariensis forest. *Geoderma* 151, 303–310. doi:10.1016/j.geoderma.2009.04.019

Rumpel, C., and Kogel-Knabner, I. (2011). K?gel-Knabner, IDeep soil organic matter—A key but poorly understood component of terrestrial C cycle. *Plant Soil* 338, 143–158. doi:10.1007/s11104-010-0391-5

Sterner, R. W., and Elser, J. J. (2017). "Ecological stoichiometry," in *Ecological stoichiometry* (Princeton, New Jersey, United States: Princeton university press).

Tian, D., Reich, P. B., Chen, H., Xiang, Y., Luo, Y., Ying, S., et al. (2018). Global changes alter plant multi-element stoichiometric coupling. *New Phytol.* 221, 807–817. doi:10.1111/nph.15428

Tian, H., Wang, S., Liu, J., Pan, S., Chen, H., Zhang, C., et al. (2006). Patterns of soil nitrogen storage in China. *Glob. Biogeochem. Cycles* 20, 1001. doi:10.1029/2005GB002464

Tyler, G. (2003). [Forum: Calcium and plant species richness] || some ecophysiological and historical approaches to species richness and calcicole/calcifuge behaviour: Contribution to a debate. *Folia Geobot.* 38, 419–428. doi:10.1007/bf02803249

Verhoeven, J., Verhoeven, Jos T A, Lawniczak, A., E., and Guesewell, S. (2009). Effect of N:K supply ratios on the performance of three grass species from herbaceous wetlands. *Basic Appl. Ecol.* 10, 715–725. doi:10.1016/j.baae.2009.05.004

Yue, K., Fornara, D. A., Yang, W., Peng, Y., Li, Z., Wu, F., et al. (2016). Effects of three global change drivers on terrestrial C:N:P stoichiometry: A global synthesis. *Glob. Chang. Biol.* 23, 2450–2463. doi:10.1111/gcb.13569

Zavaleta, E. S., Pasari, J. R., Hulvey, K. B., and Tilman, G. D. (2010). Sustaining multiple ecosystem functions in grassland communities requires higher biodiversity. *Proc. Natl. Acad. Sci. U. S. A.* 107, 1443–1446. doi:10.1073/pnas.0906829107

Zhang, J., Wu, X., Shi, Y., Jin, C., Wang, J., Wei, X., et al. (2021). A slight increase in soil pH benefits soil organic carbon and nitrogen storage in a semi-arid grassland. *Ecol. Indic.* 130, 108037. doi:10.1016/j.ecolind.2021.108037

Zhang, X. T., and Wu, X. Q. (2021). Spatiotemporal variation of NPP in Yunnan faulted basin from 2005 to 2019 based on CASA model. *Acta Geosci. Sin.* 42, 426–434.

Zhao, Z., Liu, G., Liu, Q., Chong, H., He, L., and Wu, C. (2018). Distribution characteristics and seasonal variation of soil nutrients in the mun river basin, Thailand. *Int. J. Environ. Res. Public Health* 15, 1818. doi:10.3390/ijerph15091818

Zuo, X. A., Zhao, X. Y., Zhao, H. L., Guo, Y. R., Zhang, T. H., and Cui, J. Y. (2010). Spatial pattern and heterogeneity of soil organic carbon and nitrogen in sand dunes related to vegetation change and geomorphic position in Horqin Sandy Land, Northern China. *Environ. Monit. Assess.* 164, 29–42. doi:10.1007/s10661-009-0872-2

frontiers | Frontiers in Environmental Science

ORIGINAL RESEARCH
published: 19 July 2022
doi: 10.3389/fenvs.2022.883533

Soil Mapping Using Electromagnetic Induction to Assess the Suitability of Land for Growing *Leptospermum nitens* in Western Australia

Hira Shaukat[1], *Ken C. Flower*[1,2] *and Matthias Leopold*[1,2,3]*

[1]UWA School of Agriculture and Environment, Soil Matrix Group, The University of Western Australia, Perth, WA, Australia, [2]UWA Institute of Agriculture, The University of Western Australia, Perth, WA, Australia, [3]Cooperative Research Centre for Honey Bee Products, Yanchep, WA, Australia

OPEN ACCESS

Edited by:
Niall Patrick Hanan,
New Mexico State University,
United States

Reviewed by:
Ilan Stavi,
Dead Sea and Arava Science Center,
Israel
Lorenzo De Carlo,
National Research Council (CNR), Italy

***Correspondence:**
Matthias Leopold
matthias.leopold@uwa.edu.au

Specialty section:
This article was submitted to Drylands,
a section of the journal
Frontiers in Environmental Science

Received: 25 February 2022
Accepted: 17 June 2022
Published: 19 July 2022

Citation:
Shaukat H, Flower KC and Leopold M (2022) Soil Mapping Using Electromagnetic Induction to Assess the Suitability of Land for Growing Leptospermum nitens in Western Australia.
Front. Environ. Sci. 10:883533.
doi: 10.3389/fenvs.2022.883533

Leptospermum sp. with dihydroxyacetone in their nectar are a source of high-value medicinal honey production and can provide income from agriculturally marginal lands. The current study was from two newly planted *Leptospermum nitens* sites, one with duplex soil and the other in deep sandy soil, in the low rainfall areas of the south-west of Western Australia, with the aim of identifying key soil parameters influencing the plantation's survival and growth. Electromagnetic induction (EMI) at different depths was used to investigate the possible impact of soil variability on the *Leptospermum nitens* plantations. Two EMI surveys were conducted at each site, at different times of the year, to account for soil moisture variability (relatively dry and wet conditions). A least-square inversion algorithm was used to determine true electrical conductivities at three different soil depths (0–0.5, 0.5–0.8, and 0.8–1.6 m) to produce quasi-3D maps of soil inverted electrical conductivity. Corresponding soil samples from each depth were used for the physico-chemical analysis of soil parameters and to develop laboratory-based electrical resistivity to soil volumetric moisture calibrations with R^2 values between 0.95 and 0.99. Shrub survival and growth (canopy diameter) were estimated using unmanned aerial vehicle (UAV) images and machine learning. Comparing EMI soil mapping with UAV imagery results showed significantly greater shrub survival and growth ($p < 0.001$) in areas with higher ECa ranges of 12–24 mS m^{-1} at the variable textured site and 6–9 mS m^{-1} at the uniformly sandy site. Overall, the variable textured site, with an 82% survival rate, had a significantly higher shrub count and larger plants than the uniformly sandy site, with a 75% survival rate. A principal component analysis (PCA) identified inverted EC to be strongly correlated with soil moisture > pH > soil texture. Such soil mapping may be a robust and effective method for risk assessment of new shrub plantations.

Keywords: electromagnetic induction (EMI), inversion, volumetric soil moisture, UAV, *Leptospermum*, electrical resistivity tomography (ERT), dryland, soil mapping

1 INTRODUCTION

Land degradation and associated dry land salinity is a major challenge in Australia caused by the removal of native vegetation (Stirzaker et al., 2002). Land clearing and intensive cereal/annual pasture rotations have exposed surface soils to excessive wind and water erosion, often in combination with dryland salinity issues, under semi-arid rain-fed conditions (Lamb, 2014). In response, most farmers have adopted no-tillage cropping practices with crop residue retention (D'Emden et al., 2008). According to the latest estimate, more than 1 million ha of south-west Western Australia (WA) is affected by salinity resulting in the loss of at least $519 million per year (Australian Bureau of Statistics, 2002; Furby et al., 2010). Indeed, the current scale of this degradation problem now requires landscape level mitigation responses such as reforestation (George et al., 2012). Species identified for mitigation are mainly selected based on their ecological role; however, estimated costs of such reforestation plans often exceed the value of the land (Lamb, 2014; Harper et al., 2017). A major factor affecting large-scale reforestation is to obtain an impactful hydrological response without displacing farm production (Harper et al., 2014). Therefore, market-driven reforestation has the potential to encourage the integration of perennial plants into existing farming systems (Mendham et al., 2011). A recent report on high-value honey derived from *Leptospermum* species in Australia has identified the opportunity for bioactive honey production at a commercial scale, either by diversifying traditional agricultural regions such as the WA wheatbelt region or by using unproductive lands through revegetation-focused projects (Cokcetin et al., 2019).

Leptospermum is a member of the Myrtaceae family, with 300 genera and more than 3,800 species, with 85 out of 88 identified *Leptospermum* species in this region being native to Australia (Bean, 1992, 2004), and 15 of which are native to WA. *Leptospermum* is endemic Australian species (Thompson, 1989), closely related to the widely studied and commercially successful *L. scoparium*, found in Tasmania, the north-west mainland of Australia, and in New Zealand (Porter and Wilkins, 1999; Stephens et al., 2005; Adams et al., 2009; Wicaksono et al., 2016; Thrimawithana et al., 2019). These species are renowned for their essential oils and nectar production for honey and are also used as ornamental shrubs. *Leptospermum* honey is popular for its synergistic impact with common antifungal and antibacterial agents (Lu et al., 2013; Cokcetin et al., 2016). The high/medicinal value of *Leptospermum* honey is due to the presence of the chemical component methyl glyoxal (MGO), which is formed from its precursor dihydroxyacetone (DHA) (Adams et al., 2008; Mavric et al., 2008). Not all *Leptospermum* species produce DHA in their nectar. The WA's species, *Leptospermum Nitens* (Turcz), has been shown to produce higher DHA and MGO levels than *L. scoparium* (Williams et al., 2018).

Leptospermum is a common seral shrub in succession to forest. They are usually known as a woody weed of pastures (Burrell, 1965) and are useful for erosion control (Marden and Phillips, 2015), carbon sequestration (Scott et al., 2000; Beets et al., 2014), and vegetation restoration (Marden and Phillips, 2015). Mostly, they are dominant in low fertility, poorly drained environments (Thompson, 1989), grasslands, woodlands, and heathlands (Burrell, 1981; Bennett, 1994). Since these plants can adapt to various soil and climatic conditions (Dodson et al., 1995; Hageer et al., 2017), it is expected that they will be responsive to managed cultivations (Cokcetin et al., 2019). Developing the commercial aspects of this species from an ornamental plant to a pharmacologically active plant can make it a potential priority candidate for agroforestry (Cokcetin et al., 2019).

Site assessments are useful practical tools for planning agricultural land management, but limited information is available regarding the impact of soil variations on the establishment of new native shrub plantations. Electromagnetic induction (EMI) may be a promising tool for soil surveying when establishing new native plantations. EMI sensors, which can take readings at different depths simultaneously, provide the simplest and least expensive method to assess soil variations on a broad scale. These non-invasive sensors measure the contactless bulk soil electrical properties that contribute to the apparent electrical conductivity (ECa). The measured soil Eca is a response to conductive soil parameters such as salt content, soil moisture, organic matter, soil texture, bulk density, stratigraphic layers, or bedrock (van Wesenbeeck and Kachanoski, 1988; Triantafilis et al., 2000; James et al., 2003; Corwin and Lesch, 2013; Doolittle and Brevik, 2014; Dakak et al., 2017). Generally, EMI assessments are used in agriculture (Hedley and Yule, 2009; Hanssens et al., 2019; Arshad et al., 2020; Shaukat et al., 2022) and especially for quantifying the risks related to salinity (Scudiero et al., 2017; Paz et al., 2020; Farzamian et al., 2021). However, Bennett and George (1995) conducted an EMI survey to quantify salinity for the new plantations of *Eucalyptus globulus* and suggested that this method could be used for assessing soil variations for risk assessments before establishing new plantations.

Moreover, remote sensing methods are becoming mainstream in planning for tree plantations and their management (Charron et al., 2020; Dainelli et al., 2021; Dixon et al., 2021). In particular, drones/unmanned aerial vehicles (UAVs) provide efficient aerial mapping and estimation of deforestation rates, quantifying above ground biomass, monitoring climatic impacts on land use, woodlands, and forest ecosystems, and getting information from the sites that are difficult to reach (Pádua et al., 2017; Raparelli and Bajocco, 2019). A combination of new technologies for both soil and aerial surveys with quick turn-around times can provide data-driven decisions for agroforestry (Pádua et al., 2017).

L. nitens is one of the species identified with the potential of making the unproductive low fertility areas in the "wheatbelt" region of WA a "hot spot" for generating bioactive honey (Cokcetin et al., 2019). Limited information is available on a field scale to understand the impact of soil limitations, such as shallow, saline- or nutrient-deficient soils, on the survival and growth rate of *L. nitens*. Such information could possibly identify factors correlated to the yield and quality of nectar production for medicinal honey. The hypothesis of the current study was that EMI could be used to identify soil parameters related to *L. nitens* survival and growth across the two soil

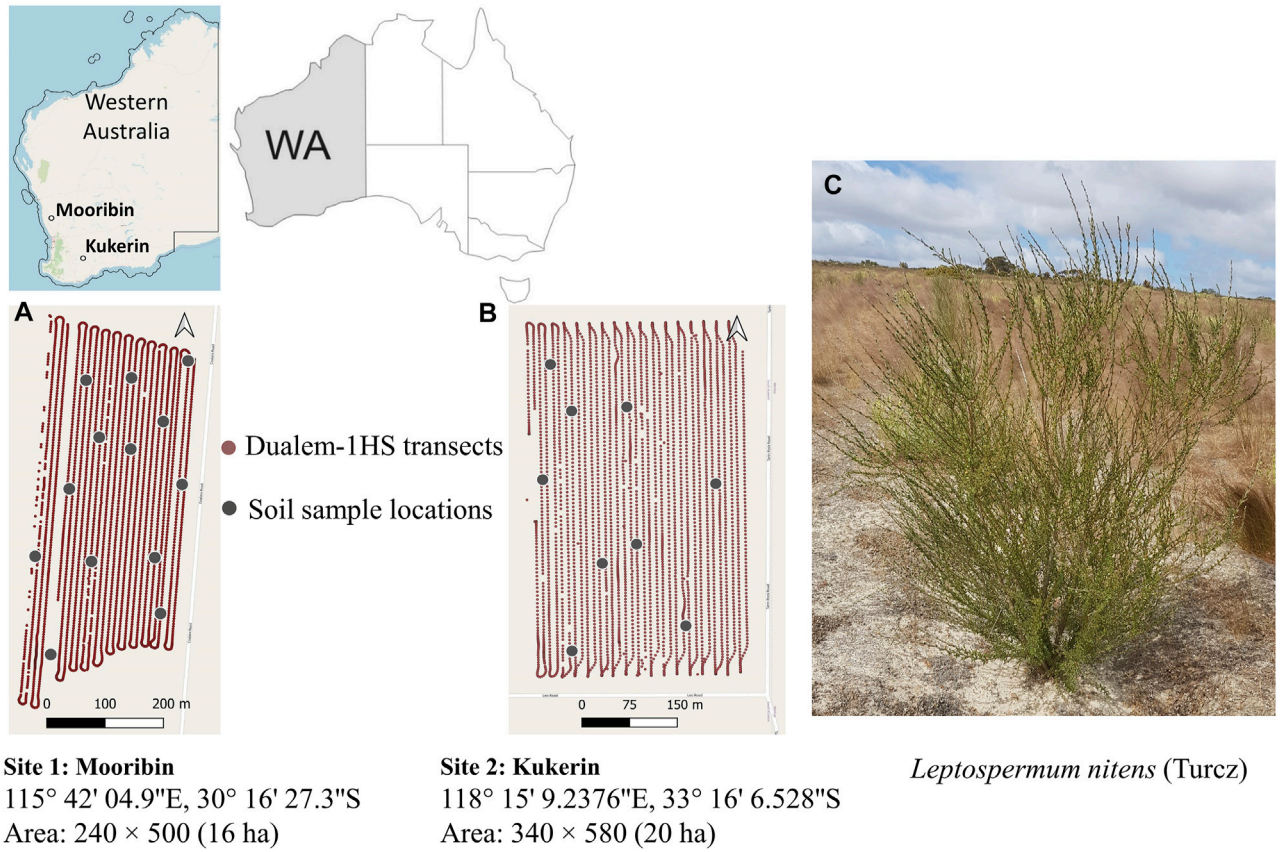

FIGURE 1 | Top, location of the study area in Western Australia. Bottom, **(A)** Site 1–Mooribin and **(B)** site 2–Kukerin. ECa transects with EMI reading points (red dots) and soil sample locations (gray dots) **(C)** *Leptospermum nitens* plant.

types. The overall aim was to develop a robust, rapid, and non-invasive soil mapping system to identify soil parameters influencing the performance of *L. nitens* for potential commercial cultivation across different soil types. A prognosis for the most suitable soil conditions for commercialization of *L. nitens* in WA is presented.

2 MATERIALS AND METHODS

Two sites with contrasting soils and newly planted *L. nitens* shrubs were selected for this study to understand the survival and growth of this species with respect to soil characteristics. The area has a Mediterranean–type climate with mild, wet winters and hot, dry summers. A Dualem-1HS EMI sensor was used for two soil surveys at each site, at two different times of the year, to include variable (relatively dry and wet) soil moisture conditions. Soil samples were also collected from the study sites to measure soil physical and chemical properties and to develop soil moisture vs. resistivity calibration curves for the different soil depths under laboratory conditions. In addition, shrub count (survival) and shrub canopy diameter (growth) estimation were done using unmanned aerial vehicle–UAV images and machine learning. EMI soil mapping was related to drone imagery results to understand the influence of soil variability on newly planted shrub survival (count) and growth.

2.1 Study Sites

2.1.1 Mooribin Badgingarra

This study site is 16 ha located in Mooribin Badgingarra in the Shire of Dandaragan, about 200 km north of Perth (115° 42′ 04.9″ E, 30° 16′ 27.3″ S; **Figure 1A**). From 1965 to 2021, the recorded mean daily temperature was 7.6°C in July and 34.6°C in January. The average annual rainfall was 530 mm, with 430 mm falling between May and October during the growing season and 100 mm between November and April during summer and autumn, with a mean annual cumulative evapotranspiration rate of 2,376 mm [Badgingarra research station, BADG 009037 (BOM, 2021)]. The soil is classified as an Arenosol by both the Australian classification system (ACS) (Isbell and National Committee on Soil and Terrain, 2021) and the international WRB system (IUSS, 2014). This area is classified under the Northern Kwongan or Sandplains and is recorded as a botanically important area (Griffin, 1994). General soil properties are brown to red-brown sands, which are non-wetting with subsurface acidity. The pH ($CaCl_2$) range is 4.2 in the top 30 cm to 4.9 at 90 cm depth. Mixed farming operations are practiced in this area mostly focused on sheep

TABLE 1 | Summary of EMI field surveys.

Site	Survey date	Transects		
		Length (m)	Distance between (m)	Total no
Mooribin (~16 ha)	7 June 2019	~550	12	25
	19 August 2019	~550	12	25
Kukerin (~20 ha)	4 June 2019	~550	6	68
	22 August 2019	~550	12	35

and beef cattle production along with lupins and wheat crop rotations.

2.1.2 Kukerin

This site is 20 ha, located near South Kukerin in the Shire of Dumbleyung, about 320 km south-east of Perth (33° 16′ 6.528″ S 118° 15′ 9.2376″ E; **Figure 1B**). From 1965 to 2021, mean daily minimum temperatures were 15.4°C in July and 31.2°C in January. Average annual rainfall is around 400 mm, with 300 mm falling from May to October and 100 mm from November to April, with a mean annual cumulative evapotranspiration rate of 1873 mm [Wagin weather station no. 010647 (BOM, 2021)]. The soil is classified as Brown Chromosol based on the Australian classification system (ACS) (Isbell, 2016) or Luvisols based on the international WRB system (IUSS, 2014). General soil features are a combination of sandy topsoils and red-brown sandy loams or sandy clay loams as the subsoil, typical of duplex soils (McKenzie et al., 2004). The pH ($CaCl_2$) range is 4.7 in the top 30 cm to 5.6 at 90 cm depth. The land is mostly used for growing wheat and sheep farming.

2.1.3 *L. nitens* Plantation

L. nitens (**Figure 1C**) seedlings of 250 mm height and 2 mm stem diameter were planted with a row spacing of 6 and 2 m between plants with an average of ~830 stems ha^{-1}.

2.2 EMI Setup and Data Collection

An electromagnetic induction (EMI) sensor (Dualem-1HS) was used for soil surveys at both sites. This is a non-intrusive sensor with a fixed frequency, and it measures the apparent soil electrical conductivity (ECa). This sensor was portable and contained a transmitter coil (Tx) and two pairs of receiver coils (Rx) with depths of exploration (DOE) of 0.3, 0.5, 0.8, and 1.6 m from the surface. The DOE accounts for 70% of the array's sensitivity (McNeill, 1980) and is determined by orientation and distance between Tx and Rx coils.

Two EMI surveys were conducted at both study sites in June (dry season) and August (after rains) 2019 (**Table 1**). To conduct the survey, the Dualem-1Hs was placed on a non-conductive polyethylene sled containing a GPS antenna. A light vehicle towed this sled across the fields at a speed of ~5.5 ms^{-1}. A recording was taken every two seconds, and each point was georeferenced with a horizontal accuracy of less than 0.5 m using the Beacon DGPS function of the Hemisphere GPS R130 unit.

2.3 Soil Sampling and Laboratory Analysis

Soil samples for laboratory analysis were taken up to a depth of 1 m. The sample locations were chosen using the initial EMI survey, where uniform ECa areas were identified using natural breaks classification in QGIS software (QGIS.org, 2022). There were twelve soil sample locations at Mooribin and nine soil samples at Kukerin (**Figure 1**). The soil samples were collected using a percussion drill rig with an 8 cm diameter and 1 m long thick steel probe immediately after the surveys in August 2019. The soil samples were bulked by depth into 0–0.5, 0.5–0.8, and 0.8–1 m depths, which broadly corresponded to the main soil horizon boundary of the duplex soils at Kukerin.

Laboratory analysis included: gravimetric moisture content, particle size analysis (PSA) using laser diffraction, pH ($CaCl_2$), electrical conductivity of soil saturated paste (EC_e), cation exchange capacity (CEC), exchangeable aluminum (Al), potassium (K), calcium (Ca), magnesium (Mg), and sodium (Na) by atomic emission spectrometry with inductively coupled plasma (ICP–OES) using Perkin Elmer Optima 7300DV optical emission spectrometer (Nicia et al., 2018), extractable phosphorus (P) using colorimetric analysis–0.5 M $NaHCO_3$ and UV-VIS spectrophotometer, and total carbon and nitrogen using CN elemental analyzer. All measurement techniques followed protocols used by Rayment and Lyons (2011) and McKenzie et al. (2002).

2.4 Laboratory Estimation of Soil Moisture (θ) Using Electrical Resistivity Tomography

To correlate ECa with soil moisture, laboratory-based calibration curves between volumetric moisture content (θ) and soil bulk electrical resistivity ρ_r were developed. Since resistivity (R) is inversely related to conductivity(C) (R = 1/C), this simple calibration relation provides reliable estimates of soil moisture status from an ECa map (Leopold et al., 2021). Soil sub samples with similar laboratory EC_e (<10 μS m^{-1} difference) and texture were bulked together to reduce the number of samples for developing volumetric moisture (%) calibration equations. Furthermore, for the Mooribin site, which is uniformly sandy throughout, soil moisture calibrations for all the inverted soil depth slices (0–0.5, 0.5–0.8, and 0.8–1.6 m) were done using the single calibration equation. For the Kukerin site, soil moisture calibration for 0.8–1.6 m depth slice was done using the calibration curve developed from 0.5–0.8 m depth slice soil because this is a duplex soil with similar textural characteristics at these depths (**Table 2**).

TABLE 2 | Summary results of soil analysis for the two study sites.

Soil parameter		Mooribin Depths (m)			Kukerin Depths (m)		
		0–0.5	0.5–0.8	0.8–1.0	0–0.5	0.5–0.8	0.8–1.0
Gravimetric water (%)	Mean	3.7	3.8	4.3	6.3	8.6	9.9
	Max	6.4	5.9	5.4	10.7	12.4	13.1
	Min	1.4	2.6	3.6	2.5	2.9	7.4
	SD	1.5	0.8	0.6	2.8	2.7	1.9
Clay (%)	Mean	0.2	0.1	0.1	1.6	5.2	6.4
	Max	2.7	0.4	0.5	4.6	11.9	9.7
	Min	0.0	0.0	0.0	0.0	1.0	0.7
	SD	0.7	0.1	0.1	1.4	3.9	3.1
Silt (%)	Mean	1.2	0.2	0.3	4.1	8.2	8.9
	Max	10.6	1.2	1.3	12	16.5	19.9
	Min	0.0	0.0	0.0	0.0	1.5	2.0
	SD	2.8	0.3	0.4	3.8	5.02	6.6
Sand (%)	Mean	98.6	99.7	99.6	94	86.5	84.6
	Max	100	100	100	100	97.1	97.2
	Min	86.5	98.3	98.1	83	77.2	70.9
	SD	3.6	0.4	0.6	5.3	8.1	8.8
CEC (mEq/100 g)	Mean	0.8	0.2	0.2	1.26	2.53	3.52
	Max	1.6	0.5	0.7	2.18	5.66	5.22
	Min	<0.01	<0.01	<0.01	0.25	<0.01	0.77
	SD	0.5	0.2	0.29	0.68	2.11	0.04
Ex-Al (mEq/100 g)	Mean	<0.01	<0.01	<0.01	0.02	0.03	0.04
	Max	<0.01	0.01	0.02	0.13	0.22	0.11
	Min	<0.01	<0.01	<0.01	<0.01	<0.01	<0.01
	SD	<0.01	<0.01	<0.01	0.04	0.07	0.04
Ex-Ca (mEq/100 g)	Mean	0.60	0.05	0.09	0.64	0.30	0.26
	Max	1.12	0.13	0.38	1.31	0.57	0.43
	Min	0.15	0.02	<0.01	0.06	0.04	0.03
	SD	0.32	0.03	0.11	0.38	0.22	0.15
Ex-K (mEq/100 g)	Mean	<0.01	<0.01	<0.01	0.02	0.02	0.02
	Max	0.03	0.01	0.05	0.04	0.09	0.14
	Min	<0.01	<0.01	<0.01	<0.01	<0.01	<0.01
	SD	0.01	0.01	0.02	0.01	0.03	0.05
Ex-Mg (mEq/100 g)	Mean	0.11	0.02	0.03	0.28	1.60	2.26
	Max	0.24	0.06	0.12	0.48	4.06	3.51
	Min	0.04	0.00	0.00	0.07	0.10	0.26
	SD	0.04	0.01	0.03	0.14	1.62	1.09
Ex-Na (mEq/100 g)	Mean	0.03	0.01	0.01	0.04	0.30	0.41
	Max	0.06	0.02	0.03	0.07	1.17	0.93
	Min	0.02	0.00	0.00	0.01	0.01	0.05
	SD	0.01	0.00	0.00	0.02	0.41	0.29
Bic P (mg/kg)	Mean	3.8	3.5	4.2	1.8	0.0	0.0
	Max	8.9	7.8	10.8	4.1	0.5	0.2
	Min	0.5	0.2	0.0	0.2	0.0	0.0
	SD	2.1	2.8	4.1	1.2	0.4	0.3
Total C (%)	Mean	0.51	0.07	0.06	0.5	0.12	0.09
	Max	1.17	0.14	0.12	0.81	0.32	0.11
	Min	0.15	0.04	0.03	0.09	0.04	0.03
	SD	0.25	0.03	0.02	0.23	0.08	0.02
Total N (%)	Mean	0.03	0	0	0.04	0.01	0.01
	Max	0.1	0.01	0.01	0.06	0.03	0.02
	Min	0.01	0.00	0.00	0.00	0.00	0.00
	SD	0.02	0.00	0.00	0.02	0.00	0.00
pH ($CaCl_2$)	Mean	4.5	4.6	4.9	4.7	5.4	5.6
	Max	4.8	4.8	5.3	5.9	6.1	6.1
	Min	4.2	4.5	4.6	4.2	4.9	4.9
	SD	0.2	0.1	0.2	0.6	0.4	0.4
EC_e (mS/m)	Mean	54.6	7.5	6.3	48.9	36.44	38.4
	Max	90.7	10.2	10.1	78.5	78.28	55.3
	Min	23.6	3.2	4.9	25.1	11.28	14.8
	SD	21.5	1.9	1.4	18.1	24.96	15.3

The resistivity to soil water calibration curves was developed using the same method as described by Shaukat et al. (2022); in brief, a sub-sample of each soil depth was placed in a 10 cm × 6.25 cm × 4 cm plastic container and saturated with deionized water. A bulk density of 1.6 g cm^{-3} was used for Mooribin and 1.5 g cm^{-3} for Kukerin. Four electrodes at 1 cm spacing were inserted in the saturated soil sample, with the resistivity measured hourly. The whole setup was placed on an automatic scale (0.00 g) to track the weight difference over time of sample drying in a temperature control room at 25°C.

To validate the accuracy of prediction, this predicted soil moisture content was compared with the moisture content derived from the soil samples, which was converted from gravimetric to volumetric moisture units.

2.5 Measurement of *L. nitens* Survival and Growth

UAV imaging surveys were done at Mooribin on 11 December 2020 and at Kukerin on 12 December 2020 to map the survival (tree counting) and growth (shrub canopy diameter) of planted *L. nitens*. A DJI M600 6 Rotor drone provided with red, green, and blue (RGB) FC550 (15 mm focal length) camera to capture the images (**Supplementary Appendices 1 and 2**). UAV imaging was carried out around mid-day under a clear sky at the height of 106 m for Mooribin and 100 m for Kukerin. To improve the positional accuracy of the images, four ground control points (GCPs) were identified using a handheld RTK system and used for dereferencing the photogrammetry processing workflow. Imaging metadata is provided in **Supplementary Appendices 1 and 2**.

3 DATA PROCESSING

In brief, the EMI data was cleaned, and outliers were removed and then inverted to the depths of 0–0.5, 0.5–0.8, and 0.8–1.6 m. The inverted ECa was used to predict field-scale soil moisture using ERT–EMI power-law calibration equations, as previously described. Then, a deep-learning framework for automatically counting the shrubs in the UAV (drone) images was developed. Statistical analysis was performed to determine the main soil parameters at each site that may influence *L. nitens* survival and growth. The newly planted *L. nitens* survival and growth data were then compared across the different soil (ECa) zones/areas within each site to relate shrub performance to soil characteristics/map.

3.1 Outlier Correction

A python-based outlier detection algorithm, "*hampel filter*", was used for the EMI field data attributed to any surface metallic objects. The filter works with the configurable moving median window and defined number of standard deviations (Delefortrie et al., 2014; Pearson et al., 2016). Here, we used the size of ten data points with three standard deviations to detect the outlier and replace it with the representative median value. Based on the set threshold, the detected outliers were less than 1% of the data in all the arrays. The code for this filter is available in the GitHub repository (Lewinson, 2019).

3.2 Quasi-3D Inversion of Electromagnetic Conductivity Imaging

ECa obtained from the EMI surveys was a weighted average of conductivity over a full depth of exploration. EM4Soil software (EMTOMO, 2018) package was used to invert these weighted averages to depth-specific conductivities or true conductivities (σ, mS m^{-1}) (Monteiro Santos et al., 2010, 2011), which are further mentioned as inverted EC. The quasi-3D inversion algorithm used was based on the assumption that 1-dimensional variation of true electrical conductivity is constrained by neighboring variations for each measured ECa location (Monteiro Santos, 2004; Monteiro Santos et al., 2011). EM4Soil requires a forward model based on linear cumulative function (CF) (McNeill, 1980) or non-linear full solution (FS) (Frischknecht, 1988). The inversion algorithm uses Occam regularization (Sasaki, 1989, 2001) and a damping factor (λ) to balance between data misfit and smoothness of Electromagnetic conductivity imaging (EMCI). Based on the lowest misfit, RMSE, and highest coefficient of determination between modeled and observed data, best inversion results were obtained using the cumulative function model, S2 algorithm with 0.07 λ for 10 iterations.

For quantitative comparison of field ECa, temperature correction for 25°C was performed using correction factors by Ma et al. (2011). Out of our four Dualem-1Hs arrays, we excluded the top 0.5 PRP (DOE 0.3 m) for not being the true representative of 70% of the EMI signal at the top 0.3 m due to the sensor height (10 cm) above the ground resulting in very low to zero conductivity values. A three-layered inversion model was selected based on the used geophysical arrays (Triantafilis et al., 2013), resulting in depth slices of 00.5, 0.5–0.8, and 0.8–1.6 m. The inverted EC was kriged using a 5 m grid in VESPER (Variogram Estimation and Spatial Prediction plus Error) software (Minasny et al., 2005).

3.4 Frequency Conversion of Inverted EC

Results of measuring electrical resistivity and conductivity are frequency-dependent. For estimating volumetric soil moisture from inverted EC, the differences in frequency of Dualem-1HS (9 kHz) and laboratory-based electrical resistivity tomography (ERT) measurement (4.16 Hz) were accounted for using the "Modified Portela Model" described by Moura et al. (2018).

3.5 Digital Photogrammetry Using Machine-Learning Algorithms

Raw UAV images at 1.8 cm ground resolution were stitched together to develop an Orthophoto and a 3D point cloud, followed by 3D data classification to produce a canopy height model (CHM). A machine-learning algorithm called "YOLOv5" was used for the *L. nitens* plant detection for surviving shrubs count. YOLO refers to "You Only Look Once", a family of algorithms introduced by Redmon et al. (2016). This algorithm is designed to detect individual objects by drawing

bounding boxes and identifying classes of objects such as cars, humans, and signs. Unlike segmentation models such as Unet (Ronneberger et al., 2015), where accurate delineation of objects is an important quality indicator, YOLO deals with classification (identifying if the object is present in the image) and accurate localization of objects (prediction of the bounding box around the required object in the image).

For our deep learning training, bounding box samples were collected in 250 images covering shrubs of various sizes and shapes. The actual training was conducted on 80% of the dataset (200 images, including 1,500 shrubs), and the remainder was used for validation. The trained model was tested in two test areas, with 90 and 5,600 m^2, to assess the model performance.

Four quality metrics were used to evaluate the object detection model performance: 1) Precision–the percentage of our correct predictions. 2) Recall–the percentage of all the positive predictions. 3) Intersection of union (IoU)–a value used in object detection to measure the overlap of a predicted vs. actual bounding box for an object, and 4) Mean average precision (mAP)–the average of average precision (AP). AP is calculated for each class and averaged to get the mAP.

For modeling of shrub canopy diameter, shrubs were segmented into pixels using circles and estimating the average intensity of pixels within these circles. Given that the intensity values of the shrub and the bare ground were known, the diameter of the shrub (circle around the plant) was set when the average intensity values within the circles were closer to the bare ground than the shrub. For shrub diameter growth, ground-truthing was done by manually taking the diameter of randomly selected 530 shrubs at the Mooribin site. Diameter from each shrub was measured at three heights; top (1/3 plant), middle (widest part), and bottom (1/3 plant) part of the shrub and locations of the shrubs were noted for comparison.

3.6 Statistical Analysis

3.6.1 Principal Component Analysis

Principal component analysis (PCA) was used to identify the main soil variables that may influence the *L. nitens* survival and growth (R Core Team, 2020). The input matrix comprised soil physico-chemical analysis data and related inverted EC from 10 m around the soil sampling points at both sites.

3.6.2 Tests of Significance

The non-parametric Wilcoxon test was used to test the difference between measured volumetric water content from the soil samples and EMI predicted volumetric water content for each depth slice. The Kruskal–Wallis test was used to compare the modeled (UAV-derived) and manual shrub diameter measurements taken from three parts (top, middle, and bottom) of a plant. This test was also used to compare shrub diameters within the different EMI mapped (inverted EC) soil zones/areas for each site. This test was performed using the R software package (R Core Team, 2020).

4 RESULTS

4.1 Soil Physico-Chemical Properties

EC_e values for all the soil samples were less than 200 mS m^{-1} (**Table 2**), which indicates that both study sites were non-saline (Simons and Bennett, 2021). In addition, average pH values of Mooribin for all three depth slices ranged from 4.5 to 4.9 (SD 0.1) and in Kukerin from 4.7 to 5.6 (SD 0.4). PSA of all the three depth slices of Mooribin showed it to be a relatively uniform sandy site with a mean of 99% sand (SD 3.6). Kukerin soils showed variable textures both vertically and horizontally, with the topsoil being more sandy to loamy and the subsoils being more loamy (**Table 2**).

Average CEC (mEq 100 g^{-1}) for all the soil depth slices of Mooribin and Kukerin ranged from 0 to 1.6 (SD 0.5) and 0 to 5 (SD 1), respectively. Similarly, exchangeable Al, Ca, K, Mg, and Na were <1 mEq 100 g^{-1}, and total C and N were <1% in all the depth slices of both sites. BicP (mg kg^{-1}) concentration at Mooribin ranged from 0 to 8 (SD 2.0), 0 to 7 (2.8), and 0 to 10 (SD 4.1) mg kg^{-1} for depth slices of 0–0.3, 0.3–0.5, and 0.5–1.0 m, respectively, while for Kukerin Bic P ranged from 0 to 4 mg kg^{-1} throughout all the measured depth slices.

4.2 Electromagnetic Conductivity Imaging of Inverted Soil Layers

Figure 2 shows the spatial distribution of inverted EC at three depth slices of 0–0.5, 0.5–0.8, and 0.8–1.6 m. For Mooribin, the inversion model misfit was 0.2% with RMSE of 0.2 mS m^{-1} for the dry season survey and model misfit of 0.6% with RMSE of 0.3 mS m^{-1} for the wet season survey. For Kukerin, the model misfit was 5.4 with RMSE of 6 mS m^{-1} for the dry season survey and model misfit of 6% with RMSE of 7 mS m^{-1} for the wet season survey. Inverted EC in the wet season survey was higher than during the dry season and was lower at Mooribin across the site and along the measured depths (0–9 mS m^{-1}) than at the Kukerin site (0–36 mS m^{-1}). The inverted EC was grouped into three ranges according to the measured values at both sites.

At Mooribin, the dry season had the lowest inverted EC range of 0–3 mS m^{-1} in the top measured depth slice of 0–0.5 m (**Figure 2A**). The rest of the two depth slices (**Figures 2B and C**) showed the inverted EC range of 3–6 mS m^{-1} in most of the area, with patches of 0–3 and 6–9 mS m^{-1}. For the wet season, the top two depth slices, 0–0.5 m (**Figure 2B**) and 0.5–0.8 m (**Figure 2E**), mostly had an inverted EC range of 3–6 mS m^{-1}, with some patches of 6–9 mS m^{-1}, especially in the second depth slice. The deepest measured depth slice of 0.8–1.6 m (**Figure 2F**) had the highest inverted EC range of 6–9 mS m^{-1}. The percentage difference maps (**Figures 2G–I**) show the change in spatial inverted EC distribution from the dry to wet season, which was most prominent in the top (0–0.5 m, **Figure 2F**) and the deepest depth slice (0.8–1.6 m, **Figure 2H**) toward the higher values. Overall, this site showed relatively homogenous inverted EC for the dry and wet season measurements, as expected for uniformly sandy soil.

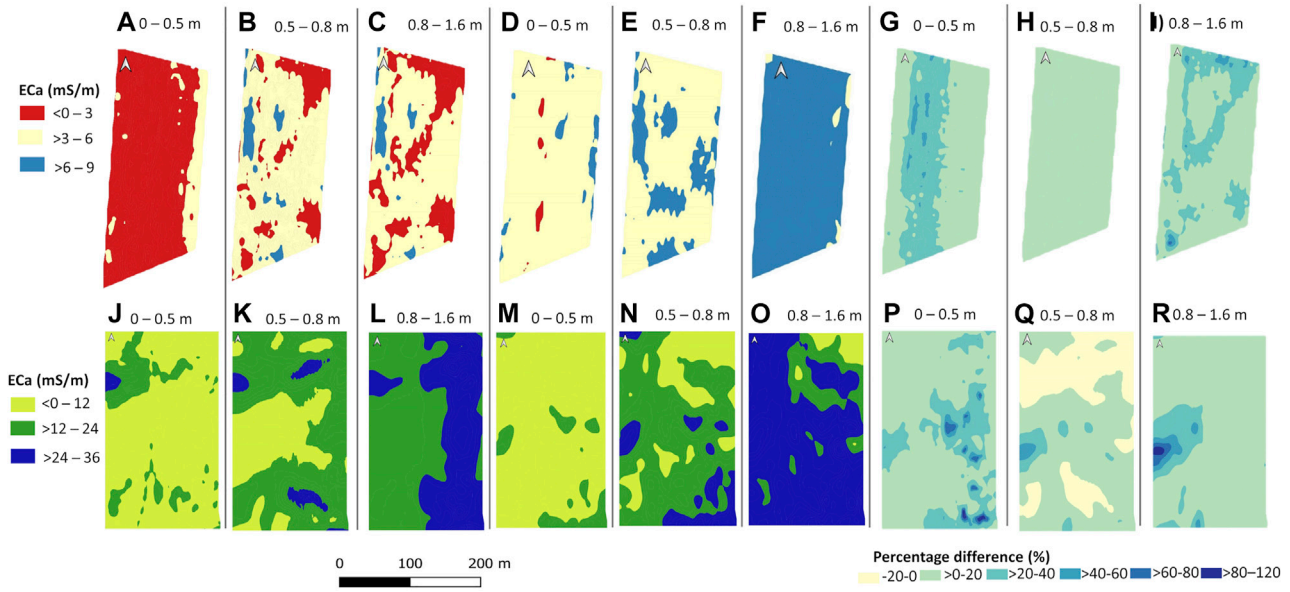

FIGURE 2 | Inverted electrical conductivity (EC) at three depths of 0–0.5, 0.5–0.8, and 0.8–1.6 m at the Mooribin site taken on 7 June 2019 [(dry season—**A**–**C**)], on 19 August 2019 [(wet season—**D**–**F**)]. Percentage difference between the inverted EC of two surveys at three depths **(G**–**I)**. Similarly, at the Kukerin site on 4 June 2019 [(dry season—**J**–**L**) and on 22 August 2019 (wet season—**M**–**O**)], and percentage difference maps of two surveys relative to the dry season at three depths **(P**–**R)**.

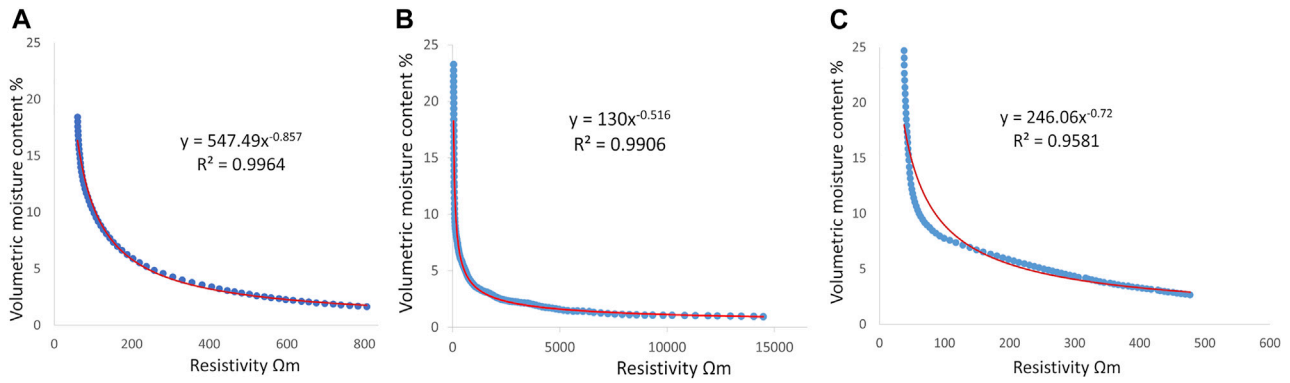

FIGURE 3 | Power-law relationships between volumetric moisture content (%) and electrical resistivity (Ωm) for all the depths of Mooribin site **(A)** and Kukerin site for lower inverted EC range of 0–12 mS m^{-1} **(B)** and higher inverted EC range of 12–36 mS m^{-1} **(C)**. The red line is the fitted power-law.

For Kukerin, the site had a variable spatial distribution of inverted EC, which changed with the season and increased with soil depth. For both seasons, the top depth slice of 0–0.5 m (**Figures 2J and M**) had the lowest measured inverted EC range of 0–12 mS m^{-1}. However, for the dry season (**Figure 2J**), the top western part of the field showed an area with mid-range inverted EC of 12–24 mS m^{-1}. The inverted EC appeared to decrease in this top western part of the field in the wet season, compared to the dry season, except for a small area of 12–24 mS m^{-1} in the bottom east corner (**Figure 2M**). The highest spatial inverted ECa distribution variability was in the second depth slice for both dry and wet seasons, where most of the area showed the mid-range inverted EC of 12–24 mS m^{-1}. The lower-range inverted EC of 0–12 mS m^{-1} in the middle of the field in the dry season (**Figure 2K**) and in the top east corner in the wet season (**Figure 2N**). During the dry season (**Figure 2L**), the last depth slice of 0.8–1.6 m showed the west half of the field with mid-range inverted EC (12–24 mS m^{-1}) and the east half with high-range inverted EC (24–36 mS m^{-1}). The last depth slice for the wet season survey (**Figure 2O**) showed high-range (24–36 mS m^{-1}) inverted EC except for the top east corner.

The percentage difference maps from the dry to wet season survey show a relatively large change in the south-east part of the top depth slice (0–0.5 m; **Figure 2P**). For the second depth slice (0.5–0.8 m; **Figure 2Q**), inverted EC

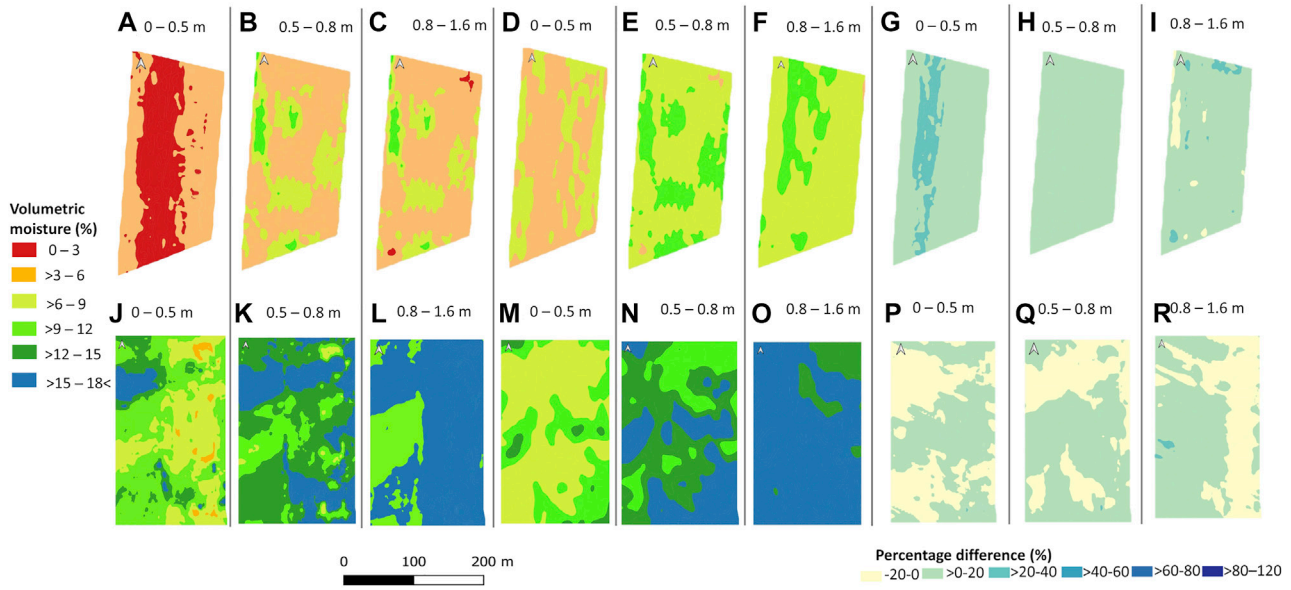

FIGURE 4 | Predicted volumetric moisture content based on inverted EC of three depths (0–0.5, 0.5–0.8, and 0.8–1.6 m) at the Mooribin site [(dry season—**A–C** and wet season—**D–F**)] and percentage difference between the volumetric moisture content of both seasons **(G–I)**. Similarly, predicted volumetric moisture content at the Kukerin site (dry season—**J–L** and wet season—**M–O**) and percentage difference relative to dry season between the volumetric moisture content of both seasons **(P–R)**.

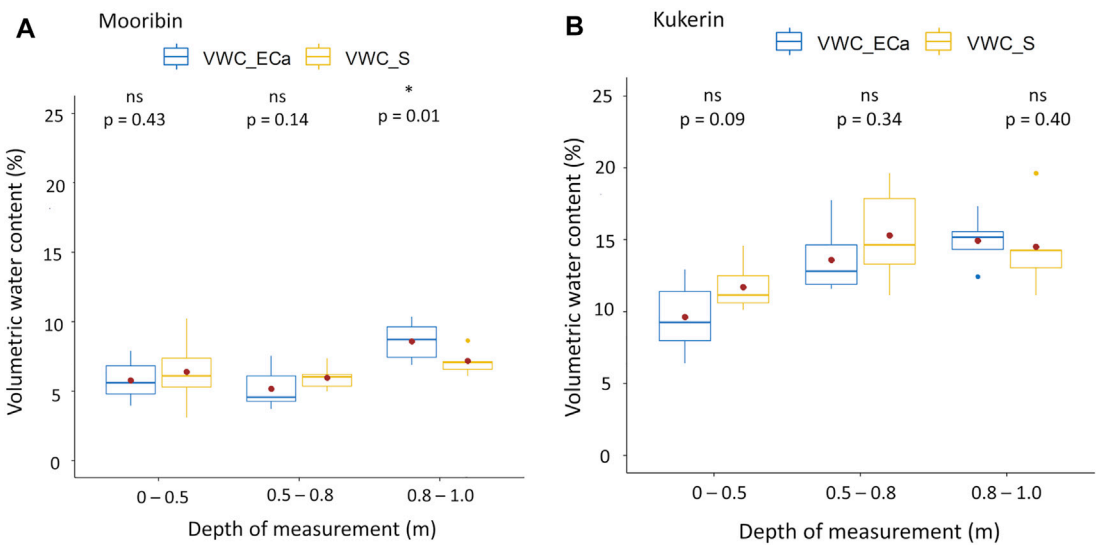

FIGURE 5 | Comparison of measured volumetric water content (%) from soil samples (VWC_S) vs. predicted volumetric water content using ERT–EMI calibration curves (VWC_ECa) from inverted EC of the wet season (both taken in August 2019) **(A)** at Mooribin **(B)** at Kukerin site. Whiskers indicate the maximum and minimum values at the 95% confidence level, the top and bottom of the box show the 25th and 75th percentiles, the line inside the box is the median value, the dot inside is the mean value, and *p* values are determined using Wilcoxon test.

increased in the mid-west and decreased in the north part of the site, while in the last depth slice of 0.8–1.6 m (**Figure 2R**), the maximum increase in inverted EC was in the mid-west part of the field.

4.3 Spatial Distribution of Calculated θ(%)

Figure 3 shows the resistivity to volumetric moisture power-law curves used for calculating the spatial distribution of volumetric moisture content % (**Figure 4**) for both sites

TABLE 3 | Shrub count accuracy assessment result.

Class	Trained data		Tested data	
	Precision	Recall	Precision	Recall
Shrub	0.57	0.97	0.54	0.94
mAP[a]	0.89		0.86	
IoU[b]	0.93		0.89	

[a]*Mean average precision.*
[b]*Intersection over union.*

using the inverted ECa (**Figure 2**). In the case of Mooribin, the overall volumetric moisture content in the wet season was slightly higher than in the dry season, as expected. The top depth slice of 0–0.5 m (**Figures 4A and D**) showed the lowest predicted volumetric moisture of 0–6% in the dry season and >3–6% in the wet season in most of the area with the patches of 6–9%. The other two depth slices showed similar moisture distribution patterns, with >3–6% moisture prediction in most of the areas with patches of 6–9% in the dry season (**Figures 4B,C**) and mostly >6–9% moisture prediction with patches of 9–12% moisture in the wet season (**Figures 4E,F**). The percentage difference maps showed the maximum soil moisture change in the top depth slice (0–0.5 m; **Figure 4G**), with <20% change in deeper depths (**Figures 4H,I**).

In the case of Kukerin, spatial moisture distribution prediction showed high variability in the top two depth slices of both seasons (**Figures 4J, K, M, and N**). Broadly, for the dry season, the top depth slice of 0–0.5 m (**Figure 4J**) had >6–9% moisture in the east half and >9–12% moisture in the west half of the field, except for the top west part with higher moisture prediction of >12–15%. In the wet season, the top depth slice of 0–0.5 m (**Figure 4M**) had the low-range (>6–9%) moisture in most of the area except for the middle and bottom east corner with mid-range (>9–12%) moisture. For the second depth slice of 0.5–0.8 m, in the dry season (**Figure 4K**), high-range (>12 to 18< %) moisture values were prominent, especially in most of the top and bottom east part of the site except for the middle west part with mid-range >9–12% moisture. The second depth slice in the wet season (**Figure 4N**) showed similar moisture prediction ranges, but their spatial distribution was different. The deepest depth slice of 0.8–1.6 m showed the relatively high moisture values in most parts of the site, except for the mid-west part with >9–12% moisture in the dry season (**Figure 4L**) and in the top east corner with >12–15% moisture in the wet season (**Figure 4O**).

Percentage difference maps (**Figures 4P–R**) showed a relatively high difference in the spatial moisture distribution across the site as compared to the changes in the absolute moisture values change from dry to wet season, which was mostly around 20% in all the measured depth slices.

The Wilcoxon test resulted in no significant difference between the measured and predicted volumetric moisture % values except for the third depth slice of Mooribin (**Figure 5A**). However, this difference is accounting the moisture range of only 3%–9% in the sandy textured soil of this site. Furthermore, at Kukerin, the volumetric moisture % increased with the increasing depth, especially from the top depth to the second depth slice (**Figure 5B**).

4.4 Accuracy Assessment of UAV Imagery

Table 3 presents the quality measures of model performance for trained and tested data sets of *L. nitens* shrub detection. The results obtained had a higher IoU of 93% and 89% for trained and tested data than the recommended PASCAL VOC challenge requirement, which is 50% (Everingham et al., 2010). Visual examples are shown in **Figures 6A–C**.

UAV-based automated shrub diameter prediction was compared with a manual diameter (cm) taken from three parts of the shrub at Mooribin. Kruskal–Wallis test (**Figure 7**) showed that shrub prediction using UAV imagery for machine learning was significantly different from the manual shrub diameter measurement for all three measuring areas. Out of all the three manually measured parts of the shrub, measurements from the bottom of the shrub appeared nearest to the machine learning results with an RMSE of 17.1.

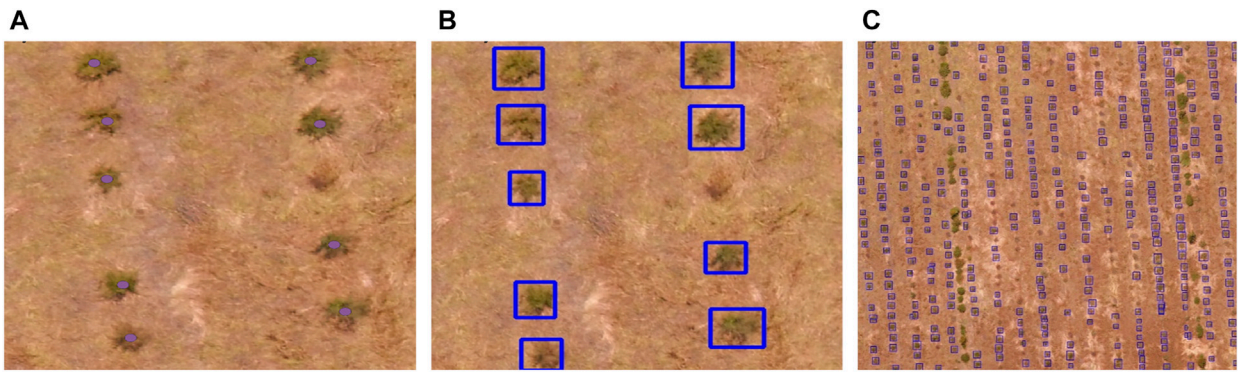

FIGURE 6 | Accuracy assessment of UAV imagery and model training example on test set at Mooribin site **(A)** manually captured shrubs, **(B)** automated result and **(C)** sample of automated shrub count results.

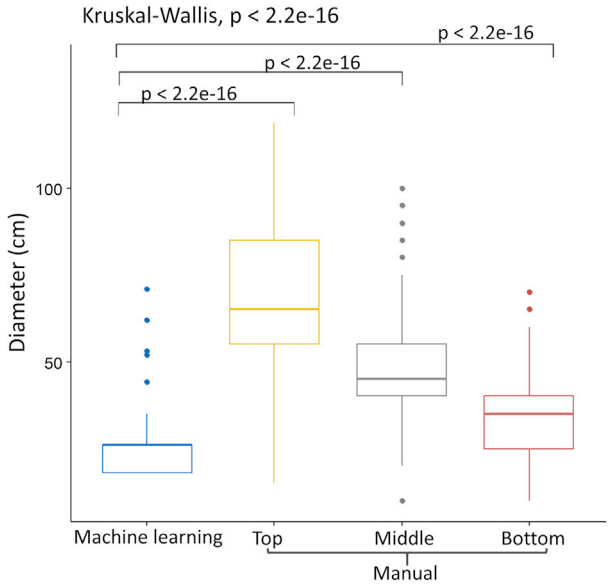

FIGURE 7 | Kruskal–Wallis test of manually measured diameter from three heights of *Leptospermum* plant (top, middle, and bottom) vs. automated canopy diameter estimation using UAV imagery and ML.

4.5 Shrub Survival and Growth Within Mapped Inverted EC Areas/Zones

Shrub survival and growth patterns estimates from ML were compared from the second inverted EC depth slices (**Figures 2B and K**) of the dry season survey, which showed the maximum variability at both sites. There were significant differences in estimated *L. nitens* shrub diameter between areas with different soil inverted EC (**Figure 8**). In the case of Mooribin, maximum shrub diameter was within the inverted EC range of >6 to 9 mS m^{-1} (mean 32 cm, SD 7), while the inverted EC ranges of 0–3 and >3 to 6 mS m^{-1} had shrub diameter of 18–26 cm (**Figure 8A**). In the case of Kukerin, the inverted EC areas of >12 to 24 and >24 to 36 mS m^{-1} had a similar average shrub diameter of 31 cm (SD 11) (**Figure 8B**). However, the range in shrub diameter varied more at >12–24 mS m^{-1} areas with 18–74 cm than the high inverted EC areas with shrub diameter of 18–55 cm. Furthermore, there was a significant difference in the number of shrubs between these mapped inverted EC areas at both sites, with an overall 77% survival at Mooribin and 82% survival at Kukerin (**Table 4**).

4.6 Principal Component Analysis

Figures 9 and **10** present the PCA for the Mooribin and Kukerin sites. The scree plot (**Figures 9A** and **10A**) showed the percentages of variations held by each principal component (PC). The first 3 PCs were retained based on eigenvalues >1 rule (Kaiser et al., 1992), accounting for ~73% (eigenvalues 7.5, 2.1, and 1.6) and ~72% (eigenvalues 5.6, 3.4, and 1.8) variation for Mooribin site and Kukerin site, respectively. In **Figures 9B** and **10B**, the projection of the arrows represents the variable loading in their respective PCs.

TABLE 4 | Shrub survival count based on inverted EC mapped areas.

ECa (mS m^{-1})	Shrub count ha^{-1}	Survival (%)	*p*-value
0–3	537	64	0.001
3–6	604	73	
6–9	721	87	
0–12	606	73	0.01
12–24	754	91	
24–36	693	83	

Furthermore, all the soil parameters contributed in the first three PCs; however, the variables contributing above the cut-off line (**Figures 9C**, **10C**) could be considered important in explaining the spatial soil variation influencing *L. nitens* plantation establishment.

For Mooribin (**Figure 9**), the variability explained by PC1 and PC2 was 63%, and inverted EC was strongly correlated to pH > volumetric moisture content > clay and silt and negatively correlated to sand and BicP. There was no correlation between ECa and ex-Mg, Total N, Total C, CEC, ex-Ca, and ex-Na. In PC3 (explaining 10% of the variability), inverted EC was again strongly correlated to pH, followed by silt, clay, and volumetric water content. There was no correlation with the rest of the elements.

For Kukerin (**Figure 10**), PC1 and PC2 explained a similar amount of variability (62%), and ECa was strongly correlated to volumetric water content > ex-Na > pH, CEC > clay and silt and negatively correlated to ex-Ca, Total N, Total C, BicP, and sand. In PC3 (explaining 12% of the variability), inverted EC had a relatively small contribution but was correlated to volumetric water content, pH, and sand. It showed little or no correlation with silt and clay and a negative correlation with the rest of the parameters.

5 DISCUSSION

In this study, a non-invasive EMI survey was used to map soil spatial variability at two sites already planted with *L. nitens* shrubs. The mapped spatial soil variability was related to newly planted *L. nitens* survival and growth (shrub canopy diameter) patterns. There was a significant difference in shrub count in the EMI mapped areas at both sites and, overall, a higher shrub count at the variable textured site (Kukerin) as compared to the uniformly sandy site (Mooribin). Areas with higher inverted soil EC were also found to have significantly larger shrub diameters at both the uniform and variable textured site. Therefore, EMI spatial soil mapping can be used to identify areas with different potential for *L. nitens* plantation establishment.

In areas with low salt concentrations, EMI signal variations generally correspond to differences in soil moisture and soil texture (Brevik and Fenton, 2002). Indeed, the PCA showed inverted EC being inversely correlated to sand and positively correlated to soil moisture. Mooribin was a uniformly deep sandy site with low agronomic value due to water repellence and lower

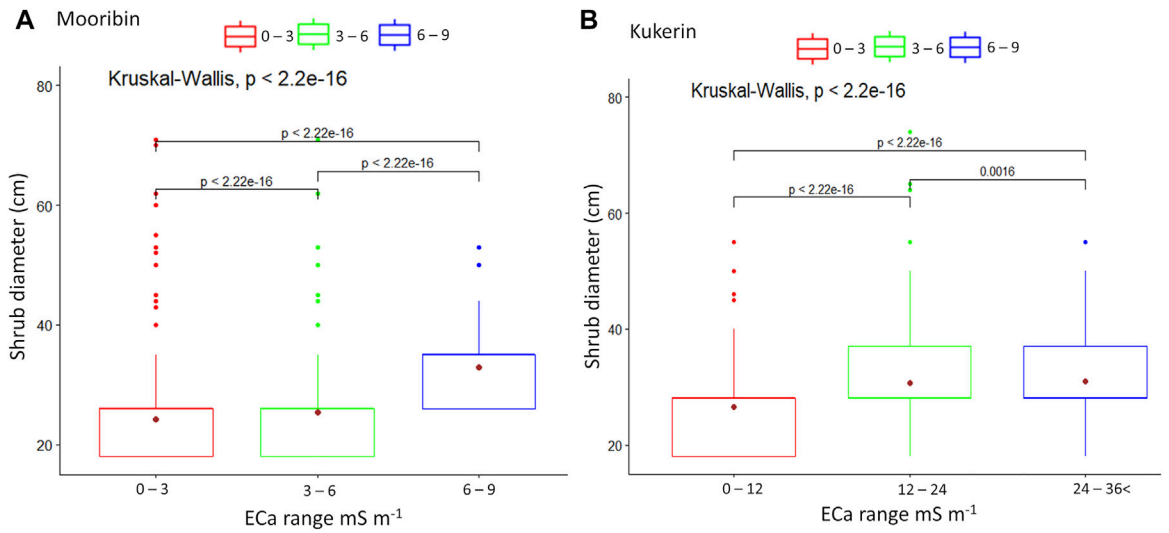

FIGURE 8 | Kruskal–Wallis comparison of shrub canopy diameter (cm) (based on UAV-derived ML method) across the sites with three different inverted EC ranges measured at 0.5–0.8 m soil depth (**Figures 2B and K**) at Mooribin **(A)** and at Kukerin **(B)**. Whiskers indicate the maximum and minimum values at the 95% confidence level, the top and bottom of the box show the 25th and 75th percentiles, and the dot inside is the mean value.

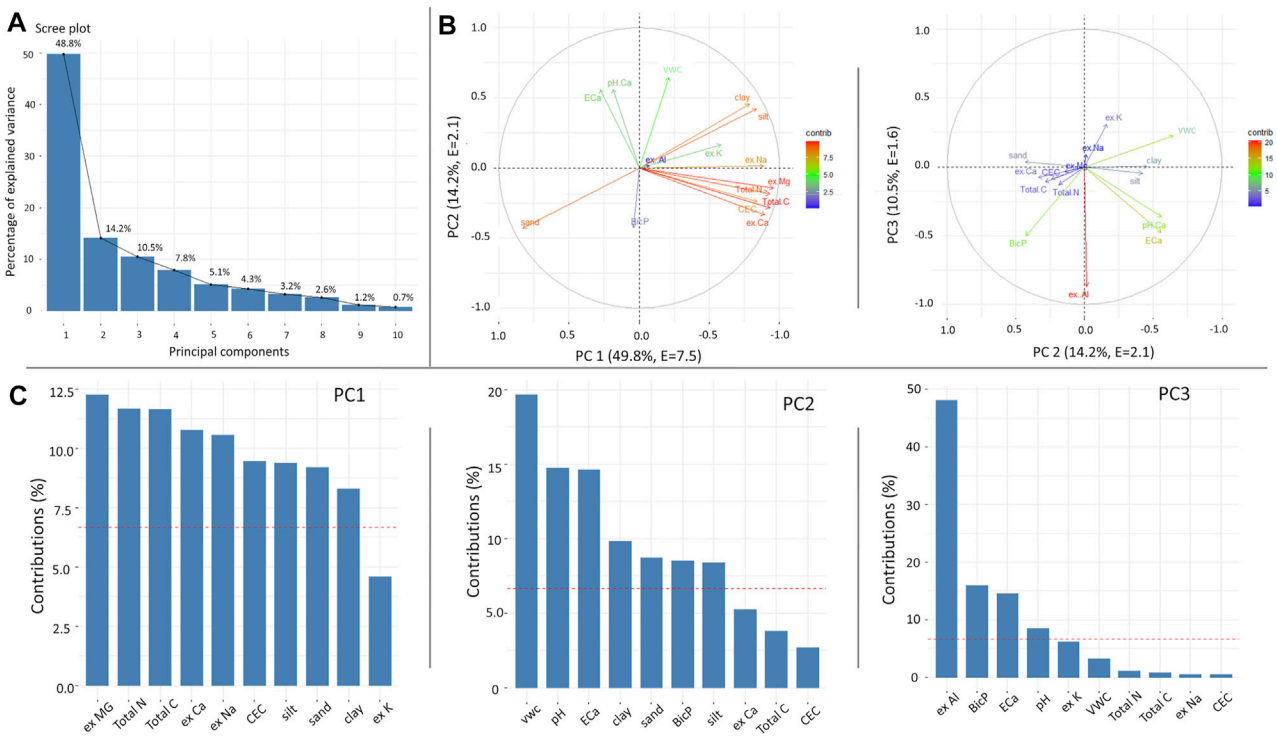

FIGURE 9 | Principal component analysis for Mooribin soil parameters showing **(A)** scree plot, **(B)** variables highlighted based on their percent contribution in correlation plots, and **(C)** contribution of variables in selected PCs, where the red line shows the expected average contribution (cut-off). The soil variables included are sand, silt, clay, volumetric water content, pH, CEC, Total N &Total C, ex Mg, ex Na, ex Ca, ex Al, ex K, BicP, and inverted EC from 10 m around each sample.

water retention rate (Roper et al., 2015). EMI surveys of this site had lower ECa values, and the ECa values increased from the dry to the wet season. Since soil water was the main variable factor between the seasons, the differences in ECa most likely corresponded to the differences in soil moisture. Our EMI–ERT volumetric moisture prediction values (**Figure 5A**)

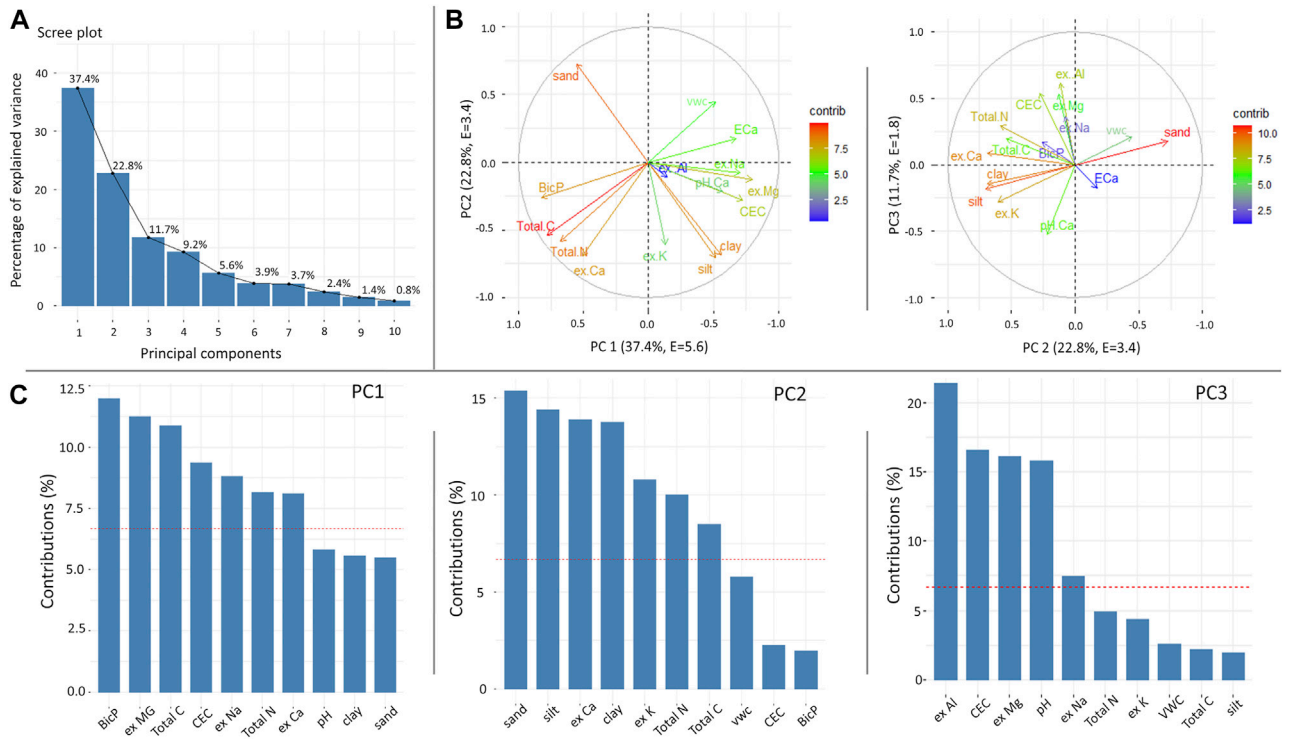

FIGURE 10 | Principal component analysis for Kukerin soil parameters showing **(A)** scree plot, **(B)** variables highlighted based on their percent contribution in correlation plots, and **(C)** contribution of variables in selected PCs, where the red line shows the expected average contribution (cut-off). The soil variables included are sand, silt, clay, volumetric water content, pH, CEC, Total N &Total C, ex Mg, ex Na, ex Ca, ex Al, ex K, BicP, and inverted EC from 10 m around each sample.

TABLE 5 | *Leptospermum nitens* performance in different soil textures.

Parameter		Deep sandy soil	Sandy top and loamy subsoil	Loamy top and loamy subsoil	Loamy top and clayey subsoil
Shrub survival/ha (%)		75	88	89	83
Shrub growth (Diameter cm)	Median	27	28	37	28
	Average	26	25	38	33

were within the range of deep sandy soil moisture rates (Tsoar, 2005). *Leptospermum* plants performed well in this deep sandy soil, with an overall 75% survival rate ha^{-1}. The 2021 season was relatively wet, and it was also observed that the flowering of shrubs at this site was good, regardless of shrub diameter. EMI survey at variable textured soils of Kukerin had higher ECa values than the uniformly sandy site with overall higher shrub survival (82%) and growth rate. A detailed comparison of shrub survival and growth patterns has shown that sandy loam and loamy textured areas resulted in higher *L. nitens* survival and growth rate. However, further increase in the clay content did not improve the shrub survival count or diameter (**Table 5**). This suggests that the performance of *Leptospermum* plantations at such sites is strongly influenced by soil moisture and is susceptible to drought periods; especially as the water retention of sands is low and soil water availability plays an important role in the successful establishment of native shrubs (Hahs et al., 1999). Moreover, for *L. scoparium*, studied under controlled conditions, Williams et al. (2014) found that soil composition had little to no impact on the growth and quality of nectar produced. However, water stress was reported to affect the nectar yield (Villarreal and Freeman, 1990; Carroll et al., 2001; Nickless et al., 2017).

Summarized shrub performance with respect to soil texture areas (**Table 5**) showed that a robust and detailed spatial map of variability could be generated in broad acre sites using EMI surveys. This would effectively improve the soil assessments for planning new plantations and site selection for reforestation or successfully introducing native shrubs in agricultural cropping areas. The EMI survey clearly mapped the different textural classes at the variable site. For example, at Kukerin, the top soil depth slice of 0–0.5 m (2J) had a higher inverted EC toward the top west part of the field during the dry season survey. This was an area of higher clay content and indicated that during the dry soil conditions, soil texture was

the most important factor contributing to the ECa values, as found by Abdu et al. (2017) and Doolittle and Brevik (2014).

Generally, medium-textured areas have shown the best shrub establishment rate; however, this textural class is most suitable for agriculture due to their nutrient holding capacity, better aeration, and drainage capacity, as compared to sandy or clayey soils (Salter and Williams, 1965). Nevertheless, heavier textured soil had a survival rate on par with medium-textured soils, so areas with higher clay content and high cost of production for growing crops can be suitable for planting *L. nitens*. Moreover, *L. nitens* survival of 75% in deep sandy soil, although the growth rate was lower, can be a good option for utilizing areas with low water retention and repellence rather than cropping.

6 LIMITATION

UAV-based monitoring system helps in reducing the high cost to cover a large area and temporal resolution limitations of satellite sensors (Asner et al., 2009; Kellenberger et al., 2017); nevertheless, for vegetation applications, their 3D point clouds only point to the upper canopy surface and critically miss the sub-canopy structure information (Baltsavias et al., 2008). In this study, the UAV survey for shrub canopy diameter detection was conducted when the shrubs were 2 years old. As such, *L. nitens* shrubs are not dense when they are young. Therefore, the circles used to model the intensity value of shrub and bare ground might have further contributed to the shrub diameter underestimation. Moreover, there was a gap between the UAV survey and manual diameter measurements of shrubs, which further added to the difference in comparison. It is important to consider the time of UAV imagery survey and ground-truthing as close as possible to get comparable data.

In order to expand the soil-type recommendations for *L. nitens*, further surveys should be conducted on heavy clay and saline soils, as the current study only considered deep sands and medium-textured soils, which were non-saline. With regards to *L. nitens* growth on saline soils, Cassaniti et al., 2009 demonstrated relative salt tolerance by *L. scoparium* plants treated with saline water, where despite high ion concentration in the leaves, plant growth was not affected. However, the quality of nectar produced by their flowers was not studied.

7 CONCLUSION

A real-time ECa mapping of the marginal soils showed the impact of spatial soil variability on the establishment and growth patterns of *L. nitens* plantation. This method was robust and quick to determine the spatial soil variability at both uniform and variable textured sites and in different rainfall seasons. This study demonstrated that the *L. nitens* cultivations could thrive on marginal agricultural lands. Based on the comprehensive analysis the main conclusions were:

1. *L. nitens* plantation thrived in a range of soil textures with low fertility; however, there was a significantly larger shrub survival and growth rate in medium and heavier texture areas than in deep sandy areas.
2. Soil moisture can be a limiting factor in shrub survival and growth (shrub canopy diameter) as areas with high inverted EC corresponding to medium texture soil and higher soil moisture retention resulted in higher shrub count and shrub diameter and vice versa. Further studies are required to study the quality and quantity of nectar production by this shrub with respect to EMI mapped areas with different shrub counts and diameter growth.
3. Dry season ECa survey can provide a useful map for marking the soil textural variability, and a wet season map is useful for delineating localized soil management zones, which is particularly useful for intercropping with *Leptospermum* shrubs.

DATA AVAILABILITY STATEMENT

Data supporting the findings of this study are included in the article/**Supplementary Material**. Raw data that support the findings of this study are available from the corresponding author, upon reasonable request.

AUTHOR CONTRIBUTIONS

HSS–Main researcher, data acquisition, data analysis, software user, original draft preparation. KFS–Project Supervision, methodology, queries, writing-review and editing. MLS–Project Supervision, methodology and conceptualization review, writing-review.

FUNDING

This research has been generously supported by the Cooperative Research Centre for Honey Bee Products (CRCHBP), Department of Industry, Science, Energy, and Resources Australia (Grant # 20160042).

ACKNOWLEDGMENTS

The first author acknowledges the Australian Government Department of Education and Training that provided her with the Research Training Programme Scholarship. The authors acknowledge Honey for Life group for providing access to the study sites.

SUPPLEMENTARY MATERIAL

The Supplementary Material for this article can be found online at: https://www.frontiersin.org/articles/10.3389/fenvs.2022.883533/full#supplementary-material

REFERENCES

Abdu, H., Robinson, D. A., Boettinger, J., and Jones, S. B. (2017). Electromagnetic Induction Mapping at Varied Soil Moisture Reveals Field-Scale Soil Textural Patterns and Gravel Lenses. *Front. Agr. Sci. Eng.* 4, 135–145. doi:10.15302/J-FASE-2017143

Adams, C. J., Boult, C. H., Deadman, B. J., Farr, J. M., Grainger, M. N. C., Manley-Harris, M., et al. (2008). Isolation by HPLC and Characterisation of the Bioactive Fraction of New Zealand Manuka (*Leptospermum scoparium*) Honey. *Carbohydr. Res.* 343, 651–659. doi:10.1016/j.carres.2007.12.011

Adams, C. J., Manley-Harris, M., and Molan, P. C. (2009). The Origin of Methylglyoxal in New Zealand Manuka (*Leptospermum scoparium*) Honey. *Carbohydr. Res.* 344, 1050–1053. doi:10.1016/j.carres.2009.03.020

Arshad, M., Li, N., Bella, L. D., and Triantafilis, J. (2020). Field-scale Digital Soil Mapping of Clay: Combining Different Proximal Sensed Data and Comparing Various Statistical Models. *Soil Sci. Soc. Am. J.* 84, 314–330. doi:10.1002/saj2.20008

Asner, G. P., Flint Hughes, R., Varga, T. A., Knapp, D. E., and Kennedy-Bowdoin, T. (2009). Environmental and Biotic Controls over Aboveground Biomass throughout a Tropical Rain Forest. *Ecosystems* 12, 261–278. doi:10.1007/s10021-008-9221-5

Australian Bureau of Statistics (2002). *Salinity on Australian Farms 2002, Bulletin 4615*. Available at: https://www.abs.gov.au/ausstats/abs@.nsf/mf/4615.0.

Baltsavias, E., Gruen, A., Eisenbeiss, H., Zhang, L., and Waser, L. T. (2008). High-quality Image Matching and Automated Generation of 3D Tree Models. *Int. J. Remote Sens.* 29, 1243–1259. doi:10.1080/01431160701736513

Bean, A. R. (1992). The Genus Leptospermum Forst. Et. Forst. F. (Myrtaceae) in Northern Australia and Malesia. *Austrobaileya* 3, 643–659. doi:10.2307/41738808

Bean, T. (2004). Three New Species of Leptospermum (Myrtaceae) from Queensland and Northern New South Wales. *Telopea* 10, 831–838.

Beets, P., Kimberley, M., Paul, T., Oliver, G., Pearce, S., and Buswell, J. (2014). The Inventory of Carbon Stocks in New Zealand's Post-1989 Natural Forest for Reporting under the Kyoto Protocol. *Forests* 5, 2230–2252. doi:10.3390/f5092230

Bennett, D. L., and George, R. J. (1995). Using the EM38 to Measure the Effect of Soil Salinity on Eucalyptus Globulus in South-Western Australia. *Agric. Water Manag.* 27, 69–85. doi:10.1016/0378-3774(95)91232-V

Bennett, L. (1994). The Expansion of Leptospermum Laevigatum on the Yanakie Isthmus, Wilson's Promontory, under Changes in the Burning and Grazing Regimes. *Aust. J. Bot.* 42, 555–564. doi:10.1071/BT9940555

Bittelli, M. (2011). Measuring Soil Water Content: A Review. *hortte* 21, 293–300. doi:10.21273/horttech.21.3.293

BOM (2021). Climate Statistics of Australian Locations. Available at: http://www.bom.gov.au/climate/data/index.shtml.

Brevik, E. C., and Fenton, T. E. (2002). Influence of Soil Water Content, Clay, Temperature, and Carbonate Minerals on Electrical Conductivity Readings Taken with an EM-38. *Soil Surv. Horizons* 43, 9. doi:10.2136/sh2002.1.0009

Burrell, J. (1965). Ecology ofLeptospermumin Otago. *N. Z. J. Bot.* 3, 3–16. doi:10.1080/0028825X.1965.10428708

Burrell, J. (1981). Invasion of Coastal Heaths of Victoria by Leptospermum Laevigatum (J. Gaertn.) F. Muell. *Aust. J. Bot.* 29, 747–764. doi:10.1071/bt9810747

Carroll, A. B., Pallardy, S. G., and Galen, C. (2001). Drought Stress, Plant Water Status, and Floral Trait Expression in Fireweed, Epilobium Angustifolium (Onagraceae). *Am. J. Bot.* 88, 438–446. doi:10.2307/2657108

Cassaniti, C., Leonardi, C., and Flowers, T. J. (2009). The Effects of Sodium Chloride on Ornamental Shrubs. *Sci. Hortic.* 122, 586–593. doi:10.1016/j.scienta.2009.06.032

Charron, G., Robichaud-Courteau, T., La Vigne, H., Weintraub, S., Hill, A., Justice, D., et al. (2020). The DeLeaves: a UAV Device for Efficient Tree Canopy Sampling. *J. Unmanned Veh. Sys.* 8, 245–264. doi:10.1139/juvs-2020-0005

Cokcetin, N. N., Pappalardo, M., Campbell, L. T., Brooks, P., Carter, D. A., Blair, S. E., et al. (2016). The Antibacterial Activity of Australian Leptospermum Honey Correlates with Methylglyoxal Levels. *PLoS One* 11, e0167780. doi:10.1371/journal.pone.0167780

Cokcetin, N., Williams, S., Blair, S., Carter, D., Brooks, P., and Harry, L. (2019). Active Australian Leptospermum Honey: New Sources and Their Bioactivity. Available at: https://www.agrifutures.com.au/wp-content/uploads/2019/10/19-037.pdf.

Corwin, D. L., and Lesch, S. M. (2013). Protocols and Guidelines for Field-Scale Measurement of Soil Salinity Distribution with ECa-Directed Soil Sampling. *Jeeg* 18, 1–25. doi:10.2113/JEEG18.1.1

Dainelli, R., Toscano, P., Di Gennaro, S. F., and Matese, A. (2021). Recent Advances in Unmanned Aerial Vehicle Forest Remote Sensing-A Systematic Review. Part I: A General Framework. *Forests* 12, 327. doi:10.3390/f12030327

Dakak, H., Huang, J., Zouahri, A., Douaik, A., and Triantafilis, J. (2017). Mapping Soil Salinity in 3-dimensions Using an EM38 and EM4Soil Inversion Modelling at the Reconnaissance Scale in Central Morocco. *Soil Use Manage* 33, 553–567. doi:10.1111/sum.12370

Delefortrie, S., Saey, T., Van De Vijver, E., De Smedt, P., Missiaen, T., Demerre, I., et al. (2014). Frequency Domain Electromagnetic Induction Survey in the Intertidal Zone: Limitations of Low-Induction-Number and Depth of Exploration. *J. Appl. Geophys.* 100, 14–22. doi:10.1016/j.jappgeo.2013.10.005

D'Emden, F. H., Llewellyn, R. S., and Burton, M. P. (2008). Factors Influencing Adoption of Conservation Tillage in Australian Cropping Regions. *Aust. J. Agric. Res. Econ.* 52, 169–182. doi:10.1111/j.1467-8489.2008.00409.x

Dixon, D. J., Callow, J. N., Duncan, J. M. A., Setterfield, S. A., and Pauli, N. (2021). Satellite Prediction of Forest Flowering Phenology. *Remote Sens. Environ.* 255, 112197. doi:10.1016/j.rse.2020.112197

Dodson, J. R., Kershaw, A. P., Arroyo M, F. M. D., and Zedler, P. H. (1995). "Evolution and History of Mediterranean Vegetation Types in Australia," in *Ecology and Biogeography of Mediterranean Ecosystems in Chile, California, and AustraliaEcological Studies (Analysis and Synthesis)* (New York, NY: Springer), 21–40. doi:10.1007/978-1-4612-2490-7_2

Doolittle, J. A., and Brevik, E. C. (2014). The Use of Electromagnetic Induction Techniques in Soils Studies. *Geoderma* 223-225, 33–45. doi:10.1016/j.geoderma.2014.01.027

EMTOMO (2018). EM4Soil: Software for Electromagnetic Tomograph. Available at: https://www.emtomo.com/products/em4soil.

Everingham, M., Van Gool, L., Williams, C. K. I., Winn, J., and Zisserman, A. (2010). The Pascal Visual Object Classes (VOC) Challenge. *Int. J. Comput. Vis.* 88, 303–338. doi:10.1007/s11263-009-0275-4

Farzamian, M., Autovino, D., Basile, A., De Mascellis, R., Dragonetti, G., Monteiro Santos, F., et al. (2021). Assessing the Dynamics of Soil Salinity with Time-Lapse Inversion of Electromagnetic Data Guided by Hydrological Modelling. *Hydrol. Earth Syst. Sci.* 25, 1509–1527. doi:10.5194/hess-25-1509-2021

Frischknecht, F. C. (1988). "6. Electromagnetic Physical Scale Modeling," in *Electromagnetic Methods in Applied Geophysics:*Theory *Investigations in Geophysics* (Houston, TX: Society of Exploration Geophysicists), Vol. 1, 364–441. doi:10.1190/1.9781560802631.ch6

Furby, S., Caccetta, P., and Wallace, J. (2010). Salinity Monitoring in Western Australia Using Remotely Sensed and Other Spatial Data. *J. Environ. Qual.* 39, 16–25. doi:10.2134/jeq2009.0036

George, S. J., Harper, R. J., Hobbs, R. J., and Tibbett, M. (2012). A Sustainable Agricultural Landscape for Australia: A Review of Interlacing Carbon Sequestration, Biodiversity and Salinity Management in Agroforestry Systems. *Agric. Ecosyst. Environ.* 163, 28–36. doi:10.1016/j.agee.2012.06.022

Griffin, E. A. (1994). *Floristic Survey of Remnanat Vegetation in the Dandaragan Area, Western Australia*. Western Australia: Department of Agriculture and Food. Perth.

Hageer, Y., Esperón-Rodríguez, M., Baumgartner, J. B., and Beaumont, L. J. (2017). Climate, Soil or Both? Which Variables Are Better Predictors of the Distributions of Australian Shrub Species? *PeerJ* 5, e3446. doi:10.7717/peerj.3446

Hahs, A., Enright, N. J., and Thomas, I. (1999). Plant Communities, Species Richness and Their Environmental Correlates in the Sandy Heaths of Little Desert National Park, Victoria. *Aust. J. Ecol.* 24, 249–257. doi:10.1046/j.1442-9993.1999.00969.x

Hanssens, D., Delefortrie, S., Bobe, C., Hermans, T., and De Smedt, P. (2019). Improving the Reliability of Soil EC-Mapping: Robust Apparent Electrical Conductivity (rECa) Estimation in Ground-Based Frequency Domain Electromagnetics. *Geoderma* 337, 1155–1163. doi:10.1016/j.geoderma.2018.11.030

Harper, R. J., Sochacki, S. J., and McGrath, J. F. (2017). The Development of Reforestation Options for Dryland Farmland in South-Western Australia: a Review. *South. For. a J. For. Sci.* 79, 185–196. doi:10.2989/20702620.2016.1255417

Harper, R. J., Sochacki, S. J., Smettem, K. R. J., and Robinson, N. (2014). Managing Water in Agricultural Landscapes with Short-Rotation Biomass Plantations. *GCB Bioenergy* 6, 544–555. doi:10.1111/gcbb.12090

Hedley, C. B., and Yule, I. J. (2009). Soil Water Status Mapping and Two Variable-Rate Irrigation Scenarios. *Precis. Agric.* 10, 342–355. doi:10.1007/s11119-009-9119-z

Isbell and National Committee on Soil and Terrain (2021). *The Australian Soil Classification. Third. CSIRO Publishing*. Available at: https://www.soilscienceaustralia.org.au/asc/re/arenosols.htm.

Isbell, R. (2016). *The Australian Soil Classification*. Victoria: CSIRO Publishing.

Iuss, W. R. B. (2014). "World Reference Base for Soil Resources 2014, Update 2015 International Soil Classification System for Naming Soils and Creating Legends for Soil Maps," in *World Soil Resources Reports No. 106* (Rome: FAO).

James, I. T., Waine, T. W., Bradley, R. I., Taylor, J. C., and Godwin, R. J. (2003). Determination of Soil Type Boundaries Using Electromagnetic Induction Scanning Techniques. *Biosyst. Eng.* 86, 421–430. doi:10.1016/j.biosystemseng.2003.09.001

Kaiser, E. A., Mueller, T., Joergensen, R. G., Insam, H., and Heinemeyer, O. (1992). Evaluation of Methods to Estimate the Soil Microbial Biomass and the Relationship with Soil Texture and Organic Matter. *Soil Biol. Biochem.* 24, 675–683. doi:10.1016/0038-0717(92)90046-Z

Kellenberger, B., Volpi, M., and Tuia, D. (2017). "Fast Animal Detection in UAV Images Using Convolutional Neural Networks," in *2017 IEEE International Geoscience and Remote Sensing Symposium* (Fort Worth: IGARSS), 866–869. doi:10.1109/IGARSS.2017.8127090

Lamb, D. (2014). *Large-Scale Forest Restoration*. 1st ed. London, UK: Routledge, Taylor & Francis Group. doi:10.4324/9780203071649

Leopold, M., Gupanis-Broadway, C., Baker, A., Hankin, S., and Treble, P. (2021). Time Lapse Electric Resistivity Tomography to Portray Infiltration and Hydrologic Flow Paths from Surface to Cave. *J. Hydrology* 593, 125810. doi:10.1016/j.jhydrol.2020.125810

Lewinson, E. (2019). outlier_detection_hampel_filter.ipynb. Available at: https://github.com/erykml/medium_articles/blob/master/Machine Learning/outlier_detection_hampel_filter.ipynb.

Lu, J., Carter, D. A., Turnbull, L., Rosendale, D., Hedderley, D., Stephens, J., et al. (2013). The Effect of New Zealand Kanuka, Manuka and Clover Honeys on Bacterial Growth Dynamics and Cellular Morphology Varies According to the Species. *PLoS One* 8, e55898. doi:10.1371/journal.pone.0055898

Ma, R., McBratney, A., Whelan, B., Minasny, B., and Short, M. (2011). Comparing Temperature Correction Models for Soil Electrical Conductivity Measurement. *Precis. Agric.* 12, 55–66. doi:10.1007/s11119-009-9156-7

Marden, M., and Phillips, C. (2015). *A Review of Research on the Erosion Control Effectiveness of Naturally Reverting Mānuka (*Leptospermum scoparium*) and Kānuka (Kunzea Ericoides Complex): Implications for Erosion Mitigation of Space-Planted Mānuka on Marginal Hill Country. Report No LC2280. Envirolink Report CO9X1424, Prepared for Hawke's Bay Regional Council 1562-HBRC210*.

Mavric, E., Wittmann, S., Barth, G., and Henle, T. (2008). Identification and Quantification of Methylglyoxal as the Dominant Antibacterial Constituent of Manuka (*Leptospermum scoparium*)honeys from New Zealand. *Mol. Nutr. Food Res.* 52, 483–489. doi:10.1002/mnfr.200700282

McKenzie, N., Coughlan, K., and Cresswell, H. (2002). *Soil Physical Measurement and Interpretation for Land Evaluation*. Melbourne: CSIRO Publishing. Available at: http://hdl.handle.net/102.100.100/198241?index=1.

McKenzie, N., Jacquier, D., Isbell, R., and Brown, K. (2004). *Australian Soils and Landscapes: An Illustrated Compendium*. Collingwood, Victoria: CSIRO publishing.

McNeill, J. D. (1980). *Electromagnetic Terrain Conductivity Measurement at Low Induction Numbers*. TN-6. Geonics Limited Mississauga, ON, Canada doi. Available at http://www.geonics.com/pdfs/technicalnotes/tn6.pdf.

Mendham, D. S., White, D. A., Battaglia, M., McGrath, J. F., Short, T. M., Ogden, G. N., et al. (2011). Soil Water Depletion and Replenishment during First- and Early Second-Rotation Eucalyptus Globulus Plantations with Deep Soil Profiles. *Agric. For. Meteorology* 151, 1568–1579. doi:10.1016/j.agrformet.2011.06.014

Minasny, B., McBratney, A., and Whelan, B. M. (2005). *VESPER Version 1.62*. Sydney: The University of Sydney, NSW. Australian Centre for Precision Agriculture, McMillan Building A05. Available at: http://www.usyd.edu.au/su/agric/acpa.

Monteiro Santos, F. A. (2004). 1-D Laterally Constrained Inversion of EM34 Profiling Data. *J. Appl. Geophys.* 56, 123–134. doi:10.1016/j.jappgeo.2004.04.005

Monteiro Santos, F. A., Triantafilis, J., and Bruzgulis, K. (2011). A Spatially Constrained 1D Inversion Algorithm for quasi-3D Conductivity Imaging: Application to DUALEM-421 Data Collected in a Riverine Plain. *Geophysics* 76, B43–B53. doi:10.1190/1.3537834

Moura, R., Pereira, T., Barros, M. T., Alipio, R., Lima, A. C. S., and Schroeder, M. A. (2018). "Analysis of Frequency-Dependence of Soil Resisitivity: Emphasis at Low Frequencies," in Conference: International Conference on Grounding and Earthing & 8th International Conference on Lightning Physics and Effects (Pirenopolis, Brazil).

Nicia, P., Bejger, R., Zadrożny, P., and Sterzyńska, M. (2018). The Impact of Restoration Processes on the Selected Soil Properties and Organic Matter Transformation of Mountain Fens under Caltho-Alnetum Community in the Babiogórski National Park in Outer Flysch Carpathians, Poland. *J. Soils Sediments* 18, 2770–2776. doi:10.1007/s11368-017-1909-8

Nickless, E. M., Anderson, C. W. N., Hamilton, G., Stephens, J. M., and Wargent, J. (2017). Soil Influences on Plant Growth, Floral Density and Nectar Yield in Three Cultivars of Mānuka (*Leptospermum scoparium*). *N. Z. J. Bot.* 55, 100–117. doi:10.1080/0028825X.2016.1247732

Pádua, L., Vanko, J., Hruška, J., Adão, T., Sousa, J. J., Peres, E., et al. (2017). UAS, Sensors, and Data Processing in Agroforestry: a Review towards Practical Applications. *Int. J. Remote Sens.* 38, 2349–2391. doi:10.1080/01431161.2017.1297548

Paz, M. C., Farzamian, M., Paz, A. M., Castanheira, N. L., Gonçalves, M. C., and Monteiro Santos, F. (2020). Assessing Soil Salinity Dynamics Using Time-Lapse Electromagnetic Conductivity Imaging. *SOIL* 6, 499–511. doi:10.5194/soil-6-499-2020

Pearson, R. K., Neuvo, Y., Astola, J., and Gabbouj, M. (2016). Generalized Hampel Filters. *EURASIP J. Adv. Signal Process.* 2016, 1–18. doi:10.1186/s13634-016-0383-6

Porter, N. G., and Wilkins, A. L. (1999). Chemical, Physical and Antimicrobial Properties of Essential Oils of *Leptospermum scoparium* and Kunzea Ericoides. *Phytochemistry* 50, 407–415. doi:10.1016/s0031-9422(98)00548-2

QGIS.org (2022). QGIS Geographic Information System. Available at: http://www.qgis.org.

R Core Team (2020). R: A Language and Environment for Statistical Computing. Available at: https://www.r-project.org/.

Raparelli, E., and Bajocco, S. (2019). A Bibliometric Analysis on the Use of Unmanned Aerial Vehicles in Agricultural and Forestry Studies. *Int. J. Remote Sens.* 40, 9070–9083. doi:10.1080/01431161.2019.1569793

Rayment, G. E., and Lyons, D. J. (2011). *Soil Chemical Methods: Australasia*. Collingwood, VIC: CSIRO publishing.

Redmon, J., Divvala, S., Girshick, R., and Farhadi, A. (2016). *You Only Look once: Unified, Real-Time Object Detection*. doi:10.1109/CVPR.2016.91

Ronneberger, O., Fischer, P., and Brox, T. (2015). "U-net: Convolutional Networks for Biomedical Image Segmentation," in *Medical Image Computing and Computer-Assisted Intervention – MICCAI 2015*. Editors F. A. N. Navab, J. Hornegger, and W. Wells (Springer International Publishing), 234–241. arXiv:1505.04597. doi:10.1007/978-3-319-24574-4_28

Roper, M. M., Davies, S. L., Blackwell, P. S., Hall, D. J. M., Bakker, D. M., Jongepier, R., et al. (2015). Management Options for Water-Repellent Soils in Australian Dryland Agriculture. *Soil Res.* 53, 786–806. doi:10.1071/SR14330

Salter, P. J., and Williams, J. B. (1965). The Influence of Texture on the Moisture Characteristics of Soils. *J. Soil Sci.* 16, 310–317. doi:10.1111/j.1365-2389.1965.tb01442.x

Santos, F. A. M., Triantafilis, J., Bruzgulis, K. E., and Roe, J. A. E. (2010). Inversion of Multiconfiguration Electromagnetic (DUALEM-421) Profiling Data Using a One-Dimensional Laterally Constrained Algorithm. *Vadose Zo. J.* 9, 117–125. doi:10.2136/vzj2009.0088

Sasaki, Y. (2001). Full 3-D Inversion of Electromagnetic Data on PC. *J. Appl. Geophys.* 46, 45–54. doi:10.1016/S0926-9851(00)00038-0

Sasaki, Y. (1989). Two-dimensional Joint Inversion of Magnetotelluric and Dipole-dipole Resistivity Data. *Geophysics* 54, 254–262. doi:10.1190/1.1442649

Scott, N. A., White, J. D., Townsend, J. A., Whitehead, D., Leathwick, J. R., Hall, G. M., et al. (2000). Carbon and Nitrogen Distribution and Accumulation in a New Zealand Scrubland Ecosystem. *Can. J. For. Res.* 30, 1246–1255. doi:10.1139/x00-048

Scudiero, E., Skaggs, T. H., and Corwin, D. L. (2017). Simplifying Field-Scale Assessment of Spatiotemporal Changes of Soil Salinity. *Sci. Total Environ.* 587-588, 273–281. doi:10.1016/j.scitotenv.2017.02.136

Shaukat, H., Flower, K. C., and Leopold, M. (2022). Quasi-3D Mapping of Soil Moisture in Agricultural Fields Using Electrical Conductivity Sensing. *Agric. Water Manag.* 259, 107246. doi:10.1016/j.agwat.2021.107246

Simons, J., and Bennett, D. (2021). Measuring Soil Salinity. *Dep. Prim. Ind. Reg. Dev.* Available at: https://www.agric.wa.gov.au/soil-salinity/measuring-soil-salinity (Accessed February 16, 2022).

Stephens, J. M. C., Molan, P. C., and Clarkson, B. D. (2005). A Review ofLeptospermum scoparium(Myrtaceae) in New Zealand. *N. Z. J. Bot.* 43, 431–449. doi:10.1080/0028825X.2005.9512966

Stirzaker, R. J., Vertessy, R. A., and Sarre, A. (2002). *Trees, Water and Salt: An Australian Guide to Using Trees for Healthy Catchments and Productive Farms*. Canberra: Joint Venture Agroforestry Program and CSIRO. RIRDC publication number: 01/086.

Thompson, J. (1989). A Revision of the Genus Leptospermum (Myrtaceae). *Telopea* 3, 301–449449. doi:10.7751/telopea19894902

Thrimawithana, A. H., Jones, D., Hilario, E., Grierson, E., Ngo, H. M., Liachko, I., et al. (2019). A Whole Genome Assembly of *Leptospermum scoparium* (Myrtaceae) for Mānuka Research. *N. Z. J. Crop Hortic. Sci.* 47, 233–260. doi:10.1080/01140671.2019.1657911

Triantafilis, J., Laslett, G. M., and McBratney, A. B. (2000). Calibrating an Electromagnetic Induction Instrument to Measure Salinity in Soil under Irrigated Cotton. *Soil Sci. Soc. Am. J.* 64, 1009–1017. doi:10.2136/sssaj2000.6431009x

Triantafilis, J., Terhune, C. H., and Monteiro Santos, F. A. (2013). An Inversion Approach to Generate Electromagnetic Conductivity Images from Signal Data. *Environ. Model. Softw.* 43, 88–95. doi:10.1016/j.envsoft.2013.01.012

Tsoar, H. (2005). "Sand Dunes," in *Encyclopedia of Soils in the Environment*. Editor D. B. T. Hillel (Oxford: Elsevier), 462–471. doi:10.1016/B0-12-348530-4/00410-0

van Wesenbeeck, I. J., and Kachanoski, R. G. (1988). Spatial and Temporal Distribution of Soil Water in the Tilled Layer under a Corn Crop. *Soil Sci. Soc. Am. J.* 52, 363–368. doi:10.2136/sssaj1988.03615995005200020011x

Villarreal, A. G., and Freeman, C. E. (1990). Effects of Temperature and Water Stress on Some Floral Nectar Characteristics in Ipomopsis Longiflora (Polemoniaceae) under Controlled Conditions. *Bot. Gaz.* 151, 5–9. doi:10.1086/337797

Wicaksono, W. A., Jones, E. E., Monk, J., and Ridgway, H. J. (2016). The Bacterial Signature of *Leptospermum scoparium* (Mānuka) Reveals Core and Accessory Communities with Bioactive Properties. *PLoS One* 11, e0163717. doi:10.1371/journal.pone.0163717

Williams, S. D., Pappalardo, L., Bishop, J., and Brooks, P. R. (2018). Dihydroxyacetone Production in the Nectar of Australian Leptospermum Is Species Dependent. *J. Agric. Food Chem.* 66, 11133–11140. doi:10.1021/acs.jafc.8b04363

Williams, S., King, J., Revell, M., Manley-Harris, M., Balks, M., Janusch, F., et al. (2014). Regional, Annual, and Individual Variations in the Dihydroxyacetone Content of the Nectar of Mānuka (*Leptospermum scoparium*) in New Zealand. *J. Agric. Food Chem.* 62, 10332–10340. doi:10.1021/jf5045958

Conflict of Interest: ML was employed by CRC for Honey Bee Products.

The remaining authors declare that the research was conducted in the absence of any commercial or financial relationships that could be construed as a potential conflict of interest.

Publisher's Note: All claims expressed in this article are solely those of the authors and do not necessarily represent those of their affiliated organizations, or those of the publisher, the editors, and the reviewers. Any product that may be evaluated in this article, or claim that may be made by its manufacturer, is not guaranteed or endorsed by the publisher.

frontiers | Frontiers in Environmental Science

TYPE Original Research
PUBLISHED 21 September 2022
DOI 10.3389/fenvs.2022.940943

OPEN ACCESS

EDITED BY
Anping Chen,
Colorado State University, United States

REVIEWED BY
Alison Post,
Northern Arizona University, United States
Qiang Yu,
Chinese Academy of Agricultural Sciences (CAAS), China

*CORRESPONDENCE
Matthew C. Roby,
matthew.roby@usda.gov

SPECIALTY SECTION
This article was submitted to Drylands, a section of the journal Frontiers in Environmental Science

RECEIVED 10 May 2022
ACCEPTED 31 August 2022
PUBLISHED 21 September 2022

CITATION
Roby MC, Scott RL, Biederman JA, Smith WK and Moore DJP (2022), Response of soil carbon dioxide efflux to temporal repackaging of rainfall into fewer, larger events in a semiarid grassland.
Front. Environ. Sci. 10:940943.
doi: 10.3389/fenvs.2022.940943

Response of soil carbon dioxide efflux to temporal repackaging of rainfall into fewer, larger events in a semiarid grassland

Matthew C. Roby[1,2,3]*, Russell L. Scott[2], Joel A. Biederman[2], William K. Smith[1] and David J. P. Moore[1]

[1]School of Natural Resources and the Environment, University of Arizona, Tucson, AZ, United States, [2]Southwest Watershed Research Center, USDA-ARS, Tucson, AZ, United States, [3]Sustainable Agricultural Water Systems Research Unit, USDA-ARS, Davis, CA, United States

Changing rainfall patterns will alter soil water availability to plants and microbes and likely impact soil CO_2 efflux (F_s) in semiarid ecosystems. However, our understanding of the response of F_s to compound changes in rainfall event size and frequency remains relatively limited. To address this knowledge gap, we examined how compound changes in rainfall size and frequency impact F_s in a semiarid grassland by deploying automated soil chambers at a rainfall manipulation experiment. All plots within the experiment received equal total summer growing season precipitation that was temporally repackaged into regular events of inversely varied size and frequency, with event sizes ranging from 5 to 50 mm and dry intervals ranging from 3.5 to 21 days. We found that repackaging rainfall into few/large events with long dry intervals decreased seasonal cumulative F_s. Repackaging influenced key aspects of pulses including mean, maximum, and antecedent (day before irrigation) values of soil moisture and F_s and their rate of decline during drying intervals. Soil moisture explained substantial variation in F_s ($R^2 > 0.84$) for all treatments; however, the sensitivity of F_s to soil moisture decreased in the few/large regime compared to the reference and many/small regimes. Dynamics in plant phenology (quantified by plot greenness) and soil temperature interacted with soil moisture to influence the seasonal evolution of F_s pulses and cumulative efflux. Our findings demonstrate that soil moisture and vegetation responses to changes in rainfall size and frequency impact soil CO_2 efflux pulses and seasonal emissions in semiarid grasslands. These results, coupled with the knowledge that CO_2 efflux pulses play an outsized role in dryland carbon exchange, indicate the possibility of future climate-mediated shifts in the carbon cycling of semiarid ecosystems.

KEYWORDS

soil respiration, soil efflux, rainfall intensification, soil moisture, pulse, semiarid

Introduction

Intensification of precipitation driven by climate warming is changing the intensity, frequency, and length of time between storms (McCabe et al., 2010; Polade et al., 2014; Guerreiro et al., 2018; Fowler et al., 2021). In the southwest United States, widespread warming has been accompanied by increases in precipitation variability and the frequency of prolonged drought (Demaria et al., 2019; Zhang et al., 2021), and general circulation models predict further intensification of precipitation, with a shift toward larger, fewer events with longer dry intervals (Cook et al., 2020; Moustakis et al., 2021). Due to tight carbon-water coupling in globally-expansive arid and semiarid ecosystems (Noy-Meir, 1973; Huxman et al., 2004; Schwinning and Sala, 2004), precipitation changes that alter the amount and timing of soil moisture availability have implications for the terrestrial carbon sink (Poulter et al., 2014; Ahlström et al., 2015; Biederman et al., 2016).

Soil moisture regulates the metabolic activity of plants and soil organisms in arid and semiarid ecosystems (Jenerette et al., 2008) and therefore exerts strong control over soil CO_2 efflux (F_s). F_s, the soil-atmosphere flux of carbon dioxide, is the sum of heterotrophic respiration and belowground autotrophic (root) respiration. In arid and semiarid ecosystems, F_s has a pulsed response to rainfall driven by physical and microbial responses to soil wetting (Birch, 1958; Huxman et al., 2004; Schwinning and Sala, 2004). Understanding F_s responses to rainfall is important because F_s indicates rates of ecosystem metabolism and nutrient cycling (Orchard and Cook, 1983; Luo and Zhou, 2006) and often dominates ecosystem-scale carbon exchange immediately after rain events (Huxman et al., 2004; Sponseller, 2007; López-Ballesteros et al., 2016). Because the temporal pattern of rainfall is a key control on soil moisture and F_s dynamics (Porporato et al., 2002; Vargas et al., 2012; Leon et al., 2014), it is necessary to examine how F_s will respond to shifts in precipitation timing and intensity.

Although prior work has examined F_s responses to key precipitation metrics—including seasonal amount (Liu et al., 2009; Zhao et al., 2021), event size/timing (Thomey et al., 2011; Vargas et al., 2018; Post & Knapp, 2021), and interstorm duration (Sponseller, 2007)—it remains unclear how F_s will respond to compound changes in event size and frequency. Projected shifts in rainfall toward infrequent, larger events may enable larger post-wetting F_s pulses due to increased soil moisture relative to antecedent conditions (Austin et al., 2004; Cable et al., 2008; Niu et al., 2019) and substrate accumulation during long dry intervals (Franzluebbers et al., 2000; Sponseller, 2007); however, soil moisture stress during prolonged dry periods is known to reduce F_s (Knapp et al., 2008). In contrast, a rainfall regime with many small events would support smaller post-wetting F_s pulses but more frequent activation of metabolic activity in near-surface soils where soil organic carbon and microbial activity are concentrated (Garcia-Pichel & Belnap, 1996; Vargas et al., 2018). Moreover, it is likely that F_s responses to event size and frequency are modulated by changes in autotrophic respiration associated with plant responses to root-zone infiltration, such as rhizosphere priming and photosynthetic substrate supply (Ogle & Reynolds, 2004; Kuzyakov & Gavrichkova, 2010; Yan et al., 2011; Liu W et al., 2017; Wang et al., 2019). Interactions among these environmental and vegetative drivers of respiration processes challenge predictions of F_s responses to rainfall intensification (Barron-Gafford et al., 2011; Roby et al., 2019).

Rainfall manipulation experiments are a useful tool to examine how interactive aspects of precipitation impact ecosystem processes (Knapp et al., 2015). Whereas many studies have investigated plant responses to rainfall manipulation (e.g., Heisler-White et al., 2008; Gherardi and Sala, 2015), comparatively few have examined the response of soil processes to simultaneous changes in event size and frequency (Griffin-Nolan et al., 2021; Rousk and Brangarí 2022). Although prior studies have provided useful information on ecosystem-scale respiration responses to repackaging (Liu Z et al., 2017), automated chamber systems can better capture transient F_s patterns during wetting-drydown cycles characteristic of semiarid regions (Huxman et al., 2004; Savage et al., 2009). Such an approach may increase our understanding of how soil and plant processes modulate F_s responses to rainfall intensification. To address this gap, we examined how compound changes in rainfall size and frequency impact F_s in a semiarid grassland by deploying automated soil chambers within a rainfall manipulation experiment. Our objective was to address the following questions: 1) How does temporal repackaging of rainfall impact F_s pulses and cumulative growing season F_s? and 2) How do changes in environmental and vegetative drivers under rainfall repackaging scenarios impact F_s rates and the seasonal evolution of F_s pulses?

Materials and methods

Site description

We conducted this experiment at the Rainfall Manipulation in the Santa Rita Experimental Range (RainManSR) site in southeast Arizona, United States (31.79° N, 110.90° W; elevation: 1,075 m). While the experiment was conducted in plots under rainout-exclusion shelters, the surrounding ecosystem is a semiarid grassland that has experienced significant increases in mesquite (Prosopis velutina) shrub cover in the 20th century. The ecosystem is composed mainly of perennial bunchgrasses, short trees/shrubs, and bare soil which can support annual grasses and forbs given adequate rainfall. Mean annual temperature is 18.6°C and mean annual

precipitation (1922–2021) is 377 mm, roughly 50% of which occurs during the summer (July–September) monsoon season (https://cals.arizona.edu/SRER/data.html). Soils are well-drained sandy loams (78% sand, 8% clay, 14% silt). Plots within the experiment represent a mixture of C4 perennial bunchgrasses, C4 annual grasses, and C3 forbs. Because the ambient ecosystem has inherently heterogeneous cover, native perennial bunchgrass (*Digitaria californica*) seedlings were transplanted in November 2019 into all plots at a density of 20 plants m^{-2}. This was done to ensure a relatively consistent plant community at the start of the experiment and to better capture vegetation responses to rainfall manipulation and potential impacts on the plant-mediated component of F_s.

Experiment design and precipitation manipulation

To block all ambient precipitation, large rainout-exclusion shelters were covered with transparent film with each shelter covering 12 plots (1.2 by 1.5 m). To hydrologically isolate the plots, the perimeter of each plot was trenched to a depth of 80 cm and wrapped in polyethylene film. Plots were then lined with steel flashing which extended from a depth of 50 cm to 10 cm above the soil surface. We used a completely randomized design with two replicates of each irrigation treatment in each shelter (n = 4 plots per treatment). All plots received 205 mm of total summer irrigation (the long-term mean seasonal precipitation amount) and were hand-irrigated using a digital flow meter. Irrigation was applied to the area within soil collars when the automated chambers were in the open position. The experiment began on July 14 when 38 mm was applied to all plots. Thereafter, irrigation treatments were imposed with the following combinations of mean event size and dry intervals: many/small (9 mm; 3.5 days); reference (34 mm; 7 days, which is the climatic normal precipitation frequency at this site), and few/large (51 mm; 21 days). For more details about the experimental design of RainManSR, Zhang et al. (2022).

Soil CO_2 efflux measurements

We measured the net efflux of carbon dioxide (CO_2) at the soil-atmosphere interface (F_s; μmol CO_2 m^{-2} s^{-1}) hourly using automated chambers connected to a multiplexer and infrared gas analyzer (LI-8100, LI-COR, Nebraska, United States). One week before data collection began, we inserted 20 cm diameter soil collars into the ground with roughly 3 cm of the collar extending above the soil surface. Soil within the collars was weeded by hand weekly to exclude aboveground vegetation from the sampled volume. Data were collected continuously during day and night hours, and F_s was determined each hour by fitting an exponential curve to the change in CO_2 molar fraction during a 120 s observation period. We excluded F_s estimates when the fitted exponential curve had a coefficient of determination below 0.95 and/or when individual chambers malfunctioned (poor seals between chamber heads and baseplates, ruptured tubing, power loss, etc.). Overall, 11% of data was discarded and gaps in the hourly chamber data were filled with treatment means for missing hours.

Environmental variables

We measured half-hourly volumetric water content (soil moisture, θ; m^3 m^{-3}) and soil temperature (T_s; °C) using Campbell Scientific CS655 probes inserted into the soil at 30° from vertical to integrate the measurement across the upper 10 cm of soil. Hourly means were calculated from half-hourly data to match the temporal resolution of soil chamber data. We also monitored plot-level phenology using nadir-oriented RGB images taken half-hourly from 09:00 to 16:00 local time with a Raspberry Pi Camera Module V2 (Raspberry Pi Foundation, Cambridge, United Kingdom). For each plot, half-hourly RGB images for the entire plot area were used to calculate a spatially-averaged, daily timeseries of the green chromatic coordinate (GCC) using the *phenopix* R package (Filippa et al., 2016). Daily GCC was calculated as the 90th percentile of all half-hourly values to minimize diurnal changes in illumination.

Data analysis

To quantify the effects of rainfall repackaging on F_s, T_s, θ, and GCC we used the R package *lme4* to build linear mixed-effects models with irrigation treatment, time, and their interaction as fixed effects and plot ID as a random effect to account for the repeated measurements (Bates et al., 2014). Variables were log-transformed when necessary to meet assumptions of normality. Cumulative F_s was calculated as the sum of daily mean F_s. To compare total seasonal F_s among repackaging treatments, we first used Levene's test for homogeneity of variance and found that the many/small regime had outsize variance compared to the other repackaging treatments ($F = 6.72$, $p < 0.05$; compare the variance in seasonal total F_s reported in Table 2). To account for unequal variance, we tried log-transforming the data and using the Kruskal-Wallis test, but did not find strong evidence of a difference in total seasonal F_s (ΣFs) when including the many/small treatment. Therefore, to reduce the chance of type II error we conducted one-way analysis of variance (ANOVA) on total seasonal F_s values for the reference and few/large regimes. We used linear regression to quantify the relationship between daily F_s and θ as well as F_s

TABLE 1 Linear mixed-effects model results for daily mean soil CO_2 efflux (F_s), soil moisture (θ), soil temperature (T_s), and green chromatic coordinate (GCC) normalized anomalies.

Term	F_s			θ			T_s			GCC		
	df	*F*	*p*	df	*F*	*p*	df	*F*	*p*	df	*F*	*p*
Treatment	2	2.42	0.14	2	0.34	0.72	2	3.22	0.08	2	0.17	0.85
DOY	91	123.27	<0.001	90	297.06	<0.001	90	1441.20	<0.001	91	26.06	<0.001
Treatment × DOY	182	16.96	<0.001	180	76.19	<0.001	180	34.66	<0.001	182	5.49	<0.001

and GCC. We compared the slope of the $F_g - \theta$ relationship among rainfall repackaging treatments using analysis of covariance (ANCOVA) with the *aoctool* in MATLAB (MathWorks, Massachusetts, United States). For each treatment group, ANCOVA fits a separate line to the continuous variables F_s and θ; differences in slopes among treatments were assessed using Tukey's honestly significant difference for pairwise comparisons. To focus on temporal dynamics in greenness, we report normalized anomalies of GCC. We quantified the rapid increase in post-wetting F_s (Δ) and the rate of decay of F_s during interstorm periods (τ) by fitting a pulse model based on Kurc and Small (2004):

$$F_s(t) = \Delta e^{-\frac{t}{\tau}} + F_{ant}$$

where Δ (μmol CO_2 m^{-2} s^{-1}) is the difference between maximum post-wetting F_s and antecedent F_s (day before irrigation), t is time in days since irrigation, and τ (days) is the exponential time constant, also known as the e-folding time during which the initial pulse magnitude, Δ, has diminished by a factor of 1/e = 0.37. The model was fit and coefficient estimates for τ were obtained using the *fitnlm* function in MATLAB.

Results

Dynamics in soil CO_2 efflux and drivers under rainfall repackaging

The effects of rainfall repackaging on F_s, T_s, θ, and GCC were strongly time-dependent ($p < 0.01$; Table 1), which resulted in pronounced temporal dynamics in F_s and environmental drivers (Figure 1). At the beginning of the growing season, all plots exhibited low F_s and low GCC associated with low θ and high T_s. A uniform 38 mm irrigation event applied on 14 July resulted in similar increases in θ and F_s, and similar declines in T_s among treatments. After this uniform initial event, changes in irrigation event size and frequency caused patterns of F_s and environmental drivers to vary among treatments. As expected, plots irrigated with many/small events had smaller F_s pulses and reduced θ extremes, whereas plots irrigated with few/large events had larger F_s pulses separated by prolonged dry intervals with low F_s. We also observed differences in pulse patterns of T_s and seasonal dynamics in GCC under rainfall repackaging scenarios. Immediately after irrigation, T_s in the few/large regime decreased relative to the many/small regime; however, this difference reversed during prolonged dry intervals. Repackaging rainfall into few/large events delayed the timing of peak GCC relative to the many/small regime and decreased the duration of wet soil moisture conditions for much of the growing season (Supplementary Figure S1).

Temporal rainfall repackaging alters cumulative soil CO_2 efflux

Differences in pulse dynamics compounded to influence seasonal cumulative F_s (Figure 2; Table 2). Repackaging equal summer rainfall (205 mm) into fewer, larger events with long dry intervals decreased seasonal cumulative F_s by 8.3% relative to the reference regime ($p < 0.05$). Although seasonal cumulative F_s was greatest for the many/small regime, substantial variability among replicates for this treatment precluded the detection of significant differences among the many/small repackaging scenario and the other treatments. Differences in cumulative F_s were established during the first month of the experiment, after which a cumulative sum of 100 mm of water had been applied to all plots. The reduction in cumulative F_s for the few/large regime was thereafter maintained through the end of the growing season, which indicates that the size and timing of a few storms can drive divergent responses in seasonal carbon losses.

Coherent pulse responses of soil CO_2 efflux and soil moisture

We next focus on a complete wetting-drying cycle to examine how tradeoffs in event size and frequency

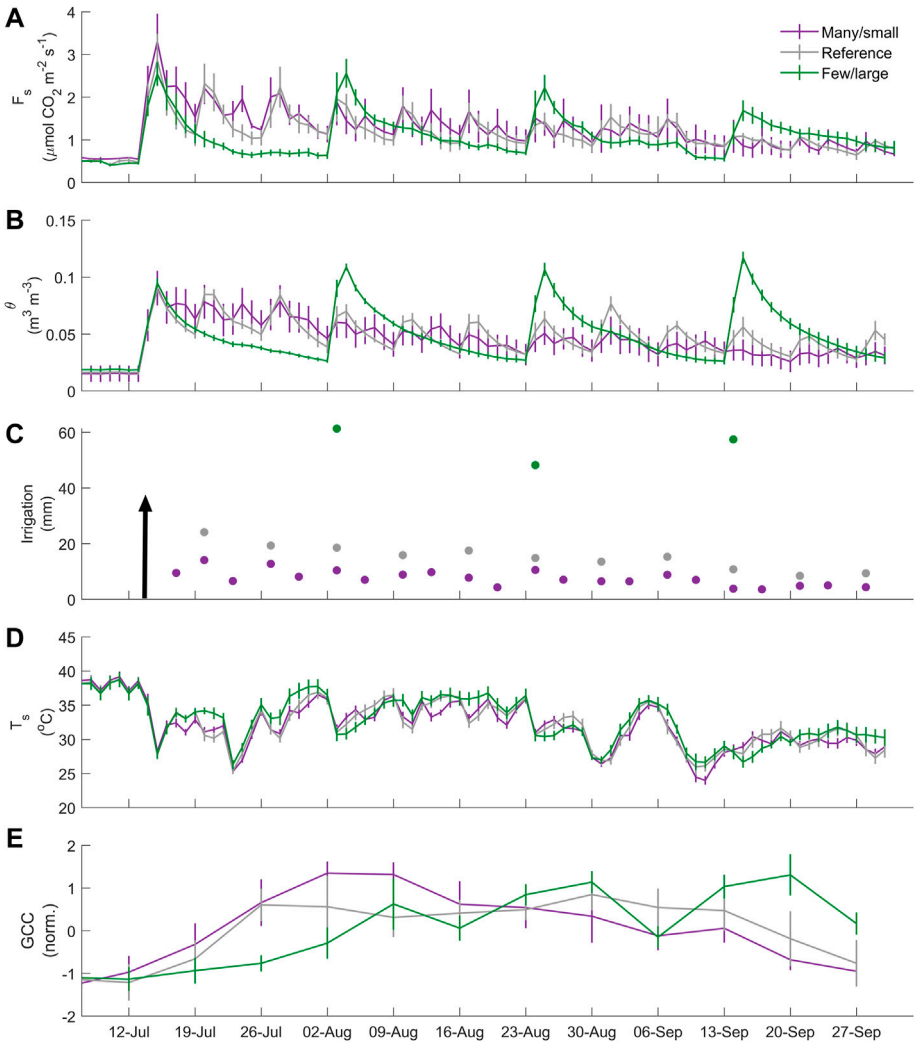

FIGURE 1
Growing season dynamics in **(A)** daily mean soil CO_2 efflux (F_s), **(B)** daily mean volumetric soil moisture (θ), 0–10 cm, **(C)** irrigation amount, **(D)** daily mean soil temperature (T_s, 0–10 cm), and **(E)** and weekly-average of daily mean green chromatic coordinate (GCC) normalized anomalies under three levels of rainfall repackaging. Arrow denotes uniform 38 mm irrigation event on 14 July. Vertical lines indicate standard deviation.

modulated pulse responses of F_s and θ (Figure 3A). Although plots with few/large events had larger post-wetting F_s pulses and increased F_s in the first week after irrigation, they experienced longer dry intervals with decreased F_s relative to plots with many/small events. During the few/large regime's prolonged interstorm periods, plots with reference and many/small treatments experienced additional events that kept F_s and θ relatively high. Averaged over the season, plots irrigated with few/large events had 38% and 67% higher maximum F_s and θ during pulses than plots in the many small/regime (Figures 3B,C). Average antecedent values (day before irrigation, which is also the last day of the previous dry-down cycle) of F_s and θ were 42% and 33% lower for few/large events than for many/small events.

Environmental and vegetative controls on soil CO_2 efflux

To explain the strong coherence among pulse patterns of θ and F_s, we examined the response of F_s to soil moisture (Figure 4) and used analysis of covariance (ANCOVA) to test for differences in the slope of the $F_s - \theta$ relationship. F_s showed a strong linear relationship with θ ($p < 0.01$) and variation in θ explained 84%–86% of F_s variability. The slope coefficient was decreased for plots subject to few/large events compared to those with many/small events ($p < 0.01$) and the reference regime ($p < 0.01$), which indicates that rainfall repackaging influenced the sensitivity of F_s to θ. When comparing the many/small repackaging scenario to reference rainfall size and frequency,

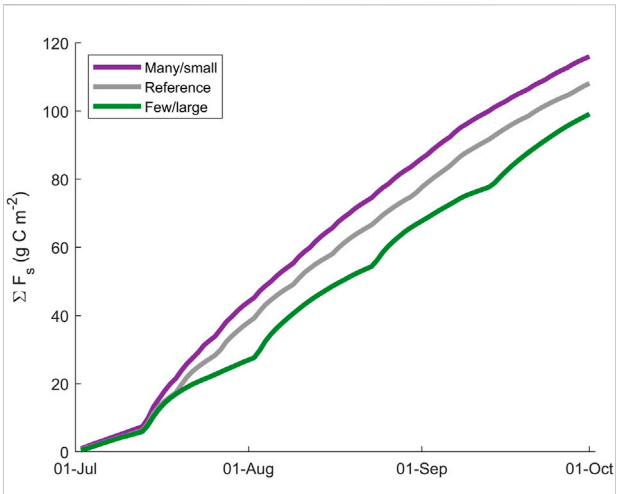

FIGURE 2
Cumulative daily soil CO_2 efflux (F_s) during the 2020 growing season.

TABLE 2 Mean and standard deviation (parentheses) of seasonal average daily mean soil CO_2 efflux (F_s), soil moisture (θ), soil temperature (T_s), and seasonal total F_s (ΣF_s) for the three levels of rainfall repackaging.

Treatment	F_s	ΣF_s	θ	T_s
Many/small	1.24 (0.537)	112.13 (19.52)	0.0441 (0.0161)	32.0 (3.35)
Reference	1.16 (0.447)	104.32 (3.66)	0.0469 (0.0167)	32.5 (3.30)
Few/large	1.06 (0.481)	95.99 (3.99)	0.0475 (0.0234)	32.8 (3.35)

we did not find strong evidence for a significant difference in the slopes ($p > 0.05$). We also investigated the response of F_s to soil temperature (T_s). Although the relationship between F_s and T_s was unclear at the daily scale, hourly F_s increased with T_s when θ was non-limiting (Supplementary Figure S2). Moreover, decreased T_s late in the season appeared to contribute to the reduction in the sensitivity of F_s to θ for the few/large plots (Supplementary Figure S3).

We next examined the relationship between F_s and green chromatic coordinate (GCC), a measure of plot-scale canopy greenness, which is correlated with vegetation gross productivity in open-canopy ecosystems (Yan et al., 2019; Zhang et al., 2022). This decision was based on prior work in this system, which found that vegetation productivity (quantified using ecosystem-scale photosynthesis) is a driver of F_s (Roby et al., 2019), and our observation that peak GCC timing varied among treatments (Figure 1E; see also Zhang et al., 2022). Whereas the relationship between daily F_s and GCC was unclear when θ was high, a positive relationship emerged during drier conditions ($\theta < 0.06$), during which GCC explained 34%–47% of F_s (Figure 5).

Seasonal evolution of soil CO_2 efflux pulses

We next examined the seasonal evolution of F_s and environmental drivers during pulse events (Figure 6). Average F_s and θ during pulses decreased seasonally for the many/small and reference treatments, but were relatively constant for the few/large treatment (Figures 6A,D). As the summer growing season progressed, we observed broadly decreasing trends in both pulse magnitude (Δ) and T_s for all treatments (Figures 6B,E). Whereas the rate of decay of pulses (τ) for the many/small and reference treatments was relatively constant during the experiment, τ and GCC for the few/large plots increased as the growing season progressed (Figures 6C,F).

Discussion

Repackaging equal total rainfall into fewer, larger events decreased summer growing season cumulative F_s relative to reference event size and frequency (Figure 2; Table 2), due to suppressed F_s during prolonged dry intervals (Figure 3) and a reduction in the sensitivity of F_s to soil moisture (Figure 4). These results demonstrate that the effects of rainfall repackaging on F_s varied over time and were modulated by soil moisture responses to interactions between event size and frequency (Table 1; Figure 1). Repackaging rainfall into fewer, larger events caused large fluctuations in θ that increased post-wetting F_s magnitude but suppressed F_s during prolonged dry intervals (Figures 1, 3). Long dry intervals result in dry antecedent conditions which stimulate large post-wetting F_s pulses (Birch, 1958; Xu et al., 2004; Cable et al., 2008; Yan et al., 2014) due to mineralization of microbial-derived carbon and physical displacement of CO_2 by infiltrating water (Fierer and Schimel, 2003; Luo and Zhou, 2006; Unger et al., 2010). Decreased F_s during longer dry intervals indicates a reduction in substrate diffusion and microbial activity associated with water stress (Orchard & Cook, 1983; Davidson et al., 1998; Moyano et al., 2013). Therefore, microbial responses to water stress during long dry intervals likely combined with reductions in oxygen availability during brief periods of saturation immediately after large irrigation events to decrease the sensitivity of F_s to θ in the few/large regime (Figure 4). In contrast, repackaging rainfall into many small events resulted in smaller F_s pulses but maintained higher F_s rates during brief interstorm periods (Figures 1, 3). Frequent wetting supported F_s activation likely by maintaining favorable soil moisture conditions in surface soils where microbes are concentrated (Garcia-Pichel and Belnap, 1996; Moyano et al., 2013). Ultimately, frequent wetting compensated for smaller pulses and increased the sensitivity of F_s to θ

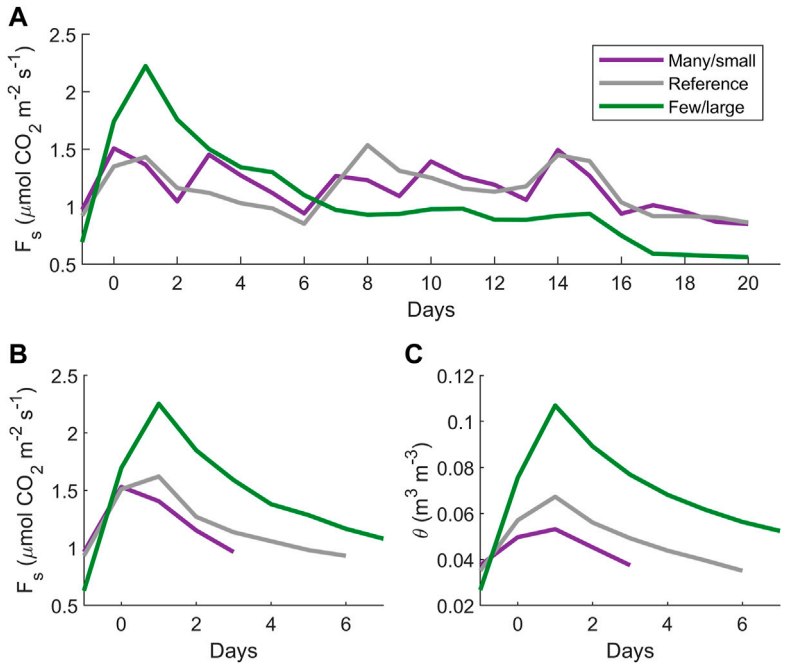

FIGURE 3
(A) Representative mid-growing season period showing soil CO_2 efflux (F_s) responses to irrigation events observed 23 August–13 September 2020 with x-axis showing days since 23 August. Lower panels show the first 7 days of the mean pulse response of **(B)** F_s and **(C)** 0–10 cm volumetric soil moisture (θ) for the three levels of rainfall repackaging averaged across all irrigation events for the entire duration of the experiment. In **(B)** and **(C)** the x-axis indicates days since irrigation event.

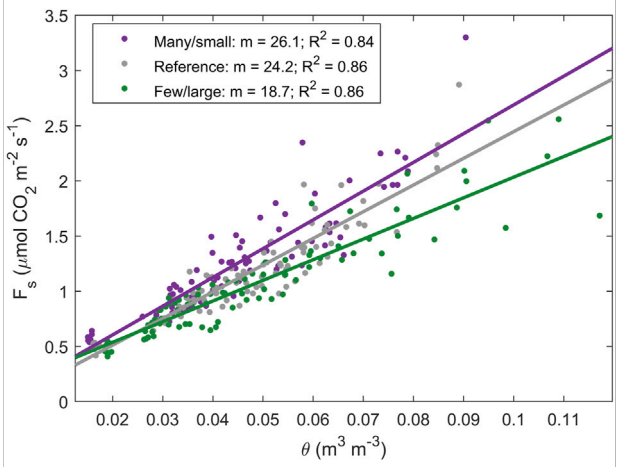

FIGURE 4
Response of daily mean soil CO_2 efflux (F_s) to soil moisture (θ) colored by rainfall repackaging treatment. Note *m* is the slope of the regression line for each treatment.

(Figure 4), resulting in increased seasonal cumulative emissions (Figure 2). Because all plots received equal total water, these findings suggest that the influence of rainfall frequency on the moisture sensitivity of F_s plays a key role in regulating soil CO_2 emissions in semiarid ecosystems.

Plot greenness (GCC) and soil temperature (T_s) were additional controls on F_s that interacted with θ to influence the seasonal evolution of pulses. We found a positive relationship between F_s and GCC during periods of low soil moisture (Figure 5), which likely indicates that measurements of plot greenness can capture the stimulatory effect of plant activity on F_s associated with root respiration and decomposition of recent plant-derived carbon in the rhizosphere (Ogle and Reynolds, 2004; Kuzyakov and Gavrichkova, 2010; Wang et al., 2019). Whereas F_s and GCC were decoupled immediately after irrigation events, a strong positive relationship emerged during drydowns (θ < 0.06; Figure 5). Because microbial respiration responds more rapidly to soil wetting than plant-mediated respiration (Carbone et al., 2011), our finding that the F_s-GCC relationship is conditional on θ suggests that microbial responses to wetting dominate F_s immediately after rainfall, whereas plant activity modulates F_s during interstorm periods by regulating substrate availability. Prior work in this system has shown that repackaging rainfall into larger, fewer events delays peak plant productivity (Zhang et al., 2022). In this study, we observed a delayed increase in GCC for the few/large regime that was accompanied by an increase in pulse duration

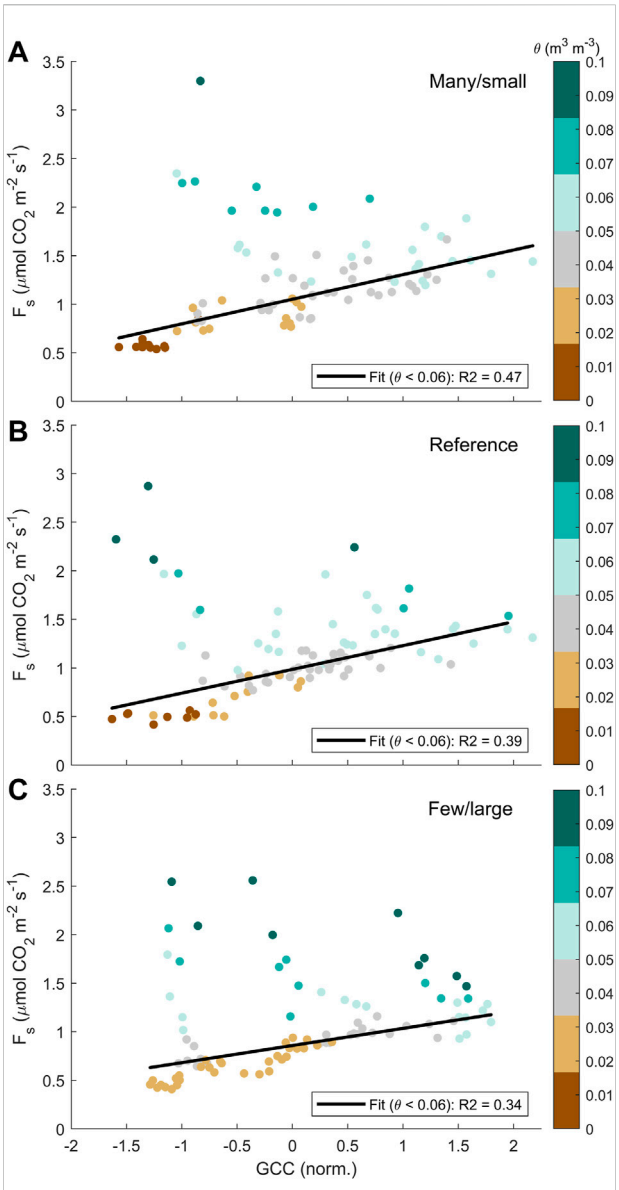

FIGURE 5
Response of daily mean soil CO_2 efflux (F_s) to normalized anomalies in green chromatic coordinate (GCC) colored by soil moisture (θ) for the three levels of rainfall repackaging. The regression line is only fit to low soil moisture values ($\theta < 0.06$).

(quantified as τ) and a decrease in pulse magnitude (Δ; Figure 6). Pulse-average F_s was relatively steady for the few/large treatment, which suggests that increasing autotrophic respiration linked to plant growth led to more sustained pulses late in the season that offset the reduction in pulse magnitude. If we interpret GCC as a proxy for active plant biomass, the linear response (Figure 5) could be caused by the relationship between plant biomass/growth and autotrophic respiration, and through the influence of plant biomass on substrate quantity or quality used for heterotrophic respiration. Thus, the ability of GCC to capture how seasonality in plant growth shapes key aspects of F_s pulses indicates that greenness data may be a useful tool for examining plant and microbial contributions to F_s in future work.

Although F_s had no clear dependency on temperature at the daily scale, hourly F_s increased with T_s when θ was non-limiting (Supplementary Figure S2). These results provide additional evidence that water availability regulates the temperature response of F_s in arid and semiarid ecosystems (Conant et al., 2004; Roby et al., 2019; Wang B. et al., 2014; Chatterjee and Jenerette, 2011). We also observed seasonal reductions in pulse magnitude associated with decreasing T_s (Figure 6) and evidence that reduced T_s late in the season contributed to the decreased sensitivity of F_s to θ in the few/large treatment (Figure 1, Supplementary Figure S3).

Together, these results indicate that changes in environmental and vegetative drivers influenced the seasonal pattern of cumulative soil CO_2 emissions. The observed difference in cumulative F_s was established early in the season when higher F_s in the many/small and reference plots was supported by abundant moisture, warm temperatures, and increased substrate supply associated with an expanding plant canopy. The difference was maintained through the end of the season as decreasing temperatures decreased pulse magnitude and reduced the sensitivity of F_s to θ in the few/large plots. These findings build on studies of generalized pulse responses to rainfall (Knapp et al., 2008; Cable et al., 2013; Vargas et al., 2018; Roby et al., 2019) by demonstrating how soil and plant responses to event size and frequency modulate F_s in semiarid grasslands. The dependence of pulse responses on antecedent θ, T_s, and plant-mediated substrate supply indicates that seasonal changes in the timing of water inputs can influence F_s independent of changes in rainfall amount. Our results demonstrate that water stress effects on F_s during prolonged dry intervals may explain reported reductions in ecosystem-scale respiration to growing season rainfall repackaging in semiarid regions (Liu W. et al., 2017). Because a few individual events drove differences in cumulative F_s, this research indicates the potential for increased variability in the carbon cycling of water-limited regions in response to ongoing changes in precipitation (Sloat et al., 2018; Zhang et al., 2021).

Dryland ecosystems have high spatial heterogeneity in soil properties and vegetation distribution, which presents challenges for understanding ecosystem responses to changes in climate, including rainfall size and frequency (Osborne et al., 2022). Because we observed large variability in seasonal total F_s for the many/small regime (Table 2), future research should examine how spatial heterogeneity and co-limitation of multiple resources (e.g., water, carbon, nutrients) mediate carbon cycling responses to rainfall repackaging (Choi et al., 2022; Osborne et al., 2022). There is also a

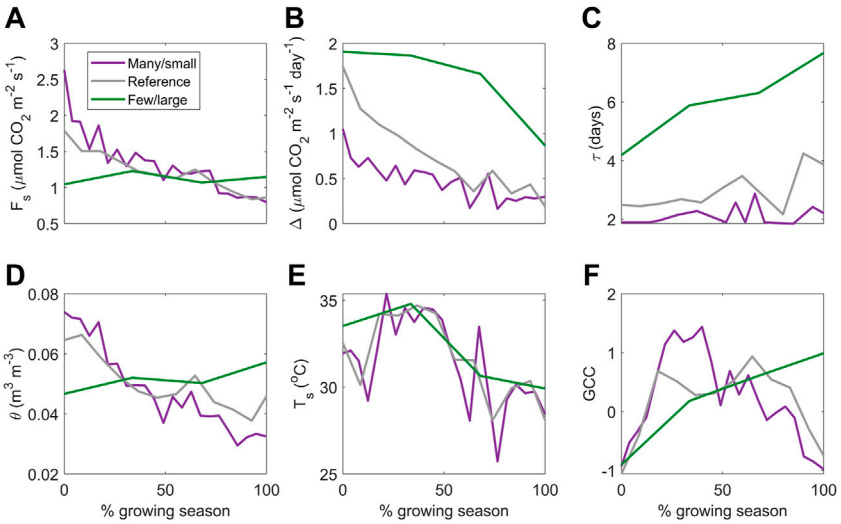

FIGURE 6
Seasonal evolution of the **(A)** average daily rate, **(B)** magnitude of pulse increase (Δ) and **(C)** exponential time decay constant (τ) of soil CO_2 efflux (F_s) during pulse events. Bottom row shows average daily **(D)** soil moisture (θ), **(E)** soil temperature (T_s), and **(F)** normalized anomalies of green chromatic coordinate (GCC) during pulse events. Colors denote the three levels of rainfall repackaging.

need to better understand how soil texture shapes F_s responses to rainfall repackaging. Soil texture is a key determinant of F_s pulse responses (Cable et al., 2008) and although high infiltration capacity of the sandy soils precluded extended periods of saturation in this study, F_s may exhibit different responses to rainfall repackaging in soils with greater clay content. For example, increased clay content may cause oxygen limitation after large events that decrease F_s, whereas increased water holding capacity during interstorm periods may increase F_s associated with moisture-dependent microbial and plant processes (Franzluebbers et al., 2000; Yan et al., 2018).

Climate models project continued changes in rainfall toward extreme events separated by longer dry intervals (Ficklin et al., 2022). Our results show that such changes in rainfall patterns may result in reductions in F_s from semiarid regions. Given the widespread nature of pulse behavior, these results have broad relevance for how changing rainfall patterns influence carbon cycling in water-limited ecosystems (Feldman et al., 2018). Our results also highlight the need for models that can account for how changes in plant-mediated substrate and soil temperature interact with water availability to drive seasonality in F_s pulses (Zhang et al., 2014). Future plot-scale work should examine the response of net ecosystem carbon exchange to contrasting compound extremes (Hoover et al., 2022); for example, to test if the observed reductions in F_s with larger, less-frequent events offset losses in productivity caused by plant responses to stress (e.g., high atmospheric demand) during prolonged interstorm periods (Roby et al., 2020).

In conclusion, our findings suggest that projected changes in rainfall size and timing will likely have important effects on carbon losses from semiarid grasslands. Here we show that holding total amount constant, repackaging rainfall into fewer, larger events imposed more water stress that decreased cumulative seasonal soil CO_2 efflux in a semiarid grassland. We also found evidence that temporal rainfall repackaging affects the seasonality of F_s pulses and likely alters plant and microbial contributions to soil CO_2 emissions. Due to the high spatial heterogeneity characteristic of dryland ecosystems, future studies should further examine how spatial variability in co-limiting resources mediates soil CO_2 efflux responses to changes in rainfall distribution. Our study advances understanding on how changes in rainfall timing and frequency alter environmental and vegetative factors that control respiratory losses of CO_2 from soil. Because pulses exert strong influence on dryland carbon exchanges, our study indicates the potential for future climate-mediated shifts in the carbon cycling of water-limited regions.

Data availability statement

The raw data supporting the conclusion of this article will be made available by the authors, without undue reservation.

Author contributions

MR analyzed the data and wrote the manuscript with input from all coauthors. JB and WS designed the rainfall manipulation experiment and identified the repackaging treatments. MR, RS, JB, WS, and DM designed the soil chamber experiment. MR installed and maintained soil chamber systems with assistance from JB and WS.

Funding

Partial funding for this research came from USDA-ARS National Program 211.

Acknowledgments

We thank N. Pierce for managing the field experiment and C. Devine for installing the camera system used to quantify plot greenness. Thank you R. Bryant (USDA-ARS) for helping deploy and repair the soil chamber systems. USDA-ARS is an equal opportunity employer. We thank the two reviewers for insightful comments that improved the clarity of this manuscript.

Conflict of interest

The authors declare that the research was conducted in the absence of any commercial or financial relationships that could be construed as a potential conflict of interest.

Publisher's note

Supplementary material

The Supplementary Material for this article can be found online at: https://www.frontiersin.org/articles/10.3389/fenvs.2022.940943/full#supplementary-material

References

Ahlström, A., Raupach, M. R., Schurgers, G., and Smith, B. (2015). The dominant role of semi-arid ecosystems in the trend and variability of the land CO2 sink. *Science* 348, 895–899. doi:10.1126/science.aaa166Available at: https://science.sciencemag.org/content/348/6237/895.abstract.

Austin, A. T., Yahdjian, L., Stark, J. M., Belnap, J., Porporato, A., Norton, U., et al. (2004). Water pulses and biogeochemical cycles in arid and semiarid ecosystems. *Oecologia* 141 (2), 221–235. doi:10.1007/s00442-004-1519-1

Barron-Gafford, G. A., Scott, R. L., Jenerette, G. D., and Huxman, T. E. (2011). The relative controls of temperature, soil moisture, and plant functional group on soil CO2 efflux at diel, seasonal, and annual scales. *J. Geophys. Res.* 116 (G1), G01023. doi:10.1029/2010jg001442

Bates, D., Mächler, M., Bolker, B., and Walker, S., 2014. Fitting linear mixed-effects models using lme4. *arXiv preprint arXiv*:1406.5823. Available at:.

Biederman, J. A., Scott, R. L., Goulden, M. L., Vargas, R., Litvak, M. E., Kolb, T. E., et al. (2016). Terrestrial carbon balance in a drier world: The effects of water availability in southwestern north America. *Glob. Chang. Biol.* 22 (5), 1867–1879. doi:10.1111/gcb.13222

Birch, H. F. (1958). The effect of soil drying on humus decomposition and nitrogen availability. *Plant Soil* 10 (1), 9–31. doi:10.1007/bf01343734

Cable, J. M., Ogle, K., Barron-Gafford, G. A., Bentley, L. P., Cable, W. L., Scott, R. L., et al. (2013). Antecedent conditions influence soil respiration differences in shrub and grass patches. *Ecosystems* 16 (7), 1230–1247. doi:10.1007/s10021-013-9679-7

Cable, J. M., Ogle, K., Williams, D. G., Weltzin, J. F., and Huxman, T. E. (2008). Soil texture drives responses of soil respiration to precipitation pulses in the sonoran desert: Implications for climate change. *Ecosystems* 11 (6), 961–979. doi:10.1007/s10021-008-9172-x

Carbone, M. S., Still, C. J., Ambrose, A. R., Dawson, T. E., Williams, A. P., Boot, C. M., et al. (2011). Seasonal and episodic moisture controls on plant and microbial contributions to soil respiration. *Oecologia* 167 (1), 265–278. doi:10.1007/s00442-011-1975-3

Chatterjee, A., and Jenerette, G. D. (2011). Changes in soil respiration Q10 during drying–rewetting along a semi-arid elevation gradient. *Geoderma* 163 (3-4), 171–177. doi:10.1016/j.geoderma.2011.04.003

Choi, R. T., Reed, S. C., and Tucker, C. L. (2022). Multiple resource limitation of dryland soil microbial carbon cycling on the Colorado Plateau. *Ecology* 103, e3671. doi:10.1002/ecy.3671

Conant, R. T., Dalla-Betta, P., Klopatek, C. C., and Klopatek, J. M. (2004). Controls on soil respiration in semiarid soils. *Soil Biol. Biochem.* 36 (6), 945–951. doi:10.1016/j.soilbio.2004.02.013

Cook, B. I., Mankin, J. S., Marvel, K., Williams, A. P., Smerdon, J. E., and Anchukaitis, K. J. (2020). Twenty-first century drought projections in the CMIP6 forcing scenarios. *Earth's. Future* 8 (6). doi:10.1029/2019ef001461

Davidson, E. A., Belk, E., and Boone, R. D. (1998). Soil water content and temperature as independent or confounded factors controlling soil respiration in a temperate mixed hardwood forest. *Glob. Change Biol.* 4, 217–227. doi:10.1046/j.1365-2486.1998.00128.x

Demaria, E. M. C., Hazenberg, P., Scott, R. L., Meles, M. B., Nichols, M., and Goodrich, D. (2019). Intensification of the north American monsoon rainfall as observed from a long-term high-density gauge network. *Geophys. Res. Lett.* 46 (12), 6839–6847. doi:10.1029/2019gl082461

Feldman, A. F., Short Gianotti, D. J., Konings, A. G., McColl, K. A., Akbar, R., Salvucci, G. D., et al. (2018). Moisture pulse-reserve in the soil-plant continuum observed across biomes. *Nat. Plants* 4 (12), 1026–1033. doi:10.1038/s41477-018-0304-9

Ficklin, D. L., Null, S. E., Abatzoglou, J. T., Novick, K. A., and Myers, D. T. (2022). Hydrological intensification will increase the complexity of water resource management. *Earth's. Future* 10 (3), e2021EF002487. doi:10.1029/2021ef002487

Fierer, N., and Schimel, J. P. (2003). A proposed mechanism for the pulse in carbon dioxide production commonly observed following the rapid rewetting of a dry soil. *Soil Sci. Soc. Am. J.* 67 (3), 798–805. doi:10.2136/sssaj2003.0798

Filippa, G., Cremonese, E., Migliavacca, M., Galvagno, M., Forkel, M., Wingate, L., et al. (2016). Phenopix: A R package for image-based vegetation phenology. *Agric. For. Meteorology* 220, 141–150. doi:10.1016/j.agrformet.2016.01.006

Fowler, H. J., Lenderink, G., Prein, A. F., Westra, S., Allan, R. P., Ban, N., et al. (2021). Anthropogenic intensification of short-duration rainfall extremes. *Nat. Rev. Earth Environ.* 2 (2), 107–122. doi:10.1038/s43017-020-00128-6

Franzluebbers, A. J., Haney, R. L., Honeycutt, C. W., Schomberg, H. H., and Hons, F. M. (2000). Flush of carbon dioxide following rewetting of dried soil relates to active organic pools. *Soil Sci. Soc. Am. J.* 64 (2), 613–623. doi:10.2136/sssaj2000.642613x

Garcia-Pichel, F., and Belnap, J. (1996). Microenvironments and microscale productivity of cyanobacterial desert crusts1. *J. Phycol.* 32 (5), 774–782. doi:10.1111/j.0022-3646.1996.00774.x

Gherardi, L. A., and Sala, O. E. (2015). Enhanced precipitation variability decreases grass- and increases shrub-productivity. *Proc. Natl. Acad. Sci. U. S. A.* 112 (41), 12735–12740. doi:10.1073/pnas.1506433112

Griffin-Nolan, R. J., Slette, I. J., and Knapp, A. K. (2021). Deconstructing precipitation variability: Rainfall event size and timing uniquely alter ecosystem dynamics. *J. Ecol.* 109 (9), 3356–3369. doi:10.1111/1365-2745.13724

Guerreiro, S. B., Fowler, H. J., Barbero, R., Westra, S., Lenderink, G., Blenkinsop, S., et al. (2018). Detection of continental-scale intensification of hourly rainfall extremes. *Nat. Clim. Chang.* 8 (9), 803–807. doi:10.1038/s41558-018-0245-3

Heisler-White, J. L., Knapp, A. K., and Kelly, E. F. (2008). Increasing precipitation event size increases aboveground net primary productivity in a semi-arid grassland. *Oecologia* 158 (1), 129–140. doi:10.1007/s00442-008-1116-9

Hoover, D. L., Hajek, O. L., Smith, M. D., Wilkins, K., Slette, I. J., and Knapp, A. K. (2022). Compound hydroclimatic extremes in a semi-arid grassland: Drought, deluge, and the carbon cycle. *Glob. Change Biol.* 28 (8), 2611–2621. doi:10.1111/gcb.16081

Huxman, T. E., Snyder, K. A., Tissue, D., Leffler, A. J., Ogle, K., Pockman, W. T., et al. (2004). Precipitation pulses and carbon fluxes in semiarid and arid ecosystems. *Oecologia* 141 (2), 254–268. doi:10.1007/s00442-004-1682-4

Jenerette, G. D., Scott, R. L., and Huxman, T. E. (2008). Whole ecosystem metabolic pulses following precipitation events. *Funct. Ecol.* 22 (5), 924–930. doi:10.1111/j.1365-2435.2008.01450.x

Knapp, A. K., Beier, C., Briske, D. D., Classen, A. T., Luo, Y., Reichstein, M., et al. (2008). Consequences of more extreme precipitation regimes for terrestrial ecosystems. *Bioscience* 58 (9), 811–821. doi:10.1641/b580908

Knapp, A. K., Hoover, D. L., Wilcox, K. R., Avolio, M. L., Koerner, S. E., La Pierre, K. J., et al. (2015). Characterizing differences in precipitation regimes of extreme wet and dry years: Implications for climate change experiments. *Glob. Chang. Biol.* 21 (7), 2624–2633. doi:10.1111/gcb.12888

Kurc, S. A., and Small, E. E. (2004). Dynamics of evapotranspiration in semiarid grassland and shrubland ecosystems during the summer monsoon season, central New Mexico. *Water Resour. Res.* 40 (9). doi:10.1029/2004wr003068

Kuzyakov, Y., and Gavrichkova, O. (2010). Review: Time lag between photosynthesis and carbon dioxide efflux from soil: A review of mechanisms and controls: Time lag between photosynthesis and CO2 efflux from soil. *Glob. Change Biol.* 16 (12), 3386–3406. doi:10.1111/j.1365-2486.2010.02179.x

Leon, E., Vargas, R., Bullock, S., Lopez, E., Panosso, A. R., and La Scala, N. (2014). Hot spots, hot moments, and spatio-temporal controls on soil CO2 efflux in a water-limited ecosystem. *Soil Biol. Biochem.* 77, 12–21. doi:10.1016/j.soilbio.2014.05.029

Liu W, W. J., Li, L. F., Biederman, J. A., Hao, Y. B., Zhang, H., Kang, X. M., et al. (2017). Repackaging precipitation into fewer, larger storms reduces ecosystem exchanges of CO2 and H2O in a semiarid steppe. *Agric. For. Meteorology* 247, 356–364. doi:10.1016/j.agrformet.2017.08.029

Liu, W., Zhang, Z., and Wan, S. (2009). Predominant role of water in regulating soil and microbial respiration and their responses to climate change in a semiarid grassland. *Glob. Change Biol.* 15 (1), 184–195. doi:10.1111/j.1365-2486.2008.01728.x

Liu Z, Z., Zhang, Y., Fa, K., Qin, S., and She, W. (2017). Rainfall pulses modify soil carbon emission in a semiarid desert. *Catena* 155, 147–155. doi:10.1016/j.catena.2017.03.011

López-Ballesteros, A., Serrano-Ortiz, P., Sánchez-Cañete, E. P., Oyonarte, C., Kowalski, A. S., Pérez-Priego, Ó., et al. (2016). Enhancement of the net CO2release of a semiarid grassland in SE Spain by rain pulses: Rain Pulses Enhance Net CO2Release. *J. Geophys. Res. Biogeosci.* 121 (1), 52–66. doi:10.1002/2015jg003091

Luo, Y., and Zhou, X. (2006). "Chapter 5 - controlling factors," in *Soil respiration and the environment*. Editors Y. Luo and X. Zhou (Burlington: Academic Press), 79–105.

McCabe, G. J., Legates, D. R., and Lins, H. F. (2010). Variability and trends in dry day frequency and dry event length in the southwestern United States. *J. Geophys. Res.* 115 (D7), D07108. doi:10.1029/2009jd012866

Moustakis, Y., Papalexiou, S. M., Onof, C. J., and Paschalis, A. (2021). Seasonality, intensity, and duration of rainfall extremes change in a warmer climate. *Earth's. Future* 9 (3), ef001824. doi:10.1029/2020ef001824

Moyano, F. E., Manzoni, S., and Chenu, C. (2013). Responses of soil heterotrophic respiration to moisture availability: An exploration of processes and models. *Soil Biol. Biochem.* 59, 72–85. doi:10.1016/j.soilbio.2013.01.002

Niu, F., Chen, J., Xiong, P., Wang, Z., Zhang, H., and Xu, B. (2019). Responses of soil respiration to rainfall pulses in a natural grassland community on the semi-arid Loess Plateau of China. *Catena* 178, 199–208. doi:10.1016/j.catena.2019.03.020

Noy-Meir, I. (1973). Desert ecosystems: Environment and producers. *Annu. Rev. Ecol. Syst.* 4 (1), 25–51. doi:10.1146/annurev.es.04.110173.000325

Ogle, K., and Reynolds, J. F. (2004). Plant responses to precipitation in desert ecosystems: Integrating functional types, pulses, thresholds, and delays. *Oecologia* 141 (2), 282–294. doi:10.1007/s00442-004-1507-5

Orchard, V. A., and Cook, F. J. (1983). Relationship between soil respiration and soil moisture. *Soil Biol. Biochem.* 15 (4), 447–453. doi:10.1016/0038-0717(83)90010-x

Osborne, B. B., Bestelmeyer, B. T., Currier, C. M., Homyak, P. M., Throop, H. L., Young, K., et al. (2022). The consequences of climate change for dryland biogeochemistry. *New Phytol.* doi:10.1111/nph.18312

Polade, S. D., Pierce, D. W., Cayan, D. R., Gershunov, A., and Dettinger, M. D. (2014). The key role of dry days in changing regional climate and precipitation regimes. *Sci. Rep.* 4, 4364. doi:10.1038/srep04364

Porporato, A., D'odorico, P., Laio, F., Ridolfi, L., and Rodriguez-Iturbe, I. (2002). Ecohydrology of water-controlled ecosystems. *Adv. Water Resour.* 25 (8-12), 1335–1348. doi:10.1016/s0309-1708(02)00058-1

Post, A. K., and Knapp, A. K. (2021). How big is big enough? Surprising responses of a semiarid grassland to increasing deluge size. *Glob. Chang. Biol.* 27 (6), 1157–1169. doi:10.1111/gcb.15479

Poulter, B., Frank, D., Ciais, P., Myneni, R. B., Andela, N., Bi, J., et al. (2014). Contribution of semi-arid ecosystems to interannual variability of the global carbon cycle. *Nature* 509 (7502), 600–603. doi:10.1038/nature13376

Roby, M. C., Scott, R. L., Barron-Gafford, G. A., Hamerlynck, E. P., and Moore, D. J. P. (2019). Environmental and vegetative controls on soil CO2 efflux in three semiarid ecosystems. *Soil Syst.* 3 (1), 6. doi:10.3390/soilsystems3010006

Roby, M. C., Scott, R. L., and Moore, D. J. P. (2020). High vapor pressure deficit decreases the productivity and water use efficiency of rain-induced pulses in semiarid ecosystems. *J. Geophys. Res. Biogeosci.* 125 (10), jg005665. doi:10.1029/2020jg005665

Rousk, J., and Brangarí, A. C. (2022). Do the respiration pulses induced by drying–rewetting matter for the soil–atmosphere carbon balance? *Glob. Change Biol.* 28, 3486–3488. doi:10.1111/gcb.16163

Savage, K., Davidson, E. A., Richardson, A. D., and Hollinger, D. Y. (2009). Three scales of temporal resolution from automated soil respiration measurements. *Agric. For. Meteorology* 149 (11), 2012–2021. doi:10.1016/j.agrformet.2009.07.008

Schwinning, S., and Sala, O. E. (2004). Hierarchy of responses to resource pulses in arid and semi-arid ecosystems. *Oecologia* 141 (2), 211–220. doi:10.1007/s00442-004-1520-8

Sloat, L. L., Gerber, J. S., Samberg, L. H., Smith, W. K., Herrero, M., Ferreira, L. G., et al. (2018). Increasing importance of precipitation variability on global livestock grazing lands. *Nat. Clim. Chang.* 8, 214–218. doi:10.1038/s41558-018-0081-5

Sponseller, R. A. (2007). Precipitation pulses and soil CO2flux in a Sonoran Desert ecosystem. *Glob. Chang. Biol.* 13 (2), 426–436. doi:10.1111/j.1365-2486.2006.01307.x

Thomey, M. L., Collins, S. L., Vargas, R., Johnson, J. E., Brown, R. F., Natvig, D. O., et al. (2011). Effect of precipitation variability on net primary production and soil respiration in a chihuahuan desert grassland: Precipitation variability in desert grassland. *Glob. Change Biol.* 17 (4), 1505–1515. doi:10.1111/j.1365-2486.2010.02363.x

Unger, S., Máguas, C., Pereira, J. S., David, T. S., and Werner, C. (2010). The influence of precipitation pulses on soil respiration – assessing the "Birch effect" by stable carbon isotopes. *Soil Biol. Biochem.* 42 (10), 1800–1810. doi:10.1016/j.soilbio.2010.06.019

Vargas, R., Collins, S. L., Thomey, M. L., Johnson, J. E., Brown, R. F., Natvig, D. O., et al. (2012). Precipitation variability and fire influence the temporal dynamics of soil CO2 efflux in an arid grassland. *Glob. Chang. Biol.* 18 (4), 1401–1411. doi:10.1111/j.1365-2486.2011.02628.x

Vargas, R., Sánchez-Cañete, P., E., Serrano-Ortiz, P., Curiel Yuste, J., Domingo, F., López-Ballesteros, A., et al. (2018). Hot-Moments of soil CO2 efflux in a water-limited grassland. *Soil Syst.* 2 (3), 47. doi:10.3390/soilsystems2030047

Wang, B., Zha, T. S., Jia, X., Wu, B., Zhang, Y. Q., and Qin, S. G. (2014). Soil moisture modifies the response of soil respiration to temperature in a desert shrub ecosystem. *Biogeosciences* 11 (2), 259–268. doi:10.5194/bg-11-259-2014

Wang, Y., Li, X., Zhang, C., Wu, X., Du, E., Wu, H., et al. (2019). Responses of soil respiration to rainfall addition in a desert ecosystem: Linking physiological activities and rainfall pattern. *Sci. Total Environ.*, 650(Pt 2), 3007–3016. doi:10.1016/j.scitotenv.2018.10.057

Xu, L., Baldocchi, D. D., and Tang, J. (2004). How soil moisture, rain pulses, and growth alter the response of ecosystem respiration to temperature: RAIN, growth, and respiration. *Glob. Biogeochem. Cycles* 18 (4), gb002281. doi:10.1029/2004gb002281

Yan, D., Scott, R. L., Moore, D. J. P., Biederman, J. A., and Smith, W. K. (2019). Understanding the relationship between vegetation greenness and productivity across dryland ecosystems through the integration of PhenoCam, satellite, and eddy covariance data. *Remote Sens. Environ.* 223, 50–62. doi:10.1016/j.rse.2018.12.029

Yan, L., Chen, S., Huang, J., and Lin, G. (2011). Water regulated effects of photosynthetic substrate supply on soil respiration in a semiarid steppe. *Glob. Change Biol.* 17 (5), 1990–2001. doi:10.1111/j.1365-2486.2010.02365.x

Yan, L., Chen, S., Xia, J., and Luo, Y. (2014). Precipitation regime shift enhanced the rain pulse effect on soil respiration in a semi-arid steppe. *PloS One* 9 (8), e104217. doi:10.1371/journal.pone.0104217

Yan, Z., Bond-Lamberty, B., Todd-Brown, K. E., Bailey, V. L., Li, S., Liu, C., et al. (2018). A moisture function of soil heterotrophic respiration that incorporates microscale processes. *Nat. Commun.* 9 (1), 2562–2610. doi:10.1038/s41467-018-04971-6

Zhang, F., Biederman, J. A., Pierce, N., Potts, D., Devine, C., Yanbin, H., et al. (2022). Precipitation temporal repackaging into fewer, larger storms delayed seasonal timing of peak photosynthesis in a semi-arid grassland. *Funct. Ecol.* 36, 646–658. doi:10.1111/1365-2435.13980

Zhang, F., Biederman, J. A., Dannenberg, M. P., Yan, D., Reed, S. C., and Smith, W. K. (2021). Five decades of observed daily precipitation reveal longer and more variable drought events across much of the western United States. *Geophys. Res. Lett.* 48 (7), e2020GL092293. doi:10.1029/2020gl092293

Zhang, X., Niu, G. Y., Elshall, A. S., Ye, M., Barron-Gafford, G. A., and Pavao-Zuckerman, M. (2014). Assessing five evolving microbial enzyme models against field measurements from a semiarid savannah—what are the mechanisms of soil respiration pulses? *Geophys. Res. Lett.* 41 (18), 6428–6434. doi:10.1002/2014gl061399

Zhao, M., Guo, S., and Wang, R. (2021). Diverse soil respiration responses to extreme precipitation patterns in arid and semiarid ecosystems. *Appl. Soil Ecol.* 163, 103928. doi:10.1016/j.apsoil.2021.103928

frontiers | Frontiers in Environmental Science

ORIGINAL RESEARCH
published: 07 July 2022
doi: 10.3389/fenvs.2022.896702

Monitoring Dryland Trees With Remote Sensing. Part A: Beyond CORONA—Historical HEXAGON Satellite Imagery as a New Data Source for Mapping Open-Canopy Woodlands on the Tree Level

Irene Marzolff[1], Mario Kirchhoff[2], Robin Stephan[1], Manuel Seeger[2], Ali Aït Hssaine[3] and Johannes B. Ries[2]*

[1]Department of Physical Geography, Goethe University Frankfurt am Main, Frankfurt am Main, Germany, [2]Department of Physical Geography, Trier University, Trier, Germany, [3]Department of Geography, Ibn Zohr University, Agadir, Morocco

OPEN ACCESS

Edited by:
Niall Patrick Hanan,
New Mexico State University,
United States

Reviewed by:
Juan Carlos Laso Bayas,
International Institute for Applied Systems Analysis (IIASA), Austria
Nathan Moore,
Michigan State University,
United States
Brianna Lind,
New Mexico State University,
United States

***Correspondence:**
Irene Marzolff
marzolff@em.uni-frankfurt.de

Specialty section:
This article was submitted to Drylands, a section of the journal Frontiers in Environmental Science

Received: *15 March 2022*
Accepted: *10 May 2022*
Published: *07 July 2022*

Citation:
Marzolff I, Kirchhoff M, Stephan R, Seeger M, Aït Hssaine A and Ries JB (2022) Monitoring Dryland Trees With Remote Sensing. Part A: Beyond CORONA—Historical HEXAGON Satellite Imagery as a New Data Source for Mapping Open-Canopy Woodlands on the Tree Level. Front. Environ. Sci. 10:896702. doi: 10.3389/fenvs.2022.896702

Monitoring woody cover by remote sensing is considered a key methodology towards sustainable management of trees in dryland forests. However, while modern very high resolution satellite (VHRS) sensors allow woodland mapping at the individual tree level, the historical perspective is often hindered by lack of appropriate image data. In this first study employing the newly accessible historical HEXAGON KH-9 stereo-panoramic camera images for environmental research, we propose their use for mapping trees in open-canopy conditions. The 2–4 feet resolution panchromatic HEXAGON satellite photographs were taken 1971–1986 within the American reconnaissance programs that are better known to the scientific community for their lower-resolution CORONA images. Our aim is to evaluate the potential of combining historical CORONA and HEXAGON with recent WorldView VHRS imagery for retrospective woodland change mapping on the tree level. We mapped all trees on 30 1-ha test sites in open-canopy argan woodlands in Morocco in the field and from the VHRS imagery for estimating changes of tree density and size between 1967/1972 and 2018. Prior to image interpretation, we used simulations based on unmanned aerial system (UAS) imagery for exemplarily examining the role of illumination, viewing geometry and image resolution on the appearance of trees and their shadows in the historical panchromatic images. We show that understanding these parameters is imperative for correct detection and size-estimation of tree crowns. Our results confirm that tree maps derived solely from VHRS image analysis generally underestimate the number of small trees and trees in clumped-canopy groups. Nevertheless, HEXAGON images compare remarkably well with WorldView images and have much higher tree-mapping potential than CORONA. By classifying the trees in three sizes, we were able to measure tree-cover changes on an ordinal scale. Although we found no clear trend of forest degradation or recovery, our argan forest sites show varying patterns of change, which are further analysed in Part B of our study. We conclude that the HEXAGON stereo-panoramic camera images, of which 670,000 worldwide will soon be

available, open exciting opportunities for retrospective monitoring of trees in open-canopy conditions and other woody vegetation patterns back into the 1980s and 1970s.

Keywords: very high resolution satellite imagery, HEXAGON, CORONA, change mapping, open-canopy woodland, dryland forest, tree density, woody cover

1 INTRODUCTION

Open-canopy woodlands cover around 30 percent of the world's drylands (FAO, 2019). Trees outside of closed-canopy conditions grow in savannah and dry woodland ecoregions, on rangeland and farmland in silvo-pastoral or agroforestry systems and sparsely scattered as desert woodlands. They contribute significantly to rural livelihoods, carbon storage, dryland biodiversity, watershed protection, desertification control and numerous other ecosystem services (Chidumayo and Gumbo, 2010; Hanan et al., 2021). Dryland forests and woodlands are under increasing anthropogenic pressure such as livestock overgrazing and browsing, coppicing and cutting for fuelwood and charcoal production and conversion into agricultural land or managed forests (Chidumayo and Gumbo, 2010; Gaisberger et al., 2017; FAO, 2019). They are also vulnerable to climate change, as water availability in most drylands is expected to decline further by long-term increases in temperature, changing precipitation patterns and increasing depletion of water resources (Mirzabaev et al., 2019; Hanan et al., 2021).

In the context of global change and the UN's Sustainable Development Goals, mapping and monitoring the deforestation and degradation of dryland forests is of high importance. And yet, open-canopy woodlands are not well represented in global maps and data products on woody biomass, tree cover and forest change (Bastin et al., 2017; Brandt et al., 2018; Fagan, 2020). The low density and scattered nature of trees and the highly variable contrast with the appearance of intertree areas, which range from bare desert soils to dense crops, make it difficult to detect forests with open canopy structures in 10–30 m-resolution remote sensing imagery. This leads to their exclusion or lack of representation in widely-used datasets such as the Global Forest Change Map by Hansen et al. (2013), the Global Forest Cover Change Map by Sexton et al. (2013) or the Global Palsar Forest Map by Shimada et al. (2014). Mapping forest degradation and quantifying different types of disturbances is even more difficult, since degradation may lead to structural changes on the individual tree level rather than canopy cover changes (Gao et al., 2020).

Several recent studies on dryland forests have therefore resorted to aerial imagery or very high resolution satellite (VHRS) imagery (~0.5–2 m spatial resolution) from the commercial Quickbird, WorldView and GeoEye satellites that are suitable for mapping open-canopy woodlands on the individual tree level. For example, object-based and segmentation approaches were used for delineating tree crowns from aerial images in deserts (Isaacson et al., 2017; Silver et al., 2019) and from VHRS imagery in savannahs (Axelsson and Hanan, 2017). Moreover, object-based and machine learning approaches were found suitable for mapping different tree species in semi-arid agroforestry parklands (Karlson et al., 2016; Lelong et al., 2020). Brandt et al. (2020) used deep learning to map 1.8 billion trees in a wall-to-wall map of African open-canopy woodlands, and Bastin et al. (2017) mapped trees in 210,000 sample plots across the world's drylands by visual interpretation of VHRS imagery. Most of these authors found VHRS-based approaches capable of mapping individual trees >2 m diameter/> 3 m^2, but prone to errors for smaller trees and clumped canopies, which are usually found to be separable to a limited degree only.

Modern very high resolution sensors (available since ~ year 2000) together with the foreseeable advancements in canopy-classification algorithms thus have a huge potential for individual tree mapping on regional to global scale and for changing our view of woody-plant ecosystems (Hanan and Anchang, 2020). However, sustainable management of dryland forests and woodlands requires data not only on current canopy cover, but also about their development during and beyond the lifetime of individual trees—particularly so in regions with high anthropogenic impact. Forest degradation is a gradual progress, and individual crown-size changes and patterns of dieback, felling, regeneration or planting over time may give important clues for understanding the state of woodlands today. To this end, analogue remote sensing photos reaching back into the 20th century provide an excellent yet challenging information source for monitoring changes on the tree level.

The highest available spatial resolutions are provided by standard aerial photographs (APs) taken for topographic mapping throughout the world, beginning with World War I and increasingly since the 1950s. During the 20th century Colonial Era, APs were for example acquired over large parts of Africa, mostly by French, British and Belgian military forces or national mapping agencies. Unfortunately, only very few of these are available through digital archives (Fradley, 2021; Nyssen et al., 2021), analogue prints are often not or very difficult to get from today's responsible authorities, and the original material is greatly threatened by chemical degradation (Michel, 2018). A more globally available alternative are analogue satellite photos of the American cold-war reconnaissance programs (described in more detail in **Section 2**). Among these, the 6–9 feet resolution CORONA KH-4 images have become valuable for environmental and cultural history research, since they cover much larger extents than APs and may be ordered conveniently through digital archives. The latest addition to these data collections are the 2–4 feet resolution HEXAGON KH-9 images taken from 1971 to 1986, which are in the focus of our study.

Regrettably, the need for manual georeferencing and the complex geometric distortions make the use of historical aerial or satellite photography for regional or large-area studies laborious. Also, the lack of spectral resolution and radiometry calibration of the panchromatic films inhibit automated classification approaches (cf. Fensham et al., 2002). Therefore, visual interpretation of changes in tree counts is the most

common method employed in monitoring woodlands on the tree-level (Schlesinger and Gramenopoulos, 1996; Gonzalez et al., 2012; le Polain de Waroux and Lambin, 2012; Usman and Nichol, 2018). The lower size limit for tree detection differs between studies, since the spatial resolution and radiometric quality of historical AP and VHRS images varies considerably. Some authors found black-and-white AP also suitable for tree-crown delineation (and thus calculation of percentage woody cover; Lahav-Ginott et al., 2001; Moustakas et al., 2006), but this is not feasible with the lower-resolution CORONA VHRS images (Dendoncker et al., 2020). Although various studies use CORONA images for mapping forest-ecosystem changes (e.g., Tappan et al., 2004; Frost and Epstein, 2014; Nita et al., 2018), quantification of woody cover change on the tree level is rarely achieved. The most comprehensive work on limitations and potential of tree detection in CORONA images was done by Andersen (2006); (Andersen and Krzywinski, 2007), who is one of the few authors scrutinizing the inhibiting role of shadows for canopy measurements from panchromatic images. She has, however, not investigated how the shadowing problem may be overcome for enabling accurate tree-cover quantification.

In summary, we believe that a gap of historical data for mapping woodland change existed until recently between small-area, higher-resolution APs (suitable for tree size estimation) and large-area, lower-resolution VHRS photographs (suitable for detection of larger trees). This paper addresses the question if the newly accessible historical HEXAGON VHRS images are capable of closing this gap. To this end, we aim to evaluate the potential of combining historical and recent VHRS imagery for mapping woodland change on the tree-level, using the case of open-canopy *Argania spinosa* forests in South Morocco. Specifically, we aim at:

(i) examining the role of illumination, viewing geometry and image resolution on the appearance of trees in two different types of historical panchromatic VHRS (CORONA and HEXAGON) imagery by using simulations based on unmanned aerial system (UAS) images;
(ii) investigating the recognizability of individual trees in the historical and recent VHRS imagery for tree-density change mapping;
(iii) exploring the feasibility of crown-size classification and thus tree-cover change mapping based on these images.

This paper is part A of our research on tree-cover changes in argan woodlands of South Morocco and results in a tree-changes database for 30 test sites. Part B of our study (Kirchhoff et al., 2022) focusses on utilising this dataset to evaluate deforestation, degradation and recovery processes of the argan forest sites.

2 AVAILABILITY AND CHARACTERISTICS OF HEXAGON VS CORONA VHRS IMAGERY

Following World War II, the United States initiated a series of satellite reconnaissance programs that operated throughout the period of the Cold War. Between 1959 and 1986, the CORONA, ARGON, LANYARD, GAMBIT and HEXAGON programs encompassed approx. 150 successful missions of a few weeks to few months each. More than 1.5 million photographs were acquired and retrieved from orbit in hundreds of "film buckets" via a re-entry capsule (Wheelon, 1997; McDonald and Widlake, 2012; USGS, 2018a; USGS, 2018b; USGS, 2018c). Classified as top secret for decades, the images have become declassified in several steps in 1995, 2002 and 2011, releasing a breathtaking resource of historical Earth observation data to the civilian community. The ingestion of image records including browse imagery into online accessible digital archives and ordering systems, however, is not yet completed.

Today, there are three main archives providing access to these data: 1) The National Archives and Records Administration (NARA) holds the original film and hard copies of the technical mission-related documents for onsite inspection; 2) the National Reconnaissance Office (NRO) provides online access to scans of technical documents—such as specification sheets, handbooks and mission reports—processed under the Freedom of Information Act (FOIA), and 3) scans of the satellite photographs may be ordered for US$ 30 each through the EarthExplorer portal of the Earth Resources Observation and Science Center of the United States Geological Survey (USGS EROS)[1]. The CORONA images and lower-resolution mapping-camera HEXAGON images[2] have been available from the USGS web portals for about 20 and 10 years, respectively. Online access to the high-resolution panoramic-camera HEXAGON images used in this study has begun only in summer 2020 (R. Longhenry, USGS, pers. comm.), and the ingestion process of over 670,000 images with 2–4 feet resolution is still ongoing at the time of writing.

A variety of different camera systems, usually identified by their satellite codenames KH-1 to KH-9, was used in the CORONA to HEXAGON programs (Perry, 1973a; Perry, 1973b; Oder et al., 1988; Oder et al., 1992; Dashora et al., 2007). They mostly comprised several cameras with different viewing perspectives and focal lengths. The highest ground resolutions (or ground resolved distances GRD), which are suitable for tree-level mapping, were achieved by the stereo-panoramic cameras of the CORONA KH-4a, KH-4b, HEXAGON KH-9 missions and the monoscopic cameras of GAMBIT KH-7 and KH-8 (**Table 1**). While the GAMBIT missions focussed on small target areas, CORONA and above all HEXAGON covered much larger areas worldwide. The geometry and cross-track scanning operation of the stereo camera systems result in complex variations of geometric

[1]After first-time order of scans from the USGS, the images become open access for subsequent users. This has encouraged the development of the open-access CORONA Atlas, which collects and disseminates manually georeferenced images of selected areas worldwide, particularly landscapes of archaeological interest. The atlas also employs its own online georeferencing tool sunspot, which allows users to upload and interactively georeference CORONA images for expanding the archive (Casana, 2020).

[2]Note that so far, published studies referring to HEXAGON images have used this 20–30 feet resolution "mapping" or "terrain camera" only, as higher-res panoramic imagery was not yet accessible (e.g. Dehecq et al. (2020) and HEXAGON-based studies referenced therein).

TABLE 1 | Overview of very high resolution historical imagery from United States satellite reconnaissance programs featuring resolutions suitable for tree-level mapping (based on Perry, 1973a; McDonald and Widlake 2012; USGS, 2018a; USGS, 2018b; USGS, 2018c and own research). Scans of the analogue photographs are available through the USGS EarthExplorer for US$ 30 each at first-time order, and may be downloaded free of charge for subsequent users.

Program	Camera Type	Ground Resolved Distance (GRD)[a]	Dates	Missions	Images Available in USGS EarthExplorer
CORONA KH-4a	stereo-panoramic cameras	~9 feet	Aug 1963—September 1969	1001–1052	248,339 Aft 249,678 Forward
CORONA KH-4b	stereo-panoramic cameras	~6 feet	Sep 1967—May 1972	1101–1117	90,757 Aft 82,161 Forward
GAMBIT KH-7	monoscopic camera	~2–4 feet	July 1963—June 1967	4001–4038	17,607
GAMBIT KH-8 (still unavailable)	monoscopic camera	<2 feet	July 1966—April 1984	4301–4354	none
HEXAGON KH-9	stereo-panoramic cameras	~2–4 feet	June 1971—April 1986	1201–1220	198,022 Aft 210,250 Forward (as at 27 Apr 2022; total of 670,000 announced in USGS, 2018c)

[a]*The resolutions given here follow the dataset-characterizing indications given by the USGS (2018a, 2018b, 2018c) and refer to the approximate ground resolved distances of the photographic film. Actual ground resolutions may be lower towards the edges of the panoramic film, and specifications vary in the technical documents (NRO, 1970; 1972; Oder et al., 1988, 1992; Perry 1973a,b).*

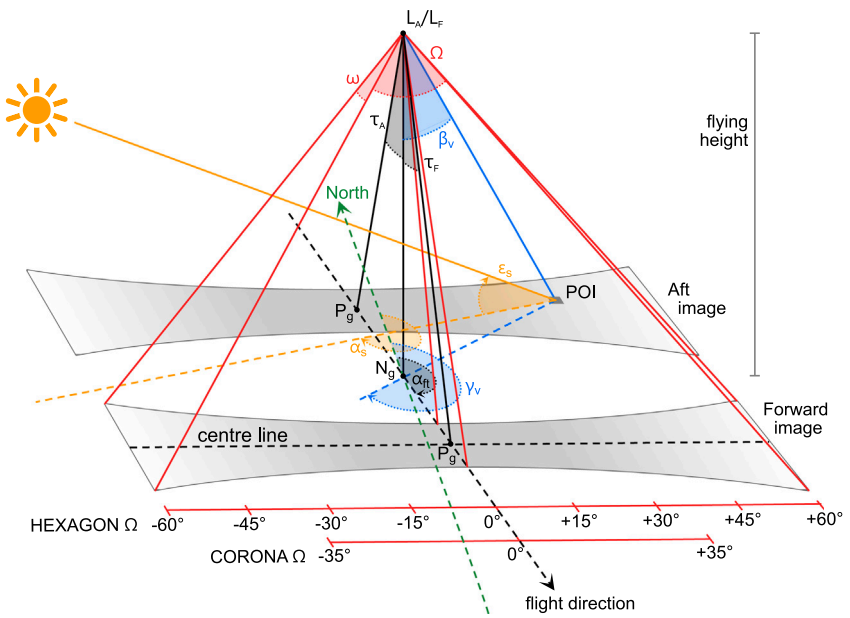

FIGURE 1 | Schematic diagram of images taken with the stereo-panoramic cameras of the CORONA and HEXAGON programs, showing exemplary image footprints of the maximum possible 120° HEXAGON scan width. Forward diagram shows image geometry; L_A/L_F: exposure stations of dual camera system; Ω: across-track camera field of view; ω: along-track camera field of view; τ_A/τ_F: camera tilt angle against/towards flight direction; α_{fl}: azimuth of flight track towards North; N_g: ground nadir point (vertical projection of L onto the ground); P_g: ground principal point (projection of optical image centre on the ground). Aft diagram shows illumination geometry; POI: given point of interest, α_S: sun azimuth; ε_S: sun elevation; γ_v: horizontal viewing angle, β_v: vertical viewing angle. Note the colour codes for sun angles (orange) and viewing angles (blue), which are used again in arrows of **Figures 3–5**.

distortion (Sohn et al., 2004; Scollar et al., 2016), spatial resolution, radial displacement of relief and high objects, and illumination across each image. **Figure 1** and **Table 2** summarize important characteristics of the cameras and images used in this study based on information taken from declassified technical documents or reconstructed from our image data.

The CORONA KH-4a (as well as KH-4b) and HEXAGON KH-9 systems each comprise two cameras tilted forward and backward (aft) along the flight track to provide stereo coverage. Each film strip is 5–6° wide and exposed during an across-track scanning motion (similar to opto-mechanical "whiskbroom" satellite scanners such as for LANDSAT 1–7 MSS/TM/ETM or AQUA/TERRA MODIS). While the across-track viewing angle is fixed with the CORONA cameras at 35° to the left and right of the track, it varies for the HEXAGON images. Here, the programmed camera field of view—30°, 60°, 90° or 120°—could be centred at 0°,

TABLE 2 | Characteristics of CORONA KH-4a and HEXAGON KH-9 stereo-panoramic camera systems and images. Italic entries are parameters that are specific to the data in this study and not generally applicable for all KH-4a and KH-9 images.

	CORONA KH-4a	HEXAGON KH-9
	Mission 1039–1 (23.2.1967)	***Mission 1203–2 (16.7.1972) and 1203–4 (23.8.1972)***
Camera type	stereo-panoramic camera (J-1) (forward/aft)	stereo-panoramic camera (forward/aft)
Focal length (*calibrated*)	24 in/609.6 mm[a] *F: 609.628 mm* *A: 609.628 mm*[c]	60 in/1,524 mm[b] *F: 1,523.314 mm* *A: 1,523.441 mm*[d]
Tilt angle aft/forward τ_A/τ_F	F: +15°/A: −15°[a]	F: +10°/A: −10°[b]
Along-track camera field of view ω	5°[a]	5.73°[b]
Across-track camera field of view Ω	70° centered at 0°[a]	30°/60°/90°/120° centered at 0°, ±15°, ±30° or ±45° (depending on scan mode)[b] *30° centered at +30° (1203–2) and 30° centered at -15° (1203–4)*
Flying altitude	varying; minimum heights (perigees) between 149 and 240 km[a,e] *182.5 km*[c]	varying; minimum heights (perigees) between 152 and 184 km[e,f] *181.3 km*[g]
Ground area length × smallest width	~207 km × 14.4 km—337 km × 23.3 km (depending on flying height)[a] *268 km * 18.4 km*[g]	~101 km × 19.1 km—677 km × 19.1 km (in centered modes at the nominal 185 km flying altitude, depending on scan mode) [adapted from b] *135 km * 19 km (1203–2) and 102 km * 18 km (1203–4)*[g]
Image resolution (film ground resolved distance (GRD)/scan ground sampling distance (GSD))	~7–10 feet/2.1–3 m (depending on flying height)[h] *2.2–2.5 m GSD (at test sites)*[g]	~2–6 feet/0.6–1.8 m GRD[b] *0.86–1.2 m GSD (at test sites)*[g]

Sources: [a] NPIC (1967), [b] NRO (1972), [c] NRO (1967), [d] SAFSP (1972), [e] NASA (2022), [f] USGS (2018c), [g] reconstructed/measured from our image data, [h] Perry (1973a:187).

15°, 30° or 45° to the left or right of the flight track. This results in large differences of image footprint sizes and shapes for the HEXAGON imagery. Deviating from the simplified schematic diagram in **Figure 1**, non-centred modes result in asymmetrically curved footprints. The chosen HEXAGON mode as well as 5° scan-angle marks are recorded on the edge of the film frame (NRO, 1972). The scan mode is not (or not yet) part of the metadata reported in the USGS EarthExplorer system; the only possibility to roughly judge the scan width and centre position of an image prior to ordering is to inspect the size and shape of the simplified (trapezoidal) footprint.

The orbital characteristics of the CORONA and HEXAGON missions vary. Most missions used an elliptical near-polar orbit, which could be flexibly adjusted but usually had its perigee (lowest orbit point that resulted in the highest image resolution) over the latitudes of the "Sino-Soviet Bloc" (Oder et al., 1992). The routinely used altitude is 185 km (100 nautical miles; McDonald and Widlake, 2012; Perry, 1973a), but the perigees vary between 149 and 240 km (see orbital details for each mission in NASA, 2022). During each revolution, the cameras were switched on for short periods of time over the target regions. Since the purpose of the imagery was military reconnaissance, the acquisition was preferably timed for low sun angles: Long shadows were desirable as they enable to interpret and calculate shapes and heights of buildings (cf. Hall, 2003; McDonald and Widlake, 2012). The exact UTC times with start and end coordinates including altitudes of the imaging flight tracks were recorded, along with other details of the orbit and cameras, in a flight data book or mission profile report. However, these documents have so far been declassified by NRO FOIA for a few missions only (e.g., NRO, 1967). In the case of our study, we had to reconstruct the acquisition time and flying altitude for the HEXAGON data from the imagery themselves (see **Section 4**).

3 STUDY AREA

The open-canopy forests formed by the endemic argan tree (*Argania spinosa*) in South Morocco are well suited for our study on tree-level change mapping based on VHRS imagery, since they are dominated by a single tree species with varying distribution patterns and tree architecture. This slow-growing tree, which may easily reach more than 200 years of age, is well adapted to aridity and drought. Its leaf-flushing and leaf-fall phenology is highly variable depending on water availability and drought and also differs strongly between tree genotypes. While some trees may get completely defoliated during dry periods, others may keep all or part of their leaves even during longer droughts (Zahidi et al., 2013). The argan woodlands are the basis of a traditional agro-silvopastoral system involving rain-fed agriculture, pasturing of goats, sheep and camels, and oil production (Lybbert et al., 2011; Msanda et al., 2021). Due to the high grazing pressure, the trees show various morphological traits and growth forms that are strongly

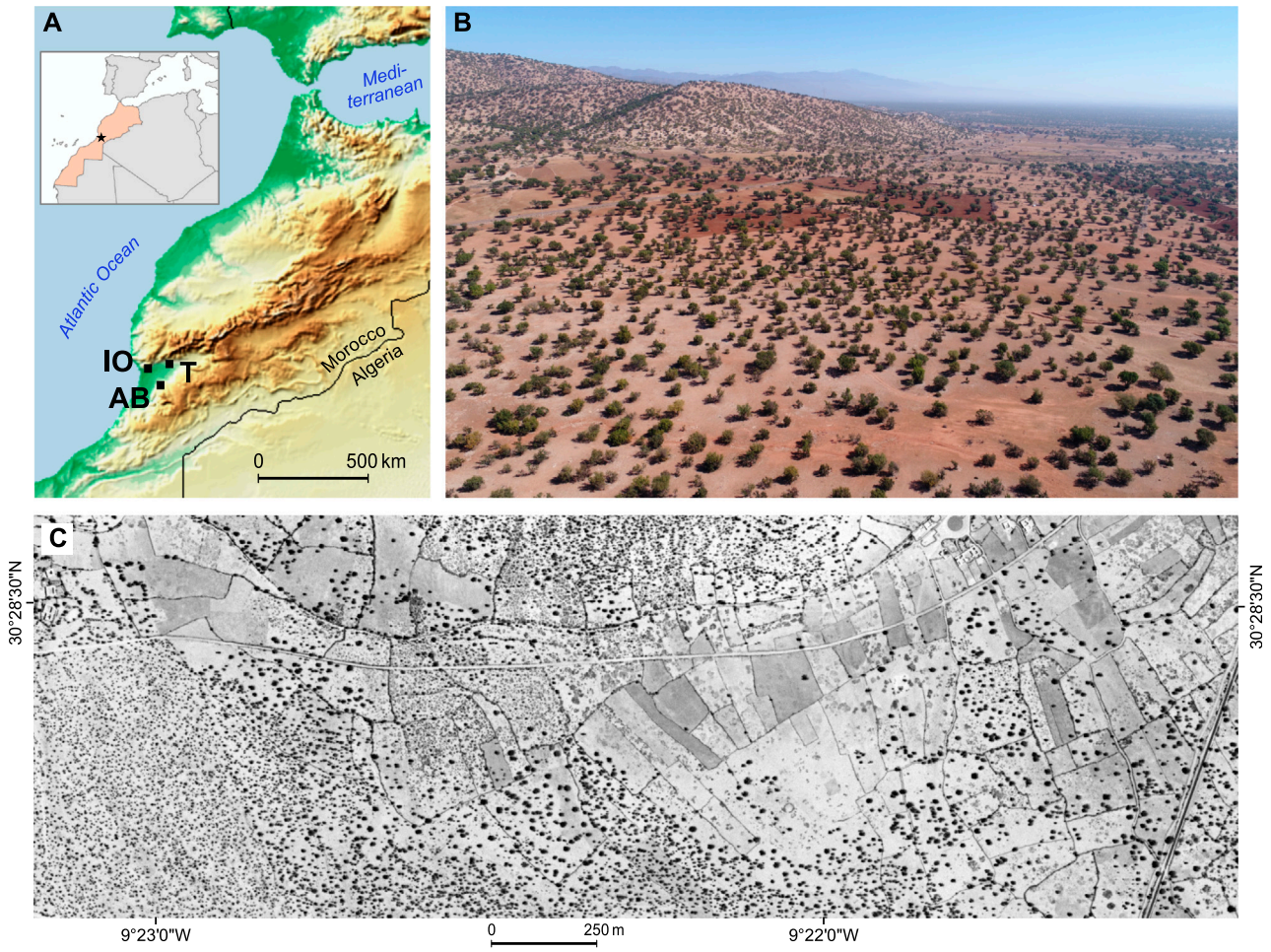

FIGURE 2 | (A) The location of the study areas Ida-Outanane (IO), Aït Baha (AB) and Taroudant (T) in the Souss Basin, Morocco. **(B)** View towards east over argan forests in the foothills of the High Atlas Mountains (Ida-Outanane study area); oblique UAS image of March 2019. Part of the area in the middle distance has been freshly ploughed for cereal cultivation, while the woodlands in the foreground are used as silvopasture. The area is classified as "0% trees" in the 2015 Global Forest Cover Change Map (Sexton et al., 2013). **(C)** View of the same area in HEXAGON KH-9 stereo-panoramic satellite photograph, 16 July 1972 (subset of image ID D3C1203-200152A016, georeferenced).

related to browsing intensity (see Kirchhoff et al., 2022). Widespread clearing of the once ubiquitous argan forests has been undertaken in the 12th to 17th century and again in the 20th century (Morton and Voss, 1987; Aït Hssaine, 2002; le Polain de Waroux and Lambin, 2012). The remaining argan woodlands have continued to decline due to firewood extraction, charcoal-making, overgrazing and soil degradation. Numerous studies suggest that tree density and canopy cover have been generally decreasing for the last 200 years. However, with the exception of the study by le Polain de Waroux and Lambin (2012), there is little quantitative and spatially explicit information about these forest-cover dynamics.

We chose three study areas in the Souss Basin in South Morocco (30–31° N, 7–9° W): Taroudant and Ida-Outanane in the southern foothills of the High Atlas and Aït Baha in the northern foothills of the Anti-Atlas (**Figure 2**). These study areas differ in the geologies of the High Atlas and the Anti-Atlas Mountains and in climate from maritime to more continental due to their varying proximity to the Atlantic Ocean. The annual precipitation rates range from an average 220 mm at Taroudant and 300 mm at Aït Baha to nearly 400 mm at Ida-Outanane with the most chance of rainfall in the late autumn to early spring, but the interannual variability is very high (Kirchhoff et al., 2019). To encompass varying land uses, altitudes, slope positions and tree densities, 30 test sites of 1 ha each were selected in these three study areas. The sites differed in the following characteristics: afforestation or reforestation sites (a); excessively browsed sites leading to cone-shaped growth of trees/bushes (b); recent or former crop cultivation (c); high canopy density due to large crowns or a high number of trees (d); incised by gully erosion (g); sites that were logged in the past with only few trees left (l); typical silvopastoral usage but otherwise nonspecific (n); high rock fragment cover (r); steep slopes >10° (s); terraced (t); sites under grazing exclusion (x). Each test site may have several of these attributes, but we mostly chose neighbouring sites contrasting in one of them; the most

salient attribute is recorded as suffix in the test site codes. For more details, see Kirchhoff et al. (2022) and **Supplementary Table S1**.

4 IMAGE MATERIAL AND PREPROCESSING

Since the argan-tree phenology reacts strongly on precipitation and temperature variations, precise timing of satellite imagery for leaves-on conditions is difficult, especially given the low temporal resolution of VHRS imagery. In average years, the highest foliage cover can be expected between March and June (Zahidi et al., 2013). Since no historical precipitation data were available for our study area and only few dates of historical VHRS images, we had to rely on image dates closest to the average humid season to ensure good contrast between tree crowns and intertree areas. The following image data and their derivatives were used in this study (see also **Supplementary Table S2**):

4.1 CORONA Satellite Images of 1967

Via the USGS EarthExplorer portal, we acquired scans of panchromatic satellite photos taken with the stereo-panoramic KH-4a camera at 23 February 1967 during CORONA mission 1039. The 2.76 inch × 29.8 inch negatives were scanned on demand with 3,600 dpi by USGS EROS in four parts and delivered as non-georeferenced TIF files.

We georectified each image file to the orthorectified WorldView images using ESRI ArcGIS Desktop 10.8 (ESRI Inc., Redlands CA, United States) in a two-step-approach: The entire image was georectified first using 10–15 well-distributed ground control points (e.g., small, well-defined trees, corners of buildings, road junctions). 10–30 additional control points were then placed around and within each of our test sites to increase local accuracy. A piecewise polynomial transformation (spline) was chosen, which is an exact transformation method and results in zero residual error. The quality of the co-registration with the WorldView imagery was assessed visually. It was not possible to achieve a precise matching of each tree crown, since crown and shadow mostly merge into one dark tree spot and because the radial displacement of the crown varies with local viewing angle and tree height (see also **Section 5.1**). Due to the panoramic film camera geometry, the spatial resolution or ground sampling distance (GSD) of the scanned CORONA images varies at our test sites between 2.2 and 2.5 m from west to east. We reconstructed the positions of the image nadir points from the known camera tilt angles and principal-point positions of the georeferenced images. The flying height and precise time of image acquisition was given in the mission's flight data book (NRO 1967). We then calculated the viewing angles and illumination angles given in the following sections from the geometrical relationships shown in **Figure 1** and using the online SunCalc tool (www.suncalc.org). More information on reconstructing and calculating these parameters is given in **Supplementary Workflow S1** and **Supplementary Workflow S2**.

4.2 HEXAGON Satellite Images of 1972

On-demand scans of panchromatic satellite photos taken with the stereo-panoramic KH-9 camera at 16 July 1972 and 23 August 1972 during HEXAGON mission 1203 were also acquired from USGS EROS. The scanning and georectifying procedures of the images were the same as for the CORONA images. As no flight data book has been declassified for this mission, we determined the time of day by comparing shadow direction of selected high buildings with sun azimuth given for the location in the SunCalc tool. Using the geometrical relationships shown in **Figure 1**, we reconstructed the flying height from the lengths of the georeferenced image strips and subsequently calculated the positions of the nadir points, viewing angles and illumination angles (see also **Supplementary Workflow S1** and **Supplementary Workflow S2**). The spatial resolution of the HEXAGON images varies at our test sites between 0.8 and 1.1 m from west to east.

4.3 WorldView Satellite Images of 2017/2018

We acquired very high resolution satellite (VHRS) images from the WorldView 2, 3 and (for just one test site) GeoEye satellites from the European Space Agency (ESA) through the Third Party's Mission scheme. The image dates vary between test sites due to limited availability (July 2017 and March 2018, see **Supplementary Table S2**), but 2017 results could be updated to 2018 with the help of UAS imagery (see below). In the following, we refer to the whole dataset as "WorldView 2018" for ease of wording. Using ERDAS Imagine 2018 image-processing software, we orthorectified the multispectral (VIS and NIR, 2 m GSD) and panchromatic (0.5 m GSD) bands to UTM Zone 29 using the rational polynomial coefficients (RPC) sensor models and a 12 m-resolution TanDEM-X elevation model. We then pansharpened the lower-resolution multispectral images to 0.5 m resolution using the associated higher-resolution panchromatic band.

4.4 Small-Format Aerial Photography (SFAP) Taken with an Unmanned Aerial System (UAS) in 2018–2020

Within the framework of the ARGAN research project (Kirchhoff et al., 2019), aerial surveys with a quadcopter UAS (DJI Phantom 4 Pro) were repeatedly conducted at all test sites in 2018–2020. We took overlapping RGB images at 50 m flying height following a flight scheme designed to capture full 3D tree shape (Aber et al., 2019:160; Marzolff et al., 2020). Georeferencing was provided by 14 ground control points per test site whose coordinates we measured with an RTK GNSS. A standard Structure-from-Motion (SfM)-photogrammetric processing workflow with Agisoft Metashape 1.6 (Agisoft LLC, St. Petersburg, Russia) was then employed for extracting dense RGB-coloured 3D point clouds (cf. Cunliffe et al., 2021). We classified the 3D point clouds into vegetation points and ground points (with sub-classes tree shadow/no tree shadow) and subsequently computed 3 cm-resolution digital surface models (DSMs)

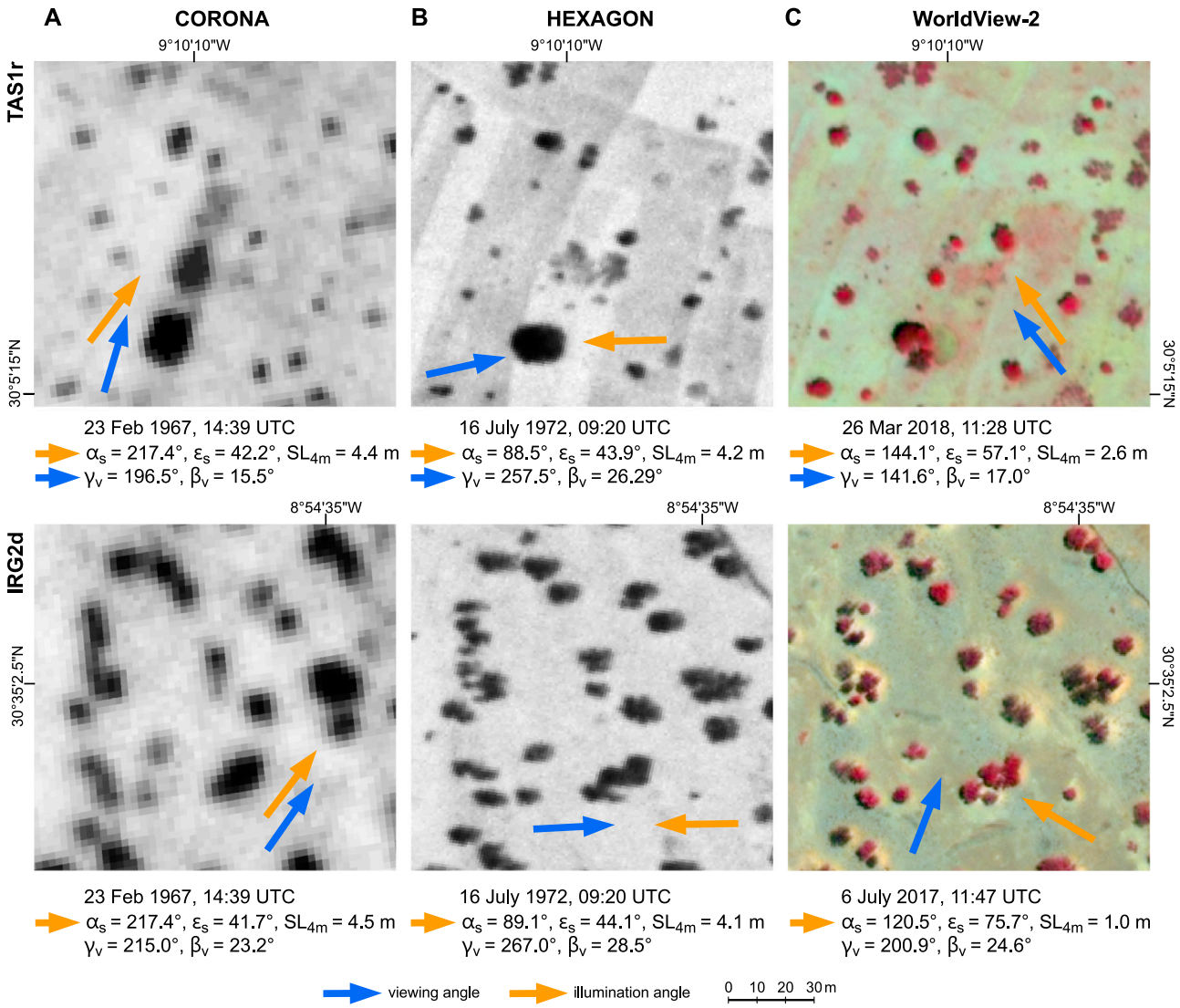

FIGURE 3 | Combined effects of varying spatial resolutions, illumination angles (orange arrows) and viewing angles (blue arrows) on the appearance of trees in CORONA **(A)**, HEXAGON **(B)** and false-colour infrared WorldView-2 **(C)** imagery of test site TAS1r (top row) and IRG2d (bottom row). α_S: sun azimuth; ε_S: sun elevation; SL_{4m}: shadow length of 4 m high object; γ_v: horizontal viewing angle of camera; β_v: vertical viewing angle of camera. Note the 5-years gap between the two historical image dates and the change of tree cover in the centre of TAS1r.

and digital terrain models (DTMs) as well as 1.5 cm-resolution orthophoto mosaics. We used ESRI ArcGIS Desktop 10.8 and CloudCompare 2.12 for creating simulated CORONA and HEXAGON imagery by altering spectral and spatial resolution and viewing angles of the UAS data. Together, these UAS data served for the following purposes:

- All orthophoto mosaics: as ultrahigh-resolution reference dataset for training and verification of argan-tree presence and size during the mapping process based on visual image interpretation of the WorldView imagery
- Selected orthophoto mosaics: for verifying that no significant changes had taken place between summer 2017 and spring 2018 for 9 of 30 test sites, since no WorldView images had been available for the latter date in this area
- Selected orthophoto mosaics degraded to panchromatic 2.2 m or 1.0 m resolution, respectively: for simulating the appearance of variously-sized trees at the poorer spatial and spectral resolutions of CORONA and HEXAGON imagery
- Selected 3D point cloud: for simulating and quantifying the influence of tree shadow on the apparent size of the tree crown in the CORONA and HEXAGON imagery at different viewing angles.

In addition to the image data, we used a database with all trees mapped on our 30 test sites in the field in 2018. This

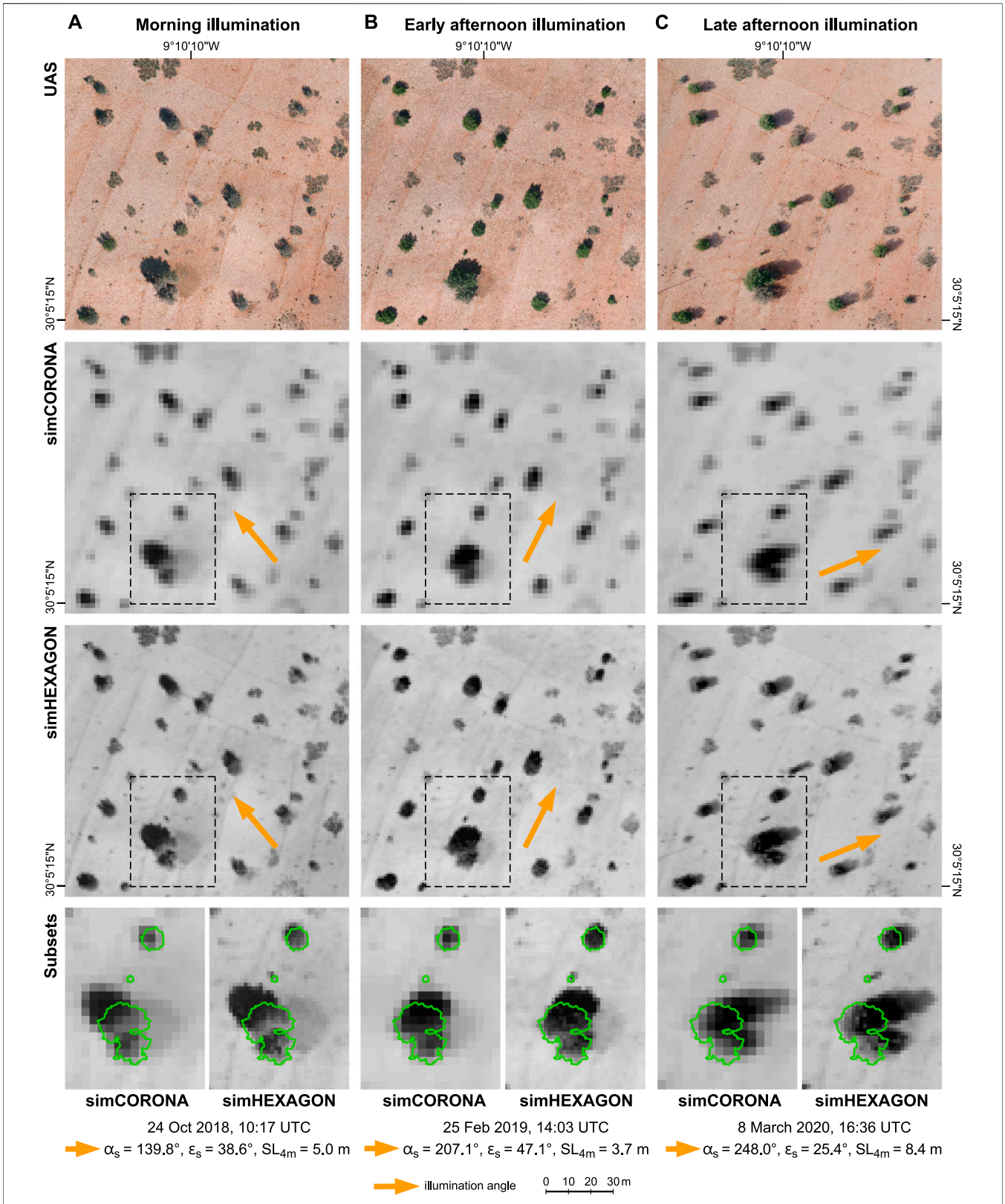

FIGURE 4 | Effect of varying sun illuminations (sun azimuth α_S shown as orange arrow) on the appearance of individual trees at test site TAS1r. Morning **(A)**, early afternoon **(B)** and late afternoon illumination **(C)** are shown in UAS imagery (1.5 cm resolution, top row), simulated CORONA imagery (2.2 m resolution, second row) and simulated HEXAGON imagery (1.0 m resolution, third row). Note that illumination condition B is very similar in date, time and sun angles to the original CORONA image of this site (**Figure 3A**, top row). Subsets (bottom row) show examples for merging of crown and shadow in the appearance of small, medium and large trees (true crown areas outlined in green). For parameter abbreviations, see **Figure 3**.

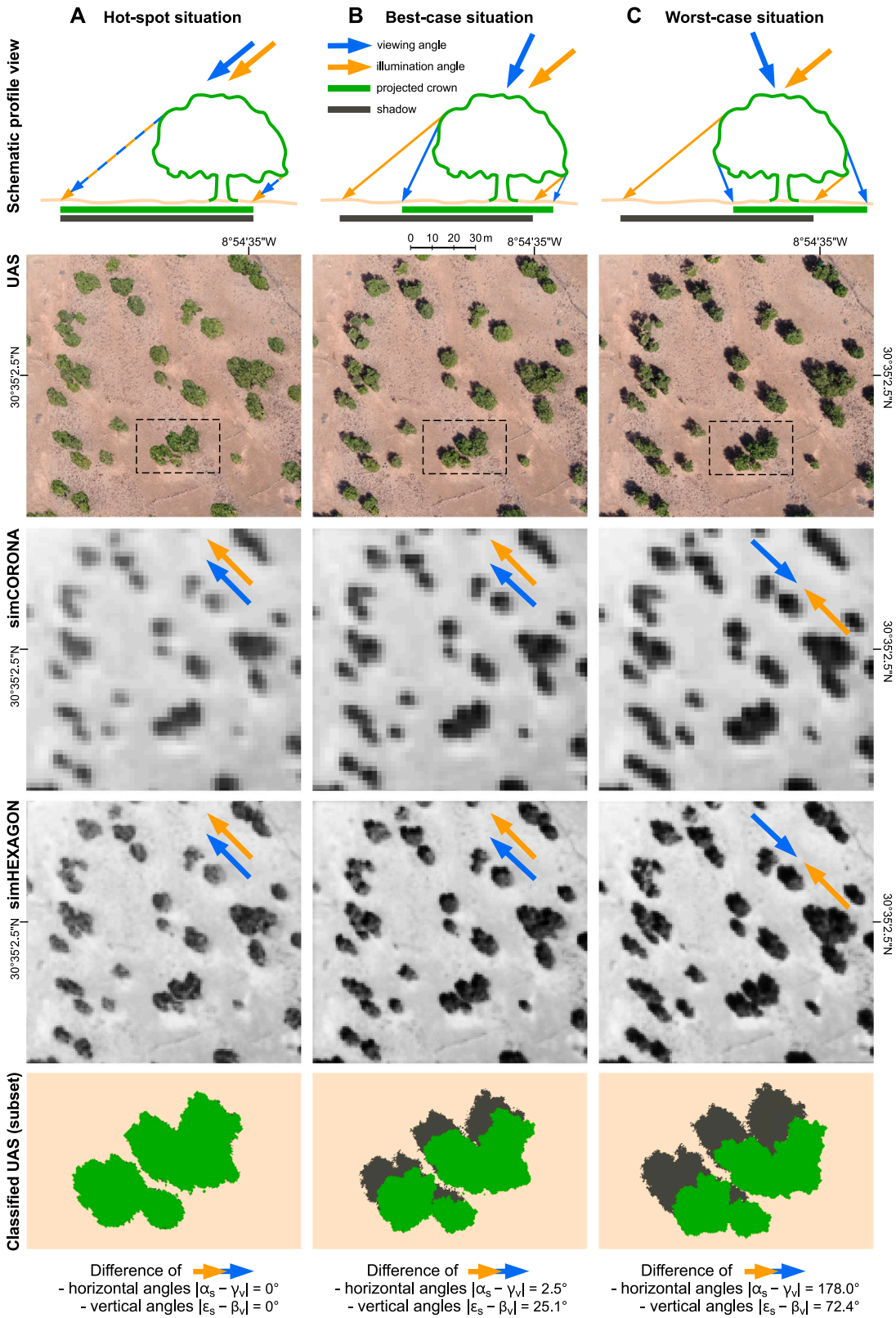

FIGURE 5 | Effect of varying viewing directions (blue arrows) relative to sun illumination (orange arrows) on the appearance of individual trees at test site IRG2d, showing theoretical hot-spot situation **(A)**, actual best-case **(B)** and actual worst-case situation **(C)** in UAS imagery simulated from 3D point clouds (top row), simulated CORONA imagery (2.2 m resolution, second row) and simulated HEXAGON imagery (1.0 m resolution, third row). Subsets (bottom row) show exemplary tree spots classified into crown and shadow area. Crown/shadow percentages at test site vary from 100%/0% **(A)** over 70%/30% **(B)** to 59%/41% **(C)**. For parameter abbreviations, see **Figure 3**.

database records the location of each individual argan tree (2,494 in total), its architecture class and single trunk/multi-trunk status (for further details, see Kirchhoff et al., 2022).

5 EVALUATION OF HISTORICAL AND RECENT VHRS IMAGERY FOR MAPPING WOODLAND CHANGE ON THE TREE-LEVEL

5.1 The Appearance of Trees in Historical CORONA and HEXAGON Images

The characteristics of the CORONA and HEXAGON programs outlined above result in several factors that influence the appearance of a tree in the panchromatic imagery. Size, shape, boundary definability and location of the dark spot representing the tree in the image depends on local GSD, contrast, camera observation angle and date and time of the image. For mapping and monitoring woodlands aiming at quantitative measures of tree density and tree-cover change, a thorough understanding of these factors is essential (cf. Fensham and Fairfax, 2002). To this end, we will in the following discuss their combined effects in exemplary subsets of original CORONA and HEXAGON photographs (**Figure 3**) and their individual variability with simulations based on UAS imagery (**Figures 4**, **5**).

For both panoramic cameras, image GSD varies with mission flying height, but also across the image. This is due to the panoramic scanning with fields of view Ω up to 120° (**Table 2**; **Figure 1**). Generally speaking, the spatial resolution of the newly available HEXAGON images is at least twice as good than that of the commonly used CORONA images (and similar to the very rare GAMBIT KH-7 images; **Table 1**). The significance of this difference for tree mapping is clearly evident from **Figure 3**, where the visibility of small trees, the shape of larger trees and the separability of clumped canopies differs greatly between the two historical image types. Apart from a felled tree and cleared shrubs in the centre of TAS1r (**Figure 3** top row), the tree cover remained unchanged between 1967 and 1972. The difference in its appearance in the historical images, however, is not only due to spatial resolution, but also to varying illumination and viewing angles: While sun elevation and shadow lengths are quite similar for both sites and dates, the direction and visibility of the cast shadows vary strongly (see orange and blue arrows in **Figure 3**). An influence of these angles on shadow visibility is also given for the WorldView images, as these modern-date VHRS sensors can be tilted to support multi-swath and stereo imaging. But other than for the panchromatic images, crown and shadow are easily distinguished in the multispectral images. Note that the largest tree on TAS1r (shown also in bottom-row subsets of **Figure 4**) has changed its crown form by 2018, as it was split by multi-trunk breakage after 1972.

Figure 4 illustrates the effects of different sun azimuths and elevations on the appearance of today's woodland at test site TAS1r for simulated spectral and spatial resolutions of CORONA and HEXAGON images. This test site represents the full range of argan-tree sizes present in our study area. In the panchromatic images, the dark spot representing a tree comprises both tree crown and its shadow and thus, lower sun elevations lead to elongated tree spots in the imagery. The sun-facing part of the crown may appear considerably lighter, resulting in a visual displacement of the tree spot. The effect is present in both CORONA and HEXAGON images, but easier recognized in the latter due to the smaller GSD and sharper outlines of the tree spots.

Although shadowing compromises the shape of the tree spot in the panchromatic images, its darkness and elongated shape helps to distinguish between elevated dense crowns of argan trees and the lower and sparser foliage of shrubs such as *Launaea arborescens* or *Ziziphus lotus* (present at some of our test sites, e.g. top and right edge of TAS1r). Note how these lighter-coloured spots do not change shape with varying sun azimuths in **Figure 4**. With the poorer resolution of the CORONA imagery, however, small trees < GSD may result in similar medium-grey pixel values as shrubs with ~ GSD diameter—especially so for higher sun elevations and shorter shadows.

Most importantly, the HEXAGON resolution allows the identification of much smaller trees, particularly at low sun elevation (see subsets in **Figure 4**, bottom row). Comparing our simulated images with crown-size measurements from the original UAS data, we found that the identification of trees with diameters <3 m is uncertain in CORONA, but trees ~1.5 m diameter are still clearly visible in HEXAGON images. We also found that the latter compare quite well with the pansharpened WorldView images (cf. **Figure 3C**), whose nominal 0.5 m GSD results from merging the panchromatic band with the much lower-resolving multispectral information.

As tree shadow impairs crown-size measurements in the historical VHRS imagery, we also need an understanding of its share in the dark tree spot. The visible area of shadow on the ground is dependent not only on sun elevation, but also on the viewing perspective onto the tree crown. Our simulation in **Figure 4** is based on a true orthophoto mosaic (geocorrected with a digital surface model) and hence has an orthographic viewing perspective. This is not the case for the satellite imagery in **Figure 3**, where trees appear in central perspective. From the geometries shown in **Figure 1** and **Table 2**, we may estimate that the stereo-panoramic KH-4a and KH-9 cameras give local vertical viewing angles (β_v) for a given point of interest (POI) ranging from a minimum 12.4° and 7.1° to a maximum 37.5° and 60.2°, respectively. Thus, all objects appear in a more or less oblique perspective and experience radial displacement relative to the nadir point N depending on their height. The direction of the radial displacement depends on the local horizontal viewing angle (γ_v), which also varies throughout the image (see **Figure 1**). Where local sun angle and viewing angle coincide, any shadow will be concealed by the object casting it: this phenomenon is known as hot spot or opposition effect (Aber et al., 2019:42). Conversely, when the viewing direction is towards the sun, the amount of visible shadow is maximised.

Figure 5 illustrates this by simulating different viewing directions relative to the sun for test site IRG2d and its appearance in simulated CORONA and HEXAGON images.

We chose this test site for three reasons: Here of all 30 sites, the illumination/viewing conditions in our actual CORONA and HEXAGON images (see **Figure 3** bottom row) are the most and least favourable, respectively; UAS imagery was taken at a similar shadow length (albeit different sun azimuth) to the historical imagery; and the tree cover has changed little in 50 years. In the theoretical scenario of **Figure 5A**, the hot-spot situation hides all tree shadow behind the crowns, resulting in a tree spot accurately representing the crown size. This situation is improbable for CORONA and HEXAGON images, as shadow effects were explicitly aimed for in mission planning. Conversely, the theoretical worst-case scenario in terms of shadow visibility would appear if the horizontal viewing direction were opposite the sun and the vertical viewing angle were maximised, i.e., the POI located at the farthest edge of the film strip.

Figure 5B represents the actual best viewing condition for our 30 test sites (corresponding to **Figure 3A**, bottom row): The difference in horizontal illumination and viewing angles is negligible, but the vertical sun angle is 25.1° lower than the vertical viewing angle. On average, the dark tree spots at our test site contain 30% shadow (see classified subset of tree group in last row of **Figure 5**). This shadow fraction is maximised to 41% for the actual worst viewing condition at our test sites (**Figure 5C**, corresponding to **Figure 3B**, bottom row). Here, the horizontal viewing angle is nearly exactly opposite the sun, and the large difference between vertical angles exposes most of the trees' shadows.

With increasing difference in viewing and illumination angles, the proportion of leaf shadow within the crown increases and the reflectance of the foliage decreases due to the multi-angular nature of canopy reflectivity (cf. Aber et al., 2019:45). This is well visible in the UAS imagery in **Figure 5** (top row), where the tree crowns become darker from left to right, and further exacerbates the difficulty of distinguishing crown from shadow in the panchromatic images. However, we found that in many cases the superior radiometric quality of the HEXAGON data, together with the smaller GSD, retains some intensity difference between crown and shadow both in the simulated images (e.g., **Figures 4**, **5**, third row) and the original images (**Figure 3B**). For the CORONA images, there is little chance of visually separating crown and shadow.

The combined effects of spatial resolution, illumination and viewing angles illustrated in **Figures 4**, **5** not only determine if single trees can be identified and measured, but also if clumped canopies can be separated into individual trees. Moderate shadowing and a small GSD—as in the HEXAGON images of **Figure 5B**, third row—are desirable in this case as they help to model the round shape of the crowns and improve separability. But it is still hardly possible in either the historical or recent VHRS imagery to identify close-growing individuals in tree groups with highly overlapping and merging canopies.

5.2 Mapping Tree Density With Historical and Recent VHRS Imagery

We learned from our simulations of historical VHRS images on the basis of UAS imagery that tree crowns <3 m (CORONA) or <1.5 m (HEXAGON) diameter cannot be reliably identified on the panchromatic images, and that current UAS imagery may help to interpret ambiguous features. To a lesser degree, this also applies to recent multispectral VHRS images from WorldView and similar satellite sensors, where very small trees may not be recognizable. In all types of images, above all CORONA, clumped crowns of tree groups may not be visually separable. Thus, VHRS-based change analyses of open-canopy woodlands on the individual tree level must always be expected to underestimate tree number and density. In order to evaluate the reliability of our data for tree-density change mapping, we created three different datasets of argan-tree maps for our 30 test sites:

Field-based dataset for all dates (FB): Tree locations in 2018 were known a-priori from field mapping. Tree existence at these locations for previous dates was verified by visual interpretation of the CORONA and HEXAGON images, and trees visually identifiable in 1967 or 1972 but lost until 2018 were supplemented.

WorldView-based dataset for all dates (WB): All visually identifiable trees in 2018 were mapped independently from WorldView images, i.e., typical recent VHRS data. Tree verification and supplementing for 1967 or 1972 was done in the same way as for the FB dataset.

HEXAGON-based dataset for 1972 (HB): All visually identifiable trees in 1972 were mapped independently from HEXAGON images, i.e., the currently best available historical VHRS data.

In the retrospective mapping process for the field-based (FB) and WorldView-based (WB) datasets, we classified all trees as already existent in 1967 or 1972 unless they were clearly not recognizable, thus retaining many group trees and some small trees which otherwise might not have been resolvable in the satellite images. The workflow for this mapping process is explained in more detail in the **Supplementary Figure S1**. We did not create a CORONA-based dataset by independent mapping as we deemed the uncertainty for trees <3 m diameter (common for all sites) and individuals in tree groups (common for some sites) too high.

Figure 6A shows the number of trees mapped in the FB, WB and HB datasets for 2018, 1972 and 1967. Of the 2,494 trees mapped in the field in 2018, we recognized 2,220 trees as already existing in the 1972 HEXAGON images. 272 trees mapped for 1972 were lost until 2018. In the CORONA images of 1967—only 5 years earlier—we could only recognize 1,549 of today's trees, plus 106 which had been lost since. The number of trees drops drastically in the WB dataset: only 1,506 (60%) of the trees mapped in the field could be identified on the contemporaneous WorldView images. On inspection of the trees missing in the WB dataset, we found that only 11% field-mapped trees (nearly all <3 m diameter) had not been recognized at all on WorldView, and the remaining gap of 29% is due to fewer individuals recognized in tree groups (see also **Supplementary Figure S2**). Accordingly, retrospective mapping for 1972 and 1967 based on the WB tree locations also yields much lower tree numbers (minus 34%), although the relative changes

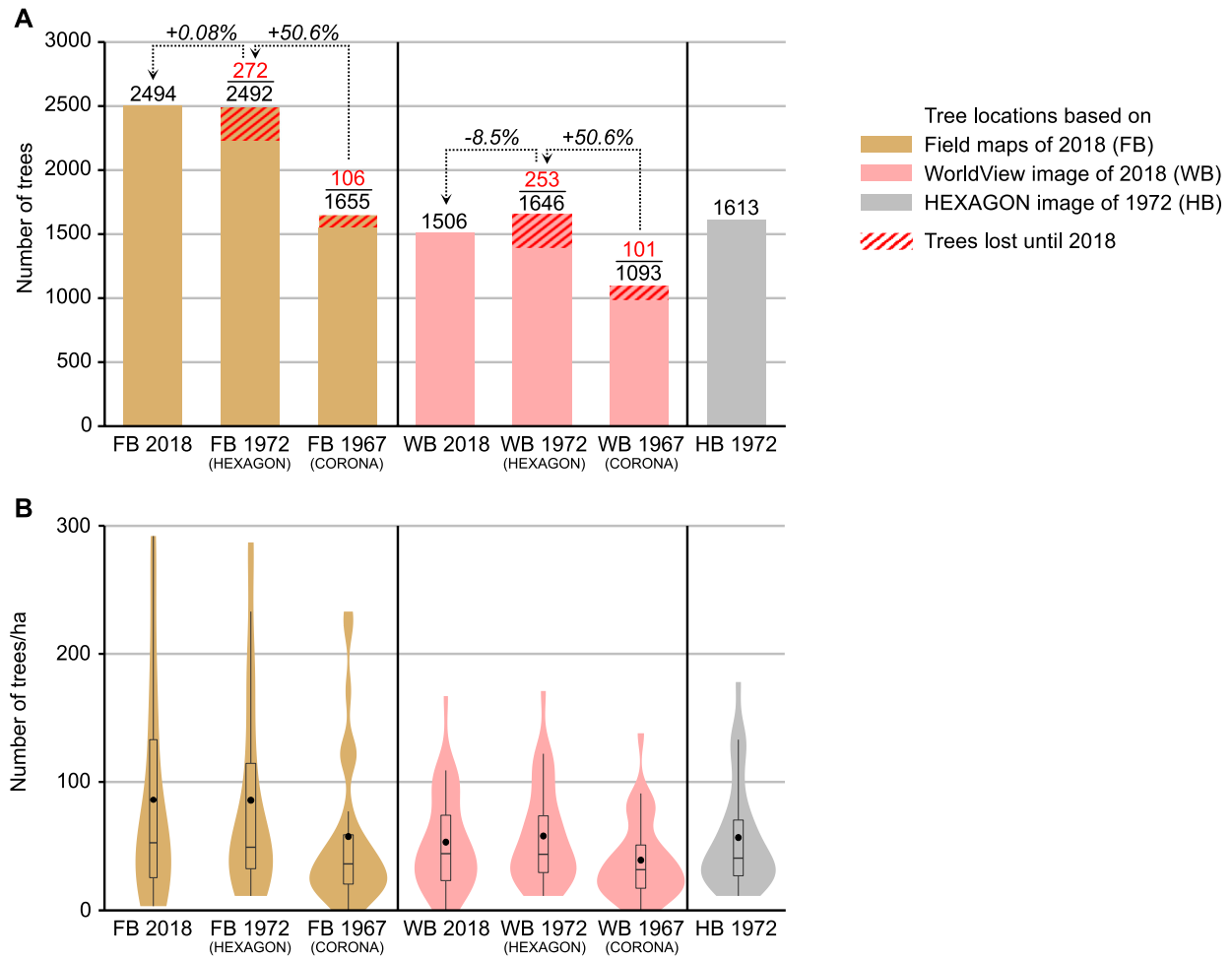

FIGURE 6 | Results of argan-tree mapping on the 30 test sites in 2018, 1972 and 1967 according to the field-based (FB), WorldView-based (WB) and HEXAGON-based (HB) datasets. **(A)** Total numbers and net changes between dates; **(B)** Distribution of tree densities over the 30 test sites shown as violin plots (boxplot shows median and upper/lower quartiles; black dot shows mean). Note the difference in the shape of the violin plots between FB and WB and the similarity between WB 1972 and HB 1972.

between the dates are the same as for the FB dataset. The slightly lower number of trees mapped as lost until 2018 in the WB dataset also concerns very small trees or trees in clumped canopies: We had a tendency to pinpoint such trees in the HEXAGON and CORONA images more readily during retrospective mapping in the FB dataset, as the knowledge of today's tree location trained us to accept even smaller or denser tree spots as individual trees.

Obviously, the choice of initial mapping base for retrospective monitoring has implications for the accuracy of the tree-density change quantification. While our FB dataset, which cautiously retains small and group trees not mappable from the satellite images, results in a negligible net change (+0.08% or +2 trees) between 1972 and 2018, the WB dataset suggests an 8.5% loss (-140 trees). The apparent 50% increase of tree numbers between 1967 and 1972 recorded in both the FB and WB dataset is clearly not realistic. We found that nearly all of these "new" trees in 1972 are too small (<< 3 m diameter) to be safely identified on CORONA images (cf. small tree crown in **Figure 4**, last row): They could either have regrown from felled stumps since 1967, or have been very small trees already existing in 1967. Given the slow growth rate of argan trees, it is improbable that a seedling emerged after 1967 would be large enough to be visible in HEXAGON imagery after only 5 years.

The different approaches to tree mapping also show in the distribution of tree densities over our 30 test sites (**Figure 6B**; for detailed results of each test site see **Supplementary Table S3**). According to the FB 2018 dataset, the maximum density is 292 trees/ha, but the unimodal distribution is positively skewed: The mean density is 86 trees/ha, and the median (50% threshold) much lower at 52.5 trees/ha. In the WB 2018 dataset, the mean and median densities are 53 and 44 trees/ha, and no test site reaches more than 167 trees/ha. The slightly tri-modal violin-plot shape and boxplot indicate that the FB and WB datasets agree much better for the lower-density test sites, while tree numbers at the denser sites (i.e., with smaller trees and more group trees) are clearly underestimated in the WorldView-based maps. Similar

density distributions result from the FB and WB datasets for 1972. In contrast, the distributions for 1967—mapped from CORONA imagery—are even more strongly skewed towards low tree densities. As the retrospective mapping approach retains a high number of field-mapped group-tree locations in the FB dataset, but fails to identify isolated small trees for 1967 due to the poor CORONA resolution, the FB 1967 violin plot has a strongly multi-modal shape caused by 6 test sites where tree groups are particularly common. This effect is less pronounced in the WB dataset, where trees in clumped-canopy groups are generally underrepresented for all dates.

Interestingly, the highest agreements across mapping approaches are given for the HB 1972 compared to the WB 1972 dataset. The total number of trees (**Figure 6A**) mapped for 1972 from the HEXAGON images, independently of tree locations known a-priori from field mapping or from WorldView images, is nearly identical to the WorldView-based WB 1972 tree count (1,613 vs 1,646). Also, the tree-density distributions (**Figure 6B**) for HB 1972 compare very well to those for WB 1972, with means of 56.6 or 57.8 and medians of 40.5 or 43.5, respectively (see also **Supplementary Figure S3**). This indicates that the suitability of HEXAGON images for (manual) tree mapping is indeed similar to that of recent VHRS imagery, in spite of lower spatial and spectral resolutions. For trees >1.5 m diameter, which we found well visible on the recent and historical VHRS images, we may therefore assume quite realistic monitoring results using the WB mapping approach. Typical in our study area, however, is a large proportion of small trees, often in dwarfed growth forms like cone-shaped cushions, that are underrepresented in the WB dataset. Cone-shaped cushions frequently develop after a tree was cut close to the ground for charcoal or firewood, when the multiple new shoots from the stump (Morton and Voss, 1987) cannot regrow into stems due to continuous high browsing pressure (Kirchhoff et al., 2022). Natural regeneration is not or very rarely possible under the high grazing pressure. Dieback over time leads to a lower tree density and a higher percentage of soil without protection from erosion or soil degradation, which in turn leaves less favourable conditions for developing young argan sprouts (le Polain de Waroux and Lambin, 2012).

In light of this situation, it is likely that most of the small trees we missed in the WB dataset for want of conspicuousness have already been there in 1967/1972, possibly as recently cut stumps or as heavily pollarded trees (cf. Andersen, 2006). Our field data on tree architecture (Kirchhoff et al., 2022) confirms that 73% of these trees have growth forms indicating regrowth from felled trees. The FB 1967 and 1972 datasets include those of them that we could recognize in the historical VHRS images since their location was known a priori from field mapping. Consequently, we have used the FB dataset for further analysis of tree crown sizes and cover changes below and in Kirchhoff et al. (2022).

5.3 Monitoring Tree-Crown Size With Historical and Recent VHRS Imagery

The development of tree number and density between 1967/1972 and 2018 shown in **Figure 6** indicates little net change of the argan woodlands over the last 50 years. But tree count is clearly too simple an indicator for forest dynamics when trees are at risk of unsustainable use due to high demands on livestock forage, firewood and charcoal. Tree canopy cover—composed of individual tree-crown sizes—is more interesting, because soil conditions under the crown differ significantly from the area between the tree crowns and would thus give an indication about relative differences in e.g., soil water content, soil organic carbon or aggregate stability (Kirchhoff et al., 2019; Kirchhoff et al., 2021).

From our evaluation of the factors influencing the appearance of trees in CORONA and HEXAGON imagery, we concluded that the latter is clearly superior for tree mapping to the former, but both types do not lend themselves to map and measure crown sizes on a continuous scale, as the uncertainties would be too high for allowing reliable interpretations of cover change. However, we decided that the range of tree sizes and changes in the argan forests may be well described by classifying the trees in small (S; < 3 m diameter), medium (M; 3–7 m) and large trees (L; > 7 m). We symbolized each field-mapped tree with a 3 m/7 m double-ring symbol in order to interpret its size class from the images (see **Supplementary Figure S1**). We classified the FB 2018 dataset first, and then recorded the changes since 1967 and 1972 by retrospective interpretation of the CORONA and HEXAGON images, taking into account the effects of viewing and illumination angles (including radial displacement of taller trees) in the historical VHRS imagery during interpretation. Any trees where change into another size class was not visually certain were given the same size class as 2018.

As a representative example for the resulting maps, **Figure 7** shows the test site MAO1n, where the overall tree density and cover change is quite similar to the average of all 30 test sites. Map A displays change since 1967 and clearly reflects the CORONA imagery's uncertainties discussed above: The HEXAGON-based map B (change since 1972) shows 17 more small trees (7 of them lost by 2018). Although some trees may have propagated from seeds within 5 years, they would still be too small to be visible at HEXAGON resolution given their slow growth rate, so natural regeneration seems unlikely. All "new" trees in 1972 are smaller than the CORONA visibility threshold, and those remaining until today exhibit architectural traits indicating high probability of resprouting from stumps after felling. The same applies for the 10 trees mapped as new between 1972 and 2018 (**Figure 7B**, green rings), which are mostly multi-stemmed and possess strongly developed basal cushions (cf. Kirchhoff et al., 2022). Altogether, 33 (or 60%) of the 1972 trees at MAO1n have remained in the same size class (yellow circles), 14 are smaller or lost (red and red-crossed circles), 18 are new or larger (green rings and circles). However, positive change only occurs in one-class increments (not present to S, or S to M), but negative change also in two- and three-class increments (M to not present, L to not present). Thus, in spite of the unchanged total number of trees, this site shows considerable ambiguity in change with a slight tendency towards net decrease of woody cover.

Figure 8 shows results for the monitoring of tree cover 1972–2018 at all 30 test sites. The development on the 30 test sites is highly heterogeneous and ranges from nearly complete deforestation (IRG3l) to considerable recovery (TAS1r). Three

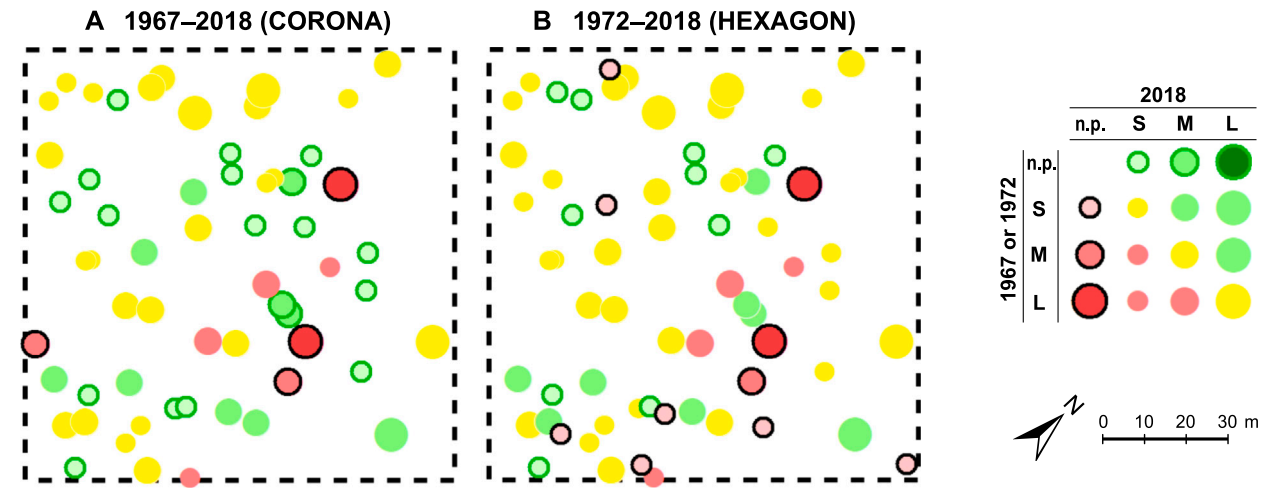

FIGURE 7 | Change maps for argan trees at test site MAO1n **(A)** between 1967 and 2018 and **(B)** 1972–2018, based on the FB 1967, FB 1972 and FB 2018 datasets (location is 9°07′51″W, 30°04′09″N). Symbol colours indicate size changes since 1967 or 1972 (green: crown-size increase and new trees, yellow: unchanged, red: crown-size decrease and lost trees). Symbol outlines indicate new (green outline) and lost trees (black outline). Symbol sizes vary by tree size in 2018 (for prevailing trees). n. p. = not present, S = < 3 m, M = 3–7 m, L = > 7 m diameter. Note that the differences between **(A)** and **(B)** are caused by the poorer resolution of the CORONA imagery rather than actual change of the slow-growing argan trees between 1967 and 2018.

test sites (ABH2c, ABH2t, AOU1a) show predominantly forest degradation with high percentages of cleared trees or smaller crown sizes. However, a clear trend of argan forest change at our test sites cannot be observed. Even within the three geographically distinct study areas, the developments between 1972 and 2018 vary substantially. These spatial associations of positive and negative changes within argan-tree populations raise questions about potential patterns of ambivalence and influences of ecological or forest-use related factors, which are given closer attention in Part B of our study (Kirchhoff et al., 2022).

6 DISCUSSION

6.1 Factors Influencing the Appearance of Trees in Historical VHRS Images

The newly accessible historical HEXAGON satellite photographs taken with the KH-9 stereo-panoramic cameras have proven clearly superior to the well-recognized CORONA KH-4 images in our study on tree-level mapping of open-canopy woodlands. This can mainly be attributed to the much higher spatial resolution—in our case, GSDs of approx. 1 m (HEXAGON) vs 2.2 m (CORONA). Since both image types are panchromatic, spatial resolution is the single most determining factor for the identification of individual trees: It influences both the threshold of minimum visible crown size and the separability of trees with clumped canopies.

It should be understood that the GSDs given for our data are not generally transferable to all HEXAGON or CORONA images. Spatial resolution varies between image centre and edge due to the panoramic distortion of the cameras and optical effects but it also varies with flying height between missions, haze, and target reflectance and contrast. Together with the film grain and lens modulation transfer function, which determine film resolution, all of these factors affect the ground resolved distance (GRD) of the photograph (NRO, 1970; NRO, 1972; McDonald and Widlake, 2012). This translates into the ground sampling distance (GSD) of the georeferenced digital image via the scanning process and is thus dependent on scanning resolution. The highest scan resolution offered by the USGS for CORONA and HEXAGON imagery is 7 µm or 3,600 dpi (USGS, 2018a; USGS, 2018c), which by Leachtenauer et al. (1998) was deemed coarser than lossless digitizing (4 µm). From our experience, however, we can agree with other authors who found the 7 µm scans quite sufficient (e.g., Galiatsatos, 2004; Fowler, 2005; Gheyle et al., 2011). The tree crowns in both our CORONA and HEXAGON images already have more or less blurred edges, and we would not expect any improvement of crown definition from higher scanning resolutions.

We have not investigated the role of radiometric image quality and image contrast for identifying and measuring individual trees in the historical VHRS images. In dryland conditions, contrast between trees and intertree areas is generally quite high but varies with seasonal dynamics: Leaf-on situation and bare or sparsely vegetated surroundings (as given for most of the image dates and test sites in our study) provide the best contrast for differentiating tree crowns from intertree areas. Leaf-off conditions, degraded and fractured tree canopies and dense grass or crop cover in the intertree areas reduce the visibility of individual trees and require finer radiometric resolution. Generally, the photographic films used in the HEXAGON (mostly EASTMAN KODAK type 1414) are of higher quality than in the CORONA mission (type 3404 and 3414; NPIC, 1967; Galiatsatos, 2004; McDonald and Widlake, 2012). However, image contrast is a function of film gradation, lens modulation transfer function and reflectance of an object compared to its surroundings, and the quality of the scanned product varies with many more factors including film processing. The discussion of these influences on the appearance of individual

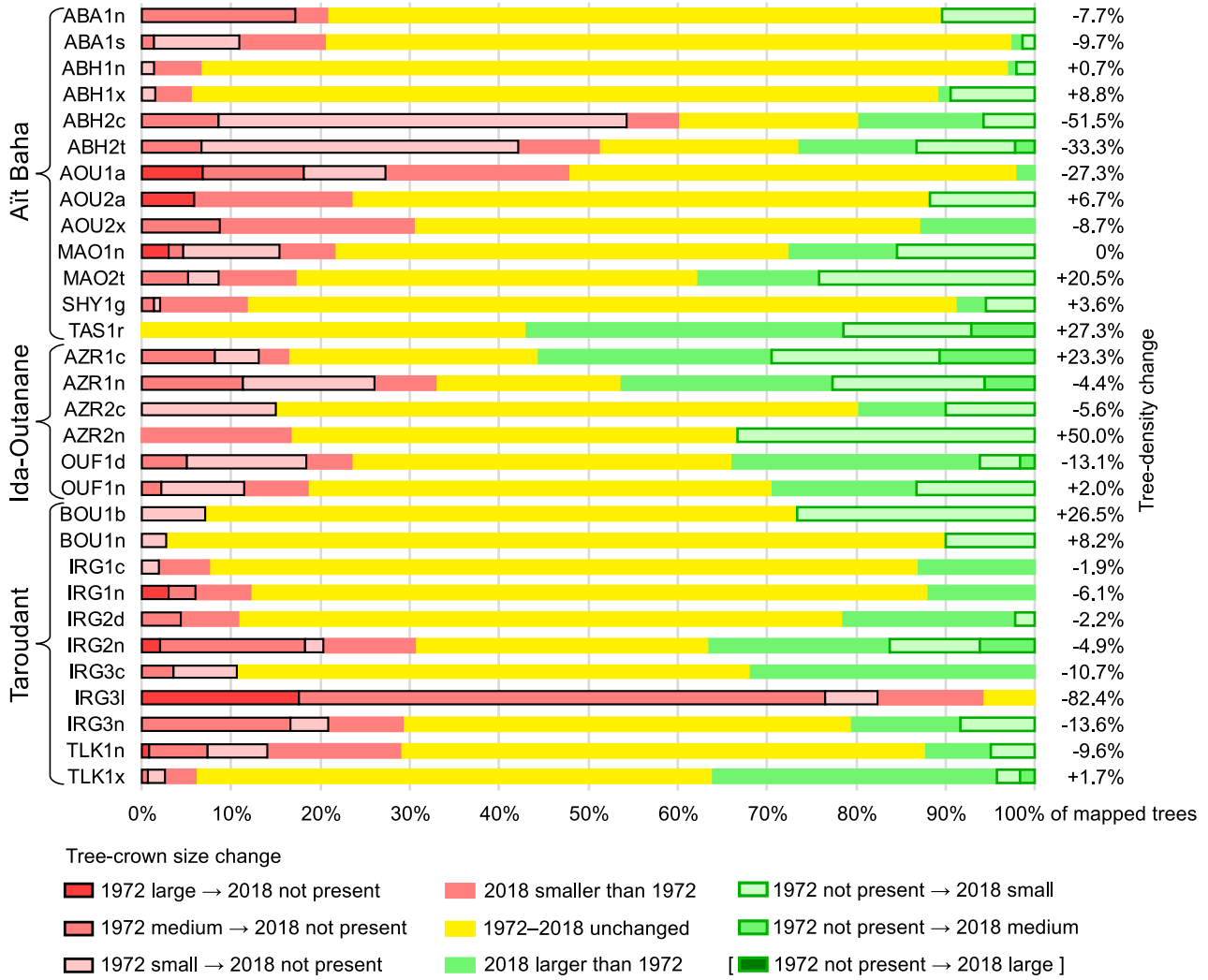

FIGURE 8 | Relative contribution of tree-size changes for argan trees between 1972 and 2018 at all 30 test sites, based on the FB 1972 and FB 2018 datasets. The stacked bars show trees lost since 1972 on the left (red shades with black outlines), trees changed and unchanged in size in the middle (red, yellow and green) and new trees until 2018 on the right (green shades with green outlines). Tree-density change for each test site is given as net change of tree count per hectare.

trees is beyond the scope of our paper, but useful observations regarding tree mapping from CORONA images and panchromatic APs may be found in Andersen (2006) and Fensham and Fairfax (2002).

Our systematic simulations of the historical panchromatic VHRS imagery based on UAS images have revealed the significant role of local illumination and viewing geometry for the shapes of the tree spots, which comprise both crown and cast shadow. Knowledge and understanding of these parameters is highly important for correctly interpreting the shape and size of the tree crown, and thus for measures of tree density and canopy cover. Long shadows are aimed for in military reconnaissance imagery (Hall, 2003), and the amount of shadowing in our images must be considered quite typical: We found that on average for our test sites, shadow contributes between 30 and 41% to the dark spot representing a tree. Disregarding this aspect in mapping and monitoring of woodland trees would not only lead to an overestimation of canopy size, but also to errors in tree counts (and thus density estimates) and misjudgements of tree-size changes between different images and dates.

While the shadowing effect may be beneficial in detecting trees, it forbids the use of simple image thresholding techniques for tree-crown mapping and canopy cover quantification, i.e., automatic classification methods not modelling and correcting shadow contribution to the tree spot. This point is also strongly emphasized by Andersen (2006) and Fensham and Fairfax (2002), but surprisingly disregarded by some authors mapping individual tree canopies from panchromatic aerial photographs (e.g., Lahav-Ginott et al., 2001; Moustakas et al., 2006) or single-band VHRS images (Shafeian et al., 2021). Tree mapping from multispectral VHRS images, such as our WorldView data, is much less affected by the shadowing problem, as tree crown and shadow are usually easy to tell

apart, especially in the near-infrared spectral band. Here, the presence of a contrasting shadow may be exploited by visual (e.g., Bastin et al., 2017) as well as object-oriented and machine-learning mapping approaches (Alsharrah et al., 2016; Brandt et al., 2020) to distinguish between trees and lower-height shrub or grass cover. On the other hand, cast shadow as well as crown self-shadow may be eliminated in multispectral images by using indices such as the NDVI, as ratioing cancels out the darkening factor. The NDVI also helps to distinguish tree crowns from less-vegetated background, and is used by numerous authors for mapping individual trees (Fisher et al., 2017; Isaacson et al., 2017; Lelong et al., 2020). The deep-learning model by Brandt et al. (2020) uses both cast shadow and high NDVI as conditions for tree-crown identification.

Although the above-mentioned methods operating in the spectral domain cannot be used for panchromatic images, the spatial domain may provide a further option in the third dimension: Owing to their height differences, tree crown and cast shadow may be visually separated by stereoscopic viewing, as was demonstrated by Fensham et al. (2002) for both panchromatic and colour AP. Quick tests we made with stereopairs of aft and forward images confirmed that this is also the case for our HEXAGON KH-9 photographs, whose stereo capability was designed for interpreting intelligence targets such as military facilities and industrial buildings (Oder et al., 1992). We tested both Agisoft Metashape (commercial software) and StereoPhoto Maker (freeware; stereo.jpn.org) and found that an assessment of size, height and even structure of the trees is indeed considerably aided by stereoviewing if one is willing to accept the obliquity of the stereomodel and the effort of constantly re-adjusting the stereopair alignment while moving through the model. Stereoviewing is possible in the same way for CORONA images, but lack of crown—shadow contrast and lower spatial resolution largely impede the 3D appearance of trees.

6.2 Mapping Trees With HEXAGON vs Other Very High Resolution Imagery

We have found that by training ourselves with the help of the UAS-simulated examples of tree-spot appearances, we were able to compensate for the shadowing effect with sufficient confidence while performing visual interpretation of different tree-size classes (small, medium and large, as defined in **Figure 7**). We chose thresholds of 3 and 7 m diameter between these classes as this classification scheme allowed the comparison of CORONA and HEXAGON images and represents typical argan-tree sizes in our study area. The 3 m-threshold (i.e., 7 m^2) for small trees also corresponds well to the minimum detectable crown size of 6 m^2 for desert trees given by Andersen (2006) for CORONA KH-4a imagery. Schlesinger and Gramenopoulos (1996) and Usman and Nichol (2018) observed a detection threshold of approx. 4 m diameter for trees on CORONA images of western Sudan and northern Nigeria, respectively. On HEXAGON KH-9 imagery, though, we could safely have defined the smallest tree-size class as < 2 m, and more classes with smaller size ranges could have been distinguished. Our UAS-based simulations confirm that trees as small as 1.5 m diameter may well be identified on these images, especially with low sun elevations (see **Figure 4**). For larger trees and favourable illumination and canopy reflectance conditions, it would also be possible to delineate tree crowns manually from HEXAGON: We found the radiometric quality good enough to differentiate between lighter crown and darker shadow in many cases. This is, however, not the case for the CORONA images, as was already observed by Dendoncker et al. (2020) and Andersen (2006).

As in other studies using historical imagery for tree mapping, the lack of reference data did not allow us to estimate the commission error, i.e. missing trees in our maps for 1967/1972. We therefore chose to evaluate the reliability of tree counts obtained from the historical and recent VHRS imagery by comparing three different mapping approaches: A field-based (FB) and a WorldView-based (WB) dataset of argan-tree maps, where the location of each tree in 2018 was known a priori from the field or WorldView image, respectively, and then checked on and supplemented by the 1967 CORONA and 1972 HEXAGON images; and a HEXAGON-image based (HB) dataset for 1972. CORONA images were found to be much less reliable for identifying trees (particularly small trees) than HEXAGON. However, KH-4a and KH4b imagery do have their value for longer-term woodland monitoring since they reach back 8 more years (see **Table 1**), thus allowing to capture especially deforestation processes in the 1960s to early 1970s. We would therefore still encourage their use in environments with dynamic forest change, especially of larger trees >3 m diameter, and where HEXAGON coverage is not available.

Compared to the FB dataset, we found tree counts for all dates 34–40% lower in the WB dataset owing, above all, to our inability to visually separate all trees with overlapping crowns growing in clumped-canopy groups: We missed 29% of the field-mapped group trees in the WorldView images. This problem is reported in many studies that quantify tree-density (e.g., Axelsson and Hanan, 2017; Dendoncker et al., 2020). Brandt et al. (2020) reported their dryland tree-mapping model to have missed 3.8% of the reference trees due to inclusion in clumped canopies. Considering that these reference trees were mapped manually from WorldView-type imagery—as in our WB approach—we may conclude that their tree-density measures (though not canopy-cover values) also considerably underestimate the true number of individual trees.

Regarding the changes of argan woodland we found at our 30 test sites in the Souss region of Morocco between 1972 and 2018 (**Figure 8**), it should be noted that our retrospective mapping method is a very conservative approach, opting for stability in case of doubt: Any trees that did not clearly have another size in 1972 were given the same size class as 2018, i.e. unchanged size (yellow bar sections in **Figure 8**). Tree-cover change is thus underestimated rather than overestimated. Since small trees >1.5 m diameter could have been missed on the HEXAGON imagery, the number of trees lost until 2018 might have been higher than recorded here. In any case, we could not observe an overall trend to increase or decrease of woody cover in our study areas, but a high degree of unchanged tree sizes and unspecific change patterns. The tree-cover change data resulting from our study described here are further analysed in combination with

plant architecture data in the companion paper (Part B of our study) by Kirchhoff et al. (2022), where we show that in spite of comparatively stable tree size and density, the argan forest shows signs of continuing degradation.

6.3 The HEXAGON Heritage: Future Opportunities and Challenges for Dryland Forest Mapping

One of the key findings of our study is the remarkably similar potential of the HEXAGON image for identifying individual trees compared to the WorldView images: The total number and test-site densities of tree for 1972 in the WB and HB datasets (**Figures 6A,B**) are nearly identical. At least for manual mapping approaches based on human visual interpretation, we would therefore consider HEXAGON images combined with recent VHRS imagery far superior not only to CORONA images, but also to historical aerial photographs (APs). Typical historical APs with image scales 1:30,000–1:50,000 yield image resolutions around or only slightly better than the 1 m GSD of HEXAGON KH-9. But the common 15 cm focal lengths of survey cameras cover only 48–132 km^2 at these scales, compared to typical HEXAGON images such as ours with ~2,500 km^2 (or even larger depending on scan angle; see **Figure 1** and **Table 2**). Moreover, the typical survey-camera field of view Ω is approx. 74°. This means that the variability of viewing angles and radial displacement (and their associated effects on tree crown/shadow appearance as described with **Figure 5**) is very high within each individual AP's extent, but negligible within the same area in a HEXAGON image, which was taken from 25 to 40 times the flying height.

Obviously, the analogue nature of both HEXAGON and CORONA images, with lack of automatically collected digital metadata and georeferencing, encumbers their use in effective large-area mapping. We chose a manual control-point approach for precisely registering the historical to recent VHRS images at our 30 test sites. A better solution for larger areas—unless the landscape has changed dramatically between dates—would be automatic placement of a large amount of control-points, which is offered by most GIS and remote sensing software packages and was found to work well in our argan woodlands, too. Another option for georeferencing large numbers of images could be crowd-sourcing orthorectification, which has been tested by the open-access CORONA Atlas project but was found to be a challenging task for non-experts (Casana, 2020). More sophisticated approaches for orthorectifying CORONA images or historical AP with the help of DEMs are based on feature-matching or photogrammetric reconstruction of image orientation in space (Nita et al., 2018; Pinto et al., 2019; Zhang et al., 2021). These approaches should generally be transferable to the HEXAGON photographs and will need to be explored and developed further.

As we have shown, an at least approximate knowledge of viewing and illumination angles is imperative for tree mapping from historical VHRS images. Other than for recent VHRS sensors, where acquisition times, sensor tilt angles, field of view, sun azimuth and elevation etc. are recorded in the image metadata, very few metadata are available for the scanned HEXAGON and CORONA images. We could partly retrieve the values for the required parameters (shown in **Figure 1**) from declassified technical documents, and reconstruct others from the images themselves. We used simplified trigonometric calculations disregarding earth curvature, which was quite sufficient for our purpose (see in **Supplementary Workflow S2**). Currently, the only available metadata in the USGS EarthExplorer prior to ordering of HEXAGON KH-9 imagery are date, mission number, frame number and orientation (aft/forward) and the simplified (trapezoidal) footprint coordinates. Since illumination and viewing angle are of great importance for assessing the shadowing conditions in an area of interest, the inclusion of acquisition time and scan mode in the HEXAGON metadata would be of great value. The scan mode is recorded on the edge of the film frame (not visible in preview quicklooks) and would need to be read and ingested into the metadatabase by USGS EROS staff for each mission revolution. The time of day is recorded in flight data books or mission profile reports, but these are not (yet) available for HEXAGON missions, and so far no alternative online records exist with this crucial information. A method proposed by Fowler (2011) for modelling acquisition times of CORONA imagery to within 20 s accuracy might also be applicable to HEXAGON missions but was not tested by us, since the reconstruction via shadow direction was sufficient for our purpose.

Automated tree detection and mapping methods for HEXAGON imagery would certainly encourage larger-area studies and wall-to-wall dryland forest mapping beyond the confined extents or plot-sampling strategies that are workable with the manual interpretation and mapping method presented in our study. Considering recent advancements in deep-learning techniques for mapping individual trees in forests, plantations or urban environments, we believe that it would be worth exploring the possibility of training machine-learning classifiers to recognise tree crowns in HEXAGON imagery. By incorporating information on illumination and viewing angles and by sensitising the classifier to fine radiometric differences, estimates of shadow percentages in the tree spot and separation of crown and shadow might become possible. Such approaches could add the historical dimension to the new focus on quantifying woody cover and forest degradation on the individual tree level called for in several recent publications (Brandt et al., 2020; Fagan, 2020; Gao et al., 2020; Hanan and Anchang, 2020) in order to improve long-term monitoring, protection and restoration of trees in arid and semi-arid environments.

In conclusion, we have shown that the newly accessible historical HEXAGON VHRS images have a great potential for mapping individual trees if the factors affecting tree-crown appearance are respected in the evaluation process. The possibility of comparing them with recent VHRS imagery such as WorldView opens exciting opportunities for retrospective monitoring of sparse dryland forests and open-canopy woodlands back into the 1980s and 1970s. Beyond these ecosystems, HEXAGON data could also support other research on plant spatial distribution, from alpine treeline dynamics to periodic woody vegetation patterns such as Sahelian "tiger bush". Once the ingestion into the USGS EarthExplorer archive and ordering system is completed, the HEXAGON KH-9 dataset will double the availability of VHRS

reconnaissance images, hitherto provided by CORONA KH-4a/b and GAMBIT KH-7. We hope that our findings on the superiority of HEXAGON over the already well-recognized CORONA imagery will encourage the scientific community to tap into this invaluable resource of historical Earth observation data for environmental monitoring.

DATA AVAILABILITY STATEMENT

The HEXAGON and CORONA images used in this study are freely available from the USGS EarthExplorer. UAS imagery and derivatives as well as the tree database containing the FB, WB and HB datasets may be obtained from the corresponding author on reasonable request.

AUTHOR CONTRIBUTIONS

IM, MK, MS, and JR designed the study; AAH provided resources and logistical support; IM, MS, AAH, and JR supervised the research activities; IM, MK, and RS acquired the data; IM, MK, MS, and JR performed the analysis and interpretation; IM and JR acquired funding; IM and MK wrote the original draft. All authors performed review and editing of the final version of the manuscript.

FUNDING

Funding of this study by the Deutsche Forschungsgemeinschaft (DFG) as part of the ARGAN research project und project no. MA 2549/6-1 and RI 835/24 is gratefully acknowledged. WorldView and GeoEye satellite data were provided by the European Space Agency (ESA) under the Third Party's Mission scheme, project no. 36256. TanDEM-X elevation data (used in orthorectification) were provided by the German Space Agency (DLR) under project no. DEM_HYDR1131.

ACKNOWLEDGMENTS

We thank the responsible local, regional and national Moroccan authorities for supporting our studies and allowing access to their territories. We are also grateful to Abdellatif Hanna and Khalil Hamouch for their considerable help with our fieldwork.

SUPPLEMENTARY MATERIAL

The Supplementary Material for this article can be found online at: https://www.frontiersin.org/articles/10.3389/fenvs.2022.896702/full#supplementary-material

REFERENCES

Aber, J. S., Marzolff, I., Ries, J. B., and Aber, S. W. (2019). *Small-format Aerial Photography and UAS Imagery: Principles, Techniques and Geoscience Applications*. Amsterdam: Elsevier Academic Press.

Aït Hssaine, A. (2002). "Le cadre physique de la Dépression du Souss et la dégradation de l'environment sédimentaire," in *L'espace rural dans le Souss: Heritage et changements: Actes du Colloque organisé le 15 et 16 Mars 1996*. Editor M. Bouchelkha, 22–27.

Alsharrah, S. A., Bouabid, R., Bruce, D. A., Somenahalli, S., and Corcoran, P. A. (2016). Use of Shadow for Enhancing Mapping of Perennial Desert Plants from High-Spatial Resolution Multispectral and gh Panchromatic Satellite Imagery. *J. Appl. Remote Sens.* 10, 036008. doi:10.1117/1.JRS.10.036008

Andersen, G. L., and Krzywinski, K. (2007). Mortality, Recruitment and Change of Desert Tree Populations in a Hyper-Arid Environment. *Plos One* 2, e208. doi:10.1371/journal.pone.0000208

Andersen, G. L. (2006). How to Detect Desert Trees Using CORONA Images: Discovering Historical Ecological Data. *J. Arid Environ.* 65, 491–511. doi:10.1016/j.jaridenv.2005.07.010

Axelsson, C. R., and Hanan, N. P. (2017). Patterns in Woody Vegetation Structure across African Savannas. *Biogeosciences* 14, 3239–3252. doi:10.5194/bg-14-3239-2017

Bastin, J.-F., Berrahmouni, N., Grainger, A., Maniatis, D., Mollicone, D., Moore, R., et al. (2017). The Extent of Forest in Dryland Biomes. *Science* 356, 635–638. doi:10.1126/science.aam6527

Brandt, M., Rasmussen, K., Hiernaux, P., Herrmann, S., Tucker, C. J., Tong, X., et al. (2018). Reduction of Tree Cover in West African Woodlands and Promotion in Semi-arid Farmlands. *Nat. Geosci.* 11, 328–333. doi:10.1038/s41561-018-0092-x

Brandt, M., Tucker, C. J., Kariryaa, A., Rasmussen, K., Abel, C., Small, J., et al. (2020). An Unexpectedly Large Count of Trees in the West African Sahara and Sahel. *Nature* 587, 78–82. doi:10.1038/s41586-020-2824-5

Casana, J. (2020). Global-Scale Archaeological Prospection Using CORONA Satellite Imagery: Automated, Crowd-Sourced, and Expert-Led Approaches. *J. Field Archaeol.* 45, S89. doi:10.1080/00934690.2020.1713285

Chidumayo, E. N., and Gumbo, D. J. (2010). *The Dry Forests and Woodlands of Africa: Managing for Products and Services*. London: Earthscan.

Cunliffe, A. M., Anderson, K., Boschetti, F., Brazier, R. E., Graham, H. A., Myers-Smith, I. H., et al. (2021). Global Application of an Unoccupied Aerial Vehicle Photogrammetry Protocol for Predicting Aboveground Biomass in Non-forest Ecosystems. *Remote Sens. Ecol. Conserv.* 8, 57–71. doi:10.1002/rse2.228

Dashora, A., Lohani, B., and Malik, J. N. (2007). A Repository of Earth Resource Information - CORONA Satellite Programme. *Curr. Sci.* 92, 926–932.

Dehecq, A., Gardner, A. S., Alexandrov, O., McMichael, S., Hugonnet, R., Shean, D., et al. (2020). Automated Processing of Declassified KH-9 Hexagon Satellite Images for Global Elevation Change Analysis since the 1970s. *Front. Earth Sci.* 8, 566802. doi:10.3389/feart.2020.566802

Dendoncker, M., Brandt, M., Rasmussen, K., Taugourdeau, S., Fensholt, R., Tucker, C. J., et al. (2020). 50 Years of Woody Vegetation Changes in the Ferlo (Senegal) Assessed by High-Resolution Imagery and Field Surveys. *Reg. Environ. Change* 20, 1–13. doi:10.1007/s10113-020-01724-4

Fagan, M. E. (2020). A Lesson Unlearned? Underestimating Tree Cover in Drylands Biases Global Restoration Maps. *Glob. Change Biol.* 26, 4679–4690. doi:10.1111/gcb.15187

FAO (Food and Agriculture Organization of the United Nations) (2019). *Trees, Forests and Land Use in Drylands: The First Global Assessment, Full Report*. Rome: Food and Agriculture Organization of the United Nations.

Fensham, R. J., and Fairfax, R. J. (2002). Aerial Photography for Assessing Vegetation Change: a Review of Applications and the Relevance of Findings for Australian Vegetation History. *Aust. J. Bot.* 50, 415. doi:10.1071/BT01032

Fensham, R. J., Fairfax, R. J., Holman, J. E., and Whitehead, P. J. (2002). Quantitative Assessment of Vegetation Structural Attributes from Aerial Photography. *Int. J. Remote Sens.* 23, 2293–2317. doi:10.1080/01431160110106050

Fisher, A., Danaher, T., and Gill, T. (2017). Mapping Trees in High Resolution Imagery across Large Areas Using Locally Variable Thresholds Guided by Medium Resolution Tree Maps. *Int. J. Appl. Earth Obs. Geo.* 58, 86–96. doi:10.1016/j.jag.2017.02.004

Fowler, M. J. F. (2005). An Evaluation of Scanned CORONA Intelligence Satellite Photography. *AARGnews* 31, 34–37.

Fowler, M. J. F. (2011). Modelling the Acquisition Times of CORONA Satellite Photographs: Accuracy and Application. *Int. J. Remote Sens.* 32, 8865–8879. doi:10.1080/01431161.2010.542207

Fradley, M. (2021). British Inter-war Aerial Photogrammetric Mapping in the MENA Region: Archives, Access and Research Potential. *Levant* 64, 1–11. doi:10.1080/00758914.2021.1992879

Frost, G. V., and Epstein, H. E. (2014). Tall Shrub and Tree Expansion in Siberian Tundra Ecotones since the 1960s. *Glob. Change Biol.* 20, 1264–1277. doi:10.1111/gcb.12406

Gaisberger, H., Kindt, R., Loo, J., Schmidt, M., Bognounou, F., Da, S. S., et al. (2017). Spatially Explicit Multi-Threat Assessment of Food Tree Species in Burkina Faso: A Fine-Scale Approach. *Plos One* 12, e0184457. doi:10.1371/journal.pone.0184457

Galiatsatos, N. (2004). *Assessment of the CORONA Series of Satellite Imagery for Landscape Archaeology: A Case Study from the Orontes Valley, Syria. PhD Dissertation*. Durham: Durham University.

Gao, Y., Skutsch, M., Paneque-Gálvez, J., and Ghilardi, A. (2020). Remote Sensing of Forest Degradation: a Review. *Environ. Res. Lett.* 15, 103001. doi:10.1088/1748-9326/abaad7

Gheyle, W., Bourgeois, J., Goossens, R., and Jacobsen, K. (2011). Scan Problems in Digital CORONA Satellite Images from USGS Archives. *Photogramm. Eng. remote Sens.* 77, 1257–1264. doi:10.14358/PERS.77.12.1257

Gonzalez, P., Tucker, C. J., and Sy, H. (2012). Tree Density and Species Decline in the African Sahel Attributable to Climate. *J. Arid Environ.* 78, 55–64. doi:10.1016/j.jaridenv.2011.11.001

Hall, R. C. (2003). *The 14 April 1956 Overflight of Nor1l'sk*. U.S.S.R.

Hanan, N. P., and Anchang, J. Y. (2020). Satellites Could Soon Map Every Tree on Earth. *Nature* 587, 42–43. doi:10.1038/d41586-020-02830-3

Hanan, N. P., Milne, E., Aynekulu, E., Yu, Q., and Anchang, J. (2021). A Role for Drylands in a Carbon Neutral World? *Front. Environ. Sci.* 9, 1–10. doi:10.3389/fenvs.2021.786087

Hansen, M. C., Potapov, P. V., Moore, R., Hancher, M., Turubanova, S. A., Tyukavina, A., et al. (2013). High-resolution Global Maps of 21st-Century Forest Cover Change. *Science* 342, 850–853. doi:10.1126/science.1244693

Isaacson, S., Ephrath, J. E., Rachmilevitch, S., Maman, S., Ginat, H., and Blumberg, D. G. (2017). Long and Short Term Population Dynamics of acacia Trees via Remote Sensing and Spatial Analysis: Case Study in the Southern Negev Desert. *Remote Sens. Environ.* 198, 95–104. doi:10.1016/j.rse.2017.05.035

Karlson, M., Ostwald, M., Reese, H., Bazié, H. R., and Tankoano, B. (2016). Assessing the Potential of Multi-Seasonal WorldView-2 Imagery for Mapping West African Agroforestry Tree Species. *Int. J. Appl. Earth Obs. Geo.* 50, 80–88. doi:10.1016/j.jag.2016.03.004

Kirchhoff, M., Engelmann, L., Zimmermann, L. L., Seeger, M., Marzolff, I., Aït Hssaine, A., et al. (2019). Geomorphodynamics in Argan Woodlands, South Morocco. *Water* 11, 2193. doi:10.3390/w11102193

Kirchhoff, M., Romes, T., Marzolff, I., Seeger, M., Aït Hssaine, A., and Ries, J. B. (2021). Spatial Distribution of Argan Tree Influence on Soil Properties in Southern Morocco. *SOIL* 7, 511–524. doi:10.5194/soil-7-511-2021

Kirchhoff, M., Marzolff, I., Stephan, R., Seeger, M., Aït Hssaine, A., and Ries, J. B. (2022). Monitoring Dryland Trees with Remote Sensing. Part B: Combining Tree Cover and Plant Architecture Data to Assess Degradation and Recovery of Argan Woodlands of South Morocco. Submitt. *Front. Environ. Sci.*

Lahav-Ginott, S., Kadmon, R., and Gersani, M. (2001). Evaluating the Viability of Acacia Populations in the Negev Desert: a Remote Sensing Approach. *Biol. Conserv.* 98, 127–137. doi:10.1016/S0006-3207(00)00147-6

le Polain de Waroux, Y., and Lambin, E. F. (2012). Monitoring Degradation in Arid and Semi-arid Forests and Woodlands: The Case of the Argan Woodlands (Morocco). *Appl. Geogr.* 32, 777–786. doi:10.1016/j.apgeog.2011.08.005

Leachtenauer, J., Daniel, K., and Vogl, T. (1998). Digitizing Satellite Imagery: Quality and Cost Considerations. *Photogrammetric Eng. Remote Sens.* 64, 29–34.

Lelong, C. C. D., Tshingomba, U. K., and Soti, V. (2020). Assessing Worldview-3 Multispectral Imaging Abilities to Map the Tree Diversity in Semi-arid Parklands. *Int. J. Appl. Earth Obs. Geo.* 93, 102211. doi:10.1016/j.jag.2020.102211

Lybbert, T. J., Aboudrare, A., Chaloud, D., Magnan, N., and Nash, M. (2011). Booming Markets for Moroccan Argan Oil Appear to Benefit Some Rural Households while Threatening the Endemic Argan Forest. *Proc. Natl. Acad. Sci. U.S.A.* 108, 13963–13968. doi:10.1073/pnas.1106382108

Marzolff, I., Stephan, R., Kirchhoff, M., Seeger, M., Aït Hssaine, A., and Ries, J. B. (2020). UAV-based Classification of Tree-Browsing Intensity in Open Woodlands. *EGU General Assem.* Online, 4–8 May 2020, 1–13. Available at: https://meetingorganizer.copernicus.org/EGU2020/EGU2020-10301.html.

McDonald, R. A., and Widlake, P. (2012). Looking Closer and Looking Broader: Gambit and Hexagon – the Peak of Film-Return Space Reconnaissance after Corona. *Natl. Reconnaissance J. Discip. Pract.*, 39–74.

Michel, N. (2018). Patrimoine: d'anciennes photographies aériennes de l'Afrique menacées de destruction. *Jeune Afr.* 4, 12. Available at: https://www.jeuneafrique.com/677525/culture/patrimoine-danciennes-photographies-aeriennes-de-lafrique-menacees-de-destruction/ (Accessed February 06, 2022).

Mirzabaev, A., Wu, J., Evans, J., García-Oliva, F., Hussein, I., Iqbal, M. H., et al. (2019). "Chapter 3: Desertification," in *Climate Change and Land: An IPCC Special Report on Climate Change, Desertification, Land Degradation, Sustainable Land Management, Food Security, and Greenhouse Gas Fluxes in Terrestrial Ecosystems*. Editors P. R. Shukla, J. Skea, E. Calvo Buendia, V. Masson-Delmotte, H. O. Pörtner, and D. C. Roberts.

Morton, J. F., and Voss, G. L. (1987). The Argan Tree (Argania Sideroxylon, Sapotaceae), a Desert Source of Edible Oil. *Econ. Bot.* 41, 221–233. doi:10.1007/BF02858970

Moustakas, A., Guenther, M., Wiegand, K., Mueller, K. H., Ward, D., Meyer, K. M., et al. (2006). Long-Term mortality Patterns of the Deep-Rooted Acacia Erioloba: The Middle Class Shall die! *J. Veg. Sci.* 17, 473–480. doi:10.1111/j.1654-1103.2006.tb02468.x

Msanda, F., Mayad, E. H., and Furze, J. N. (2021). Floristic Biodiversity, Biogeographical Significance, and Importance of Morocco's Arganeraie Biosphere Reserve. *Environ. Sci. Pollut. Res.* 28, 64156–64165. doi:10.1007/s11356-020-11936-0

NASA (2022). NASA Space Science Data Coordinated Archive. Available at: https://nssdc.gsfc.nasa.gov/nmc (Accessed February 06, 2022).

Nita, M. D., Munteanu, C., Gutman, G., Abrudan, I. V., and Radeloff, V. C. (2018). Widespread Forest Cutting in the Aftermath of World War II Captured by Broad-Scale Historical Corona Spy Satellite Photography. *Remote Sens. Environ.* 204, 322–332. doi:10.1016/j.rse.2017.10.021

NPIC (National Photographic Interpretation Center) (1967). The KH-4a Camera System. Available at: https://www.nro.gov/Portals/65/documents/foia/CAL-Records/Cabinet2/DrawerC/2%20C%200061.pdf.

NRO (National Reconnaissance Office) (1967). Corona J Flight Data Book 1039-1. Available at: https://www.nro.gov/Portals/65/documents/foia/CAL-Records/Cabinet5/DrawerA/5%20A%200027.pdf.

NRO (National Reconnaissance Office) (1970). CRYSPER-C Performance Prediction Program. Memorandum for the Record. Available at: https://www.nro.gov/Portals/65/documents/foia/CAL-Records/Cabinet3/DrawerC/3%20C%200008.pdf.

NRO (National Reconnaissance Office) (1972). Hexagon Camera User Guide. Available at: https://www.nro.gov/Portals/65/documents/foia/declass/ForAll/101917/F-2017-00094.pdf.

Nyssen, J., Debever, M., Gebremeskel, G., De Wit, B., Hadgu, K. M., De Vriese, S., et al. (2021). Online Digital Archive of Aerial Photographs (1935–1941) of Ethiopia. *Geosci. Data J.*, 1–34. doi:10.1002/gdj3.115

Oder, F., Fitzpatrick, J. C., and Worthman, P. E. (1988). *The Corona Story*. National Reconnaissance Office.

Oder, F., Fitzpatrick, J. C., and Worthman, P. E. (1992). *The Hexagon Story*. National Reconnaissance Office.

Perry, R. (1973a). *A History of Satellite Reconnaissance*. CORONA. National Reconnaissance Office.

Perry, R. (1973b). *A History of Satellite Reconnaissance*. HEXAGON. National Reconnaissance Office.

Pinto, A. T., Gonçalves, J. A., Beja, P., and Pradinho Honrado, J. (2019). From Archived Historical Aerial Imagery to Informative Orthophotos: A Framework for Retrieving the Past in Long-Term Socioecological Research. *Remote Sens.* 11, 1388. doi:10.3390/rs11111388

SAFSP (Directorate of Special Projects, Office of the Secretary of the Air Force)(1972). *Performance Evaluation Team Mission 1203*. Available at: https://www.nro.gov/Portals/65/documents/foia/declass/ForAll/041921/F-2020-00083_C05129988.pdf.

Schlesinger, W. H., and Gramenopoulos, N. (1996). Archival Photographs Show No Climate-Induced Changes in Woody Vegetation in the Sudan, 1943-1994*. *Glob. Change Biol.* 2, 137–141. doi:10.1111/j.1365-2486.1996.tb00058.x

Scollar, I., Galiatsatos, N., and Mugnier, C. (2016). Mapping from CORONA: Geometric Distortion in KH4 Images. *Photogram Engng Rem. Sens.* 82, 7–13. doi:10.14358/PERS.83.1.7

Sexton, J. O., Song, X.-P., Feng, M., Noojipady, P., Anand, A., Huang, C., et al. (2013). Global, 30-m Resolution Continuous Fields of Tree Cover: Landsat-Based Rescaling of MODIS Vegetation Continuous Fields with Lidar-Based Estimates of Error. *Int. J. Digital Earth* 6, 427–448. doi:10.1080/17538947.2013.786146

Shafeian, E., Fassnacht, F. E., and Latifi, H. (2021). Mapping Fractional Woody Cover in an Extensive Semi-arid Woodland Area at Different Spatial Grains with Sentinel-2 and Very High-Resolution Data. *Int. J. Appl. Earth Obs. Geo.* 105, 102621. doi:10.1016/j.jag.2021.102621

Shimada, M., Itoh, T., Motooka, T., Watanabe, M., Shiraishi, T., Thapa, R., et al. (2014). New Global Forest/non-Forest Maps from ALOS PALSAR Data (2007–2010). *Remote Sens. Environ.* 155, 13–31. doi:10.1016/j.rse.2014.04.014

Silver, M., Tiwari, A., and Karnieli, A. (2019). Identifying Vegetation in Arid Regions Using Object-Based Image Analysis with RGB-Only Aerial Imagery. *Remote Sens.* 11, 2308. doi:10.3390/rs11192308

Sohn, H.-G., Kim, G.-H., and Yom, J.-H. (2004). Mathematical Modelling of Historical Reconnaissance CORONA KH-4B Imagery. *Photogramm. Rec.* 19, 51–66. doi:10.1046/j.0031-868X.2003.00257.x

Tappan, G. G., Sall, M., Wood, E. C., and Cushing, M. (2004). Ecoregions and Land Cover Trends in Senegal. *J. Arid Environ.* 59, 427–462. doi:10.1016/j.jaridenv.2004.03.018

USGS (2018a). USGS EROS Archive - Declassified Data - Declassified Satellite Imagery – 1. Available at: https://www.usgs.gov/centers/eros/science/usgs-eros-archive-declassified-data-declassified-satellite-imagery-1 (Accessed February 06, 2022).

USGS (2018b). USGS EROS Archive - Declassified Data - Declassified Satellite Imagery – 2. Available at: https://www.usgs.gov/centers/eros/science/usgs-eros-archive-declassified-data-declassified-satellite-imagery-2 (Accessed February 06, 2022).

USGS (2018c). USGS EROS Archive - Declassified Data - Declassified Satellite Imagery – 3. Available at: https://www.usgs.gov/centers/eros/science/usgs-eros-archive-declassified-data-declassified-satellite-imagery-3 (Accessed February 06, 2022).

Usman, M., and Nichol, J. E. (2018). Remarkable Increase in Tree Density and Fuelwood Production in the Croplands of Northern Nigeria. *Land Use Policy* 78, 410–419. doi:10.1016/j.landusepol.2018.04.046

Wheelon, A. D. (1997). Corona: The First Reconnaissance Satellites. *Phys. Today* 50, 24–30. doi:10.1063/1.881677

Zahidi, A., Bani-Aameur, F., and El Mousadik, A. (2013). Seasonal Change Effects on Phenology of *Argania Spinosa* (L.) in the Fields. *J. Ecol. Nat. Environ.* 5, 189–205. doi:10.5897/JENE2013.0373

Zhang, L., Rupnik, E., and Pierrot-Deseilligny, M. (2021). Feature Matching for Multi-Epoch Historical Aerial Images. *ISPRS J. Photogramm. Remote Sens.* 182, 176–189. doi:10.1016/j.isprsjprs.2021.10.008

Conflict of Interest: The authors declare that the research was conducted in the absence of any commercial or financial relationships that could be construed as a potential conflict of interest.

Publisher's Note: All claims expressed in this article are solely those of the authors and do not necessarily represent those of their affiliated organizations, or those of the publisher, the editors and the reviewers. Any product that may be evaluated in this article, or claim that may be made by its manufacturer, is not guaranteed or endorsed by the publisher.

frontiers | Frontiers in Environmental Science

TYPE Original Research
PUBLISHED 07 October 2022
DOI 10.3389/fenvs.2022.896703

OPEN ACCESS

EDITED BY
Niall Patrick Hanan,
New Mexico State University,
United States

REVIEWED BY
Salma Sai Kachout,
Institut National de la Recherche Agronomique de Tunisie (INRAT),
Tunisia
Abdoul Aziz Diouf,
Centre de Suivi Ecologique, Senegal
Niall Patrick Hanan,
New Mexico State University,
United States

*CORRESPONDENCE
Mario Kirchhoff,
kirchhoff@uni-trier.de

SPECIALTY SECTION
This article was submitted to Drylands, a section of the journal Frontiers in Environmental Science

RECEIVED 15 March 2022
ACCEPTED 21 September 2022
PUBLISHED 07 October 2022

CITATION
Kirchhoff M, Marzolff I, Stephan R, Seeger M, Aït Hssaine A and Ries JB (2022), Monitoring dryland trees with remote sensing. Part B: Combining tree cover and plant architecture data to assess degradation and recovery of Argania spinosa woodlands of South Morocco.
Front. Environ. Sci. 10:896703.
doi: 10.3389/fenvs.2022.896703

Monitoring dryland trees with remote sensing. Part B: Combining tree cover and plant architecture data to assess degradation and recovery of *Argania spinosa* woodlands of South Morocco

Mario Kirchhoff[1]*, Irene Marzolff[2], Robin Stephan[2], Manuel Seeger[1], Ali Aït Hssaine[3] and Johannes B. Ries[1]

[1]Department of Physical Geography, Trier University, Trier, Germany, [2]Department of Physical Geography, Goethe University Frankfurt am Main, Frankfurt am Main, Germany, [3]Department of Geography, Ibn Zohr University, Agadir, Morocco

The argan woodlands of South Morocco represent an open-canopy dryland forest with traditional silvopastoral usage that includes browsing by goats, sheep and camels, oil production as well as agricultural use. In the past, these forests have undergone extensive clearing, but are now protected by the state. However, the remaining argan woodlands are still under pressure from intensive grazing and illegal firewood collection. Although the argan-forest area seems to be overall decreasing due to large forest clearings for intensive agriculture, little quantitative data is available on the dynamics and overall state of the remaining argan forest. To determine how the argan woodlands in the High Atlas and the Anti-Atlas had changed in tree-crown cover from 1972 to 2018 we used historical black and white HEXAGON satellite images as well as recent WorldView satellite images (see Part A of our study). Because tree shadows can oftentimes not be separated from the tree crown on panchromatic satellite images, individual trees were mapped in three size categories to determine if trees were unchanged, had decreased/increased in crown size or had disappeared or newly grown. The current state of the argan trees was evaluated by mapping tree architectures in the field. Tree-cover changes varied highly between the test sites. Trees that remained unchanged between 1972 and 2018 were in the majority, while tree mortality and tree establishment were nearly even. Small unchanged trees made up 48.4% of all remaining trees, of these 51% showed degraded tree architectures. 40% of small (re-) grown trees were so overbrowsed that they only appeared as bushes, while medium (3–7 m crown diameter) and large trees (>7 m) showed less degraded trees regardless if they had changed or not. Approaches like grazing exclusion or cereal cultivation lead to a positive influence on tree architecture and less tree-cover decrease. Although the woodland was found to be mostly unchanged 1972–2018, the analysis of tree architecture reveals that a lot of

(mostly small) trees remained stable but in a degraded state. This stability might be the result of the small trees' high degradation status and shows the heavy pressure on the argan forest.

KEYWORDS

open-canopy woodland, tree density, woody cover, plant architecture, forest degradation, argan tree, change mapping, HEXAGON

1 Introduction

Forest degradation by way of excessive wood exploitation, logging or overgrazing is a serious issue around the world (Lund, 2009; FAO, 2011) and especially in North Africa (Barbero et al., 1990; Wojterski, 1990). These forests have been used by locals for subsistence since the Neolithic, but with an increase in population and intensifying usage the already vulnerable ecosystems cannot regenerate fast enough (Barbero et al., 1990; Médail and Quézel, 1997), leading to forest-density decline (Le Polain de Waroux and Lambin, 2012). A reduced number of trees leaves a part of the soil without cover to shield it from erosion and soil degradation, thus creating less favourable conditions for saplings to develop (Alados and El Aich, 2008; Schnabel et al., 2009; Le Polain de Waroux and Lambin, 2012).

In rural, poorer areas, these dryland forests can provide a source of income for the local population who harvest the wood and turn it into charcoal (Rueda et al., 2015). The impact of charcoal production is still under discussion in the literature and ranges from sustainable forest protection and recovery (Hosier, 1993; Rueda et al., 2015) to forest degradation by selective cutting of suitable trees (Kouami et al., 2009; Ndegwa et al., 2016; Sedano et al., 2016; Kiruki et al., 2017). Charcoal production as a source of income might lead to a financial incentive for preservation of dryland forests (Rueda et al., 2015) but could also lead to excessive logging (Hosier, 1993; Faouzi, 2013). Sustainable solutions of coppicing with subsequent regrowth can be pursued, but an interplay of multiple pressure factors may lead to a degraded system all the same, e.g., failed regrowth due to heavy grazing pressure on young saplings (Hosier, 1993; Le Polain de Waroux and Lambin, 2012).

One such case is the *Argania spinosa* forest, which covered ~950,000 ha in South Morocco in 2015 (Lefhaili and Amhajar, 2020). The argan population is seen as strongly degraded (Culmsee, 2004; Le Polain de Waroux and Lambin, 2012), especially due to overgrazing and browsing by goats, sheep and dromedaries but also due to the now illegal wood cutting and the encroachment of agricultural areas into formerly wooded regions (Lybbert et al., 2010; Le Polain de Waroux and Lambin, 2012; Kirchhoff et al., 2019a). The argan tree is the source of the valuable argan oil, which is used for cosmetic and alimentary purposes (Gharby and Charrouf, 2022). It has been produced by the locals for centuries (Charrouf and Guillaume, 2009), today it is produced by women's cooperatives and marketed all around the world (Lybbert et al., 2010; Defaa et al., 2015). Due to the newly found income, the argan tree is seen as a source of revenue for a part of the population, which in turn helps to preserve the argan forest. In 1998, the *Arganeraie* was designated a UNESCO Biosphere Reserve (Charrouf and Guillaume, 2018).

However, the argan tree is also known among the local population for its high fuel value, especially when turned into charcoal (Faouzi, 2013). This resulted in the deforestation of 800,000 ha of argan forest in the 12th to 17th century for the use of firewood in the sugarcane industry (Berthier, 1966; Aït Hssaine, 2002). An increase of *Argania spinosa* forest, probably as pre-steppe scrub forest, in the 19th century could be measured using pollen archives (McGregor et al., 2009). Yet in the beginning of the 20th century, the argan forest was seen as degraded, which is why several protection measures were passed, declaring the argan forest property of the state (1925) and granting several usage rights to the local population (Monnier, 1965; Davis, 2005; Faouzi, 2013). Since the late 1990 s reforestation measures were implemented with grazing exclusion (Defaa et al., 2015) and paid contractors guarding the sites.

Monnier (1965) states that in 1965 700,000 ha of argan on state-owned land remained, with an additional 10,000–20,000 ha on private property. In recent years the argan forest covered between 870,000 (2013) and ~950,000 ha (2015) (Faouzi, 2013; Lefhaili and Amhajar, 2020), depending on the source; the spatial extent is currently being analysed in a remote-sensing study (Sebbar et al., 2021). In their case study in Awluz in the Province of Taroudant, Le Polain de Waroux and Lambin (2012) compared aerial photographs from 1970 with satellite images from 2007 and revealed a 44.5% decline of forest density during this period. This rapid decline was explained by a multitude of factors, but namely fuelwood extraction and increasing aridity. Browsing and grazing herds of goats, sheep and dromedaries might be partially to blame for the loss of regrowth by feeding on saplings but are mostly responsible for tree degradation due to overbrowsing (Culmsee, 2005; Le Polain de Waroux and Lambin, 2012).

The diverse reports on argan-forest extent as well as argan-density decline show that the current state of the *Arganeraie* cannot be judged by the covered area alone (Le Polain de Waroux and Lambin, 2012). The knowledge of forest-density change is especially important for sustainable management, since bare land is more susceptible to soil degradation and erosion, leaving less fertile land for natural regrowth or reforestation measures. In this context, the change of the composition of the argan forest

(trees/shrubs, canopy cover change, size of the trees) can be an additional factor to determine forest degradation or recovery (Culmsee, 2005; Dendoncker et al., 2020).

Specifically, this study aims to determine the development and state of the remaining argan woodlands on 30 test sites over three study areas in the Souss Basin. To this end, we aim at

1) examining the development of tree cover from 1972 to 2018 by way of tree density and crown size changes;
2) describing the current state of the argan woodlands by investigating tree architecture or browsing and cutting-related growth forms;
3) identifying specific land uses that influence tree-cover changes positively.

Ultimately, the objective of this research is to determine degradation or recovery on the chosen test sites. This is especially necessary because Morocco does not monitor the possible degradation of their forests (Lefhaili and Amhajar, 2020). Modern very high resolution satellite (VHRS) sensors such as WorldView have already proved their potential for individual tree mapping and tree-density and canopy-cover estimation (Hanan and Anchang, 2020). For the historical perspective on the last 50 years, 0.6–1.2 m resolution panchromatic satellite photographs taken 1971–1986 during the American reconnaissance programme HEXAGON have recently become accessible. Field records as well as ultra-high-resolution images taken with an unoccupied aerial system (UAS) are used to validate and give further information, as has been shown before for the Sahel zone (Dendoncker et al., 2020).

This paper is Part B of our research on monitoring dryland trees in South Morocco and uses the argan-tree database resulting from Part A of our study (Marzolff et al., 2022, this issue), where we investigated the potential of historical HEXAGON satellite imagery as a new data source for mapping open-canopy woodlands on the tree level.

2 Materials and methods

2.1 Study areas

The three study areas Ida-Outanane, Taroudant and Aït Baha are situated in the Souss Basin, an alluvial depression between the High Atlas and Anti-Atlas Mountains in Morocco (Figure 1). 30 test sites of 1 ha each were chosen to encompass varying altitudes, climate conditions, soil types and tree densities (see Supplementary Table S1; see also Kirchhoff et al., 2019a). The sites differ in various use-related, tree-cover and relief characteristics. Each test site may have several of these attributes, but we mostly chose neighbouring sites contrasting in one of them; the most salient attribute is recorded as suffix in the test site codes. Sites with code -n have no specific characteristics besides typical silvopastoral usage.

The study area of Ida-Outanane is located near Agadir and the Atlantic Ocean on the southern foothills of the High Atlas. Its climate is maritime with an annual precipitation of 230–260 mm (data for the suburbs of Agadir, 20 km away, Díaz-Barradas et al., 2010) and a mean annual temperature of 18.4°C (data for Agadir, Saidi, 1995). The Paleozoic, Mesozoic and Cenozoic rocks of the High Atlas (Hssaisoune et al., 2016) are covered by mostly immature soils like Regosols, Leptosols and Fluvisols (Jones et al., 2013). The test sites are either used silvopastorally or for rainfed cultivation of wheat.

Like Ida-Outanane, the study area of Taroudant is situated on the southern foothills of the High Atlas. About 80 km from the coast, its climate is more continental (220 mm annual precipitation, 20°C mean annual temperature; Peter et al., 2014; Saidi, 1995). Four test sites are located in the foothills of the High Atlas, while seven lie on an alluvial fan that originates from the High Atlas and covers the Pliocene and Quaternary fluvial, fluvio-lacustrine and aeolian deposits of the Souss Basin (Aït Hssaine and Bridgland, 2009; Chakir et al., 2014). Besides *Argania spinosa*, shrubs and bushes such as *Launaea arborescens*, *Ziziphus lotus*, *Acacia gummifera*, *Euphorbia* spec. and *Artemisia* spec. make up the vegetation in this study area (Peter et al., 2014; Ain-Lhout et al., 2016; Zunzunegui et al., 2017). The Souss region, and especially the study area of Taroudant, has been dominated by a dynamic land use change, where traditional speculative rainfed agriculture is replaced by more profitable citrus plantations and greenhouses for banana and vegetable cultivation (d'Oleire-Oltmanns et al., 2012; Kirchhoff et al., 2019b; Peter et al., 2014).

The study area of Aït Baha is situated in the northern foothills of the Anti-Atlas Mountains. Closer to the Atlantic Ocean than Taroudant, its precipitation ranges from 250 to 350 mm annually with an average annual temperature of 18.7°C (Seif-Ennasr et al., 2016). Fluvisols, Regosols and Leptosols cover the Precambrian and Palaeozoic rocks of the Anti-Atlas (Jones et al., 2013). At three test sites cereals are cultivated on ploughing terraces, at three test sites argan trees are planted for reforestation purposes.

The 30 test sites listed in Supplementary Table S1 have been subject to extensive research in previous studies by the authors that focussed on the trees' potential influence on the soil, including infiltration and soil erosion by wind and water (Kirchhoff et al., 2019a; Marzen et al., 2020; Kirchhoff et al., 2021). However, the state and long-term development of the argan woodlands themselves were not subject of these studies.

2.2 Study design

Part A of our study on tree-cover mapping by way of panchromatic (black and white) satellite images showed that results can be prone to errors, because depending on the image

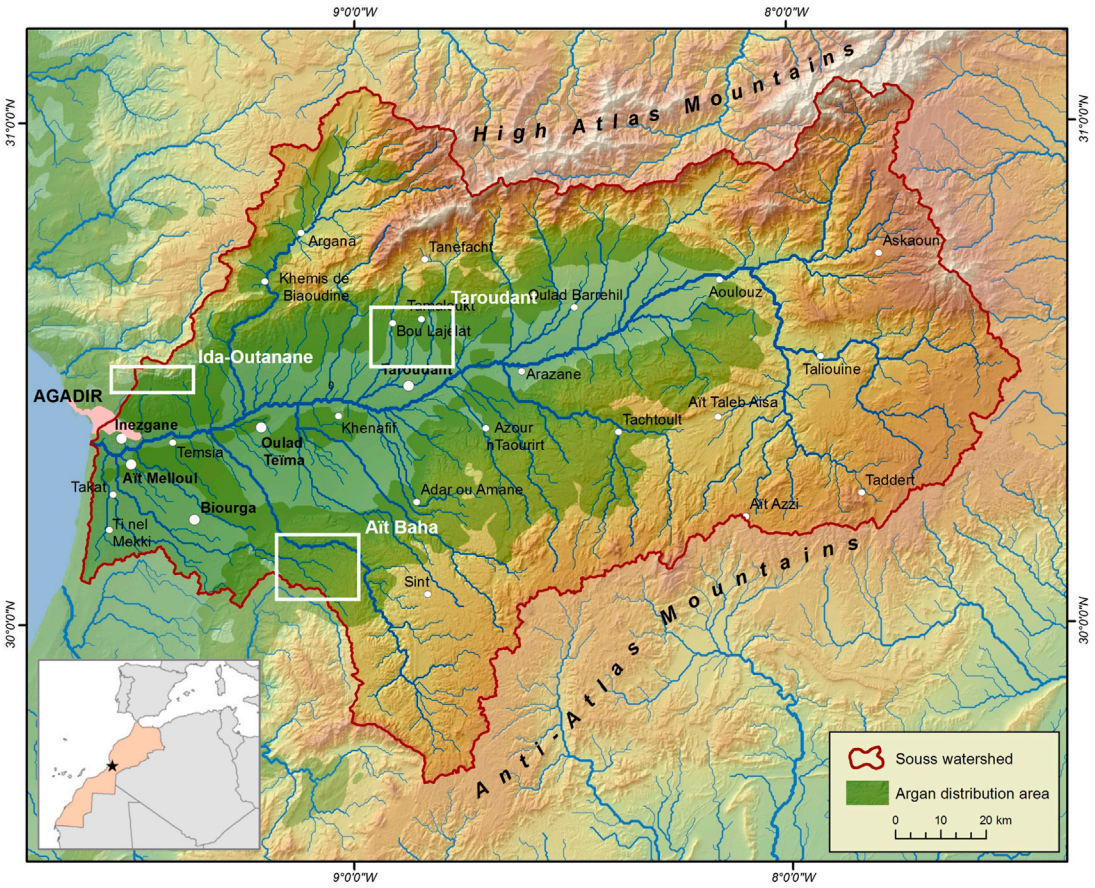

FIGURE 1
The location of the study areas Aït Baha, Ida-Outanane and Taroudant (white boxes) in the Souss Basin, Morocco. The argan distribution area is shown in green shades (see Msanda et al., 2005); the position of the main map is indicated with a star in the smaller location map.

viewing geometry and illumination angle, tree shadows cannot be separated visually from the tree crown. With the most unfavourable conditions in the case of our study, shadows can make up over 40% of the mapped tree, which may lead to severe miscalculations and misinterpretations of forest cover if disregarded (Marzolff et al., 2022). To avoid potential errors associated with inaccurate tree-crown delineations, we did not map tree canopy cover on a continuous scale, but opted for measuring tree-cover changes on an ordinal scale. In the following, we will use the term "tree-crown size" for the ordinal crown sizes small, medium and large, and the term "tree-cover change" for the resulting ordinal change classes, which integrate increased or decreased crown size, loss or establishment of trees (see 2.4 as well as Marzolff et al., 2022). Vegetation cover in general may change (positively or negatively) or stay unchanged (Ries, 2005; Sloan et al., 2019). In undisturbed forests, we would expect tree changes in size between the years 1972 and 2018 as well as some dieback and regeneration. When left to grow the trees would increase in size or new trees could grow, therefore increasing tree cover. Since the argan woodlands are a multi-use silvopastoral system, a tree is normally influenced by a multitude of factors unless it is purposely protected. Whole branches may be cut as firewood, diminishing the tree in size and canopy density. The tree may be pollarded or cut completely for charcoal or firewood. If the tree is cut, it will usually resprout with multiple new shoots that need to be protected from browsing to grow. If a small argan tree or saplings from a stump are continually browsed, they will not develop into a tall-stemmed tree but become a dense shrub. Owing to this multitude of factors influencing argan cover, we will determine the tree-crown size change and tree-cover change of all trees on the chosen test sites. We may expect tree sizes and tree cover to have changed on every test site if trees are not hindered from growing. Due to the variety of test sites (usage, distance from settlements etc.) the degree of tree-cover change will also differ between sites. By incorporating knowledge about tree-cover change, tree-crown sizes and plant architecture in 2018 (see Sections 2.3, 2.4), a conclusion about degradation or recovery can be drawn.

10.3389/fenvs.2022.896703

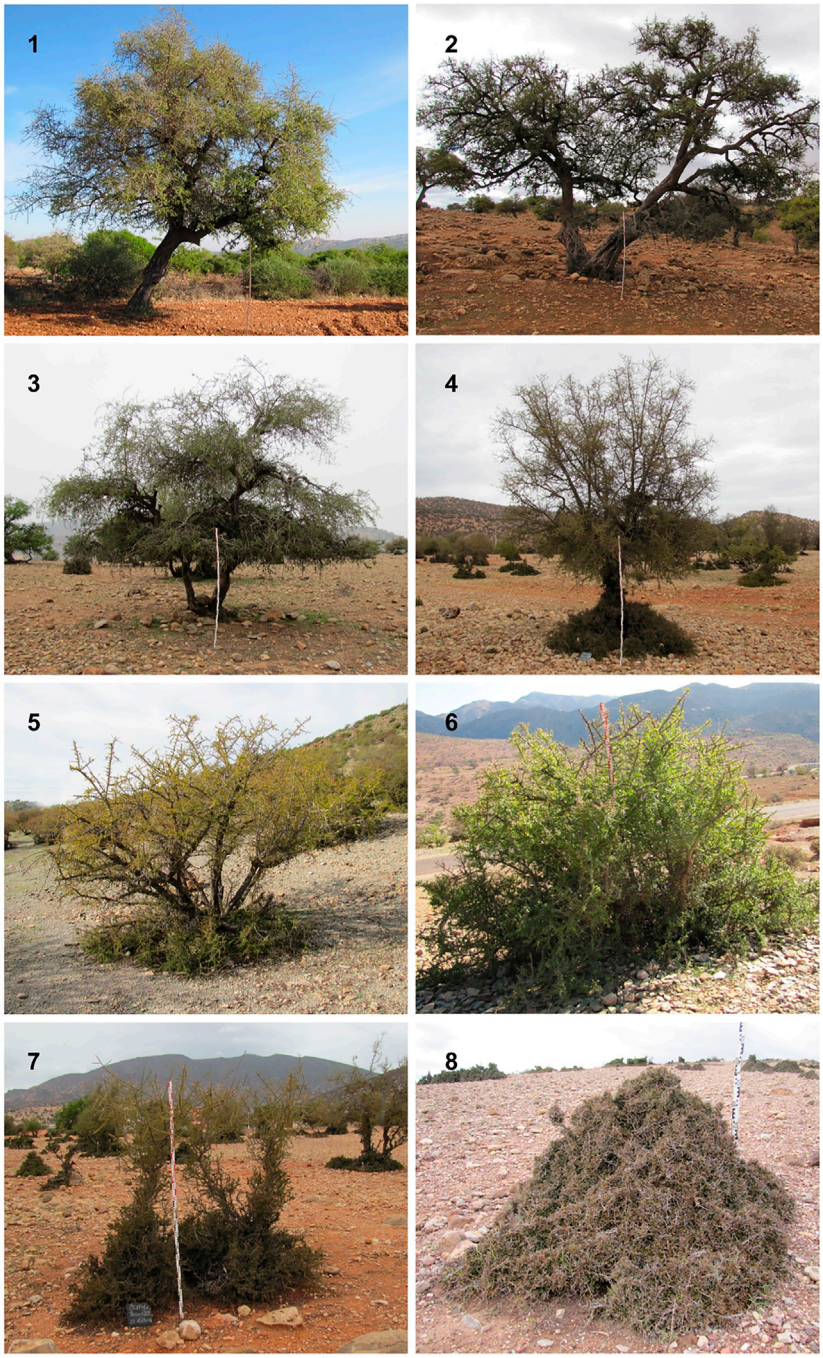

FIGURE 2
Tree architecture classes from 1 to 8 with increasing tree degradation (classification modified and expanded from Culmsee, 2004). 1: Tree with big, round crown, one or multiple trunks easily visible; 2: Tree with multiple, diverging trunks, no densification of branches and leaves; 3: Tree with denser crown, one or multiple trunks are visible despite basal cushions (if present), crown is umbrella-shaped, where branches are pulled down- or upward; 4: Tree with one or multiple trunks, strongly developed basal cushion, possible umbrella-shaped crown; 5: Transition form between tree and shrub with multiple visible trunks, often low in height; 6: Shrub with dense crown, number of trunks due to basal cushion not visible; 7: Shrub with some outgrowing branches, dense, number of trunks not visible (cone-shaped cushion); 8: Low, compact shrub (cone-shaped cushion), dense to very dense.

2.3 Field mapping and tree architecture classification

We mapped the location of each individual argan tree (2,494 in total) on our 30 test sites in the field in 2018. This enabled us to record small trees as well and also to clearly identify the individual trees in overlapping canopy clusters. Argan trees often have more than one trunk (Culmsee, 2004; Buernor et al., 2021) and form coalescing crowns, but in the field, we could differentiate between multi-stemmed trees (counted as one plant) and single-stemmed trees growing in close groups with clumped canopies. In addition to mapping the trees, each tree was assigned a field number and an architecture class based on its overall appearance (Figure 2), following and modifying the categorisation first described by Culmsee (2004). Tree architecture has been shown to relate strongly to browsing intensities (Culmsee, 2004; Fornara and Du Toit, 2007; Moncrieff et al., 2011) as well as other influences such as cutting, coppicing or pollarding. Trees of architecture class 1–2 are not or little affected by browsing. Trees of classes 3–4 show increasing signs of browsing by climbing goats, but are less limited in their functions (like e.g., fruit production) than trees in architecture classes 5–8, which take the form of shrubs and cushion-like bushes. In addition, we recorded if the trees had multiple trunks, which could be an indication of coppicing in the past.

2.4 Satellite-based tree-cover change mapping

For quantifying tree-cover change between July 1972 and March 2018, we used two types of very high resolution satellite (VHRS) imagery: historical panchromatic satellite photographs taken with the KH-9 camera of the military reconnaissance program HEXAGON (approx. 1 m resolution) and recent multispectral images from the WorldView satellites (pansharpened to 0.5 m resolution); see exemplary subsets in Figure 3. The analogue scanned HEXAGON images were manually georeferenced to the orthorectified WorldView images using a spline transformation. We verified the existence of each field-mapped tree on the HEXAGON images, and trees visually identifiable in 1972 but lost until 2018 were added to the database. First for 2018, then for 1972, the trees were classified into four classes by visual image interpretation of their crown diameters: small (<3 m diameter), medium (3–7 m), large (>7 m) or not present in 1972 or 2018. During this retrospective mapping process, we classified all trees as already existent in 1972 unless they were clearly not recognizable on the HEXAGON image. Any trees where change into another size class was not visually certain were given the same size class as 2018, i.e., unchanged size. For some sites, WorldView images dated from 1 year earlier (July 2017), but tree-crown size or presence could be updated to 2018 with the help of UAS imagery taken in March 2018.

In Part A of our study (Marzolff et al., 2022) we found that HEXAGON imagery has a remarkably similar potential for identifying individual trees compared to the WorldView images, although both have limited ability for mapping small trees and trees in clumped-canopy groups. By using the combination of tree locations known a priori from field mapping with a retrospective mapping approach opting for stability in case of doubt, we could ensure very high accuracy for tree-density and tree-cover measures in 2018 and a conservative tendency towards underestimation rather than overestimation of change. More details on the tree-mapping procedure, especially concerning the complex effects of resolution, viewing and illumination angles in the historical HEXAGON imagery, may be found in Part A of our study (Marzolff et al., 2022).

In order to quantify tree-cover change, we defined seven change classes from −3 to +3 reflecting size-class increase or decrease from 1972 to 2018 (Table 1), and attributed all trees accordingly. The tree-cover change class +3 (from not present 1972 to large tree 2018) could effectively not be observed in this study, and is indeed rather improbable since argan trees grow very slowly (Morton and Voss, 1987), especially under continuing grazing and usage pressure.

2.5 Statistical analysis

The tree-cover change classes were analysed using descriptive statistics, and net change sums derived from the tree-cover change classes were calculated to find woodland trends for each test site. Averages for tree mortality and tree establishment for each test site were compared using a Wilcoxon-Test. Furthermore, to determine if there were significant differences between excluded and non-excluded as well as cultivated and non-cultivated test sites (see attributes in Supplementary Table S1), a Mann-Whitney-U-Test was carried out. All statistical analyses were performed with the software IBM SPSS Statistics for Windows, Version 25.0 (IBM Corp., Armonk, NY, United States).

3 Results

3.1 Changes of tree cover and density 1972–2018

As a representative example for the tree-cover change maps 1972–2018, Figure 4 shows the test site MAO1n, where the overall tree density and cover change is quite similar to the average of all 30 test sites (compare with change map Figure 7 in Marzolff et al., 2022). The tree density at MAO1n remained

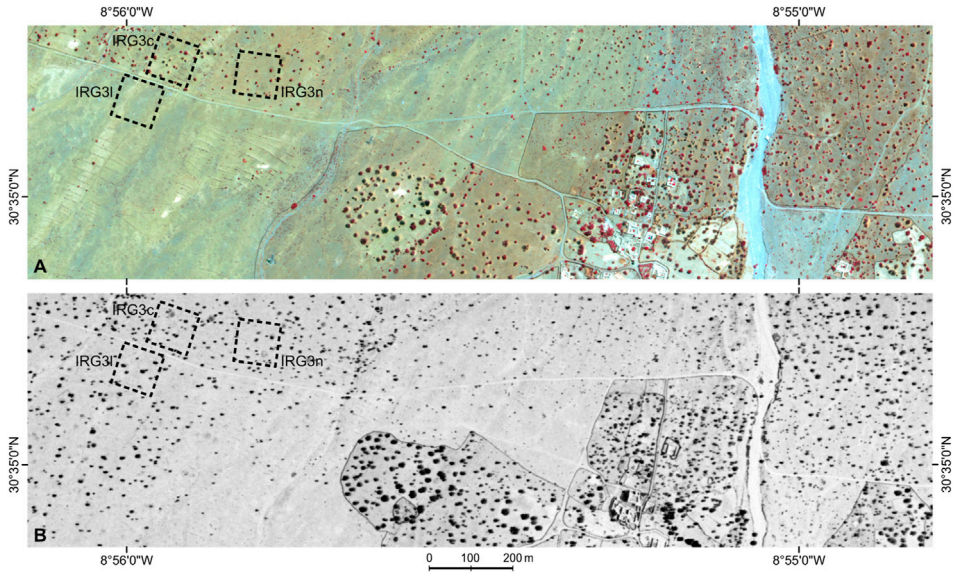

FIGURE 3
Exemplary subsets of the satellite imagery used for tree-cover change mapping. Part of the Taroudant study area, with three test sites marked in dashed lines. The village of Aït Bou Hamida in the lower right was once specialised in charcoal production, which is reflected in the low tree densities in its surroundings. Some remains of charcoal kilns are visible as grey marks on and between IRG3c and IRG2n (see Figure 11B). **(A)** False-colour infrared WorldView-2 image of 6 July 2017 **(B)** panchromatic HEXAGON KH-9 stereo-panoramic camera photograph of 16 July 1972. Note the striking comparability of woodland details and other landscape features in the two images in spite of the very different sensor generations and types.

TABLE 1 Tree-cover change classification based on HEXAGON satellite images 1972 and WorldView satellite images 2018. Change-class values indicate ordinal-scaled positive or negative change between the tree-crown size classes.

		2018			
	Tree-crown size class	**Class 0: not present**	**Class 1: small**	**Class 2: medium**	**Class 3:large**
1972	**Class 0: not present**	n/a	+1	+2	+3
	Class 1: small (< 3 m)	−1	0	+1	+2
	Class 2: medium (3–7 m)	−2	−1	0	+1
	Class 3: large (> 7 m)	−3	−2	−1	0

unchanged at 55 trees ha^{-1}, and 33 (or 60%) of the 1972 trees remained in the same size class (yellow circles). 18 trees increased in crown size or were mapped as new (green), while only 14 trees decreased in crown size or were lost (red). However, positive change only reaches class +1, while the negative change classes −2 and −3 occur for 3 and 2 trees, respectively. Thus, in spite of the unchanged total number of trees, this site shows considerable ambiguity in change with a slight tendency towards net decrease of woody cover.

Figure 5 shows the tree-cover change class distributions on the test sites. Some test sites show a highly dynamic tree-cover change between 1972 and 2018, despite a governmental logging ban, with numerous decreasing and increasing trees. However, unchanged trees are in the majority, with 62.3% of all mapped trees remaining in the same size class as in 1972. The highest percentage of unchanged trees (90.2%) can be found on test site ABH1n. With 20.7% of all mapped trees, tree-cover change +1 is the second most frequent class, indicating that either small new trees have grown or trees have grown to a larger size between 1972 and 2018 (e.g., from small to medium trees, from medium to large trees). 11.6% of all trees have decreased one size class (class −1, from large to medium trees, from medium to small trees, disappeared small trees). Classes −2, +2, and −3 are rarer with 3.5%, 1.4%, and 0.4%, respectively. These classes indicate greater changes, e.g., faster tree growth or logging/coppicing of large or medium trees. Positive and negative changes occurred on

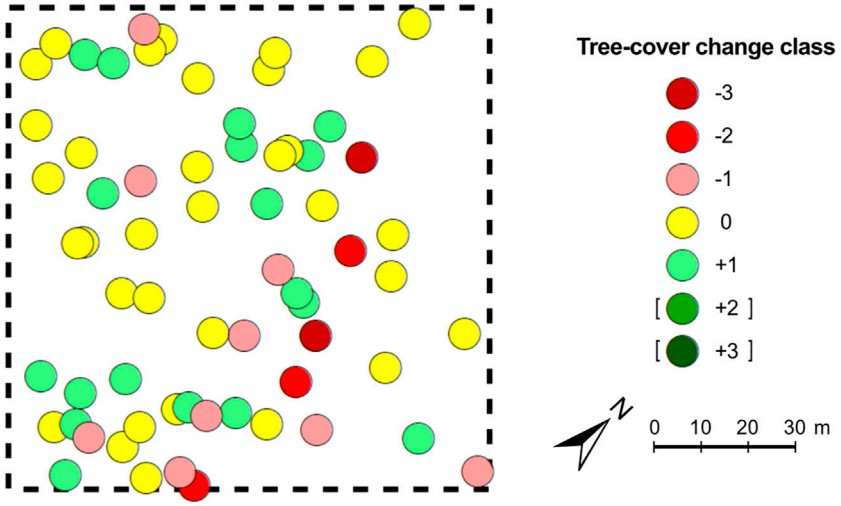

FIGURE 4
Map of tree-cover change 1972–2018 at test site MAO1n (30°04′09″N, 9°07′51″W). Change classes are defined according to Table 1; positive change (green) shows crown-size increase and new trees, negative change (red) shows crown-size decrease and lost trees. Unchanged trees are shown in yellow. This map is a representative example of tree-cover change although there is a high heterogeneity from site to site (see Figure 5).

nearly every test site. However, one test site, IRG3l, shows 94.1% of negative change: It was specifically chosen as an example of a logged test site, featuring only three remaining argan shrubs in 2018 (see Figure 3).

Tree establishment (newly grown trees) and tree mortality (lost trees) are similar on the test sites. Overall, 292 trees have newly grown on the 30 test sites, 281 trees disappeared. On average 9.7 trees ha^{-1} have established themselves, while 9.4 trees ha^{-1} were lost between 1972 and 2018 (standard deviations: 11.2 and 8.4, respectively). Significant differences using a Wilcoxon-Test could not be found between the means.

The distribution of tree-cover change classes on each test site reveals the predominant changes on the test sites between 1972 and 2018. Figure 6 shows boxplots of the tree-cover change classes. Since great change in that time is rare, the upper and lower quartiles reach mostly from tree-cover change -1 to +1, while tree-cover change classes −3, −2 and +2 are outliers. For some test sites the upper and lower quartiles are both set on 0 because most trees on these test sites remained unchanged. The means as well as net change sums (NCS) also point in the direction of predominant change on the test site. They are especially low on test site IRG3l (as explained above) due to logging of trees. The length of the whiskers as well as the standard deviation show if the degree of change on the test site was similar (e.g., mostly tree-cover change class −1). For example, test site IRG2n has a mean of −0.06 indicating that nearly no net change has taken place, but a standard deviation of 1.27 due to the co-occurance of positive and negative tree-cover change classes on this site. This indicates a high ambivalence of change, which is also visible on the test sites ABH2t with a slightly more negative trend and on AZR1n. The test site AZR1c shows a high standard deviation (1.08) as well, which is not only due to positive and negative change on the test site but mainly due to the positive change differing (+1, +2). Trends in increasing and decreasing tree-cover can be found; sites with only positive or negative change, however, are rare. This is only the case for the test sites TAS1r (increasing change) and IRG3l (decreasing change). The aforementioned test site MAO1n (Figure 4) has a mean and net change sum which are both negative, although more trees show positive than negative change (Figure 5): This is due to the negative changes reaching the greater classes up to -3, while the positive changes occur only in the lowest class +1—a variability also reflected in the rather high standard deviation of 0.94. The rest of the test sites show mostly no change (10 test sites where upper and lower quartile are both 0), mostly positive change (9 test sites where lower quartile is 0, upper quartile is 1 and mean is in between) or mostly negative change (7 test sites where upper quartile is 0 or below).

3.2 Architecture classes and tree-crown sizes as indicators of woodland state in 2018

Using the tree-cover change classes we were able to determine how the trees on our test sites changed between 1972 and 2018. Since we also recorded the architecture class of every tree in 2018 it is possible to give a more complete picture of the state of the argan trees in our study areas and on our test sites. This enables us to determine which trees are most at risk of

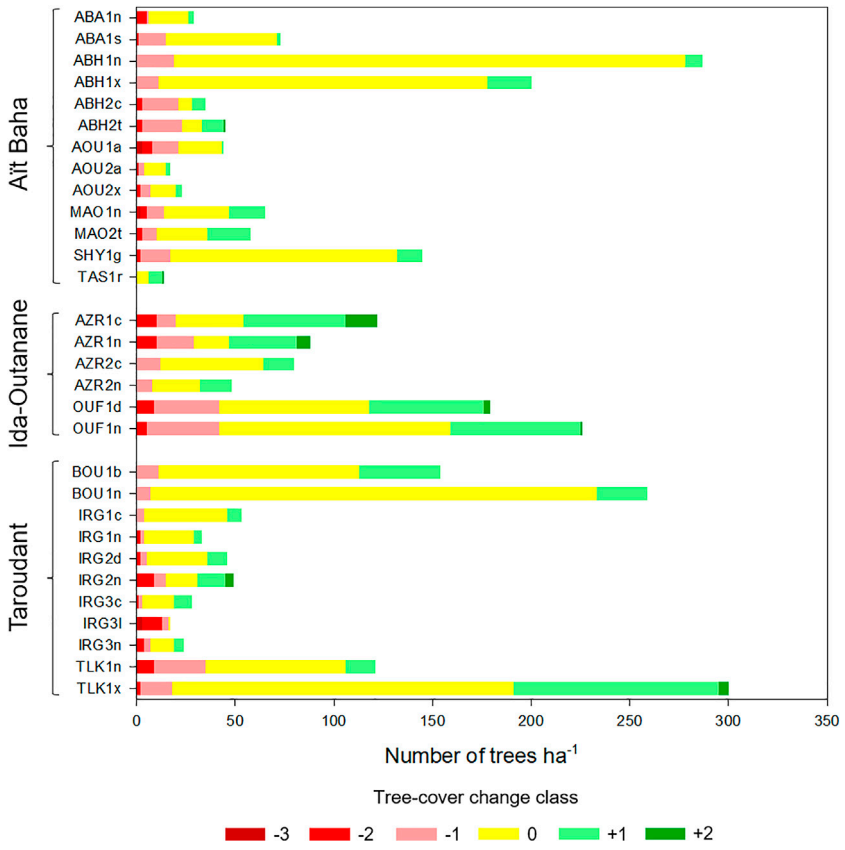

FIGURE 5
Distribution of tree-cover change classes (as defined in Table 1) between 1972 and 2018 at all 30 test sites. The stacked bars show the number of trees with negative changes on the left (crown-size decrease or loss of trees, red shades), unchanged in the middle (yellow) and with positive changes on the right (crown-size increase or new trees, green shades). Tree densities and development on the test sites are very heterogeneous.

(further) degradation. In the tree-architecture classification scheme described with Figure 2 (Section 2.3), classes 1 to 4 describe less degraded trees (still recognizable as trees), while classes 5 to 8 characterize trees/shrubs in a higher state of degradation. Trees in architecture classes 7 or 8 are by definition of small size, since they mostly resemble shrubs and are hindered by browsing from growing larger. Trees in architecture classes 5 or 6 are mostly small but might grow to a medium size. Trees in architecture classes 1 to 4 can be of any size, although classes 1 and 2 should mostly be of large or medium size.

Figure 7 shows the distribution of architecture classes for each combination of tree-cover change class and 2018 tree-crown size class. Overall, small trees are in the majority regardless of tree-cover change class, and small unchanged trees (0/small) account for nearly half (48.4%) of all remaining trees. 51% of these trees are in the degraded half of architecture classes; 19.5% of them are in the most degraded architecture class 8. These trees could have been cut, regrown and overbrowsed, or they are stable in a degraded state. Two thirds of newly grown small trees (part of tree-cover change class +1) show the more degraded stages 5–8, most of them are classified as architecture class 8 (40.3%). These are most likely cases where regrowth has been overbrowsed and could not develop into a fully grown tree. The change from medium to small trees—i.e., −1/small in Figures 7 — results in less degraded trees overall (64% in architecture classes 1–4), but also in 21.6% of trees classified as small overbrowsed shrubs (architecture class 8).

34.2% of mapped trees in 2018 are medium-sized trees (3–7 m crown diameter), and most of these have not changed in crown size between 1972 and 2018. They are less degraded than small trees, with most trees classified as architecture class 3. This architecture class shows signs of browsing (goats can climb the trees) but is recognizable as a tree with a typical stem-and-crown tree shape unlike architecture classes 5–8, which only make up 7.5% of medium unchanged trees. This indicates that trees are safer from degradation by browsing when they have reached a certain size, in this case >3 m crown diameter. While large trees are in good condition (none in architecture classes 5, 6, 7 or 8), medium-sized trees are in their best condition when they

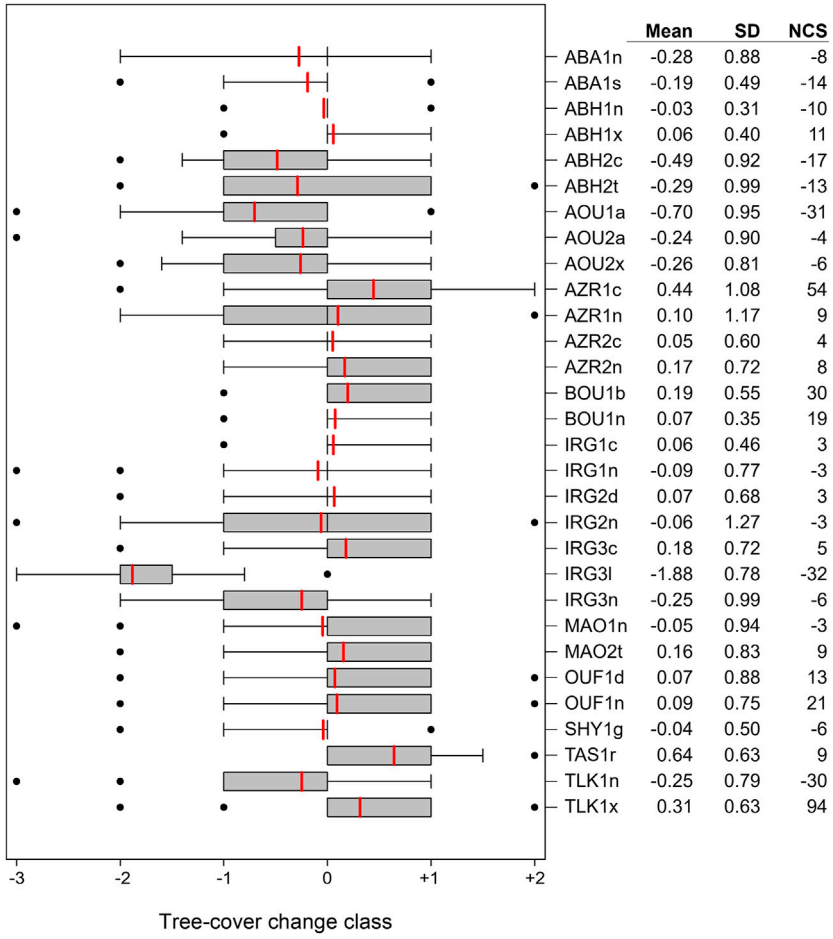

FIGURE 6
Boxplots of tree-cover change classes (as defined in Table 1) showing predominant trends (positive/negative change or no change) on the test sites. Means are shown in red as well as in the first table column; dots show outliers. Where boxes are not displayed, the upper and lower quartile are both 0, showing a predominantly unchanged test site. Standard deviations (SD; second table column) indicate variability of change; net change sums (NCS; third table column) show the weighted dominant change on each test site regardless of unchanged trees.

are in tree-cover change class −1 (3.3% in architecture classes 5–8). This suggests that the change from large trees to medium trees rarely affects the architecture class: this change is possibly caused by the trimming of branches. Large trees only make up 2.9% of all mapped trees in 2018; they mostly have architecture class 2 when increased in size or architecture class 1 when unchanged.

Most of the mapped trees have more than one tree trunk regardless of their size or tree-cover change class. Unchanged medium trees show the highest percentage of single-stemmed trees (48.7%) as well as medium trees that have decreased one size class (−1/medium; 40%). 38.4% of trees changed from medium to small (−1/small) have only one trunk, which makes the interpretation of cutting and regrowth improbable for these trees. Small unchanged trees as well as small newly grown trees (+1/small) have the lowest percentages of single-stemmed trees (26.5% and 18.6%, respectively), indicating that these trees have been cut and (re-)grown, probably several times, and that the supposed new trees are actually regrowth of a cut tree which could not be observed on the Hexagon image of 1972.

3.3 Tree-cover change and woodland state in the different study areas

In order to investigate possible regional differences, we summarized the tree-cover changes per tree-crown size classes for each study area between 1972 and 2018 in Figure 8. The study area of Aït Baha is dominated by mostly unchanged small (53.1%) and medium (17.1%) trees with only little deforestation (8.8%), size changes (12.1% decrease/

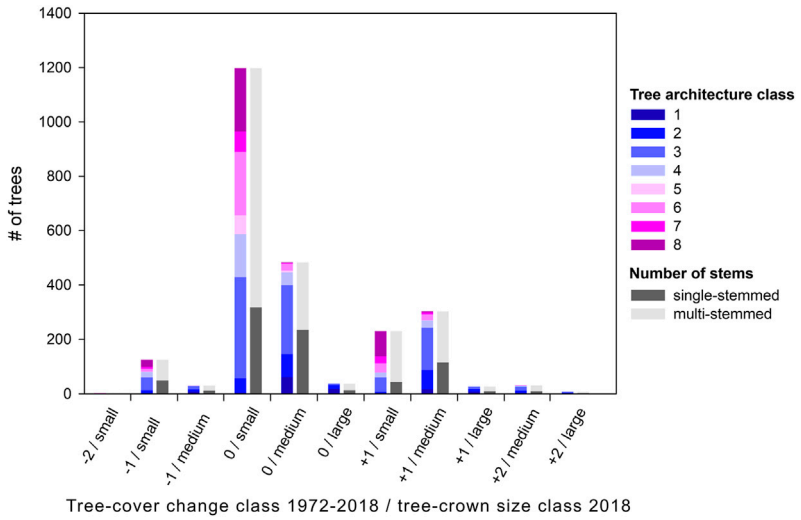

FIGURE 7
Distribution of architecture classes and stem numbers for each combination of tree-cover change class and 2018 tree-crown size class (for trees still present in 2018). Less degraded architecture classes 1 to 4 are shown in blue shades, more degraded classes 5 to 8 in pink shades. The second bar shows the percentage of single- and multi-stemmed trees. The x-axis shows the tree-cover change class 1972-2018 and crown-size class in 2018 (for further details see Table 1), e.g., –1/small thus describes small trees in 2018 that were of medium size in 1972.

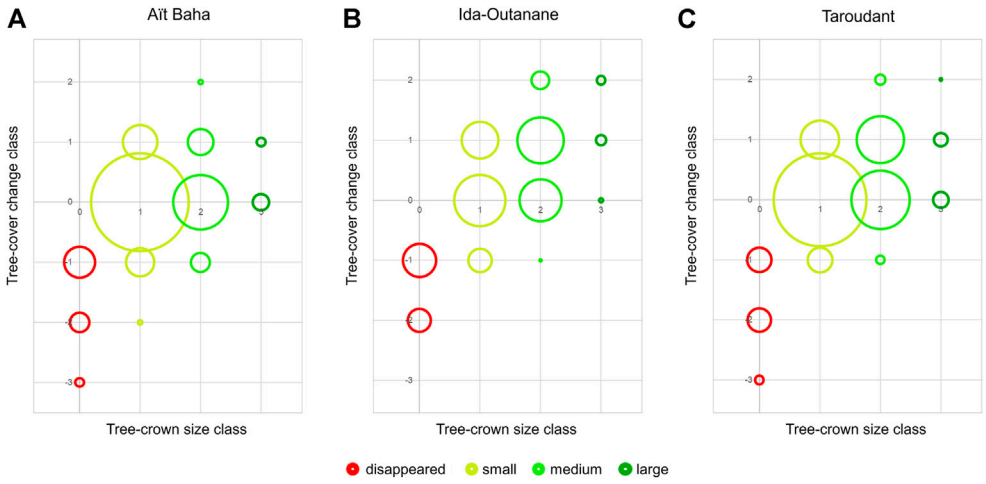

FIGURE 8
Bubble diagrams showing the tree-cover changes and tree-crown size distribution in the study areas Aït Baha **(A)**, Ida-Outanane **(B)** and Taroudant **(C)**. Tree-crown sizes (as defined in Table 1) are shown on the x-axis and marked in colours (red: 0 = disappeared, yellow: 1 = small, light green: 2 = medium, dark green: 3 = large). The y-axis describes the tree-cover change class from -3 (large tree in 1972, disappeared in 2018) to +2 (regrowth from not present in 1972 to medium tree in 2018 or small tree in 1972 to large tree in 2018), for further details on tree-cover change classes see Table 1. The size of the bubbles is proportional to the percentage of each tree-cover change/tree-size class combination in each study area.

increase) or new (re-)growth (7.1%). Architecture class 6 is found often in Aït Baha (28.2%). In contrast, Ida-Outanane shows a larger proportion of changed trees. Ida-Outanane has a higher percentage of medium trees than the other two study areas, possibly due to the more maritime climate. The proximity to the city of Agadir also offers other occupation possibilities, whereas the rural population in the study areas of Aït Baha and Taroudant often makes their livelihoods from the herding and

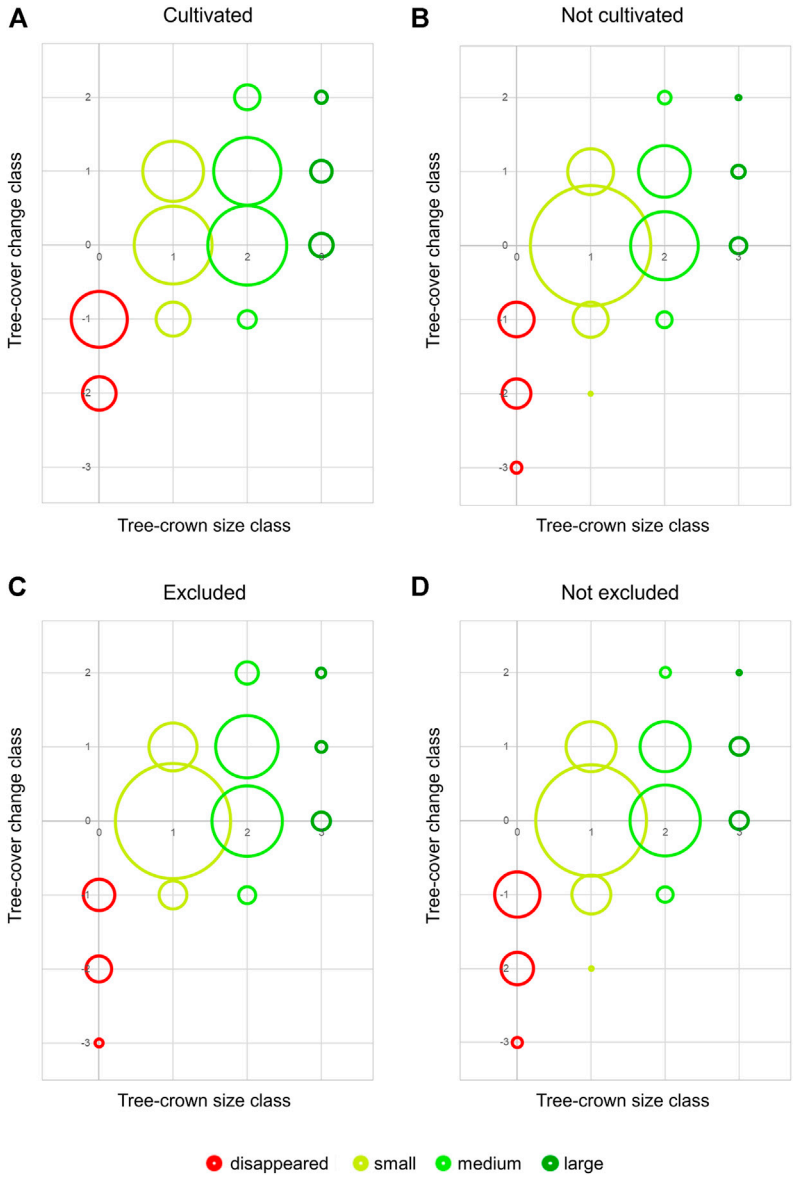

FIGURE 9
Bubble diagrams showing the tree-cover changes and tree-crown size distribution for cultivated/non-cultivated **(A,B)** and excluded/non-excluded **(C,D)** test sites. Tree-crown sizes (as defined in Table 1) are shown on the x-axis and marked in colours (red: 0 = disappeared, yellow: 1 = small, light green: 2 = medium, dark green: 3 = large). The y-axis describes the tree-cover change class from −3 (large tree in 1972, disappeared in 2018) to +2 (regrowth from not present in 1972 to medium tree in 2018 or small tree in 1972 to large tree in 2018). The size of the bubbles is proportional to the percentage of each tree-cover change/tree-crown size class combination at cultivated/non-cultivated **(A,B)** and excluded/non-excluded **(C,D)** test sites.

sale of argan-browsing goats or sheep. The proportion of newly or re-grown trees is also quite high (15.9%). Although 15.6% of trees have disappeared, a larger part of this study area has positively changed. Most of the trees in Ida-Outanane have changed positively and are in good condition (75.2% in architecture classes 1–4), but many are heavily browsed (16.4% in architecture class 8) or have disappeared completely. As in the other two study areas, most trees in Taroudant are small and have not changed (45.9%). When changed, the trees have only changed little (change class +1: 21.7%) and show more positive change (22.5%) than negative (11.5%) in this study area. The most deforested test site IRG3l is also located in this study area. Taroudant has the highest percentage of trees in architecture classes 7 (6.2%) and 8 (23.5%), which is mostly due to the two test sites BOU1b and BOU1n.

3.4 Tree-cover change and woodland state on test sites under different usages

All test sites were chosen for different attributes, mostly based on land use. On some test sites grazing animals are excluded by fences or thorny hedges for preventing damage to young seedlings in reforestation measures or to protect the harvest on cultivated land. Hypothetically, trees on test sites under cultivation—even when easily accessible—are less grazed, since local shepherds lead their herds away from these test sites traditionally used for cultivation by acquainted locals. All test sites can be allocated to cultivated (i.e., showing present or past signs of cultivation) or non-cultivated test sites as well as excluded or non-excluded test sites (Figure 9). Cultivated (Figure 9A) compared to non-cultivated sites (Figure 9B) show both higher negative (cultivated: 21.0% vs. non-cultivated: 14.1%) and higher positive changes (33.9% vs. 18.8%) and less unchanged trees (45.1% vs. 67.1%) using the total number of trees. Most of the negative changes on cultivated test sites (73%) occurred due to the removal of trees. Excluded (Figure 9C) compared to non-excluded sites (Figure 9D) overall showed a slightly higher percentage of unchanged trees (excluded 64.0% vs. non-excluded: 61.1%) but lower negative (10.9% vs. 18.9%) and slightly higher positive changes (25.0% vs. 20.0%), while the difference mostly affected medium trees (size class 2 with tree-cover change classes 1 and 2 are higher for excluded, lower for non-excluded test sites). A Mann-Whitney-U-Test found significant differences between the percentage of positive changes on cultivated and non-cultivated test sites ($p < 0.05$) and more specifically between the percentage of change class +1 ($p < 0.05$). There are no significant differences for excluded and non-excluded test sites.

Cultivated/excluded and non-cultivated/non-excluded test sites can also be compared according to the distribution of architecture classes. Both cultivated and excluded sites show higher values than their counterparts for architecture classes 1, 2, and 3 and lower values for architecture classes 6, 7, and 8. Significant differences (using a Mann-Whitney-U-Test, $p < 0.05$) between cultivated and non-cultivated test sites can only be found for architecture class 8 with means of 4.4% and 15% for cultivated and non-cultivated, respectively. For excluded and non-excluded test sites significant differences are present for architecture class 7 (averages of 0.8% and 7.1%, respectively), between the sum of architecture classes 1, 2, 3, and 4 (the less degraded half, averages of 85.7% and 64.1%, respectively) and the sum of architecture classes 5, 6, 7, and 8 (the degraded half, means of 14.3% and 35.9%, respectively).

4 Discussion

The results show the high heterogeneity of tree-cover change in argan woodlands, ranging from mostly positive change (increase of crown sizes, regrowth) and relatively stable growth forms to near-total deforestation (IRG3l) with the remaining trees as degraded shrubs. As is evident from Figures 5, 6 our test sites do not show one direction of evolution but several. Most test sites have a high percentage of unchanged trees, i.e., trees that did not cross size class boundaries, although they might have grown or have been reduced in size. Also, very small trees or trees growing in clumped-canopy groups were more difficult to identify in the panchromatic historical HEXAGON images than the recent multispectral WorldView images. Where in doubt, our retrospective mapping approach therefore opted for unchanged size, and thus slightly overestimated woodland stability (see Marzolff et al., 2022). However, it is clearly evident that on nearly all test sites, many of the analysed trees stayed relatively unchanged over a period of 46 years.

4.1 Tree-density changes of argan woodlands

The degradation of the argan woodlands (in any form) has been discussed previously (Culmsee, 2005; Le Polain de Waroux and Lambin, 2012; Defaa et al., 2015; Kirchhoff et al., 2019a). Regarding tree-density change as a measure of degradation, our results—an average tree-density increase of 0.4%—are in contrast to the argan-forest decline of −44.5% observed by Le Polain de Waroux and Lambin (2012) between 1970 and 2007 some 60 km further east, in the hillslopes of the Anti-Atlas Mountains. However, while our tree counts are based on field mapping 2018 and a retrospective monitoring approach (FB approach; Marzolff et al., 2022), the densities reported by Le Polain de Waroux and Lambin (2012) are based on a remote sensing imagery. Their method is more similar to our WorldView-based (WB) approach, which tends to overestimate negative change. Using this approach, we found an average −8.5% density decrease, with 3 of 30 sites losing 40%–100% of trees. Our study areas also span a larger regional variety with higher heterogeneity in argan woodland evolution, and generally have higher tree densities: Le Polain de Waroux and Lambin report a mean change from 27.4 to 15.2 trees/ha, as compared to our WorldView-based 57.8 to 53 trees/ha (Marzolff et al., 2022, Figure 6B; WB 1972 and WB 2018).

4.2 Factors influencing argan woodland change: forest clearing and wood cutting

For this study, we looked only at the situation on our test sites (wooded in 2018, except most of IRG3l) and explicitly not at historic or recent argan degradation on a large scale, which would have to include the forest clearings in the 1970s to make room for the irrigated cultivation of legumes or citrus plantations (El

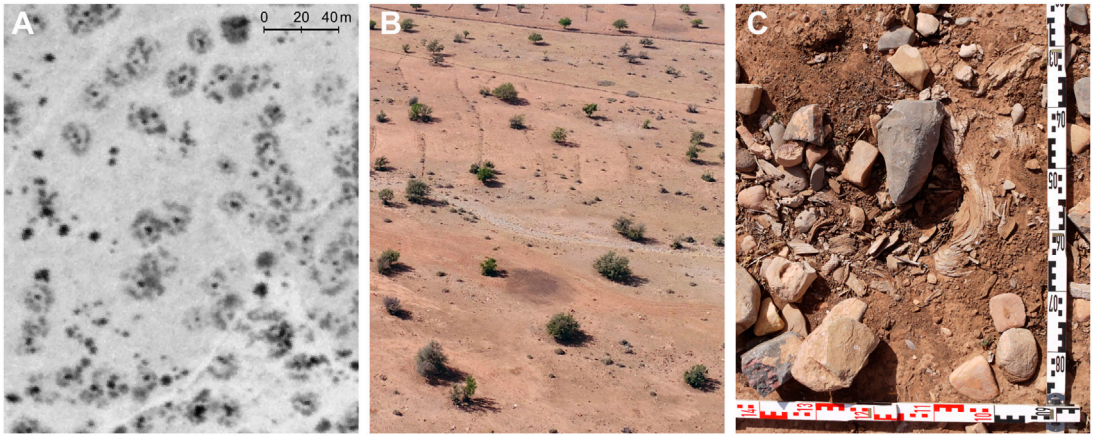

FIGURE 10
Evidences of argan-forest clearing activities. **(A)** Heavy pollarding and clear-cutting in progress west of IRG3 test sites (8°57′10″W, 30°35′30″N), as seen on HEXAGON satellite imagery of July 1972 (4.5 ha subset of 200 ha clearing area). Cut branches are piled up in rings around the remains of tree stems. **(B)** Site of a charcoal kiln on test site IRG3n (8°55′54.8″W, 30°35′14.8″N) as seen on oblique UAS image of October 2018 (a second kiln site is visible in the upper right corner). The ash-darkened sites are already present on 1967 CORONA satellite imagery; 98 of them can still be seen today, covering an area of 170 ha. **(C)** Site of a large tree cut after 1972; parts of the root remain visible in the field (March 2020).

Alaoui, 1999). Ouassou et al. (2006) state that the loss of forest is mainly due to fuelwood collection while land clearance was secondary, possibly due to the rising awareness regarding deforestation in the 1990s (El Alaoui, 1999) and the subsequent designation of the argan forest as a UNESCO Biosphere Reserve in 1998 (Charrouf and Guillaume, 2018), which could be an explanation for the regrowth on some test sites. In the end of the 1990s the trade with argan charcoal diminished (Le Polain de Waroux, 2013), which had been very popular due to its combustive properties (Rocher, 1926) in some villages that specialised on carbonisation of argan wood between 1970 and 1990. This was also the reason for the change on test site IRG2n (which showed ambivalent tendencies in Figure 6) and the clearing of the test site IRG3l. Since not only old trunks or underbrush were taken but fully intact trees (Rocher, 1926), there were fears that without state intervention the argan forest would disappear completely (Boudy and Chalot, 1935). Figure 10B shows an example for charcoal-production evidences (kilns used by the French military during the colonisation) that can be found on and near our test sites. The test sites where argan trees had once been cut—long before 1972—show different tendencies from increasing, decreasing or ambivalent tree-cover change. Only IRG3l was deforested so irredeemably—after 1972—that it is still bare today. Figure 10A shows forest-clearing activities in 1972 2 km west of the aforementioned test sites, where trees were pollarded heavily rather than clear-cut and (most) have since regrown. However, cutting the trunk at ground-level was also common, even with removal of the roots (Rocher, 1926) or cutting of regrowth (explanations for disappeared trees), and Figure 10C shows the remains of a root where a tree once stood.

4.3 Factors influencing argan woodland change: charcoal production and overbrowsing

Since there are no active charcoal kilns in the region today due to bottled gas being readily available as fuel, recent deforestation for the transformation to charcoal is not visible on our test sites. Faouzi (2013) states, however, that many households can still not afford gas or charcoal for cooking and thus use wood taken from the forest or the cuttings of citrus plantations, which could be a reason for trees decreased in size (parts of tree-cover change classes −1 and −2). Wood cutting is acknowledged by locals as part of the problem (Le Polain et Waroux and Lambin, 2012) while grazing/browsing of argan trees by local herds is seen as less of a problem for tree survival but rather for the short-term harvest (Lybbert et al., 2010). Excessive browsing/grazing as well as soil compaction by trampling may make regrowth from seedlings exceedingly difficult (c.f. Fornara and Du Toit, 2007; Rasmussen et al., 2018), which could also explain trees decreased in size (cutting and regrowth) or unchanged trees. Since natural regeneration is very rarely possible, coppicing can be a method of rejuvenation for mature argan forests (Morton and Voss, 1987; Nouaim et al., 2002). If the argan tree is cut, it can rejuvenate with multiple saplings from the old wood (Morton and Voss, 1987), thus resulting in multiple trunks (see Figure 7). This regrowth must, however, be protected against overgrazing/overbrowsing. A tree's recovery after cutting could be delayed or halted if grazing pressure continued during the growing phase (Hosier, 1993). A low growth rate could also indicate that the tree has been degraded in the past (by cutting and/or overbrowsing),

is now in a stable state where it cannot degrade much further but is also prevented from growing (by, e.g., overbrowsing). The stability of the trees can be caused by their high degradation status. This is probably the case on the test sites BOU1b and BOU1n (>66% change class 0, mostly architecture classes 7 and 8). Both sites have obviously been clear-cut prior to 1972, and stump regrowth has since been contained by extreme grazing pressure to the slow development of highly densified cone-shaped cushions (see Figure 2, architecture class 8). Culmsee (2005) makes the argument that cone-shaped cushions (architecture classes 7 and 8) are maximally browsed and are thus shaped only by grazing pressure. This is possible if young trees are continually browsed, but it can also be a combination of felled trees that are now hindered from regrowing. Small unchanged trees are the majority of trees mapped for this study, of these 51.0% of trees are in the degraded half of architecture classes suggesting stability in a degraded state. Medium unchanged trees do not show this tendency and are clearly recognizable as trees. If a tree has reached a certain crown size, in this case >3 m diameter, they seem to be secure from degradation to a shrub, although still browsed (as seen in the high percentage of architecture class 3). Tree architecture is in general shaped by the selective pressures of their environment (Archibald and Bond, 2003; Moncrieff et al., 2014), which are numerous for the argan tree. Although argan trees are resilient in their harsh environment, the high demand for charcoal coupled with high grazing pressure led to a degradation described by many authors (Boudy and Chalot, 1935; Nouaim et al., 2002; Le Polain de Waroux and Lambin, 2012; Le Polain de Waroux, 2013). Since land-usage rights in argan woodlands are complex, this could lead to a behaviour focusing on overexploitation in the short-term (Ouassou et al., 2006), especially in parts of the forest that are free to use for everyone (Lavauden, 1941). A study by Lybbert et al. (2011), analysing vegetation-index (NDVI) time series from before and after 1998, found that the argan woodlands had not visibly improved since being designated a Biosphere Reserve, especially in proximity to argan-oil markets, which corresponds to our results, since most mapped trees are unchanged. This also means that the space between trees has not changed, the soil is unprotected and vulnerable to water and wind erosion making a rehabilitation on the test sites very improbable (Kirchhoff et al., 2019a; Marzen et al., 2020; Kirchhoff et al., 2021).

4.4 Influence of land use: grazing exclusion and cultivation

Fencing-off test sites to exclude grazing and browsing herds has a slightly positive effect on the argan trees in our study. However, many trees still remain unchanged, possibly due to the test sites having been excluded for only a short time. However, this could be due to one test site (TLK1×), which has the highest tree density and which has been fenced in since at least October 2004. Other excluded test sites are AOU1a and AOU2×, which showed decreases in woody cover. Yet, trees on excluded test sites are mostly in less degraded architecture classes than trees on non-excluded sites. Cultivation, in turn, leads to the removal of some trees but leads to an increase in tree size and density over time. Since cultivated sites are not grazed, younger trees are protected and less trees are fully degraded to cone-shaped cushions (architecture class 8). Grazing exclusion without the cooperation of the local population is not necessarily the best way to protect, since top-down approaches like installing fences around areas used by the local population might result in break-ins of herds (Defaa et al., 2015). Cultivation on (parts of) a test site, however, seems to protect most of the existing trees, at least on our test sites, since the population is able to use the land and overgrazing is prevented. Blanco et al. (2015) found similar results for acacia trees in Southwestern Morocco, with high regeneration and recruitment on cultivated lands.

4.5 Degradation or recovery?

Degraded forests are generally connected with a loss of function and ecosystem services (Chazdon, 2008; Vásquez-Grandón et al., 2018). The identification as a degraded forest can vary depending on the definition of forest and forest degradation (Lund, 2009; Vásquez-Grandón et al., 2018; Gao et al., 2020). While Lund (2009) proposes a human-induced tree loss in the forest, Vásquez-Grandón et al. (2018) also mention loss of canopy cover but add changes in structure, composition as well as low or a lack of regeneration. These factors are found on most of our test sites, although we unfortunately have no data about tree architecture in 1972. A change in structure or composition is, however, not improbable (see Figure 7). Since we found a recovery of argan woodlands on some test sites and a degradation on others, a clear trend in one direction cannot be identified.

4.6 Future possibilities and challenges

Our results, which combine tree-cover and plant-architecture data, confirm the importance of forest structure estimations emphasised by Vásquez-Grandón et al. (2018) and Gao et al. (2020). In our study, tree-cover change was analysed from very high resolution satellite images, and tree architecture was mapped in the field. Data on tree-canopy cover on a continuous scale—rather than ordinal size classes—may reliably be mapped from VHRS images for larger trees and from UAS imagery also for small trees. However, the historical perspective, i.e., precise canopy-cover change, is hindered by the difficulties of delineating and measuring exact sizes of tree crowns in the HEXAGON images (Marzolff et al., 2022). A time-effective alternative to field surveys of every tree

FIGURE 11
Tree shadows as indicator of tree architecture on test site SHY1g. Vertical UAS image taken on 8 March 2020, 16:15 local time. Note the different shadow shapes and lengths as well as the appearance of the crown (dense, sparse), which give insight into the growth form and architecture class affiliation of the tree (see Figure 2). Small and dense shadows are architecture classes 5–8, while large, fragmented shadows occur for architecture classes 1–4. Exemplary architecture classes are shown as numbers next to shadows.

can be tree-structural information obtained from UAS imagery or 3D point clouds from LiDAR or photogrammetric analysis (Gao et al., 2020; Gobbi et al., 2020; Marzolff et al., 2020). Even a simple visual interpretation of shadows on UAS images can give important clues to the shape of a three-dimensional object (Aber et al., 2019:53), in this case the tree's architecture. During our field campaigns, we also conducted aerial surveys with a quadcopter UAS (see Part A of our study; Marzolff et al., 2022, and Marzolff et al., 2020), and one example for a late-afternoon image is shown in Figure 11. The different shadow shapes, densities and lengths distinguish more shrub-like compact plants of architecture classes 6 and 7 from larger and taller single-stemmed and multi-stemmed trees of architecture classes 1–4. Insight about the height of the tree is given by different lengths of shadows, about the crown density by the compactness or fragmentation of the shadow; both can help to interpret a tree's state not solely by its crown size. Despite the shadows' distortion, many plant-architectural characteristics familiar from the normal ground-perspective (Figure 2) are recognizable and classifiable (possibly automatically). In the near future it is probable that UAS images will be increasingly available via data repositories and social networks; a shadow-based analysis of dryland tree cover and state could thus become possible worldwide by using such imagery from random sample sites. Citizen-science approaches could help gather UAS images where none are available and could be an efficient alternative to the more detailed but very time-consuming field-based approach for large-area forest structure estimation.

5 Conclusion

In conclusion, we have shown that the tree-cover change between 1972 and 2018 showed a high heterogeneity on the argan test sites. Only few sites showed mostly positive or mostly negative tree-cover changes with few unchanged trees. However, 48% of all studied trees remained small (<3 m diameter) and unchanged with half of them being in a degraded state. Due to the pressure on the argan forest by wood cutting, overgrazing etc. these trees are hindered from growing but remain stable in a degraded state. The degradation of the tree can thus cause the stability found in the tree-cover change classes. The trees' protection of the soil is therefore limited, with bare intertree areas degrading and leaving a less fertile base for young seedlings. Since overgrazing is a problem in southern Morocco, trees on sites with protection from browsing (however achieved) can grow relatively undisturbed. Some trees were cut to make room for cultivation or—before the ban on cutting—due to charcoal production, and regrowth seemed to be mostly protected from overbrowsing on these test sites. With financial incentives focused on specific sites they can be protected while afforestation sites (not planned with involvement of the

local population) are subject to break-ins and further overgrazing. Herds of goats, sheep and sometimes dromedaries can roam the argan woodlands leaving little chance for regrowth. However, our data show an increase in tree density and tree size on few test sites, demonstrating that regrowth is possible under some circumstances. A regeneration of the argan forest could therefore be achievable with the support of the local population if grazing is controlled. Additional monitoring at regional scale could show argan woodland dynamics and would be an important resource to further understand their current status and future trends.

Data availability statement

The HEXAGON images used in this study are freely available from the USGS EarthExplorer. The argan-tree database may be obtained from the corresponding author on reasonable request.

Author contributions

MK, IM, MS, and JR designed the study; AAH provided resources and logistical support; IM, MS, AAH, and JR supervised the research activities; MK, IM and RS acquired the data; MK, IM, MS, and JR performed the analysis and interpretation; JR and IM acquired funding; MK and IM wrote the original draft. All authors performed review and editing of the final version of the manuscript.

Funding

Funding of this study by the Deutsche Forschungsgemeinschaft (DFG) as part of the ARGAN research project with project no. RI 835/24 and MA 2549/6-1 is gratefully acknowledged. WorldView and GeoEye satellite data were provided by the European Space Agency (ESA) under the Third Party's Mission scheme, project no. 36256. TanDEM-X elevation data (used in orthorectification) were provided by the German Space Agency (DLR) under project no. DEM_HYDR1131. The publication was funded by the Open Access Fund of Universität Trier and the German Research Foundation (DFG) within the Open Access Publishing funding programme.

Acknowledgments

We thank the responsible local, regional and national Moroccan authorities for supporting our studies and allowing access to their territories. We are also grateful to Abdellatif Hanna and Khalil Hamouch for their considerable help with our fieldwork.

Conflict of interest

The authors declare that the research was conducted in the absence of any commercial or financial relationships that could be construed as a potential conflict of interest.

Publisher's note

All claims expressed in this article are solely those of the authors and do not necessarily represent those of their affiliated organizations, or those of the publisher, the editors and the reviewers. Any product that may be evaluated in this article, or claim that may be made by its manufacturer, is not guaranteed or endorsed by the publisher.

Supplementary material

The Supplementary Material for this article can be found online at: https://www.frontiersin.org/articles/10.3389/fenvs.2022.896703/full#supplementary-material

References

Aber, J. S., Marzolff, I., Ries, J. B., and Aber, S. E. W. (2019). *Small-format aerial photography and UAS imagery – principles, techniques and geoscience applications*. Amsterdam, Netherlands: Elsevier.

Ain-Lhout, F., Boutaleb, S., Diaz-Barradas, M. C., Jauregui, J., and Zunzunegui, M. (2016). Monitoring the evolution of soil moisture in root zone system of *Argania spinosa* using electrical resistivity imaging. *Agric. Water Manag.* 164 (1), 158–166. doi:10.1016/j.agwat.2015.08.007

Aït Hssaine, A., and Bridgland, D. (2009). Pliocene-quaternary fluvial and aeolian records in the Souss Basin, southwest Morocco: A geomorphological model. *Glob. Planet. Change* 68 (4), 288–296. doi:10.1016/j.gloplacha.2009.03.002

Aït Hssaine, A. (2002). L'érosion des sols à Taroudant entre nature et societé. *Bull. Réseau Eros.* 21, 295–300.

Alados, C. L., and El Aich, A. (2008). Stress assessment of argan (*Argania spinosa* (L.) Skeels) in response to land uses across an aridity gradient. Translational asymmetry and branch fractal dimension. *J. Arid Environ.* 72 (4), 338–349. doi:10.1016/j.jaridenv.2007.06.015

Archibald, S., and Bond, W. J. (2003). Growing tall vs growing wide: Tree architecture and allometry of *Acacia karoo* in forest, savanna, and arid environments. *Oikos* 102, 3–14. doi:10.1034/j.1600-0706.2003.12181.x

Barbero, M., Bonin, G., Loisel, R., and Quézel, P. (1990). Changes and disturbances of forest ecosystems caused by human activities in the Western part of the Mediterranean Basin. *Vegetatio* 87, 151–173. doi:10.1007/bf00042952

Benismail, M. C., Bouzit, Z., Zabir, K., and Bouchaouch, S. (2013). "Eléments de conduite des arganiers en culture intensive: La "taille" des arbres," in *Actes du 2ème Congrès International de l'Arganier Agadir 9-11 décembre 2013* (Agadir, Morocco: ANDZOA).

Berthier, P. (1966). Les anciennes sucreries du Maroc et leurs réseaux hydrauliques. Rabat, Morocco: L'Université Mohammed V de Rabat. [dissertation thesis].

Blanco, J., Genin, D., and Carrière, S. M. (2015). The influence of Saharan agro-pastoralism on the structure and dynamics of acacia stands. *Agric. Ecosyst. Environ.* 213, 21–31. doi:10.1016/j.agee.2015.07.013

Boudy, P., and Chalot, J. P. (1935). Le rôle économique de la forêt marocaine. *Bull. Soc. Éco. Maroc. II* 8, 98–104.

Buernor, A., Amri, A., Birouk, A., Analy, C., Kehel, Z., and Aitlhaj, A. (2021). Contribution to the identification of morphological descriptors for the genetic diversity of argan tree (*Argania spinosa* L. Skeels). *Glob. J. Ecol.* 6 (1), 051–061. doi:10.17352/gje.000044

Chakir, L., Aït Hssaine, A., and Bridgland, D. (2014). Morphogenesis and morphometry of alluvial fans in the high Atlas, Morocco: A geomorphological model of the fans of the wadi beni mhammed, Souss valley. *Int. J. Environ.* 3 (3), 294–311. doi:10.3126/ije.v3i3.11090

Charrouf, Z., and Guillaume, D. (2009). Sustainable development in northern Africa: The argan forest case. *Sustainability* 1 (4), 1012–1022. doi:10.3390/su1041012

Charrouf, Z., and Guillaume, D. (2018). The argan oil project: Going from utopia to reality in 20 years. *OCL* 25 (2), D209. doi:10.1051/ocl/2018006

Chazdon, R. L. (2008). Beyond deforestation: Restoring forests and ecosystem services on degraded lands. *Science* 320, 1458–1460. doi:10.1126/science.1155365

Culmsee, H. (2005). "An assessment of sustainability from the geobotanical perspective," in *Vegetation and pastoral use in the Western High Atlas Mountains (Morocco)Publications de la Faculté des Lettres et des Sciences Humaines de Rabat. Série: Colloques et Séminairesd*. Editors M. Aït Hamza and H. Popp (Rabat, Morocco: Actes du 7eme Colloque Maroco-Alleman), 67–80.

Culmsee, H. (2004). Vegetation und Weidenutzung im Westlichen Hohen Atlas (Marokko). Eine Nachhaltigkeitsbewertung aus geobotanischer Sicht. *Diss. Bot.* 389, 1–244.

d'Oleire-Oltmanns, S., Marzolff, I., Peter, K. D., and Ries, J. B. (2012). Unmanned aerial vehicle (UAV) for monitoring soil erosion in Morocco. *Remote Sens.* 4, 3390–3416. doi:10.3390/rs4113390

Davis, D. K. (2005). Potential forests: Degradation narratives, science, and environmental policy in protectorate Morocco, 1912-1956. *Environ. Hist.* 10 (2), 211–238. doi:10.1093/envhis/10.2.211

Dendoncker, M., Brandt, M., Rasmussen, K., Taugourdeau, S., Fensholt, R., Tucker, C. J., et al. (2020). 50 years of woody vegetation changes in the Ferlo (Senegal) assessed by high-resolution imagery and field surveys. *Reg. Environ. Change* 20, 137. doi:10.1007/s10113-020-01724-4

Defaa, C., Elantry, S., El Alami, S.L., Achour, A., El Mousadik, A., and Msanda, F. (2015). Effects of Tree Shelters on the Survival and Growth of *Argania spinosa* Seedlings in Mediterranean Arid Environment. *International Journal of Ecology* 1, 6. doi:10.1155/2015/124075

Díaz-Barradas, M. C., Zunzunegui, M., Ain-Lhout, F., Jáuregui, J., Boutaleb, S., Álvarez-Cansino, L., et al. (2010). Seasonal physiological responses of *Argania spinosa* tree from Mediterranean to semi-arid climate. *Plant Soil* 337, 217–231. doi:10.1007/s11104-010-0518-8

El Alaoui, N. (1999). Paysages, usages et voyages d'*Argania spinosa* (L.) Skeels (IXe-Xe siècles). *jatba.* 41 (2), 45–79. doi:10.3406/jatba.1999.3711

FAO (2011). "Assessing forest degradation. Towards the development of globally applicable guidelines," in *Forest resources assessment* (Rome: FAO).

Faouzi, H. (2013). L'exploitation du bois-énergie dans les arganeraies: Entre soutenabilité et degradation (région des haha, haut-atlas Occidental, maroc). *com.* 262, 155–182. doi:10.4000/com.6832

Fornara, D. A., and Du Toit, J. T. (2007). Browsing lawns? Responses of Acacia nigrescens to ungulate browsing in an african savanna. *Ecology* 88 (1), 200–209. doi:10.1890/0012-9658(2007)88[200:BLROAN]2.0.CO;2

Gao, Y., Skutsch, M., Paneque-Gálvez, J., and Ghilardi, A. (2020). Remote sensing of forest degradation: A review. *Environ. Res. Lett.* 15, 103001. doi:10.1088/1748-9326/abaad7

Gharby, S., and Charrouf, Z. (2022). Argan oil: Chemical composition, extraction process, and quality control. *Front. Nutr.* 8, 804587. doi:10.3389/fnut.2021.804587

Gobbi, B., van Rompaey, A., Loto, D., Gasparri, I., and Vanacker, V. (2020). Comparing forest structural attributes derived from UAV-based point clouds with conventional forest inventories in the Dry Chaco. *Remote Sens.* 12, 4005. doi:10.3390/rs12234005

Hanan, N. P., and Anchang, J. Y. (2020). Satellites could soon map every tree on Earth. *Nature* 587, 42–43. doi:10.1038/d41586-020-02830-3

Hosier, R. H. (1993). Charcoal production and environmental degradation: Environmental history, selective harvesting, and post-harvest management. *Energy Policy* 21 (5), 491–509. doi:10.1016/0301-4215(93)90037-g

Hssaisoune, M., Boutaleb, S., Benssaou, M., Bouaakkaz, B., and Bouchaou, L. (2016). in *Physical geography, geology, and water resource availability of the souss-massa river BasinThe souss-massa river basin, Morocco*. Editors R. Choukr-Allah, R. Ragab, L. Bouchaou, and D. Barceló (Basel, Switzerland: Springer International Publishing), 27–56. doi:10.1007/698_2016_68

Jones, A., Breuning-Madsen, H., Brossard, M., Dampha, A., Deckers, J., Dewitte, O., et al. (2013). *Soil Atlas of Africa*. Luxembourg: Publications Office of the European Union.

Kirchhoff, M., Engelmann, L., Zimmermann, L. L., Seeger, M., Marzolff, I., Aït Hssaine, A., et al. (2019a). Geomorphodynamics in argan woodlands, South Morocco. *Water* 11, 2193. doi:10.3390/w11102193

Kirchhoff, M., Peter, K. D., Aït Hssaine, A., and Ries, J. B. (2019b). Land use in the Souss region, South Morocco and its influence on wadi dynamics. *Zfg_suppl.* 62, 137–160. doi:10.1127/zfg_suppl/2019/0525

Kirchhoff, M., Romes, T., Marzolff, I., Seeger, M., Aït Hssaine, A., and Ries, J. B. (2021). Spatial distribution of argan tree influence on soil properties in southern Morocco. *SOIL* 7, 511–524. doi:10.5194/soil-7-511-2021

Kiruki, H. M., van der Zanden, E. H., Malek, Ž., and Verburg, P. H. (2017). Land cover change and woodland degradation in a charcoal producing semi-arid area in Kenya. *Land Degrad. Dev.* 28, 472–481. doi:10.1002/ldr.2545

Kouami, K., Yaovi, N., and Honan, A. (2009). Impact of charcoal production on woody plant species in west Africa: A case study in Togo. *Sci. Res. Essays* 4 (9), 881–893.

Lavauden, L. (1941). Les forêts de la France. Mémoire couronné par l'Académie des Sciences colonials. *jatba.* 21 (239-240), 285–365. doi:10.3406/jatba.1941.2133

Le Polain de Waroux, Y. (2013). Environmental degradation and economic development in the argan woodlands of Aoulouz (Morocco). *Sécheresse* 24, 29–38. doi:10.1684/sec.2013.0373

Le Polain de Waroux, Y., and Lambin, E. F. (2012). Monitoring degradation in arid and semi-arid forests and woodlands: The case of the argan woodlands (Morocco). *Appl. Geogr.* 32, 777–786. doi:10.1016/j.apgeog.2011.08.005

Lefhaili, A., and Amhajar, M. (2020). *Évaluation des ressources forestières mondiales 2020*. Rome: FAO.

Lund, H. G. (2009). *What is a degraded forest? White paper prepared for FAO*. Gainesville, Virginia, USA: Forest Information Services, 39. AvaliableAt: https://www.researchgate.net/publication/280921178_What_is_a_degraded_forest (Accessed 09 13, 2021).

Lybbert, T. J., Aboudrare, A., Chaloud, D., Magnan, N., and Nash, M. (2011). Booming markets for Moroccan argan oil appear to benefit some rural households while threatening the endemic argan forest. *Proc. Natl. Acad. Sci. U. S. A.* 108 (34), 13963–13968. doi:10.1073/pnas.1106382108

Lybbert, T. J., Magnan, N., and Aboudrare, A. (2010). Household and local forest impacts of Morocco's argan oil bonanza. *Environ. Dev. Econ.* 15, 439–464. doi:10.1017/S1355770X10000136

Marzen, M., Kirchhoff, M., Marzolff, I., Aït Hssaine, A., and Ries, J. B. (2020). Relative quantification of wind erosion in argan woodlands in the Souss Basin, Morocco. *Earth Surf. Process. Landf.* 45, 3808–3823. doi:10.1002/esp.5002

Marzolff, I., Kirchhoff, M., Stephan, R., Seeger, M., Aït Hssaine, A., and Ries, J. B. (2022). Monitoring dryland trees with remote sensing. Part A: Beyond CORONA—historical HEXAGON satellite imagery as a new data source for mapping open-canopy woodlands on the tree level. *Front. Environ. Sci.* 10, 896702. doi:10.3389/fenvs.2022.896702

Marzolff, I., Stephan, R., Kirchhoff, M., Seeger, M., Aït Hssaine, A., and Ries, J. B. (2020). UAV-based classification of tree-browsing intensity in open woodlands. *EGU General Assem*. doi:10.5194/egusphere-egu2020-10301

McGregor, H. V., Dupont, L., Stuut, J.-B. W., and Kuhlmann, H. (2009). Vegetation change, goats, and religion: A 2000-year history of land use in southern Morocco. *Quat. Sci. Rev.* 28, 1434–1448. doi:10.1016/j.quascirev.2009.02.012

Médail, F., and Quézel, P. (1997). Hot-spots analysis for conservation of plant biodiversity in the mediterranean basin. *Ann. Mo. Botanical Gard.* 84 (1), 112–127. doi:10.2307/2399957

Moncrieff, G. R., Chamaillé-Jammes, S., Higgins, S. I., O'Hara, R. B., and Bond, W. J. (2011). Tree allometries reflect a lifetime of herbivory in an African savanna. *Ecology* 92 (12), 2310–2315. doi:10.1890/11-0230.1

Moncrieff, G. R., Lehmann, C. E. R., Schnitzler, J., Gambiza, J., Hiernaux, P., Ryan, C. M., et al. (2014). Contrasting architecture of key African and Australian savanna tree taxa drives intercontinental structural divergence. *Glob. Ecol. Biogeogr.* 23, 1235–1244. doi:10.1111/geb.12205

Monnier, Y. (1965). Les problèmes actuels de l'arganeraie marocaine. *Rev. For. Fr.* 11, 750–767. doi:10.4267/2042/24697

Morton, J. F., and Voss, G. L. (1987). The argan tree (*Argania sideroxylon, sapotaceae*), A desert source of edible oil. *Econ. Bot.* 41 (2), 221–233. doi:10.1007/bf02858970

Msanda, F., El Aboudi, A., and Peltier, J-P. (2005). Biodiversité et biogéographie de l'arganeraie marocaine. *Cah. Agric.* 14 (4), 357–364.

Ndegwa, G. M., Nehren, U., Grüninger, F., Iiyama, M., and Anhuf, D. (2016). Charcoal production through selective logging leads to degradation of dry woodlands: A case study from mutomo district, Kenya. *J. Arid. Land* 8 (4), 618–631. doi:10.1007/s40333-016-0124-6

Nouaim, R., Mangin, G., Breuil, M. C., and Chaussod, R. (2002). The argan tree (*Argania spinosa*) in Morocco: Propagation by seeds, cutting and *in-vitro* techniques. *Agrofor. Syst.* 54, 71–81. doi:10.1023/a:1014236025396

Ouassou, A., Amziane, T. H., and Lajouad, L. (2006). "State of natural resources. Degradation in Morocco and plan of action for desertification and drought control," in *Desertification in the mediterranean region: A security issue*. Editors W. G. Kepner, J. L. Rubio, D. A. Mouat, and F. Pedrazzini (Netherlands: Springer), 251–268.

Peter, K. D., d'Oleire-Oltmanns, S., Ries, J. B., Marzolff, I., and Aït Hssaine, A. (2014). Soil erosion in gully catchments affected by land-levelling measures in the Souss basin, Morocco, analysed by rainfall simulation and UAV remote sensing data. *Catena* 113, 24–40. doi:10.1016/j.catena.2013.09.004

Rasmussen, K., Brandt, M., Tong, X., Hiernaux, P., Diouf, A. A., Assouma, M. H., et al. (2018). Does grazing cause land degradation? Evidence from the sandy *ferlo* in northern Senegal. *Land Degrad. Dev.* 29, 4337–4347. doi:10.1002/ldr.3170

Ries, J. B. (2005). Soil erosion on abandoned fields in mediterranean Mountains – monitoring of processes and development. *J. Mediterr. Ecol.* 6 (1), 43–52.

Rocher, P. (1926). L'arganier. *Ann. Géogr.* 35 (195), 259–267. doi:10.3406/geo.1926.8452

Rueda, C. V., Baldi, G., Gasparri, I., and Jobbágy, E. G. (2015). Charcoal production in the Argentine Dry Chaco: Where, how and who? *Energy Sustain. Dev.* 27, 46–53. doi:10.1016/j.esd.2015.04.006

Saidi, M. E. M. (1995). Contribution à l'hydrologie profonde et superficielle du bassin du Souss (Maroc). Climatologie, Hydrogéologie, crues et bilans hydrologiques en milieu sub-aride. Paris, France: Université Paris IV, Sorbonne. [dissertation thesis].

Schnabel, S., Gómez Gutiérrez, A., and Lavado Contador, J. F. (2009). "Grazing and soil erosion in dehesas of SW Spain," in *Advances in studies on desertification*. Editors A. Romero Diaz, F. Belmonte Serrato, F. Alonso Sarria, and F. Lopez Bermudez (Murcia, Spain: Ediciones de la Universidad de Murcia), 725–728.

Sebbar, B., Moumni, A., Lahrouni, A., Chehbouni, A., Belghazi, T., and Maksoudi, B. (2021). Remotely sensed phenology monitoring and land-cover classification for the localization of the endemic argan tree in the southern-west of Morocco. *J. Sustain. For.* 1, 15. doi:10.1080/10549811.2021.1897018

Sedano, F., Silva, J. A., Machoco, R., Meque, C. H., Sitoe, A., Ribeiro, N., et al. (2016). The impact of charcoal production on forest degradation: A case study in tete, Mozambique. *Environ. Res. Lett.* 11, 094020. doi:10.1088/1748-9326/11/9/094020

Seif-Ennasr, M., Zaaboul, R., Hirich, A., Caroletti, G. N., Bouchaou, L., El Abidine El Morjani, Z., et al. (2016). Climate change and adaptive water management measures in Chtouka Aït Baha region (Morocco). *Sci. Total Environ.* 573, 862–875. doi:10.1016/j.scitotenv.2016.08.170

Sloan, S., Meyfroidt, P., Rudel, T. K., Bongers, F., and Chazdon, R. (2019). The forest transformation: Planted tree cover and regional dynamics of tree gains and losses. *Glob. Environ. Change* 59, 101988. doi:10.1016/j.gloenvcha.2019.101988

Vásquez-Grandón, A., Donoso, P. J., and Gerding, V. (2018). Forest degradation: When is a forest degraded? *Forests* 9, 726. doi:10.3390/f9110726

Wojterski, T. W. (1990). Degradation stages of the oak forests in the area of Algiers. *Vegetatio* 87, 135–143. doi:10.1007/bf00042950

Zunzunegui, M., Boutaleb, S., Díaz Barradas, M. C., Esquivias, M. P., Valera, J., Jáuregui, J., et al. (2017). Reliance on deep soil water in the tree species *Argania spinosa*. *Tree Physiol.* 38, 678–689. doi:10.1093/treephys/tpx152

frontiers | Frontiers in Environmental Science

TYPE Original Research
PUBLISHED 29 September 2022
DOI 10.3389/fenvs.2022.931299

OPEN ACCESS

EDITED BY
Lindsay Beaumont Hutley,
Charles Darwin University, Australia

REVIEWED BY
Abel Ramoelo,
University of Pretoria, South Africa
Niall Patrick Hanan,
New Mexico State University,
United States

*CORRESPONDENCE
Adama Lo,
loadama11@gmail.com

SPECIALTY SECTION
This article was submitted to Drylands, a section of the journal Frontiers in Environmental Science

RECEIVED 28 April 2022
ACCEPTED 07 September 2022
PUBLISHED 29 September 2022

CITATION
Lo A, Diouf AA, Diedhiou I, Bassène CDE, Leroux L, Tagesson T, Fensholt R, Hiernaux P, Mottet A, Taugourdeau S, Ngom D, Touré I, Ndao B and Sarr MA (2022), Dry season forage assessment across senegalese rangelands using earth observation data. *Front. Environ. Sci.* 10:931299. doi: 10.3389/fenvs.2022.931299

Dry season forage assessment across senegalese rangelands using earth observation data

Adama Lo[1,2]*, Abdoul Aziz Diouf[1], Ibrahima Diedhiou[2], Cyrille Djitamagne Edouard Bassène[1,3], Louise Leroux[4,5], Torbern Tagesson[6,7], Rasmus Fensholt[6], Pierre Hiernaux[8], Anne Mottet[9], Simon Taugourdeau[10,11], Daouda Ngom[3], Ibra Touré[10], Babacar Ndao[1] and Mamadou Adama Sarr[1,12]

[1]Centre de Suivi Ecologique, Dakar, Sénégal, [2]ENSA, Université Iba Der Thiam de Thiès, Thiès, Sénégal, [3]UCAD, Département de Biologie Végétale, Dakar, Sénégal, [4]CIRAD, UPR AIDA, Dakar, Sénégal, [5]AIDA, Univ Montpellier, CIRAD, Montpellier, France, [6]Department of Geosciences and Natural Resource Management, Faculty of Science, University of Copenhagen, Copenhagen, Denmark, [7]Department of Physical Geography and Ecosystem Sciences, Lund University, Lund, Sweden, [8]Pastoralisme Conseil, Caylus, France, [9]Food and Agriculture Organization of the United Nations, Animal Production and Health Division, Rome, Italy, [10]CIRAD, UMR SELMET-PPZS, Dakar, Sénégal, [11]UMR SELMET, Univ Montpellier CIRAD INRAE Institut AGRO, Montpellier, France, [12]Section de Géographie, UFR Lettres et Sciences Humaines, Université Gaston Berger (UGB), Saint-Louis, Sénégal

Strengthening of feed security in the Sahel is urgently needed given the climate change and growing human population. A prerequisite to this is sustainable use of rangeland forage resources for livestock. Many studies have focused on the assessment of rangeland resources during the rainy season, while only a few have focused on the dry season which is the longest and most demanding period for livestock in Sahelian rangelands. The objective of this study is to develop remote sensing-based models for estimating dry season forage vegetation mass. To that end, 29 vegetation indices calculated from each of the MODIS-MCD43A4 (500 m), Landsat-8 (30 m), and Sentinel-2 (10 m) satellite products were used and tested against in situ data collected during three field-measurement campaigns in 2021 at eleven monitoring sites across Senegalese rangelands. Four statistical models were tested, namely, random forest, gradient boosting machines, and simple linear and multiple linear regressions. The two main vegetation mass variables modeled from remote sensing imagery were the standing herbaceous and litter dry mass (BH) and total forage dry mass (BT) with a dry mass of woody plant leaves added to BH. Overall, Sentinel-2 data provided the best performance for the assessment of BH with multiple linear regression (R^2 = 0.74; RMSE = 378 kg DM/ha) using NDI5 (Normalized Difference Index5), GRCI (Green Residue Cover Index), SRI (Simple Ratio Index), TCARI (Transformed Chlorophyll Absorption in Reflectance Index), and DFI (Dead Fuel Index) indices. For BT, the best model was also obtained from Sentinel-2 data, including RVI3 (Ratio Vegetation Index3) (R^2 = 0.78; RMSE = 496 kg DM/ha). Results showed the suitability of combining the red, green, blue, NIR, SWIR1, and SWIR2 bands in monitoring forage availability during the dry season. Our study revealed that the spectral richness of the optical sensor systems Sentinel-2, Landsat-8, and MODIS-MCD43A4 allowed for accurate assessments of dry-season forage

mass of semi-arid rangelands. Adding to this, the high spatial and temporal resolution of Sentinel-2 satellite imagery makes this a promising data source for timely monitoring. These findings can support the monitoring of the animal feed balance in Sahelian countries and contribute to enhancing the resilience of pastoralism toward feed shortage through early warning systems.

KEYWORDS

forage dry mass, dry season, MODIS MCD43A4, Landsat-8, Sentinel-2, food security, statistical modeling, Senegalese rangelands

1 Introduction

Livestock production is the primary livelihood strategy to generate income for the Sahelian population, particularly in West Africa (Dicko et al., 2006), where many pastoral households depend on their livestock for both milk and meat production (Sayre et al., 2013). Livestock is, therefore, a strong guarantee for food security in this region (Sloat et al., 2018). Livestock income was found to be important for purchasing food, engaging in non-farm activities, and acting as a safety net in case of crop failure (Loison & Bignebat, 2017). However, the pastoral livelihood system is highly dependent on forage availability from rangelands, which is the predominant source of feed for the livestock.

Rangelands play multiple essential roles both in relation to the balance of the Sahelian ecosystem and in the lives of human populations (Hiernaux et al., 2018). Rangelands are fundamental for food security (ISRA, 2003) and play an important ecological role in allowing for improved soil fixation, carbon uptake, and biodiversity conservation (Holechek et al., 2020). However, pastoral systems in the Sahel have faced major crises since the 1970s, accentuated by climate change, increasingly threatening the region. Climate change has led to an increase in rainfall variability (Sloat et al., 2018; Zhang et al., 2017), impacting mainly the processes that control ecosystem functioning (Zhang et al., 2018). In particular, biological activity and productivity have been affected, as well as the floristic composition of herbaceous components in rangelands (Hiernaux et al., 2009; Briske et al., 2015; Delon et al., 2015; Brandt et al., 2016). Consequently, animal feeding, growth, and reproduction are all impacted (Chirat et al., 2014). Optimal use of pasture as a fodder source is vital for successful production (Otgonbayar et al., 2019), particularly in the dry season (the longest and most difficult period of the year, during which livestock can experience increasing food shortages) when the amount of forage decreases, severely impacting livestock (Jacques et al., 2014). Timely monitoring and estimation of plant vegetation mass during the dry season, therefore, are essential for forage resource management in Sahelian rangelands (Diouf et al., 2015).

Many studies have been conducted in the Sahel to improve the quantification of forage mass (Diouf et al., 2014; Diouf et al., 2015; Garba et al., 2015, Garba et al.,2017). Recently, the FAO (Food and Agriculture Organization of the United Nations) and CIRAD (*Centre de coopération internationale en recherche agronomique pour le développement*) have provided guidelines to propose a harmonized feed balance methodology and feed balance sheet that is being implemented already in five countries in the Sahel (FAO, 2020). These guidelines, in particular, recommend a better description of the available forage according to its type and its nutritional value at different periods of the year. Indeed, forage balances are often used for evaluations at different scales, such as in the context of competition between animal and human food (Mottet et al., 2017). In addition, over the past decades, food security information systems like AGRHYMET (*Centre régional de formation et d'applications agronomique, hydrologique et météorologique*) (Traore et al., 2014), SMIAR (*Système Mondial d'Information et d'Alerte Rapide*) (Jost, 1996) and specific systems to pastoral monitoring, e.g., SIG Sahel (pastoral monitoring system of action against hunger in the Sahel) (Ham & Fillol, 2012), GEOGLAM RAPP (Group on Earth Observations Global Agricultural Monitoring Rangelands and Pasture Productivity) (Guerschman et al., 2015) have shown significant progress.

Remote sensing techniques are currently used with good success to monitor vegetation mass over large areas using both Lidar and multispectral sensors (Rana et al., 2014). Jin et al. (2015) used Landsat-8 images and textural layers to estimate maize residue cover in Northeast China. Otgonbayar et al. (2019) also used Landsat-8 images to map pasture vegetation mass in Mongolia using Random Forest regression. Najaf et al. (2019) compared Sentinel-2 and Landsat-8 data to map and characterize residues of crops in the east of the Azerbaijan province (Iran). Since the 1970s, regular remote sensing monitoring of rainy-season vegetation mass has been conducted throughout the Sahel for better management of pastoral resources (Tucker et al., 1985; Diallo et al., 1991). Several parametric models have been established to assess forage vegetation mass at the end of the rainy season in the Sahel using vegetation indices such as the NDVI (Normalized Difference Vegetation Index) (Diouf & Lambin, 2001; Fensholt et al., 2004; Tucker et al., 1985). Jacques et al. (2014) tested combinations of MODIS (Moderate Resolution Imaging Spectroradiometer) bands (NBAR collection 5) to quantify forage vegetation mass during the dry season in the Sahelian zone. Their study was

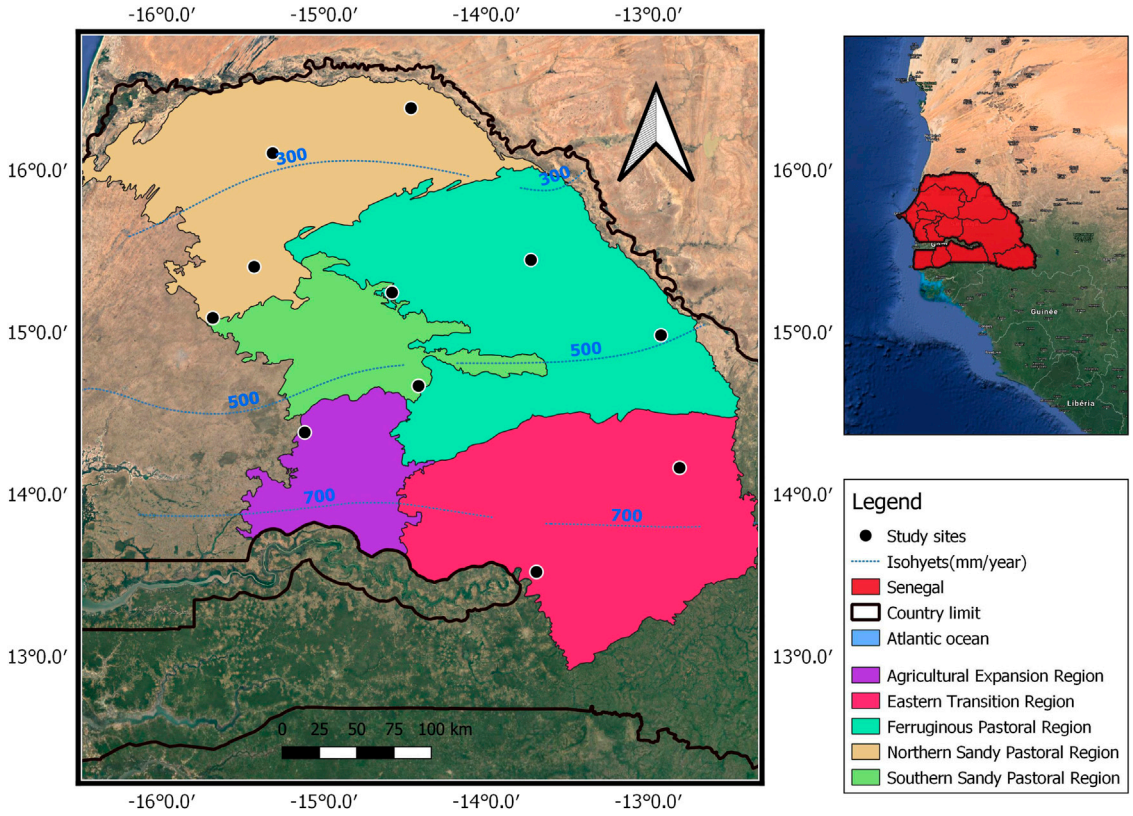

FIGURE 1
Map of the study area with isohyets corresponding to the average annual rainfall for the period 1981–2010.

based on MODIS SWIR (short-wave infrared) bands that were found to be relevant due to their sensitivity to components such as lignin, cellulose, and hemicellulose (Daughtry, 2001). Kergoat et al. (2015) used field-based radiometer measurements and MODIS images to estimate dry vegetation mass and cover fraction throughout the dry season across the Sahel using the SWIR1.6 and SWIR2.1 bands. Over the years, several other spectral indices have been suggested to estimate vegetation mass during the dry season based on different sensors, e.g., Landsat Thematic Mapper, Landsat Enhanced Thematic Mapper, MODIS, and ASTER (Advanced Spaceborne Thermal Emission and Reflection Radiometer); normalized difference indices such as Normalized Difference Index 5—NDI5 (Mcnairn & Protz, 1993); chlorophyll detection indices such as Triangular Vegetation Index—TVI (Broge & Leblanc, 2001); indices with correction for atmospheric or soil effects such as Soil-Adjusted Vegetation Index—SAVI (Huete, 1988), and vegetation indices by ratio such as Soil Tillage Index—STI (Van Deventer et al., 1997).

Taking advantage of the ever-increasing quality of satellite sensor technology and surface reflectance products readily available to the users, the main objective of this study is to estimate the forage availability during the dry season using spectral indices computed from satellite images for Senegalese rangelands. We aim to address the following research questions: what would be the most efficient approach to assess dry season vegetation mass in Senegalese rangelands from remote sensing data and what are the dynamics of vegetation mass during the dry season according to the best performing model?

2 Materials and methods

2.1 Study area

The study area covers almost the entire silvopastoral zone of Senegal, with a total area of 101.609 km^2. It is located in the Sahel belt and is characterized by two seasons: a dry season from November to June and a rainy season from July to October, each year. The climate is arid to semi-arid, with a minimum and maximum annual rainfall of 200 and 980 mm, respectively. Generally, it is during the rainy season that herbaceous

vegetation develops and reaches its maximum growth. At the end of this season, the vegetation begins to dry out. During the dry season, a thin dry herbaceous layer covers the ground. As elsewhere in the pastoral Sahel, the vegetation is dominated by annual herbaceous species, with scattered trees and shrubs (Kergoat et al., 2015).

The study area covers five ecoregions: the northern and southern sandy pastoral regions, the ferruginous pastoral region, the eastern transitional region, and the agricultural expansion region (Figure 1) (Tappan et al., 2004). Field measurements were collected at 11 monitoring sites: 10 sites of the CSE (*Centre de Suivi Ecologique*) (Diouf et al., 2015) and the Dahra field site (Tagesson et al., 2015).

2.2 Data acquisition and processing

2.2.1 Field measurement

2.2.1.1 Collection and calculation of standing herbaceous and litter dry mass

Standing herbaceous dry mass was collected during three field campaigns in the 2021 dry season (January 31 to February 10; March 25 to April 04; May 15 to May 25) following the sampling protocol of Kergoat et al. (2015) at the 11 monitoring sites. At each site, we used a 500-m transect subdivided into 500 plots of 1 m^2. Each of the 500 1 m^2 plots was visually classified into one of the four levels of productivity; bare soil, low-, medium-, and high-level productivity. Bare soil was assumed to have no dry mass, and randomly, three plots were selected in the low level, six plots in the medium level, and three plots in the high level. At each of these 12 plots, geographic coordinates, the nadir pointing vertical photos taken at 1.2 m height above the top of the vegetation, and species composition were recorded. Also, the dominant species was recorded (from the contribution of each herbaceous species to the cover in a given plot). Then, within each of these 12 plots, aboveground vegetation mass was cut and weighed to obtain the fresh mass. Litter was also collected and weighed separately. At the Dahra site, the collection protocol was similar to that of the other sites, but the sampling plots followed, instead, two perpendicular transects of 250 m as proposed by Mbow et al. (2013). All samples were thereafter dried at 80°C for 48 h and weighed to retrieve the dry weight mass (DM). The dry matter rate was estimated as the ratio of DM to fresh mass.

The resulting DM was then incorporated into the following equation to calculate the standing herbaceous dry mass (SBH) at the site level:

$$SBH = \sum_{i=1}^{3} \mathrm{FM}_i * \mathrm{ani} * \mathrm{ms} * 10 \quad (1)$$

where ***SBH*** is the total standing herbaceous dry mass of the site (kg DM/ha), ***FMi*** is the average fresh mass of the production level (i) measured in the field (g/m^2), ***ani*** is the fraction of occurrence of the specific productivity level (i) along the 500 m transect, ***ms*** is the dry matter rate (the ratio of DM to fresh mass), and 10 is the conversion factor of g/m^2 to kg/ha.

This weighting was not applied for litter mass because it did not vary between the productivity levels. The litter mass was calculated taking into account the percentage of bare soil (BS) using the following formula:

$$Lit = \sum_{i=1}^{12} \frac{M.lit * ms}{12} * (1 - \mathrm{BS}) * 10 \quad (2)$$

where ***Lit*** is the total dry mass of the litter for the site (kg DM/ha), ***M.lit*** is the mass of the litter per plot (g/m^2), ***ms*** is the dry matter rate, ***BS*** is the percentage of bare soil, and 10 was used to convert g/m^2 to kg/ha.

2.2.1.2 Collection and calculation of the woody foliage mass

Foliage mass of woody plants was also collected during the three campaigns. An inventory of dominant tree species was made in two circular plots with the center located at 200 and 400 m from the beginning of the 500-m transects (Supplementary Figure S1). For the Dahra site, four circular plots were used, instead, located at the beginning and end of the perpendicular transects due to the difference between the sampling schemes. The radius of the plots was 28 m in the four northernmost sites and 20 m in the remaining sites, taking into account vegetation density which is higher in the southern sites. For each of the dominant woody species, five twigs with 2-cm diameter were cut, defoliated, and leaves (only) were weighed. The samples of around 200 g were then dried in an oven at 80°C for 48 h, and foliage was again weighted to obtain DM. The site-level foliage dry mass of woody plants was then calculated as follows:

$$BL = \sum_{i=1}^{n} \left(\frac{Mv * ms}{Mss}\right) * \left(aC^b\right) * \left(\frac{1}{S}\right) \quad (3)$$

where ***BL*** is the sum of foliage dry mass of woody plants in kg DM/ha, **n** is the number of dominant species listed, ***Mv*** is the average weight of fresh foliage mass (g) of the five twigs for each species, ***ms*** is the dry matter rate, ***Mss*** is the average standard dry foliage mass of five twigs for each woody species (g) (Hiernaux, 1980), $\boldsymbol{aC^b}$ is the foliage dry mass produced for all trees and shrubs for each species in kg where a and b are species dependent constants (Diouf & Lambin, 2001), ***C*** is the base circumference of the trunk at 1.3 m above the ground measured on the ground in cm, and S is the area of the circular sample plots in ha.

Finally, the total forage dry mass (BT) of each site was calculated by adding the standing herbaceous dry mass (SHB), litter dry mass (Lit), and foliage dry mass (BL). The herbaceous dry mass (BH) is the sum of the standing herbaceous dry mass (SBH) and litter dry mass (Lit).

TABLE 1 Description of the sensors used in the study.

Sensor	Landsat-8/OLI central wavelengths		Sentinel-2A/MSI central wavelengths		MODIS/TERRA-AQUA central wavelengths	
Launch date	2013		2015		1999	
Spatial resolution	30 m		10 m/20 m/60 m		250 m/500 m/1000 m	
Temporal resolution	16 days		5–10 days		1–2 days	
Spectral bands and wavelengths (micrometer)	B1 Aerosols	0.443	B1 Coastal Aerosols	0.443	B1 Red	0.659
	B2 Blue	0.482	B2 Blue	0.492	B2 NIR	0.865
	B3 Green	0.561	B3 Green	0.560	B3 Blue	0.470
	B4 Red	0.655	B4 Red	0.665	B4 Green	0.555
	B5 NIR	0.865	B5 VRedEdge	0.704	B5 NIR	1.240
	B6 SWIR1	1.609	B6 VRedEdge	0.740	B6 SWIR1	1.640
	B7 SWIR2	2.200	B7 VRedEdge	0.783	B7 SWIR2	2.130
			B8 NIR	0.833		
			B8A Narrow NIR	0.865		
			B9 Water vapor	0.945		
			B10 SWIR Cirrus	1.373		
			B11 SWIR 1	1.614		
			B12 SWIR 2	2.202		

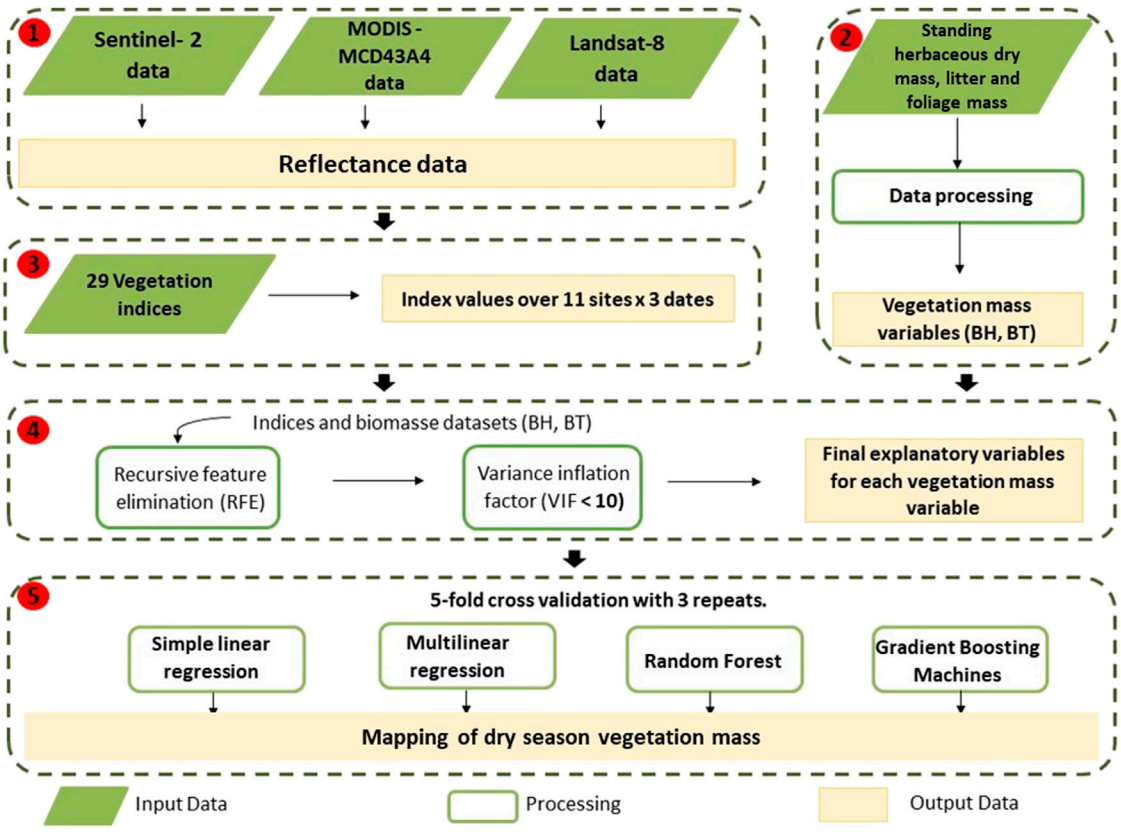

FIGURE 2
Flowchart of the main steps of the study with 1) satellite data pre-processing, 2) preparation of field observed BH and BT, 3) satellite index calculation, 4) selection of explanatory variables, and 5) parameterization and validation of models.

2.2.2 Satellite image acquisition and processing

Three different satellite data sets were used to study their suitability for dry season vegetation mass monitoring: MODIS, Landsat-8, and Sentinel-2 (Table 1). The acquisition dates of the images were chosen to correspond, as closely as possible, to the dates of the field campaigns.

2.2.2.1 Moderate-resolution imaging spectroradiometer

The MODIS-NBAR (Nadir BRDF-Adjusted Reflectance) collection 6 (MCD43A4) product with 500-m spatial resolution (Schaaf & Wang, 2015) was downloaded with the MODIStsp platform (Busetto & Ranghetti, 2016). The NBAR product with a temporal resolution of 1–2 days was chosen because reflectance is less-affected by view angle effects. The quality layer from the MCD43A2 product was used to exclude pixels with clouds (i.e., quality value > 2) (Jacques et al., 2014). The seven bands (bands 1–7) were used to calculate spectral indices.

2.2.2.2 Landsat-8

With a spatial resolution of 30 m and a temporal resolution of 16 days, Landsat-8 OLI (operational land imager) data collection 2 level 2 (EROS, 2020) was downloaded from the Earth Explorer platform. These images were geometrically and atmospherically corrected prior to downloading. Images with less than 10% cloud cover were downloaded following a visual inspection to ensure that clouds were not present over the specific study sites.

2.2.2.3 Sentinel-2

Sentinel-2 L2A images, atmospherically corrected (Drusch et al., 2012) with less than 5% clouds, were downloaded from the Copernicus Open Access Hub. The spatial resolution of Sentinel-2 is varying between 10 and 60 m, and the temporal resolution is 5 days. All bands were resampled (nearest neighbor method) to a 10-m spatial resolution using the Sentinel Application Platform (SNAP).

2.2.3 Spectral indices

Initially, a literature review was conducted in order to list the most suitable remote sensing indices for monitoring dry vegetation and crop residues. Then, from this review, several indices for green vegetation were suggested to be very useful for mapping dry vegetation and crop residues and were subsequently used in this study. These indices were also used to capture the chlorophyll activity left on the vegetation at the beginning of the dry season. In total, 29 spectral indices were calculated for monitoring foliage dry mass during the dry season (Supplementary Table S1). These indices were grouped into four categories: 1) normalized difference vegetation indices, 2) chlorophyll detection indices, 3) vegetation indices with correction for atmospheric or soil effects, and 4) vegetation indices by ratio. All indices were averaged for each site within a 500-meter buffer.

2.3 Methods

The overall approach for developing the models to monitor dry season forage mass followed five processing steps is given in Figure 2.

2.3.1 Selection of explanatory variables of vegetation mass

A performance test was applied to identify the most relevant satellite variables and eliminate non-performing spectral indices for predicting each of the dry mass variables (BH (herbaceous dry mass) and BT (total forage dry mass)). To do this, the recursive feature elimination algorithm (RFE) was used (Kuhn et al., 2021). To assess and select the best collection of spectral indices, the random forest classifier was used with 5-fold cross-validation. Additionally, the variance inflation factor (VIF) was applied to detect the collinearity or dependence between the spectral indices (Thompson et al., 2017) and avoid its amplifying effect on the standard error of the model (Miles, 2014). The VIF uses multiple regression in order to eliminate satellite variables that could impact the performance of the models, e.g., create overfitting. A VIF threshold >10 (only predictors with a VIF less than or equal to 10 were retained) was used to exclude collinear spectral indices from the dataset (Midi & Bagheri, 2010) and retrieve the optimal number of variables used to build the final models.

$$VIF = \frac{1}{1 - R^2} \tag{4}$$

where R^2 is the coefficient of determination from a multiple linear regression with the predictor variable against the other independent variables that gives the proportion of the variance in the outcome associated with the explanatory variables.

2.3.2 Model approaches

Four regression modeling approaches were used to estimate the dry season forage vegetation mass across the study area: two linear regression models (simple and multiple) and two machine learning algorithms (random forest and gradient boosting machines). Independent variables were BH and BT, and the spectral indices checked for collinearity were used as explanatory variables. Since the dataset available for this study was relatively small, the k-fold cross-validation method was applied with five folds and three repetitions (Kuhn et al., 2021). For each modeling approach, the different possible combinations that could emerge from the final base obtained after the VIF test for each vegetation mass variable (BH and BT) have been assessed. Each combination (a minimum of two for ordinary least squares (OLS) models and a minimum of three for machines learning (ML) models) constituted a separate model. In total, for all types of images, 619 models were tested for BH and 987 models for BT (Supplementary Table S2).

TABLE 2 List of the vegetation indices used in the development of the models.

Indices	Definition	Formula	Source
NDI5	Normalized Difference Vegetation Index	$NDI5 = \frac{(NIR-SWIR1)}{(NIR+SWIR1)}$	Rouse et al. (1974)
DFI	Dead Fuel Index	$DFI = 100^{*}(1 - \frac{SWIR2}{SWIR1})^{*}(\frac{Red}{NIR})$	Cao et al. (2010)
TCARI	Transformed CARI	$TCARI = 3^{*}[(NIR - Red) - 0,2(NIR - Green)^{*}(\frac{NIR}{Red})]$	Haboudane et al. (2002)
GRCI	Green Residue Cover Index	$GRCI = \frac{(Green-Blue)}{(Green+Blue)}$	Kavoosi et al. (2020)
SRI	Simple Ratio Index	$SRI = \frac{NIR}{Red}$	Rondeaux et al. (1996)
RVI2	Ratio Vegetation Index2	$RVI2 = \frac{Green}{Red}$	Jordan, (1969)
CRC	Crop Residue Cover	$CRC = \frac{SWIR1-Green}{SWIR1+Green}$	Sullivan et al. (2006)
RVI3	Ratio Vegetation Index3	$RVI3 = \frac{Green}{Blue}$	Jordan (1969)

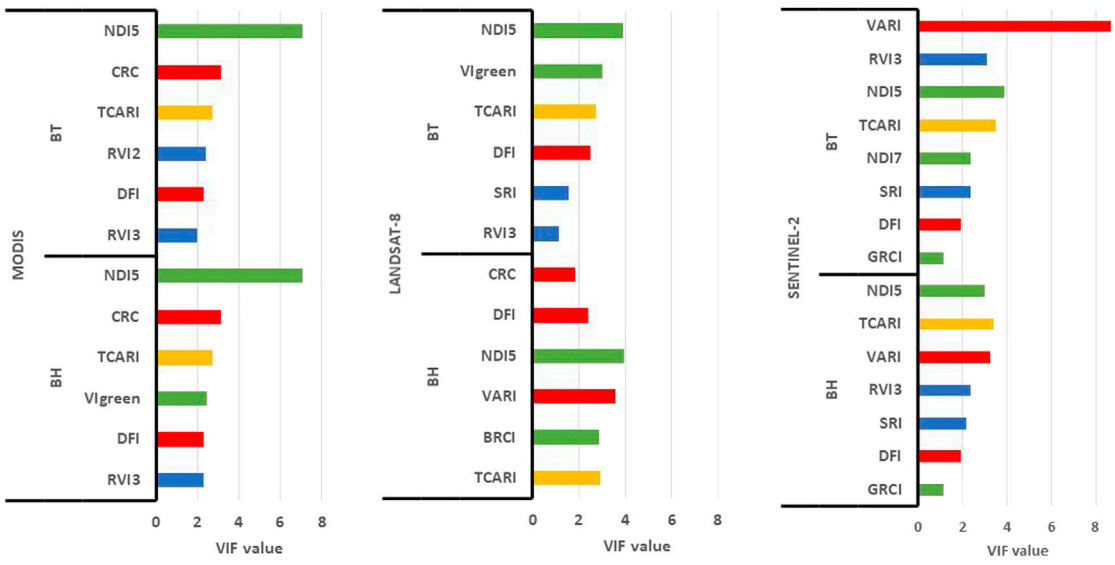

FIGURE 3
Selected explanatory variables after performance and collinearity tests. The included variables are colored as follows: vegetation indices by normalized difference (green), chlorophyll detection indices (yellow), vegetation indices with correction for atmospheric or soil effects (red), and vegetation indices by the ratio (blue).

2.3.2.1 Random forest

To run the random forest (RF) model (Liaw & Wiener, 2002), the number of features to use at each split (mtry) was set to the half number of included explanatory variables, while the number of trees to grow (ntree) were set to 1,000. All combinations starting at three up to the total number of explanatory variables retained after the RFE and VIF tests were tested for each independent variable. The model with the lowest RMSE was selected and optimized based on these three input parameters: mtry, ntree, and minimum node size. The final result of the optimization used the following values: 1 for mtry, 100 for ntree, and 2 for minimum node size (Supplementary Table S3). The optimization was carried out by rescaling the model with the prediction variables of the best model. By iteration, the best mtry was integrated as a parameter of the model, and the latter was re-run to search for the best ntree. Then, the best ntree and mtry were integrated with the parameters of the model to search for the best node size.

2.3.2.2 Gradient boosting machines

Several combinations of explanatory variables (starting at three) were also tested with gradient boosting machines (GBM) (Ridgeway, 2020). The model run and optimization involved the total number of trees (ntrees), the maximum depth of variable interactions (interaction depth), the learning rate (shrinkage), and the minimum number of observations in

TABLE 3 Model performance for estimating dry season herbaceous dry mass (BH) and total ecosystem foliage dry mass (BT) (upper and lower row, respectively) for the three satellite sensor systems.

	Model	Dry mass variable	R^2	RMSE (kg DM/ha)	RRMSE (%)	NSE
Landsat-8	MLS	BH	0.37	569	40	0.30
		BT	0.45	906	45	0.32
	MML	BH	0.62	437	30	0.70
		BT	0.77	526	26	0.82
	RF	BH	0.63	476	33	0.48
		BT	0.64	688	34	0.52
	GBM	BH	0.68	450	31	0.90
		BT	0.63	622	31	0.97
MODIS	MLS	BH	0.42	575	40	0.33
		BT	0.51	923	46	0.25
	MML	BH	0.65	414	29	0.70
		BT	0.69	551	27	0.77
	RF	BH	0.57	482	34	0.45
		BT	0.64	694	35	0.49
	GBM	BH	0.55	469	33	0.81
		BT	0.69	605	30	0.76
Sentinel-2	MLS	BH	0.43	567	39	0.30
		BT	0.36	901	45	0.22
	MML	BH	0.74	378	26	0.76
		BT	0.78	496	25	0.81
	RF	BH	0.45	544	38	0.28
		BT	0.53	816	41	0.27
	GBM	BH	0.53	476	33	0.92
		BT	0.57	712	35	0.97

the tree's terminal nodes (n. minobsinnode) (Supplementary Table S4). After the iteration process, the GBM model with the lowest RMSE was obtained using the following values: ntrees (200), interaction. depth (3), shrinkage (0.1), and n. minobsinnode (3).

2.3.2.3 Linear regression

Simple linear regression (MLS) was carried out for each of the vegetation indices, and multiple linear regressions (MML) were tested for all possible combinations of vegetation indices. A comparison between the linear model developed by Jacques et al. (2014) and the one developed in this study was carried out for the herbaceous dry mass estimation (Supplementary Table S5).

2.3.3 Assessment of model performance

Four parameters were used to assess the accuracy of the models: coefficient of determination (R^2), root mean square error (RMSE), relative root mean square error (RRMSE), and Nash Sutcliff Efficiency (NSE). NSE shows the relative magnitude of the residual variance compared to the measured data variance and varies in the range of $-\infty$ to 1 (Nash & Sutcliffe, 1970). A value of NSE = 1 reflects that between the modeled and measured values, there is a perfect match (Nadiri et al., 2020).

The residuals of the best model for each vegetation mass variable and each sensor were also used to analyze existing variability over the dry season (Supplementary Figure S2).

2.3.4 Upscaling of dry season vegetation mass

The indices included in the best models for BH and BT were computed across the study area using the Google Earth Engine platform (Gorelick et al., 2017) for the three study periods (January–February, March–April, and May). For each composite image (MODIS-MCD43A4, Landsat-8, and Sentinel-2), cloud masks were applied to remove residual noises from the final output images.

TABLE 4 Best model and sensor for estimating dry season herbaceous dry mass (BH) and total ecosystem foliage dry mass (BT) in the silvopastoral zone in Senegal.

Best model	Dry mass variable	R^2	RMSE (kg DM/ha)	RRMSE (%)	NSE	Sensor
MML	BH	0.74	378	26	0.76	Sentinel-2
	BT	0.78	496	25	0.81	

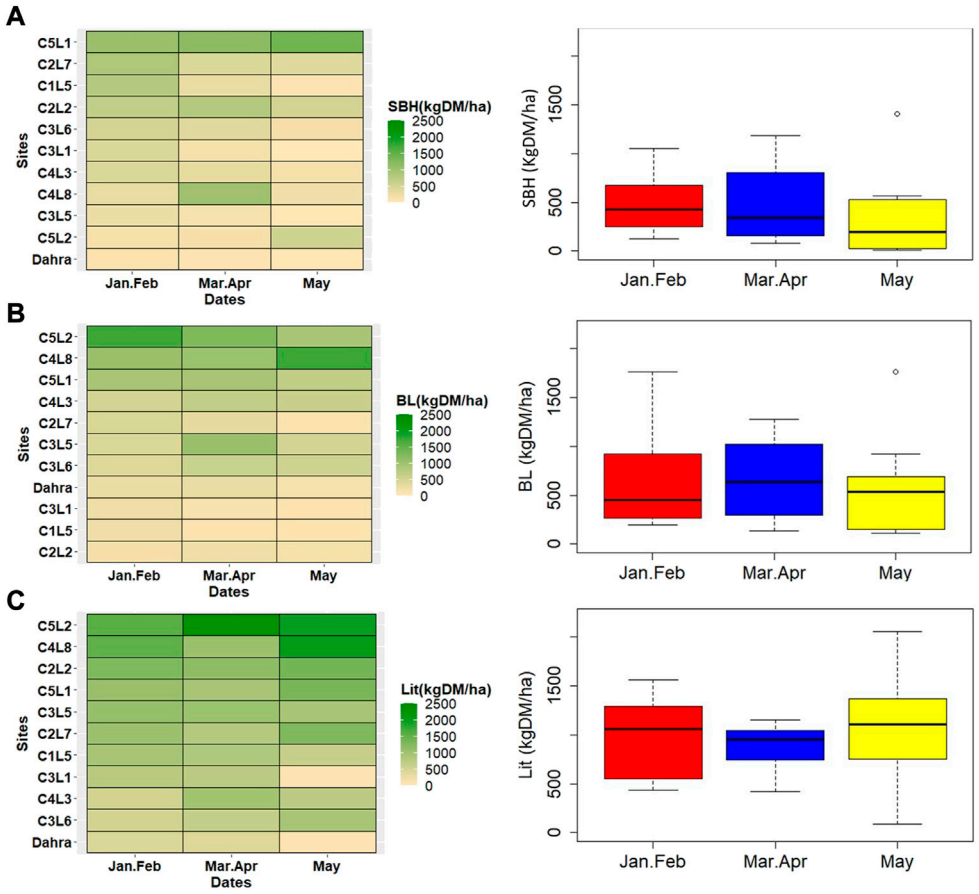

FIGURE 4
Variation of field observed SBH **(A)**, BL **(B)**, and Lit **(C)** during the dry season. Jan.Feb = January–February, Mar.Apr = March–April. The values in the first column of heatmaps were sorted in descending order from the top to bottom.

3 Results

3.1 Vegetation index relation with dry season forage variability

After the exploratory analysis of the explanatory variables (i.e., RFE and VIF test), eight of the 29 vegetation indices were selected for development of the models (Table 2). It is noted that TCARI, DFI, and NDI5 were retained for each of the dry mass variables and for all sensors (Figure 3). The explanatory variables for each dry mass variable and each sensor contain at least one index belonging to the four-index group with a dominance of normalized difference vegetation indices and vegetation indices with correction for atmospheric or soil effects (Figure 3).

3.2 Models adapted for monitoring vegetation dry mass variables

On the basis of R^2, RMSE, RRMSE, and NSE, the multilinear model (MML) showed the best performance among the four tested models for the estimation of both BH and BT (Table 3) and for all

sensor types (Supplementary Tables S6–S8). The multilinear model applied to Sentinel-2 was found to be the best model for estimating dry vegetation mass in the silvopastoral zone of Senegal (Table 4).

3.3 Dry season dynamics in herbaceous dry mass and total foliage dry mass

3.3.1 Field observed variation during the dry season

A boxplot analysis (Figure 4) shows that herbaceous standing dry mass (SHB) showed a decrease over the dry season, while the litter dry mass (Lit) increased slightly between January and May. An increase in foliage dry mass (BL) was observed between January and April and then decreased between April and May.

Spatiotemporal analysis from the heatmap (Figure 4) showed a spatial variability with BL with an increase along a north–south gradient. On the other hand, temporal variability is observed for SBH.

3.3.2 Spatialization maps for BH and BT with the best Sahelian model outputs

The multilinear model applied on a Sentinel-2 image was found to be effective in predicting BH and BT data over the entire study area with the following model equations:

$$BH = 3326.60 + 16221.51*\mathbf{NDI5} - 721.34*\mathbf{GRCI} + 84.72*\mathbf{DFI} - 19074.62*\mathbf{TCARI} + 1638.59*\mathbf{SRI} \quad (5)$$

$$BT = 5684.40 + 20292.26*\mathbf{NDI5} + 4363.24*\mathbf{SRI} - 30111.55*\mathbf{TCARI} + 102.60*\mathbf{DFI} - 646.06*\mathbf{GRCI} - 2531.03*\mathbf{RVI3} \quad (6)$$

The extrapolated results with these best models reflected, through the scatterplots, that a strong and significant relationship exists between the observed and predicted dry mass by the model. This implies that these models are capable of predicting total dry mass spatially (Figure 5) and temporally at 10-m resolution (Figure 6).

4 Discussion

4.1 Best approach to estimate dry season vegetation mass

4.1.1 Most suited sensor(s) and indices for monitoring dry season vegetation mass

Sentinel-2 data generally yielded better performances for BH and BT estimation (Table 3) with a finer spatial resolution and a higher capacity to differentiate signals from the woody and herbaceous components.

Indices such as NDI5, DFI, and TCARI are essential for monitoring of dry vegetation mass (Figure 3). These indices used the red, green, blue, NIR, SWIR1, and SWIR2 bands. In particular, the SWIR1 and SWIR2 bands play an important role in forage estimation with low model accuracy when omitted. Kergoat et al. (2015) showed the relevance of using the SWIR1 and SWIR2 bands for dry season vegetation mass estimation in the Sahel. Similarly, Kavoosi et al. (2020) showed that indices based on SWIR1 and SWIR2 bands were able to provide more accurate predictions of crop residue cover. In fact, without the SWIR (i.e., 2100 nm region), the estimation of crop residues on the soil surface likely provides a high RMSE as shown by Najaf et al. (2019). This is mainly due to the absorption signature of the cellulose which increases in the SWIR region, around 2,100 nm (Daughtry et al., 2004).

Previous studies have reported the relevance of other indices, also tested in this study, to quantify dry vegetation mass. For example, Kavoosi et al. (2020) identified the DFI as the most suitable for monitoring the cover of crop residues, and it was found here to be an important variable for estimation of both BH and BT. Therefore, we can confirm its relevance in monitoring dry vegetation in semi-arid areas. According to Ji et al. (2020), the red and NIR bands from Sentinel-2 were identified to be effective in improving the accuracy of non-photosynthetic vegetation cover fraction estimation. Kowalski et al. (2022) pointed out that non-photosynthetic vegetation often had a stronger reflectance increase in the red edge to the NIR wavelength region (different from soil reflectance). Furthermore, we suggest the use of these indices that differentiate the soil from non-photosynthetic vegetation for dry mass monitoring, and as stated by Verrelst et al. (2015), there is no reason to limit the estimation to two-band indices when multiple bands are available.

This study also showed that a saturation of the estimates occurs at thresholds equal to 2,200 kg DM/ha for BH and 3,000 kg DM/ha for BT regardless of the sensor type (Supplementary Figure S3). Our results are thereby in line with those of Jacques et al. (2014) who showed a saturation of the herbaceous mass estimation with values above 2,500 kg DM/ha using the STI based on SWIR1 and SWIR2 bands from MODIS.

4.1.2 Selection of modeling approach

The multilinear regression model (the best model of this study) (Table 3) showed better performance than the random forest and gradient boosting machines models, regardless of sensor type. The weaker performance of the machine learning algorithms could be explained by the small size of the dataset (33 samples). In fact, Li et al. (2014) showed that the larger the dataset, the better the performance of the random forest model in their study on improving the linkage affinity prediction of scoring functions on the substitution of random forest for linear regression. This conclusion was also reached by Ding et al. (2020) in their study on the comparison of empirical regressions and machine learning methods for crop residue cover estimation using Sentinel-2 data, as well as by Wang et al. (2016) in their study on wheat biomass estimation using the random forest regression algorithm and remote sensing data.

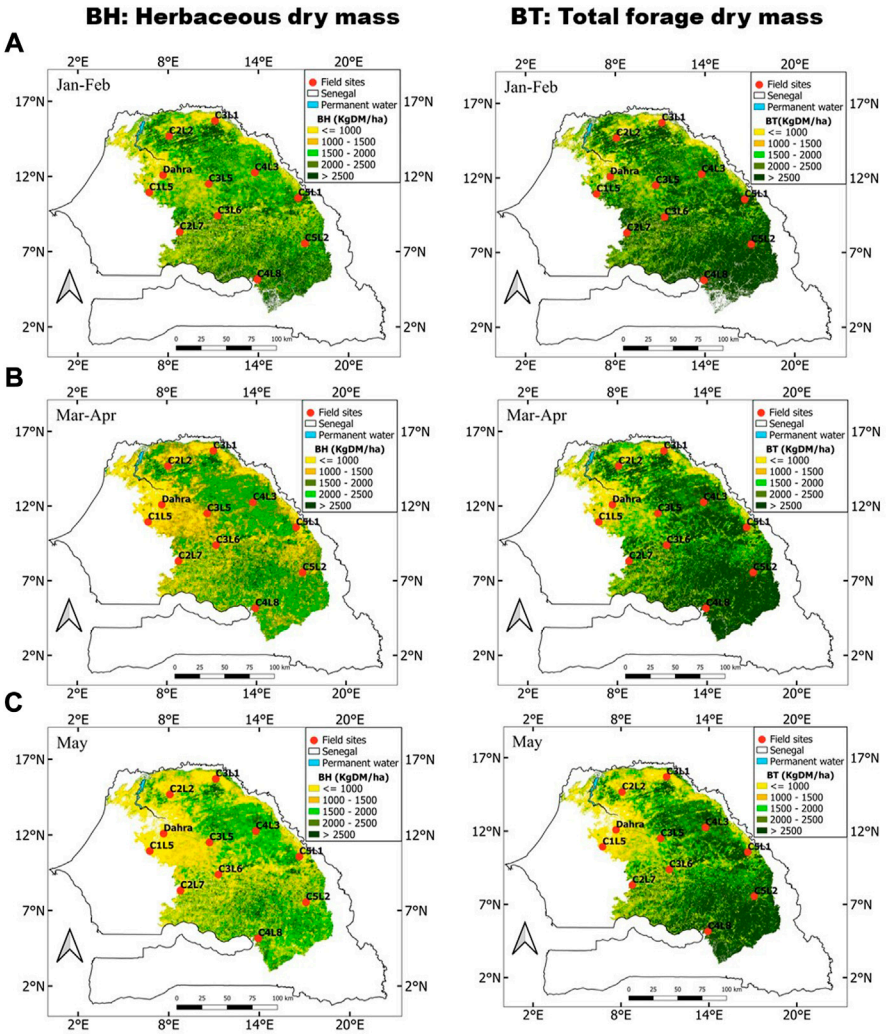

FIGURE 5
Prediction maps of herbaceous dry mass and total forage dry mass in **(A)** January–February, **(B)** March–April, and **(C)** May with the best model to estimate BH and BT.

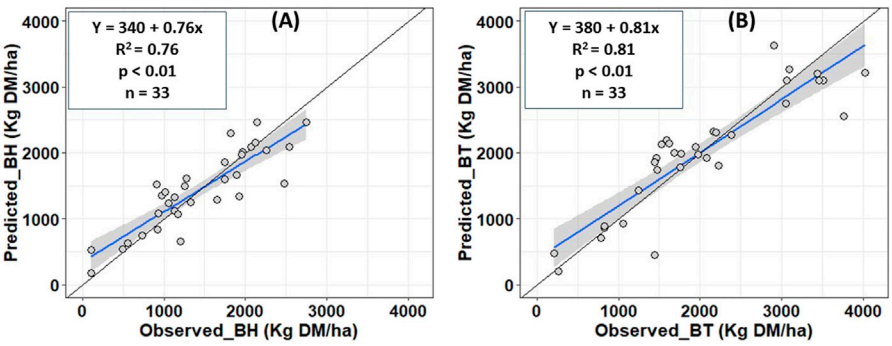

FIGURE 6
Scatterplot between observed and predicted (data over all the three periods) data using the best model for each dry mass variable with **(A)**: BH and **(B)**: BT.

They all reported that the accuracy of the machine learning approaches was improved when increasing the training sample size relative to the total sample population.

4.2 Dynamics of vegetation mass throughout the dry-season

Our results showed a diminution in forage dry mass during the dry season, from January to May (Figure 5). These results are consistent with those of Sanon et al. (2015) who showed that the availability of herbaceous forage and grazed forage was significantly reduced during the dry season in their study on the seasonal dynamics of herbaceous forage production in Sahelian pastures used by domestic ruminants. Furthermore, Sanon et al. (2015) indicated that, in addition to biological aging, this reduction in dry mass during the dry season could be accentuated by livestock trampling and human activities such as cutting wood for charcoal and cutting certain herbaceous species such as *Andropogon gayanus* to obtain straw or bushfire.

4.3 Comparison of the best herbaceous dry mass estimation model with Jacques's model on moderate resolution imaging spectroradiometer images

The STI index has been proven suitable to monitor dry vegetation mass in the Gourma region of Mali but is potentially suitable for many other semi-arid areas (Jacques et al., 2014).

The simple linear model developed in this study using only the STI index and the one developed by Jacques et al. (2014) based on MODIS images (Supplementary Figure S4) showed a similar correlation coefficient of 0.53. The dry vegetation mass estimation model of the Malian Gourma (Jacques et al., 2014) was implemented through a set of field measurements (26 sites) along the 1-km transect and over the 7-year period (2004–2011). In their study, the best results were obtained with indices such as the short-wave infrared bands (R^2 = 66%, n = 126, RRMSE = 44%, index = STI). In contrast to several studies that reported the relevance of the STI for estimating dry vegetation mass such as that by Jacques et al. (2014) or Kergoat et al. (2015), this study showed that this index (Supplementary Table S5) was not the most suited for monitoring dry vegetation mass in Senegalese rangelands (R^2 = 42%, RRMSE = 39%).

5 Conclusion

The performance assessment of estimation models of dry season forage dry mass through several modeling approaches and vegetation indices derived from three widely used satellite sensor systems (i.e., MODIS, Landsat-8, and Sentinel-2) allowed the following conclusions:

- Sentinel-2 overall provides better estimates of herbaceous dry mass (BH) and total forage dry mass (BT) in silvopastoral ecosystems in Senegal;
- MODIS and Landsat-8 data could also be used for predicting BH and BT in the study area with nearly similar performance;
- a multilinear model is preferred for estimating dry season vegetation when only limited numbers of sample points are available;
- The indices NDI5, DFI, GRCI, TCARI, SRI, and RVI3 are all relevant to estimate BH and BT in Sahelian drylands.

This study demonstrated that dry season vegetation mass could be accurately predicted (RRMSE = 26%) using multilinear models and satellite indices that include several spectral bands covering both visible, near-infrared, and shortwave infrared wavelengths. Most countries in the Sahel region calculate feed balances only once a year, using estimated forage dry mass toward the end of the rainy season. This constitutes a shortcoming as such assessment offers increasingly less detailed information on the feed status and potential forage deficits as the dry season, lasting up to 9 months, progresses. It also hinders the efficiency of response measures potentially to be taken to alleviate such deficit. While several countries in West Africa are currently improving their national feed balance inventory tools, better estimates of available dry mass over the year and during the dry season, in particular, are timely signs of progress. As a perspective to this study, we recommend further increasing the number of sampling sites, taking into account the size of the ecoregions as well as performing further analysis of the impact of fires on the satellite-based estimation of forage resources.

Data availability statement

The raw data supporting the conclusions of this article will be made available by the authors, without undue reservation.

Author contributions

AL, AD, LL, and CB contributed to the research design, acquisition, analysis, interpretation of data, and writing of the manuscript. ST, PH, RF, TT, and BN provided comments and suggestions on the acquired data and data analysis. All authors contributed to the final version of the manuscript.

Funding

This research was financed by "Carbon sequestration and greenhouse gas emissions in (agro) silvopastoral ecosystems in the Sahelian CILSS states" (CaSSECS) project (FOOD/2019/410-169) supported by European Union under the "Development Smart Innovation through Research in Agriculture" (DeSIRA) Initiative. TT was additionally funded by the Swedish National Space Agency (SNSA 2021-00144; 2021-00111) and FORMAS (Dnr. 2021-00644).

Conflict of interest

The authors declare that the research was conducted in the absence of any commercial or financial relationships that could be construed as a potential conflict of interest.

Publisher's note

All claims expressed in this article are solely those of the authors and do not necessarily represent those of their affiliated organizations, or those of the publisher, the editors, and the reviewers. Any product that may be evaluated in this article, or claim that may be made by its manufacturer, is not guaranteed or endorsed by the publisher.

Supplementary material

The Supplementary Material for this article can be found online at: https://www.frontiersin.org/articles/10.3389/fenvs.2022.931299/full#supplementary-material

SUPPLEMENTARY TABLE S1
List of the 29 vegetation indices used in this study.

SUPPLEMENTARY TABLE S2
Number of models tested to estimate BH and BT.

SUPPLEMENTARY TABLE S3
Optimization parameters used with random forest.

SUPPLEMENTARY TABLE S4
Optimization parameters used with Gradient Bosting Machines.

SUPPLEMENTARY TABLE S5
Simple linear models for the assessment of the herbaceous biomass during the dry-season developed by Jacques et al. (2014) and in this study, both using the STI index based on MODIS and the best model using Sentinel-2 images.

SUPPLEMENTARY TABLE S6
Performance of MLS, MML, RF and GBM models with Landsat-8.

SUPPLEMENTARY TABLE S7
Performance of MLS, MML, RF and GBM models with MODIS.

SUPPLEMENTARY TABLE S8
Performance of MLS, MML, RF and GBM models with Sentinel-2.

References

Brandt, M., Hiernaux, P., Tagesson, T., Verger, A., Rasmussen, K., Diouf, A. A., et al. (2016). Woody plant cover estimation in drylands from Earth Observation based seasonal metrics. *Remote Sens. Environ.* 172, 28–38. doi:10.1016/j.rse.2015.10.036

Briske, D. D., Joyce, L. A., Polley, H. W., Brown, J. R., Wolter, K., Morgan, J. A., et al. (2015). Climate-change adaptation on rangelands: Linking regional exposure with diverse adaptive capacity. *Front. Ecol. Environ.* 13 (5), 249–256. doi:10.1890/140266

Broge, N. H., and Leblanc, E. (2001). Comparing prediction power and stability of broadband and hyperspectral vegetation indices for estimation of green leaf area index and canopy chlorophyll density. *Remote Sens. Environ.* 76 (2), 156–172. doi:10.1016/S0034-4257(00)00197-8

Busetto, L., and Ranghetti, L. (2016). MODIStsp: an R package for automatic preprocessing of MODIS Land Products time series. *Comput. Geosci.* 97, 40–48. doi:10.1016/j.cageo.2016.08.020

Cao, X., Chen, J., Matsushita, B., and Imura, H. (2010). Developing a MODIS-based index to discriminate dead fuel from photosynthetic vegetation and soil background in the Asian steppe area. *Int. J. Remote Sens.* 31 (6), 1589–1604. doi:10.1080/01431160903475274

Chirat, G., Groot, J. C. J., Messad, S., Bocquier, F., and Ickowicz, A. (2014). Instantaneous intake rate of free-grazing cattle as affected by herbage characteristics in heterogeneous tropical agro-pastoral landscapes. *Appl. Animal Behav. Sci.* 157, 48–60. doi:10.1016/j.applanim.2014.06.003

Daughtry, C. S. T. (2001). Agroclimatology: Discriminating crop residues from soil by shortwave infrared reflectance. *Agron. J.* 93 (1), 125–131. doi:10.2134/agronj2001.931125x

Daughtry, C. S. T., Hunt, E. R., and Mcmurtrey, J. E. (2004). Assessing crop residue cover using shortwave infrared reflectance. *Remote Sens. Environ.* 90, 126. doi:10.1016/j.rse.2003.10.023

Delon, C., Mougin, E., Serça, D., Grippa, M., Hiernaux, P., Diawara, M., et al. (2015). Biogenic NO emissions from soils in a Sahelian rangeland Modelling the effect of soil moisture and organic matter degradation on biogenic NO emissions from soils in Sahel rangeland (Mali) Biogenic NO emissions from soils in a Sahelian rangeland. *Biogeosciences Discuss.* 12, 1155–1203. doi:10.5194/bgd-12-1155-2015

Diallo, O., Diouf, A., Hanan, N. P., Ndiaye, A., and Prévost, Y. (1991). AVHRR monitoring of savanna primary production in Senegal, west Africa: 1987-1988. *Int. J. Remote Sens.* 12 (6), 1259–1279. doi:10.1080/01431169108929725

Dicko, M. S., Djitèye, M. A., and Sangaré, M. (2006). Les systèmes de production animale au Sahel. *Sci. Changements Planétaires /Sécheresse* 17 (1), 83–97. Available at: http://www.jle.com/fr/revues/sec/e-docs/les_systemes_de_production_animale_au_sahel_270090/article.phtml?tab=texte.

Ding, Y., Zhang, H., Wang, Z., Xie, Q., Wang, Y., Liu, L., et al. (2020). *Remote Sens. (Basel).*, 12(9), 1470. doi:10.3390/rs12091470Available at: https://sci-hub.se/https://www.mdpi.com/2072-4292/12/9/1470.

Diouf, A. A., Brandt, M., Verger, A., Jarroudi, M., Djaby, B., Fensholt, R., et al. (2015). Fodder biomass monitoring in sahelian rangelands using phenological metrics from FAPAR time series. *Remote Sens.* 7 (7), 9122–9148. doi:10.3390/rs70709122

Diouf, A. A., Djaby, B., Diop, M. B., Wele, A., Ndione, J.-A., and Tychon, B. (2014). "Fonctions d'ajustement pour l'estimation de la production fourragère herbacée des parcours naturels du Sénégal à partir du NDVI S10 de SPOT-vegetation," in XXVIIème Colloque de l'Association Internationale de Climatologie, Dijon, France, July 2–5, 2014.

Diouf, A., and Lambin, E. F. (2001). Monitoring land-cover changes in semi-arid regions: Remote sensing data and field observations in the Ferlo, Senegal. *J. Arid Environ.* 48 (2), 129–148. doi:10.1006/jare.2000.0744

Drusch, M., Del Bello, U., Carlier, S., Colin, O., Fernandez, V., Gascon, F., et al. (2012). Sentinel-2: ESA's optical high-resolution mission for GMES operational services. *Remote Sens. Environ.* 120, 25–36. doi:10.1016/J.RSE.2011.11.026

EROS. (2020). *USGS EROS archive - Landsat archives - Landsat 8-9 OLI/TIRS collection 2 level-2 science products* | US, U.S. Geological Survey. Available at: https://www.usgs.gov/centers/eros/science/usgs-eros-archive-landsat-archives-landsat-8-9-olitirs-collection-2-level-2.

FAO (2020). *Estimation des bilans fourragers dans la région du Sahel d'Afrique de l'Ouest et Centrale*. doi:10.4060/ca9111fr

Fensholt, R., Sandholt, I., and Rasmussen, M. S. (2004). Evaluation of MODIS LAI, fAPAR and the relation between fAPAR and NDVI in a semi-arid

environment using *in situ* measurements. *Remote Sens. Environ.* 91, 490. doi:10.1016/j.rse.2004.04.009

Garba, I., Djaby, B., Salifou, I., Boureima, A., Toure, I., and Tychon, B. (2015). Evaluation des ressources pastorales au sahel nigérien à l'aide des données NDVI issues de SPOT-vegetation et MODIS. *Eur. J. Remote. Sens.* 1, 13–28.

Garba, I., Djaby, B., Salifou, I., Toure, I., Samba, A., Yapo, Y., et al. (2017). Improving fodder biomass modeling in the sahelian zone of Niger using the multiple linear regression method. Available at: www.ijraset.com.

Gorelick, N., Hancher, M., Dixon, M., Ilyushchenko, S., Thau, D., and Moore, R. (2017). Google Earth engine: Planetary-scale geospatial analysis for everyone. *Remote Sens. Environ.* 202, 18–27. doi:10.1016/J.RSE.2017.06.031

Guerschman, J., Held, A., Donohue, R., Renzullo, L., Sims, N., Kerblat, F., et al. (2015). L'activité GEOGLAM sur les parcours et la productivité des pâturages : Progrès récents et orientations futures - NASA/ADS. Available at: https://ui.adsabs.harvard.edu/abs/2015AGUFM.B43A0531G/abstract.

Haboudane, D., Miller, J. R., Tremblay, N., Zarco-Tejada, P. J., and Dextraze, L. (2002). Integrated narrow-band vegetation indices for prediction of crop chlorophyll content for application to precision agriculture. *Remote Sens. Environ.* 81 (2–3), 416–426. doi:10.1016/S0034-4257(02)00018-4

Ham, F., and Fillol, E. (2012). Pastoral surveillance system and feed inventory in the Sahel. Available at: http://web.vgt.vito.be/documents/BioPar/g2-BP-RP-BP053-ProductUserManu- Hiernaux.

Hiernaux, P. (1980). "Inventory of the browse potential of bushes, trees and shrubs in an area of the sahel in Mali: Method and initial results," in *Browse in AfricaILCA: Addis ababa, Ethiopia*. Editor H. N. L. Houerou. Available at: https://books.google.bf/books?hl=en&lr&id=f8wzMTZzPZYC&oi=fnd&pg=PA197&ots=OtA4WBbo1Z&sig=q-CtP-_mT64_BttQu2rCjECWXxQ&redir_esc=y#v=onepage&q&f=false.

Hiernaux, P., Ayantunde, A., Kalilou, A., Mougin, E., Gérard, B., Baup, F., et al. (2009). Trends in productivity of crops, fallow and rangelands in Southwest Niger: Impact of land use, management and variable rainfall. *J. Hydrology* 375 (1–2), 65–77. doi:10.1016/j.jhydrol.2009.01.032

Hiernaux, P., Diawara, M. O., and Assouma, M. H. (2018). Au Sahel, maintenir l'élevage pastoral pour s'adapter au changement climatique. Available at: https://agritrop.cirad.fr/593558/1/Article dans le Monde.pdf.

Holechek, J. L., Geli, H. M. E., Cibils, A. F., and Sawalhah, M. N. (2020). Climate change, rangelands, and sustainability of ranching in the Western United States. *Sustain. Switz.* 12 (12), 4942. doi:10.3390/SU12124942

Huete, A. R. (1988). A soil-adjusted vegetation index (SAVI). *Remote Sens. Environ.* 25, 295–309. doi:10.1016/0034-4257(88)90106-x

ISRA (2003). *Rapport national sur L'état des ressources phytogénétiques pour L'alimentation et L'agriculture sénégal*.

Jacques, D. C., Kergoat, L., Hiernaux, P., Mougin, E., and Defourny, P. (2014). Monitoring dry vegetation masses in semi-arid areas with MODIS SWIR bands. *Remote Sens. Environ.* 153, 40–49. doi:10.1016/j.rse.2014.07.027

Ji, C., Li, X., Wei, H., and Li, S. (2020). Comparison of different multispectral sensors for photosynthetic and non-photosynthetic vegetation-fraction retrieval. *Remote Sens.* 12 (1), 115. *Page 115*. doi:10.3390/RS12010115

Jin, X., Ma, J., Wen, Z., Song, K., Ozdogan, M., Bajwa, S., et al. (2015). Estimation of maize residue cover using landsat-8 OLI image spectral information and textural features. *Remote Sens. (Basel).* 7, 14559–14575. doi:10.3390/rs71114559

Jordan, C. F. (1969). Derivation of Leaf-Area Index from quality of light on the forest floor. *Ecology* 50 (4), 663–666. doi:10.2307/1936256

Jost, S. (1996). *Le Système mondial d'information et d'alerte rapide de la FAO*.

Kavoosi, Z., Raoufat, M. H., Dehghani, M., Abdolabbas, J., Kazemeini, S. A., and Nazemossadat, M. J. (2020). Feasibility of satellite and drone images for monitoring soil residue cover. *J. Saudi Soc. Agric. Sci.* 19 (1), 56–64. doi:10.1016/j.jssas.2018.06.001

Kergoat, L., Hiernaux, P., Dardel, C., Pierre, C., Guichard, F., and Kalilou, A. (2015). Dry-season vegetation mass and cover fraction from SWIR1.6 and SWIR2.1 band ratio: Ground-radiometer and MODIS data in the Sahel. *Int. J. Appl. Earth Observation Geoinformation* 39, 56–64. doi:10.1016/j.jag.2015.02.011

Kowalski, K., Okujeni, A., Brell, M., and Hostert, P. (2022). Quantifying drought effects in Central European grasslands through regression-based unmixing of intra-annual Sentinel-2 time series. *Remote Sens. Environ.* 268, 112781. doi:10.1016/J.RSE.2021.112781

Kuhn, M., Wing, J., Weston, S., Williams, A., Keefer, C., Engelhardt, A., et al. (2021). caret: Classification and regression training version 6.0-90 from CRAN. Available at: https://rdrr.io/cran/caret/.

Li, H., Leung, K. S., Wong, M. H., and Ballester, P. J. (2014). Substituting random forest for multiple linear regression improves binding affinity prediction of scoring functions: Cyscore as a case study. *BMC Bioinforma.* 15 (1), 291. doi:10.1186/1471-2105-15-291

Liaw, A., and Wiener, M. (2002). Classification and regression by randomForest. Available at: http://www.stat.berkeley.edu/.23

Loison, S. alobo, and Bignebat, C. (2017). *Patterns and determinants of household income diversification in rural Senegal and Kenya**. BIGNEBAT 93-126 Patterns and Determinants of Household Income Diversification in Rural Senegal and Kenya.pdf https://agritrop.cirad.fr/584564/1/JPAID 8%281%29 ALOBO LOISON %26.

Mbow, C., Fensholt, R., Rasmussen, K., and Diop, D. (2013). Can vegetation productivity be derived from greenness in a semi-arid environment? Evidence from ground-based measurements. *J. Arid Environ.* 97, 56–65. doi:10.1016/j.jaridenv.2013.05.011

Mcnairn, H., and Protz, R. (1993). Mapping corn residue cover on agricultural fields in oxford county, ontario, using thematic mapper. *Can. J. Remote Sens.* 19 (2), 152–159. doi:10.1080/07038992.1993.10874543

Midi, H., and Bagheri, A. (2010). Robust multicollinearity diagnostic measure in collinear data set respondent driven sampling method view project data mining view project arezoo Bagheri national population studies robust multicollinearity diagnostic measure in collinear data set. Available at: https://www.researchgate.net/publication/265284031.

Miles, J. (2014). *Tolerance and variance inflation factor*.

Mottet, A., de Haan, C., Falcucci, A., Tempio, G., Opio, C., and Gerber, P. (2017)., 14. Elsevier B.V, 1–8. doi:10.1016/j.gfs.2017.01.001Livestock: On our plates or eating at our table? A new analysis of the feed/food debate*Glob. Food Secur.*

Nadiri, A. A., Khatibi, R., Khalifi, P., and Feizizadeh, B. (2020). A study of subsidence hotspots by mapping vulnerability indices through innovatory 'ALPRIFT' using artificial intelligence at two levels. *Bull. Eng. Geol. Environ.* 79 (88), 3989–4003. doi:10.1007/S10064-020-01781-3

Najaf, P., Navid, H., Feizizadeh, B., Eskandar, I., and Blaschke, T. (2019). *Sci-Hub | Fuzzy Object-Based Image Analysis Methods Using Sentinel-2A Landsat-8 Data Map Charact. Soil Surf. Residue. Remote Sens.*, 11(21), 2583 | doi:10.3390/rs11212583Available at: https://sci-hub.se/10.3390/rs11212583

Nash, J. E., and Sutcliffe, J. V. (1970). River flow forecasting through conceptual models part I - A discussion of principles. *J. Hydrology* 10 (3), 282–290. doi:10.1016/0022-1694(70)90255-6

Otgonbayar, M., Atzberger, C., Chambers, J., and Damdinsuren, A. (2019). Mapping pasture biomass in Mongolia using partial least squares, random forest regression and Landsat 8 imagery. *Int. J. Remote Sens.* 40, 3204–3226. doi:10.1080/01431161.2018.1541110

Rana, P., Korhonen, L., Gautam, B., and Tokola, T. (2014). Effect of field plot location on estimating tropical forest above-ground biomass in Nepal using airborne laser scanning data. *Isprs J. Photogrammetry Remote Sens.* 94, 55–62. doi:10.1016/j.isprsjprs.2014.04.012

Ridgeway, G. (2020). *Generalized boosted models: A guide to the gbm package*.

Rondeaux, G., Steven, M., and Baret, F. (1996). Optimization of soil-adjusted vegetation indices. *Remote Sens. Environ.* 55 (2), 95–107. doi:10.1016/0034-4257(95)00186-7

Rouse, W. J., Haas, R. H., Schell, J. A., and Deering, D. W. (1974). *Monitoring vegetation systems in the Great Plains with Erts*. Patent No. PAPER-A20). doi:10.1021/jf60203a024

Sanon, O., Ouattara, F., and Savadogo, M. (2015). Seasonal dynamic of herbaceous fodder production in the Sahelian pastures used by domestic ruminants. *J. Agric. Environ. Int. Dev. (JAEID)* 109 (1), 123–138. doi:10.12895/JAEID.20151.317

Sayre, N. F., McAllister, R. R., Bestelmeyer, B. T., Moritz, M., and Turner, M. D. (2013). Earth stewardship of rangelands: Coping with ecological, economic, and political marginality. *Front. Ecol. Environ.* 11 (7), 348–354. doi:10.1890/120333

Schaaf, C., and Wang, Z. (2015). MODIS bidirectional reflectance distribution function (BRDF) /albedo parameter. Available at: https://modis.gsfc.nasa.gov/data/dataprod/mod43.php.

Sloat, L. L., Gerber, J. S., Samberg, L. H., Smith, W. K., Herrero, M., Ferreira, L. G., et al. (2018). Increasing importance of precipitation variability on global livestock grazing lands. *Nat. Clim. Chang.* 8 (3), 214–218. doi:10.1038/s41558-018-0081-5

Sullivan, D. G., Truman, C. C., Schomberg, H. H., Endale, D. M., and Strickland, T. C. (2006). Evaluating techniques for determining tillage regime in the southeastern Coastal Plain and Piedmont. *Agron. J.* 98, 1236–1246. doi:10.2134/agronj2005.0294

Tagesson, T., Fensholt, R., Cropley, F., Guiro, I., Horion, S., Ehammer, A., et al. (2015). *Dynamics in carbon exchange fluxes for a grazed semi-arid savanna ecosystem in West Africa*. doi:10.1016/j.agee.2015.02.017

Tappan, G. G., Sall, M., Wood, E. C., and Cushing, M. (2004). Ecoregions and land cover trends in Senegal. *J. Arid Environ.* 59, 427–462. doi:10.1016/j.jaridenv.2004.03.018

Thompson, C. G., Kim, R. S., Aloe, A. M., and Becker, B. J. (2017). *Basic and applied social psychology extracting the variance inflation factor and other multicollinearity diagnostics from typical regression results*. doi:10.1080/01973533.2016.1277529

Traore, S. B., Ali, A., Tinni, S. H., Samake, M., Garba, I., Maigari, I., et al. (2014). Agrhymet: A drought monitoring and capacity building center in the west Africa region. *Weather Clim. Extrem.* (3), 22–30. doi:10.1016/J.WACE.2014.03.008

Tucker, C. J., Vanpraet, C. L., Sharman, M. J., and Van Ittersum, G. (1985). Satellite remote sensing of total herbaceous biomass production in the senegalese sahel: 1980-1984. *Remote Sens. Environ.* 17 (3), 233–249. doi:10.1016/0034-4257(85)90097-5

Van Deventer, A. P., Ward, A. D., Gowda, P. H., and Lyon, J. G. (1997). Using thematic mapper data to identify contrasting soil plains and tillage practices. *Photogrammetric Eng. Remote Sens.* 63 (1), 87–93.

Verrelst, J., Rivera, J. P., Veroustraete, F., Muñoz-Marí, J., Clevers, J. G. P. W., Camps-Valls, G., et al. (2015). *Experimental Sentinel-2 LAI estimation using parametric, non-parametric and physical retrieval methods â€“ A comparison*. doi:10.1016/j.isprsjprs.2015.04.013

Wang, ai, Zhou, X., Zhu, X., Dong, Z., and Guo, W. (2016). *Estimation of biomass in wheat using random forest regression algorithm and remote sensing data*. doi:10.1016/j.cj.2016.01.008

Zhang, W., Brandt, M., Guichard, F., Tian, Q., and Fensholt, R. (2017). Using long-term daily satellite based rainfall data (1983–2015) to analyze spatio-temporal changes in the sahelian rainfall regime. Available at: https://www.elsevier.com/open-access/userlicense/1.0/.

Zhang, W., Brandt, M., Tong, X., Tian, Q., and Fensholt, R. (2018). Impacts of the seasonal distribution of rainfall on vegetation productivity across the Sahel. *Biogeosciences* 15 (1), 319–330. doi:10.5194/bg-15-319-2018

frontiers | Frontiers in Environmental Science

TYPE Original Research
PUBLISHED 07 September 2022
DOI 10.3389/fenvs.2022.928351

OPEN ACCESS

EDITED BY
Mengtian Huang,
Chinese Academy of Meteorological Sciences, China

REVIEWED BY
Haijun Deng,
Fujian Normal University, China
Nicholas Chrisman,
Retired, Bellingham, WA, United States

*CORRESPONDENCE
Xiaoyu Meng,
mengxiaoyu@henu.edu.cn

†These authors share first authorship

SPECIALTY SECTION
This article was submitted to Drylands, a section of the journal Frontiers in Environmental Science

RECEIVED 25 April 2022
ACCEPTED 16 August 2022
PUBLISHED 07 September 2022

CITATION
He P, Ma X, Han Z, Meng X and Sun Z (2022), Uncertainties of gross primary productivity of Chinese grasslands based on multi-source estimation. *Front. Environ. Sci.* 10:928351. doi: 10.3389/fenvs.2022.928351

Uncertainties of gross primary productivity of Chinese grasslands based on multi-source estimation

Panxing He[1†], Xiaoliang Ma[1,2†], Zhiming Han[3], Xiaoyu Meng[4*] and Zongjiu Sun[1]

[1]Grassland Ministry of Education Key Laboratory for Western Arid Region Grassland Resources and Ecology, College of Grassland, Xinjiang Agricultural University, Urumqi, China, [2]State Key Laboratory of Grassland Agro-ecosystems, College of Pastoral Agriculture Science and Technology, Lanzhou University, Lanzhou, China, [3]College of Resources and Environment, Northwest A&F University, Yangling, China, [4]Development Collaborative Innovation Center on Yellow River Civilization, Key Research Institute of Yellow River Civilization and Sustainable, Henan University, Kaifeng, China

Gross primary productivity (GPP) is an important parameter in the carbon cycle and climate change studies. The results of GPP fluxes estimated based on multiple models or remote sensing vary widely, but current studies of GPP in Chinese grasslands tend to ignore data uncertainty. In this study, uncertainty analysis of GPP datasets estimated based on terrestrial ecosystem models and remote sensing was conducted using cross-validation, standard error statistics, and ensemble empirical modal decomposition. We found that 1) the fit coefficients R^2 of two-by-two cross-validation of GPP datasets mostly exceeded 0.8 at the global scale. 2) GPP from different sources were consistent in portraying the spatial and temporal patterns of GPP in Chinese grasslands. However, due to many differences in model structure, parameterization and driving data, some uncertainties still exist, especially in the parts of dry-cold areas where the standard deviations are relatively large. 3) Uncertainties were higher for future scenarios than for historical periods, and GPP uncertainties were much higher for future high-emissions scenarios than for low- and medium-emissions scenarios. This study highlighted the need for uncertainty analysis when GPP is applied to spatio-temporal analysis, and suggested that when comparing and assessing carbon balance conditions, multiple source data sets should be combined to avoid misleading conclusion due to uncertainty.

KEYWORDS

gross primary productivity, uncertainty, Chinese grasslands, MsTIMP, ISIMIP

1 Introduction

The ability to evaluate the strengths and weaknesses of gross primary productivity (GPP) between site observations, model simulations, and remote sensing estimates can be evaluated by comparing multiple source datasets against each other (Randerson et al., 2009). Eddy covariance techniques can accurately measure net ecosystem CO_2 exchange, and ecosystem respiration can be removed from this variable to directly obtain GPP observations from flux towers at the site scale (Falge et al., 2001; Morales et al., 2021). However, flux towers only provide a composite measure of CO_2 fluxes over the footprint (the area upwind of the flux tower measurement), whose size and shape (ranging from several hundred meters to several kilometers) vary with tower height, physical properties of the canopy, and wind speed (Osmond et al., 2004). The observation footprint is so small that it is not suitable for use in evaluating models and remotely sensed coarse resolution GPP datasets. In addition, there are not yet enough effective observation systems for long periods and large scales in Chinese grasslands because of the spatio-temporal constraints and high cost of flux tower site observations (Yuan et al., 2014). To accurately assess the large-scale GPP dynamics in Chinese grasslands, the spatio-temporal applicability of models and remote sensing GPP in Chinese grasslands needs to be analyzed from macroscopic and long series. Therefore, when there is a lack of validation of the actual measurement data, uncertainty analysis can only be done on GPP data from different sources.

Based on the observed ecophysiological, biophysical, and biogeochemical processes (Sitch et al., 2008; Huang et al., 2015), terrestrial ecosystem models can theoretically obtain a high enough resolution grid GPP and are currently an effective method for studying GPP variability and its climate effects at large spatial and temporal scales (Yuan et al., 2021). However, the accuracy of model GPP is limited by the uncertainty of input parameters, model-driven data, and defects in the physical structure of the model, leading to large uncertainties in the GPP simulated by individual models (Zaehle et al., 2005; Cheng et al., 2017). In addition, using satellite-derived GPP, Mao et al. (2012) pointed out that remote sensing provides large-scale information on real changes in vegetation, land use, and landforms, which can provide valuable observations at large scales for terrestrial ecosystem models to correct model GPP products.

To analyze the uncertainty among the models, the four Inter-Sectoral Impact Model Intercomparison Project (ISIMIP) and four Multi-scale Synthesis and Terrestrial Model Intercomparison Project (MsTMIP) models covered above were used to analyze GPP data uncertainty. The ISIMIP and MsTMIP projects were originally established to assess the physical mechanisms of climate feedback differences among models and were used to explore the reasons for the different results between models for the same driving data outputs. Currently, a small number of studies on model uncertainty have been conducted for ISIMIP and MsTMIP (Shao et al., 2016; Krysanova et al., 2017; Exbrayat et al., 2018), but the spatio-temporal applicability of the two sets of model GPP data in Chinese grasslands has still not been compared.

The purpose of this study is to assess the capability of eight terrestrial ecosystem models in ISIMIP and MsTMIP to simulate GPP, explore the influence of initial conditions and model structure on model GPP uncertainty, and propose to address 1) cross-validation of GPP products from global-scale ISIMIP, MsTMIP, Global Land Surface Satellite (GLASS), and Multisource data Synergized Quantitative (MuSYQ) on an pixel-by-pixel basis; 2) study the GPP simulation capability of ISIMIP and MsTMIP by comparing with GLASS and MuSYQ remote sensing observations of GPP, investigate the ability of ISIMIP and MsTMIP to simulate the historical phase (1981–2005) of the mean climate state and long-term trend of GPP for grasslands in China through comparative analysis with GLASS and MuSYQ remote sensing observations of GPP; 3) explore the future scenarios of different models in ISIMIP for typical emission pathways RCP2.6, RCP6.0, and RCP8.5 (LPJmL model only) (2005–2099) for China's grassland GPP.

2 Data and methods

2.1 Dataset description

The GPP data used in this study mainly include eight simulated GPP datasets provided by ISIMIP and MsTMIP, two observation GPP datasets provided by GLASS and MuSyQ. Descriptions of the relevant datasets have been published in our previous analysis (He et al., 2022), but the difference is that this study focuses on GPP uncertainty.

Ecological process models are the only means to study the impact of global change factors on the carbon cycle of ecosystems in the context of past, present and future global change (Wei et al., 2014). Schimel et al. (2000) simulated several different ecosystem process models and found that, due to the huge differences in complexity, input parameters and simulation algorithms of different models, researchers should used multi-model simulation and intercomparison to quantify the uncertainty of GPP in terrestrial ecosystems. At present, the International Comparison Scheme of Multi-Terrestrial Ecosystem Models has developed rapidly, such as ISIMIP (https://www.isimip.org/), MsTMIP (https://nacp.ornl.gov/MsTMIP.shtml), and TRENDY (http://globalcarbonproject.org/) for the annual global carbon balance report. Moreover, MsTMIP and ISIMIP are publicly available free of charge without application.

(1) The MsTMIP is a model comparison program designed to diagnose differences in simulations of historical terrestrial carbon cycle dynamics between models (Huntzinger et al., 2013). The ecological process models participating in MsTMIP all use the same driving data to provide GPP output products for historical periods (Wei et al., 2014; Zscheischler et al., 2014). In the latest release of model simulations (https://doi.org/10.3334/ORNLDAAC/1225), MsTMIP provides monthly-valued GPP products with a spatial resolution of 0.5°, and a time span of 1901–2010. Based on the need for sensitivity analysis, we selected four terrestrial ecosystem models in MsTMIP for multiple scenarios based on the findings of previous studies (Zhou et al., 2017): Community Land Model version 4(CLM4) (Mao et al., 2012), CLM4-Variable Infiltration Capacity model (CLM4VIC) (Li et al., 2011), Dynamic Land Ecosystem Model (DLEM) (Tian et al., 2012), and Integrated Science Assessment Model (ISAM) (Jain et al., 2013) were used as the basis dataset for this study. The MsTMIP model provides multi-simulation GPP results for different scenarios, and only the BG1 scenario of MsTMIP (with all environmental drivers) was used in our study.

(2) The ISIMIP is a model comparison program that assesses a comprehensive and consistent description of global climate dynamics under different climate change scenarios (Rosenzweig et al., 2017), and aims to provide international organizations and individual countries with a framework for sustainable projections of climate change and its impacts (https://esg.pik-potsdam.de/projects/isimip/). The four terrestrial GPP datasat providing GPP data, were screened for historical period (1901–2005) and future (2006–2099) scenarios under strict adherence to the ISIMIP2b standard protocol. The ISIMIP applied the atmospheric circulation model IPSL-CM5A-LR as meteorological forcing data, and output products of the global terrestrial vegetation dynamics model (monthly, 0.5°). We used Ecosystem Models: CARbon Assimilation In the Biosphere (CARAIB) (Warnant et al., 1994), Lund-Potsdam-Jena: General Ecosystem Simulator (LPJ GUESS) (Smith et al., 2014), Lund-Potsdam-Jena managed Land (LPJmL) (Bondeau et al., 2007), and Organizing Carbon and Hydrology in Dynamic EcosystEms: Dynamic Global Vegetation Model (ORCHIDEE DGVM) (Guimberteau et al., 2018) in this study.

(3) The GLASS is widely used in the study of global change. Among them, the ecosystem GPP is the most important product dataset of GLASS, which spans nearly 40 years (1982–2018), and becomes the primary choice for the current study of long-term evolution characteristics of GPP due to its relatively high spatio-temporal resolution (0.05°, 8 days). Previous research found that GLASS GPP can better characterize the photosynthetic productivity of major ecosystem types than other satellite-based GPP models (Yuan et al., 2014). The link to access this GLASS GPP is: http://www.glass.umd.edu/Download.html.

In addition, to avoid misleading results from a single remote sensing algorithm inversion of GPP, another MuSyQ GPP algorithm based on photosynthetic use efficiency model was used in this study to compare the accuracy of GLASS GPP results (Wang et al., 2021). The MuSyQ GPP (8 days and 0.05°) products for 1982–2018 are available. Crucially, when cross-validating with the model GPP data, we resampled the remotely sensing GPP to half-degree resolution in line with the model GPP.

(4) The CRU climate dataset uses an extrapolated spatial interpolation algorithm to obtain a global image-by-image gridded product by integrating measured information from various meteorological stations on a global scale (Harris et al., 2020). In this study, we used temperature and precipitation data with a temporal resolution of 1 month and a spatial resolution of 0.5° provided by CRU TS Version 4.02 (https://crudata.uea.ac.uk/cru/data/hrg/).

2.2 Methods

(1) In this study, the Manner-Kendall (M-K) nonparametric test was applied to calculate the trend of GPP over time (Kendall and Gibbons 1957; Culotta 1995). Assuming a time series with n years (x_1,. . ., x_n), for all k, j ≤ n, and $k \neq j$, the distributions of x_j and x_k are different, the test statistic S is calculated with the following equation.

$$S = \sum_{k=1}^{n-1} \sum_{j=k+1}^{n} Sgn\left(x_j - x_k\right) \tag{1}$$

$$Sgn\left(x_j - x_k\right) = \begin{bmatrix} +1\left(x_j - x_k\right) > 0 \\ 0\left(x_j - x_k\right) = 0 \\ -1\left(x_j - x_k\right) < 0 \end{bmatrix} \tag{2}$$

S is normally distributed with mean 0 and variance $Var(S) = n\,(n-1)\,(2n+5)/18$. When $n > 10$, the standard normal statistic variable is calculated by the following equation.

$$Z = \begin{bmatrix} \frac{S-1}{\sqrt{Var\,(S)}} S > 0 \\ \frac{S-1}{\sqrt{Var\,(S)}} S < 0 \end{bmatrix} \tag{3}$$

For statistical values, greater than 0 indicates an increase in the series; the opposite is true for a decrease. However, since the M-K nonparametric test can only provide the sign and statistical significance of the trend of the variable, it cannot clarify the size of the trend of the variable. Therefore, the Sen's slope estimation method was introduced in this study to quantify the degree of change in the trend of the variables.

The Sen's slope estimation method is a method for robustly fitting a line to a sampled point in the plane (simple linear regression) by selecting the median of the slope of all lines at paired points, which provides a good response to the degree of change in the series trend, and the Sen's slope K is given by the following

$$K = median(\theta_i) \tag{4}$$

$$\theta_i = \frac{x_j - x_k}{j - k} \tag{5}$$

where i is a constant taking value of (1,2,. . .,n); n is the length of the time series; x_j and x_k are the sequences of j and k, respectively; and $j > k$ is satisfied.

The statistical method was implemented in MATLAB software (Note: The statistics and plots in this study are based on MATLAB software unless otherwise stated).

(2) The Empirical Mode Decomposition (EMD) method is an adaptive time-frequency method first proposed, which is widely used in climate signal processing. EMD is applied to decompose the original signal into a series of Intrinsic Mode Function (IMF) signals. However, EMD suffers from the modal mixing problem, and the components of IMF may lose their practical meaning. To solve this problem, researcher proposed Ensemble Empirical Mode Decomposition (EEMD) (Wu and Huang 2009), a method to aid data analysis by controlled addition of white noise, which can improve EMD performance overall.

$$x(t) = \sum_{i=1}^{n} C_i(t) + R_n(t) \tag{6}$$

As can be seen from the equation, EEMD decomposes a time series into a series of eigenmodal function IMF components. The resulting IMF signal must satisfy two conditions: the number of extremes and the number of zero crossings must be equal or differ by one, and the mean of the two envelopes is defined by local maxima and local minima. IMF is the same as the original time series but with differences in frequency and amplitude, from IMF one to IMF X, the frequency decreases sequentially. The residual component is monotonic and contains only one extreme value, so it can be considered as the overall trend of the original series. In this study, the amplitude of white noise is added as 1/5 times the standard deviation of the original time series GPP data, the number of IMFs is five, and the number of pooled average members is 100.

3 Results

3.1 Global-scale cross-validation of GPP data from multiple sources

The cross-validation of the GPPs of each source at the whole Earth showed that the GPPs of the two combinations are in good agreement (Figure 1). The R^2 values of ISIMIP, MsTMIP, GLASS, and MuSyQ are all high among each other, especially the R^2 between IMSMIP and GLASS is close to 0.85, and even the combination of ISIMIIP and MuSyQ with the lowest R^2 is over 0.79. This reflects that the model simulation and remote sensing observation GPPs fit well on the global with high consistency. When compared the remotely sensed GPP of different algorithms, we found that the fitted R^2 of GLASS with MsTMIP and ISIMIP model GPP is obviously higher, 0.85 and 0.84, respectively, which is significantly higher than 0.79 and 0.80 of MuSyQ. This represents that GLASS GPP may be able to portray the true value of GPP at global better than MuSyQ.

Most of the global pixel values are concentrated within the value of 1,000 g C m^{-3}. The prominent feature of value threshold data is that the GPP simulated by the ISIMIP model is significantly above the 1:1 value line, which is significantly higher than the remotely sensed GPP, represents a possible overestimation of ISIMIP at the low value threshold GPP. However, the same modeled MsTMIP GPP, the low-value threshold is clearly lower than the two remotely sensed datasets, represents that MsTMIP may underestimate GPP.

3.2 Uncertainty analysis of grassland GPP data in China during the historical period

Before analyzed the uncertainty of the spatial mean state of GPP in Chinese grasslands during the historical period, the spatial distribution of GPP from various sources in Chinese grasslands was shown, and the influence of environmental factors (temperature, precipitation) on the spatial distribution of GPP in ecosystems is initially explored. Figure 2 showed the spatial distribution of GPP from multiple sources, indicated that each GPP maintains a similar spatial pattern, with higher GPP values closer to the east and a gradual decrease in GPP closer to the inland northwest. The high value area includes the eastern part of the Inner Mongolia steppe, the middle-eastern part of Qinghai-Tibet Plateau and the southeastern part of Loess Plateau, while the low value area includes the western part of Inner Mongolia steppe, most of Qinghai-Tibet Plateau, Xinjiang and the northwestern part of Loess Plateau. The spatial divergence is obviously related to the combination of water and heat resources. When the mean values of ecosystem GPP in different precipitation and temperature intervals were analyzed, we found that the high value areas of GPP in Chinese grasslands were mostly located in areas with higher temperature and more abundant precipitation, while the low value areas were mostly concentrated in areas with water scarcity and temperature limitation (Figure 3).

As shown in Figure 4, the GPP mean states based on models and remote sensing differed, and there were also differences between GPPs at different spatial scales. The difference between the GPP simulated by different ISIMIP models is very obvious for

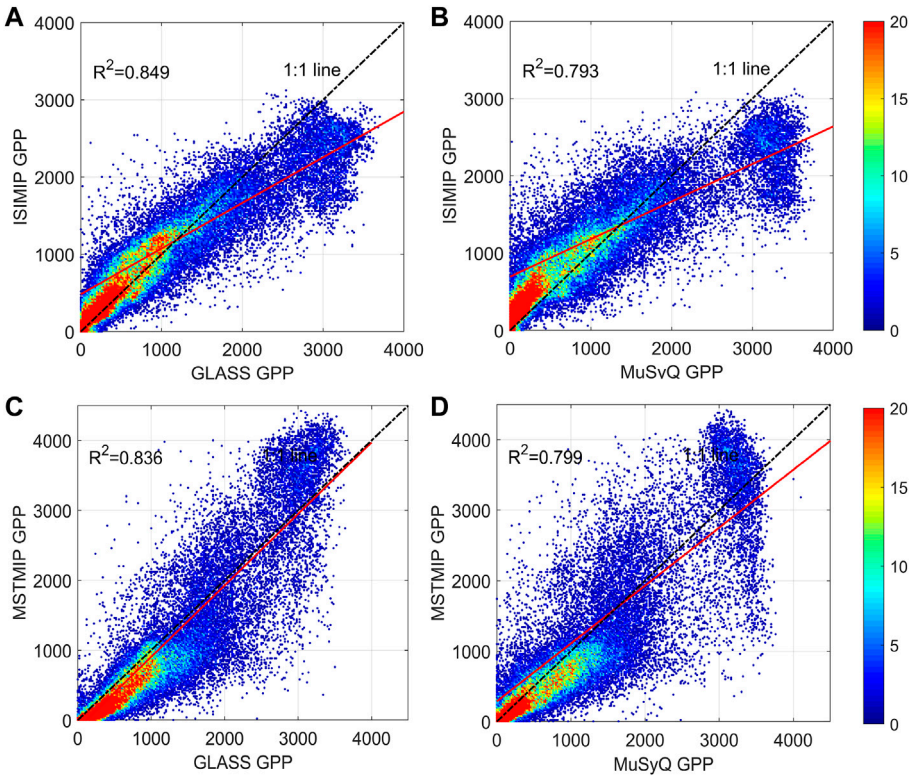

FIGURE 1
Cross-validation between four different sources of GPP data at the global scale per pixel. **(A)** ISIMIP vs. GLASS; **(B)** ISIMIP vs. MuSyQ; **(C)** MsTMIP vs. GLASS; **(D)** MsTMIP vs. MuSyQ.

Chinese grasslands, with a maximum of 720 g C m^{-2} and a minimum of 380 g C m^{-2}, and the extreme difference is nearly double. The simulation results of MsTMIP multi-model are closer, and the same two remote sensing GPP estimation results are similar. Compared the absolute values of GPP for each source at both national and global scales, we found that the GPP values are closer, which is consistent with the findings in Section 3.1 that multi-source GPP may have a better match at the global scale, but the error may be large at the regional scale. This reminds that in regional studies, a single model or remotely sensed GPP should not be selected as the base data, but rather a multi-source dataset should be used to judge whether the conclusion obtained from a single data are reliable. Multiple source datasets can provide multiple conclusion that increase the robustness and applicability of the conclusion, and also avoid misleading findings as much as possible.

Considerd that the simulation of GPP by different models is influenced by the model complexity and climate state settings, the accuracy of GPP obtained from the simulation should be more concerned with the consistency of its evolution characteristics over time rather than its mean size (Dirmeyer et al., 2004). To eliminate the effect of differences in the climate state of GPP between different models, the distance level of GPP over the time series was first calculated. The time series of the mean GPP distance levels for the four different sources were shown in Figure 5A. To facilitate comparison between ISIMIP and MsTMIP multi-models, doubled standard deviation was used to indicate the variability between the two groups of terrestrial ecosystem model members. The analysis revealed that the ensemble averages of the two groups of models showed very similar patterns of change during the period 1901–2005, with both showed a significant upward trend and a significantly faster rate of increased since 1980. Comparison with the two remotely sensed GPPs also showed that the evolution characteristics of model GPP and remotely sensed GPP over time are consistent overall (Figure 5A). Figure 5B reflected the time series of the simulated standard deviations of the two GPP ensembles, ISIMIP and MsTMIP, and we found that the standard deviations of the two GPP models are significantly different over time.

To quantitatively assess the inter-model uncertainty, the relative standard deviation (relative standard deviation was defined as the ratio of standard deviation to mean GPP) between the members of the ISIMIP and MsTMIP models was then obtained. The relative standard deviation, which is more applicable than the standard deviation, was used in this

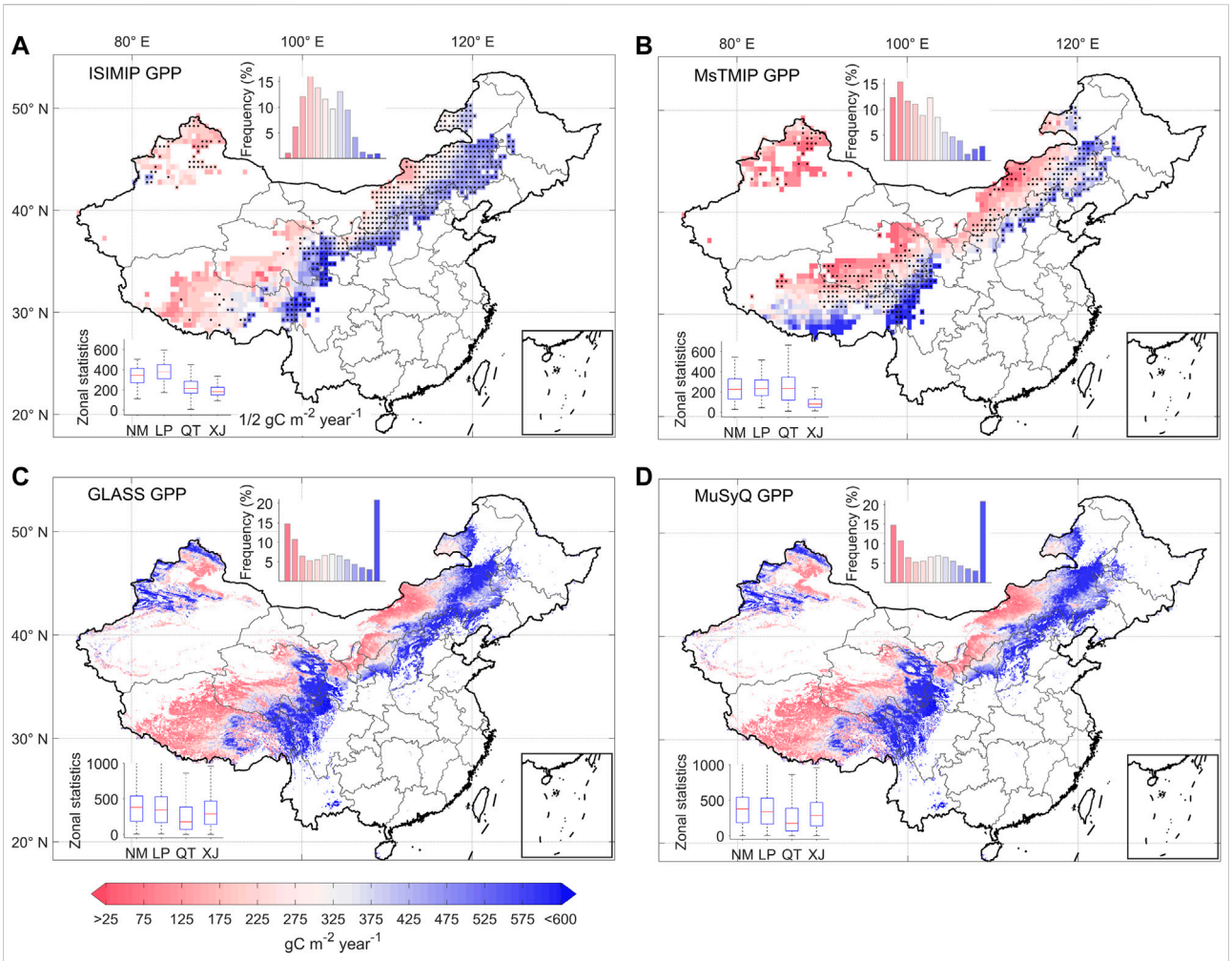

FIGURE 2
Spatial patterns of ecosystem GPP value per pixel estimated based on process model simulations and remote sensing datasets for the period 1982–2005. **(A)** ISIMIP; **(B)** MsTMIP; **(C)** GLASS; **(D)** MuSyQ. The results of averaging over multiple model ensembles to reduce inter-model errors were used in Figure **(A,B)**. Black dots represent standard deviations between members that exceed 50% of the mean of the model ensemble. The regional average trend values are counted as box plots in the lower left corner, NM, LP, QT, and XJ represent grasslands in Inner Mongolia, Loess Plateau, Qinghai-Tibet Plateau, and Xinjiang, respectively, red dots represent GPP anomalies.

study because it is considered that the relative standard deviation can effectively eliminate GPP units and facilitate the intercomparison of the two groups of models in different climate zones. From the analysis of Figure 6, we point out that the differences between different ISIMIP simulations are greater than MsTMIP (Figures 6A,B), and the relative standard deviation among the four ISIMIP models is less than 20% of the ensemble average for 26.71% of the pixels in Chinese grasslands, while 28.43% of the pixels are greater than 50% of the ensemble average and they are mostly located in the grasslands of eastern Inner Mongolia, western Qinghai-Tibet Plateau, and Xinjiang. In contrast, 69.36% and 90.02% of the pixels were less than 20% and 50% of the ensemble average, respectively, for MsTMIP. Therefore, the relative standard deviation of MsTMIP is significantly smaller than that of ISIMIP, which means that there is less variation among GPP results output from MsTMIP at the image element scale.

The above studies used standard deviation to demonstrate the uncertainty among models, but the standard deviation is essentially an averaging value that does not fully reflect the subtle differences among different members of the models. Therefore, in our study, time series distance levels of GPP simulated by eight terrestrial ecosystem models for the period 1901–2005 were calculated (Figure 7A). We found that the results vary among model members but the trends are nearly consistent, i.e., individual models all showed an upward trend while showing interannual fluctuations of varying amplitudes. In addition, we found that the pooled averaging (black line in Figure 7A) effectively eliminates the interannual fluctuations of the model, and makes the data show only low-frequency

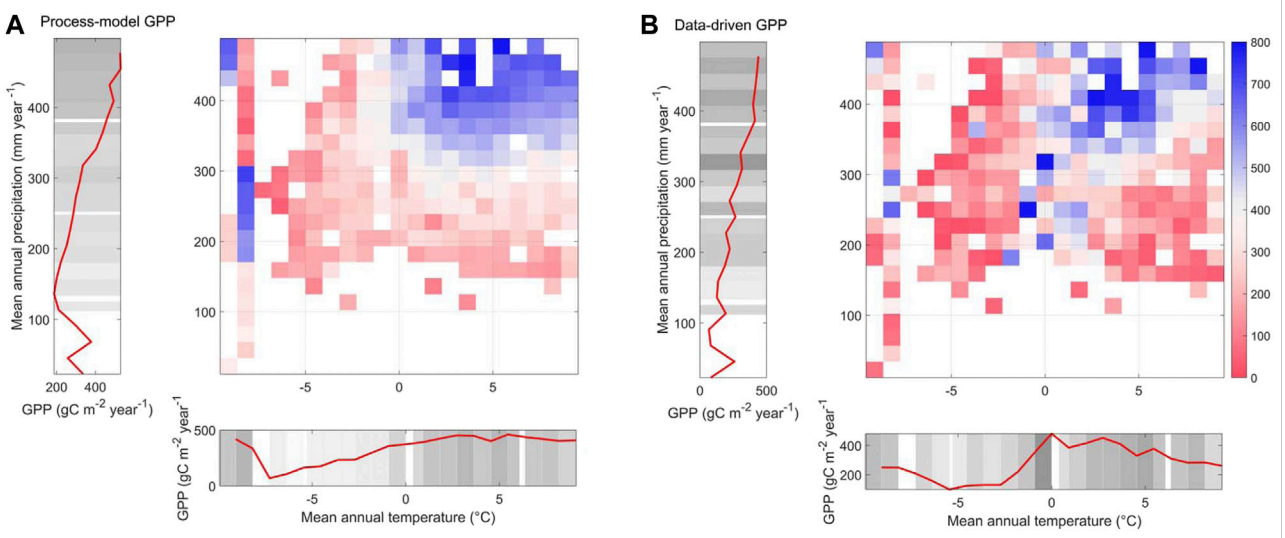

FIGURE 3
Mean values of GPP of Chinese grasslands in different temperature and precipitation intervals. The precipitation and temperature variables here are the multi-year average annual total precipitation and the multi-year average annual average temperature, respectively. The red curve in the figure represents the mean value of GPP at that temperature and precipitation value threshold. The gray shading represents the uncertainty, and the darker the color reflects the greater uncertainty of GPP. **(A)** Simulated GPP based on ecosystem process model; **(B)** Estimated GPP based on remote sensing dataset.

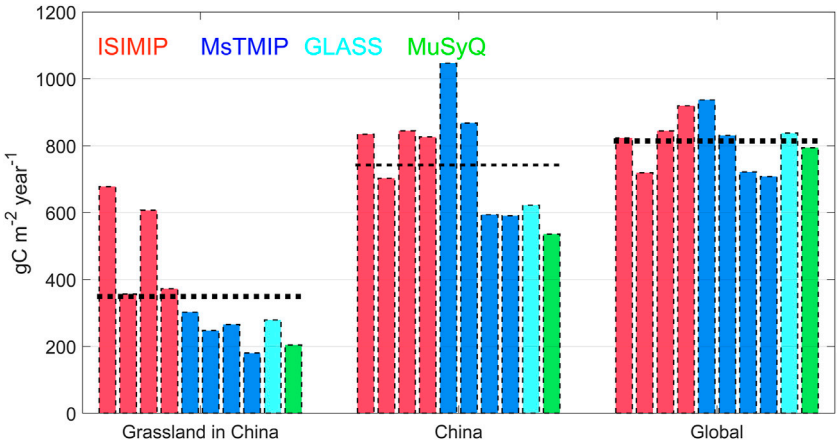

FIGURE 4
Average GPP from multiple sources for Chinese grasslands, China, and globally during 1982–2005. The black dashed line parallel to the *x*-axis is the ensemble mean of the four ISIMIP process models and the four MsTMIP process models.

signals. Since interannual fluctuations generally contain a large amount of uncertain information about the internal variability of the model, pooled averaging is an important way to effectively eliminate the uncertainty of the internal variability of the model.

To further explore the uncertainty of the model results on different time scales, the GPP of each model on the original time series was decomposed into five IMF components and residuals at different time scales by the EEMD method. Figures 7B–G showed the variation curves of IFM1 to IFM5 with time series, representing the GPP signals at different time scales from high frequency to low frequency, and the residuals represent the long-term trend of GPP. The analysis showed that the five IMFs have different periodic signals, and their variation periods are shortening while their amplitudes are becoming larger as the signal frequency decreases. However, we noted that there are differences in the simulated curves of IMF3 and IMF4, which

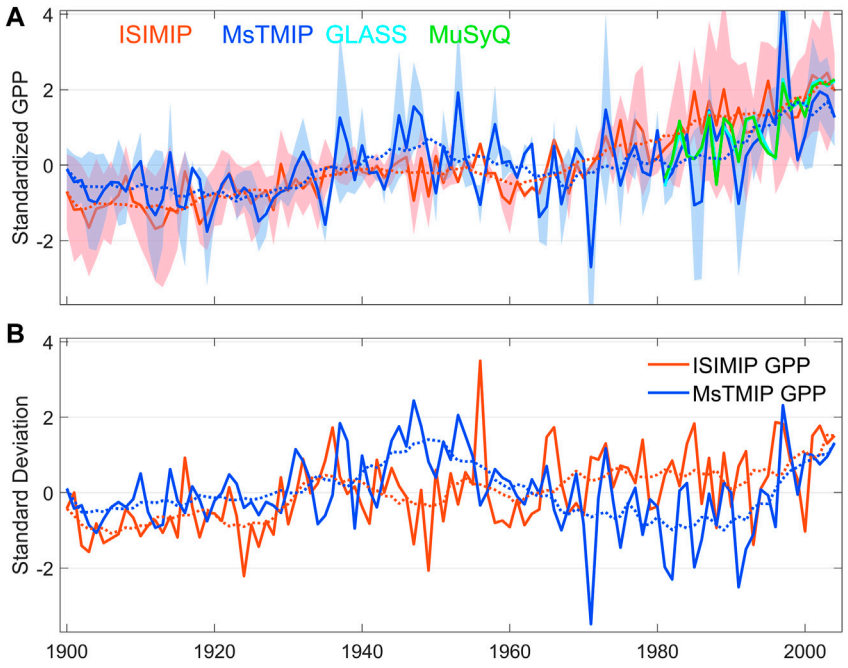

FIGURE 5
Time series of annual average GPP distance levels based on multiple data sources. Shading represents the doubled standard deviation of the four model members. Dotted dashed lines are 20-years moving average of ISIMIP GPP and MsTMIP GPP. **(A)** Annual average GPP; **(B)** model GPP standard deviation.

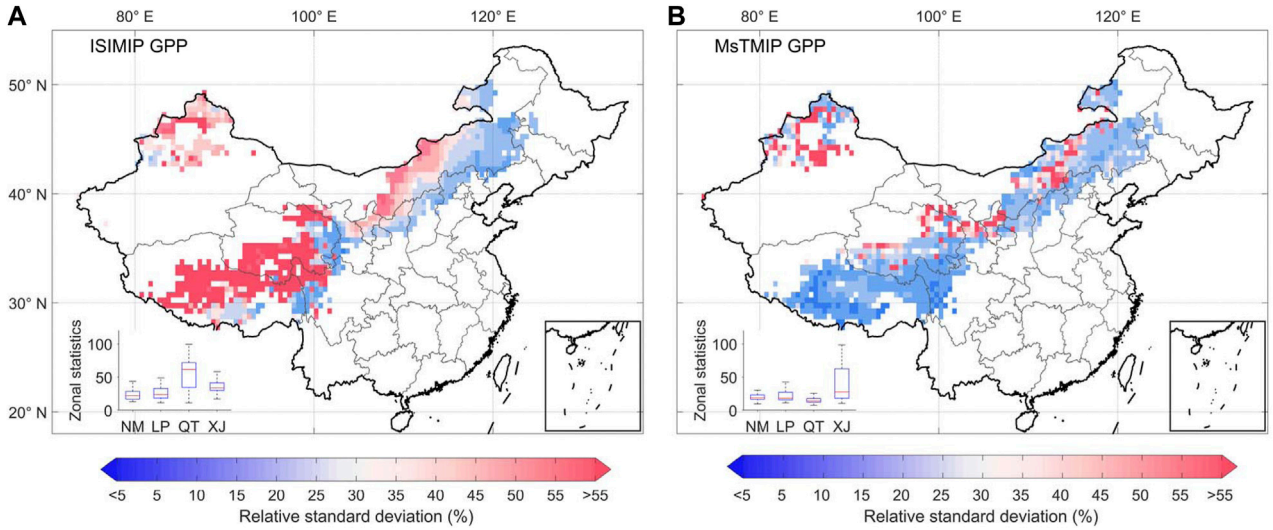

FIGURE 6
Spatial patterns of the relative standard deviations of the **(A)** ISIMIP, and **(B)** MsTMIP simulations for the period 1901–2005.

indicated that the model complexity can lead to uncertainty in the model GPP at each time scale. As seen in the residual signals, the eight models exhibit a generally consistent upward trend, and this is consistent with the conclusive information presented in Figure 6A. However, the long-run signals of the residuals whose starting values in 1901 and 2005 are inconsistent suggest that there is still some uncertainty in the simulated GPP for each model.

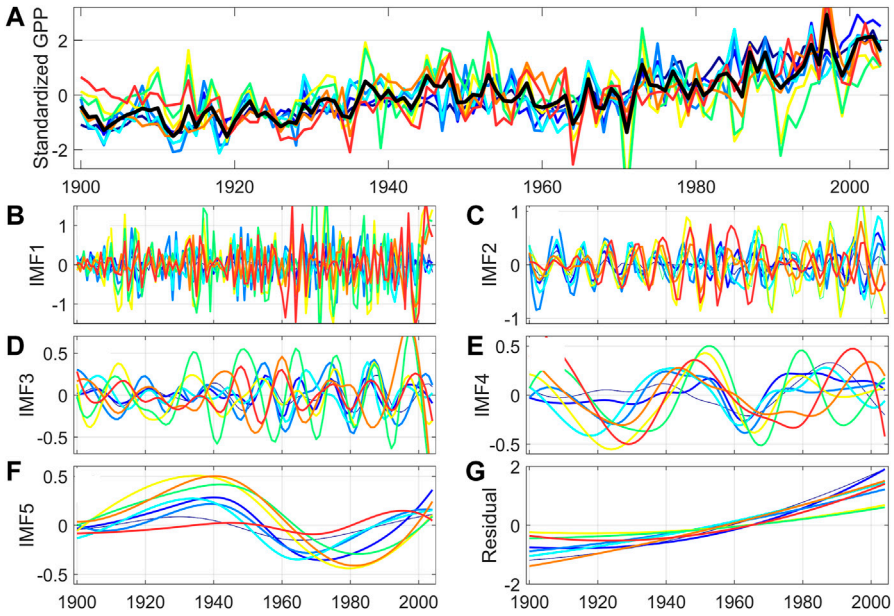

FIGURE 7
Average GPP distance levels for 1901–2005 and IMF1...IMF5, and the time series of residuals. **(A)** Time series of simulated GPP distance levels for the four ISIMIP and four MsTMIP models, the black line is the result of the average of the eight model ensembles; **(B–F)** time series of IMF1 to IMF5 extracted by the EEMD method; **(G)** residuals extracted by the EEMD method.

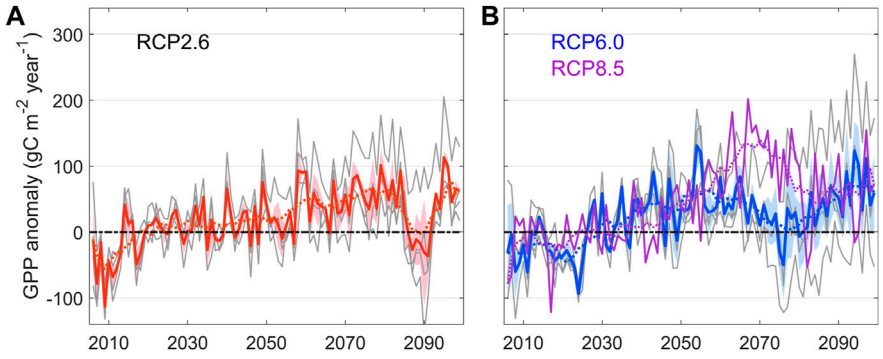

FIGURE 8
Time series of ISIMIP annual average GPP distance levels for future periods, distance levels are based on 2006–2025 average. **(A)** RCP2.6; **(B)** RCP6.0 and RCP8.5, note that the RCP8.5 model only provides the LPJmL model so only its curves are plotted. The gray lines in the figure represent the distance level of the four models in the time series for the RCP2.6 **(A)** and RCP6.0 **(B)** scenarios, and the shading represents the doubled standard deviation of the four model members. The dotted dashed line is the 20-years moving average for ISIMIP GPP and MsTMIP GPP.

3.3 Uncertainty analysis of China's grassland GPP data in the future period

Since only the ISIMIP model comparison program provides GPP products under future emission scenarios, the uncertainty of the ISIMIP GPP dataset under future scenarios is then analyzed. Figure 8 showed the long-term change curves of the GPP models for each future scenario, which showed that the overall Chinese grassland GPP maintains some increase from 2006 to 2099 for the low, medium, and high scenarios. The analysis of the change curves and doubling standard deviation of each model showed that the difference between the models is relatively small in the first half of the 21st century, while the uncertainty increases in the second half of the century with increasing standard deviation.

When compared the standard deviations within the Chinese grassland pixels for each future scenario, we found that the

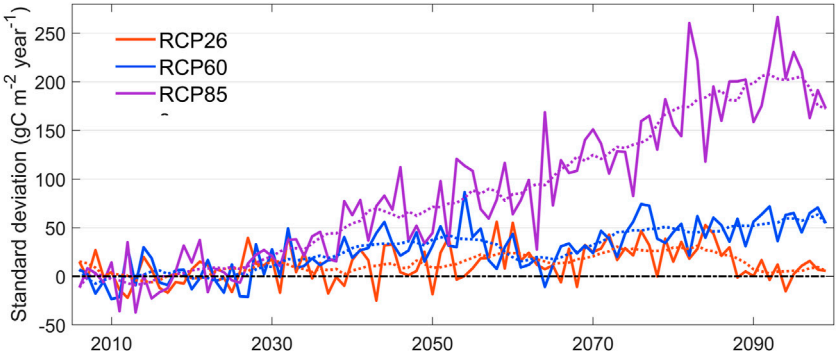

FIGURE 9
Time series of ISIMIP simulated standard distance levels for GPP in China grasslands for each emission scenario in the future period, with distance levels based on the 2006–2025 average.

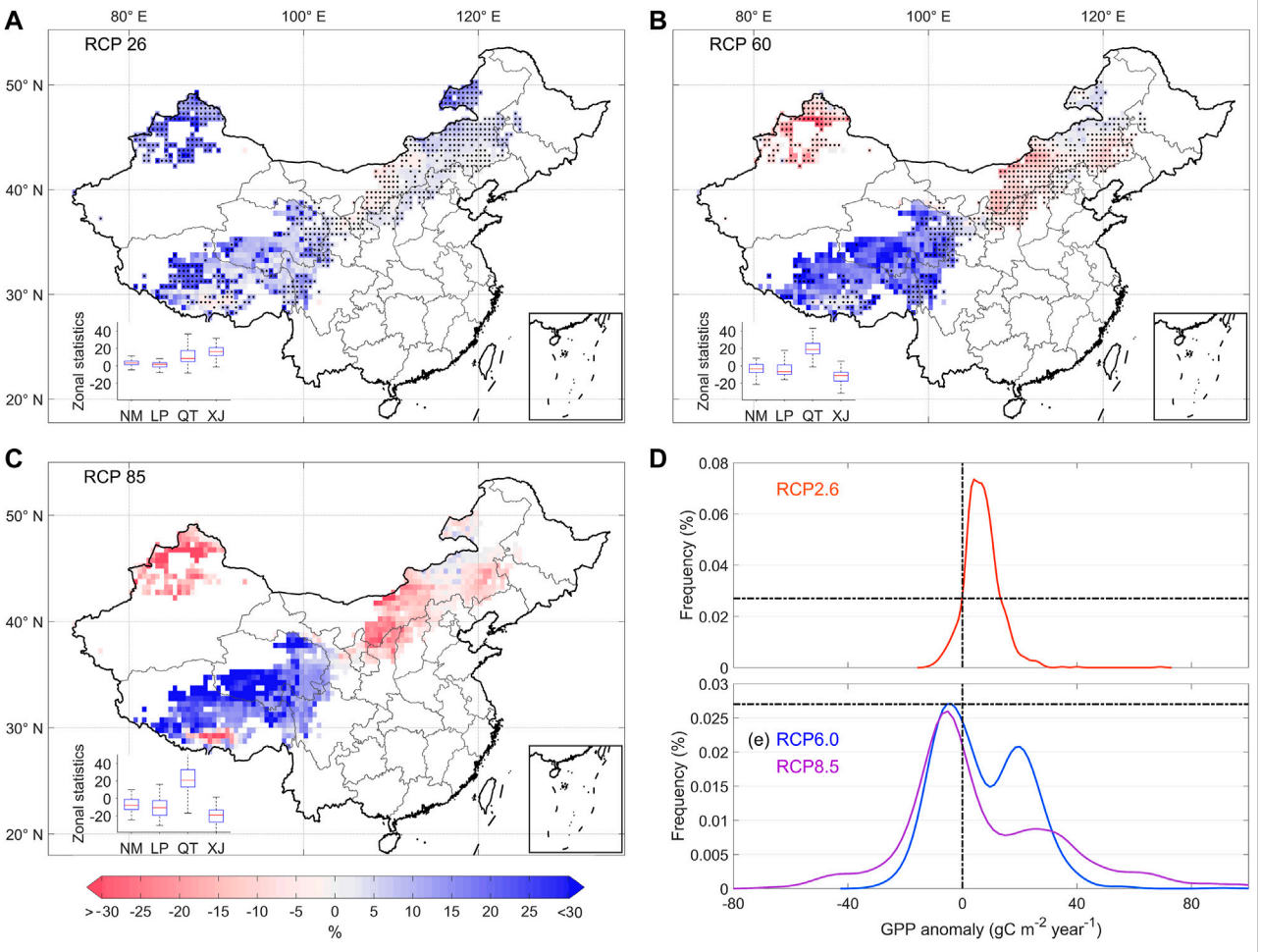

FIGURE 10
Percentage change in mean GPP from 2050 to 2099 compared to 2006–2049 over the Chinese grassland. **(A)** RCP2.6; **(B)** RCP6.0; **(C)** RCP8.5; **(D)** distribution density of percentages in the RCP2.6 scenario; **(E)** distribution density of percentages in the RCP6.0 and RCP8.5 scenarios. Where the black dots in figure **(A,B)** represent three of the four models where the positive and negative directions of percentages are consistent.

standard deviations of RCP2.6 and RCP6.0 were relatively low (Figure 9), reflecting that the differences among regions of Chinese grassland under the low-moderate emission scenario were relatively small and maintained a range in the time series. The standard deviation of Chinese grassland under the high emission scenario of RCP8.5 showed a gradual increase from 2030 onward, indicated that the standard deviation of Chinese grasslands under the RCP8.5 high emission scenario increased gradually after 2030, indicated that the simulated GPP between regions of Chinese grasslands became more spatially heterogeneous and the internal uncertainty increased with time.

After analyzing the percentage change between the second half and the first half of the 21st century (Figure 10), we found that under the RCP2.6 low emission scenario, the GPP values of most of the Chinese grasslands would exceed those of the first half of the century in the second half of the century, and the density distribution curve was more distributed to the right of the 0-value line, and most of the models showed a consistent percentage change in the direction. The RCP8.5 scenario showed the same direction of GPP percentage change as RCP6.0. We concluded that the GPP of Chinese grasslands will not continue to grow steadily under the medium and high emission scenarios in the future, and continued high emissions will limit the productivity accumulation of Chinese temperate grassland and Xinjiang grassland. However, the special point is that the simulation of the direction of the percentage change differs greatly among models for each future scenario Tibetan Plateau grassland in the second half of the century despite showing a stronger increase in GPP, reflecting the great challenge for the models to accurately portray the GPP change on the Tibetan Plateau.

4 Discussion

We indicated that terrestrial ecosystem models have significant uncertainties in model structure, parameterization, and driving data, and the correction and deterministic assessment of model data become important scientific issues (Shao et al., 2016; Cheng et al., 2017). We previously suggested that remote sensing technology provides near real-time indicators related to global vegetation growth and gross primary production, which can be a global-scale constraint for assessing the reliability of the information provided by ecological process models (Mao et al., 2012). In this study, based on the cross-validation results of the model and remotely sensed GPP, we found that the model is an important way to accurately portray the true GPP at the global scale, and its R^2 fit coefficient between the model and remotely sensed data was as high as 0.8, which is consistent with the findings of Mao et al. (2012). However, the comparison with remotely sensed GPP data also reveals that there is a significant overestimation or underestimation of GPP in both models, especially in the pixels in the low GPP region. The reason for this discrepancy may be related to the uncertainty of the model input data in addition to the uncertainty of the model itself. For example, the climate information, system noise and processing bias input to the model can affect the accurate simulation of GPP at the regional scale (Wei et al., 2014; Cheng et al., 2017). In particular, the selected historical climate dataset inputs may cause considerable uncertainty in the estimated GPP with output fluctuations of 9%–20% (Jung et al., 2007; Barman et al., 2014; Wu et al., 2017). In our study, the input climate datasets selected in the MsTMIP model comparison program were mainly CRU-NCEP reanalysis data (Wei et al., 2014), while ISIMIP selected climate datasets from the IPSL-CM6A-LR climate model output (Boucher et al., 2020). Therefore, it is possible that the differences in the selection of climate input parameters led to the differences in the Chinese grassland GPP output from the two model datasets. In addition, other environmental drivers and related data are different between the two model sets, including time-varying atmospheric CO_2 concentration, time-varying N deposition, C_3/C_4 fraction, major crop distribution, phenology, and soil characteristics, which may also be another reason for the existence of over- or under-estimation of model-simulated Chinese grassland GPP (Wei et al., 2014; Shao et al., 2016; Exbrayat et al., 2018).

Grassland GPP uncertainty in China showed an increasing pattern from southeast to northwest, which may be related to the differences in model responses under different environmental stresses. During the historical period, the grasslands of the Qinghai-Tibet Plateau, Xinjiang, and eastern Inner Mongolia had colder and drier climates, and the environmental stresses of moisture and temperature had a greater impact on the accuracy of model simulations (Jia et al., 2018), so the historical GPP based on model simulations also had large uncertainties in colder and drier environments (Shao et al., 2016). In contrast, for future emission scenarios, the uncertainty in model GPP increased in the second half of the 21st century and spatially showed that except for the Qinghai-Tibet Plateau (and the direction of change is not consistent among models), grasslands in other regions exhibit consistent decreasing GPP changes. This aspect reflects that the future GPP of Chinese grasslands will not consistently increase along with rising CO_2 concentration and warming all the time. With the exception of the temperature-constrained Tibetan Plateau, the carbon sequestration capacity of the other grasslands, which are more sensitive to water (especially drought), will be greatly limited in the future (Wu and Wang 2022). On the other hand, we also be seen that accurately simulating the cold-dry Tibetan Plateau GPP in the future will still be quite difficult.

In addition, our study found that ensemble averaging can effectively eliminate the uncertainty of the internal variability among model GPPs, and make the results exhibit low-frequency signals, which is a reasonable and necessary treatment for multi-model ensemble averaging than the results of single-model simulations. The results of EEMD analysis showed that the amplitude of each IMF component after model ensemble

averaging is significantly lower than the time series of the original values, which is consistent with the results of previous studies consistent with previous findings that the ensemble averaging method is not only effective in eliminating the effect of model internal variability, but also may filter out the interdecadal scale signal (Cheng et al., 2017), which is meaningful in many fields. Therefore, in the future, a new method that can eliminate the internal variability and retain the interdecadal scale signal in a more scientific way needs to be explored to resolve this conflict.

5 Conclusion

Uncertainty analysis of GPP datasets based on terrestrial ecosystem models and remote sensing estimates was conducted using cross-validation, standard error statistics and ensemble empirical modal decomposition. We found that 1) the R^2 of the fit coefficients for two-by-two cross-validation of the GPP datasets mostly exceeded 0.8 globally. 2) GPP from different sources were consistent in portraying the spatiotemporal patterns of GPP in Chinese grasslands. However, due to many differences in model structure, parameterization, and driving data, uncertainties still exist, especially in the relatively large standard deviations in some arid-cold areas. 3) The uncertainties of future scenarios are higher than those of historical periods, and the GPP uncertainties of future high-emission scenarios are much higher than those of medium-low emission scenarios. In summary, we found that the uncertainty between different data is very large. Therefore, we recommend that multi-source data (including models and remote sensing) should be used when analyzing ecosystem GPP dynamics in the future, to avoid the shortcomings of a single data that is not sufficient to fully and truly reflect changes in ecosystem productivity.

Data availability statement

The original contributions presented in the study are included in the article/supplementary material, further inquiries can be directed to the corresponding author.

Author contributions

Conceptualization, ZS and PH; Methodology, XYM and PH; Software, PH; Validation, PH and XYM; Formal analysis, PH; Investigation, PH and XYM; Re-sources, HP; Data curation, HP; Writing—original draft preparation, XLM, ZH, and PH; Writing—review and editing, XLM, XYM, and PH; Visualization, PH; Supervision, PH; Project administration, ZS and PH; Funding acquisition, ZS and PH. All authors have read and agreed to the published version of the manuscript.

Funding

This research was funded by Foundation items: National Natural Science Foundation of China, No. 32060408; National Basic Resources Survey Special, No. 2017FY100200; the Scientific Innovation Project of Postgraduates of Xinjiang Uygur Autonomous Region, China, No. XJ 2021G169.

Conflict of interest

The authors declare that the research was conducted in the absence of any commercial or financial relationships that could be construed as a potential conflict of interest.

Publisher's note

All claims expressed in this article are solely those of the authors and do not necessarily represent those of their affiliated organizations, or those of the publisher, the editors and the reviewers. Any product that may be evaluated in this article, or claim that may be made by its manufacturer, is not guaranteed or endorsed by the publisher.

References

Barman, R., Jain, A., and Liang, M. (2014). Climate-driven uncertainties in modeling terrestrial gross primary production: A site level to global-scale analysis. *Glob. Chang. Biol.* 20 (5), 1394–1411. doi:10.1111/gcb.12474

Bondeau, A., Smith, P., Zaehle, S., Schaphoff, S., Lucht, W., Cramer, W., et al. (2007). Modelling the role of agriculture for the 20th century global terrestrial carbon balance. *Glob. Chang. Biol.* 13 (3), 679–706. doi:10.1111/j.1365-2486.2006.01305.x

Boucher, O., Servonnat, J., Albright, A., Aumont, O., Balkanski, Y., Bastrikov, V., et al. (2020). Presentation and evaluation of the IPSL-CM6A-LR climate model. *J. Adv. Model. Earth Syst.* 12 (7), 1–25. doi:10.1029/2019MS002010

Cheng, S., Huang, J., Ji, F., and Lin, L. (2017). Uncertainties of soil moisture in historical simulations and future projections: Uncertainties of soil moisture. *J. Geophys. Res. Atmos.* 122 (4), 2239–2253. doi:10.1002/2016JD025871

Culotta, E. (1995). Will plants profit from high CO_2? *Science* 268 (5211), 654–656. doi:10.1126/science.268.5211.654

Dirmeyer, P., Guo, Z., and Gao, X. (2004). Comparison, validation, and transferability of eight multiyear global soil wetness products. *J. Hydrometeorol.* 5 (6), 1011–1033. doi:10.1175/JHM-388.1

Exbrayat, J., Bloom, A., Falloon, P., Ito, A., Smallman, T. L., and Williams, M. (2018). Reliability ensemble averaging of 21st century projections of terrestrial net primary productivity reduces global and regional uncertainties. *Earth Syst. Dyn.* 9 (1), 153–165. doi:10.5194/esd-9-153-2018

Falge, E., Baldocchi, D., Olson, R., Anthoni, P., Aubinet, M., Bernhofer, C., et al. (2001). Gap filling strategies for long term energy flux data sets. *Agric. For. Meteorology* 107 (1), 71–77. doi:10.1016/s0168-1923(00)00235-5

Guimberteau, M., Zhu, D., Maignan, F., Huang, Y., Yue, C., Dantec-Nédélec, S., et al. (2018). ORCHIDEE-MICT (v8.4.1), a land surface model for the high latitudes: Model description and validation. *Geosci. Model Dev.* 11 (1), 121–163. doi:10.5194/gmd-11-121-2018

Harris, I., Osborn, T., Jones, P., and Lister, D. (2020). Version 4 of the CRU TS monthly high-resolution gridded multivariate climate dataset. *Sci. Data* 7 (1), 109. doi:10.1038/s41597-020-0453-3

He, P., Ma, X., Meng, X., Han, Z., Liu, H., and Sun, Z. (2022). Spatiotemporal evolutionary and mechanism analysis of grassland GPP in China. *Ecol. Indic.* 143. doi:10.1016/j.ecolind.2022.109323

Huang, M., Piao, S., and Zeng, Z. (2015). Seasonal responses of terrestrial ecosystem water-use efficiency to climate change[J]. *Glob. Change Biol.* 22 (6), 2165–2177. doi:10.1111/gcb.13180

Huntzinger, D., Schwalm, C., Michalak, A., Schaefer, K., King, A. W., Wei, Y., et al. (2013). the north American carbon program multi-scale synthesis and terrestrial model intercomparison project – Part 1: Overview and experimental design. *Geosci. Model Dev.* 6 (6), 2121–2133. doi:10.5194/gmd-6-2121-2013

Jain, A., Meiyappan, P., Song, Y., and House, J. (2013). CO_2 emissions from land-use change affected more by nitrogen cycle, than by the choice of land cover data. *Glob. Chang. Biol.* 19 (9), 2893–2906. doi:10.1111/gcb.12207

Jia, W., Liu, M., Wang, D., he, H., Shi, P., Li, Y., et al. (2018). Uncertainty in simulating regional gross primary productivity from satellite-based models over northern China grassland. *Ecol. Indic.* 88 (5), 134–143. doi:10.1016/j.ecolind.2018.01.028

Jung, M., Vetter, M., Herold, M., Churkina, G., Reichstein, M., Zaehle, S., et al. (2007). Uncertainties of modeling gross primary productivity over europe: A systematic study on the effects of using different drivers and terrestrial biosphere models. *Glob. Biogeochem. Cycles* 21 (4), 1–12. doi:10.1029/2006GB002915

Kendall, M., and Gibbons, J. (1957). Rank correlation methods. *Biometrika* 44 (2), 298. doi:10.2307/2333282

Krysanova, V., Vetter, T., Eisner, S., Huang, S. C., Pechlivanidis, I., Strauch, M., et al. (2017). Intercomparison of regional-scale hydrological models and climate change impacts projected for 12 large river basins worldwide-a synthesis. *Environ. Res. Lett.* 12 (10), 105002. doi:10.1088/1748-9326/aa8359

Li, H., Huang, M., Wigmosta, M., Ke, Y., Coleman, A. M., Leung, L. R., et al. (2011). Evaluating runoff simulations from the Community Land Model 4.0 using observations from flux towers and a mountainous watershed. *J. Geophys. Res.* 116 (D24), 1–19. doi:10.1029/2011jd016276

Mao, J., Thornton, P., Shi, X., Zhao, M., and Post, W. (2012). Remote sensing evaluation of CLM4 GPP for the period 2000-09. *J. Clim.* 25 (15), 5327–5342. doi:10.1175/JCLI-D-11-00401.1

Morales, L., Hernandez, A., Rodriguez, N., and Jimenez, R. (2021). Carbon exchange and accumulation in an orinoco high plains native savanna ecosystem as measured by eddy covariance. *Front. Environ. Sci.* 9, 673932. doi:10.3389/fenvs.2021.673932

Osmond, B., Ananyev, G., Berry, J., Langdon, C., Kolber, Z., Lin, G., et al. (2004). Changing the way we think about global change research: Scaling up in experimental ecosystem science. *Glob. Chang. Biol.* 10 (4), 393–407. doi:10.1111/j.1529-8817.2003.00747.x

Randerson, J., Hoffman, F., Thornton, P., Mahowald, N., Lindsay, K., Lee, Y.-H., et al. (2009). Systematic assessment of terrestrial biogeochemistry in coupled climate-carbon models. *Glob. Chang. Biol.* 15 (10), 2462–2484. doi:10.1111/j.1365-2486.2009.01912.x

Rosenzweig, C., Arnell, N., Ebi, K., Lotze-Campen, H., Raes, F., Rapley, C., et al. (2017). Assessing inter-sectoral climate change risks: The role of ISIMIP. *Environ. Res. Lett.* 12 (1), 010301. doi:10.1088/1748-9326/12/1/010301

Schimel, D., Melillo, J., Tian, H., McGuire, A., Kicklighter, D., Kittel, T., et al. (2000). Contribution of increasing CO2 and climate to carbon storage by ecosystems in the United States. *Sci. (New York, N.Y.)* 287 (1), 2004–2006. doi:10.1126/science.287.5460.2004

Shao, J., Zhou, X., Luo, Y., Zhang, G. D., Yan, W., Li, J. X., et al. (2016). Uncertainty analysis of terrestrial net primary productivity and net biome productivity in China during 1901-2005. *J. Geophys. Res. Biogeosci.* 121 (5), 1372–1393. doi:10.1002/2015JG003062

Sitch, S., Huntingford, C., and Gedney, N. (2008). Evaluation of the terrestrial carbon cycle, future plant geography and climate-carbon cycle feedbacks using five Dynamic Global Vegetation Models (DGVMs)[J]. *Glob. Change Biol.* 14 (9), 2015–2039. doi:10.1111/j.1365-2486.2008.01626.x

Smith, B., Wårlind, D., Arneth, A., Hickler, T., Leadley, P., Siltberg, J., et al. (2014). Implications of incorporating N cycling and N limitations on primary production in an individual-based dynamic vegetation model. *Biogeosciences* 11 (7), 2027–2054. doi:10.5194/bg-11-2027-2014

Tian, H., Chen, G., Zhang, C., Liu, M., Sun, G., Chappelka, A., et al. (2012). Century-scale responses of ecosystem carbon storage and flux to multiple environmental changes in the Southern United States. *Ecosystems* 15 (4), 674–694. doi:10.1007/s10021-012-9539-x

Wang, J., Sun, R., Zhang, H., Xiao, Z., Zhu, A., Wang, M., et al. (2021). New global MuSyQ GPP/NPP remote sensing products from 1981 to 2018. *IEEE J. Sel. Top. Appl. Earth Obs. Remote Sens.* 14 (1), 5596–5612. doi:10.1109/jstars.2021.3076075

Warnant, P., François, L., Strivay, D., and Gerard, J. C. (1994). Caraib: A global model of terrestrial biological productivity. *Glob. Biogeochem. Cycles* 8 (3), 255–270. doi:10.1029/94GB00850

Wei, Y., Liu, S., Huntzinger, D., Michalak, A. M., Viovy, N., Post, W. M., et al. (2014). the north American carbon program multi-scale synthesis and terrestrial model intercomparison project-part 2: Environmental driver data. *Geosci. Model Dev.* 7 (6), 2875–2893. doi:10.5194/gmd-7-2875-2014

Wu, C., and Wang, T. (2022). Evaluating cumulative drought effect on global vegetation photosynthesis using numerous GPP products. *Front. Environ. Sci.* 10 (1). doi:10.3389/fenvs.2022.908875

Wu, Z., Ahlström, A., Smith, B., Ardö, J., Eklundh, L., Fensholt, R., et al. (2017). Climate data induced uncertainty in model based estimations of terrestrial primary productivity. *Environ. Res. Lett.* 12 (6), 064013. doi:10.1088/1748-9326/aa6fd8

Wu, Z., and Huang, N. (2009). Ensemble empirical mode decomposition: A noise-assisted data analysis method. *Adv. Adapt. Data Anal.* 1 (1), 1–41. doi:10.1142/S1793536909000047

Yuan, W., Cai, W., Xia, J., Chen, J., Liu, S., Dong, W., et al. (2014). Global comparison of light use efficiency models for simulating terrestrial vegetation gross primary production based on the LaThuile database. *Agric. For. Meteorology* 192 (15), 108–120. doi:10.1016/j.agrformet.2014.03.007

Zaehle, S., Sitch, S., Smith, B., and Hatterman, F. (2005). Effects of parameter uncertainties on the modeling of terrestrial biosphere dynamics. *Glob. Biogeochem. Cycles* 19 (3), 1–16. doi:10.1029/2004GB002395

Zhou, S., Yu, B., Schwalm, C., Ciais, P., Zhang, Y., Fisher, J., et al. (2017). Response of water use efficiency to global environmental change based on output from terrestrial biosphere models: Drivers of WUE variability. *Glob. Biogeochem. Cycles* 31 (11), 1639–1655. doi:10.1002/2017GB005733

Zscheischler, J., Michalak, A., Schwalm, C., Mahecha, M., Huntzinger, D., Reichstein, M., et al. (2014). Impact of large-scale climate extremes on biospheric carbon fluxes: An intercomparison based on MsTMIP data. *Glob. Biogeochem. Cycles* 28 (6), 585–600. doi:10.1002/2014GB004826

frontiers | Frontiers in Environmental Science

ORIGINAL RESEARCH
published: 27 April 2022
doi: 10.3389/fenvs.2022.790200

Assessing Model Predictions of Carbon Dynamics in Global Drylands

Dominic Fawcett[1,2†], Andrew M. Cunliffe[2†], Stephen Sitch[2], Michael O'Sullivan[3], Karen Anderson[1], Richard E. Brazier[4], Timothy C. Hill[2], Peter Anthoni[5], Almut Arneth[5], Vivek K. Arora[6], Peter R. Briggs[7], Daniel S. Goll[8], Atul K. Jain[9], Xiaojun Li[10], Danica Lombardozzi[11], Julia E. M. S. Nabel[12], Benjamin Poulter[13], Roland Séférian[14], Hanqin Tian[15], Nicolas Viovy[16], Jean-Pierre Wigneron[10], Andy Wiltshire[17] and Soenke Zaehle[12]*

[1]Environment and Sustainability Institute, University of Exeter, Penryn, United Kingdom, [2]Department of Geography, College of Life and Environmental Sciences, University of Exeter, Exeter, United Kingdom, [3]Department of Mathematics, College of Engineering, Mathematics and Physical Sciences, University of Exeter, Exeter, United Kingdom, [4]Centre for Resilience in Environment, Water and Waste, Geography, College of Life and Environmental Sciences, University of Exeter, Exeter, United Kingdom, [5]Karlsruhe Institute of Technology, Institute of Meteorology and Climate, Research/Atmospheric Environmental Research, Garmisch-Partenkirchen, Germany, [6]Canadian Centre for Climate Modelling and Analysis, Environment and Climate Change Canada, Victoria, BC, Canada, [7]Climate Science Centre, CSIRO Oceans and Atmosphere, Canberra, ACT, Australia, [8]Université Paris Saclay, CEA-CNRS-UVSQ, LSCE/IPSL, Gif sur Yvette, France, [9]Department of Atmospheric Sciences, University of Illinois, Urbana, IL, United States, [10]INRAE, UMR 1391 ISPA, Université de Bordeaux, Villenave d'Ornon, France, [11]Climate and Global Dynamics Laboratory, National Center for Atmospheric Research, Boulder, CO, United States, [12]Max Planck Institute for Biogeochemistry, Max Planck Institute for Meteorology, Jena, Germany, [13]NASA GSFC, Earth Science Division, Biospheric Sciences Laboratory, Greenbelt, MD, United States, [14]CNRS, CNRM, Université de Toulouse, Toulouse, France, [15]International Center for Climate and Global Change Research, School of Forestry and Wildlife Sciences, Auburn University, Auburn, AL, United States, [16]LSCE, Université Paris-Saclay, Gif sur Yvette, France, [17]Met Office Hadley Centre, Exeter, United Kingdom

OPEN ACCESS

Edited by:
Lara Prihodko, New Mexico State University, United States

Reviewed by:
Ning Chen, Lanzhou University, China
Joel Biederman, United States Department of Agriculture, United States

***Correspondence:**
Dominic Fawcett
d.fawcett@exeter.ac.uk

[†]These authors have contributed equally to this work and share first authorship

Specialty section:
This article was submitted to Drylands, a section of the journal Frontiers in Environmental Science

Received: *06 October 2021*
Accepted: *04 April 2022*
Published: *27 April 2022*

Citation:
Fawcett D, Cunliffe AM, Sitch S, O'Sullivan M, Anderson K, Brazier RE, Hill TC, Anthoni P, Arneth A, Arora VK, Briggs PR, Goll DS, Jain AK, Li X, Lombardozzi D, Nabel JEMS, Poulter B, Séférian R, Tian H, Viovy N, Wigneron J-P Wiltshire A and Zaehle S (2022) Assessing Model Predictions of Carbon Dynamics in Global Drylands. Front. Environ. Sci. 10:790200. doi: 10.3389/fenvs.2022.790200

Drylands cover ca. 40% of the land surface and are hypothesised to play a major role in the global carbon cycle, controlling both long-term trends and interannual variation. These insights originate from land surface models (LSMs) that have not been extensively calibrated and evaluated for water-limited ecosystems. We need to learn more about dryland carbon dynamics, particularly as the transitory response and rapid turnover rates of semi-arid systems may limit their function as a carbon sink over multi-decadal scales. We quantified aboveground biomass carbon (AGC; inferred from SMOS L-band vegetation optical depth) and gross primary productivity (GPP; from PML-v2 inferred from MODIS observations) and tested their spatial and temporal correspondence with estimates from the TRENDY ensemble of LSMs. We found strong correspondence in GPP between LSMs and PML-v2 both in spatial patterns (Pearson's r = 0.9 for TRENDY-mean) and in inter-annual variability, but not in trends. Conversely, for AGC we found lesser correspondence in space (Pearson's r = 0.75 for TRENDY-mean, strong biases for individual models) and in the magnitude of inter-annual variability compared to satellite retrievals. These disagreements likely arise from limited representation of ecosystem responses to plant water availability, fire, and photodegradation that drive dryland carbon dynamics. We assessed inter-model agreement and drivers of long-term change in carbon stocks over centennial timescales. This analysis suggested that the simulated trend of increasing carbon stocks in drylands is in soils and primarily driven by increased productivity due to CO_2 enrichment. However, there is limited empirical

evidence of this 50-year sink in dryland soils. Our findings highlight important uncertainties in simulations of dryland ecosystems by current LSMs, suggesting a need for continued model refinements and for greater caution when interpreting LSM estimates with regards to current and future carbon dynamics in drylands and by extension the global carbon cycle.

Keywords: land surface models (LSM), drylands, productivity, aboveground biomass, model evaluation, vegetation optical depth (VOD)

INTRODUCTION

Drylands play an important role in the global carbon cycle and are vulnerable to global climate and land-use changes (Sietz et al., 2011; Ahlström et al., 2015). Yet, despite their importance, we have limited understanding of drylands and their ecological responses to climate change and other drivers (Huang et al., 2017). Defined by their climatic aridity, dryland ecosystems cover ca. 40% of the land surface and are expanding as evapotranspiration increases faster than precipitation (Huang et al., 2016; Archer et al., 2018; Yao et al., 2020; IPCC, 2021). Despite being characterised by relatively low-biomass densities relative to forest biomes, drylands, and particularly semi-arid ecosystems, are thought to dominate both the longer term (>50-year) trend and year-to-year variability in the land carbon sink (Poulter et al., 2014; Ahlström et al., 2015; Piao et al., 2020). There is a pressing need to learn more about the future efficacy of drylands as a sink of anthropogenic carbon emissions (Friedlingstein et al., 2019). Particularly semi-arid ecosystems are thought to have a potentially transitory response to large perturbations causing enhanced uptake followed by rapid turnover of carbon through decomposition and loss through fire (Poulter et al., 2014), implying that they may only have the capacity to function as a significant carbon sink for a finite period (Schlesinger et al., 2009). Drylands furthermore provide provisioning and regulating services that directly support over a third of the human population worldwide (SRCCL, 2020). Many of these people are experiencing increasing insecurity due to the triple threat of climate change, population growth, and increasing pressure on finite natural resources (Huang et al., 2016; Archer et al., 2018; Xu et al., 2020).

There is considerable uncertainty in current and projected storage and fluxes of carbon in drylands (Schlesinger et al., 2009; Haverd et al., 2016; Schlesinger, 2016; Yao et al., 2020). Much of our understanding of the processes behind these global changes relies on simulations of land surface models (LSMs) or dynamic global vegetation models (DGVMs, in this manuscript collectively labelled as LSMs; Ahlström et al., 2015; Piao et al., 2020; Poulter et al., 2014). Yet we know that LSMs often perform more poorly in water-limited drylands relative to energy-limited biomes (Harper et al., 2020; Yang et al., 2020; MacBean et al., 2021). Much of this poorer performance is attributed to incomplete representations of ecosystem responses to plant water availability in terms of carbon inputs (Harper et al., 2020; MacBean et al., 2021) and processes controlling the release of carbon such as fire and photodegradation (Bond et al., 2005; Berenstecher et al., 2020). This is compounded by limitations in parameterisation data on land use and localised precipitation (Yang et al., 2020). This uncertainty is further exacerbated by a backdrop of changing environmental conditions including CO_2 fertilization, increasing plant water use efficiency, fire suppression, woody shrub encroachment, and increasingly variable precipitation, leaving considerable uncertainty around the resilience of dryland ecosystem function (Gonsamo et al., 2021; Maestre et al., 2021; Walker et al., 2021).

To constrain uncertainty in predictions of the current and future functioning of dryland ecosystems, further evaluations are needed to assess LSM performance (Forkel et al., 2019; Piao et al., 2020). LSM intercomparison efforts are common and include those that focus on "Trends in net land carbon exchange" (TRENDY) (Sitch et al., 2015). However, historically there has been a lack of observational data from water-limited drylands, and the data that do exist have not been extensively used for evaluating model performance in these settings (Ciais et al., 2011). New satellite-derived datasets have recently become available with global coverage over recent decades (Smith et al., 2019). For example, productivity describes the uptake of carbon by the ecosystems and can be inferred from satellite observations using light use efficiency models. Critically, light use efficiency is modulated by changing atmospheric carbon dioxide concentrations (Long et al., 2004). The PML-v2 gross primary productivity (GPP) product is modelled based on MODIS observations and has been demonstrated to have less error compared to other products with regards to site-level eddy covariance observations (Gan et al., 2018; Zhang et al., 2019a). Most evaluations of LSM performance have focused on fluxes rather than carbon stocks (Blyth et al., 2011; Yang et al., 2020; Yao et al., 2020; MacBean et al., 2021). Vegetation optical depth (VOD) provides a metric for vegetation structural characterisation, by measuring the attenuation of microwaves by water content in vegetation (Chaparro et al., 2019). Recent studies have found L-band frequency (1–2 GHz or 15–30 cm wavelength) VOD (L-VOD) is strongly related to aboveground biomass carbon (AGC) in dryland ecosystems (Brandt et al., 2018). Another advantage of this product is its multi-year availability, which is imperative for evaluating trends and interannual variability in biomass carbon stocks.

The long-term trends of dryland carbon stocks over centennial timescales and their future state is critically important yet highly uncertain given their potential transitory responses. However, these timescales lie beyond the temporal limit of widespread observational data, hindering evaluations of LSM estimates. To assess model performance and evaluate long-term changes in

dryland carbon stocks, we undertook a model intercomparison. By evaluating the consistency of different model estimates over time, we can better constrain the uncertainty associated with ensemble estimates over multi-decadal periods. If different models agree, this increases confidence in their ensemble predictions over longer timescales. Conversely, if models differ over time, then ensemble predictions should be treated with caution and different ways of assessing models should be selected by considering them as falsifiable hypotheses (Goldstein et al., 2013).

This study aims to investigate the correspondence between simulated and retrieved productivity and biomass carbon in dryland landscapes. Specifically, we addressed the following questions:

1) How well are TRENDY models able to reproduce a) spatial distribution, b) temporal trends, and c) interannual variability in GPP compared to estimates from the satellite-derived PML-v2 product?
2) How well are TRENDY models able to reproduce a) spatial distribution, b) temporal trends, and c) interannual variability in aboveground vegetation carbon compared to estimates from the satellite-derived L-VOD product?
3) How consistent are TRENDY simulations of vegetation and soil carbon stocks among models through time?

METHODS

Dryland Delineation

We classified climatic drylands based on the aridity index, using a threshold of <0.65 for the ratio of mean annual precipitation (P) to mean annual potential evapotranspiration (PET) (Yao et al., 2020) calculated using the 2.5 arc minutes 1981–2010 TerraClimate mean gridded surface climatology (Abatzoglou et al., 2018). The fine grain of the TerraClimate product corresponded more closely to physical reality than coarser resolution products (**Supplementary Table S1** for details of these gridded products). We excluded drylands >55° north and south of the Equator to omit "cold" permafrost drylands, resulting in a global dryland area of 59.1×10^6 km^2. While LSMs do not always simulate drylands exactly coincident with this climatic mask, this masking approach is standard (e.g., Ahlström et al., 2015; Yao et al., 2020; Gonsamo et al., 2021).

Gross Primary Productivity From MODIS

We used the PML-v2 (v016) GPP product derived using a light use efficiency model based on MODIS observations (Zhang et al., 2019a). This product has a spatial resolution of 500 m, revisit frequency of 8 days, and was available from 26/03/2000 to 26/12/2020. Importantly, the PML-v2 product couples evapotranspiration and GPP resulting in a more robust estimation of GPP while partly accounting for water use efficiency, and explicitly accounts for the influence of changing CO_2 concentration on carbon assimilation via a simplified photosynthesis model (Gan et al., 2018). PML-v2 has been evaluated at 95 eddy covariance flux tower sites, 40 of which lie within our delineated drylands (Zhang et al., 2019a). Over the 95 sites, PML-v2 outperformed other GPP products available at the time for 8-day and site mean GPP, with smaller bias, lower RMSE, and higher R^2 compared to the MOD17A2H, FluxCom GPP, and VPM GPP products; (Zhang et al., 2019a), while performance regarding annual anomalies was comparable. We calculated annual integrated productivity for spatial comparison with the LSM predictions and temporal analysis.

Above Ground Carbon Density From L-Band Vegetation Optical Depth

We inferred AGC in biomass from L-VOD retrieved from the Soil Moisture and Ocean Salinity (SMOS) mission L-band observations from 2011 to 2018 (SMOS-IC V2; Wigneron et al., 2021; **Figure 1**). Soil moisture and L-VOD are derived from a two-parameter inversion of the L-MEB model (L-band microwave emission of the biosphere) from the multi-angular and dual-polarized SMOS observations (Wigneron et al., 2021). The SMOS-IC products are mostly independent of other Earth observation datasets or simulations from atmospheric models (Wigneron et al., 2021). The L-VOD product consists of ascending and descending orbit datasets with a maximum 3-day revisit time. L-VOD is sensitive to radio frequency interference (RFI) over some specific geographic regions (particularly central Asia and southern Europe) and noise when retrieved over areas of variable topography or frozen ground (Fernandez-Moran et al., 2017). L-VOD data require filtering to retrieve reproducible signals, so we filtered observations by quality flags to exclude pixels containing more than 10% water, ice, or urban land cover (based on the MODIS MCD12Q1 product and IGBP classification scheme), extreme topography (Mialon et al., 2008) and frozen ground (ECMWF soil temperature <273 K) (Fernandez-Moran et al., 2017). L-VOD retrievals above a noise threshold between measured and L-MEB modelled brightness temperature values (8 K) were discarded to remove strong RFI (Fernandez-Moran et al., 2017). We selected four regions with sufficient data coverage (North America, South America, Australia, and Africa) and total dryland area 37.9×10^6 km^2, as RFI precluded reliable retrieval of L-VOD in other dryland regions. Filtered observations (mean of 102 per pixel annually) were aggregated to annual median ascending and descending L-VOD. Where fewer than 20 observations per year were available, the pixel was excluded (Brandt et al., 2018). Large differences between annual average ascending and descending L-VOD can indicate remaining RFI, therefore pixels where this difference was greater than 0.05 L-VOD were excluded. This filtering also excluded a part of North America due to an L-VOD anomaly in 2011. L-VOD retrievals are sensitive to both vegetation biomass and water stress (Konings et al., 2019). However, we expect trends in annual median L-VOD to be largely unaffected by inter-annual variability in vegetation water content. We assume that any trend in vegetation water content would correspond to a trend in vegetation biomass in these predominantly water-limited ecosystems (Abel et al., 2021; Frappart et al., 2020). We assumed a linear relationship between plant water content and biomass in these generally

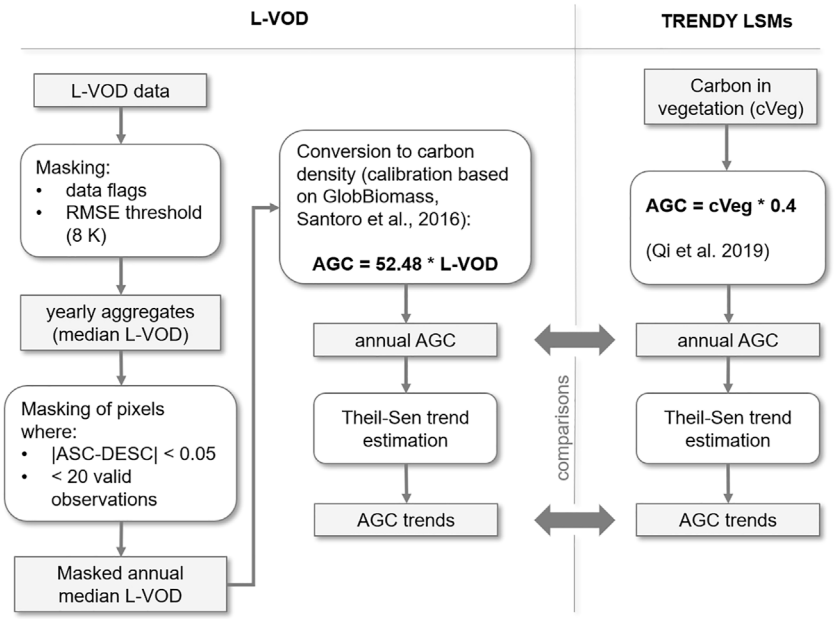

FIGURE 1 | Processing of L-VOD data and TRENDY simulated above ground carbon (AGC) to obtain annual average carbon density and trends. ASC and DESC refer to ascending and descending L-VOD data. Bold arrows indicate products compared.

sparsely vegetated drylands, which was supported by the findings of (Brandt et al., 2019; Fan et al., 2019; Konings et al., 2017; Liu et al., 2015; Mialon et al., 2020; Rodríguez-Fernández et al., 2018; Tian et al., 2016). Annual average carbon density (Mg C ha^{-1}) was estimated from ascending L-VOD, which is acquired at dawn when plant water storage usually peaks (Tian et al., 2018). **Equation 1** was used to estimate AGC which was derived from an OLS regression of L-VOD against a global biomass map (Santoro et al., 2018), converted to AGC following the 47% biomass:carbon density ratio (Paustian et al., 2006; Chave et al., 2019). We developed a drylands-specific biomass transfer function because previous linear models (e.g., Brandt et al., 2018) calibrated against data including high-biomass ecosystems like tropical forests tend to overestimate dryland biomass (**Supplementary Figure S3**). The GlobBiomass map was selected as it showed a higher correlation with L-VOD for drylands than available alternatives (**Supplementary Table S2**).

$$AGC = 52.48 \times LVOD \quad [Mg\,\mathrm{C\,ha^{-1}}] \tag{1}$$

Land Surface Models Simulated Productivity and Biomass

To test the correspondence of state-of-the-art LSMs with retrieved biomass and productivity estimates, we used the simulation outputs from 12 LSMs from the TRENDY v8 project (Friedlingstein et al., 2019). This TRENDY ensemble of models includes CABLE-POP, CLASS-CTEM, CLM5.0, DLEM, ISBA-CTRIP, ISAM, JSBACH, JULES-ES-1.0, LPJ-GUESS, OCN, ORCHIDEE, and ORCHIDEE-CNP (**Supplementary Table S3** for details). For these comparisons we focused on the most comprehensive simulations with time-varying CO_2, observed climate and land-use forcing (TRENDY "S3" simulations). Using the ensemble mean of these LSMs allows us to filter some of the inter-model variability to examine the overall model estimates. Six of these models include representation of fire processes [**Supplementary Table S3** and (Friedlingstein et al., 2019) for details]. We annually aggregated GPP and mean annual biomass of the LSMs, from 01/01/2001 to 31/12/2018 and 01/01/2011 to 31/12/2018 respectively. We used AGC where this was quantified by the LSMs (CABLE-POP, CLASS-CTEM, CLM, ISAM). For the LSMs that did not explicitly partition carbon into above and below pools in TRENDYv8 outputs, we assumed 40% of simulated total biomass carbon was aboveground, using the average root to shoot ratios of grasslands, shrublands, savannas and woody savanna biomes that together dominate total dryland biomass (Liu et al., 2015; Qi et al., 2019). Though this ratio will vary regionally according to environmental factors and plant functional types, there is insufficient information available to enable accurate spatially explicit exploration.

Land Surface Models Intercomparison

To assess the implications of different model simulations over climate-relevant time scales, we evaluated changes in predicted soil C (cSoil, including necromass as litter and coarse woody debris where simulated), vegetation carbon (cVeg), and net ecosystem (cEco = cSoil + cVeg) stocks from 1901 to 2018. At the end of this period, we quantified how much each model diverged from the TRENDY mean in units of standard deviation of the ensemble mean (Goldstein et al., 2013). We excluded ISBA-CTRIP from this portion of the analysis because this model had issues with 1) insufficient soil carbon storage under trees and 2) high productivity of crops causing excessive soil inputs (Boysen

et al., 2020) (subsequently resolved by the addition of a crop sub-model). To diagnose the causes of the differences in simulated carbon stocks over time and between models, we isolated the effects of CO_2, climate change, and land-use change by looking at the contribution associated with the TRENDY "S1" (including CO_2 forcing), "S2" (including CO_2 and climate change forcing), and "S3" simulations (Friedlingstein et al., 2019).

Fire

To understand the extent to which model-data differences in GPP and AGC related to fire, a process not represented in all LSMs, we investigated these spatially in relation to fire frequency. Using the most recent MCD64A1 version 6 burned area product (Giglio et al., 2015), we calculated the sum of the burned area between 2001 and 2018 per 1° grid cell and divided it by the length of the data record. This period was chosen to best encapsulate the influence of fires on GPP and AGC.

Statistical Analysis

We tested the spatial correspondence between LSM simulations and biomass carbon retrieved from L-VOD or GPP retrieved from MODIS respectively. To maintain a consistent sample size across models, we used bilinear interpolation to resample the outputs from TRENDY models to a common spatial resolution of 1°. To appropriately handle boundary effects and partial coverage due to quality filtering of satellite retrieved L-VOD and GPP, we computed weights for the model pixels using the "exactextractr" package in R (Baston, 2020, v0.5.1). We computed weighted pairwise Pearson's r (R package "weights", Pasek, 2020, v1.0.1), and used weighted total least squares regression (R package "deming", Therneau, 2018, v1.4) to fit linear models that account for uncertainty on both axes to quantify the agreement as the slope of the fitted model.

To test the temporal correspondence at annual resolution between biomass carbon inferred from L-VOD and simulated with LSMs and between GPP inferred from MODIS and simulated with LSMs, we summed the weighted dryland values at the native spatial resolution of each dataset using "exactextractr", and for the biomass comparison considered only the areas with reliable L-VOD data for all years (**Figure 1** and **Supplementary Figure S2**). We quantified bias as the mean error between the summed model predictions and the satellite retrievals. Both GPP and AGC measurements were highly sensitive to the approaches used to resample data. Sensitivity analysis revealed that the inclusion or exclusion of cells only partially within our spatial region of interest potentially introduces a 6-fold difference in the total productivity and biomass retrieved for drylands (**Supplementary Figures S17–19**). To minimise this issue when undertaking this analysis across datasets with different native resolutions, we used weighted extraction methods to account for the partial coverage of cells within a mask.

We used a Theil-Sen estimator to robustly fit linear models to the time series of productivity and AGC (Myers-Smith et al., 2020). To assess correspondence in inter-annual variability, we normalised each time series to its mean and detrended the series using the Theil-Sen model slope. The goodness-of-fit was then quantified as the mean absolute error between the series.

RESULTS

Correspondence in Gross Primary Productivity

We found good spatial correlation between the mean GPP PML-v2 inferred from MODIS observations and GPP simulated by the TRENDY model ensemble (**Figure 2**; **Table 1**) over arid and semi-arid regions between 2001 and 2018. Correlation coefficients were moderately high across the 12 models, with Pearson's r ranging from 0.71 to 0.90. The spatial patterns shown in **Figure 2B** are common across most LSMs (**Supplementary Figure S6**), with overestimation of productivity in the African Sahel and underestimation of productivity in southern African and South American drylands. The linear model slopes between the model and the satellite retrievals ranged from 0.56 to 1.18. The TRENDY mean exhibited strong correspondence with the satellite retrievals, with r of 0.9 and a slope of 0.88. We found no overarching relationship between fire frequency and bias in GPP although several models (JULES, CLASS-CTEM, ORCHIDEE-CNP, and OCN) did systematically overestimate GPP in more frequently burned areas (**Supplementary Figure S11**).

We found strong correspondence in inter-annual anomalies in GPP between MODIS-derived and all TRENDY models between 2001 and 2018. There was relatively little bias in mean GPP between the TRENDY mean and MODIS PML-v2 product (ME −1.5 Pg C yr^{-1}, 5.7%) (**Figure 3C**; **Table 1**). All 12 models and consequently the TRENDY-mean exhibited positive trends in productivity over time (11 of 12 trends were significant at α 0.05), while the retrieved GPP had no trend over the 18 years (**Figure 3A**, **Supplementary Table S4**). GPP trends differed spatially, increasing in some areas and decreasing in others (**Supplementary Figures S5, S7**).

Correspondence in Aboveground Biomass Carbon

We found often poor agreement in the spatial patterns of remotely-sensed and model-simulated biomass for the regions analysed (Africa, Australia, North and South America) (**Figure 4**, **Table 1**). Correlation coefficients were moderate across the 12 models, with Pearson's r ranging from 0.52 to 0.75. The bias between the models and the satellite retrievals was often extreme, with most models exhibiting substantial bias and linear model slopes ranging between 0.2 and 5.2. The TRENDY mean exhibited slightly stronger correspondence with the satellite retrievals, with r of 0.75 and a slope of 1.13. For most models, we found little relation between observed burn frequency and model - data residuals, apart from JULES and CLASS-CTEM which overestimated biomass in more frequently burned regions (**Supplementary Figure S12**).

Detection of temporal change in biomass was hindered by the short (2011–2018) period included in the L-VOD product. There was generally poor agreement in the temporal patterns of simulated and remotely-sensed above ground carbon. There was a large range in bias between models and the satellite retrieval with MEs from −8.7 to 8.4 Pg C (−84.4

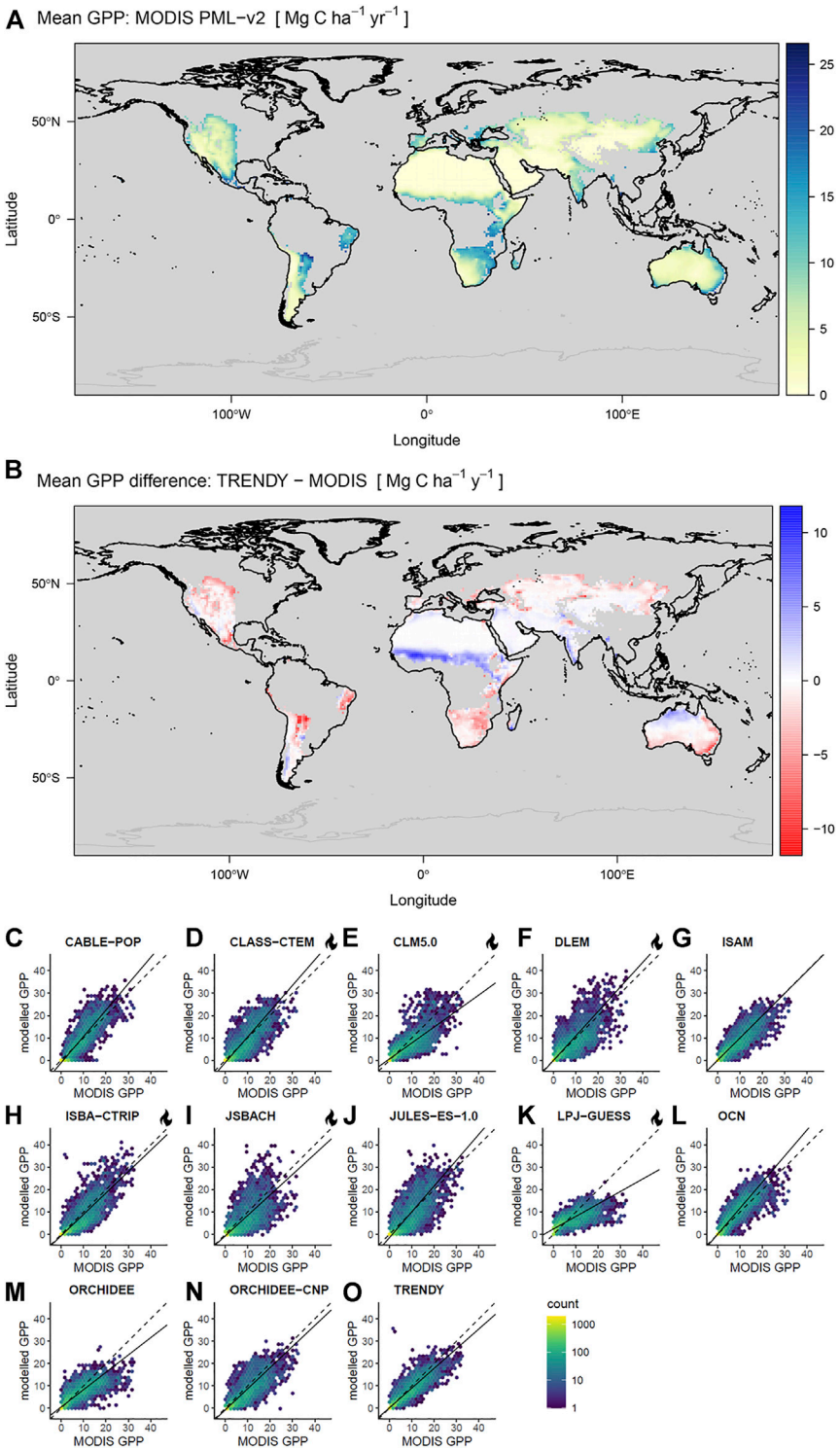

FIGURE 2 | (A) Mean productivity retrieved from MODIS PML-v2, **(B)** difference between MODIS PML-v2 minus TRENDY-mean productivity over arid and semi-arid regions. The regions analysed are shown in bold. **(C–O)** Pairwise pixel covariance in annual GPP means over global dryland regions (2001–2018) estimated from MODIS PML-v2 and TRENDY models, displayed as counts per hexagonal bin. Dashed lines represent 1:1, and solid lines are linear models fitted with total least squares. Units are GPP (Mg C ha^{-1} y^{-1}) and all means are calculated over the common 2001–2018 time period. Note that in **(C–O)** models are fitted to weighted values but weights are not illustrated while **(A,B)** include only grid cells with centroids within the dryland mask. LSMs with explicit representation of fire are indicated with a flame icon.

TABLE 1 | Correspondence between model simulations and satellite retrieved GPP and AGC from MODIS PML-v2 and L-VOD respectively. Where Pearson's r indicates the weighted Pearson's r, slope is the slope of the linear model fitted to the pairwise pixel comparison with weighted total least squares regression, bias in time is the mean error of the annually aggregated values (percentages in brackets show the relative error), and the sensitivity to interannual variability is quantified by the mean-normalised mean absolute error. Shading indicates the relative performance of each model, with darker shading indicating better correspondence. Regression slopes were shaded by their $\log_{10}$ absolute value. * indicates models including explicit representation of fire.

Model	Productivity space		Time			Biomass space		Time		
	Pearson's r	Regr. slope	Bias (ME)	–	Sens (norm. MAE)	Pearson's r	Regr. slope	Bias (ME)	–	Sens (norm. MAE)
CABLE-POP	0.900	1.175	−1.343	(−5.1%)	0.441	0.558	3.801	3.489	(+33.7%)	0.148
CLASS-CTEM*	0.831	1.147	−2.406	(−9.06%)	0.465	0.573	5.175	8.433	(+81.5%)	0.196
CLM5.0*	0.812	0.715	−3.960	(−14.9%)	0.470	0.606	1.780	−1.616	(−15.6%)	0.149
DLEM*	0.787	1.097	3.793	(+14.3%)	0.490	0.694	1.213	−0.249	(−2.4%)	0.155
ISAM	0.905	0.995	1.012	(+3.8%)	0.449	0.633	1.687	−4.011	(−38.8%)	0.190
ISBA-CTRIP*	0.852	0.955	−3.906	(−14.7%)	0.439	0.716	0.944	−3.587	(−34.7%)	0.161
JSBACH*	0.711	0.915	−6.394	(−24.1%)	0.543	0.526	0.211	−8.727	(−84.4%)	0.162
JULES-ES-1.0	0.749	1.156	−4.838	(−18.2%)	0.482	0.521	3.539	5.039	(+48.7%)	0.185
LPJ-GUESS*	0.761	0.560	2.590	(+9.8%)	0.555	0.583	0.291	−5.821	(−56.3%)	0.162
OCN	0.905	1.168	4.128	(+15.5%)	0.665	0.710	0.974	−3.562	(-34.4%)	0.127
ORCHIDEE	0.834	0.775	−4.822	(−18.2%)	0.336	0.576	0.464	−6.325	(−61.1%)	0.148
ORCHIDEE-CNP	0.817	0.943	−1.921	(−7.2%)	0.408	0.615	1.662	1.579	(+15.3%)	0.171
TRENDY-mean	0.898	0.882	−1.505	(−5.7%)	0.367	0.750	1.129	−1.281	(−12.4%)	0.152

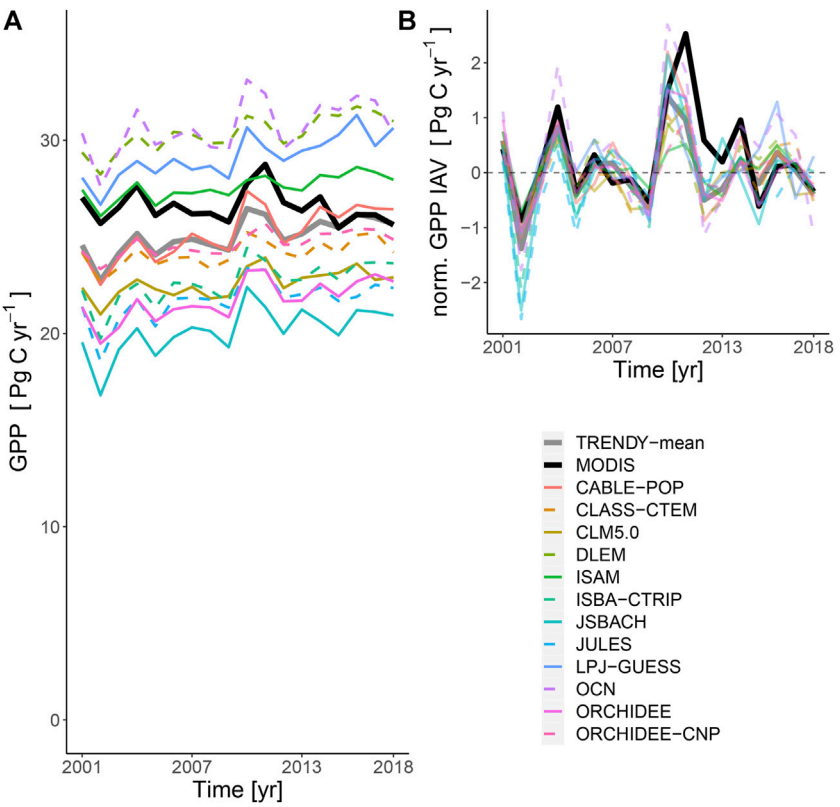

FIGURE 3 | (A) Time-series of mean annual GPP (2001–2018) of global drylands for the satellite retrieval and TRENDY models (including TRENDY mean). All 12 models simulate increasing GPP over time whereas MODIS-retrieved GPP had no clear trend. **(B)** The mean-normalised detrended time series show good agreement in interannual differences for all models.

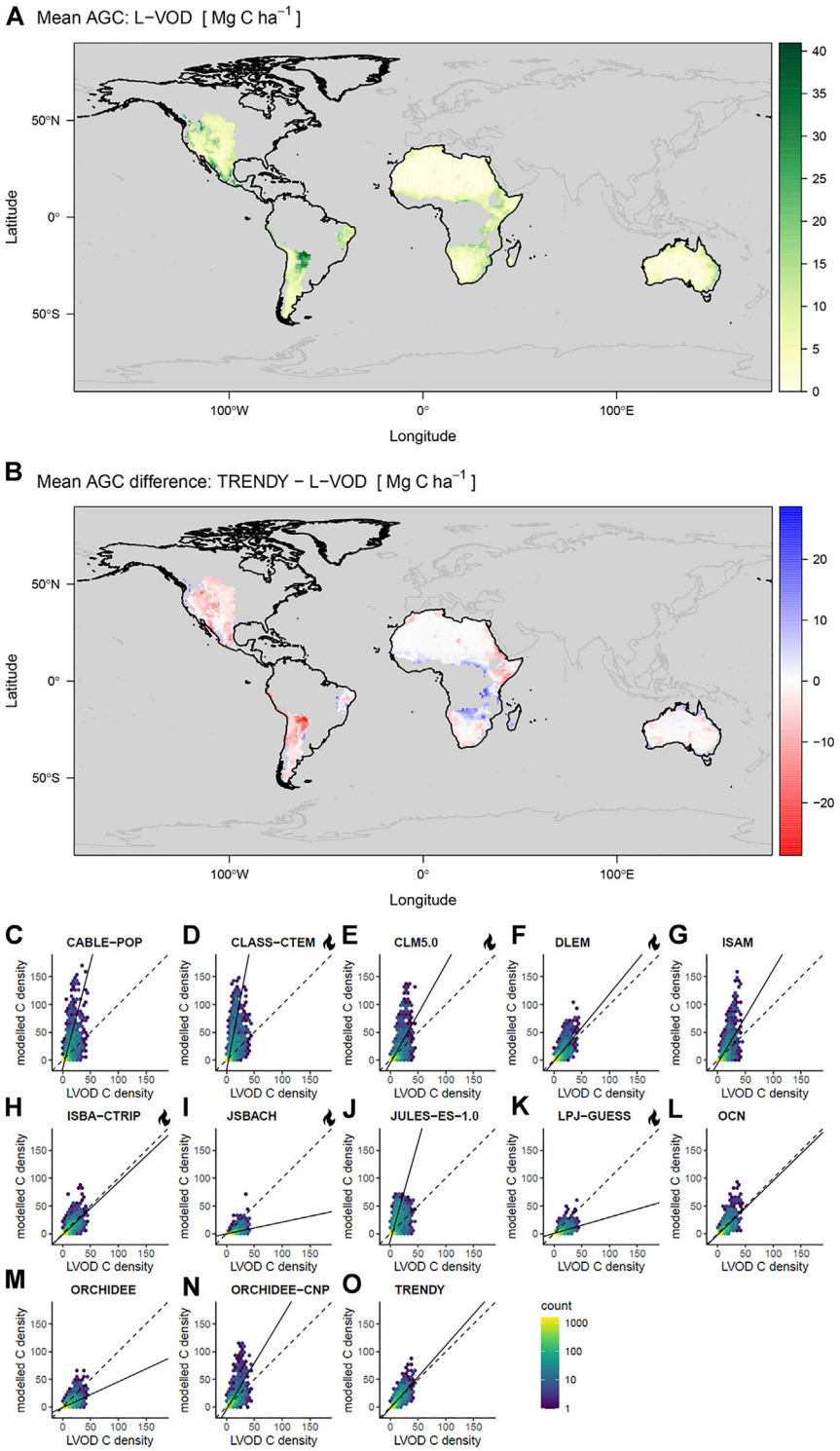

FIGURE 4 | (A) mean biomass inferred from L-VOD, **(B)** difference between L-VOD retrieval and the TRENDY mean AGC, the regions analysed are outlined in black with other regions excluded due to higher RFI. **(C–O)** Pairwise pixel covariance in mean AGC density estimated from L-VOD versus modelled values over the focal dryland regions, displayed as counts per hexagonal bin. Dashed lines represent 1:1 on the carbon density plots and solid lines are linear models fitted with total least squares. Units are biomass carbon density (Mg C ha^{-1}) and means are calculated over the 2011-2018 period. Note that in **(C–O)** models are fitted to weighted values but weights are not illustrated while **(A,B)** include only grid cells with centroids within the dryland mask. LSMs with explicit representation of fire are indicated with a flame icon.

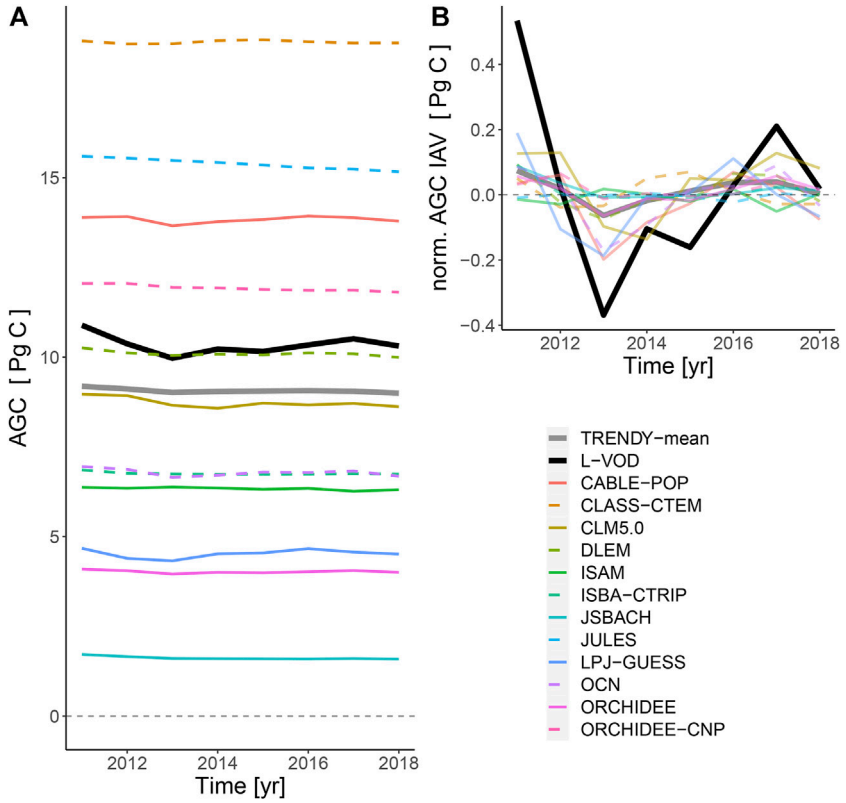

FIGURE 5 | (A) Time-series of aboveground carbon (2011–2018) in African, American and Australian drylands for the retrieval (black bold line) and models of the TRENDY ensemble. There was substantial bias between most models and models were less sensitive to temporal changes in AGC compared to the L-VOD retrieval. **(B)** The mean-normalised detrended time series show weak agreement in interannual differences for all models.

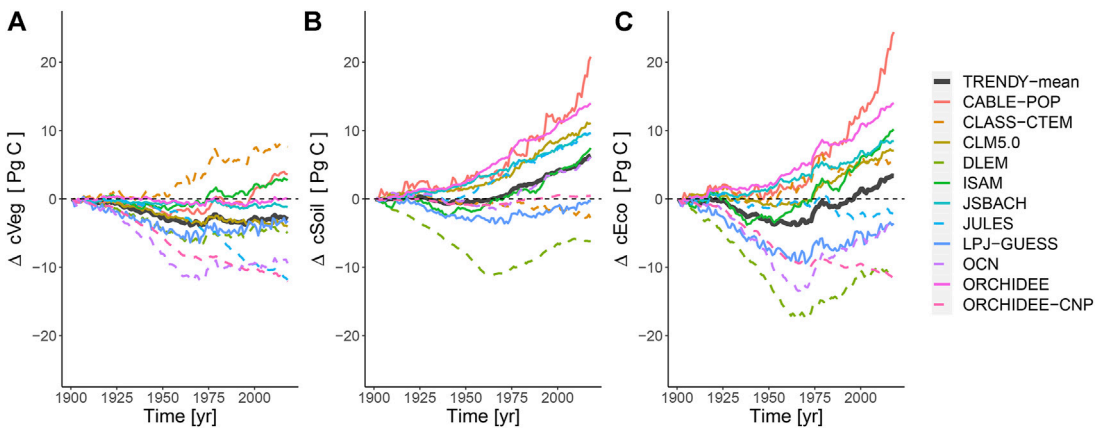

FIGURE 6 | Time-series of changes in **(A)** vegetation carbon, **(B)** soil carbon and **(C)** ecosystem carbon storage (soil plus vegetation) in global drylands between 1901 and 2018 as simulated by the models of the TRENDY ensemble. The divergence is shown relative to 1901. On average the models simulate an overall increase in ecosystem carbon over the century, particularly in the latter 70 years.

and 81.5%). Although inter-annual anomalies in AGC generally had the same sign across the L-VOD retrieval and TRENDY models (for the TRENDY mean the sign of the anomaly was consistent between TRENDY and the L-VOD in 88% of the time series), most LSMs had much smaller anomalies from the mean compared to the larger anomalies in the L-VOD-derived values (**Figure 5**). There were no meaningful trends in the time series of AGC; the few

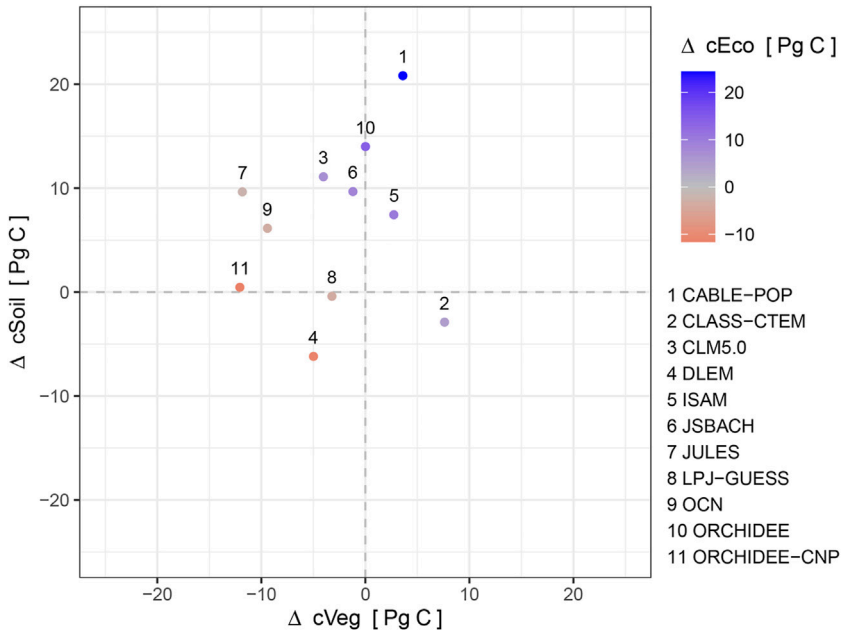

FIGURE7 | Comparison of changes in simulated vegetation and soil carbon in global drylands from 1901 to 2018. Points are coloured by the net change in ecosystem carbon, illustrating the diversity of model predictions within the ensemble.

that were statistically significant had negligible effect sizes (**Supplementary Table S4**).

Simulated Dryland Carbon Stocks Through Time

The land surface models predicted a net gain of ecosystem carbon in global drylands (mean 3.37 Pg C), due to an increase in soil carbon (mean 6.35 Pg C) that exceeds the losses in vegetation carbon (mean −2.98 Pg C) over the last 118 years (1901–2018) (**Figures 6**, **7**, **Supplementary Table S5**). There was a wide range of carbon accumulation responses across the TRENDY models (**Supplementary Table S5**). The overall loss in simulated vegetation carbon was predominantly driven by the influence of land-use change, exceeding the increase simulated due to CO_2 fertilization (**Supplementary Figure S13**). Climate change had minimal effect on the simulated dryland vegetation carbon stocks. The overall increase in simulated soil carbon was predominantly driven by the increase in litter inputs into the soil associated with the increase in net primary productivity due to CO_2 fertilization, with most models predicting a small reduction due to climate change (**Supplementary Figure S14**). The influence of land-use change on soil carbon was more varied between model simulations, with the majority showing a reduction. The overall increase in simulated ecosystem carbon was predominantly driven by the influence of CO_2 fertilization, exceeding the losses predicted due to both land-use change and, to a lesser extent, climate change (**Figure 6** and **Supplementary Figure S15**). Overall, dryland carbon stocks are simulated by models to have decreased by an average of 3.82 Pg C from 1901 to late-1960, before subsequently increasing by 7.19 Pg C up to 2018 as the CO_2 fertilisation effect increases simulated GPP in response to increasing atmospheric CO_2 concentrations.

DISCUSSION

In this study, we investigated the correspondence between LSM simulated values, a MODIS productivity product (2001–2018) and L-VOD derived AGC (2011–2018) in climatic drylands as well as the agreement of model projections of dryland carbon stocks (1901–2018). We examined LSMs' performance in terms of their ability to simulate the spatial distribution of GPP and AGC alongside the temporal trends and variability of these quantities over arid and semi-arid regions. GPP appears to be reasonably well simulated, compared to estimates from the MODIS PML-v2 product, in most LSMs. However, there were differences in simulated aboveground carbon stocks and their trends compared to the estimate from the L-VOD product. Large differences potentially arise from insufficient constraints impacting the representation of carbon allocation and release processes.

Gross Primary Productivity

Our results suggest that carbon uptake (GPP) by dryland ecosystems is broadly well represented by LSMs at the global scale. We found good agreement in the spatial distribution of GPP between simulated LSM estimates and MODIS based PML-v2 values in drylands for most models. Correlation coefficients were high and bias was low, especially for the TRENDY ensemble average. Our finding that spatial patterns of GPP were broadly in

agreement was consistent with previous evaluations of other MODIS-derived GPP products against GPP observations from dryland eddy covariance flux towers in North America (Biederman et al., 2017). Geographic biases were consistent across most LSMs, with overestimation of productivity in the African Sahel and underestimation of productivity in drylands in southern Africa and South America.

We found very strong agreement in GPP interannual variability between LSM-simulated values and those modelled based on satellite observations of photosynthetic capacity (**Figure 3B**; **Table 1**), including the large 2 Pg C yr^{-1} positive anomaly in 2010–11 caused by a severe La Niña event (Poulter et al., 2014; Haverd et al., 2016). This agreement lends some confidence that globally, LSMs capture the predominant dynamic responses controlling inputs of carbon into dryland ecosystems in response to annual-scale perturbations. However, the agreement found in IAV in GPP at the global scale contrasts with the disagreement in IAV at the site level where both MODIS and LSM simulated productivity have been found to underestimate IAV. Using eddy covariance observations from 25 dryland sites in North America, Biederman et al. (2017) found IAV in GPP was underestimated by MODIS-derived GPP. Similarly using observations from 12 eddy covariance sites in the southwestern U.S., MacBean et al. (2021) concluded LSMs underestimate IAV in dryland net ecosystem exchange. These findings underscore the ongoing need for further development and evaluations of remotely sensed GPP products in drylands (Smith et al., 2019).

All 12 LSMs consistently estimated a positive trend in dryland GPP between 2001 and 2018 (**Figure 3**; **Table 1**), mainly due to simulated CO_2 fertilization (**Supplementary Figure S16**). The CO_2 fertilization effect has been identified for drylands using satellite measurements (Donohue et al., 2013). Models predict a direct CO_2 fertilization effect (reduced photorespiration) and in water-limited systems stomatal closure for the same gain in CO_2 implies a longer growing season and higher annual productivity (Gonsamo et al., 2021), as expected from theory (Prentice et al., 2001). However, there was no trend in the satellite retrieved PML-v2 GPP product over this time. The discrepancy in GPP trends between models and PML-v2 was most pronounced in the Sahel region, where PML-v2 GPP decreased and LSM-simulated GPP increased (**Supplementary Figure S7**). While the PML-v2 product represents the effects of increasing CO_2 concentration on GPP (Zhang et al., 2019a), a comprehensive review of the effects of CO_2 enrichment on GPP by Walker et al. (2021) suggests that most remotely sensed GPP products are insufficiently sensitive to increasing CO_2. Satellite-retrieved GPP products are derived from light use efficiency models which have limitations (Smith et al., 2019; Baldocchi, 2020; Walker et al., 2021), one being the often very heterogeneous patterns of dryland vegetation and soil background signal giving rise to uncertainties, particularly in leaf area index estimations at the coarser spatial resolutions of the satellite pixels (Smith et al., 2019). Furthermore, the observations of evapotranspiration, energy, and carbon fluxes used for calibrating satellite retrieved GPP products and some of the LSMs are observed at relatively few locations globally, with short time-series, insufficient replication, and sampling biases that under-represent highly dynamic dryland ecosystems (Schimel et al., 2015; Hill et al., 2017; Jung et al., 2020). The undersampling of semi-arid settings in particular has been suggested to have a large impact on GPP upscaling errors (Jung et al., 2020).

Aboveground Biomass Carbon

Although we found reasonably good spatial agreement in AGC between L-VOD retrieved and average LSM (TRENDY-mean, Pearson's r: 0.75), individual models exhibited poor agreement both with each other and with the satellite-derived estimates (**Figure 4**; **Supplementary Figure S8**; **Table 1**). We found large biases in total AGC between models (**Figure 5A**). To some extent, inter-LSM differences arise from different representations of land surface processes (Sitch et al., 2008), for example, their representation of fire and land-use change, and native model resolutions that influence PFT fractions within grid-cells along dryland fringes or vegetation transition zones (**Supplementary Figures S17–19**). These factors also influence simulated residence times (Friend et al., 2014) and ecosystem respiration, explaining why LSMs that show better correspondence with the PML-v2 product for GPP do not necessarily correspond better for AGC (**Table 1**).

To improve the evaluation of LSM vegetation carbon stock predictions in low biomass drylands, further efforts are needed to improve the accuracy and validation of satellite-derived AGC products. A recent review concluded existing aboveground biomass products are almost entirely inconsistent across dry forests, savannas, and grasslands (Zhang et al., 2019b). Uncertainties arise from insufficient data on non-forest vegetation for calibration and validation as well as the insensitivity of remotely sensed observations to low biomass ecosystems (Duncanson et al., 2019; Cunliffe et al., 2021). Furthermore, comparisons between LSM predictions and AGC maps are strongly influenced by root-shoot ratios. These ratios are poorly constrained by observations, particularly in drylands (Qi et al., 2019), and also vary under different environmental conditions in response to differences in atmospheric CO_2, aridity and grazing pressure, amongst other factors (Mokany et al., 2006; Yan et al., 2020; Yan et al., 2021). The impact of different root-shoot ratios also relates to the functional role of roots in LSMs. For many models, root biomass does not impact function such as explicit water uptake (Warren et al., 2015), therefore adding root biomass would merely add a greater respiratory cost to the plants and lead to lower allocation to photosynthetic material (leaves) and reduced net primary productivity (Sitch et al., 2003).

Over the relatively short (8-year) time series, there was no clear trend in AGC but the year-to-year anomalies (IAV) were mostly consistent in terms of sign between models and L-VOD AGC. The positive anomaly in 2011 was largely driven by the influence of the La Niña in Australia (Poulter et al., 2014; Haverd et al., 2016). These results could imply that LSMs capture the response to key drivers on carbon inputs via photosynthesis but not necessarily the allocation between above and belowground biomass or the processes that release carbon from these environments (e.g., respiration, fire, photodegradation). The L-VOD AGC anomalies have considerably higher amplitude than those of the LSMs. It is possible that the amplitudes of

L-VOD-inferred anomalies may be exaggerated by variations in plant water stress, even though the L-VOD was averaged annually. The difference in amplitudes is furthermore sensitive to the biomass-transfer function used to calibrate the L-VOD data [e.g., linear, see this study (**Supplementary Figure S3**) and Brandt et al. (2018), or sinusoid, Fan et al. (2019)] and L-VOD data filtering. As L-VOD is a relatively recent product, methods for processing and analysing the data to best understand ecological functions are still being developed. Although longer time-series of VOD products exist, based on C, X, and Ku band microwave data, they have limitations such as increased sensitivity to water stress of foliage (Momen et al., 2017) and the necessity for intercalibration of different satellite instruments and measurements (Moesinger et al., 2020).

Long-Term Carbon Stock Predictions

Simulated dryland vegetation carbon stocks varied between LSMs and decreased on average between 1901 and 2018 (**Figures 6**, **7**) because reductions mainly due to land-use change exceeded the gains caused by CO_2 fertilization, while climate change had minimal effect in most models (**Supplementary Figure S13**). Dryland soil carbon stocks increased since 1970 despite being negatively impacted by land-use change in drylands such as the conversion of native woodlands to pasture and cropland which are often associated with degradation and can lead to decreased carbon input into soils (Cowie et al., 2011) (**Supplementary Figure S14**). These reductions in soil carbon from land-use change were counteracted by inputs from increased vegetation productivity due to CO_2 fertilization (**Figures 6**, **7**, and **Supplementary Figure S15**) (Walker et al., 2021), resulting in soil carbon dominating the increasing trend in LSM simulated dryland ecosystem carbon storage (**Figure 6**). However, current ecosystem models are considered to poorly capture the complex interactions between CO_2 fertilization and soil organic carbon stocks (Terrer et al., 2021). With a lack of long-term observations, it is difficult to be confident in the role of dryland soils in climate-carbon feedbacks. This highlights the need for longer-term observational efforts to be able to verify these model estimates. Furthermore, we found large differences in the change in modelled carbon stocks of dryland ecosystems over centennial timescales between the different LSMs (**Figures 6**, **7**). This level of disagreement in the change in carbon stocks when hindcast using relatively well-constrained climatology, CO_2 concentrations and land use is concerning because it undermines confidence in prognostic applications of these LSMs to even more uncertain future scenarios.

Improving Process Representations in Modelled Drylands

Fire is a critical process in many, but not all, dryland ecosystems, responsible for maintaining a stable ecological state in savanna ecosystems and is a major cause of carbon release (Bond et al., 2005; Lasslop et al., 2020). Land surface models increasingly include explicit representation of fire, including six of the twelve models considered here. Our analysis of these simulations found that the models with explicit fire did not show systematically better agreement with either GPP or AGC retrieved from remote sensing (**Table 1**). We found little systematic relationship between observed burn frequency and GPP residuals, although some models (JULES and CLASS-CTEM, ORCHIDEE-CNP, and OCN) did overestimate GPP in more frequently burned areas (**Supplementary Figure S11**). There was generally no relation between observed burn frequency and AGC residuals, apart from JULES and CLASS-CTEM which overestimated biomass in more frequently burned regions (**Supplementary Figure S12**). These results are consistent with the fire model intercomparisons (FireMIP), which found that while explicit fire substantially improved model-data correspondence in some regions (especially in functional drylands in South America that are excluded by our climatic definition of drylands) it worsened correspondence in other regions (Hantson et al., 2020). Vegetation models which lack explicit representation of fire contain compensatory biases which partially account for the effects of fire (Burton et al., 2019; Rabin et al., 2017). "LSMs that represent fires still do so insufficiently. For example, fire-enabled LSMs were not able to capture the global trend in burnt area (Andela et al., 2017). Uncertainties also remain regarding remote sensing observations with commonly used 500 m spatial resolution fire products significantly underestimating area burnt and fire carbon emissions (Ramo et al., 2021). Improvements to the representation of fire in LSMs are both needed and anticipated as better remotely-sensed fire products become available and we learn more about the compensatory biases present within current LSMs (Burton et al., 2019; Hantson et al., 2020; Lasslop et al., 2020)."

Simulations of terrestrial ecosystem processes in these LSMs struggle to capture many aspects of carbon dynamics in ecosystems that are subjected to severe water stress (Harper et al., 2020; MacBean et al., 2021). Limitations in model simulations of plant responses to water availability have been highlighted by MacBean et al. (2021) and Harper et al. (2020). For example, the plant functional types simulated in most models do not represent the ecophysiological adaptations present in most dryland vegetation communities (such as stomatal control and drought phenology), and simulated soils and rooting schemes are usually too shallow for these ecosystems. Furthermore, most LSMs have poor or no representation of biological soil crusts which are increasingly recognised to play critical roles in drylands including contributing ~0.6 Pg yr^{-1} of C to global net primary productivity (Chamizo et al., 2012; Rodriguez-Caballero et al., 2018). This is likely a reflection of a historical emphasis/bias of models to temperate forest phenology combined with a lack of empirical data. Differences in simulated vegetation dynamics also lead to erroneous estimates of fractional cover in key areas.

There are other processes thought to be important in drylands that LSMs do not represent. For instance, solar radiation interacting with plant litter causes photodegradation that emits gaseous carbon. Empirical evidence from decomposition (Austin & Vivanco, 2006; Day et al., 2018, 2019; Méndez et al., 2019; Berenstecher et al., 2020) and eddy covariance (Rutledge et al., 2010; Adair et al., 2017) studies suggests that photodegradation accounts for somewhere between 10% and 50% of gaseous carbon emissions in the semiarid ecosystems that dominate IAV and trends in dryland carbon dynamics (Poulter et al., 2014; Ahlström

et al., 2015). Photodegradation is therefore an important aspect of carbon emission in seasonally arid ecosystems that is not currently represented in LSMs, despite their inclusion of insolation and litter pools. As the simulated long-term trends in ecosystem carbon stocks are dominated by cSoil (including litter) (**Figures 6**, **7**), explicit representation of photodegradation would improve simulations of carbon dynamics in drylands.

CONCLUSION

The potential significance of drylands for the global carbon budget highlights the need for an improved understanding of how well LSMs simulate the carbon dynamics of these ecosystems. Comparing LSM simulations to two satellite-derived products revealed that these correspond reasonably well in terms of spatial patterns and interannual variability of dryland productivity but disagree regarding the distribution and changes in biomass. While the satellite-derived products used for this evaluation have their own limitations and uncertainties, many relating to the historic lack of observations in drylands, their synoptic coverage is suitable for global assessments of LSMs. The current limitations in how LSMs represent carbon allocation and release in dryland ecosystems in particular should be addressed through improved process representations. This includes refining existing processes such as plant responses to water availability, addressing compensatory biases in fire-enabled models, and representing photodegradation of litter that is an important pathway of carbon release in semiarid ecosystems. The increasing trend in dryland carbon storage simulated by the LSMs is dominated by increasing soil carbon; however, this change is very poorly constrained by empirical observations and needs to be addressed by future site-scale evaluations. This highlights both the need for longer-term observational efforts to be able to constrain and verify these model predictions but also that we should remain cautious in interpreting this element of LSM predictions as to the role of drylands in explaining trends in the global carbon cycle.

DATA AVAILABILITY STATEMENT

The datasets presented in this study can be found in online repositories. The names of the repository/repositories and accession number(s) can be found below: The TRENDY-v8 ensemble of simulation outputs is available upon request at https://sites.exeter.ac.uk/trendy. The PML-v2 product script is available online from https://github.com/gee-hydro/gee_PML. The SMOS-IC V2 L-VOD product was provided by Jean-Pierre Wigneron. Processing code is available at https://doi.org/10.5281/zenodo.5511724. Google Earth Engine Repository is available at: https://earthengine.googlesource.com/users/dfawcett/DRIVING_C_RS_publication (requires Google account to access).

AUTHOR CONTRIBUTIONS

Conceived the research idea: AC, DF, KA, SS, RB, and TH. Acquired funding: SS, RB, AC, KA, TH, J-PW, DG, and RS. Developed the experimental design. AC, DF, KA, and SS. Curated the data: DF, MO, XL, and J-PW. Data visualisation: DF and AC. Performed the analysis: DF and AC. Led the writing of the manuscript: AC and DF. All authors contributed to the final version of the manuscript.

FUNDING

Natural Environment Research Council (NERC) (NE/R00062X/1) awarded to RB, AC, SS, KA, and TH. ESA Climate Change Initiative RECCAP2 (contract no. 4000123002/18/I-NB) awarded to SS. SS also received support from NERC SECO grant NE/T01279X/1. DG received support from the ANR CLAND Convergence Institute. RS was supported by the European Union's Horizon 2020 research and innovation programme ESM2025—Earth System Models for the Future (Grant Agreement No 101003536).

ACKNOWLEDGMENTS

We thank Clément Albergel from the European Space Agency (ESA) for constructive feedback on an earlier version of this manuscript. The CESM project is supported primarily by the National Science Foundation (NSF). This material is based upon work supported by the National Center for Atmospheric Research, which is a major facility sponsored by the NSF under Cooperative Agreement 1852977. Computing and data storage resources, including the Cheyenne supercomputer (doi: 10.5065/D6RX99HX), were provided by the Computational and Information Systems Laboratory (CISL) at NCAR.

SUPPLEMENTARY MATERIAL

The Supplementary Material for this article can be found online at: https://www.frontiersin.org/articles/10.3389/fenvs.2022.790200/full#supplementary-material

REFERENCES

Abatzoglou, J. T., Dobrowski, S. Z., Parks, S. A., and Hegewisch, K. C. (2018). TerraClimate, a High-Resolution Global Dataset of Monthly Climate and Climatic Water Balance from 1958-2015. *Sci. Data* 5, 170191. doi:10.1038/sdata.2017.191

Abel, C., Horion, S., Tagesson, T., De Keersmaecker, W., Seddon, A. W. R., Abdi, A. M., et al. (2021). The Human-Environment Nexus and Vegetation-Rainfall Sensitivity in Tropical Drylands. *Nat. Sustain.* 4, 25–32. doi:10.1038/s41893-020-00597-z

Adair, E. C., Parton, W. J., King, J. Y., Brandt, L. A., and Lin, Y. (2017). Accounting for Photodegradation Dramatically Improves Prediction of Carbon Losses in Dryland Systems. *Ecosphere* 8, e01892. doi:10.1002/ecs2.1892

Ahlström, A., Raupach, M. R., Schurgers, G., Smith, B., Arneth, A., Jung, M., et al. (2015). The Dominant Role of Semi-arid Ecosystems in the Trend and Variability of the Land CO 2 Sink. *Science* 348, 895–899. doi:10.1126/science.aaa1668

Andela, N., Morton, D. C., Giglio, L., Chen, Y., van der Werf, G. R., Kasibhatla, P. S., et al. (2017). A Human-Driven Decline in Global Burned Area. *Science* 356, 1356–1362. doi:10.1126/science.aal4108

Archer, E., Engelbrecht, F., Hänsler, A., Landman, W., Tadross, M., and Helmschrot, J. (2018). Seasonal Prediction and Regional Climate Projections for Southern Africa. *Biodivers. Ecol.* 6, 14–21. doi:10.7809/b-e.00296

Austin, A. T., and Vivanco, L. (2006). Plant Litter Decomposition in a Semi-arid Ecosystem Controlled by Photodegradation. *Nature* 442, 555–558. doi:10.1038/nature05038

Baldocchi, D. D. (2020). How Eddy Covariance Flux Measurements Have Contributed to Our Understanding of Global Change Biology. *Glob. Change Biol.* 26, 242–260. doi:10.1111/gcb.14807

Baston, D. (2020). *Exactextractr: Fast Extraction from Raster Datasets Using Polygons*. Burlington, Vermont, United States: ISciences, LLC.

Berenstecher, P., Vivanco, L., Pérez, L. I., Ballaré, C. L., and Austin, A. T. (2020). Sunlight Doubles Aboveground Carbon Loss in a Seasonally Dry Woodland in Patagonia. *Curr. Biol.* 30, 3243–3251.e3. doi:10.1016/j.cub.2020.06.005

Biederman, J. A., Scott, R. L., Bell, T. W., Bowling, D. R., Dore, S., Garatuza-Payan, J., et al. (2017). CO 2 Exchange and Evapotranspiration across Dryland Ecosystems of Southwestern North America. *Glob. Change Biol.* 23, 4204–4221. doi:10.1111/gcb.13686

Blyth, E., Clark, D. B., Ellis, R., Huntingford, C., Los, S., Pryor, M., et al. (2011). A Comprehensive Set of Benchmark Tests for a Land Surface Model of Simultaneous Fluxes of Water and Carbon at Both the Global and Seasonal Scale. *Geosci. Model. Dev.* 4, 255–269. doi:10.5194/gmd-4-255-2011

Bond, W. J., Woodward, F. I., and Midgley, G. F. (2005). The Global Distribution of Ecosystems in a World without Fire. *New Phytol.* 165, 525–538. doi:10.1111/j.1469-8137.2004.01252.x

Boysen, L. R., Brovkin, V., Pongratz, J., Lawrence, D. M., Lawrence, P., Vuichard, N., et al. (2020). Global Climate Response to Idealized Deforestation in CMIP6 Models. *Biogeosciences* 17, 5615–5638. doi:10.5194/bg-17-5615-2020

Brandt, M., Hiernaux, P., Rasmussen, K., Tucker, C. J., Wigneron, J.-P., Diouf, A. A., et al. (2019). Changes in Rainfall Distribution Promote Woody Foliage Production in the Sahel. *Commun. Biol.* 2, 133. doi:10.1038/s42003-019-0383-9

Brandt, M., Wigneron, J.-P., Chave, J., Tagesson, T., Penuelas, J., Ciais, P., et al. (2018). Satellite Passive Microwaves Reveal Recent Climate-Induced Carbon Losses in African Drylands. *Nat. Ecol. Evol.* 2, 827–835. doi:10.1038/s41559-018-0530-6

Burton, C., Betts, R., Cardoso, M., Feldpausch, T. R., Harper, A., Jones, C. D., et al. (2019). Representation of Fire, Land-Use Change and Vegetation Dynamics in the Joint UK Land Environment Simulator vn4.9 (JULES). *Geosci. Model. Dev.* 12, 179–193. doi:10.5194/gmd-12-179-2019

Chamizo, S., Cantón, Y., Miralles, I., and Domingo, F. (2012). Biological Soil Crust Development Affects Physicochemical Characteristics of Soil Surface in Semiarid Ecosystems. *Soil Biol. Biochem.* 49, 96–105. doi:10.1016/j.soilbio.2012.02.017

Chaparro, D., Duveiller, G., Piles, M., Cescatti, A., Vall-llossera, M., Camps, A., et al. (2019). Sensitivity of L-Band Vegetation Optical Depth to Carbon Stocks in Tropical Forests: a Comparison to Higher Frequencies and Optical Indices. *Remote Sensing Environ.* 232, 111303. doi:10.1016/j.rse.2019.111303

Chave, J., Davies, S. J., Phillips, O. L., Lewis, S. L., Sist, P., Schepaschenko, D., et al. (2019). Ground Data Are Essential for Biomass Remote Sensing Missions. *Surv. Geophys.* 40, 863–880. doi:10.1007/s10712-019-09528-w

Ciais, P., Bombelli, A., Williams, M., Piao, S. L., Chave, J., Ryan, C. M., et al. (2011). The Carbon Balance of Africa: Synthesis of Recent Research Studies. *Phil. Trans. R. Soc. A.* 369, 2038–2057. doi:10.1098/rsta.2010.0328

Clark, D. B., Mercado, L. M., Sitch, S., Jones, C. D., Gedney, N., Best, M. J., et al. (2011). The Joint UK Land Environment Simulator (JULES), Model Description - Part 2: Carbon Fluxes and Vegetation Dynamics. *Geosci. Model. Dev.* 4, 701–722. doi:10.5194/gmd-4-701-2011

Cowie, A. L., Penman, T. D., Gorissen, L., Winslow, M. D., Lehmann, J., Tyrrell, T. D., et al. (2011). Towards Sustainable Land Management in the Drylands: Scientific Connections in Monitoring and Assessing Dryland Degradation, Climate Change and Biodiversity. *Land Degrad. Dev.* 22, 248–260. doi:10.1002/ldr.1086

Cunliffe, A. M., Anderson, K., Boschetti, F., Brazier, R. E., Graham, H. A., Myers-Smith, I. H., et al. (2021). Global Application of an Unoccupied Aerial Vehicle Photogrammetry Protocol for Predicting Aboveground Biomass in Non-forest Ecosystems. *Remote Sens Ecol. Conserv* 8, 57–71. doi:10.1002/rse2.228

Day, T. A., Bliss, M. S., Placek, S. K., Tomes, A. R., and Guénon, R. (2019). Thermal Abiotic Emission of CO 2 and CH 4 from Leaf Litter and its Significance in a Photodegradation Assessment. *Ecosphere* 10, e02745. doi:10.1002/ecs2.2745

Day, T. A., Bliss, M. S., Tomes, A. R., Ruhland, C. T., and Guénon, R. (2018). Desert Leaf Litter Decay: Coupling of Microbial Respiration, Water-soluble Fractions and Photodegradation. *Glob. Change Biol.* 24, 5454–5470. doi:10.1111/gcb.14438

Delire, C., Séférian, R., Decharme, B., Alkama, R., Calvet, J. C., Carrer, D., et al. (2020). The Global Land Carbon Cycle Simulated with ISBA-CTRIP: Improvements over the Last Decade. *J. Adv. Model. Earth Syst.* 12, e2019MS001886. doi:10.1029/2019MS001886

Donohue, R. J., Roderick, M. L., McVicar, T. R., and Farquhar, G. D. (2013). Impact of CO2fertilization on Maximum Foliage Cover across the globe's Warm, Arid Environments. *Geophys. Res. Lett.* 40, 3031–3035. doi:10.1002/grl.50563

Duncanson, L., Armston, J., Disney, M., Avitabile, V., Barbier, N., Calders, K., et al. (2019). The Importance of Consistent Global Forest Aboveground Biomass Product Validation. *Surv. Geophys.* 40, 979–999. doi:10.1007/s10712-019-09538-8

Fan, L., Wigneron, J.-P., Ciais, P., Chave, J., Brandt, M., Fensholt, R., et al. (2019). Satellite-observed Pantropical Carbon Dynamics. *Nat. Plants* 5, 944–951. doi:10.1038/s41477-019-0478-9

Fernandez-Moran, R., Al-Yaari, A., Mialon, A., Mahmoodi, A., Al Bitar, A., De Lannoy, G., et al. (2017). SMOS-IC: An Alternative SMOS Soil Moisture and Vegetation Optical Depth Product. *Remote Sensing* 9, 457–521. doi:10.3390/rs9050457

Forkel, M., Drüke, M., Thurner, M., Dorigo, W., Schaphoff, S., Thonicke, K., et al. (2019). Constraining Modelled Global Vegetation Dynamics and Carbon Turnover Using Multiple Satellite Observations. *Sci. Rep.* 9, 18757. doi:10.1038/s41598-019-55187-7

Frappart, F., Wigneron, J., Li, X., Liu, X., Al-yaari, A., Fan, L., et al. (2020). Global Monitoring of the Vegetation Dynamics from the Vegetation Optical Depth (VOD): A Review. *Remote Sens* 12, 7–10. doi:10.3390/rs12182915

Friedlingstein, P., Jones, M. W., O'Sullivan, M., Andrew, R. M., Hauck, J., Peters, G. P., et al. (2019). Global Carbon Budget 2019. *Earth Syst. Sci. Data* 11, 1783–1838. doi:10.5194/essd-11-1783-2019

Friend, A. D., Lucht, W., Rademacher, T. T., Keribin, R., Betts, R., Cadule, P., et al. (2014). Carbon Residence Time Dominates Uncertainty in Terrestrial Vegetation Responses to Future Climate and Atmospheric CO 2. *Proc. Natl. Acad. Sci. U.S.A.* 111, 3280–3285. doi:10.1073/pnas.1222477110

Gan, R., Zhang, Y., Shi, H., Yang, Y., Eamus, D., Cheng, L., et al. (2018). Use of Satellite Leaf Area index Estimating Evapotranspiration and Gross Assimilation for Australian Ecosystems. *Ecohydrology* 11, e1974. doi:10.1002/eco.1974

Giglio, L., Justice, C., Boschetti, L., and Roy, D. (2015). MCD64A1 MODIS/Terra+Aqua Burned Area Monthly L3 Global 500m SIN Grid V006 [Data Set] [Accessed September 20, 2021]. doi:10.5067/MODIS/MCD64A1.006

Goldstein, M., Seheult, A., and Vernon, I. (2013). "Assessing Model Adequacy," in *Environmental Modelling: Finding Simplicity in Complexity*. Editors J. Wainwright and M. Mulligan (Wiley-Blackwell), 435–449. doi:10.1002/9781118351475.ch26

Goll, D. S., Vuichard, N., Maignan, F., Jornet-Puig, A., Sardans, J., Violette, A., et al. (2017). A Representation of the Phosphorus Cycle for ORCHIDEE (Revision 4520). *Geosci. Model. Dev.* 10, 3745–3770. doi:10.5194/gmd-10-3745-2017

Gonsamo, A., Ciais, P., Miralles, D. G., Sitch, S., Dorigo, W., Lombardozzi, D., et al. (2021). Greening Drylands Despite Warming Consistent with Carbon Dioxide Fertilization Effect. *Glob. Change Biol.* 27, 3336–3349. doi:10.1111/gcb.15658

Hantson, S., Kelley, D. I., Arneth, A., Harrison, S. P., Archibald, S., Bachelet, D., et al. (2020). Quantitative Assessment of Fire and Vegetation Properties in Simulations with Fire-Enabled Vegetation Models from the Fire Model Intercomparison Project. *Geosci. Model. Dev.* 13, 3299–3318. doi:10.5194/gmd-13-3299-2020

Harper, A. B., Williams, K. E., McGuire, P. C., Duran Rojas, M. C., Hemming, D., Verhoef, A., et al. (2020). Improvement of Modelling Plant Responses to Low

Soil Moisture in JULESvn4.9 and Evaluation against Flux tower Measurements. *Geosci. Model. Dev. Discuss.*, 1–42. doi:10.5194/gmd-2020-273

Haverd, V., Smith, B., Nieradzik, L., Briggs, P. R., Woodgate, W., Trudinger, C. M., et al. (2018). A New Version of the CABLE Land Surface Model (Subversion Revision R4601) Incorporating Land Use and Land Cover Change, Woody Vegetation Demography, and a Novel Optimisation-Based Approach to Plant Coordination of Photosynthesis. *Geosci. Model. Dev.* 11, 2995–3026. doi:10.5194/gmd-11-2995-2018

Haverd, V., Smith, B., and Trudinger, C. (2016). Dryland Vegetation Response to Wet Episode, Not Inherent Shift in Sensitivity to Rainfall, behind Australia's Role in 2011 Global Carbon Sink Anomaly. *Glob. Change Biol.* 22, 2315–2316. doi:10.1111/gcb.13202

Hill, T., Chocholek, M., and Clement, R. (2017). The Case for Increasing the Statistical Power of Eddy Covariance Ecosystem Studies: Why, where and How? *Glob. Change Biol.* 23, 2154–2165. doi:10.1111/gcb.13547

Huang, J., Li, Y., Fu, C., Chen, F., Fu, Q., Dai, A., et al. (2017). Dryland Climate Change: Recent Progress and Challenges. *Rev. Geophys.* 55, 719–778. doi:10.1002/2016RG000550

Huang, J., Yu, H., Guan, X., Wang, G., and Guo, R. (2016). Accelerated Dryland Expansion under Climate Change. *Nat. Clim Change* 6, 166–171. doi:10.1038/nclimate2837

Jung, M., Schwalm, C., Migliavacca, M., Walther, S., Camps-Valls, G., Koirala, S., et al. (2020). Scaling Carbon Fluxes from Eddy Covariance Sites to globe: Synthesis and Evaluation of the FLUXCOM Approach. *Biogeosciences* 17, 1343–1365. doi:10.5194/bg-17-1343-2020

Konings, A. G., Piles, M., Das, N., and Entekhabi, D. (2017). L-band Vegetation Optical Depth and Effective Scattering Albedo Estimation from SMAP. *Remote Sensing Environ.* 198, 460–470. doi:10.1016/j.rse.2017.06.037

Konings, A. G., Rao, K., and Steele-Dunne, S. C. (2019). Macro to Micro: Microwave Remote Sensing of Plant Water Content for Physiology and Ecology. *New Phytol.* 223, 1166–1172. doi:10.1111/nph.15808

Krinner, G., Viovy, N., de Noblet-Ducoudré, N., Ogée, J., Polcher, J., Friedlingstein, P., et al. (2005). A Dynamic Global Vegetation Model for Studies of the Coupled Atmosphere-Biosphere System. *Glob. Biogeochem. Cycles* 19. doi:10.1029/2003GB002199

Lasslop, G., Hantson, S., Harrison, S. P., Bachelet, D., Burton, C., Forkel, M., et al. (2020). Global Ecosystems and Fire: Multi-model Assessment of Fire-induced Tree-cover and Carbon Storage Reduction. *Glob. Change Biol.* 26, 5027–5041. doi:10.1111/gcb.15160

Lawrence, D. M., Fisher, R. A., Koven, C. D., Oleson, K. W., Swenson, S. C., Bonan, G., et al. (2019). The Community Land Model Version 5: Description of New Features, Benchmarking, and Impact of Forcing Uncertainty. *J. Adv. Model. Earth Syst.* 11, 4245–4287. doi:10.1029/2018MS001583

Liu, Y. Y., van Dijk, A. I. J. M., de Jeu, R. A. M., Canadell, J. G., McCabe, M. F., Evans, J. P., et al. (2015). Recent Reversal in Loss of Global Terrestrial Biomass. *Nat. Clim Change* 5, 470–474. doi:10.1038/nclimate2581

Long, S. P., Ainsworth, E. A., Rogers, A., and Ort, D. R. (2004). RISING ATMOSPHERIC CARBON DIOXIDE: Plants FACE the Future. *Annu. Rev. Plant Biol.* 55, 591–628. doi:10.1146/annurev.arplant.55.031903.141610

MacBean, N., Scott, R. L., Biederman, J. A., Peylin, P., Kolb, T., Litvak, M. E., et al. (2021). Dynamic Global Vegetation Models Underestimate Net CO2 Flux Mean and Inter-annual Variability in Dryland Ecosystems. *Environ. Res. Lett.* 16, 094023. doi:10.1088/1748-9326/ac1a38

Maestre, F. T., Benito, B. M., Berdugo, M., Concostrina-Zubiri, L., Delgado-Baquerizo, M., Eldridge, D. J., et al. (2021). Biogeography of Global Drylands. *New Phytol.* 231, 540–558. doi:10.1111/nph.17395

Mauritsen, T., Bader, J., Becker, T., Behrens, J., Bittner, M., Brokopf, R., et al. (2019). Developments in the MPI-M Earth System Model Version 1.2 (MPI-ESM1.2) and its Response to Increasing CO 2. *J. Adv. Model. Earth Syst.* 11, 998–1038. doi:10.1029/2018MS001400

Meiyappan, P., Jain, A. K., and House, J. I. (2015). Increased Influence of Nitrogen Limitation on CO 2 Emissions from Future Land Use and Land Use Change. *Glob. Biogeochem. Cycles* 29, 1524–1548. doi:10.1002/2015GB005086

Melton, J. R., and Arora, V. K. (2016). Competition between Plant Functional Types in the Canadian Terrestrial Ecosystem Model (CTEM) V. 2.0. *Geosci. Model. Dev.* 9, 323–361. doi:10.5194/gmd-9-323-2016

Méndez, M. S., Martinez, M. L., Araujo, P. I., and Austin, A. T. (2019). Solar Radiation Exposure Accelerates Decomposition and Biotic Activity in Surface Litter but Not Soil in a Semiarid woodland Ecosystem in Patagonia, Argentina. *Plant Soil* 445, 483–496. doi:10.1007/s11104-019-04325-1

Mialon, A., Coret, L., Kerr, Y. H., Secherre, F., and Wigneron, J.-P. (2008). Flagging the Topographic Impact on the SMOS Signal. *IEEE Trans. Geosci. Remote Sensing* 46, 689–694. doi:10.1109/TGRS.2007.914788

Mialon, A., Rodríguez-Fernández, N. J., Santoro, M., Saatchi, S., Mermoz, S., Bousquet, E., et al. (2020). Evaluation of the Sensitivity of SMOS L-VOD to Forest Above-Ground Biomass at Global Scale. *Remote Sensing* 12, 1450. doi:10.3390/rs12091450

Moesinger, L., Dorigo, W., de Jeu, R., van der Schalie, R., Scanlon, T., Teubner, I., et al. (2020). The Global Long-Term Microwave Vegetation Optical Depth Climate Archive (VODCA). *Earth Syst. Sci. Data* 12, 177–196. doi:10.5194/essd-12-177-2020

Mokany, K., Raison, R. J., and Prokushkin, A. S. (2006). Critical Analysis of Root : Shoot Ratios in Terrestrial Biomes. *Glob. Change Biol.* 12, 84–96. doi:10.1111/j.1365-2486.2005.001043.x

Momen, M., Wood, J. D., Novick, K. A., Pangle, R., Pockman, W. T., McDowell, N. G., et al. (2017). Interacting Effects of Leaf Water Potential and Biomass on Vegetation Optical Depth. *J. Geophys. Res. Biogeosci.* 122, 3031–3046. doi:10.1002/2017JG004145

Myers-Smith, I. H., Kerby, J. T., Phoenix, G. K., Bjerke, J. W., Epstein, H. E., Assmann, J. J., et al. (2020). Complexity Revealed in the Greening of the Arctic. *Nat. Clim. Change* 10, 106–117. doi:10.1038/s41558-019-0688-1

Pasek, J. (2020). *Weights: Weighting and Weighted Statistics*.

Paustian, K., Ravindranath, N. H., and van Amstel, A. R. (2006). *2006 IPCC Guidelines for National Greenhouse Gas Inventories. [s.n.]*.

Piao, S., Wang, X., Wang, K., Li, X., Bastos, A., Canadell, J. G., et al. (2020). Interannual Variation of Terrestrial Carbon Cycle: Issues and Perspectives. *Glob. Change Biol.* 26, 300–318. doi:10.1111/gcb.14884

Poulter, B., Frank, D., Ciais, P., Myneni, R. B., Andela, N., Bi, J., et al. (2014). Contribution of Semi-arid Ecosystems to Interannual Variability of the Global Carbon Cycle. *Nature* 509, 600–603. doi:10.1038/nature13376

Prentice, I. C., Farquhar, G. D., Fasham, M. J. R., Goulden, M. L., Heimann, M., Jaramillo, V. J., et al. (2001). "The Carbon Cycle and Atmospheric Carbon Dioxide," in *Climate Change 2001: The Scientific Basis. Contribution of Working Group I to the Third Assessment Report of the Intergovernmental Panel on Climate Change*. J. T. Houghton, Y. Ding, D. J. Griggs, M. Noguer, P. J. van der Linden, X. Dai, et al. (Cambridge, UK: Cambridge University Press).

Qi, Y., Wei, W., Chen, C., and Chen, L. (2019). Plant Root-Shoot Biomass Allocation over Diverse Biomes: A Global Synthesis. *Glob. Ecol. Conservation* 18, e00606. doi:10.1016/j.gecco.2019.e00606

Ramo, R., Roteta, E., Bistinas, I., van Wees, D., Bastarrika, A., Chuvieco, E., et al. (2021). African Burned Area and Fire Carbon Emissions Are Strongly Impacted by Small Fires Undetected by Coarse Resolution Satellite Data. *Proc. Natl. Acad. Sci. U.S.A.* 118, e2011160118. doi:10.1073/pnas.2011160118

Reick, C. H., Gayler, V., Goll, D., Hagemann, S., Heidkamp, M., Nabel, J. E. M. S., et al. (2021). JSBACH 3 - The land component of the MPI Earth System Model: documentation of version 3.2. Hamburg: MPI für Meteorologie. doi:10.17617/2.3279802

Rodriguez-Caballero, E., Belnap, J., Büdel, B., Crutzen, P. J., Andreae, M. O., Pöschl, U., et al. (2018). Dryland Photoautotrophic Soil Surface Communities Endangered by Global Change. *Nat. Geosci* 11, 185–189. doi:10.1038/s41561-018-0072-1

Rodríguez-Fernández, N. J., Mialon, A., Mermoz, S., Bouvet, A., Richaume, P., Al Bitar, A., et al. (2018). An Evaluation of SMOS L-Band Vegetation Optical Depth (L-VOD) Data Sets: High Sensitivity of L-VOD to Above-Ground Biomass in Africa. *Biogeosciences* 15, 4627–4645. doi:10.5194/bg-15-4627-2018

Rutledge, S., Campbell, D. I., Baldocchi, D., and Schipper, L. A. (2010). Photodegradation Leads to Increased Carbon Dioxide Losses from Terrestrial Organic Matter. *Glob. Change Biol.* 16, no. doi:10.1111/j.1365-2486.2009.02149.x

Santoro, M., Cartus, O., Mermoz, S., Bouvet, A., Le Toan, T., Carvalhais, N., et al. (2018). GlobBiomass Global Above-Ground Biomass and Growing Stock Volume Datasets. Available at: http://globbiomass.org/products/global-mapping (Accessed September 20, 2021).

Schimel, D., Pavlick, R., Fisher, J. B., Asner, G. P., Saatchi, S., Townsend, P., et al. (2015). Observing Terrestrial Ecosystems and the Carbon Cycle from Space. *Glob. Change Biol.* 21, 1762–1776. doi:10.1111/gcb.12822

Schlesinger, W. H. (2016). An Evaluation of Abiotic Carbon Sinks in Deserts. *Glob. Change Biol.* 23, 25–27. doi:10.1111/gcb.13336

Schlesinger, W. H., Belnap, J., and Marion, G. (2009). On Carbon Sequestration in Desert Ecosystems. *Glob. Change Biol.* 15, 1488–1490. doi:10.1111/j.1365-2486.2008.01763.x

Sietz, D., Lüdeke, M. K. B., and Walther, C. (2011). Categorisation of Typical Vulnerability Patterns in Global Drylands. *Glob. Environ. Change* 21, 431–440. doi:10.1016/j.gloenvcha.2010.11.005

Sitch, S., Friedlingstein, P., Gruber, N., Jones, S. D., Murray-Tortarolo, G., Ahlström, A., et al. (2015). Recent Trends and Drivers of Regional Sources and Sinks of Carbon Dioxide. *Biogeosciences* 12, 653–679. doi:10.5194/bg-12-653-2015

Sitch, S., Huntingford, C., Gedney, N., Levy, P. E., Lomas, M., Piao, S. L., et al. (2008). Evaluation of the Terrestrial Carbon Cycle, Future Plant Geography and Climate-Carbon Cycle Feedbacks Using Five Dynamic Global Vegetation Models (DGVMs). *Glob. Change Biol.* 14, 2015–2039. doi:10.1111/j.1365-2486.2008.01626.x

Sitch, S., Smith, B., Prentice, I. C., Arneth, A., Bondeau, A., Cramer, W., et al. (2003). Evaluation of Ecosystem Dynamics, Plant Geography and Terrestrial Carbon Cycling in the LPJ Dynamic Global Vegetation Model. *Glob. Chang. Biol.* 9, 161–185. doi:10.1046/j.1365-2486.2003.00569.x

Smith, B., Wårlind, D., Arneth, A., Hickler, T., Leadley, P., Siltberg, J., et al. (2014). Implications of Incorporating N Cycling and N Limitations on Primary Production in an Individual-Based Dynamic Vegetation Model. *Biogeosciences* 11, 2027–2054. doi:10.5194/bg-11-2027-2014

Smith, W. K., Dannenberg, M. P., Yan, D., Herrmann, S., Barnes, M. L., Barron-Gafford, G. A., et al. (2019). Remote Sensing of Dryland Ecosystem Structure and Function: Progress, Challenges, and Opportunities. *Remote Sensing Environ.* 233, 111401. doi:10.1016/j.rse.2019.111401

SRCCL (2020). Special Report on Climate Change and Land, 2020. Available at: https://www.ipcc.ch/srccl/chapter/summary-for-policymakers/.

Terrer, C., Phillips, R. P., Hungate, B. A., Rosende, J., Pett-Ridge, J., Craig, M. E., et al. (2021). A Trade-Off between Plant and Soil Carbon Storage under Elevated CO2. *Nature* 591, 599–603. doi:10.1038/s41586-021-03306-8

Therneau, T. (2018). *deming*.

Tian, F., Brandt, M., Liu, Y. Y., Verger, A., Tagesson, T., Diouf, A. A., et al. (2016). Remote Sensing of Vegetation Dynamics in Drylands: Evaluating Vegetation Optical Depth (VOD) Using AVHRR NDVI and *In Situ* green Biomass Data over West African Sahel. *Remote Sensing Environ.* 177, 265–276. doi:10.1016/j.rse.2016.02.056

Tian, F., Wigneron, J.-P., Ciais, P., Chave, J., Ogée, J., Peñuelas, J., et al. (2018). Coupling of Ecosystem-Scale Plant Water Storage and Leaf Phenology Observed by Satellite. *Nat. Ecol. Evol.* 2, 1428–1435. doi:10.1038/s41559-018-0630-3

Tian, H., Chen, G., Lu, C., Xu, X., Hayes, D. J., Ren, W., et al. (2015). North American Terrestrial CO2 Uptake Largely Offset by CH4 and N2O Emissions: toward a Full Accounting of the Greenhouse Gas Budget. *Climatic Change* 129, 413–426. doi:10.1007/s10584-014-1072-9

IPCC (2021). in *Climate Change 2021: The Physical Science Basis. Contribution of Working Group I to the Sixth Assessment Report of the Intergovernmental Panel on Climate Change*. V. Masson-Delmotte, P. Zhai, A. Pirani, S. L. Connors, C. Péan, S. Berger, et al. (Cambridge University Press).

Walker, A. P., De Kauwe, M. G., Bastos, A., Belmecheri, S., Georgiou, K., Keeling, R. F., et al. (2021). Integrating the Evidence for a Terrestrial Carbon Sink Caused by Increasing Atmospheric CO 2. *New Phytol.* 229, 2413–2445. doi:10.1111/nph.16866

Warren, J. M., Hanson, P. J., Iversen, C. M., Kumar, J., Walker, A. P., and Wullschleger, S. D. (2015). Root Structural and Functional Dynamics in Terrestrial Biosphere Models - Evaluation and Recommendations. *New Phytol.* 205, 59–78. doi:10.1111/nph.13034

Wigneron, J.-P., Li, X., Frappart, F., Fan, L., Al-Yaari, A., De Lannoy, G., et al. (2021). SMOS-IC Data Record of Soil Moisture and L-VOD: Historical Development, Applications and Perspectives. *Remote Sensing Environ.* 254, 112238. doi:10.1016/j.rse.2020.112238

Xu, C., Kohler, T. A., Lenton, T. M., Svenning, J.-C., and Scheffer, M. (2020). Future of the Human Climate Niche. *Proc. Natl. Acad. Sci. U.S.A.* 117, 11350–11355. doi:10.1073/pnas.1910114117

Yan, C., Yuan, Z., Liu, Z., Zhang, J., Liu, K., Shi, X., et al. (2021). Aridity Stimulates Responses of Root Production and Turnover to Warming but Suppresses the Responses to Nitrogen Addition in Temperate Grasslands of Northern China. *Sci. Total Environ.* 753, 142018. doi:10.1016/j.scitotenv.2020.142018

Yan, L., Li, Y., Wang, L., Zhang, X., Wang, J., Wu, H., et al. (2020). Grazing Significantly Increases Root Shoot Ratio but Decreases Soil Organic Carbon in Qinghai-Tibetan Plateau Grasslands: A Hierarchical Meta-analysis. *Land Degrad. Dev.* 31, 2369–2378. doi:10.1002/ldr.3606

Yang, H., Ciais, P., Santoro, M., Huang, Y., Li, W., Wang, Y., et al. (2020). Comparison of forest Above-ground Biomass from Dynamic Global Vegetation Models with Spatially Explicit Remotely Sensed Observation-based Estimates. *Glob. Change Biol.* 26, 3997–4012. doi:10.1111/gcb.15117

Yao, J., Liu, H., Huang, J., Gao, Z., Wang, G., Li, D., et al. (2020). Accelerated Dryland Expansion Regulates Future Variability in Dryland Gross Primary Production. *Nat. Commun.* 11, 1665. doi:10.1038/s41467-020-15515-2

Zaehle, S., and Friend, A. D. (2010). Carbon and Nitrogen Cycle Dynamics in the O-CN Land Surface Model: 1. Model Description, Site-Scale Evaluation, and Sensitivity to Parameter Estimates. *Glob. Biogeochem. Cycles* 24, a–n. doi:10.1029/2009GB003521

Zhang, Y., Kong, D., Gan, R., Chiew, F. H. S., McVicar, T. R., Zhang, Q., et al. (2019a). Coupled Estimation of 500 M and 8-day Resolution Global Evapotranspiration and Gross Primary Production in 2002-2017. *Remote Sensing Environ.* 222, 165–182. doi:10.1016/j.rse.2018.12.031

Zhang, Y., Liang, S., and Yang, L. (2019b). A Review of Regional and Global Gridded Forest Biomass Datasets. *Remote Sensing* 11, 2744. doi:10.3390/rs11232744

Conflict of Interest: The authors declare that the research was conducted in the absence of any commercial or financial relationships that could be construed as a potential conflict of interest.

Publisher's Note: All claims expressed in this article are solely those of the authors and do not necessarily represent those of their affiliated organizations, or those of the publisher, the editors and the reviewers. Any product that may be evaluated in this article, or claim that may be made by its manufacturer, is not guaranteed or endorsed by the publisher.

frontiers | Frontiers in Environmental Science

TYPE Original Research
PUBLISHED 14 September 2022
DOI 10.3389/fenvs.2022.866309

OPEN ACCESS

EDITED BY
Lindsay Beaumont Hutley,
Charles Darwin University, Australia

REVIEWED BY
Panayiotis G Dimitrakopoulos,
University of the Aegean, Greece
Maya Negev,
University of Haifa, Israel

*CORRESPONDENCE
Abeer Albalawneh,
aberfer@yahoo.com

SPECIALTY SECTION
This article was submitted to Drylands, a section of the journal Frontiers in Environmental Science

RECEIVED 31 January 2022
ACCEPTED 31 August 2022
PUBLISHED 14 September 2022

CITATION
Albalawneh A, Al-Assaf A, Sweity A, Hammour WA, Kloub K, Hjazin A, Kabariti R, Abu Nowar L, Tadros MJ, Aljaafreh S, Diab M, Alwidyan J, Albashbsheh G and Haddad N (2022), Mapping cultural ecosystem services in the hyper arid environment of south of Jordan.
Front. Environ. Sci. 10:866309.
doi: 10.3389/fenvs.2022.866309

Mapping cultural ecosystem services in the hyper arid environment of south of Jordan

Abeer Albalawneh[1]*, Amani Al-Assaf[2], Amer Sweity[3], Wafa'a Abu Hammour[1], Khawla Kloub[1], Amgad Hjazin[1], Rabab Kabariti[4], Lana Abu Nowar[4], Maher J. Tadros[5], Safaa Aljaafreh[1], Mai Diab[1], Jafar Alwidyan[1], Ghadeer Albashbsheh[4] and Nizar Haddad[6]

[1]Environment and Climate Change Research Directorate, National Agricultural Research Center (NARC), Baq'a, Jordan, [2]Department of Agricultural Economics and Agribusiness, University of Jordan, Aljubeiha, Jordan, [3]Water and Soil Research Directorate, National Agricultural Research Center (NARC), Baq'a, Jordan, [4]Economic and Social Studies Research Directorate, National Agricultural Research Center (NARC), Baq'a, Jordan, [5]Department of Natural Resources and Environment, Jordan University of Science and Technology, Irbid, Jordan, [6]Bee Research Directorate, National Agricultural Research Center (NARC), Baq'a, Jordan

Cultural ecosystem services (CESs) refer to the non-monetary benefits that nature provides humans. This study aimed to allocate and map the CESs in the hyper arid region at the southern part of Wadi Araba as a unique ecosystem in Jordan. 296 residents were participated in a structured questionnaire. The respondents were prompted to indicate CES by drawing dots on a geo-referenced landscape map corresponding to any areas they considered as CES. The results showed that (81.1%) of the locals practice hiking (71.3%) of locals practice walking, and (66.2%) of the locals visit sand dunes which are all among the most CESs the locals engage with. Moreover, respondents expressed that these activities are not related to their primary source of income. The results were mapped and subjected to hot-spot and statistical analyses using a geographical information system (GIS)-based spatial evaluation and statistical analysis using the kernel density estimation (KDE) and Getis-Ord Gi* statistics with inverse distance weight (IDW) interpolation. Overall, the CESs provided by their region were appreciated by most residents. The hot-spot analysis revealed that those core hot-spots (Getis-Ord-Gi* values equal to $p = 0.01$) covered 19.6% while core cold spots covered 21.2% of the study area. The respondents expressed eagerness to contribute to a constant flow of CESs if the restoration plans are fully supported by the local community. The CES maps generated using the data collected in the present study can serve as baseline measures of the CES provisions subject to change based on the parameters of each development scenario. Furthermore, these maps could help support current and future management efforts by integrating communities' preferences into development and conservation initiatives, thereby ensuring more efficient and effective utilization of CESs.

KEYWORDS

cultural ecosystem services, human ecology, spatial analysis., ecosystem services, arid and semiarid ecosystems

Introduction

The concept of ecosystem services (ES) was adopted in the 1960s (King, 1966; Helliwell, 1969) and refers to the processes and benefits that the ecosystem provides to humanity, with an emphasis on those with economic outcomes (Chaudhary et al., 2015) and it was coined by Paul and Anne Ehrlich in 1981 (4). The common definition of ES currently includes all of the material (e.g., monetary) and non-material (e.g., aesthetic, spiritual) elements directly and indirectly derived from the biodiversity of an ecosystem that support human wellbeing in a sustainable manner (Millennium ecosystem assessment, M. E. A., 2005; Wallace, 2007). Inherent in this definition is the notion that human well-being is strongly reliant on dynamic and healthy ecosystems and natural resources, which are responsible for the constant flow of ESs from the environment to humanity. These services are classified into four classes (King, 1966): provisioning ES to provide essential services (e.g., foods, building material, water) (Helliwell, 1969); regulating ES to monitor and maintain climate stability (e.g., disease control, coastal protection, flood control); (Chaudhary et al., 2015); supporting ESs (e.g., nutrient cycling, soil formation, pollination); and (Braat and de Groot, 2012) cultural ESs (CESs) that provide "the "intangible", "subjective", "non-use", and "non-material" benefits people gained from ecosystems through spiritual enrichment, intellectual development, reflection, recreation, and aesthetic experience (education, tourism) and they are difficult to quantify" (Leemans and De Groot, 2003; Millennium ecosystem assessment, M. E. A., 2005; Haines-Young and Potschin, 2011).

The nature conservation targets cannot be achieved formally protected areas alone, and thus, conservation must be integrated into the daily activities taking place on public and private lands namely, on lands designated for production (e.g., agricultural) and non-production (e.g., residential), respectively. Therefore, many global resource management initiatives include ES concepts to align ecological conservation with socio-economic decisions related to the environment (Tallis et al., 2011). For scientists and practitioners alike, ES has become 1) a crucial link between global ecological health with human wellbeing, 2) a currency through which to determine environmental and economic policies, 3) a conceptual link between the natural and social sciences, and 4) a mechanism with which to communicate the importance of nature conservation to policymakers and the general public (de Groot et al., 2002; Cowling et al., 2008; Carpenter et al., 2009; Tallis et al., 2011).

Mapping and valuing ES is increasingly used to provide visual tools that enable decision-makers to maximize the sustainability of future developments. Mapping ES is a growing trend and the number of studies and reviews on ES mapping are on the rise (Crossman et al., 2012). Brown et al. developed a landscape values approach and public participation geographic information systems (PPGISs) to map and measure landscape tangible and non-tangible ES values (Brown and Raymond, 2007; Raymond et al., 2009; Brown et al., 2012; Brown and Weber, 2013). ES mapping is a user-friendly, useful tool for raising public awareness about ecosystem areas of interest and ES delivery relevant to their region; it identifies how humans could rely on functioning nature and provides information about interregional ES flows (Raymond et al., 2009). Allocating ES hotspots has become an essential means of integrating ES into the process of ecological conservation assessment. ES hot-spots have been described as ecological features with high service diversity and high biophysical or monetary value of services that benefit humans; while cold spots are ecological features with few services and low value (Schröter and Remme, 2016; Li et al., 2017).

As mentioned earlier, CES is an essential subset of ES derived from landscapes, yet not thoroughly researched and not fully integrated into operational frameworks or in nature protection and landscape management programs (Satz et al., 2013). Considerably, relatively few studies focus on CES (Chan et al., 2012a; Milcu et al., 2013; Leyshon, 2014; Andersson et al., 2015; Hirons et al., 2016). This is partly due to the challenges of measuring intangible and subjective values and the complex nature of CES makes it hard to quantify. Most studies focus on recreation and ecotourism while far fewer on other CES categories (Hernández-Morcillo et al., 2013; Plieninger et al., 2013). However, CES identification and quantification remains an important tool for optimal landscape planning and effective ecosystem management (Davidson, 2013).

CES's are sensitive to external impacts such as landscape changes and inappropriate management. Considering how different landscape features contribute to diverse CES provision is essential for effective landscape planning and management. This is also of interest when assessing landscape changes (Bieling et al., 2014; Plieninger et al., 2015). Consequently, the techniques being implemented in ES valuation and mapping are usually congregated in the related biophysical, socio-cultural, and economic domains (Martín-López et al., 2014). The socioeconomic status of the residents also influences which interventions are made for natural resource management; this variation is largely based on locals' natural and socio-economic conditions (Cheung and Jim, 2013). This CES socio-cultural valuation is especially important for exploring human perceptions and their preferences among existing CES valuations (Martín-López et al., 2012).

Recent efforts toward measuring CESs in Jordan have identified some relevant trends and issues (Al-assaf et al.,

2014; Alassaf et al., 2014; Shishany et al., 2020). Only a few studies have been conducted on valuing ES in Jordan in general, and on CES in particular, very few map CES and all of these were conducted on a local or landscape spatial scale (Al-assaf et al., 2014; Alassaf et al., 2014; Al-Assaf et al., 2016; Shishany et al., 2020). Social and natural science methods were combined and used to provide a holistic understanding of the socio-ecological system via the currency of ecosystem services in Wadi Araba (Sagie et al., 2013; Orenstein and Groner, 2015). Ecotourism's as CES in WA (e.g., hiking, camping, photography and filming, mountain climbing, biking, walking, sand dunes, waterfalls, bird watching, historical sites, hunting, and camelback riding) have transformed the region into an attractive and desirable tourist destination. The local population in hyper-arid areas is firmly connected to the local landscape and ecosystem (Sagie et al., 2013). Therefore, this study aimed to integrate allocating and mapping CES hot-spots specifically for recreation and ecotourism from a public participatory approach in the arid region of the Wadi Araba valley in south Jordan.

Materials and methods

Study area

Wadi Araba is a 2,000-km^2 extremely harsh desert environment that extends 170 km from the southern part of the Dead Sea shore (400 m below sea level) to the Gulf of Aqaba at the Red Sea (130 m above sea level) and occupies 2.4% of Jordan's total area (Nawash and Al-Horani, 2011; Orenstein and Groner, 2015). Six large communities reside in Wadi Araba with an estimated population of 10,500 people living in 820 households according to the most recent survey of the region in 2019 (Ministry of Interior, 2019). Wadi Araba is near Aqaba city, a recreational destination popular among citizens from other cities in Jordan and international visitors alike, which, along with Wadi Rum and Petra, constitute Jordan's most significant tourism sites (El-Naqa et al., 2010). Wadi Araba suffers from a surface water scarcity due to low rainfall rates and spatial fluctuations; in addition, the absence of valleys and permanently flowing torrents affects its ecosystem in general and ESs in particular. Only 8 million cubic meters of floodwater is associated with the valleys and torrents in the Wadi Araba region annually. Floodwater is a crucial water source for the region because it recharges groundwater and increases the moisture in the soil, which facilitates the growth of pastoral plants (Company, 2019).

Data collection: Participatory mapping

The selected study sites were all located in the southern part of Wadi Araba including Rahama, Qatar, Ar Rishah, and Beir Mathkour, which host 50% of the region's population. These were chosen for the unique diversity of the ESs in these locations (Figure 1). The study areas have a high level of ecosystem homogeneity including common climate conditions, biodiversity coverage, and natural features (e.g., waterfalls, mountains, dunes) as well as living standards. A total of 296 samples were randomly selected and equally distributed among the residents in the study areas, which represents 36% of the total households. The random selection process targeted respondents from different backgrounds and ages, without any biases in terms of the profile selection of the studied samples. Data were collected between December 2019 and January 2020 using a structured questionnaire designed to reflect the respondents' perceptions on ecotourism described as potential CESs. The question topics were chosen following sets of meetings with ten key persons in the Wadi Araba region; the key persons were nominated based on their professions and relations to the community. Throughout these meetings, the residents were unfamiliar with the "Ecosystem Services" concept, which influenced the questionnaire type and structure. Then, the questionnaire was pre-tested by interviewing 8 people and was slightly modified accordingly regarding specific topics. Later, the field researchers were trained for two days on the different sections of the questionnaire. . The questionnaire was composed of five parts to collect the information and opinions of respondents on the ESs of Wadi Araba region. The first part covered the demographic information of the respondents, such as gender, age, education, occupation, income, and family size. The second part was focused on residents' benefits and interaction with the surrounding ecosystem, such as animal production, grazing, agriculture, vegetation cover, and water-provisioning, as well as focused about the respondents' perceptions about different cultural services such as hiking, camping, photography, climbing mountains, biking, bird watching, visiting historic sites/ museums, etc. During the data collection process, the study participants were prompted to individually indicate CES by drawing dots on a geo-referenced landscape map of the areas they use as presumed CES. SPSS computer (version IBM 20) program was used for data entry. Quantitative techniques were used to assess ecosystem services' types and utilities according to respondents' perceptions and evaluations. Through the questionnaire, respondents were most of the time asked open-ended questions and close-ended questions which are noticed as most of the results are represented by frequencies, mean, and standard deviation. In other questions, respondents were asked to rate their perceptions and satisfaction with ecotourism within Wadi Araba. We asked the respondents to rank the importance of ecotourism activities within Wadi Araba and rank the importance of the local products handmade by the local community and which characterize the study area. The rating was conducted on a 10-point scale, of which 1 is not important, and 10 is extremely important. In addition, respondents were

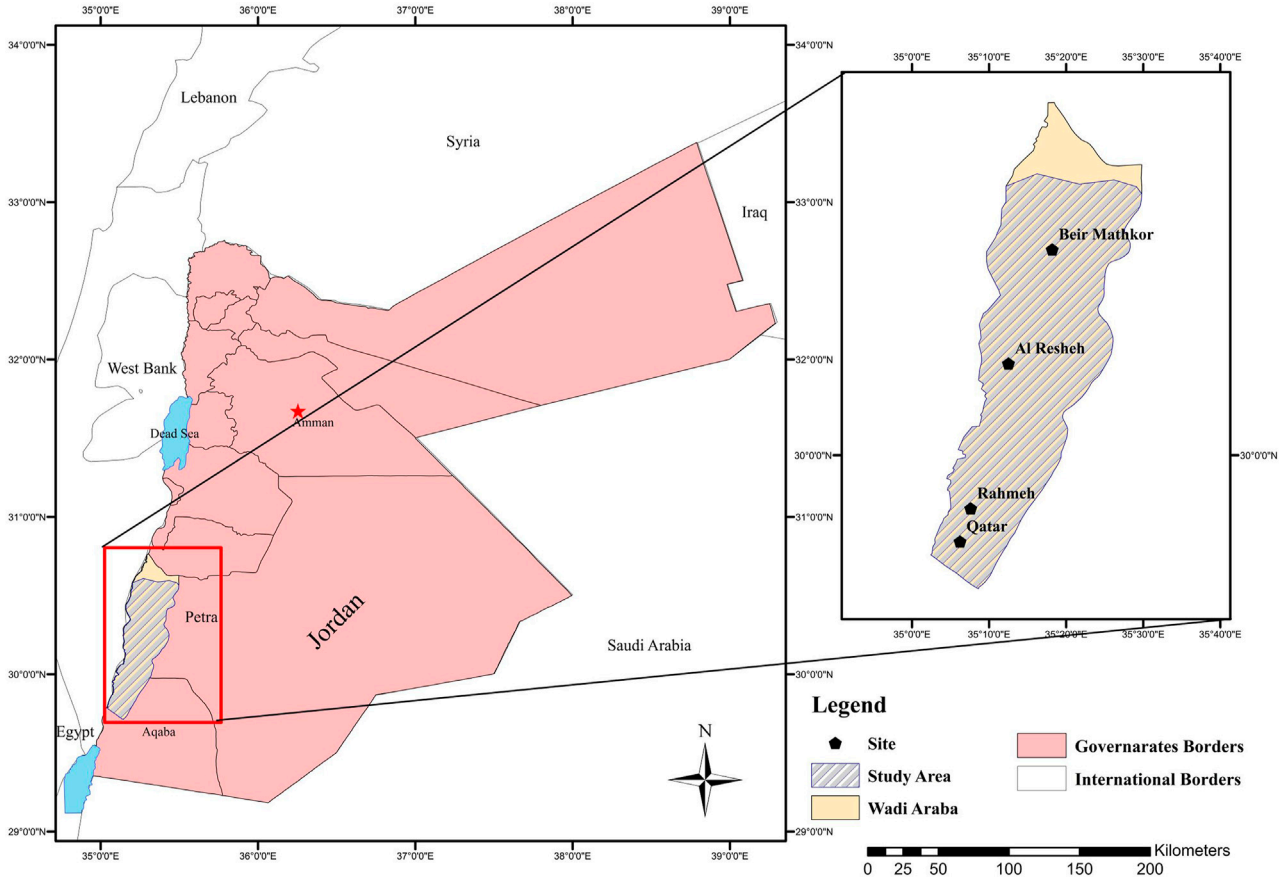

FIGURE 1
Map of the study area in the southern region of Wadi Araba. Source: NARC 2020.

asked to express their satisfaction with ecotourism's contribution to the region using the scale of strongly agree, agree, disagree, and strongly disagree.

Data pre-processing

A total of 138 coordinate points collected from the survey were projected into ArcGIS Desktop software ver. 10.6. Then, the projected social value coordinate points were transferred into the Arc GIS geodatabase. After summarizing the descriptive statistics, including the number of CES points mapped in the study area and the number of respondents who mentioned each CES as important. We next used a Chi-square test to identify significant differences regarding the numbers of respondents with certain socio-demographic characteristics who identified the various CES as important and valuable. Since the 138 CES points fell within proximity of one another, the coordinated points were combined using the 'Collect Event' tool before performing the hot-spot analysis to consolidate all of the CES events in the same geographical location with the new point feature class "ICOUNT", which was then introduced as an input feature for the hot-spot analysis tools (Singh et al., 2021).

Spatial analysis

The hot-spot analysis tools used to determine the concentration of events within a limited geographical area and to evaluate spatiotemporal patterns in CES in Wadi Araba were 1) kernel density estimation (KDE), inverse distance weight (IDW), and 3) the Getis-Ord (Gi*) statistic. KDE is a quadratic kernel function (Silverman, 2018) used to identify the location and degree of spatial clustering of ecosystem hot-spot services; it classifies the density of areas based on the total count of the frequency of geographical events over time around each raster cell output where only a circular neighborhood can create a smooth, continuous surface map to each point with a gradient of variation in the intensity of each event across the

TABLE 1 Demographic information of the study sample with permission of (Al-Assaf et al., 2021).

Demographic characteristics		%	Number
Gender	Male	68.6	204
Marital status	Married	83.1	246
Nature of work of the respondents	Retired	15.5	46
	Housewife	26.7	79
	Governmental Employee	23	68
	Private sector	6.0	18
	Farmer	2.0	6

study areas without being limited by thematic boundaries (Silverman, 2018). KDE has been widely used to characterize and analyze spatial trends generated by landscape features and the ecological connections or effects on the surrounding environment (Naidoo et al., 2008; Raymond et al., 2009; Sherrouse et al., 2011).

The IDW interpolation method estimates values by hot-spot analysis surrounding the targeted area (Besag and Newell, 1991). IDW takes the distance between the targeted points and the sample points as the weighted average; the closer the sample points to the targeted points, the greater the weight given to the sample points. The values closest to the targeted location have more influence on the targeted value than those farther away (Besag and Newell, 1991; Burrough et al., 2015). The Getis–Ord (Gi*) statistic is a hot-spot analysis developed by Getis and Ord to identify statistically distinct spatial clusters of high value (hot-spots) and low value (cold spots). It also identifies the location and degree of spatial clustering among ESs to determine whether identifiable spatial patterns exist (Ord and Getis, 1995). This tool creates a new Output Feature Class with a z-score, *p*-value, and confidence level bin (Gi_Bin) for each feature in the Input Feature Class. The Getis–Ord (Gi*) statistic is widely used to identify statistically significant high- and low-value spatial clusters (hot and cold spots, respectively) at the local level (Getis and Ord, 2010).

Results

CES in Wadi Araba

Recreation and ecotourism are among the most distinguished services in Wadi Araba (Sagie et al., 2013). Thus, this study was designed to provide detailed information about these touristic activities using a participatory approach. Participants' demographic characteristics are described in our previous publication (Al-Assaf et al., 2021) and are listed in (Table 1). The generated maps are based on the respondents who considered Wadi Araba to be a high tourist attraction area and the participatory approach, where 65.9% of the respondents confirmed that local and foreigner tourists frequently visit the region in September and October when the weather conditions are the most comfortable.

Despite the importance of the measured CESs in Wadi Araba, the respondents rarely engage in most of these activities except for hiking (81.1%), walking (71.3%), and visiting the dunes (66.2%). While the other CESs and activities were less frequently enjoyed by local residents, they were still regarded as important for locals and visitors; these activities/services include bird watching, hunting, photography, biking, and mountain climbing. These CES's provide the local community with additional knowledge of the desert environment and allow them to gain the experience required to be tour guides in the region (Figure 2).

Regardless of the diversity of the ES in this region, most of the respondents expressed that these activities are not related to their primary source of income (Figure 2). Several CESs (e.g., sand dunes, biking, photography, mountain climbing, hiking, and camping) proved to be the greatest contributors to the residents' livelihoods; specifically, the sand dunes (18.2%) and biking (19.3%) were the services most frequently acknowledged by the respondents (Figure 2). However, they pointed out that the direction of change of these activities was mostly increased except for waterfalls, which decreased by 3.6% likely in response to changes in water availability from multiple sources within the study area.

Site distribution

The distribution of CESs according to sites as reported by the respondents is presented in Figure 3. They allocated the most sites to hiking (71 sites), camping, photography, and walking (70 sites). Meanwhile, 53, 52, and 49 sites were attributed to bird watching, mountain climbing, and hunting, respectively. Moreover, 42 and 41 sites were identified for sand dunes and camelback riding. The lowest site numbers were associated with historical locations (25 sites), biking (22 sites), and waterfalls (21 sites).

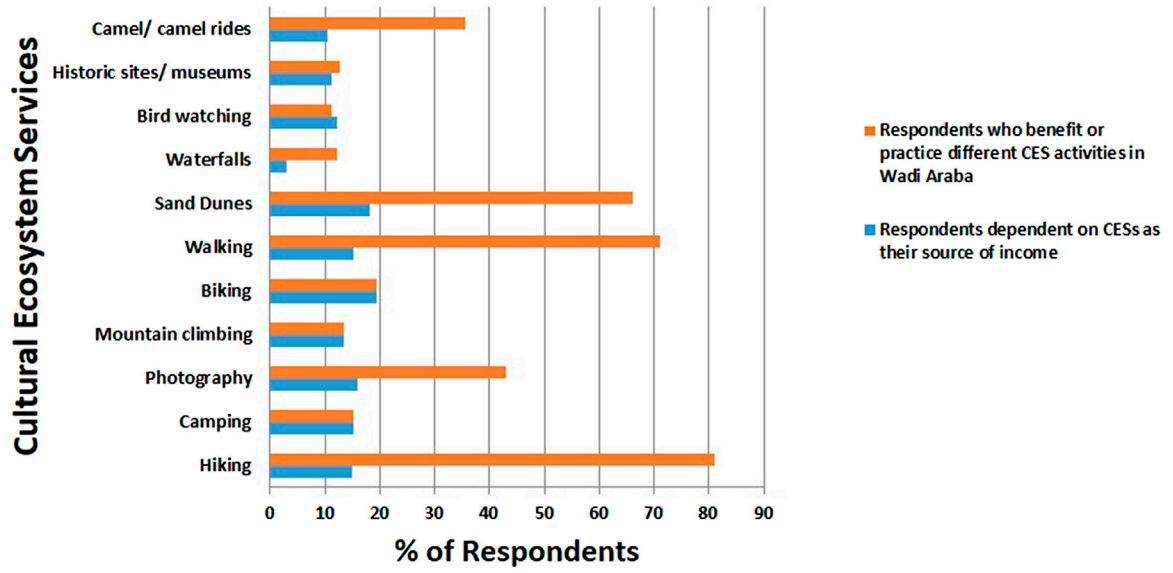

FIGURE 2
Percentage (%) of respondents who benefit or practice different CES activities in Wadi ArabaPercentage (%) of respondents dependent on CESs as their source of income.

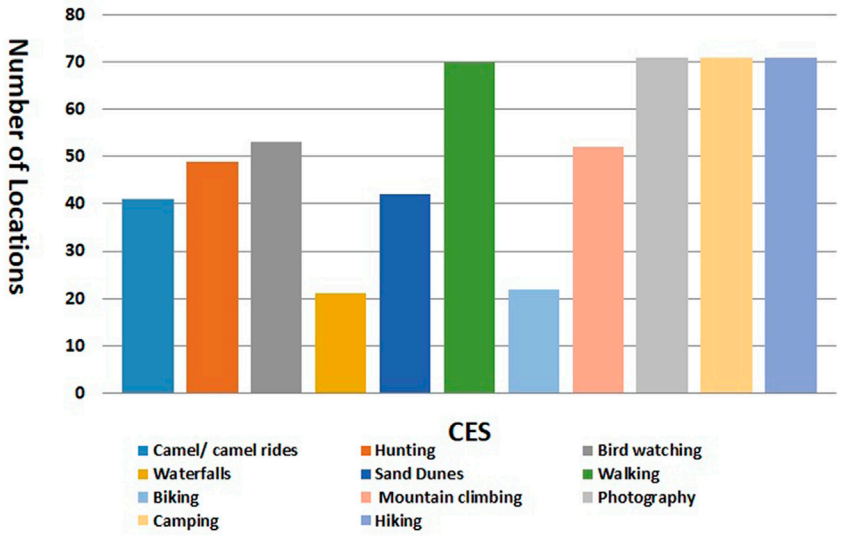

FIGURE 3
Distribution of CESs locations among ecotourism activities according to the respondents.

Economic considerations

Most of the Wadi Araba residents included in the present study reported an absence of local tourism products or brands specifically characteristic of the region. The few who reported that such items do exist cited carpets (rugs), precious stones, colored sand, wooden products, and palm fonds as examples. However, among these, carpets and palm fonds are the only ones abundantly available. Even though the respondents were not involved in the production or manufacture of these

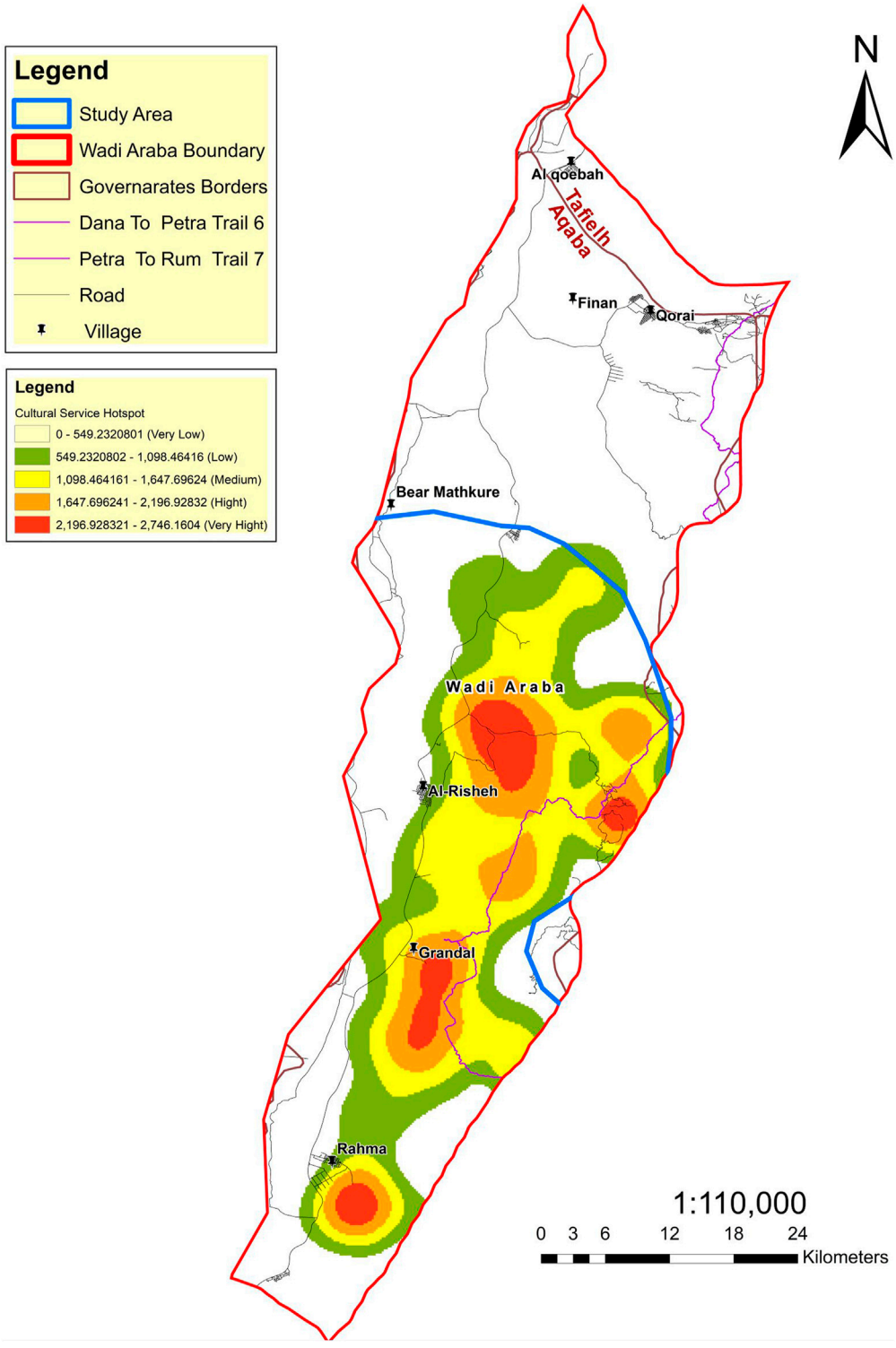

FIGURE 4
CES map constructed using the field survey information provided by the participants as hot -spots, using KDEs for point features. The point densities decrease from red (hot-spots) to orange, then yellow, and green (cold spots).

tourism products, they sell them to tourists to supplement their primary source of income. Moreover, the Wadi Araba residents reported that tourists frequently visit the region for medicinal purposes, especially to collect wild plants for traditional healing remedies (herbal medicine). Collectively, the respondents referenced 26 different wild plants collected by visitors to the Wadi Arab area including *Cleome* droserifolia (Al Moshta) (21.4%), Artemisia Judaica (Ba'ethran) (16%), and Teucrium (Ja'adeh) (12.8%). Since the locals of the Wadi Araba area are nomads and practice hunting as a traditional activity, hunting is considered a notable activity that draws tourists to the region (51.4%), even though Wadi Araba is not distinguished by a certain type of animal (59.1%). The respondents mentioned 14 types of wild animals and birds attributed to the area, the most popular of which being wild oryx (23.9%), Chlamydotis Al Habari (21.3%), and wild rabbits (12.6%). The local residents reported hunting mostly for personal consumption (36.8%) rather than selling (2.4%). Importantly, hunting is affecting the biodiversity within Wadi Araba, as indicated by most of the respondents observing a negative impact on the number of wild animals in the past 5 years (55.7%). The other reasons posited for the decreased number of wild animals in the area reported by 48.7% of the respondents were the drought (17.1%) and a lack of pastures (13.4%).

Distribution of CESs: KDE, IDW, and Getis-Ord Gi*hot-spot analyses

The CES hot-spot maps generated using the KDE method is illustrated in Figure 4. For each study area, the derived maps indicate that the CESs were not randomly distributed but, rather, aggregated into clusters and that the hot-spots were homogeneously distributed within the CESs. Only around 9% (156 of 1,600 km^2) of the study area was found to contain hot-spots with a high capacity to provide ecotourism and recreation value, as expected of CESs. The hottest spots in the Wadi Araba region tended to increase from south to north from the center of Wadi Araba. Most of the CESs reported by the respondents were located at the edges of residential areas and villages. Most of the hot-spots were allocated to the center of the study area, which has unique geography and topography. The development of the residential areas seemed to positively contribute to CESs with more total services aggregated within or close to villages. The cold spots were allocated to the east and west of the study area and are surrounded by high, steep mountains that are hard to climb and extend to the Dead Sea-Aqaba main highway and the Israeli border, an area restricted to both locals and tourists. In contrast, CES hot-spots were reported near more accessible mountains where hiking, climbing, and collecting local medicinal herbs are more feasible and readily accessible.

The hot-spot analysis results were spatially joined using a zonal statistics tool after IDW interpolation to reveal a statistical significance of the hot-spots. The hot-spot analysis calculation based on Getis-Ord Gi* statistics identified hot and cold spots among the CESs (Figure 5). Selecting the areas with the highest z-scores (i.e., the two highest confidence intervals with p = 99% and p = 95%) showed that the most significant hot-spots were located in the southern portion of the study area. These analyses also revealed a congregation of CESs areas in the center of the south of the study area. These CES hot-spots covered 41.7% of the Wadi Araba area included in this study (Figure 5). These areas contain many unique ecological features (e.g., sand dunes, medicinal plants, hiking trails, wild animals for hunting, scenic views, climbing tracks, and historical sites), as depicted in Figure 5. Despite the availability of nature-based attractions in the hot-spot-dense areas, these are not extensively utilized due to accessibility barriers and a lack of infrastructure. As such, these sites have a high potential for development in future years. Cold spot areas, on the contrary, were found to cover 38.5% of Wadi Araba, primarily in the northern portion of the study area. When considering only the core hot-spots (Getis-Ord-Gi* values equal to p = 0.01), the percentage coverage of Wadi Araba areas highly delivering CESs decreased by approximately 19.6% compared with the total hot-spot classification using the Getis-Ord Gi* approach. The relative proportions (%) of the areas covered by Gi* hot and cold spots are summarized in Table 2.

Discussion

Arid areas around the globe are relatively lacking in provisioning ESs despite having an abundance of CESs (Sagie et al., 2013). The demand for CESs is growing in industrialized societies (Guo et al., 2010) and these services have great potential to secure public support for protecting ecosystems (Guo et al., 2010; Weiler et al., 2013; Wolff et al., 2015). From a socio-ecological perspective, ecotourism and recreation are tightly coupled with the perception of the supply of and demand for CESs (Ruskule et al., 2018). The interrelated relationship between tourism and recreation derived from nature and society mutual influences each other (Mehring et al., 2017). Our results demonstrate that the Wadi Araba desert provides over 12 ecotourism practices that represent rich CESs. Local community members highlighted CESs that has been mentioned in other studies on arid landscapes (Figure 2) (Taylor et al., 2017; Cerda et al., 2018) In our previous study, the respondents emphasized the importance of these services for Wadi Arab with the average importance for all measured services ranging from 6 to 8 out of 10 (Al-Assaf et al., 2021). The dunes were rated by this sample population to be the most important activity in the region

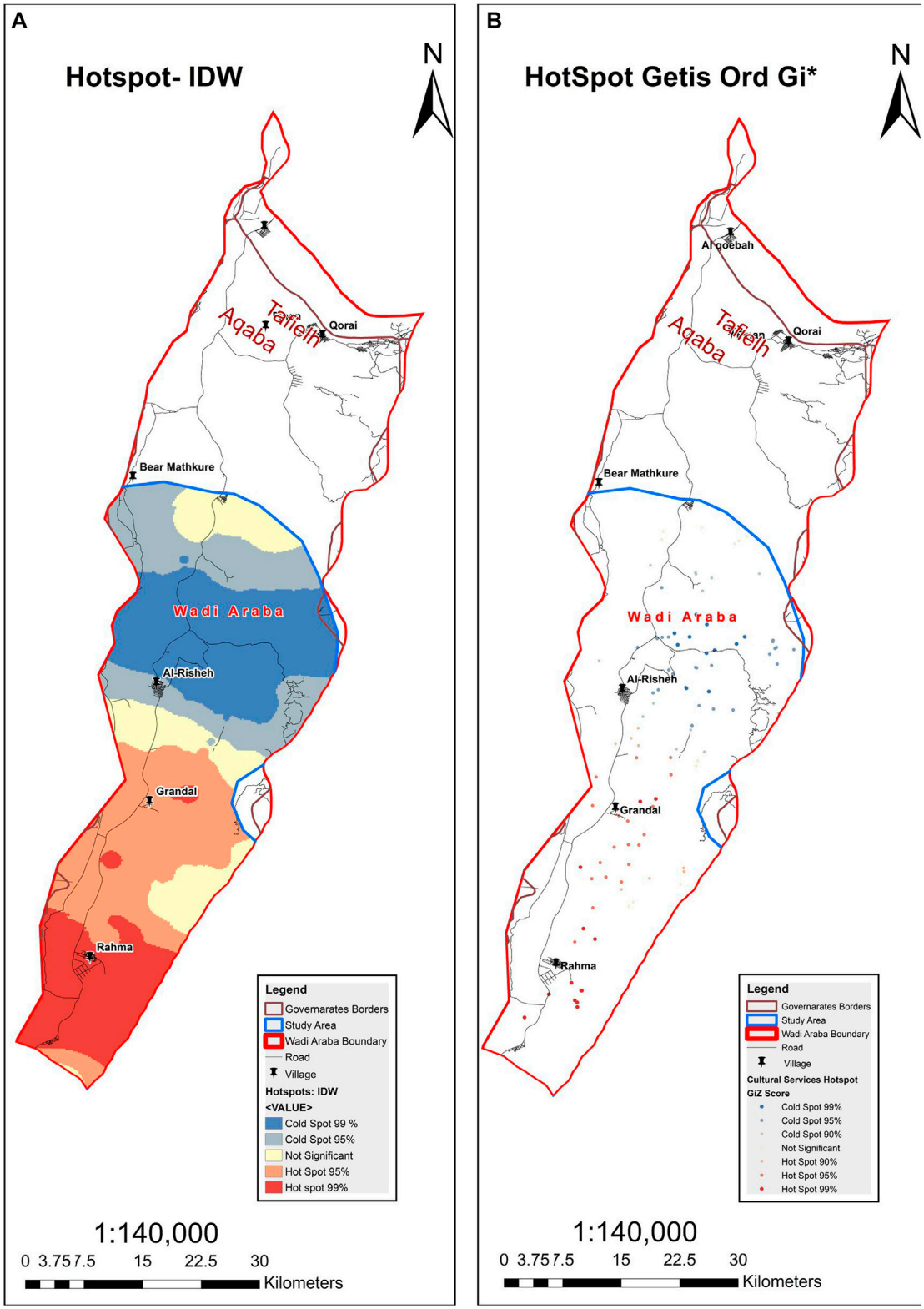

FIGURE 5
Hot-spot and coldspots analysis with different confidence levels using **(A)**. IDW interpolation and **(B).** Getis-Ord Gi* maps Hotspots and coldspots (The blue and the red color gradient indicate hotspots or coldspots are significant at 99 and 95% level respectively while the yellow color is not significant).

TABLE 2 Hot-spot classification according to Getis-Ord Gi* statistics and coverage percentage of each Gi* hot-spot.

Gi* Classification	Confidence Level	Probability (Gi* *p*-Value)	Standard Deviation (Gi* z-Score)	Area (Km^2)	Coverage (%)
Cold Spot	99%	<0.01	<−2.53	338.9	21.2
Cold Spot	95%	<0.05	<−1.96	338.6	17.3
Other areas	Not significant	Not significant	−1.65 - 1.65	413.7	19.7
Hot-Spot	95%	<0.05	>1.96	520.1	22.1
Hot-Spot	99%	<0.01	>2.53	440.1	19.6

followed by hiking and camping (Al-Assaf et al., 2021). Respondents emphasized that CESs are products of both landscape diversity and biodiversity (Sagie et al., 2013). Surprisingly, ecotourism was less recognized by the respondents, with only 38.2% stating that eco-ecotourism could greatly benefit Wadi Araba and ecotourism need not focus only on wildlife and scenic landscapes but should also feature the elements related to Bedouin culture (Sagie et al., 2013; Al-Assaf et al., 2021).

The CES literature is mostly comprised of spatially explicit studies and information concerning human-environment interactions such as green space, (bio)diversity, and recreational infrastructure. A limited amount of documentation and information exists on how a specific landscape and its associated features and ecosystem properties contribute to public perception. Hence, nature protection planning and management programs are negatively affected in terms of deriving the benefits of the landscape (Scholte et al., 2015) due to the limited resources and bad implication of these programs. In addition to a theoretical understanding regarding the extent of CESs' spatial overlap (i.e., CES hot spots), the findings described here have important practical implications for land use and conservation.

When financial resources are limited, it is vital to allocate hotspots and coldspots locations to help set priorities for maintaining essential ES (Braat and de Groot, 2012; Brown et al., 2012; Crossman et al., 2012). The KDE results in conjunction with the Getis-Ord Gi* statistics used to distinguish more clearly the hot-spot from the coldspot areas. While the KDE provides a visual representation of the hot-spots, hot-spot analysis (Getis-Ord Gi*) identifies statistically significant hot-spots using numerical values (i.e., Getis-Ord Gi* statistic) (Braithwaite and Li, 2007). Most of the residents located hot-spots within or close to their villages, which are in the midst of ongoing development processes (Figure 4). The perception of residents of CES value is influenced by their distance to residential areas, the frequency of use, and their accessibility (Jaligot et al., 2019). Our results are in line with Wang et al. (2021) who found that the residential development process contributes positively to CESs (Wang et al., 2021). CESs hot spot mapping is an essential elements in the management and protection of cultural landscapes. Generally the hotspots are over represented in comparison to the coldspots. We recommend a future place-based environmental resource research incorporate more survey methodologies to ensure respondent rates are more proportional to overcome the bias. To avoid future damages, CES hotspots should get the priority of being conserved; while for the CES coldspots, targeted measures should be taken to improve the severe status quo by analysing and sorting out local drivers of CES conflicts and degeneration (Jiang et al., 2013).

Maps that spatially visualize cultural hot-spots encourage stakeholders and managers to promote and enhance the CESs of specific sites in the study area. The act of bringing stakeholder knowledge to the consciousness of decision-makers is now a cornerstone of the sustainability paradigm (Haberl et al., 2006) of developing more effective, socially-acceptable policies and assuring social equity (Wilson and Howarth, 2002). Stakeholder input is indeed a central tenet of sustainable management theory and should be put into practice whenever possible (Clark and Clark, 2002). Without stakeholder involvement and consultation, decision-makers cannot prioritize management decisions that align with the expressed needs of the public. Areas with low CES densities, in turn, motivate planners to pay special attention to the economics and priority of the ecological objectives of these sites. The residents' perceptions of the CESs from an arid environment will grow if the tourism facilities grow and create jobs in the tourism industry (Dou et al., 2020).

Based on this preliminary research, we believe that the importance of CESs in arid regions, for example, are underestimated or missed entirely in ecological or economic assessments, despite being the most obvious and prominent ESs in social assessments (Sagie et al., 2013; Orenstein and Groner, 2015); therefore, it seemed crucial to map these services. The Wadi Araba Development Company will start to establish an integrated industrial development zone in Al-Risha (cold spot), a poor CES area. This new industrial zone will be based on light food processing industries. According to the company's studies,

this region is on the cusp of agricultural, industrial, water, and tourism development that will actualize the short- and long-term goals of Wadi Araba and Jordan. The residents of the area investigated in the current study do not object to any of the development plans in the region, as long as these plans consider the local community's privacy, their traditional way of life and offer them jobs. Rationally, the respondents are being willing to contribute to the constant flow of CESs which agree with the finding of (Sagie et al., 2013; Orenstein and Groner, 2015) who reported that locals of the Wadi Araba exhibits a high affinity to the desert landscape, its mountains, and open spaces. Providing this information to policymakers would relay the individual determination to restore and sustain ecosystem services. Neglecting cultural values, practices, and services decreases the likelihood of successfully implementing development plans (Chan et al., 2012b). Using CES maps will help to pinpoint benchmarks with which to assess the long-term provisions of selected CESs under different development scenarios (Alcamo et al., 2005), which incorporates both national and local factors. ES maps can serve as baseline measures of CES provisions that can change based on the parameters of each development scenario. The national and local factors are analogous to indicators employed by Weinger et al. (2010) that consider the potential of various changes in local land use and their impact on ES provisions (Wainger et al., 2010). It is also important to create protected areas in the region to preserve the hot and cold-spot regions. Protected areas are often more likely to provide cultural and other ESs than non-protected areas (Dudley et al., 2014; Eastwood et al., 2016).

Conclusion and recommendations

CES's were mostly appreciated by the residents of the Wadi Araba region compared to other visitors of the region. The respondents reported their willingness to contribute to the constant flow of CESs. This information can serve to inform policymakers of their constituents' determination to restore and sustain CESs. This study also demonstrates that even the harsh, dry environment of Wadi Araba is still valued among its residents. The estimated conservation value will be useful for future public policy decision-making and assist with the inclusion of ES principles in the development and implementation of these policies. Moreover, this study highlights the importance of engaging the beneficiaries and stakeholders in meaningful dialogues concerning arid ecosystem management; as such, participatory management strategies are optimal for the sustainable utilization of Wadi Araba resources. The CES maps generated using the data collected in this study provide baseline measures of CES provisions that are subject to change according to the parameters of each development scenario.

- These CES maps represent a promising means of assuring optimal land-use decision-making. Furthermore, our results enable managers to isolate and target specific individual CESs in their planning processes, which is important given that specific CESs may require more definite actions. For example, improving access to historical sites could serve to promote 'social relations', whereas improving the accessibility of open and blue spaces might enhance 'inspiration'.
- The Wadi Araba area lacks the infrastructure and accessibility required to support CES hot-spots despite the richness of their nature-based attractions. Hence, these areas are neither extensively enjoyed by local residents nor sources of valuable ecotourism.
- Improving accessibility is the most essential factor in the development of tourism and recreation-related CESs since it would allow people to freely and easily benefit from these enriching ESs (Paracchini et al., 2014).

Data availability statement

The raw data supporting the conclusions of this article will be made available by the authors, without undue reservation.

Author contributions

AA, AA-A, AS, KK, and NH performed the conceptualization and the methodology; WH, AH, RK, SA, MD, JA, and GA performed data collection and curation; WH and LN performed data entry; WH and KK processed the data; AA, AA-A, AS, and KK prepared the original draft; AA, AS, AA-A, and MT wrote and edited the paper; NH supervised and funded the APC; KK analyzed the data and AA and NH managed the project. All authors have read and agreed to publish a version of the manuscript.

Funding

This research was funded by USAID (M32-044), and the APC was funded by National Agricultural Research Center (NARC).

Acknowledgments

The authors would like to thank the local community in Wadi Araba for sharing their time and information.

Conflict of interest

The authors declare that the research was conducted in the absence of any commercial or financial relationships that could be construed as a potential conflict of interest.

Publisher's note

All claims expressed in this article are solely those of the authors and do not necessarily represent those of their affiliated organizations, or those of the publisher, the editors and the reviewers. Any product that may be evaluated in this article, or claim that may be made by its manufacturer, is not guaranteed or endorsed by the publisher.

Supplementary material

The Supplementary Material for this article can be found online at: https://www.frontiersin.org/articles/10.3389/fenvs.2022.866309/full#supplementary-material

References

Al-Assaf, A., Albalawneh, A., Majdalawi, M., Nowar, L. A., Kabariti, R., Hjazin, A., et al. (2021). Local communities' willingness to accept compensation for sustainable ecosystem management in Wadi Araba. *South Jordan* 13 (9), 5190.

Al-assaf, A., Nawash, O., and Omari, M. (2014). Identifying forest ecosystem services through socio-ecological bundles: A case study from northern Jordan. *Int. J. Sustain. Dev. World Ecol.* 21 (4), 314–321. doi:10.1080/13504509.2014.919968

Al-Assaf, A. A., Al-Asmar, Y. Y., Johnsen-Harris, B. D., and Al-Raggad, M. M. (2016). Spatial mapping of the social value of forest services: A case study of northern Jordan. *J. Sustain. For.* 35 (7), 469–485. doi:10.1080/10549811.2016.1212381

Alassaf, A., Alhunaiti, D., Dick, J., and Al-Adwan, T. (2014). Differences in perceptions, attitudes, and use of ecosystem services among diverse communities in an arid region: A case study from the south of Jordan. *J. Hum. Ecol.* 45 (2), 157–165. doi:10.1080/09709274.2014.11906689

Alcamo, J., Van Vuuren, D., Cramer, W., Alder, J., Bennett, E., Carpenter, S., et al. (2005). Changes in ecosystem services and their drivers across the scenarios. *Ecosyst. Hum. well-being* 2, 297–373.

Andersson, E., Tengö, M., McPhearson, T., and Kremer, P. (2015). Cultural ecosystem services as a gateway for improving urban sustainability. *Ecosyst. Serv.* 12, 165–168. doi:10.1016/j.ecoser.2014.08.002

Besag, J., and Newell, J. (1991). The detection of clusters in rare diseases. *J. R. Stat. Soc. Ser. A* 154 (1), 143–155. doi:10.2307/2982708

Bieling, C., Plieninger, T., Pirker, H., and Vogl, C. R. (2014). Linkages between landscapes and human well-being: An empirical exploration with short interviews. *Ecol. Econ.* 105, 19–30. doi:10.1016/j.ecolecon.2014.05.013

Braat, L. C., and de Groot, R. (2012). The ecosystem services agenda:bridging the worlds of natural science and economics, conservation and development, and public and private policy. *Ecosyst. Serv.* 1 (1), 4–15. doi:10.1016/j.ecoser.2012.07.011

Braithwaite, A., and Li, Q. (2007). Transnational terrorism hot spots: Identification and impact evaluation. *Confl. Manag. Peace Sci.* 24 (4), 281–296.

Brown, G., Montag, J. M., and Lyon, K. (2012). Public participation GIS: A method for identifying ecosystem services. *Soc. Nat. Resour.* 25 (7), 633–651. doi:10.1080/08941920.2011.621511

Brown, G., and Raymond, C. (2007). The relationship between place attachment and landscape values: Toward mapping place attachment. *Appl. Geogr.* 27 (2), 89–111. doi:10.1016/j.apgeog.2006.11.002

Brown, G., and Weber, D. (2013). A place-based approach to conservation management using public participation GIS (PPGIS). *J. Environ. Plan. Manag.* 56 (4), 455–473. doi:10.1080/09640568.2012.685628

Burrough, P. A., McDonnell, R. A., and Lloyd, C. D. (2015). *Principles of geographical information systems*. Oxford University Press.

Carpenter, S. R., Mooney, H. A., Agard, J., Capistrano, D., DeFries, R. S., Díaz, S., et al. (2009). Science for managing ecosystem services: Beyond the Millennium Ecosystem Assessment. *Proc. Natl. Acad. Sci. U. S. A.* 106 (5), 1305–1312. doi:10.1073/pnas.0808772106

Cerda, C., Fuentes, J. P., De La Maza, C. L., Louit, C., and Araos, A. N. A. (2018). Assessing visitors' preferences for ecosystem features in a desert biodiversity hotspot. *Environ. Conserv.* 45 (1), 75–82. doi:10.1017/s0376892917000200

Chan, K. M. A., Guerry, A. D., Balvanera, P., Klain, S., Satterfield, T., Basurto, X., et al. (2012). Where are cultural and social in ecosystem services? A framework for constructive engagement. *BioScience* 62 (8), 744–756. doi:10.1525/bio.2012.62.8.7

Chan, K. M. A., Satterfield, T., and Goldstein, J. (2012). Rethinking ecosystem services to better address and navigate cultural values. *Ecol. Econ.* 74, 8–18. doi:10.1016/j.ecolecon.2011.11.011

Chaudhary, S., McGregor, A., Houston, D., and Chettri, N. (2015). The evolution of ecosystem services: A time series and discourse-centered analysis. *Environ. Sci. Policy* 54, 25–34. doi:10.1016/j.envsci.2015.04.025

Cheung, L. T. O., and Jim, C. Y. (2013). Ecotourism service preference and management in Hong Kong. *Int. J. Sustain. Dev. World Ecol.* 20 (2), 182–194. doi:10.1080/13504509.2013.775192

Clark, T. W., and Clark, S. G. (2002). *The policy process: A practical guide for natural resources professionals*. Yale University Press.

Company, W. A. D. (2019). *Floods management at Wadi Araba*.

Cowling, R. M., Egoh, B., Knight, A. T., O'Farrell, P. J., Reyers, B., Rouget, M., et al. (2008). An operational model for mainstreaming ecosystem services for implementation. *Proc. Natl. Acad. Sci. U. S. A.* 105 (28), 9483–9488. doi:10.1073/pnas.0706559105

Crossman, N. D., Burkhard, B., and Nedkov, S. (2012). Quantifying and mapping ecosystem services. *Int. J. Biodivers. Sci. Ecosyst. Serv. Manag.* 8 (1-2), 1–4. doi:10.1080/21513732.2012.695229

Davidson, M. D. (2013). On the relation between ecosystem services, intrinsic value, existence value and economic valuation. *Ecol. Econ.* 95, 171–177. doi:10.1016/j.ecolecon.2013.09.002

de Groot, R. S., Wilson, M. A., and Boumans, R. M. J. (2002). A typology for the classification, description and valuation of ecosystem functions, goods and services. *Ecol. Econ.* 41 (3), 393–408. doi:10.1016/s0921-8009(02)00089-7

Dou, Y., Yu, X., Bakker, M., De Groot, R., Carsjens, G. J., Duan, H., et al. (2020). Analysis of the relationship between cross-cultural perceptions of landscapes and cultural ecosystem services in Genheyuan region, Northeast China. *Ecosyst. Serv.* 43, 101112. doi:10.1016/j.ecoser.2020.101112

Dudley, N., MacKinnon, K., and Stolton, S. (2014). The role of protected areas in supplying ten critical ecosystem services in drylands: A review. *Biodiversity* 15 (2-3), 178–184. doi:10.1080/14888386.2014.928790

Eastwood, A., Brooker, R., Irvine, R. J., Artz, R. R. E., Norton, L. R., Bullock, J. M., et al. (2016). Does nature conservation enhance ecosystem services delivery? *Ecosyst. Serv.* 17, 152–162. doi:10.1016/j.ecoser.2015.12.001

El-Naqa, A., Hammouri, N., Ibrahim, K., and Al-Taj, M. (2010). Integrated approach for groundwater exploration in Wadi Araba using remote sensing and GIS. *Jordan J. Civ. Eng.* 3.

Getis, A., and Ord, J. K. (2010). *The analysis of spatial association by use of distance statistics. Perspectives on spatial data analysis*. Springer, 127–145.

Guo, Z., Zhang, L., and Li, Y. (2010). Increased dependence of humans on ecosystem services and biodiversity. *PLOS ONE* 5 (10), e13113. doi:10.1371/journal.pone.0013113

Haberl, H., Winiwarter, V., Andersson, K., Ayres, R. U., Boone, C., Castillo, A., et al. (2006). From LTER to LTSER: Conceptualizing the socioeconomic dimension of long-term socioecological research. *Ecol. Soc. Nat. Resour.* 11 (2).

Haines-Young, R., and Potschin, M. (2011). *Common international classification of ecosystem services (CICES): 2011 update*. Nottingham: Report to the European Environmental Agency.

Helliwell, D. R. (1969). Valuation of wildlife resources. *Reg. Stud.* 3 (1), 41–47. doi:10.1080/09595236900185051

Hernández-Morcillo, M., Plieninger, T., and Bieling, C. (2013). An empirical review of cultural ecosystem service indicators. *Ecol. Indic.* 29, 434–444. doi:10.1016/j.ecolind.2013.01.013

Hirons, M., Comberti, C., and Dunford, R. (2016). Valuing cultural ecosystem services. *Annu. Rev. Environ. Resour.* 41 (1), 545–574. doi:10.1146/annurev-environ-110615-085831

Jaligot, R., Hasler, S., and Chenal, J. (2019). National assessment of cultural ecosystem services: Participatory mapping in Switzerland. *Ambio* 48 (10), 1219–1233. doi:10.1007/s13280-018-1138-4

Jiang, M., Bullock, J. M., and Hooftman, D. A. (2013). Mapping ecosystem service and biodiversity changes over 70 years in a rural E nglish county. *J. Appl. Ecol.* 50 (4), 841–850. doi:10.1111/1365-2664.12093

King, R. T. (1966). Wildlife and man. *New York Conservationist*. Editors I. A. Bailey, W. Elder, and McKinney 20 (6), 8–11.

Leemans, R., and De Groot, R. (2003). *Millennium ecosystem Assessment: Ecosystems and human well-being: A framework for assessment*.

Leyshon, C. (2014). Cultural ecosystem services and the challenge for cultural geography. *Geogr. Compass* 8 (10), 710–725. doi:10.1111/gec3.12160

Li, Y., Zhang, L., Yan, J., Wang, P., Hu, N., Cheng, W., et al. (2017). Mapping the hotspots and coldspots of ecosystem services in conservation priority setting. *J. Geogr. Sci.* 27 (6), 681–696. doi:10.1007/s11442-017-1400-x

Martín-López, B., Gómez-Baggethun, E., García-Llorente, M., and Montes, C. (2014). Trade-offs across value-domains in ecosystem services assessment. *Ecol. Indic.* 37, 220–228. doi:10.1016/j.ecolind.2013.03.003

Martín-López, B., Iniesta-Arandia, I., García-Llorente, M., Palomo, I., Casado-Arzuaga, I., Amo, D. G. D., et al. (2012). Uncovering ecosystem service bundles through social preferences. *PLOS ONE* 7 (6), e38970. doi:10.1371/journal.pone.0038970

Millennium ecosystem assessment, M. E. A. (2005). *Ecosystems and human well-being* 5, 563. Washington, DC: Island press.

Mehring, M., Zajonz, U., and Hummel, D. (2017). Social-ecological dynamics of ecosystem services: Livelihoods and the functional relation between ecosystem service supply and demand—evidence from socotra archipelago, Yemen and the sahel region, west africa. *Sustainability* 9 (7), 1037. doi:10.3390/su9071037

Milcu, A. I., Hanspach, J., Abson, D., and Fischer, J. (2013). Cultural ecosystem services A literature review and prospects for future research. *Ecol. Soc.* 18 (3).

Ministry of Interior (2019). *Household survey*.

Naidoo, R., Balmford, A., Costanza, R., Fisher, B., Green, R. E., Lehner, B., et al. (2008). Global mapping of ecosystem services and conservation priorities. *Proc. Natl. Acad. Sci. U. S. A.* 105 (28), 9495–9500. doi:10.1073/pnas.0707823105

Nawash, O., and Al-Horani, A. S. (2011). The most important medicinal plants in Wadi Araba desert in south west Jordan: A review article. *Adv. Environ. Biol.* 5, 418–425.

Ord, J. K., and Getis, A. (1995). Local spatial autocorrelation statistics: Distributional issues and an application. *Geogr. Anal.* 27 (4), 286–306. doi:10.1111/j.1538-4632.1995.tb00912.x

Orenstein, D. E., and Groner, E. (2015). "Using the ecosystem services framework in a long-term socio-ecological research (LTSER) platform: Lessons from the Wadi Araba desert, Israel and Jordan," in *Earth stewardship* (Springer), 281–296.

Paracchini, M. L., Zulian, G., Kopperoinen, L., Maes, J., Schägner, J. P., Termansen, M., et al. (2014). Mapping cultural ecosystem services: A framework to assess the potential for outdoor recreation across the eu. *Ecol. Indic.* 45, 371–385. doi:10.1016/j.ecolind.2014.04.018

Plieninger, T., Dijks, S., Oteros-Rozas, E., and Bieling, C. (2013). Assessing, mapping, and quantifying cultural ecosystem services at community level. *Land Use Policy* 33, 118–129. doi:10.1016/j.landusepol.2012.12.013

Plieninger, T., Kizos, T., Bieling, C., Le Dû-Blayo, L., Budniok, M-A., Bürgi, M., et al. (2015). Exploring ecosystem-change and society through a landscape lens: Recent progress in European landscape research. *Ecol. Soc.* 20 (2), art5. doi:10.5751/es-07443-200205

Raymond, C. M., Bryan, B. A., MacDonald, D. H., Cast, A., Strathearn, S., Grandgirard, A., et al. (2009). Mapping community values for natural capital and ecosystem services. *Ecol. Econ.* 68 (5), 1301–1315. doi:10.1016/j.ecolecon.2008.12.006

Ruskule, A., Klepers, A., and Veidemane, K. (2018). Mapping and assessment of cultural ecosystem services of Latvian coastal areas. *One Ecosyst.* 3, e25499. doi:10.3897/oneeco.3.e25499

Sagie, H., Morris, A., Rofè, Y., Orenstein, D. E., and Groner, E. (2013). Cross-cultural perceptions of ecosystem services: A social inquiry on both sides of the Israeli–Jordanian border of the southern Arava valley desert. *J. Arid Environ.* 97, 38–48. doi:10.1016/j.jaridenv.2013.05.007

Satz, D., Gould, R. K., Chan, K. M. A., Guerry, A., Norton, B., Satterfield, T., et al. (2013). The challenges of incorporating cultural ecosystem services into environmental assessment. *Ambio* 42 (6), 675–684. doi:10.1007/s13280-013-0386-6

Scholte, S. S. K., van Teeffelen, A. J. A., and Verburg, P. H. (2015). Integrating socio-cultural perspectives into ecosystem service valuation: A review of concepts and methods. *Ecol. Econ.* 114, 67–78. doi:10.1016/j.ecolecon.2015.03.007

Schröter, M., and Remme, R. P. (2016). Spatial prioritisation for conserving ecosystem services: Comparing hotspots with heuristic optimisation. *Landsc. Ecol.* 31, 431–450. doi:10.1007/s10980-015-0258-5

Sherrouse, B. C., Clement, J. M., and Semmens, D. J. (2011). A GIS application for assessing, mapping, and quantifying the social values of ecosystem services. *Appl. Geogr.* 31 (2), 748–760. doi:10.1016/j.apgeog.2010.08.002

Shishany, S., Al-Assaf, A. A., Majdalawi, M., Tabieh, M., and Tadros, M. (2020). Factors influencing local communities relational values to forest protected areas in Jordan. *J. Sustain. For.* [ahead of print], 1–19. doi:10.1080/10549811.2020.1847665

Silverman, B. W. (2018). *Density estimation for statistics and data analysis*. New York: Routledge.

Singh, P. P., Sabnani, C. S., and Kapse, V. S. (2021). Hotspot analysis of structure fires in urban agglomeration: A case of nagpur city, India. *Fire* 4 (3), 38. doi:10.3390/fire4030038

Tallis, H., Ricketts, T. H., Daily, G. C., and Polasky, S. (2011). *Natural capital: Theory and practice of mapping ecosystem services*. Oxford University Press.

Taylor, N. T., Davis, K. M., Abad, H., McClung, M. R., and Moran, M. D. (2017). Ecosystem services of the big bend region of the chihuahuan desert. *Ecosyst. Serv.* 27, 48–57. doi:10.1016/j.ecoser.2017.07.017

Wainger, L. A., King, D. M., Mack, R. N., Price, E. W., and Maslin, T. (2010). Can the concept of ecosystem services be practically applied to improve natural resource management decisions? *Ecol. Econ.* 69 (5), 978–987. doi:10.1016/j.ecolecon.2009.12.011

Wallace, K. J. (2007). Classification of ecosystem services: Problems and solutions. *Biol. Conserv.* 139 (3), 235–246. doi:10.1016/j.biocon.2007.07.015

Wang, Z., Xu, M., Lin, H., Qureshi, S., Cao, A., and Ma, Y. (2021). Understanding the dynamics and factors affecting cultural ecosystem services during urbanization through spatial pattern analysis and a mixed-methods approach. *J. Clean. Prod.* 279, 123422. doi:10.1016/j.jclepro.2020.123422

Weiler, B., Moore, S. A., and Moyle, B. D. (2013). Building and sustaining support for national parks in the 21st century: Why and how to save the national park experience from extinction. *J. Park Recreat. Adm.* 31 (2), 110–126.

Wilson, M. A., and Howarth, R. B. (2002). Discourse-based valuation of ecosystem services: Establishing fair outcomes through group deliberation. *Ecol. Econ.* 41, 431–443. doi:10.1016/s0921-8009(02)00092-7

Wolff, S., Schulp, C. J. E., and Verburg, P. H. (2015). Mapping ecosystem services demand: A review of current research and future perspectives. *Ecol. Indic.* 55, 159–171. doi:10.1016/j.ecolind.2015.03.016

Frontiers in
Environmental Science

Explores the anthropogenic impact on our natural world

An innovative journal that advances knowledge of the natural world and its intersections with human society. It supports the formulation of policies that lead to a more inhabitable and sustainable world.

Discover the latest Research Topics

See more →

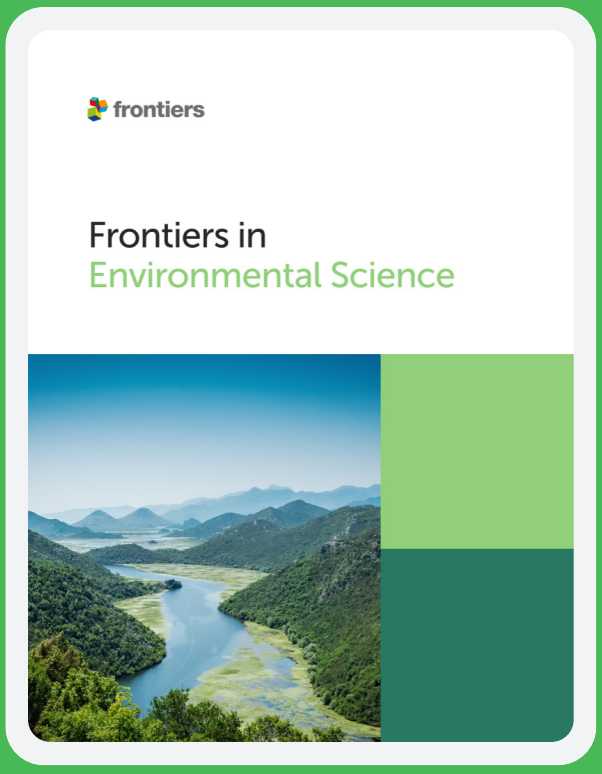

Frontiers

Avenue du Tribunal-Fédéral 34
1005 Lausanne, Switzerland
frontiersin.org

Contact us

+41 (0)21 510 17 00
frontiersin.org/about/contact